PROCEEDINGS
THIRTEENTH WORKSHOP
GEOTHERMAL RESERVOIR ENGINEERING

January 19-21, 1988



Henry J. Ramey, Jr., Paul Kruger, Frank G. Miller,
Roland N. Horne, William E. Brigham,
Jean W. Cook
Stanford Geothermal Program
Workshop Report SGP-TR-113*

*Sponsored by the Geothermal Technology Division of the U.S. Department of Energy, Stanford-DOE Contract No. DE-AS07-84ID12529

Library of Congress Catalogue Card No. 88-062529

TABLE OF CONTENTS

Page

Preface v

INTRODUCTION

An Overview of the Department of Energy Geothermal Program
J.E. Mock and R.E. Blackett 1

FIELD DATA ANALYSIS

Analysis of Production and Reservoir Performance at the Casa Diablo Geothermal Project
Richard J. Miller and Rosalinda Vasquez 5
Compressibility and Sonic Velocity in Steam/Water Mixtures
S. Sveinsson et al 19
The Beijing Geothermal System, P.R. China: Natural State and Exploitation
Modelling Study of a Low Temperature Basement Aquifer System
M.P. Hochstein and Y. Zhongke 25
Using Precision Gravity Data in Geothermal Reservoir Engineering Modelling Studies
P. Atkinson and J. Pedersen 35

WELL TESTING

Downhole Pressure, Temperature and Flowrate Measurements in Steam Wells at the Geysers Field
K.L. Enedy 41
Nedo's Project on Geothermal Reservoir Engineering - A Reservoir Engineering Study of the Kirishima Field, Japan
H. Kitamura et al 47
Well-Test Analysis for a Well in a Finite, Circular Reservoir
A.K. Ambastha and H.J. Ramey, Jr. 53
The Depth of Feed Water Influences Maximum Discharge-Pressure of Hot Water Geothermal Wells
R. James 59
Use of Derivatives for Detecting Impermeable Boundaries in the Analysis of Transient Pressure Tests
F. Ascencio and R. Molinar 305

FIELD DEVELOPMENT

Reservoir Management - As Conceived and Applied on the Palinpinon Reservoir, Phillipines
Z.F. Sarmiento and A.E. Amistoso 63
A Vapor-Dominated Reservoir Exceeding 600° F at the Geysers Sonoma County, California
M.A. Walters et al 73
A Summary of Modelling Studies of the Nesjavellir Geothermal Field, Iceland
G.S. Bodvarsson et al 83
Hydrogen Chloride in Superheated Steam and Chloride in Deep Brine at the Geysers Geothermal Field, California

J.R. Haizlip and A.H. Truesdell 93

GEOSCIENCE

Double-Diffusive Convection as a Mechanism for Transferring Heat and Mass within the Salton Sea Geothermal Brine
R.O. Fournier 101
Evolution of the Thermal Cap in Two Wells from the Salton Sea Geothermal System, California
J.N. Moore and M.C. Adams 107
A Comparison of Two Heat Transfer Models for Estimating Thermal Drawdown in Hot Dry Rock Reservoirs
B.A. Robinson and P. Kruger 113
A Hydrologic Monitoring Program to Detect Potential Impacts of Geothermal Development in Long Valley Caldera, California
M.L. Sorey 121

GEOCHEMISTRY

Chemistry of a Low Temperature Geothermal Reservoir: the Triassic Sandstone Aquifer in Melleray, France
F.D. Vuataz et al 309
Natural Flow and Vertical Heterogeneities in a Sedimentary Geothermal Reservoir (Paris Basin, France): Geochemical Investigations
A. Criaud et al 133
Geochemical Mud Logging of Geothermal Drilling
F.B. Tonani et al 141
A New Illite Geothermometer
J.M. Ballantyne and J.N. Moore 145

MODELLING, WITH NON-CONDENSABLE GASES

A Wellbore Flow Model in the Presence of CO_2 Gas
M. Takahashi 151
Computer Code of Two-Phase Flow in Geothermal Wells Producing Water and/or Water-Carbon Dioxide Mixtures
S. Tanaka and K. Nishi 159
Some Effects of Non-Condensable Gas in Geothermal Reservoirs with Steam-Water Counterflow
R. McKibbin and Karsten Pruess 165
Mathematical Modelling of Near-Critical Convection
B.L. Cox et al 173

CASE HISTORIES OF MATURE GEOTHERMAL FIELDS

Flow Rate Decline and Pressure Transient in the Larderello Geothermal Field
G. Neri 181
Reservoir Engineering of Wairakei Geothermal Field
M. A. Grant 191

FRACTURED RESERVOIRS I

The Hydraulic Fracturing of Geothermal Formations

K.B. Naceur and M.J. Economides 199
Transient Behavior in Fractured Media with Zero Matrix Permeability
E. Okandan et al 205
Fracture Network Modelling of a Hot Dry Rock Geothermal Reservoir
B.A. Robinson 211
A Semi-Analytical Method for Heat Sweep Calculations in
Fractured Reservoirs
K. Pruess and Y.S. Wu 219

FRACTURED RESERVOIRS II

A Three-Dimensional Model of Fluid, Heat, and Tracer Transport
in the Fenton Hill Hot Dry Rock Reservoir
S.A. Birdsell and B.A. Robinson 225
Locating Hydraulically Active Fracture Planes
M. Malzahn et al 231
Wellbore Interference in Fractured Media
M.V. Malzahn and H.D. Murphy 239
Tracer Measurements During Long-Term Circulation of
the Rosemanowes HDR Geothermal System
K.A. Kwakwa 245

RESERVOIR MODELLING

Pressure Interference Data Analysis for Two-Phase (Water/Steam)
Geothermal Reservoirs
S.K. Garg and J.W. Pritchett 253
A Convolution Boundary Element Method for Unsteady State
Groundwater Flow in Homogeneous Aquifers
J. Kikani and R.N. Horne 261
Analysis of Internal Wellbore Flow
M. Ripperda and D.S. Bodvarsson 269
Dual Permeability Modelling of Solute Transport in
Discrete Fracture Systems
J.D. Miller and T.M. Clemo 273

FINAL SESSION

Tracer Flow Model for Naturally Fractured Geothermal Reservoirs
J. Ramirez et al 281
ANAPPRES: An Expert System for Interference Well-Test Analysis
V.M. Arellano et al 291
VAPLIQ: Hydrothermal Systems in the Vertical Permeability of Los Azufres
Mexico Geothermal Reservoir
E. Iglesias and V. Arellano 125
Application of the Spread-Spectrum Technique in Well-Logging
C.V. Chrysikopoulos and S.D. Dadakarides 299
Chemistry of a Low Temperature Geothermal Reservoir: the Triassic
Sandstone Aquifer at Melleray, France
F.D. Vuataz et al 309
Prediction of Kizildere Reservoir Behavior under Exploitation
E. Okandan 317
Predicting Thermal Conductivity of Rocks from the Los Azufres
Geothermal Field, Mexico, from Easily Measurable Properties
A. Garcia et al 323

LIST OF PARTICIPANTS 329
SUBJECT INDEX 339
AUTHOR INDEX 343

PREFACE

The Thirteenth Workshop on Geothermal Reservoir Engineering was held at Stanford University on January 19-21, 1988. Although 1987 continued to be difficult for the domestic geothermal industry, world-wide activities continued to expand. Two invited presentations on mature geothermal systems were a keynote of the meeting. Malcolm Grant presented a detailed review of Wairakei, New Zealand and highlighted plans for new development. G. Neri summarized experience on flow rate decline and well test analysis in Larderello, Italy.

Attendance continued to be high with 128 registered participants. Eight foreign countries were represented: England, France, Iceland, Italy, New Zealand, Japan, Mexico and The Phillipines. A discussion of future workshops produced a strong recommendation that the Stanford Workshop program continue for the future.

There were forty-one technical presentations at the Workshop. All of these are published as papers in this Proceedings volume. Four technical papers not presented at the Workshop are also published. In addition to these forty five technical presentations or papers, the introductory address was given by Henry J. Ramey, Jr. from the Stanford Geothermal Program.

The Workshop Banquet speaker was Gustavo Calderon from the Inter-American Development Bank. We thank him for sharing with the Workshop participants a description of the Bank's operations in Costa Rica developing alternative energy resources, specifically Geothermal, to improve the country's economic basis. His talk appears as a paper in the back of this volume. The chairmen of the technical sessions made an important contribution to the workshop. Other than Stanford faculty members they included: J. Combs, G. T. Cole, J. Counsil, A. Drenick, H. Dykstra, K. Goyal, P. Muffler, K. Pruess, and S. K. Sanyal.

The Workshop was organized by the Stanford Geothermal Program faculty, staff and students. We would like to thank Marilyn King, Pat Oto, Terri Ramey, Bronwyn Jones, Yasmin Gulamani, and Rosalee Benelli for their valued help with the meeting arrangements and preparing the Proceedings. We also owe great thanks to our students who arranged and operated the audio-visual equipment, especially Jeralyn Luetkehans.

The Thirteenth Workshop was supported by the Geothermal Technology Division of the U.S. Department of Energy through Contract No. DE-AS07-84ID12529. We deeply appreciate this continued support.

Henry J. Ramey, Jr.
Paul Kruger
Roland N. Horne
William E. Brigham
Frank G. Miller
Jean W. Cook

August, 1988

PROCEEDINGS, Thirteenth Workshop on Geothermal Reservoir Engineering
Stanford University, Stanford, California, January 19-21, 1988
SGP-TR-113

AN OVERVIEW OF THE DEPARTMENT OF ENERGY GEOTHERMAL PROGRAM

Dr. John E. Mock, Director

Geothermal Technology Division
U.S.Department of Energy

It is a pleasure to be here again for the 13th Annual Stanford Geothermal Reservoir Engineering Workshop. At No. 13, your workshop goes back almost as far as the federal geothermal research and development program about which I am here to speak with you today. I don't need to remind many of you that the earliest Congressional mandates for federal geothermal R&D were to the Atomic Energy Commission and the National Science Foundation in the early 1970's. Many of our on-going programs have their origins in those agencies. And, still we're "at it."

Sometimes I have asked myself why this is so. Why are we still researching certain technologies after 15 years or more? Why does the structure of our R&D program not look much different from year to year?

In order to answer these and related questions, we are, in fact, currently assessing the performance of our program elements against technology objectives set 15 years ago, and defining the impact of each in solving important technical barriers, and in promoting the national goal of increased geothermal use. From this retrospective analysis we are redefining the goals and objectives for our future R&D program. We have developed three levels of quantitative objectives from this exercise:

- Level I reflecting goals for, and anticipated impacts of, the overall R&D program categories upon the cost of power from geothermal energy systems.
- Level II reflecting estimates of the impacts of the R&D on the performance and costs of the major subsystems of a geothermal energy development project, thus providing an overview of R&D program balance across the geothermal technologies.
- Level III objectives providing the mechanisms for assessing the progress of research elements, or groups of R&D elements.

As our assessment nears completion, I will look forward to an opportunity to discuss it with you and soliciting your valuable inputs.

Today however, I shall undertake to bring you up-to-date on the current emphasis of the various elements of our R&D program. Due to the limits on space and time on my presentation, this will necessarily be limited to an overview, as the title suggests.

RESERVOIR TECHNOLOGY

This R&D category embraces three major tasks -- reservoir definition, brine injection, and exploration techniques. The major goals of these tasks are, respectively, to:

- enable industry to maximize energy recovery from a resource
- reduce the adverse thermal and chemical effects of injection on geothermal reservoirs
- verify new techniques for identifying geothermal reservoirs associated with young volcanic terrains.

In FY 1988, reservoir definition R&D will be focused on reservoir technology research areas that have a direct impact on the characterization and assessment of geothermal reservoirs, topics of fundamental importance to industry. Representative activities include:

- development and testing of improved reservoir monitoring techniques to help characterize the effects of fluid recharge and pressure maintenance at producing geothermal fields
- development and testing of improved methods for determining fracture characteristics of geothermal reservoir rocks

- development and incorporation into existing computer models of realistic descriptions of geothermal brines and rock-fluid interactions.

The major emphasis of the brine injection R&D continues to be the development of high performance tracers, the analysis of tracer flow through fractures, and the interpretation of tracer return profiles. Interpretation of the profiles can indicate the speed of movement of the injected fluids through the reservoir and preferential flow between specific injection and production wells. Analysis of tracer transport is complicated by the fractured nature of many geothermal reservoirs and requires detailed investigation. The most recent success in tracer performance evaluation is the identification of 15 suitable hydrocarbon candidates for liquid-phase application which survived at 250°C; work in gas-phase tracer research is in preliminary stages.

Another focus of the injection R&D is developing modeling and measurement techniques for determining the location of and predicting the evolution of pressure, fluid, and thermal fronts which occur during injection. The ultimate purpose of these studies is to provide additional information to the reservoir engineers who model the behavior of the field and predict its performance.

The development of exploration techniques for identifying geothermal reservoirs in young volcanic environments is centered in the Cascades Range of the Pacific Northwest, specifically in the vicinity of Newberry Crater, Mt. Jefferson, and Crater Lake in Oregon. DOE has cost-shared deep thermal gradient holes with industry at these locations, obtaining core samples and geophysical well logs. Geophysical measurements from the samples and logs are compared with surface geophysical observations which helps to determine what conditions in the subsurface cause the observed surface geophysical responses. The comparison also serves to calibrate various surface and borehole geophysical tools and evaluate their performance in young volcanic environments.

HARD ROCK PENETRATION

The goal of the hard rock penetration R&D is to develop drilling/coring, lost circulation control, and wellbore technology for current and advanced geothermal application in order to decrease costs and increase the economic resource. The borehole mechanics element is emphasizing research in borehole stability, well completion, and fluid sampling. A major FY 1988 effort is construction of a flow visualization experiment to study the two-phase flow phenomenon that dictates fracture plugging mechanics for single particle, high temperature, and multiple constituent lost circulation materials.

In cooperation with industry, deficiencies in the prototype radar fracture mapping tool found during testing last year will be corrected with design changes during FY 1988. The tests, in a rock quarry, also revealed, however, that the tool does perform as predicted and has promise for locating fractures.

The Geothermal Drilling Organization (GDO), an industry/DOE non-profit cooperative formed to fund projects of value to geothermal operators, is continuing development and field testing of an acoustic borehole televiewer, field testing of hardware and procedures for deploying an expanding foam in geothermal lost circulation zones, and field testing of a downhole air turbine for drilling geothermal wells. Development of high temperature elastomers for use as drill pipe protectors and rotating head seals is also continuing.

CONVERSION TECHNOLOGY

The conversion technology R&D consists of three major tasks: heat cycle research, advanced brine chemistry, and materials research. Heat cycle R&D is focused on the development of technology for effecting the improved utilization of moderate-temperature geothermal fluids. Thus, a major emphasis of the research is improvement of the performance of geothermal binary cycles to levels approaching the practicable thermodynamic maximum. Tests are being conducted at the Heat Cycle Research Facility at East Mesa, California, to investigate the use of mixtures of non-adjacent hydrocarbons as the working fluid, with supercritical vaporization and in-tube condensation of the working fluid. Preparations are also being made to investigate the binary cycle improvements which can be achieved by allowing supersaturated vapor expansions in the turbine. These efforts are anticipated to verify that improvements of up to 28 percent in the net geofluid effectiveness (net watt hours plant output per pound of geofluid) over conventional binary power plants can be achieved. Future efforts will include testing of direct contact heat exchangers with fluids "too dirty" for conventional heat exchangers and heat rejection systems which will minimize cooling water make-up requirements while retaining a performance level approaching that of conventional wet cooling systems.

Two approaches are being pursued to define the costly operating problems associated with brine chemistry. First, numerical modeling of complex brines will allow improved prediction of the thermodynamic conditions under which problems will occur in geothermal power plants from scale deposition, corrosion, and suspended solids. Second, research is focused on detection and monitoring of constituents in the brine stream which can damage piping, valves, and wells as brine flows through the power plant and is injected back into the wellfield. Chemistry monitoring instrumentation is inserted in the brine flow lines to detect serious corrosion, scaling, and particulate matter before these problems result in plant failure.

An offshoot of the brine chemistry research is the effort to find economical means for detoxifying sludges created by treatment of hypersaline brines prior to injection. The presence of toxic metals, though small in quantity, invokes federal/state environmental requirements for disposal as hazardous wastes. This type of disposal is costly and is becoming highly uncertain with the closure of many such sites due to tightening restrictions. Thus, experiments are underway on the use of biochemical techniques to concentrate and remove the metals from the wastes. Two methods are being addressed: 1) solubilization of metals by micro-organisms which leach them out, and 2) concentration and removal by sorption on cellular materials. Both processes are applicable in situations where metals are present in large volumes of waste at concentrations unsuitable for conventional technology.

Research and development continues on materials for use in the harsh geothermal environment so that geothermal development is not constrained by the lack of such materials. Further cost reductions and extension of service life are being sought for such materials an nonmetallic heat exchanger tubing, very high temperature well completion materials, and metallic liners for well casings.

GEOPRESSURED RESEARCH

The geopressured R&D has successfully completed estimating the size and magnitude of geopressured reservoirs and is in the process of developing technology for producing and utilizing them. The Gladys McCall well in Louisiana is under test at the present time and has successfully produced over 25 million barrels of brine. The reservoir has proven larger than initial test data predicted, and research is concentrated on identifying reservoir drive mechanisms in order to improve test procedures. A comprehensive test program of variable flow rates, pressure recovery, logging, and coring is planned.

Testing will start in FY 1988 on the Pleasant Bayou well near Houston, Texas, where an Electric Power Research Institute hybrid electrical power generation experiment will be conducted. It incorporates both a geothermal binary cycle to utilize the heat of the brine and gas combustion to utilize the produced methane. This type system can produce in excess of 15 percent more electricity than the same amount of fuel and geothermal fluid used in separate power plants.

It is our hope that we can complete geopressured R&D with the testing of a former gas well contributed by industry which, at 21,000 feet, is much deeper than any tested to date. It has the potential to be economical in the near future and will serve as verification of the geopressured technology developed throughout the life of the program.

HOT DRY ROCK RESEARCH

While other methods for creating a man-made reservoir are possible in different geologic environments, our program has so far concentrated on hot crystalline rock of low initial permeability; the use of fluid pressure (hydraulic fracturing) to create flow passages and heat-transfer surface in the rock; and operation of a closed, recirculating, pressurized-water loop to extract heat from the rock and transport it to the earth's surface. Large-scale field experiments are conducted at Fenton Hill in the Jemez Mountains of northern New Mexico. Concomitant supporting activities include development of new or improved downhole equipment and instruments, field and laboratory experimental techniques, and analytical and numerical data analyses and modeling procedures. Many of these developments have been found useful in other experimental programs and in a variety of industrial applications.

The technical issues faced in HDR development are demanding. Wells must be drilled to depths where temperatures are likely to be 200 to 300°C (392-572°F), suitable for electricity generation. Even in regions with favorable geothermal gradients, such temperatures are found only at great depths, 10,000-16,000 feet. The rock formation must then be fractured at great stress, and the

fractures held open so that the permeability remains high and flow resistance is low. Furthermore, large areas of hot rock must be adequately bathed by the injected water to result in high heat production. At the same time, since all water must be provided from an external source, excessive water losses to the rock formation surrounding the fractured reservoir must be avoided.

The small Phase I reservoir created at Fenton Hill in 1977 was the world's first hot dry rock geothermal energy system. Water was produced from the man-made reservoir at temperatures and thermal power rates as high as 175°C (347°F) and 5 MW_t. A much larger Phase II reservoir was created at the site in 1983, and has been flow tested briefly. A long-term flow test is planned in order to evaluate the longevity of a hydraulically fractured HDR reservoir with power capacity of about 35 thermal megawatts. The target design for the system is a lifetime of at least 10 years with less than 20 percent thermal drawdown.

MAGMA ENERGY RESEARCH

The thrust of the magma energy extraction R&D is to determine the engineering feasibility of locating, accessing, and utilizing magma as a viable resource. This effort is a follow-on to the DOE/OBES-funded Magma Energy Research Project that determined the scientific feasibility of the magma energy concept.

Ongoing research in the area of magma energy extraction is directed at developing a fundamental understanding of the establishment and long-term operation of both closed-loop and open, direct-contact heat exchangers in a crustal magma body. The energy extraction rate has a direct influence on the economic viability of the concept. An open heat exchanger, in which fluid is circulated through the interconnecting fissures and fractures in the solidified region around drilling tubing, offers the promise of very high rates of heat transfers. Studies show that an open heat exchanger can be formed by solidifying magma around a cooled borehole and that the resulting mass will be extensively fractured by thermally-induced stresses. Numerical models indicate that high quality thermal energy can be delivered at the wellhead at nominal power levels from 25 to 30 MW electric.

Previous heat extraction research indicated that magma can be utilized at energy extraction rates that are comparable to or better than those in conventional geothermal fluids. The high temperatures of the magma resource and the corresponding high tempera tures of the working fluid lead directly to efficient, conventional techniques for generating electricity. Processes have been considered for using this high-quality energy to generate transportable fuels in addition to electricity.

A primary long range target of this effort is to conduct an energy extraction experiment directly in a molten, crustal magma body. Several key technology tasks are critical to determining engineering feasibility of this undertaking: obtaining detailed geophysical definition of potential magma targets; characterizing the magma environment and selecting compatible engineering materials; developing drilling and completion techniques for entry into a magma body; and developing heat extraction technology.

DOE GEOTHERMAL PROGRAM REVIEW

Once a year the Geothermal Technology Division sponsors a DOE Geothermal Program Review. These sessions are designed to focus the attention of personnel from DOE headquarters and operations offices, national laboratories, and contractors, as well as state and local government representatives and the private sector, exclusively on the DOE geothermal R&D program. The Reviews have functioned as an excellent mechanism for ensuring a continued high degree of interest and participation in the program.

Program Review VI, which will focus on the redefined goals and objectives for the GTD R&D program I spoke about at the beginning of my talk, is to be held in San Francisco April 12-14, and I hereby invite all of you to attend. The discussions are typically quite lively, and I believe you will enjoy the gathering while you lend assistance to our planning and R&D priority assessment. I would also like especially to urge that you encourage junior level technical personnel in your organizations to attend and become acquainted with the R&D program and its interaction with industry and academia since we need to plan now for the continuity of the interaction.

However, may I add that the list of participants in this meeting gives me a good sense of security about the future of the program. If I were to ask for a show of hands by those who have worked, in one capacity or another, for or with the Geothermal Technology Division or its predecessors for five to 10 years or more, I believe that at least half of you would so indicate. It is reassuring that the geothermal community continues to retain the knowledge, experience, and dedication of its long-time participants. Our "corporate memory" would be considerably lessened without you.

PROCEEDINGS, Thirteenth Workshop on Geothermal Reservoir Engineering
Stanford University, Stanford, California, January 19-21, 1988
SGP-TR-113

ANALYSIS OF PRODUCTION AND RESERVOIR PERFORMANCE AT THE CASA DIABLO GEOTHERMAL PROJECT

Richard J. Miller and Rosalinda Vasquez

Cascadia Pacific Corporation

Introduction

The Mammoth-Pacific geothermal project at Casa Diablo has been in production since January, 1985. The plant generates 7-8 MW of electric power using a binary system supplied by geothermal fluid production from four wells that produce about 3500 GPM of 340° F, low salinity geothermal fluid. The wells produce from a fault/fracture system that is apparently continually recharged from a deep "reservoir" with no significant drawdown in pressure or decline in flow rate over the 2 year period.

Prior to the start of production a series of well tests were conducted to determine the pumped flow capacity of the original four wells and to determine reservoir properties from pressured drawdown and build-up analysis. Since the start of operations a continuous record of production rate, flowing bottom-hole pressure, and temperature has been maintained. The well tests and production records have been evaluated to determine the nature of the reservoir and reservoir permeability and other properties. This paper presents the results of that evaluation.

Geology & Hydrology

The Long Valley KGRA exists in the collapsed caldera of a volcano that exploded 750,000 ybp. The caldera has been active since that time and has been partially filled by eruptions of tuffaceous and ryholitic material, basalt flows and the creation of several volcanic vents and other features such as the Inyo Domes. The magma body is apparently growing and possibly intruding to shallower depths causing, over time, the formation of a resurgent dome in the west central part of the caldera and considerable seismic activity.

The geology of the caldera is very complex. At depth, the remaining rocks of the original granites and metasediments exist as a large scale rubble of the collapse. These rocks occur at various depths throughout the caldera. Only a few wells have been drilled deep enough to find these rocks, but geophysical data combined with well data, indicates depths of several thousand feet. Overlying the granites and metasediments is a thick layer of tuffaceous material known as the Bishop Tuff. These rocks were erupted during and after the explosion of the caldera and occur in layers of varying thickness over most of the caldera area. Well records indicate Bishop Tuff sequences several thousand feet thick in several areas. In some cases Bishop Tuff is interbedded with rhyolites and other rocks and surface outcrops have been mapped at several places in the caldera.

In most of the caldera, but particularly in the area of the resurgent dome, the Bishop Tuff is overlain by sequences of rhyolite flows that are of variable thickness but are recorded as several hundred to 2000 ft. in some wells. The rhyolites appear to be the result of an intermittent series of eruptions and surface flows over time. Near and on the surface rhyolites are often interbedded or overlain by basalts of varying age. The basalt flows are most common in the western caldera on the southwest margin and around the resurgent dome. Finally, the partial filling of the caldera until relatively recent time by a lake resulted in the accumulation of lacustrine and deltaic deposits, particularly in the large area southeast of the resurgent dome. Glacial moraines and alluvial

deposits are the dominant surface materials at the caldera/sierra boundary.

As the result of the collapse of the caldera, subsequent magma intrusion and resurgence, and continuous seismic and tectonic activity, the entire long valley area is heavily faulted with caldera ring fault(s) circumscribing the entire valley and a large number of active and dormant faults which generally trend in a northwest-southeast direction. These fault trends and the fractured zones proximate to the faults are generally characterized by fumeroles, hot springs, volcanic vents, hydrothermal alteration of surface and subsurface rocks, and high thermal gradients.

The complex geology of the caldera and its location near a major source of meteoric precipitation in the Sierras gives rise to an equally complex hydrologic system that can be described as one of the largest geothermal systems in the U.S. Intense field geologic work, geophysical and geochemical studies, and well drilling by industry and government agencies has resulted in a large volume of data about the system. The data available indicate general system where meteoric water from the Sierras enters the subsurface system through the caldera ring faults and other faults near the base of the mountains, and flows deep into the system coming into contact with the basement rocks heated by the magma body. The water is continually heated as it flows under hydraulic head through the basement rocks and, possibly, the Bishop Tuff in a general east-southeast direction. Various estimates of the temperature of this hot water reservoir reach 219°C at depth based on geochemistry. Flow through the system is relatively slow with residence time of 2000-3000 yrs. being estimated based on chemistry.

While most of the fluid eventually exits in the Hot Creek Springs and Lake Crowley, some reaches the surface at various points throughout the caldera by traveling up faults and fractures to form the hot springs and fumeroles found at Casa Diablo, Hot Bubbling Pool, and other places. This flow to the surface requires the existence of an open flow path in the fault plane and is highly subject to occasional closure and re-opening of the flow path(s) by chemical deposition and seismic activity. The large amount of evidence of hydrothermal activity at certain points on defined faults, and the lack of evidence of activity in non-faulted areas, indicate that while the Long Valley geothermal system is pervasive at depths of 2-4 miles, access to the system for commercial development is probably limited to a few sites where fluid reaches or approaches the surface in sufficient volume and at a temperature to be useful.

Casa Diablo is one of those locations. The hot springs and fumeroles of the area have been described for over 100 years. Extensive well drilling since the early 1960's has defined, with considerable clarity, a geology and hydrologic system consistent with the overall Long Valley model. Casa Diablo lies on the west margin of a graben block, known as the Keystone graben, that extends in a south-southeasterly direction from the resurgent dome and appears to reach a convergence at a point to the southeast of Casa Diablo. The exact extent of the graben and the definition of its composite faults is not completely defined, but continued drilling will eventually complete the picture.

The graben in the area of Casa Diablo is formed by the Taylor-Bryant (TB) fault and several smaller faults with surface exposure that together trend in a shallow arc from southeast to northwest enclosing the Casa Diablo area within the arc. The surface geology consists of recent rhyolite flows to the north and northeast with several areas of hydrothermal alteration. The south-southwest border is composed of basalt flows. The low area between the resurgent dome rhyolite flows and the faulted basalt flows is a marshy area with fluvial and other sediments punctuated by hot springs and occasional mud pots.

Depending on location, wells drilled in the area encounter basalts or sediments down to 50-100 ft

of surface and then enter a sequence of rhyolite flows that extend to about 1000 ft. from surface. Detailed lithology from mud logs indicate considerable differentiation within the rhyolites with significant alteration and calcite deposition noted in fissures and fractures. Below the rhyolites, wells enter a thick sequence of Bishop Tuff that has been measured in one well to a depth of 4510 ft. At the rhyolite-tuff boundary there is some interbedding. High temperatures and geothermal fluid flows have been encountered in virtually every well drilled at Casa Diablo, although, as will be discussed below, some wells are better than others. Fluid entry points and maximum temperature points are not at uniform depth and appear to be confined to relatively thin intervals in the wells.

Development of Casa Diablo

The development area of the Casa Diablo project is relatively small comprising 40-80 acres. Present plans call for expanding the productive area in the north-northeast direction and potentially to the southeast following the evidence of fault trends and hydrothermal features, and the results of reservoir engineering and geologic evaluation.

The first wells were drilled at Casa Diablo as water wells and very shallow wells to exploit the hot springs. Commercial geothermal exploration did not occur until eight wells known as Endogenous Nos. 1-7 and M-1 were drilled by cable tool to depths of 400-800 ft. in 1959-1962. Temperature measurements were taken and the wells were completed with surface casing and open hole. None of the wells were logged and no mud logs were made except as notes on the drilling reports. All of the wells were tested in 1961 and 1963 which indicated that high flow rates of water in excess of 300° F could be obtained from shallow depths. While the flow rates varied and some difficulty with calcite deposition occurred due to steam flashing, the tests generally confirmed a geothermal resource in the immediate area of Casa Diablo. In 1979 Union Oil Co. drilled a well to 5265 ft. total depth which found basement rocks at 4510 ft. and recorded two high temperature peaks at about 400 ft. in rhyolite and 2200 ft. in Bishop Tuff.

Following an analysis of available data and completion of a resource assessment, the Ben Holt Company drilled four producing wells and an injection well at Casa Diablo and recompleted Union Mammoth No. 1 in late 1983 and early 1984. The production wells, known as Mammoth Binary Power (MBP) Nos. 1,2,4, and 5, were completed with shaft turbine pumps at depths of 650-670 ft. at locations which generally followed the surface expression of the Taylor-Bryant fault or local cross fault traces. All the wells were logged and detailed mud logs were obtained. Temperature surveys were run shortly after completion.

Subsequent to the startup of plant operation in November, 1984 MBP-3 was drilled; MBP No. 2 was abandoned; a third injection well was drilled; and a production test well has been drilled at a location to the southeast of Casa Diablo.

Well Test Program

In June, 1984 as the Mammoth Binary Power plant was nearing completion, a series of flow tests were conducted by MBPC and Pacific Resources Management, Inc. (PRMI) to determine: the stabilized flow rates to be expected from the four wells then available; if additional wells were necessary; if the two injection wells were adequate; and to obtain, if possible, any reservoir information that could be derived from pressure build-up/drawdown tests.

The test program was designed to test each well individually and to maximize the amount of reservoir data that could be obtained. The program included several steps.

1. Static pressure/temperature (P/T) profiles were taken in each well including the injection wells.

2. Each well would be produced on pump as a constant rate for a fixed time period to record flow rate, temperature, flowing BHP, and pump efficiency. The pumps had only one speed and attempts

to control rates by varying back pressure proved futile.

3. BHP was recorded during production startup and shut-in to obtain drawdown and build-up data.

4. Pressures were recorded in offset wells to determine if interference would occur between wells.

The pressure/temperature profiles were obtained uneventfully and a wireline pressure recorder was installed in Endogenous No. 2 to record interference effects if they occurred. Flow rates were measured using an orifice meter. Fluid temperature was measured by a thermocouple at the wellhead. BHP was measured using a nitrogen bubbler tube where the bottom end of the tube was set just above the top of the pump. Annulus pressure was also measured. All data points were electronically connected to a digital read-out and plotter which recorded a total of eight data points each 5 seconds.

The data measurement and recording system used during the tests was complicated and not without problems in operation such as premature disconnection of recorders and N_2 supply. Despite the problems a significant amount of data was collected and the objectives of the tests were satisfied.

Test Results

All four producing wells are completed with slotted liners in the rhyolite. The mud logs and wireline well logs show very similar characteristics in each well with some variation, particularly with depth, from well to well. Well MBP No. 4 is described here as an example.

In MBP No. 4 the well logs and the mud log on the well were analyzed to determine the apparent location of fractures and matrix porosity. The mud log indicates that the well entered rhyolite at about 80 ft. The lithology to TD varies including altered rhyolite and intervals of glassy rhyolite and demonstrates considerable calcite deposition in fissures and fractures. The Neutron-Density Logs indicate an interval of apparently high porosity from about 415 ft. to 485 ft. The high porosity is not continuous through the interval but appears to be concentrated in 4 or 5 streaks. The interval corresponds to a zone of rhyolite glass that extends above and below the interval. The caliper log indicated an extreme deviation to increased hole size over the interval with hole size diminishing to near bit gauge above and below the interval. About 10% lost circulation was recorded over the interval from 413 ft. to 443 ft. Temperatures recorded during drilling reached a maximum in the upper part of and just above the 415 ft.-485 ft. interval.

A second interval from about 595 ft. to 620 ft. appears to include a number of high porosity streaks and some minor temperature increases were recorded during drilling. Lost circulation occurred deeper in the well at 648 ft. The porosity measurements recorded by the Neutron-Density logs and the caliper deviation is generally equal to the deviation recorded for the upper interval.

It would appear that the well penetrated one or more fractures in the interval 415 ft. to 485 ft. and that these fractures are the major source of fluid flow in the well. An exact determination of the depth of a fracture or the thickness is not possible since the brittle nature of the rhyolite (glass) probably caused the rock to shatter and break up immediately about the wellbore as the succession of fractures was penetrated. It is possible that the fracture interval is the intersection of the Taylor-Bryant fault the surface trace of which passes within 40 ft. of the well surface location.

Two separate flow tests were run on the well with nearly identical results. The first test was run for almost 2 days starting at about 19:40 of June 28, 1984. After several false starts, due to mechanical problems with the pump motor, a sustained flow was established at about 22:45 on June 28. The maximum flow rate of about 1,020 gallons per minute (GPM) was maintained for about 5 minutes. The

flow rate was then reduced to allow a check of the bottom-hole pressure (BHP) data recording. The rate fluctuated between 250 and 800 GPM for about an hour while the BHP recorder was determined to be correct.

At midnight on June 28, 1984, production was increased gradually to about 890 GPM and a sustained flow was started. At this flow rate the fluid temperature was recorded continuously as 347° F. BHP was recorded as 230.6 psig with about 300 ft. of fluid over the pump.

Flow was maintained for about 5 hours after which the well was shut-in. During the flow period the rate declined gradually from 890 GPM to 810 GPM at shut-in with no change in BHP. Over that period the fluid level showed some fluctuation, but generally declined from about 300 ft. to 291 ft. over the pump while pump discharge pressure increased from 480.1 psig to 494.1 psig. Fluid temperature remained essentially constant at 347° F.

The second flow test was conducted on July 6, 1984. During this test, flow rates were held relatively constant at four successively higher rates over a total test period of about 6 hours. The results of this test are summarized in Table 1.

It is apparent that MBP No. 4 is an extremely good producing well which is probably being supplied by an extensive fracture system. The water produced was very clean and is very low salinity. While there is no direct evidence, the high flow rates, very low drawdown, high temperature, and proximity to the fumeroles and the Taylor-Bryant fault trace offer the possibility that the well penetrates a fault or the fractured area immediately proximate to the fault that is a primary fluid channel.

There is no pressure build-up analysis on this well since the small pressure drawdown offers no opportunity for significant build-up to occur.

Analysis of the other wells indicated similar geology and reservoir conditions.

In MBP No. 1 fluid entry was defined as an interval between 595 ft. and 628 ft. which is very similar to the rhyolite glass interval in MBP No. 4. The flow tests were plagued with mechanical problems and a good test was not obtained until July 7 when the well demonstrated rates of 472-632 gpm at BHP between 208.9 and 194.9 psi respectively. BHP drawdown was determined to be 19-33 psi. The average PI is 22 GPM/psi. No pressure build-up or drawdown data of value was obtained.

In MBP No. 2 the fluid entry point(s) are less clearly defined and appear to be inflows through fractures and fissures in the rhyolite too small to be apparent on logs or to cause notable fluid loss during drilling. The well ultimately had more tests run than any other well. Over a series of short duration flows the well demonstrated an ability to produce in the range of 500-600 gpm but with a considerable 50-80 psi drawdown over the period of the test. The well is apparently highly sensitive to flow rate and is not well connected to the hydrothermal system. A 100 minute flow on June 29, 1984 demonstrated a decline in flow rate from 639 gpm to 360 gpm with a corresponding decline in FBHP from 143.1 psi to 117.1 psi. Following shut-in pressure build-up to original BHP required about 3 hours.

MBP No. 5 exhibits geology and fluid entry characteristics very similar to MBP No. 4 with the exception that MBP No. 5 is on the up-thrown side of the TB fault. Fluid entry appears to be from a fractured interval at 410 ft.-450 ft. Four flow tests of short duration were run on the well. The last three tests demonstrated maximum flow of 524 GPM with a more stable range around 350-400 GPM and pressure drawdowns 40-50 psi. A fifth test run on July 3, 1984 indicated a range of flow rates from 525-646 GPM with maximum drawdown of 88 psi.

It is apparent from the production tests that performance by the wells is not uniform and that various geologic and other factors appear to influence flow rates and the drawdown/build-up response of

the individual wells. Fluid entry points are rather readily defined from a combination of data and analysis. Correlation of well performance and general geology leads to the conclusion that the most favorable performance is obtained from the wells located close to and on the down side of the Taylor-Bryant fault (MBP No. 4 & No. 1) while apparently restricted performance was obtained from MBP No. 5 (on the up side of the Taylor-Bryant fault) and from MBP No. 2 which seems to have been completed in an area where fluid connectivity through faults and fractures is not good. Both the latter wells exhibited drawdowns during production that continued throughout the test indicating a restricted fluid source.

Pressure and Build-up Analysis

In some respects the pressure build-up and drawdown tests were disappointing but as a secondary objective of the test program some very interesting results were obtained. The test of MBP No. 4 demonstrated flow rates to the maximum of pump capacity with a measured drawdown of only 2-3 psi. When production was stopped or started build-up and drawdown occurred almost instantaneously so that only one or two data points at most were obtained allowing no analysis. Intermittent pump problems and malfunctions of the N_2 system prevented any useful data collection from MBP No. 1 except to note that pressure response was very rapid following high flow rates. Only MBP No. 2 and No. 5 demonstrated sufficient drawdown or build-up to allow analysis to be done. We are then in the curious position of being able to analyze only the two least productive wells with results that probably form the base line of data regarding reservoir properties at Casa Diablo.

A series of five flow tests were run on MBP No. 5. BHP build-up analysis was done following three of the flow periods. All of the build-up analyses were re-evaluated using computer techniques in 1987. While all three contributed useful information the build-up following the second test was considered most useful. This analysis was done using cross-plotting techniques described by El-Hadidi for vertically fractured wells. Analysis indicates virtually no afterflow. The log-log plot indicates two linear flow intervals separated by a possible radial flow segment. The plot ends with an apparent radial or pseudo radial flow - segment. Other cross plot techniques indicate linear flow separated by possible radial flow segments. The parts of the data that indicate linear flow represent the surface of the fracture intersecting the well bore. The pseudo radial flow portion of the build-up curve is used to calculate Kh for the well. Pressure build-up on successive days following further flow tests indicated virtually identical performance except that the radial flow portion separating the two linear segments diminished leaving one linear portion followed by a radial flow portion. Calculated Kh from the radial flow portion increased with each test as shown in Table 2.

Among other problems MBP No. 5 had considerable lost circulation during drilling and the improved performance may well be the result of cleaning out of fractures during testing. The well does however appear to be somewhat limited in flow capacity as demonstrated by the significant drawdown in the well even during the fifth test and, as will be seen, during sustained production. This overall result is interpreted to mean that despite a very high Kh and apparent connection to a fracture/fault system the well does not have the same level of access to the flow system as do MBP Nos. 1, 3, and 4.

A series of three pressure build-up analyses in MBP No. 2 demonstrated very similar but lower level performance to MBP No. 5.

Analysis of Results

The very high Kh values, the lack of any definable after flow even in wells where some drawdown had occurred, and the virtual lack of any drawdown in MBP No. 4 seems to indicate that flow in the system is entirely fault/fracture dominated with no matrix flow. It seems clear when combined with the geology of the system, as shown in the lithology and well logs, that wells

drilled into the Casa Diablo geothermal system must contact either the Taylor-Bryant fault, one or more of the fracture zones nearby the fault, or a well connected cross fault/fracture zone.

As a result of the flow test program and the reservoir evaluation that followed the program, MBP No. 3 was drilled to provide additional flow capacity for the plant. The location of MBP No. 3 was sited based on the apparent location of the TB fault intercept at a depth essentially equivalent to MBP No. 4. Unfortunately no logs were run on the well and the lithology log is of limited value. No controlled flow tests or pressure build-up/drawdown analyses have been done. A temperature profile indicates inflow at approximately the same depth as in MBP No. 4.

Production History Evaluation

Continuous operation of the Mammoth-Pacific plant at Casa Diablo began in January, 1985 with production from MBP No. 1. The other wells began production on a continuous basis in March and April, 1985. Plant changes, shutdowns and modifications occurred with some frequency throughout early 1985 but full operation was finally achieved in late 1985. Performance of the plant and wells since that time has been generally good with production through most of 1986 and the first half of 1987 being relatively consistent. This "stabilized" production period has been used to assess the reservoir and its properties by attempting to calculate production histories that would match the actual history based on assumed reservoir conditions.

Sources of Data

The data measuring and recording system at Casa Diablo has changed considerably over the time period included in this study. These changes have some influence on the use of data for analysis and require that certain adjustments be made to some data.

Production Rates - Prior to December, 1986 total flow was recorded as plant inlet volume on an orifice meter. Individual well volumes were estimated from pump curves based on amperage. The total fluid production was then apportioned back to each well based on pump curve rates. Only MBP No. 3 was directly measured by vortex meter. Orifice meters were installed on MBP Nos. 1, 4, and 5 in December, 1986. Completion of full instrumentation on the wells had not been completed as of the time of this study, however, it appears that an 8-10% adjustment in previously recorded flow rates is warranted. Also in December, 1986 flow rates began to be reported at 60° F rather than actual flowing temperature. The result would be a correction of 1.0932 reducing the apparent or reported flow volume. The temperature correction is for standardization purposes only. The reservoir volume is at reservoir temperature and is the volume that is used for analysis. Flow rates were recorded three times per day.

Fluid Temperature - Flowing fluid temperature is recorded three times each day from a dial thermometer at wellhead.

Bottom Hole Pressure - BHP is obtained from a surface reading of an N_2 bubbler tube on each well. The bottom of the bubbler tube is located just above the pump. All readings until recently were taken at surface. Prior to April, 1986 the fluid of height above the pump discharge was recorded. Since April, 1986 the calculated BHP is reported. There is no N_2 correction from surface to BHP.

Prior to the start of analysis all the data was reviewed for obvious errors and inconsistencies. All BHP data was corrected to the mid-point of fluid entries. To the extent possible, all data were corrected for known and quantified systemic recording or reporting errors. This error correction is not considered to embrace all such errors that might be required.

Overall Production History

In general, the wells supplying the plant have performed well since the start of operation. MBP Nos. 1, 3, and 4 supply relatively equal (at April, 1987) shares of total production. MBP No. 5 is a weak

producer that is brought on intermittently as needed. MBP No. 2 was abandoned for mechanical reasons in 1985. Total production averages 3500 GPM of 340° F fluid. Large variation in flow rates is more often a function of plant and/or pump operation than any apparent well or reservoir problems.

Individual Well History/Analysis

Production rate, pressure, and temperature data for each well was obtained on a daily basis from January 1, 1985 to April 30, 1987 and was entered into a computer database. Corrections were made to the data as noted above and data points with obvious errors were noted. The data for each well was then plotted in several graphical forms to obtain a portrayal of the data over the full time frame.

In attempting to model certain aspects of the Casa Diablo system by matching calculated results to actual performance several assumptions were made and complications were considered.

1. The wells were assumed to produce from an infinite acting, recharged reservoir so that Pe was kept constant for the study period. Pe was taken as the measured SIBHP adjusted to the mid-point of fluid entry.

2. Flow rate was selected as the variable to be matched.

3. It was assumed that changes in pump efficiency, instrument deterioration, and recording errors could not be modeled or compensated.

4. Because of the relatively narrow range of data such as BHP for MBP Nos. 3 and 4, relatively small changes in input values were found to cause large variations in results.

MBP No. 3 - As the first well evaluated MBP No. 3 was used to establish a model form and equation. It became quickly apparent that the high volume and low drawdown could not be accommodated by matrix flow models and required a form of fracture flow/linear flow model. In practice, however, use of a linear flow model requires more definitive knowledge of fracture dimensions than is available. Based on the geology of the "reservoir," an infinite line source model was chosen as most representative of the conditions extant in the Casa Diablo reservoir:

$$q = \frac{0.2065\ Kh\ (Pe-Pw)}{\mu w \beta w\ ln\ (2D/rw)}$$

where "D" is the distance from the well to the line source - in this case the TB fault.

The production histories in terms of daily flow rate and flowing BHP are presented as Exhibits III-VI. The flow rates indicate considerable variability while BHP is much less variable. Reasonably good matches to the flow rates were obtained in MBP Nos. 1, 3, and 4 considering that the flow rate is not always correlatable to BHP. It was found, however, that good matches were obtained over the short periods of production/pressure stability and that these periods established a base for assessment of the fluctuation periods.

The primary difficulty in matching flow rate is the very low difference between Pe and Pw. In MBP No. 4 Pe-Pw averages 11.4 psi with a standard deviation of 1.4 psi. A change of 1 psi has a major effect in these circumstances.

In MBP No. 4 a relatively good match of flow rates was attained at Kh = 456,100 md. ft. used over the period April 1, 1986 to April 30, 1987.

In MBP No. 3 matching was generally better than for MBP No. 4 despite the same low differential between Pe and Pw using an average Kh of 554,000 md. ft. over the same period. Average Pe-Pw over the period is 9.7 psi with a standard deviation of only 1.9 psi.

The best match was obtained in MBP No. 1 where Pe-Pw averaged 25.2 psi with a standard deviation of 3.7 psi. In this well, Kh found to be about 195,000 md. ft. While this is considerably lower than MBP Nos. 3 and 4, it is consistent with the well location and geology and with well performance.

Table 1. Well Test MBP No. 4 (July 6, 1984)

Flow Rate (GPM)	Duration of Flow (minutes)	Avg. BHP (psig)	Avg. Fluid Temperature (°F)	Fluid Level (ft.)
610	55	227.9	345	310
720	65	226.8	353	310
800	100	226.0	348	289
950	65	225.9	348	288

Table 2

Date	Kh
6/27/84	74,101 md. ft.
6/28/84	199,898 md. ft.
6/29/84	417,455 md. ft.

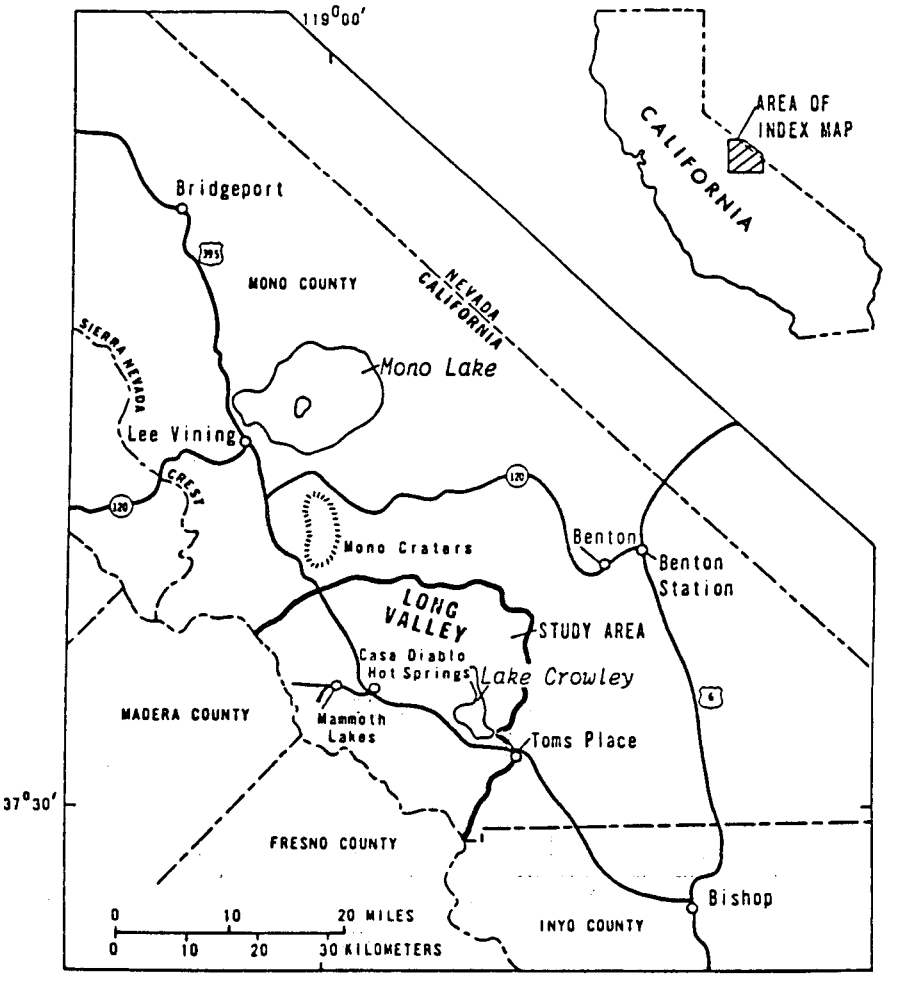


Figure 1. Regional location map - Long Valley (After Sorey et al.)

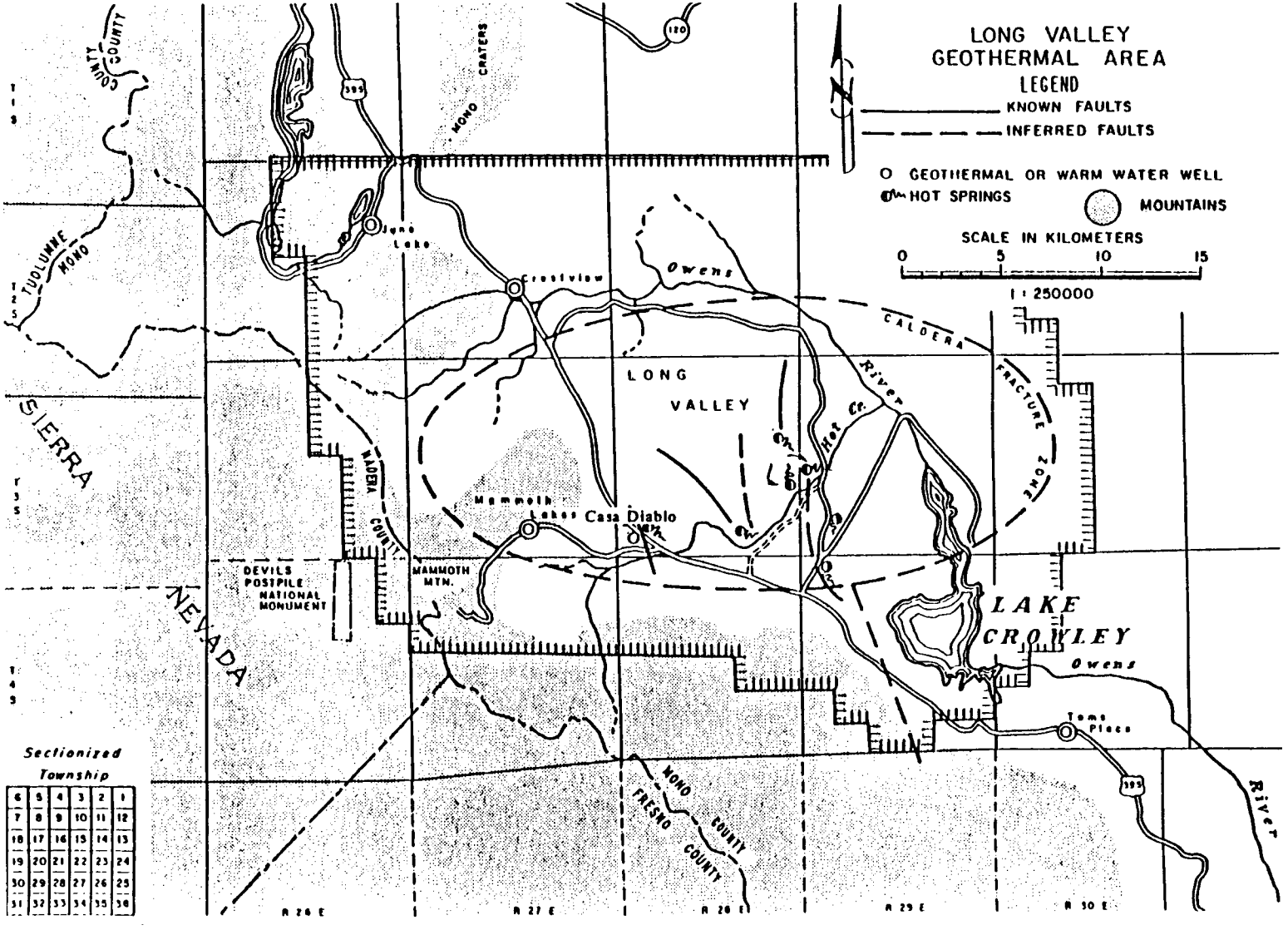


Figure 2. Area location map - Casa Diablo and Long Valley (After Sorey et al.)

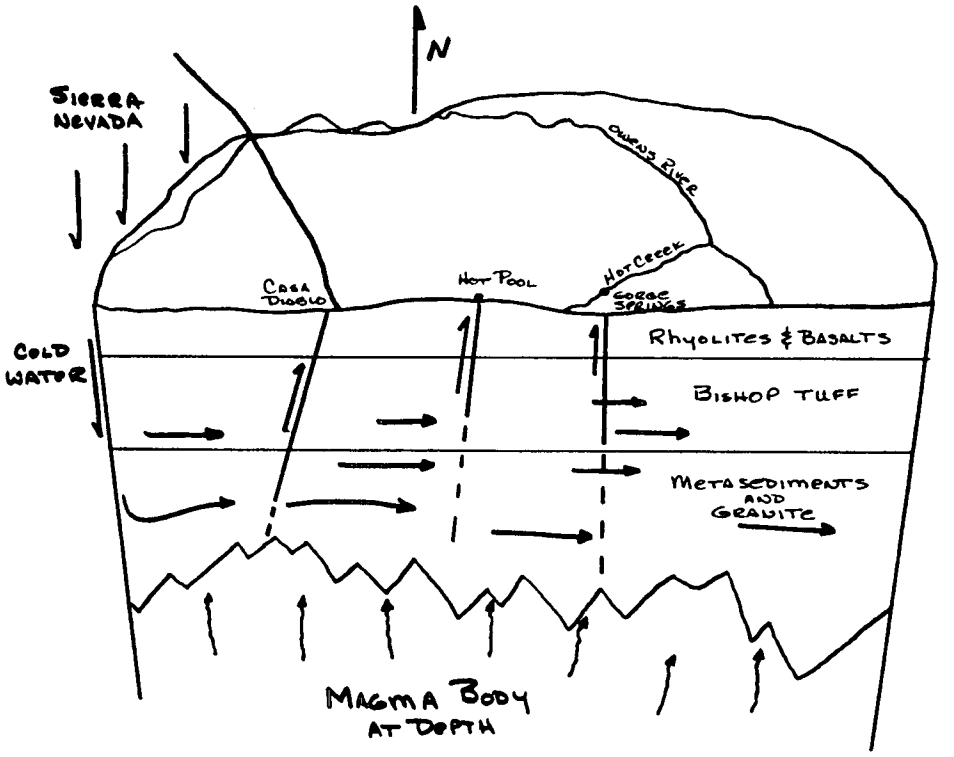


Figure 3. Conceptual model of Long Valley geologic and hydrologic system (After Sorey et al.)

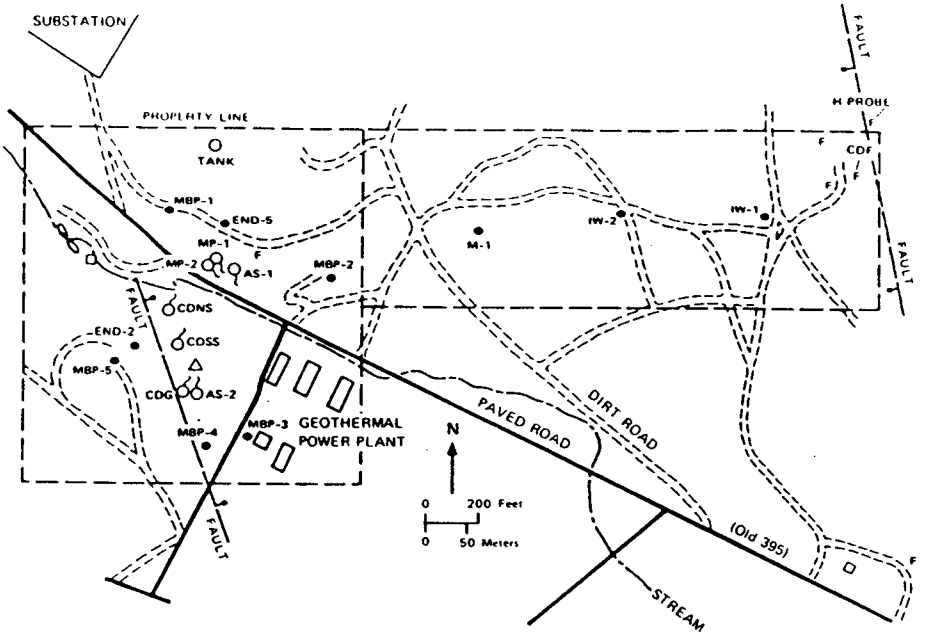


Figure 4. Casa Diablo well location map (After Farrar et al.)

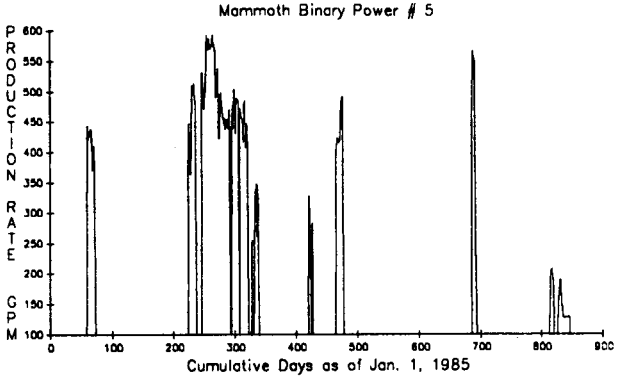


Figure 5a. Pressure buildup test on MBP No. 5 on June 27, 1984

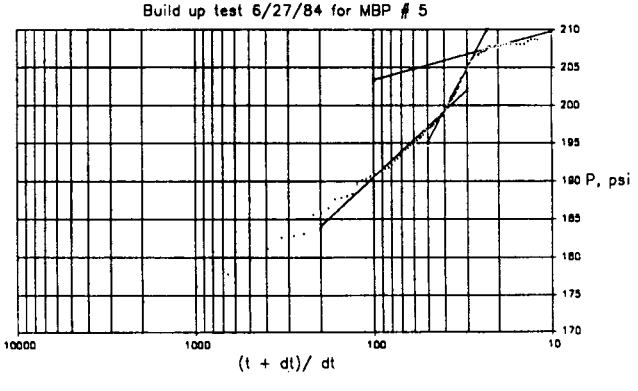
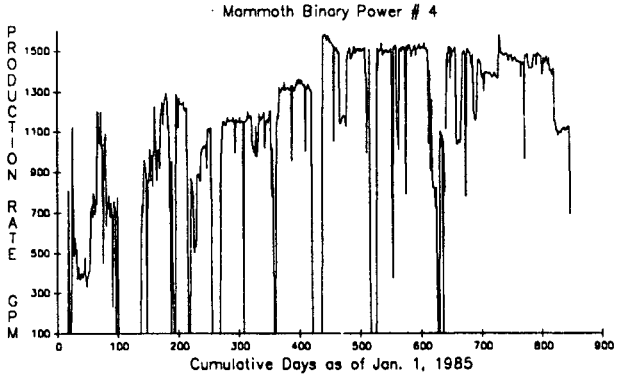


Figure 5b. Production rate performance - MBP No. 5. January 1, 1985 to April 30, 1987



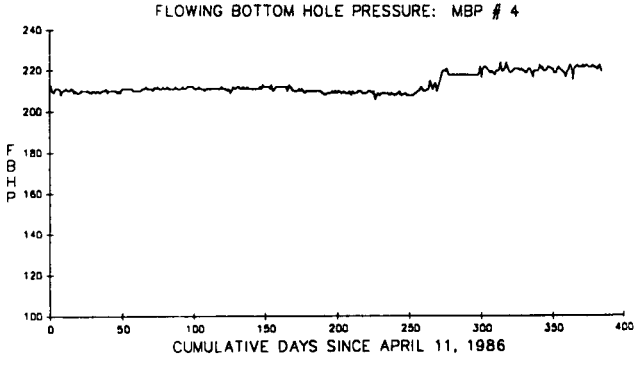
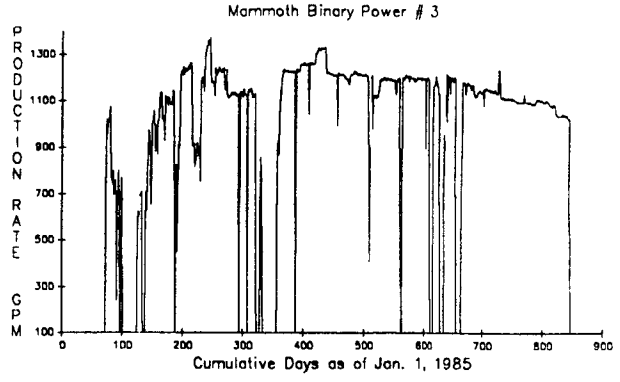


Figure 6. Flowrate and FBHP (uncorrected)- MBP No. 4. January 1, 1985 to April 30, 1987



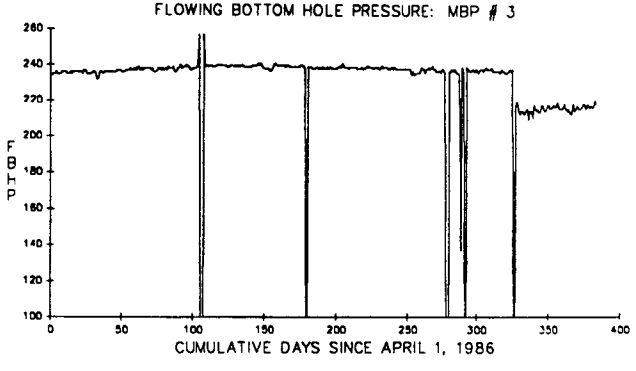
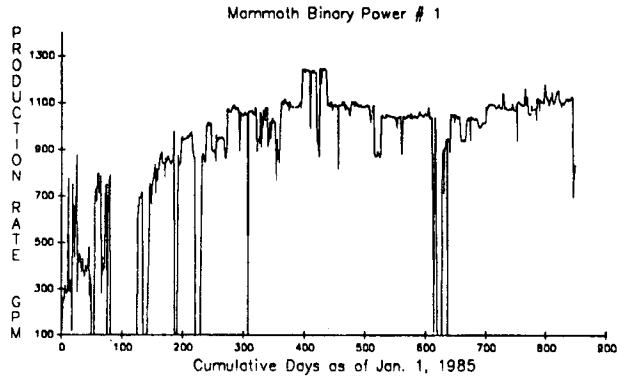


Figure 7. Flowrate and FBHP (uncorrected)- MBP No. 3. January 1, 1985 to April 30, 1987



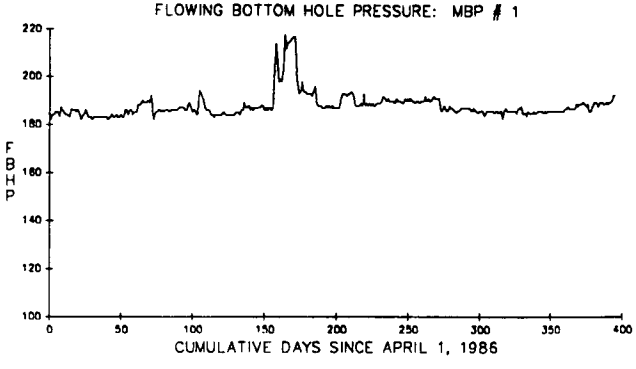


Figure 8. Flowrate and FBHP (uncorrected)- MBP No. 4. January 1, 1985 to April 30, 1987

PROCEEDINGS, Thirteenth Workshop on Geothermal Reservoir Engineering
Stanford University, Stanford, California, January 19-21, 1988
SGP-TR-113

COMPRESSIBILITY AND SONIC VELOCITY IN STEAM/WATER MIXTURES

Sigurgeir Sveinsson
Jón-Steinar Gudmundsson*
Valdimar K. Jónsson

*Geothermal Division, National Energy Authority
Mechanical Engineering Department, University of Iceland
Reykjavík, Iceland

ABSTRACT

A simplified expression is derived for the compressibility of steam/water mixtures at ideal thermodynamic conditions. It is shown how the same expression can be used to estimate the sonic velocity also. Empirical correlations are presented for both the compressibility and sonic velocity.

INTRODUCTION

The maximum fluid velocity in two-phase geothermal wells and surface equipment, is the sonic velocity of the mixture. In locations where this velocity is attained, the flow conditions are said to be choked or critical. The James-method is based on such conditions in a discharge tube (James, 1962). Also, when calculating the output of two-phase geothermal wells using a wellbore simulator, the velocity in the steam/water mixture at outlet conditions needs to be known, to check that the calculated mixture velocity does not exceed the sonic velocity (Bilicki et al., 1982).

Experimental data on sonic velocity in steam/water mixtures at geothermal wellbore conditions are not readily available. To solve this problem, theoretical calculations need to be carried out to find the sonic velocity for ideal thermodynamic conditions. Such calculations have been carried out by Kieffer (1977) and Maeder et al. (1981), for example. In both studies the results were presented in tabular and graphic form, not convenient for engineering calculations. Karamarakar and Chen (1980) reviewed several choked flow correlations for two-phase flow metering of geothermal wells. They concluded that the nuclear-industry-type correlations agreed reasonably well with the James-method correlation.

We have derived a simplified expression for the compressibility of steam/water mixtures at conditions typical in geothermal wells. The expression can be used to estimate the sonic velocity in such mixtures. We started this work to better understand the nature of two-phase flow in high-enthalpy geothermal wells, producing from boiling-dominated reservoirs (Gudmundsson, 1986a, 1986b). Many such wells flow steam vapor with a few percent liquid water. Perhaps, if the compressibility of steam/water mixtures can be found from a simple expression, it would be possible to calculate directly the pressure drop in high-enthalpy two-phase wells, using a similar method as used for steam wells (Morales G. et al., 1979). The details of our work are given by Sveinsson (1987).

DERIVATION OF COMPRESSIBILITY

Our derivation follows similar reasoning as that of Grant and Sorey (1979), who investigated the compressibility of a steam/water mixture in contact with reservoir rock. Consider a two-phase geothermal well where thermodynamic equilibrium exists between the phases and where the flow is homogeneous, steady-state and one-dimensional. Furthermore, assume the wellbore flow to be adiabatic; no heat loss or gain.

A balance equation can be written for the steam/water mixture flowing from one infinitesimal cross-section to another

$$x_1 h_{g1} + (1-x_1) h_{f1} = x_2 h_{g2} + (1-x_2) h_{f2} \quad \ldots(1)$$

where x represents the mass fraction of steam and h_g and h_f the enthalpy of steam vapor and liquid water, respecively. The equation can also be written as

$$h_{f1} + x_1 h_{fg1} = h_{f2} + x_2 h_{fg2} \quad \ldots(2)$$

We assume that the latent heat of evaporization, h_{fg}, changes negligibly between adjacent cross-sections; from one infinitesimal cross-section to another. We can hence rewrite Equation 2 in the form

$$h_{f1}-h_{f2}=(x_2-x_1)h_{fg} \quad \ldots(3)$$

An examination of Steam Table values shows that the heat of evaporization of water remains reasonably constant over a wide range. This does not mean that the heat of evaporization is constant throughout the system considered; the appropriate value is used for each saturation condition.

Next we assume that constant pressure heat capacity, C_p, can be used. For the liquid water phase we can write

$$C_{pf}\Delta T=h_{f1}-h_{f2} \quad \ldots(4)$$

and we note that the right-hand side of this equation is the same as the left-hand side of Equation 3. When liquid water evaporates due to pressure lowering, the steam/water mixture volume changes. The dominant volume change is that caused by phase change; liquid water turning into steam vapor. We ignore the slight volume change in the water and steam already present. Therefore, the change in mixture volume becomes

$$\Delta V=\Delta m(v_g-v_f) \quad \ldots(5)$$

where Δm is the mass of water changing phase and v_g and v_f the specific volume of steam and liquid, respectively. And since this mass of water is simply

$$\Delta m=(x_2-x_1)m \quad \ldots(6)$$

where m is the mass of steam/water mixture present, the change in mixture volume can be written

$$\Delta V=m(x_2-x_1)(v_g-v_f) \quad \ldots(7)$$

It is possible to define fluid compressibility in several ways, depending on what physical property is assumed constant: temperature, enthalpy, entropy. Usually the temperature is assumed constant, giving an isothermal compressibility. For two-phase wellbore flow without heat loss or gain, an adiabatic definition of compressibility seems most appropriate. Thus

$$K_h=-(1/V)(\Delta V/\Delta p) \quad \ldots(8)$$

Substituting for ΔV using Equation 7 and then Equations 3 and 4 to eliminate (x_2-x_1), the adiabatic compressibility becomes

$$K_h=-(mC_{pf}\Delta T(v_g-v_f))/(V\Delta p h_{fg}) \quad \ldots(9)$$

The total mass of the steam/water mixture, m, is given by the relationship

$$m=V(\alpha\rho_g+(1-\alpha)\rho_f) \quad \ldots(10)$$

At all conditions the steam/water mixture follows the saturation curve. Therefore, for a small pressure drop, Δp, the following will apply

$$\Delta p/\Delta T=(dp/dT)_{sat} \quad \ldots(11)$$

Combining Equations 9, 10 and 11, gives our simplified derivation for the adiabatic compressibility of steam/water mixtures

$$K_h = \frac{C_{pf}(\alpha\rho_g+(1-\alpha)\rho_f)(1/\rho_g-1/\rho_f)}{h_{fg}(dp/dT)_{sat}} \quad (12)$$

COMPRESSIBILITY AND SONIC VELOCITY

We now turn to the relationship between compressibility and sonic velocity. In our derivation above we assume an adiabatic process. Sonic velocity, c, is always defined in thermodynamic texts at isentropic conditions, s, namely

$$c^2=(dp/d\rho)_s \quad \ldots(13)$$

where ρ is the fluid density. By using the definition of compressibility at isentropic conditions

$$K_s=1/\rho(d\rho/dp)_s \quad \ldots(14)$$

the following relationship results

$$K_s=vc^{-2} \quad \ldots(15)$$

In other words, by knowing the isentropic compressibility, we also know the sonic velocity. This was the method used in the present work.

From thermodynamics we know that an isentropic process is both adiabatic and reversible. The question arises whether we can equate compressibility and sonic velocity for adiabatic and isentropic conditions. For fluid flow in wellbores and pipelines, frictional losses make the process non-reversible. This aspect of fluid flow is particularily important in situations where rapid pressure drops occur, for example in nozzles. It is less important in situations where the pressure changes gradually with distance, for example in wellbores and long pipelines. Therefore, the validity of sonic velocity values derived from adiabatic compressibility values, will depend on the flow situation. The sonic velocity obtained in our work represents an approximation.

RESULTS

Equation 12 gives the compressibility of steam/water mixtures we want to find. The properties needed are the liquid water heat capacity, the density of liquid water and steam vapor and the latent heat of evaporization. These were calculated from correlations reported by Michaelides (1981). [A few errors (in Equations 2, 3 and 21) were found in the paper - they were corrected by contacting a co-worker of the author. The corrections are given by Sveinsson (1987) and also by Gudmundsson and Thráinsson (to be published).] The liquid water heat capacity was calculated from a correlation giving enthalpy with temperature; the other properties were calculated directly. The pressure-temperature gradient on the saturation line, however, was calculated from the Clausius-Clapeyron equation.

$$(dp/dT)_{sat}=(v_g-v_f)^{-1}[h_{fg}/(T+273.15)] \quad ...(16)$$

The remaining property in Equation 12, the steam/water mixture void fraction, α, can be expressed as

$$\alpha=[1+((1-x)/x)(\rho_g/\rho_f)]^{-1} \quad ...(17)$$

where x has the usual meaning of steam mass fraction

$$x=(h_o-h_f)/h_{fg} \quad ...(18)$$

A computer program was written where the steam/water mixture enthalpy was specified and calculations performed for saturation temperature in the range 100°C to 300°C. The Michaelides (1981) physical property correlations are reasonably accurate over this temperature interval. All calculations were performed assuming saturation conditions. Examples of calculated compressibility values are shown with pressure on a semilog plot in Figure 1, for steam/water mixture enthalpy [$(1-x)h_f+xh_g$] from 1000 kJ/kg to 2400 kJ/kg, in intervals of 200 kJ/kg.

We were interested in correlating the results, to obtain an expression convenient for engineering calculations. Figure 1 shows the compressibility with saturation pressure for several constant mixture enthalpy values. We found that the results could be collapsed into a single line by plotting the compressibility, divided by the steam/water mixture density

$$\rho=(\alpha\rho_g+(1-\alpha)\rho_f) \quad ...(19)$$

with saturation pressure. The correlated results are plotted on a semilog plot in Figure 2, showing the calculated values (solid line) and fitted values (broken line). An examination of Equation 12 shows, that moving the term expressing the mixture density (Equation 18) from the right-hand-side to the left-hand-side of the equation, suggests a way to correlate the results. We used a standard power-fit program, which resulted in the following expression

$$K_h/\rho=(789.4)p^{-1.616}\ (1/GPa)(m^3/kg) \quad ...(20)$$

In the range 10-20 bara pressure, the fitted line is just above the calculated

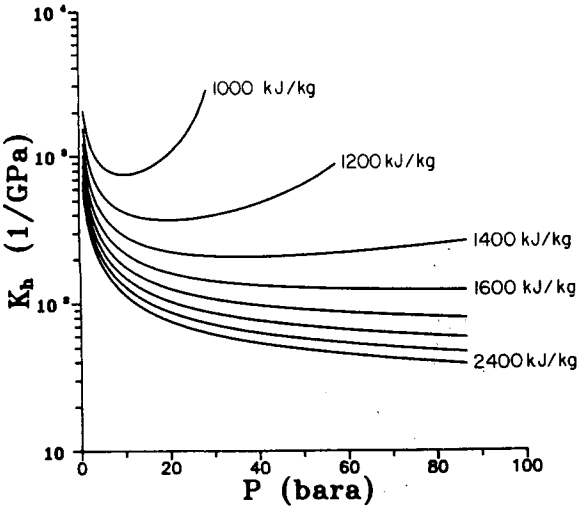


Figure 1 - Calculated compressibility with saturation pressure and steam/water mixture enthalpy.

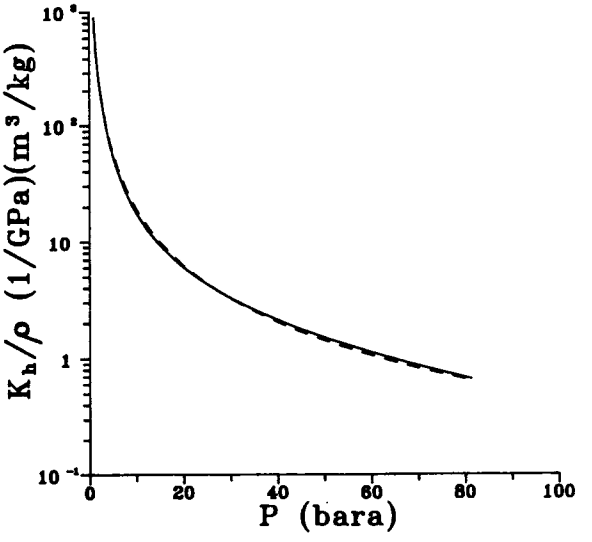


Figure 2 - Calculated (solid line) and correlated (broken line) compressibility with saturation pressure.

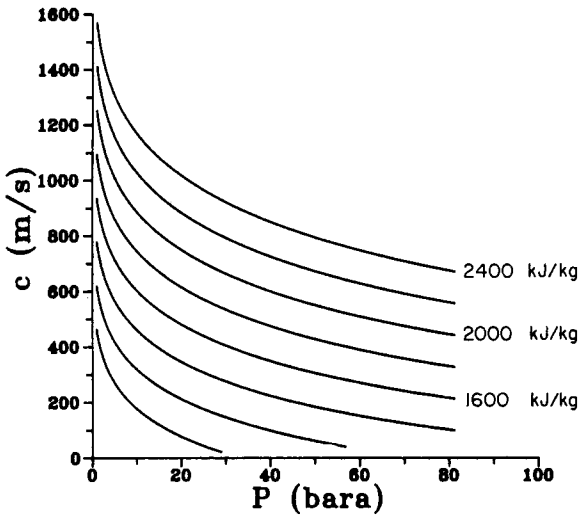


Figure 3 - Calculated sonic velocity with saturation pressure and steam/water mixture enthalpy.

values. In the range 40-80 bara the fitted line falls just below the calculated values. We did not evaluate the goodness of fit, but estimate that the calculated and fitted values differ by only a few percent at the most.

Using Equation 15, we calculated the sonic velocity, c, from the steam/water mixture compressibility values already obtained. Our results are shown on a linear plot in Figure 3. It can be shown that the compressibility correlation (Equation 20) gives rise to the following relationship for sonic velocity in terms of mass flux at choked or critical flow conditions

$$c\rho=(1125)p^{0.808} \ (kg/m^2.s) \qquad ...(21)$$

We obtained this correlation assuming thermal equilibrium between the phases, a homogeneous steam/water mixture and isentropic (adiabatic and reversible) conditions. Equation 21 is shown on a linear plot in Figure 4 (broken line), along with the calculated sonic velocity values (solid line).

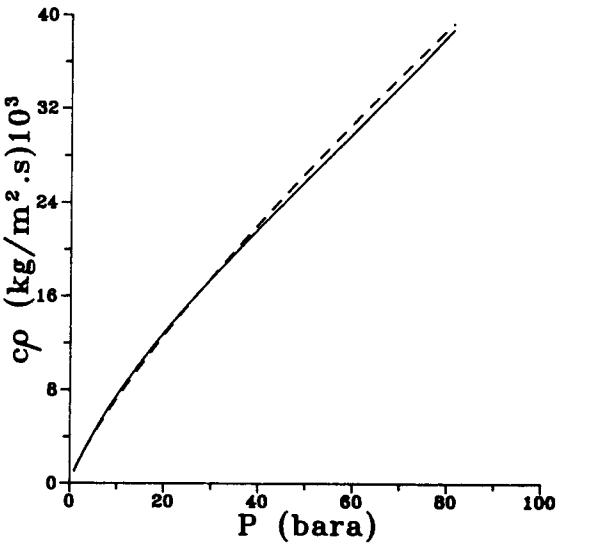


Figure 4 - Calculated (solid line) and correlated (broken line) sonic velocity with saturation pressure.

DISCUSSION

Well 11 in the Námafjall field in Iceland, was tested in 1987 to flow 20 kg/s of a steam/water mixture having an enthalpy of 2072 kJ/kg at a wellhead pressure of 27 bar-a. The steam mass fraction at these conditions should be 0.6 or 60 percent. The James-method was used to arrive at the mixture flowrate and enthalpy (James, 1966).

From Equation (21) we calculate the sonic velocity in the steam/water mixture at the wellhead, to be about 720 m/s. For comparison, from the results of Kieffer (1977), we estimate the sonic velocity to be about 400 m/s. Similarily from Meader et al. (1981) we estimate the sonic velocity to be about 350 m/s. We observe that our results give a much higher sonic velocity than estimated from the other studies.

The critical lip pressure in the Námafjall well 11 output test was 1.7-1.8 bar-g, say 1.85 bar-a. The James (1962, 1966) equation can be written

$$(Gh^{1.102}/p_c^{0.96})=16.8x10^6 \qquad ...(22)$$

where G ($kg/m^2.s$) is the mass flux, p_c (MPa) the critical lip-pressure and h (kJ) the mixture enthalpy. The mass flux at critical/choked flow conditions can be approximated by

$$G=c\rho \qquad ...(23)$$

where c is the sonic/critical/choked flow velocity and ρ the mixture density. We estimate the mixture density (from mass and energy balance and Equation 19) of Námafjall well 11 at 1.85 bar-a pressure to be 1.47 kg/m^3 and calculated the mass flux from Equation (22) to be 736.4 $kg/m^2.s$. Using these values we calculated from Equation 23 the sonic velocity to be 500 m/s. Equation (22) shows the critical mass flux in the James-tube for some mixture enthalpy and critical lip-pressure. The lip-pressure is not the pressure in the steam/water mixture immediately upsteam at the wellhead.

Table 1 - Sonic velocity (m/s) in steam/water mixtures with enthalpy corresponding to 250°C liquid water (1086 kJ/kg), flashed to lower temperatures.

Temperature (°C)	Pressure (bar)	Steam Mass Fraction	Present Work	Kieffer (1977)	Maeder (1981)
225	25.50	0.065	95	68	82
200	15.55	0.120	172	160	126
175	8.92	0.170	250	175	160
150	4.76	0.215	330	200	181

We note that our compressibility equation is a simplification of the equations used by both Kieffer (1977) and Maeder et al. (1981). [There are typographical errors in the Kieffer (1977) paper. In Equations 17 and 18 the wrong symbol is used for steam mass fraction. In Equations 17, 28 and 29, there are missing overall brackets and the exponent -1]. In our study and the two other studies, the flow is assumed frictionless. Therefore, the sonic velocity estimated from all three studies, should be greater than the empirical value obtained from the James (1962, 1966) equation. We note that the sonic velocity obtained in the present study is much greater, while the Kieffer (1977) and Maeder et al. (1981) values are smaller than the empirical James-equation value. This calls for further investigation.

To check our results in another way, we calculated the sonic velocity at several conditions typical for a two-phase geothermal well producing from liquid-dominated conditions at 250°C, see Table 1. For comparison we show the sonic velocity estimated from the results of Kieffer (1977) and Maeder et al. (1981). We observe that our results are above the others, but not by as much as for the wellhead conditions of well 11 in the Námafjall field. We note that the lower the steam mass fraction (0.07 to 0.22 in Table 1), the closer our results agree with the two other studies.

CONCLUSIONS

1. A simplified equation was derived for the compressibility of steam/water mixtures at ideal thermodynamic conditions. This equation can also give the sonic velocity in the same mixtures.
2. Calculated values of compressibility and sonic velocity were easily correlated by including the steam/water mixture density. The empirical power-fit correlations are convenient for engineering calculation.
3. The calculated sonic velocity was compared to two previous studies. The present results were 80-100 percent higher when the steam fraction was large (mainly steam vapor) and 40-80 percent higher when the steam fraction was small (mainly liquid water).

REFERENCES

Bilicki, Z., DiPippo, R., Kestin, J. and Maeder, P.F. (1982): "Available Work Analysis in the Design of Geothermal Wells," Proc., Int'l. Conf. Geothermal Energy, Florence, Italy, May, BHRA Fluid Engineering, 227-248.

Grant, M.A. and Sorey, M.L. (1979): The Compressibility and Hydraulic Diffusivity of a Water-Steam Flow," Water. Resources Res., 15 (3), 684-686.

Gudmundsson, J.S. (1986a): "Composite Model of Geothermal Reservoirs," GRC Bulletin, January, 3-10.

Gudmundsson, J.S. (1986b): "Two-Phase Wells," GRC Bulletin, March, 10-16.

Gudmundsson, J.S. and Thráinsson, H. (to be published): "Power Potential of Two-Phase Geothermal Wells.

James, R. (1962): "Steam-Water Critical Flow Through Pipes," Proc. Inst. Mech. Engrs., 176 (26), 741-748.

James, R. (1966): Measurement of Steam-water Discharging at the Speed of Sound to the Atmosphere," N.Z. Engn., October, 437-441.

Karamarakar, M. and Chen, P. (1980): A Theoretical Assessment of James' Method for the Determination of Geothermal Wellbore Discharge Characteristics, LBL Report 11498, Berkeley, California.

Kieffer, S.W. (1977): "Sound Speed in Liquid-Gas Mixtures: Water-Air and Water-Steam," J.Geoph.Res., 82 (20), 2895-2904.

Maeder, P.F., DiPippo. R., Delor, M. and Dickinson, D. (1981): The Physics of Two-Phase Flow: Choked Flow, Brown University, Report GEOFLO/10, 45 pp.

Michaelides, M.M. (1981): "Thermodynamic Properties of Geothermal Flids," Trans. GRC, 5, 361-364.

Morales G., C, Baza, J.R., Ramey, H.J. and Sanyal. S.K. (1979): "Calculations of Performance of Dry Steam Wells," Trans. GRC, 3 , 465-468.

Sveinsson, S. (1987): Compressibility and Pressure Drop in Steam Wells, Mech. Eng. Dept., University of Iceland, Project Report, 138 pp, (in Icelandic).

PROCEEDINGS, Thirteenth Workshop on Geothermal Reservoir Engineering
Stanford University, Stanford, California, January 19-21, 1988
SGP-TR-113

THE BEIJING GEOTHERMAL SYSTEM, P R CHINA: NATURAL STATE AND EXPLOITATION MODELLING STUDY OF A LOW TEMPERATURE BASEMENT AQUIFER SYSTEM

M P HOCHSTEIN
Geothermal Institute, University of Auckland, New Zealand

YANG ZHONGKE*
Institute of Geology, Academia Sinica, Beijing, P R China
(presently with Geothermal Institute, University of Auckland)

Introduction

An extensive (>800 km^2) basement aquifer confined to the top 300m of Sinian dolomites occurs beneath the Beijing Graben at 300m to 3000m depth (Fig. 1). The Beijing Geothermal Field is associated with a broad horst structure (called from now on the Beijing sub-uplift) under the SE flank where the aquifer lies typically between 600 to 1200m depth covering an area of about 70 km^2 (Fig. 2). Most of the 44 wells drilled between 1971 and 1982 were brought down on this structure and produce thermal waters at wellhead temperatures between 45 to 55°C; a few wells also produce from the deeper part of the Beijing Graben with wellhead temperatures of up to 70°C from 2600m depth. Fluid production began in 1972 and was increased to about 130 kg/s in 1985; the production rate varies significantly during the year as about 40% of the produced water is used for heating and about 60% for baths and industrial purposes (base load). As a result of this abstraction the reservoir pressure has decreased by about 3 bars. In terms of total production the Beijing Field ranks as the third largest low temperature field presently exploited in China; higher production rates are documented only for the Tianjin Field (Ouyang et al., 1986) and the Fuzhou fracture zone reservoir in Fujian Province (Huang and Goff, 1986).

A summary description of the characteristics of the Beijing Field and its utilization has been given by Zhang, Z.G. (1981), Hochstein et al. (1984), and in the final technical report of a UNDP-sponsored project (UNDP-Ministry of Geology, 1984). There was great uncertainty as to the origins of the thermal anomaly of the Beijing Field. Most of the sediments which infill the Beijing Graben have a very low permeability; temperature gradients in wells are almost linear for the sedimentary section. If one plots the temperature in the basement aquifer and the heat flow in the sediments above versus basement level, one finds that there is a higher than normal heatflow (80-90 mW/m^2) over the sub-uplift and a lower than normal flux (less than 45 mW/m^2) in the deepest part of the graben (see Fig. 3); the heat flux changes by more than a factor of two over a distance of less than 8 km (Hochstein et al., 1984). The thermal waters are of meteoric origin (Zheng, K., 1981; Zheng, K. et al., 1982).

There is still some uncertainty about management of the resource. Although the production has been moderate, the resulting pressure drop in the basement aquifer has been noticed throughout the whole production area. The permeability of the aquifer is very high as indicated by the immediate response to seasonal variations in production noticed in wells throughout the whole sub-uplift area (see Fig. 4). For economic production expensive deep well pumps cannot be used, and the presently installed shaft pumps have a lifting capacity of only about 50-60m. If production increases at the rate as measured during the period 1982-85 (i.e. from 3.5 Mt/yr to 5 Mt/yr), the data in Fig. 4 indicate that some production problems will probably be encountered when the total pressure drop reaches, say, 6 bars in the aquifer. It was uncertain whether significant natural recharge had occurred, whether re-injection was required on a larger scale to stabilize the existing pressure drop, and whether colder fluids from shallower levels were moving into the reservoir.

Some reservoir modelling was therefore required to obtain a better understanding as to which processes in the past caused the thermal anomaly of the Beijing Field and to analyze heat and mass transfer induced by past production.

Earlier models of the Beijing system

In the 1970s it was assumed that the anomalous temperatures in the basement aquifer beneath the sub-uplift were caused by some crustal hot granitic body and that deeper thermal waters ascended along deep-reaching, NE trending faults and entered the aquifer (Zheng, K., 1981). Although this simple model explains the anomalous temperatures in the uplift it does not explain the observation that the temperature in the deepest part of the graben are anomalously low (Hochstein and Caldwell, 1985); the role of deeper fracture zones was also open to criticism since anomalous temperatures near major faults, such as the Liangxiang-Qianmen Fault (see Fig. 1), had not been found.

The role of conductive heat transfer has been studied in more detail by Hochstein and Caldwell (1985). Since the thermal conductivity of the basement rocks is about 2 times greater than that of the sedimentary infill, the Beijing Graben causes a large heat flux anomaly. Detailed 2D modelling showed that about half of the anomalous increase in heat flux over the flanks (and about half the decrease in flux over the graben) could be explained by the divergence of the deep crustal heat flux. Hochstein and Caldwell inferred therefore that some additional heat transfer by secular convection is required. The temperature field of the Beijing Graben has also been modelled by members of the Institute of Geology, Academia Sinica (the study referred to in Xiong and Zhang (1986); this study also reproduced the anomalously low heat flux values over the centre of the graben using a conductive model.

Simple reservoir engineering methods have been used to assess the production potential of the Beijing Geothermal Field. Plotting observed drawdown versus accumulated production, the likely total fluid volume was estimated which could be produced for an assumed economic cut-off limit of 100m drawdown in piezometric level. For the main basement aquifer (Wumishan or Wu aquifer) this value was found to be

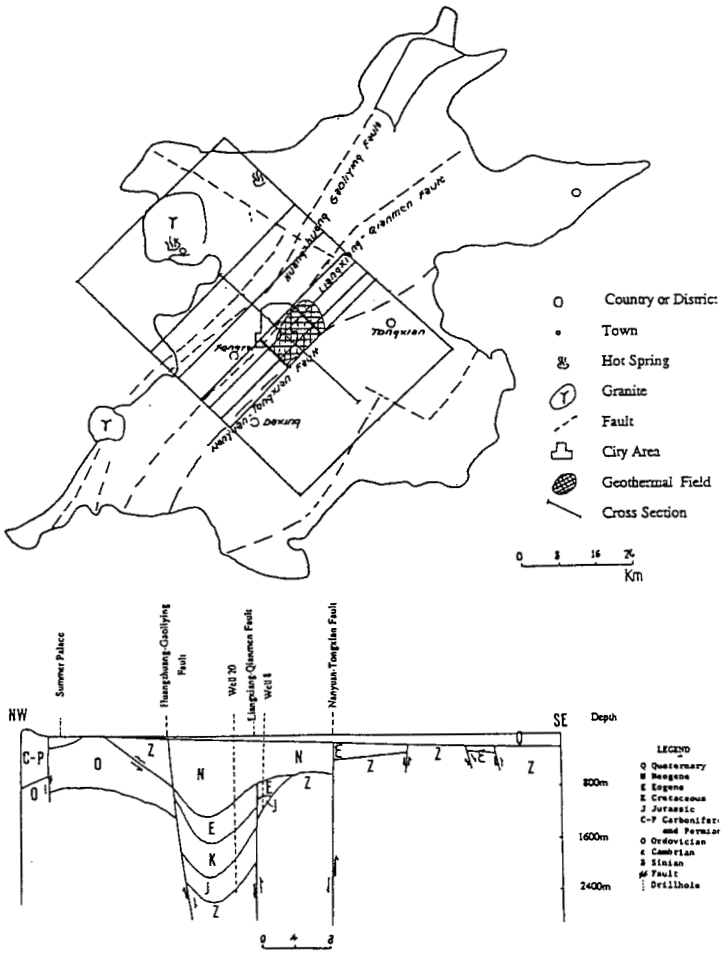


Fig. 1: Structural map and cross-section of Beijing Graben. The cross-section is perpendicular to the axis of the graben and runs through the central part of the Beijing geothermal field.

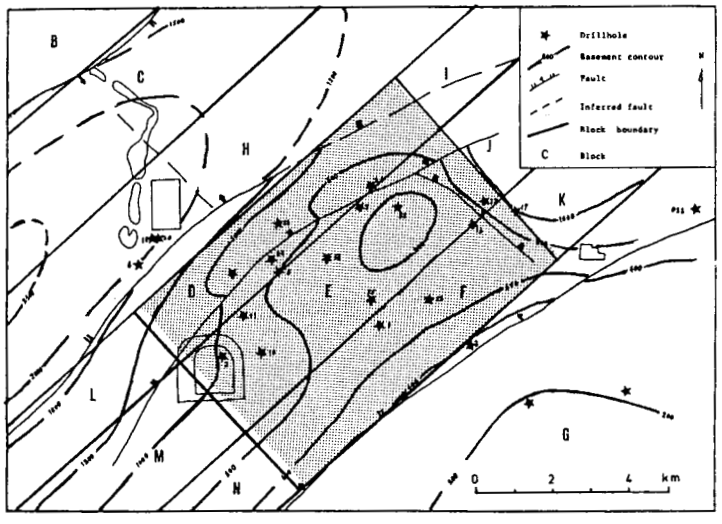


Fig. 2: Basement contour map of the Beijing sub-uplift (contour interval for stippled area is 200m; contour interval for the deeper graben shown by dashed contours is 500m). Most of the production comes from the sub-uplift (stippled pattern) covered by blocks D, E, and F; only half of the productive wells are shown.

about 350 Mt (Beijing Hydrogeological Bureau, 1984); about 10% of this inferred reserve had been produced by 1985. There is also a second basement aquifer (Tieling or Ti aquifer) at the SE margin of the sub-uplift (block F) which overlies the Wu aquifer. The total reserves of the Ti aquifer for a 100m drawdown were estimated to be 46 Mt (Beijing Hydrogeological Bureau, 1984) of which about 20% had been produced by 1985.

A stored mass-energy assessment (Hochstein, 1984) gave somewhat different figures. Considering the actual wellhead temperatures and the efficiency of existing utilization schemes (average reject temperature of 35°C), it was found that the energy potential of the Wu aquifer beneath the sub-uplift is probably no greater than 1 to 1.7 MW_{th}/km^2 for continuous load. This potential is subject to use of re-injection to stabilize reservoir pressure; a mass flow potential of 0.57 $Mt/km^2/yr$ (for 25 yr production) was inferred for the Wu aquifer.

A mass balance approach was used by Kuo (1981) to estimate the likely recharge for 1980 which was found to be about $^2/_3$ of the total annual production of 3.55 Mt. Since it can be inferred that the permeability structure in the direction of the graben axis might not vary significantly for individual units, a simple 2D reservoir model was constructed to assess the permeability of the SE recharge block (Daxing uplift; i.e. the block to the SE of the Nanyuan-Tongxian Fault in Fig. 1) which seem to control the pressure drop for any 2D model of the sub-uplift. The permeability of the Wu and Ti aquifers had been determined by pumping tests and was known to be of the order of 1 Darcy, i.e. $1E\text{-}12m^2$ (Beijing Hydrogeological Bureau, 1984). Assuming that the permeability of the rocks above and below the basement aquifer is very small ($\leq$ 1mD), and using realistic abstraction rates (22 kg/s for a 2 km wide strip), it was found that the average permeability of the recharge block was of the order of 4E-14 (i.e. 40 mD) by comparing observed and computed pressure drops in the reservoir (Hochstein, 1984); for simulation a modified SHAFT 79 program (O'Sullivan et al., 1983) was used. This simple reservoir model was also used to assess the likely pressure and temperature changes in the aquifer for an idealised "doublet scheme" where production and re-injection wells were separated by 1 km distance (Hochstein et al., 1984) and the previously cited energy potential of 1 to 1.7 Mt/km^2 was based on such "doublet schemes".

However, none of these models could explain adequately the natural heat and mass transfer in the reservoir nor could it predict actual changes in mass transfer and induced recharge inside and outside the production area. For this more detailed modelling was required.

The first conceptual model of the Beijing system (natural state)

The data described so far constitute a good data set for simulation of the Beijing system in its natural state. Such study was recently undertaken by Yang, Z. (1987). Available were the steady state temperatures in the basement aquifer for a depth range of 500 to 2600m covering almost $^2/_3$ of the central strip of the Beijing Graben in which the sub-uplift is located; in addition, some temperature data were also available for a well on the Daxing uplift and a deep (3000m) well in the deepest part of the graben. Since temperatures vary slightly for the same level in each block, a mean temperature from all wells in each block was used as observed temperature (see Table 2). Representative values were also available for rock properties (i.e. saturated density, porosity, thermal conductivity) of the major lithostratigraphic units from cores and well logs. The geological structure was known (see Fig. 1).

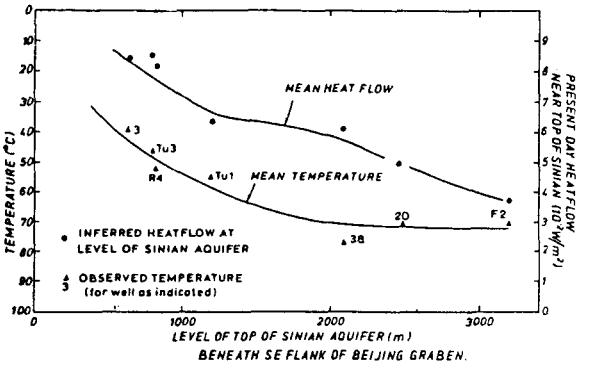


Fig. 3: Temperature at top of basement aquifer and apparent heatflow in sediments versus level of basement aquifer (Beijing Graben).

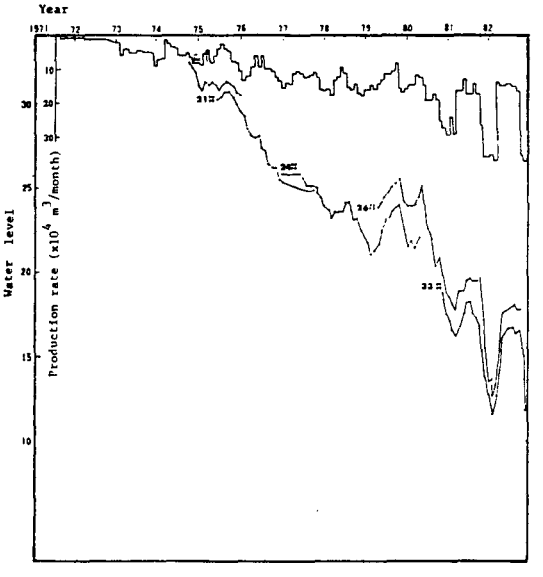


Fig. 4: Monthly production of thermal water from D and E block (see Fig. 2) and water level drawdown in selected wells of E block for period Jan. 1971 to Dec. 1982. (Note parallel tracking of WL in wells 26 and 33 which are about 5 km apart).

The permeability structure as well as the magnitude of the undisturbed heat flux at greater depths beneath the graben were poorly known; paleo-heat studies, however, indicate that the heat flux in the Neogene was probably close to 62 mW/m^2 (Prof. Wang, pers.comm.). There were, however, important constraints. The average transmissivity of the basement aquifers was known to be 300 Dm for the Wu aquifer and about 150 Dm for the Ti aquifer; both aquifers are 200 to 300m thick. The average permeability of the Jurassic and Cretaceous sediments is $\leq$ 1 mD as indicated by the observation that an uncased well which bottomed in these sediments in the centre of the graben did not fill up with water over several years. A somewhat exponential decrease in permeability was assumed for all deep rocks lying beneath the basement aquifer. The likely permeability range for rocks in the Daxing uplift (block G in Fig. 5) was known from earlier modelling (Hochstein, 1984).

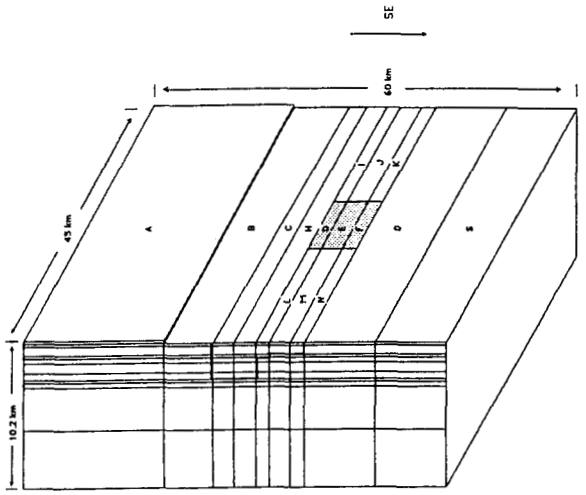


Fig. 5: Quasi 3-dimensional model of the Beijing geothermal system. Strip A represents the Yanshan mountain area where most infiltration of meteoric water occurs; strip B represents the Beijing W Rise; C and H lie over the deepest part of the Beijing Graben, the stippled blocks D,E,F define the Beijing sub-uplift, strips L,M,N and I,J,K represent the SE flank of the graben to the SW and NE respectively, strips G and S outline the Daxing uplift. The thick solid line in the section represents the Beijing Graben.

The aim of the first model study (Yang, Z., 1987) was to simulate a natural mass transfer pattern where infiltrating meteoric waters from the recharge blocks A,B as well as G and S (Fig. 5) penetrate deeply into the crust to depths greater than 5 km, where they sweep out some heat and ascend beneath the graben and the flanks into the basement aquifer. A temperature field given by the normal heatflux was used to define the initial condition; a modified SHAFT 79 program (O'Sullivan et al., 1983) was used to simulate convection until steady state conditions were reached. Matching parameter was the temperature observed in various blocks of the basement aquifer and the overlying sediments.

The first model already gave acceptable fits; simulation had to be run for a period of about 6×10^6 yr to obtain steady state conditions. Matching of observed and computed temperatures was improved by a trial and error approach during which the initial permeability structure was changed sequentially. Modelling confirmed that the vertical permeability (k_z) of the highly permeable layers had to be about one order of magnitude lower than the horizontal permeability (k_x); this phenomenon has also been inferred from modelling of high temperature systems (O'Sullivan , 1985). For the top layers a ratio of k_x/k_z of 100:1 had to be used to avoid significant cooling. The permeability structure of the best fit model (model 1) is similar to that listed in Table 1, although the data of this table describe the permeability structure of a revised model described in the next paragraph.

Tha main outcome of the simulation was that the temperature structure of the Beijing geothermal system can be explained by secular convection involving a mass transfer of only about 13 kg/s of deeper fluids which ascend into the basement aquifer beneath the sub-uplift; about half of this flow ascends to the surface and is discharged into the groundwater; the other portion constitutes a lateral outflow. Because of the high permeability of the basement aquifers, additional heat is thus transferred from the graben to the flanks. The setting-up time to reach steady state convection is of the order of 6 Mill yrs, i.e. minimum geological lifetime of the system. The observed temperatures within the graben and over the flanks can be reproduced with an error which for most blocks is less than ±2°C. The best fit model requires a natural heatflux of 56 mW/m^2 at 10 km depth; the heat-generating capacity of rocks above this level was neglected.

To test the pressure response of the model to actual production, the width in N-S extension of the model was reduced to that of the Beijing sub-uplift (i.e. about 10 km, see Fig. 2) thus neglecting any lateral flow within the graben. The model was subjected to actual abstraction rates as documented for the period 1971-1982. The overall pattern of the pressure drop as shown in Fig. 4 could be reproduced without any further changes of the model (Yang, Z., 1987).

Revised conceptual model of the Beijing system (natural state and production simulation

Although the first conceptual model could reproduce the natural state situation and thus became the first model describing the likely heat and mass transfer for the whole Beijing basement aquifer system, it could not be used for detailed reservoir modelling since it was essentially a two-dimensional model. The model was therefore revised by considering likely three-dimensional effects related to horizontal anisotropy of permeability and the geometry of the sub-uplift.

For models 3, 4, 7 and 8, separate blocks D, E and F were created which coincide with the Beijing sub-uplift (Fig. 5); for model 3, horiziontal anisotropy was neglected, otherwise its permeability structure is the same as that listed in Table 1. Model 4 was similar to that of model 3 except that horizontal permeability for all basement rocks was reduced by a factor of two in x-direction (perpendicular to the axis of the graben). The direction of the main faults running parallel to the axis of the graben indicates that jointing of the basement rocks could be significant in NE direction (y-axis of the model); minor faulting in NW direction (x-direction of model) also exists (see Fig. 1). For models 7 and 8 the geometry of the uplift was taken into account by moving the level of the top of the basement in columns D, E and F by 200m above that of the basement in the adjacent blocks I, J, K and L, M, N. The geometry of models 7 and 8 is shown in the form of sliced sections in Fig. 6. For model 7, horizontal anisotropy was neglected; for model 8, pressure interference in the basement aquifer in columns E and F was decoupled by assuming that the permeability in x-direction is 10 times less than that in y-direction (for layers SNW and SNT in Table 1 only). The natural heatflow at 10 km depth was kept constant for all 4 models ($54\ mW/m^2$).

The computed and observed temperatures for the central strip with drillhole control, i.e. for columns H, D, E and F, are shown in Fig. 7a,b,c, and d respectively. It can be seen that except for model 4 in H-block, all other models produce quite acceptable fits to observed temperatures. Even the fit of model 4 for H-block could be acceptable if one allows for the fact that the observed temperature profile for this block is based on one well only. The pressure response of each model to actual abstraction scenarios (abstraction by means of a fictitious well intersecting the basement aquifer in the centre of columns H, D, E and F), however, allowed better discrimination. Here model 8, i.e. the model with pronounced fracture permeability in the aquifer for colums E and F, produced the best fit between observed and computed pressure drop (see Fig. 8a, b for model 8 in comparison to Fig. 8c, d for the other

TABLE 1: Rock properties of model 7.

(for location of layers listed under rock types refer to Fig. 6).

ROCK TYPE	DENSITY (kg/m3)	POROSITY	PERMEABILITY (md) HORI.	VERTI.	THERMAL COND. (mW/Deg.C m)	THERMAL CAPACITY (kJ/ C kg)
QUA	2700	0.20	1000	10	1.7	900
QU1	2000	0.20	300	3	1.7	900
CE1	2000	0.12	50	0.5	1.8	900
CE2	2000	0.10	10	0.1	1.9	900
CE3	2000	0.09	7.5	0.1	1.9	900
CRE	2450	0.05	1.0	0.1	2.0	900
JUR	2520	0.04	0.5	0.05	2.4	900
YX1	2650	0.04	100	10	3.0	900
YX2	2650	0.03	80	8	3.0	900
DX1	2650	0.02	80	8	3.5	900
DX2	2650	0.01	60	6	3.5	900
DSN	2700	0.01	60	6	4.0	900
SN1	2700	0.01	100	10	4.0	900
SN2	2700	0.01	20	2	4.0	900
SN3	2700	0.01	0.2	0.02	4.0	900
SNW	2700	0.03	1000	100	4.0	900
SNT	2700	0.03	500	50	4.0	900
SWT	2700	0.01	300	30	4.0	900
GRA	2700	0.01	0.05	0.05	2.6	900

Note: For model 3 the same properties were used as in Table 1, except that horizontal permeability for layer DX2 and DSN was taken as 50 mD.
For model 4 the same properties were used as for model 3, except that the horizontal permeability in x-direction (see text) was half that of the horizontal permeability for model 1 for layers YX1, YX2, DX1, DX2, DSN, SN1, SN2, SN3, SNW, SNT, SWT.
For model 8 the same properties were used as for model 7, except that the horizontal permeability in x-direction (see text) was 1/10th of that listed in Table 1 for layers SNW and SNT (i.e. the productive horizons).

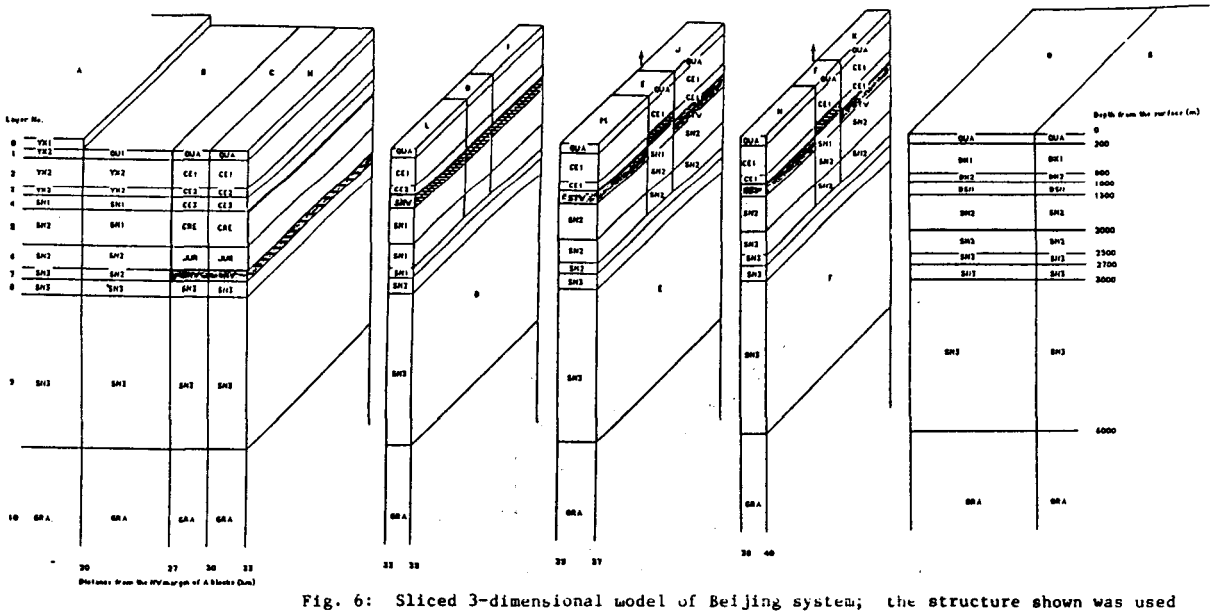


Fig. 6: Sliced 3-dimensional model of Beijing system; the structure shown was used for best fit models No. 7 and 8 referred to in the text. The darker shaded band outlines the highly permeable layers SNT, STW, and SNW coinciding with a thick karst layer at the top of the Sinian basement. The main production comes from two blocks, F3 and F3.

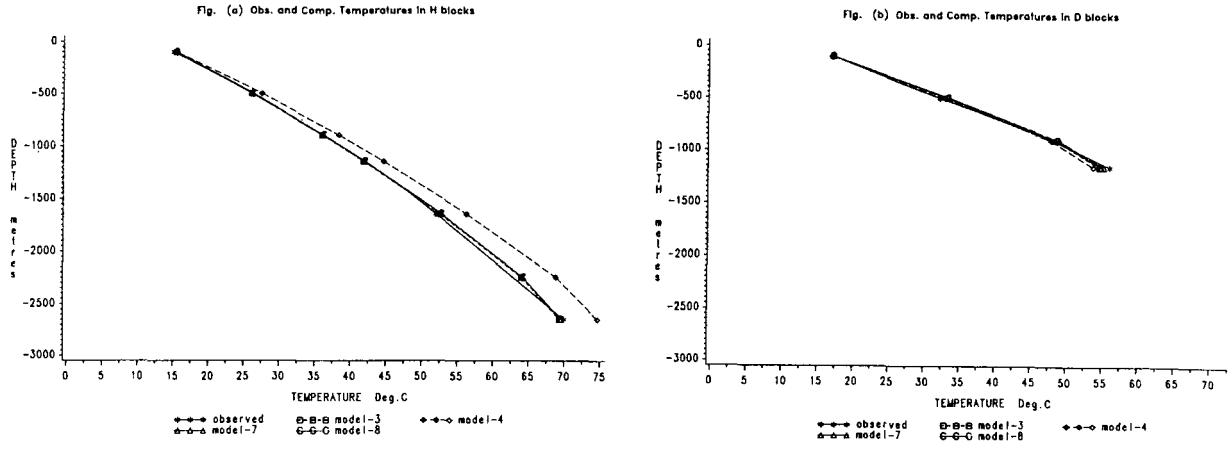


Fig. 7a,b: Observed and computed temperatures for revised models 3,4,7 and 8 of the Beijing geothermal system. Temperatures for models 7 and 8 are listed also in Table 2. Fig. 7a shows temperatures for H-block (deepest part of Beijing Graben), Figs. 7b,c,d show temperatures for D,E and F blocks respectively which are located over the Beijing sub-uplift (refer to Fig. 2).

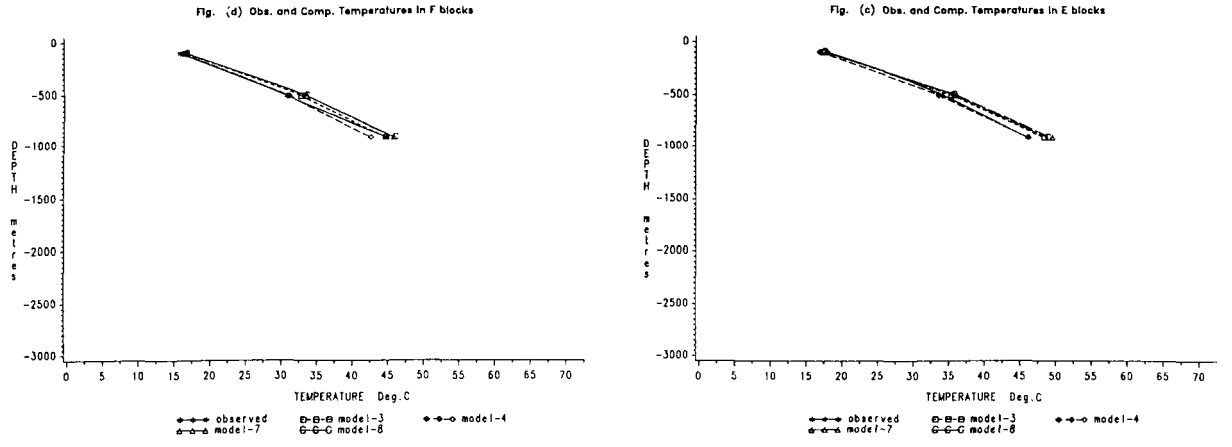


Fig. 7c,d: Observed and computed temperatures for revised models 3,4,7 and 8; for details refer to caption for Fig. 7a,b.

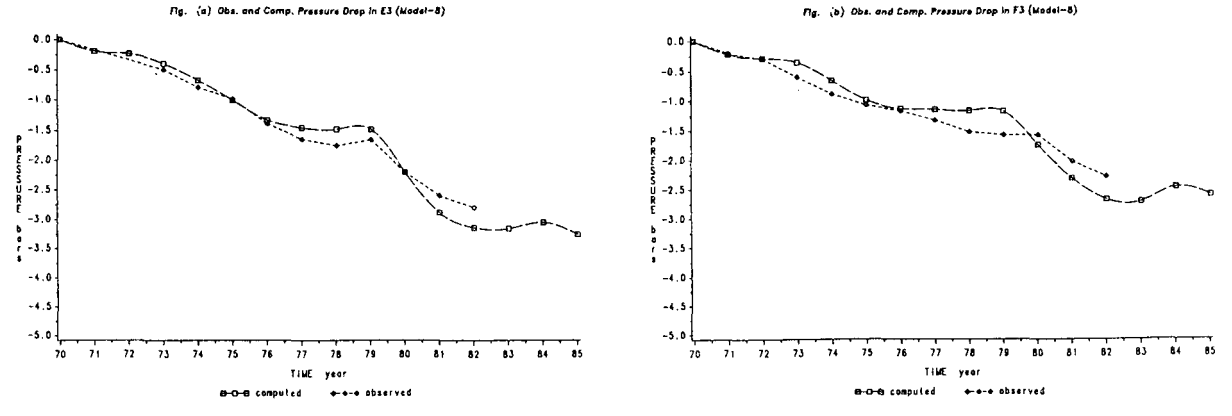
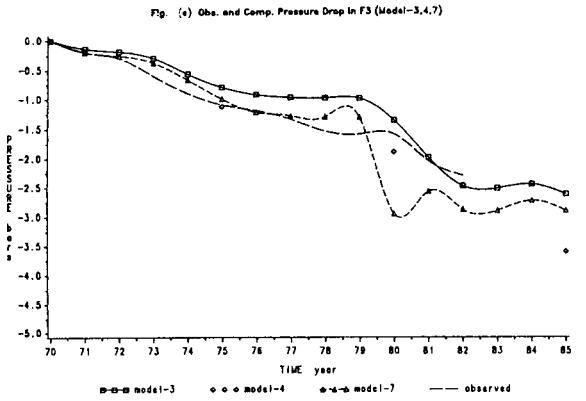


Fig. 8a,b: Observed and computed pressure drop for best fit model 8 caused by production from basement aquifer beneath Beijing sub-uplift between 1971 and 1985. Fig. 8a shows situation for production from E3 block (Wu aquifer only); Fig. 8b refers to F3 blocks (mainly Ti aquifer). For structure of E3 and F3 blocks refer to Fig. 6.



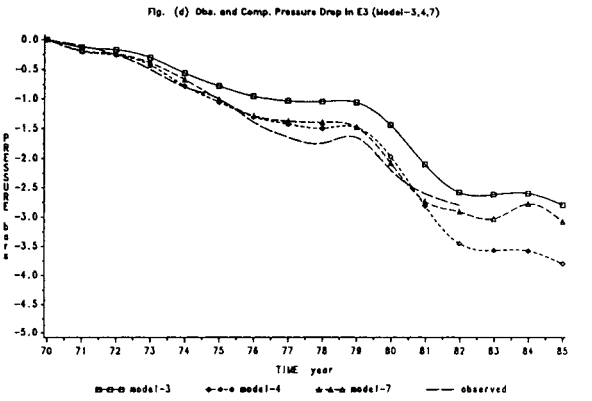


Fig. 8c,d: Observed and computed pressure drop for models 3,4 and 7 (refer to text) caused by production from basement aquifer beneath Beijing sub-uplift between 1971 and 1985. Fig. 8c depicts scenario for E3 block (Wu aquifer only). Fig. 8d refers to F3 block (mainly Ti aquifer).

models). Observed and computed temperatures of models 7 and 8 for natural state conditions are listed separately in Table 2.

The role of recharge in the revised conceptual model and implications

After obtaining a model which explains in a satisfactory way both heat and mass transfer in the natural and the dynamic stage, we can now look at the role of recharge as predicted by the best fit models (Nos. 7 and 8). By comparing net inflow rates and production rates for each productive block it was found that after one year of production almost all the produced fluids were recharged (total net imbalance was on average only about -0.2% of total production). Most of the induced recharge occurred through the bottom of the basement aquifer block (between 65 to 80% of total induced net recharge). As a result, the temperature of the produced fluids remained almost constant; the model indicates temperature changes of less than -0.1°C for a production period of 15 years, which agrees with observed data. Because of the high permeability of the basement aquifer the trend in the observed pressure drop can be explained simply in terms of increases in the average rate of production. If production remained constant at the 1985 level, pressures would stabilize within one year. The observed plateau in the pressure drop curves in Figs. 8a,b is the result of rather constant production which took place during 1977 to 1979.

The simulation has various implications for the reservoir management of the Beijing basement aquifer. Re-injection of waste fluids into the aquifer is obviously not required to achieve stabilization of reservoir pressure since such stabilization can be brought about by maintaining constant production rates. In view of the almost perfect recharge indicated by the revised reservoir model, the mass flow potential for a given pressure drop at constant production rates appears to be almost unlimited. The long term mass flow potential of the Beijing reservoir appears therefore to be limited only by the characteristics of the installed pumps. For the presently installed shaft pumps it is likely that the long term mass flow potential is reached when the pressure in the basement aquifer has dropped by about 5 to 6 bars, which implies that the annual production of about 5 Mt in 1985 can probably be increased by a factor of 2 (i.e. about 10 Mt/yr), although the yield of individual wells would decrease.

TABLE 2: Observed (T_{obs}) and computed (T_{comp}) natural state temperatures for best fit model 7 for columns H,D,E,F and G; (for position of columns refer to Fig. 6).

H

Depth (m)	T.obs (Deg.C)	T.comp (Deg.C)
100	15	15.4
500	26	26.6 (-0.4)
900	36	36,2
1150	42	42.0
1650	52	52.8
2250		64.3
2650	70	69.6

D

Depth (m)	T.obs (Deg.C)	T.comp (Deg.C)
100	17±1	17.0
500	32±2	33.4 (-0.2)
900	48±1	49.0 (-0.3)
1150	57±3	55.2
* 1162+178	**56±5	

E

Depth (m)	T.obs (Deg.C)	T.comp (Deg.C)
100	18±2	17.7 (-0.1)
500	34±4	36.0 (-0.2)
900	46±4	49.5 (-0.6)
* 799+126	**45±4	

F

Depth (m)	T.obs (Deg.C)	T.comp (Deg.C)
100	16±1	17.0
500	31±3	33.8
900	44±6	46.0 (+0.2)
* 871+183	**44±5	

G

Depth (m)	T.obs (Deg.C)	T.comp (Deg.C)
100		16.9
500	28	27.0

N.B.. * depths of the last entry in D,E, F refer to average depth of production wells in each block;
** temperatures are average wellhead temperatures.

Note: Temperature differences (°C) between model 8 and model 7 (natural state) are listed in parentheses in the T.comp column.

Summary discussion

Computer modelling of the Beijing low temperature, basement aquifer system has shown that secular natural convection of meteoric waters down to depths greater than 5 km can produce a temperature field which is similar to that observed in deep wells. Secular convection occurs within a crustal block with the approximate dimensions of 45 x 60 x 10 km; the Beijing system is probably one of the largest secular convecting systems described so far. It is driven entirely by the crustal heatflow which appears to be slightly lower (i.e. 54 mW/m^2) than the average continental heat flux. The study has several geophysical implications:

(1) The apparent natural heatflow inferred from linear temperature gradients in deep wells over large basins underlain by permeable basement aquifers is not representative for the actual crustal heatflow which probably can only be assessed from natural state modelling studies.

(2) Thermal anomalies associated with large sedimentary basins underlain by basement aquifers involve deeply penetrating meteoric waters. Although the maximum depth of penetration cannot be estimated with confidence for the Beijing system (because of uncertainties in the deeper permeability structure), it is likely that meteoric waters descend to at least 5 km depth beneath the Beijing Graben.

(3) Natural flowrates beneath the basement aquifer are very small (of the order of mm/yr), hence all water in the basement aquifer is very old water. Cation species in the thermal fluids should therefore be re-equilibrated with respect to aquifer temperature. Apparent higher equilibria temperatures, which have been associated with "deeper upflows" and the concept of mixing of deeper upflows (Beijing Hydrogeological Bureau, 1984) are open to criticism. Published high equilibrium temperatures are based on geothermometers involving sodium (Na) which might not re-equilibrate because of the absence of sodium-bearing minerals in the thick dolomite sequence.

Modelling of the observed temperatures in the natural state allows an approximate definition of the permeability structure of the Beijing system, but matching of observed and computed steady state temperatures is not sufficient to define details of the reservoir. For this, modelling of the pressure response of the reservoir under production has to be used. Although the area of the production blocks of good fit models is still very large (between 20 and 25 km^2) thus preventing any precise fits, the modelling of heat and mass transfer of the Beijing reservoir under

steady temperatures is not sufficient to define details of the reservoir. For this, modelling of the pressure response of the reservoir under production has to be used. Although the area of the production blocks of good fit models is still very large (between 20 and 25 km^2) thus preventing any precise fits, the modelling of heat and mass transfer of the Beijing reservoir under exploitation provides valuable information for the management of the resource.

(4) Over most of the Beijing sub-uplift, the basement aquifer is very homogeneous although some inhomogeneity occurs in block F; this probably also applies to other parts of the Beijing Graben.

Anisotropic flow associated with pronounced fracture permeability is probably not as significant as previously thought. High vertical permeability previously associated with inferred upflows along deep-reaching NE-trending major faults is also not significant since modelling showed that temperatures near such faults are significantly elevated in the natural state model - such higher temperatures, however, have not been observed. Estimation of average transmissivity from pump tests using line source solutions give almost the same permeability as pressure response modelling.

(5) Pressure response modelling has shown that induced recharge almost balances production (>99.7%). Most of the induced recharge (>70% by mass) enters the production blocks through the bottom; changes in temperature (enthalpy) of the produced fluids is therefore almost nil (<0.1 °C for a 15 yr period). For present-day production, stabilization of pressure drop by re-injection of colder waste fluids is not required since such stabilization can be brought about by constant production rates. If colder waste fluids are not re-injected, this also avoids cooling of the reservoir.

(6) Since induced recharge of the Beijing aquifer practically balances production, the concept of a finite mass production potential has to be revised. The final production potential is that given by the lifting capacity of the pumps at the wellhead which allow economic production of fluids for a given drawdown which, in turn, can be predicted by the reservoir model for each production block.

Acknowledgement

Prof Wang Jiyang (Institute of Geology, Academia Sinica, Beijing) provided additional temperature measurements and thermal conductivity data for wells in the Beijing Graben. Prof M J O'Sullivan (University of Auckland) offered valuable assistance for the "fine-tuning" of the models. Mr Yang Zhongke's research at the Geothermal Institute, University of Auckland, has been sponsored by a UNDP geothermal training fellowship (INT/84/011) from the Division for Global and Interregional Projects, UNDP, (New York).

References

Beijing Hydrogeological Bureau, 1984. Final Technical Report on technical evaluation of geothermal resources and their development in Beijing area. In: UNDP-Ministry of Geology and Mineral Resources of P R China. Final technical report UNDP/China/CPR/80/065, Beijing, 9-36.

HOCHSTEIN, M.P., 1984. Technical evaluation of geothermal resources and their development in the Beijing Area. In: UNDP-Ministry of Geology and Mineral Resources of P R China. Final technical report UNDP/China/CPR/80/065, Beijing, 37-112.

HOCHSTEIN, M.P., McKIBBIN, R., YANG YUTANG, 1984. Assessment of the Beijing geothermal prospect (P R China). Proc. 6th New Zealand Geothermal Workshop 1984, 91-95.

HOCHSTEIN, M.P. and CALDWELL, G., 1985. Heat source characteristics of some warm and hot spring systems in China and Thailand. 1985 Int. Symposium on Geothermal Energy, Geothermal Resources Council, Transactions 9 (Int. Volume): 557-562.

HUANG, H.F. and GOFF, F., 1986. Hydrogeochemistry and reservoir model of Fuzhou geothermal field, China. Journal of Volcanology and Geothermal Research 27: 203-227.

KUO, T., 1981. CPR/80/013 consultant report. UNDP-Beijing (unpublished), 6 pp.

O'SULLIVAN, M.J., 1985. Geothermal reservoir simulation. Energy Research 9, 319-332.

O'SULLIVAN, M.J., ZYVOLOSKI, G., BLAKELEY, M.R., 1983. Computer modelling of geothermal reservoirs. School of Engineering Report 318, University of Auckland.

OUYANG, J., O'SULLIVAN, M.J., HOCHSTEIN, M.P., 1986. Modelling of low temperature aquifers in the Tianjin Area (P R China). Proc. 8th New Zealand Geothermal Workshop 1986, 49-52.

UNDP-Ministry of Geology and Mineral Resources of P R China, 1984. Final technical report UNDP/China/CPR/80/065. UNDP Beijing, 112 pp (in English and Chinese).

XIONG, L. and ZHANG, J., 1986. Applications of finite element method to geothermal studies. Scientific Press, Beijing, 138 pp (in Chinese); (reference to the Beijing model is made on p. 60-61).

YANG, Z.K., 1987. Simulation of the Beijing geothermal system. Geothermal Institute Project Report 87.27, University of Auckland, New Zealand, 40 pp.

ZHANG, Z.G., 1981. An assessment of the geothermal resources of the N China Basin. Geothermal Institute Project Report 81.26, University of Auckland, New Zealand, 36 pp.

ZHENG, K., 1981. The features of geothermal mineral water in the SE part of Beijing. In: Symposium on geothermics of China, selected contributions. Scientific Press, Beijing, 67-74 (in Chinese).

ZHENG, K., MA, D.L., XIE, C.F., HUANG, S.Y., FENG, J.H., WU, J.S., 1982. Preliminary interpretation of isotopic studies of geothermal waters from the Beijing Region (P R China). Proc. of Pacific Geothermal Conference 1982 (incorporating the 4th New Zealand Geothermal Workshop, Part 2, 491-496.

PROCEEDINGS, Thirteenth Workshop on Geothermal Reservoir Engineering
Stanford University, Stanford, California, January 19-21, 1988
SGP-TR-113

USING PRECISION GRAVITY DATA IN GEOTHERMAL RESERVOIR ENGINEERING MODELING STUDIES

Paul G. Atkinson and Jens R. Pedersen

Unocal Geothermal Division
3576 Unocal Place
Santa Rosa, CA 95401

ABSTRACT

Precision gravity measurements taken at various times over a geothermal field can be used to derive information about influx into the reservoir. Output from a reservoir simulation program can be used to compute surface gravity fields and time histories. Comparison of such computed results with field-measured gravity data can add confidence to simulation models, and provide insight into reservoir processes. Such a comparison is made for the Bulalo field in the Philippines.

INTRODUCTION

Reservoir engineering calculations of mass and energy balances on producing geothermal reservoirs require information about in- and out-flows from the reservoir. Such information is usually available for surface flows: production and injection rates can be measured; and natural discharge rates can be estimated. Values for subsurface in- or out-flows are much more elusive. One method commonly used to estimate aquifer influx is via a history matching process whereby reservoir performance is computed for various strengths of influx, and then matched against observed performance (Gudmundsson, and Olsen, 1985). The best match is then considered to represent an estimate of influx into the reservoir. This methodology is directly analogous to the use of influx models in material balance calculations in the oil and gas industry (Craft and Hawkins, 1959).

A more direct and independent method of estimating influx is through repeat precision gravity surveys over a producing field. When such surveys are carried out with appropriate accuracy, they allow an estimate of mass loss between surveys to be made. This estimate can then be compared with net surface withdrawals (production minus injection) to compute influx. Such calculations have been made for the Wairakei field (Hunt, 1970; Hunt, 1977; Allis and Hunt, 1986).

This paper first reviews the basic principles of repeat gravity surveys as they pertain to estimating influx into producing geothermal reservoirs. It then describes the coupling of precision gravity data with reservoir simulation models. Three examples of such a coupling are then presented: two for idealized reservoirs; and one for the Bulalo field in the Philippines.

GRAVITY: THEORY AND MEASUREMENT

Gravity relates, through fundamental elements of physics, the force exerted on a body on the surface of a planet to the mass distribution surrounding the body. The gravitational pull on the surface of the earth is not uniform, and in fact, subtle variations in gravity are commonly used to identify the presence of ore bodies or geological structures. This use of gravity measurement as a geophysical prospecting tool is described in standard references such as Dobrin (1960). The magnitude of gravity on the surface of the earth is approximately 980 gals. Exploration geophysics is usually looking at variations on the order of milligals. Precision gravity measurements discussed in this paper deal with variations on the order of 0.01 milligals, or 10 microgals; hence the term "precision".

As mass is removed from a geothermal reservoir, the gravity field above the reservoir will decrease. By measuring the surface gravity field at two points in time over a producing reservoir, the change in gravity over the reservoir during the time interval can be determined. This delta-gravity field can be used in various ways. These are:

1. To qualitatively identify 100% influx, as for example was done for Wairakei, when the delta-gravity values approached zero (Hunt, 1977);

2. To integrate under the delta-gravity contours to obtain the net mass loss implied by the contours (Hunt, 1977); and

3. To model the areal detail of the observed delta-gravity contours with calculations derived from a reservoir simulator.

Instruments are commercially available to measure gravity with a precision of $\pm$ 1 microgal (e.g., LaCoste & Romberg, Model D gravimeters). When making comparisons of repeat measurements at a given site, known

temporal effects need to be corrected for. Three major effects requiring correction are subsidence (3 microgals/cm), earth tides (up to 230 microgals) and meter drift (assumed linear with time after removal of earth tides). Our field wide surveys in the Philippines are run using a tight network configuration (Lambert and Beaumont, 1977). Approximately 125 benchmarks are measured using 300 independent estimates of gravity differences between benchmark pairs. The survey takes about two months to complete. After corrections for known subsidence, earth tides and meter drift, the network is least-squares adjusted (Eckhardt, 1986). The resulting average error at a benchmark is $\pm$ 7 microgals. By comparison, typical reservoir effects can be expected to be about 100 microgals per 4 million megawatt-hrs of production. Other non-reservoir effects due mainly to seasonal effects of rainfall are $\pm$ 10 microgals.

Correcting for subsidence effects through high order levelling surveys is probably the single most expensive element of carrying out meaningful precision gravity surveys over a producing geothermal field. In general, both the gravity and levelling surveys need to extend far beyond the limits of the producing field.

NUMERICAL MODELLING OF GRAVITY FIELDS

We have developed a program which uses information from a three-dimensional reservoir simulator to compute surface gravity fields corresponding to any state of the simulator. The gravity calculation procedure uses the method of Nagy (1966) to compute the gravity effect at any surface point resulting from a subsurface stacked set of rectangular prisms comprising the cartesian discretization of a reservoir problem. Thus, we can compute the surface delta-gravity field between two times resulting from the change in mass distribution in the reservoir. The following presents such calculations for two idealized reservoirs and then presents both field results and calculations for the Bulalo field in the Philippines.

IDEALIZED RESERVOIR WITH NO INFLUX

Figure 1 presents gravity profiles at two different times over hypothetical Reservoir A in order to illustrate various points. The computed delta-gravity field has a well-defined maximum directly above the reservoir, and extends far past the edges of the reservoir. In principle such a field is measurable with an instrument whose precision is $\pm$ 1 microgal. As net mass loss from the reservoir increases, the volume under the delta-gravity surface can be seen to increase. Gauss' theorem states that this volume is directly proportional to the net mass loss from the reservoir (Hammer, 1945; LaFehr, 1965). Thus, integrating under the 10-year surface would result in twice the volume under the five-year curve.

IDEALIZED RESERVOIR WITH INFLUX

A series of calculations were next made for a rectangular hypothetical porous medium Reservoir B, in order to illustrate the impact of influx on surface gravity. The reservoir has dimensions 9000 ft x 9000 ft x 5000 ft deep, and top at a plane at 1500 ft subsea. It is initially filled with liquid at boiling-point-with-depth conditions, has 12% porosity, and 100 md permeability. Steam for 200 MW is produced from the upper part of one quadrant. 100% of the associated brine

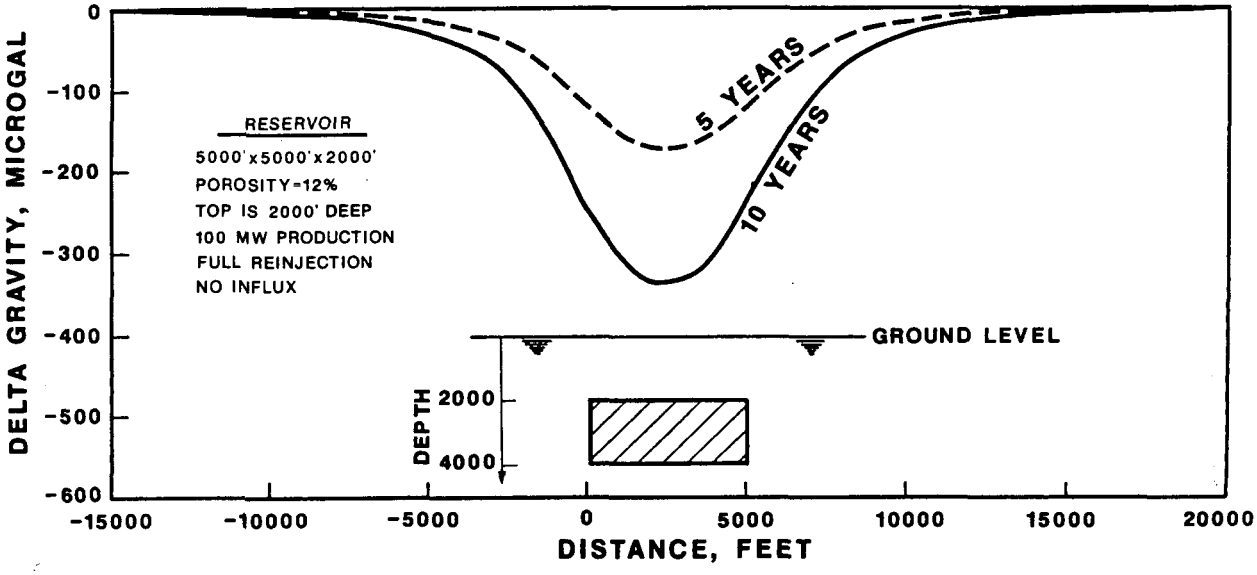


Figure 1. Delta gravity profiles over center of idealized Reservoir A

and 20% of the steam are injected as liquid into an adjacent quadrant. Case 1 was run with no influx, and Case 2 with deep hot influx along the bottom edge of the two remaining quadrants. Figure 2 illustrates this system. Both cases develop an extensive two-phase zone around the producing wells.

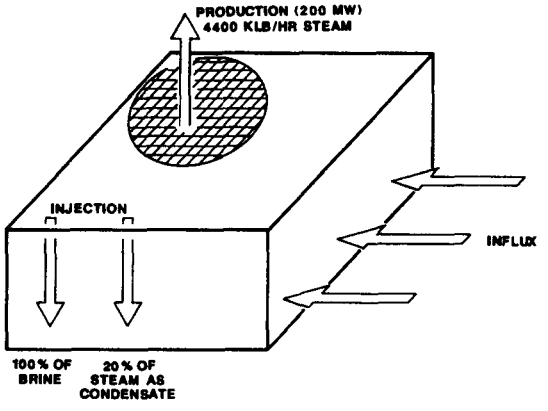


Figure 2. Schematic of idealized Reservoir B

Figure 3 illustrates the time history of gravity and various computed reservoir parameters during the ten-year period. Net mass depletion falls linearly with time for no influx. Influx has little effect on system performance until after three years of production, at which time its effects become important. The computed gravity response over the reservoir can be seen to mimic the net mass depletion curve. The details of the gravity response shown are certainly detectable with a well planned gravity survey program.

Figure 3 depicts the impact of influx on gravity as well as more traditional reservoir engineering measures for the specific configuration of Reservoir B. The effects of reservoir physics on surface gravity are subtle, and other configurations may act differently.

PRECISION GRAVITY AT BULALO

The Bulalo Geothermal Field is located in the Philippines approximately 30 miles south of Manila. The field is operated by Philippine

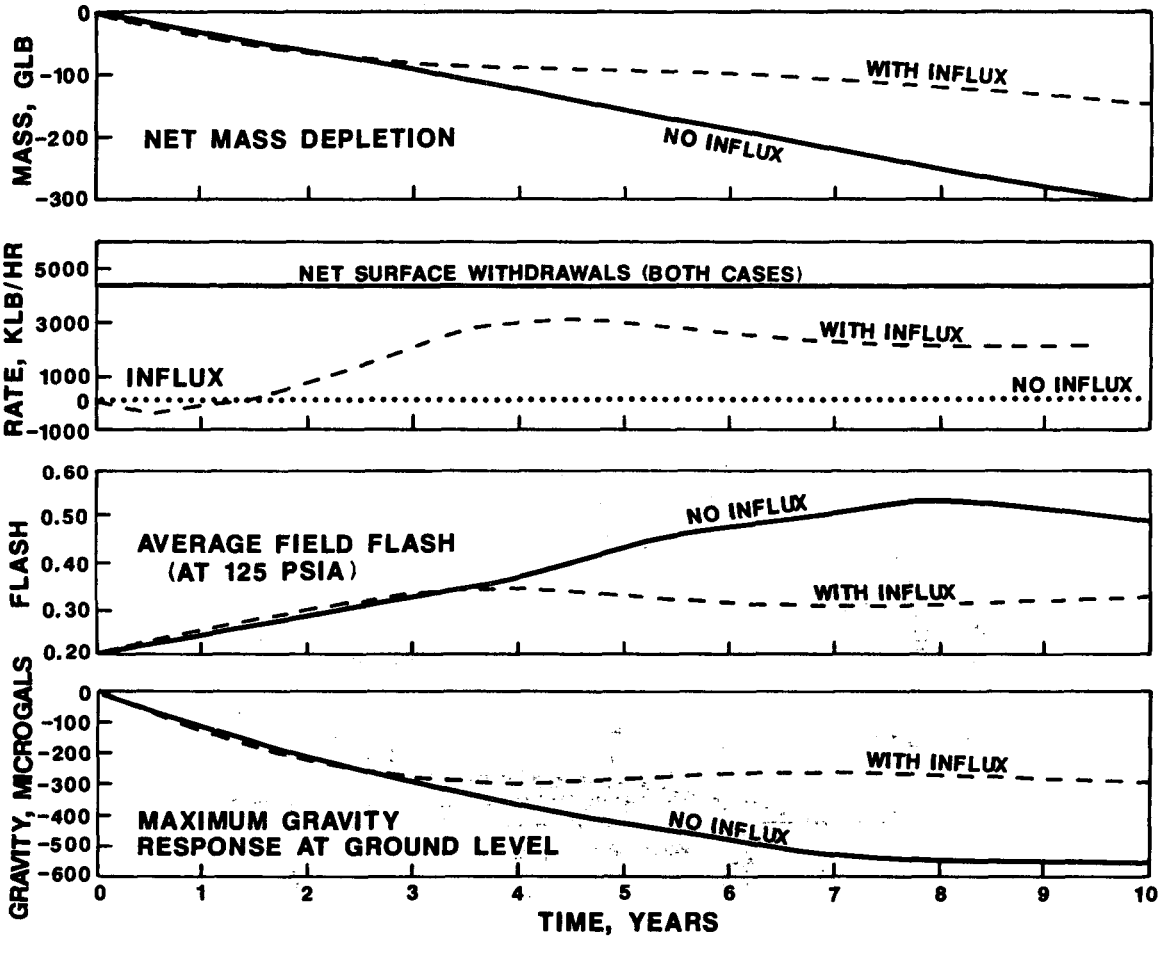


Figure 3. Computed history of Reservoir B performance

Geothermal, Inc. (PGI, a subsidiary of Unocal) under a contract with the National Power Corporation of the Philippines. The field has been producing commercially since 1979, and currently has 330 MW of installed capacity. Figure 4 presents the history of net surface production at Bulalo since 1979.

Five fieldwide precision gravity surveys have been carried out at Bulalo since 1980, as indicated on Figure 4. After 1980, each new precision gravity survey can be used to infer overall mass loss from the system over the intervening time period. When this is compared with net surface production (production minus injection), influx can be computed. Figure 4 presents the resulting influx rates averaged over each time period. Up through 1985 gravity-inferred influx is a small fraction of net production. During 1986 and 1987 gravity-inferred influx has increased significantly.

Figure 4 also presents the influx rate computed by a three-dimensional reservoir simulation model of the Bulalo Field. The model describes the Bulalo reservoir with a 1100 block double-porosity configuration. It as been calibrated against histories of individual well pressures and producing enthalpies through 1985. While the calibration can still be improved upon, the important elements of reservoir performance were reasonably well approximated by allowing only negligible influx into the reservoir. This behavior is consistent with gravity-inferred influx rates through 1985. The recent increase in gravity-inferred influx is anomalous, and is not associated with any obvious changes in reservoir performance. Our current hypothesis is that it is associated with subtle near surface or data processing effects, rather than a real increase in influx rate. The next gravity survey will be run in April-May, 1988.

Figure 5 presents a simplified map of the Bulalo field. Also shown are the locations of the power plants and various outlying wells. BM66 is a benchmark located in the center of the production area. Figure 6 presents observed and simulator delta-gravity

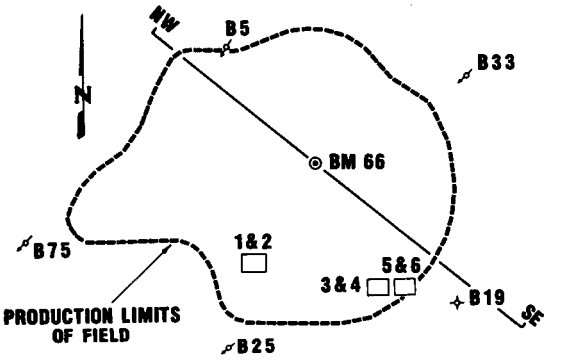


Figure 5. Simplified map of Bulalo

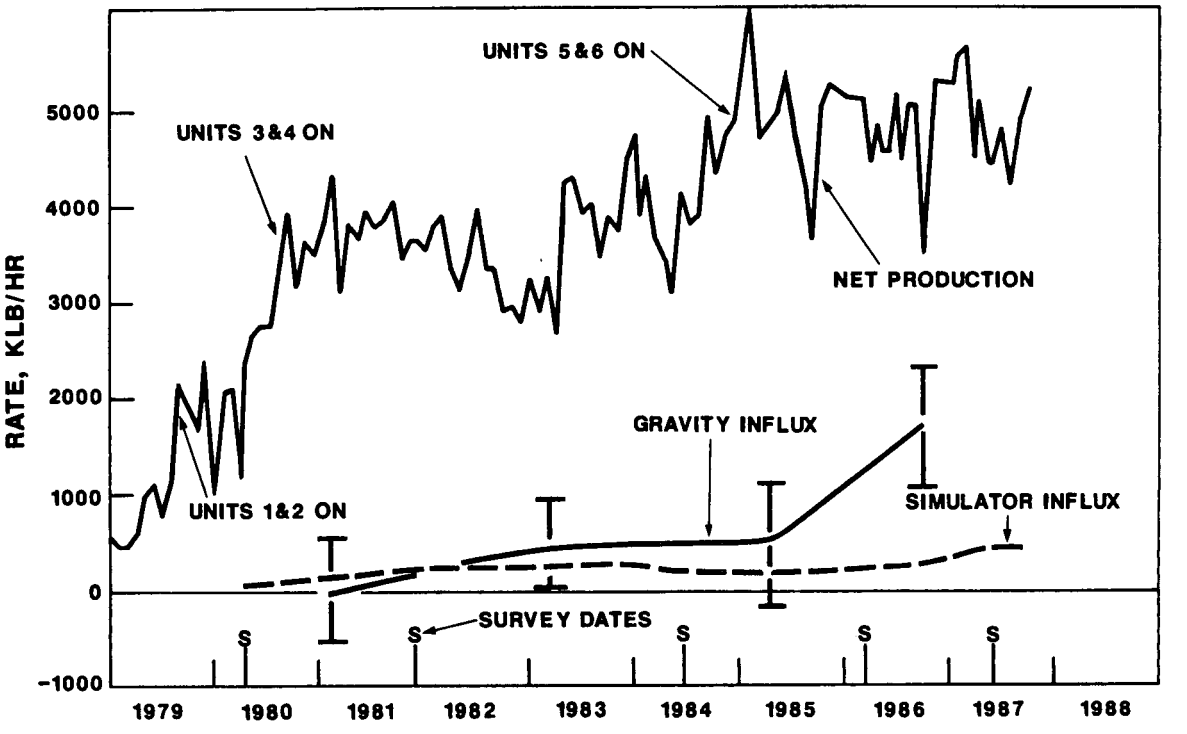


Figure 4. Bulalo Field net production and influx rates

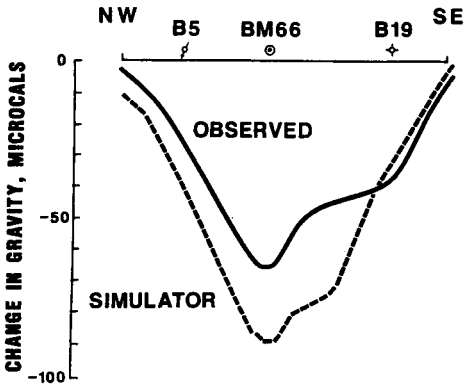


Figure 6. Observed and computed delta-gravity profiles across Bulalo for 1984 to 1986

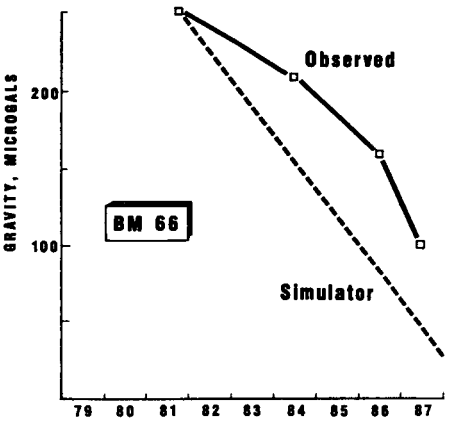


Figure 7. Observed and computed histories of gravity at Bulalo benchmark BM66

profiles on a NW-SE section through BM66, corresponding to the 1984-1986 time frame. The maximum observed gravity change is almost 70 microgals, whereas that derived from the reservoir simulation model is 90 microgals. The smaller area under the observed curve suggests that the reservoir is experiencing substantially more influx than the simulation model. However, another possibility is that depletion in the reservoir is occurring deeper than in the numerical model. This latter possibility is consistent with two observations:

1. The shapes of the two profiles in Figure 6 are similar, suggested that the fundamental reservoir physics of depletion contained in the model is a good representation of that in the reservoir; and

2. The impact of near-surface effects on precision gravity data is to add variations of $\pm$ 10 microgals to the delta-gravity field away from the productive area. This causes the tails of the observed delta-gravity distribution to be noisy. It results in uncertainty in mass loss calculations because stable benchmarks cannot be accurately defined. The error bars on the gravity-inferred influx rates in Figure 4 result partly from this effect. Thus, it may be that the observed data should be shifted down.

Figure 7 presents observed and computed delta-gravity histories for benchmark BM66. This benchmark was first installed in 1981 in the center of the field. A total observed change of 150 microgals over almost six years can be seen. The observed data initially show a flatter trend, implying either less depletion, or deeper depletion in the field than in the model.

We are currently reviewing both field and model data in order to provide a basis for improving the match between observed and simulation gravity results. Past experience with such reviews have taught us that while the gravity data can provide important insights into reservoir behavior, it can also display misleading features that have nothing to do with reservoir behavior. Sometimes these features appear to have been associated with weather patterns. We suspect that the gravity-inferred increase in influx in 1986-87 shown on Figure 4 may actually be an effect unrelated to the reservoir.

CONCLUSION

Precision gravity monitoring can be used to infer influx into geothermal reservoirs. Such data must be gathered in the field with great care, as data interpretation requirements push the limits of commercially available technology. Even when the data gathering is sufficiently accurate, non reservoir effects such as near-surface aquifer recharging due to rainfall can complicate data interpretation.

Gravity-inferred influx rates for the Bulalo field have been compared with those used in a simulation model. Conversely, simulation-computed gravity fields have been compared with observed results. These comparisons have provided us with confidence in the basic structure of the simulation model.

REFERENCES

Allis, R.G., and Hunt, T.M. (1986), "Analysis of exploitation-induced gravity changes at Wairakei geothermal field, Geophysics, v. 51, no. 8, 1647-1660.

Craft, B.C., and Hawkins, M.F. (1959), Applied Petroleum Reservoir Engineering, Prentice-Hall, Chapters 4 and 5.

Dobrin, M.B. (1960), Introduction to Geophysical Prospecting, Second Edition, McGraw-Hill.

Eckhardt, D. (1986), "Isomorphic geodetic and electrical networks: An application to the analysis of airborne gravity gradiometer survey data", Geophysics, v. 51, no. 11, 2145-2159.

Gudmundsson, J.S., and Olsen, G. (1985), "Water influx modeling of Svartsengi geothermal field, Iceland," SPE 13615, presented at the SPE 1985 California Regional Meeting, Bakersfield, California, March 27-29.

Hammer, S. (1945), "Estimating ore masses in gravity prospecting", Geophysics, v. 10, 50-62.

Hunt, T.M. (1970) "Gravity changes at Wairakei geothermal field, New Zealand", Geological Society of America Bulletin, v. 81, 529-536.

Hunt, T.M. (1977), "Recharge of water in Wairakei geothermal field determined from repeat gravity measurements", N.Z. Jour. Geol. & Geophys., v. 20, no. 2, 303-317.

LaFehr, T.R. (1965), "The estimation of the total amount of anomalous mass by Gauss's theorem", J. Geophys. Res., v. 70, no. 8, 1911-1919.

Lambert, A., and Beaumont, C. (1977), "Nano variations in gravity due to seasonal groundwater movements: Implications for gravitational detection of tectonic movements", J. Geophys. Res., v. 82, no. 2, 297-306.

Nagy, D. (1966), "The gravitational attraction of a right rectangular prism", Geophysics, v. 31, 362-371.

ACKNOWLEDGEMENTS

All reservoir simulation calculations described in this paper were made with a program developed under joint sponsorship with Technical Software & Engineering, Inc. T.D. Anderson of Unocal's Science and Technology Division wrote the software for computing surface gravity fields.

DOWNHOLE PRESSURE,TEMPERATURE AND FLOWRATE MEASUREMENTS IN STEAM WELLS AT THE GEYSERS FIELD

Kathleen L. Enedy

Geysers Geothermal Company
1160 North Dutton, Suite 200
Santa Rosa, CA 95401

ABSTRACT

Recently developed pressure-temperature-spinner (PTS) tools are used to collect reliable downhole measurements in geothermal systems, such as at The Geysers. PTS surveys in several flowing Geysers steam wells were used to quantify steam entry location and magnitude, wellbore heat loss, pressure drop due to friction, thermodynamic properties of the steam, and maximum rock temperature. Interwell cross flow/interference was identified in one well. Finally, a single-phase saturated steam wellbore model used to compare calculated to measured downhole values, was found to adequately predict the flowing pressure versus depth curves in vapor filled holes.

INTRODUCTION

Geysers Geothermal Company (GGC), the managing general partner for Freeport-McMoRan Resource Partners, Limited Partnership, supplies steam to Pacific Gas and Electric (PG&E) Units 13 and 16 and Sacramento Municipal Utility District (SMUD) GEO #1 plant. The combined generating capacity of the above plants is 320 MW net. Construction of GGC's two new projects, Bear Creek Canyon (BCC) and West Ford Flat (WFF), is underway. In the BCC and WFF projects, GGC will be both steam supplier and plant operator. These plants are scheduled to commence operations in late 1988 to early 1989 and will generate a combined 47 MW net.

GGC initiated a PTS logging program in 1986 to obtain baseline reservoir data on designated steam wells throughout GGC leases at The Geysers field, California. The purpose of this paper is to discuss and interpret PTS logs of several flowing steam wells.

A BRIEF DESCRIPTION OF PTS TOOL

Until the recent development of the PTS tool, reliable downhole information under producing conditions was difficult to obtain with conventional logging tools due to the high temperature environment of 480 °F and high fluid velocities. A sophisticated dewer-type insulator allows the tool to operate for an extended time period (up to 8 hours) in the high temperature environment. The PTS tool simultaneously measures pressure, temperature and spinner revolutions per second (rps). The independent signals are transmitted to the surface microprocessor via a single high temperature (600 °F) conductor and are then processed and recorded.

Two companies, Hot Hole Instruments Los Alamos (HHI) and Dresser Atlas, presently run PTS tools in The Geysers field. The PTS runs discussed in this paper were logged using the HHI tool. An example of a Dresser Atlas log output is shown in Figure 1.

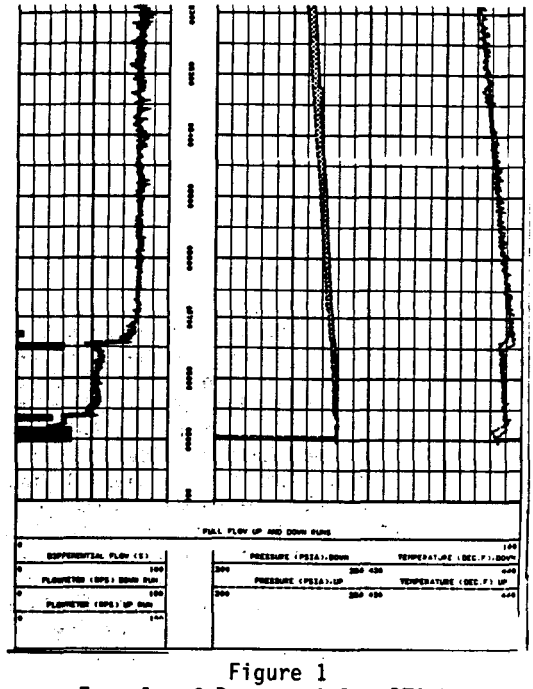


Figure 1
Example of Dresser Atlas PTS Log

USES OF PTS TOOL

Knowledge of certain reservoir parameters is essential to properly develop and model any geothermal field. The PTS tool improves measurements of key reservoir characteristics including steam entry location and magnitude, pressure and temperature profiles in the wellbore under varying flow conditions, pressure drop due to friction, wellbore heat loss, thermodynamic properties of the steam, etc.

One of the most valuable uses of the tool is to quantify the location, size and enthalpy of steam entries. Prior to the development of the PTS tool, both enthalpy and size of steam entries could only be crudely estimated while drilling the well. Newly encountered steam entries are indicated by abrupt changes in air compressor or injection pressure and/or flowline temperature increases while air drilling. These estimations are generally adequate for determining the steam entry location in the wellbore. Drilling data is often the only steam entry information available for most wells. However, since this drilling data is obtained only upon encountering new steam entries, it is often unclear how the recent entry affects production of previous steam entries. Consequently, a thief zone, for example, may be undetected unless it is extremely large.

A major advantage of the PTS over the Kuster-type tools is the ability to provide continuous surface readout of the pressure, temperature and spinner data in a producing well. Although Kuster-type tools are run frequently at The Geysers to obtain downhole pressure and temperature profiles for wells at relatively low flowrates, these profiles do not allow adequate interpretation as how individual entries perform at various flow conditions.

The PTS survey often proves to be a valuable diagnostic tool in the evaluation of problem wells. Producing wells in The Geysers may at times suffer significant losses in production due to mechanical problems in the wellbore such as scale formation, casing collapse, or bridging of the open hole. Large water entries (either injection or meteoric) into the wellbore can also cause major loss of steam production due to quenching. A PTS survey can often pinpoint the cause of the problem and allows the engineer to make recommendations for workover solutions (i.e. cleaning out the well, running a casing liner, reducing injection from offset injectors, etc).

Finally, reservoir characteristics can be determined by conducting pressure buildup, drawdown, interference, or injectivity tests in the wellbore using the PTS tool. Figure 2 is actual HHI log output of a tool hung just inside the casing shoe of a well while partially closing in the well. This type of testing is useful in wells containing water or noncondensible gas where surface pressure measurements do not yield adequate results in conventional well test analysis.

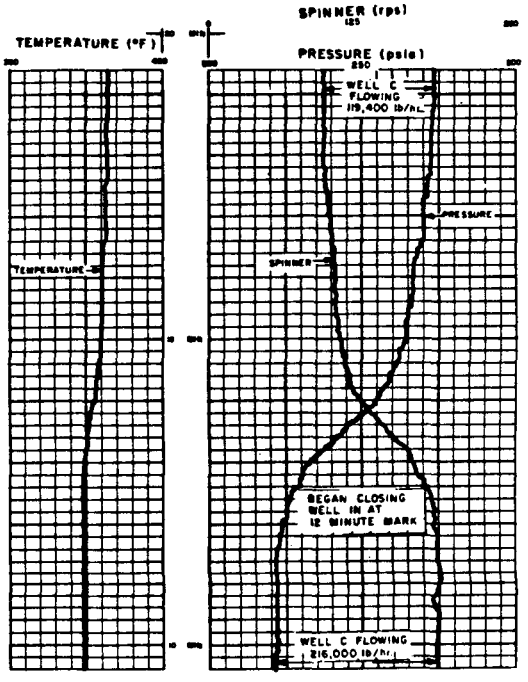


Figure 2
HHI PTS Log during partial shutin of well

EXAMPLES OF SEVERAL SURVEYED WELLS

Figures 3 and 4 represent pressure, temperature and spinner data (obtained with a PTS tool) plotted versus depth for two different GGC wells. The PTS survey indicated six distinct steam entries in Well A. Their location and casing shoe depth is noted on Figure 3 on the x-axis. The spinner data plotted versus depth on Figure 3 (Well A) indicates that all of the steam enters the wellbore above 4300'. Since the total depth of this well is approximately 5200', 900' of wellbore is a "dead-leg". Well A's temperature profile approaches a maximum rock temperature of 465 °F (Figure 3). It is also noteworthy that the pressure gradient decreases from 4.6 to 0.3 psi/100'as the tool enters the static steam column.

Well B (Figure 4) represents a well with four distinct steam entries and a 980' liquid column just below the deepest entry at 6300'. The pressure gradient increases from 2.5 to 33.9 psi/100' as the PTS tool enters the liquid column. Although Well B contains liquid, a maximum rock temperature of 480 °F is reached in its dead-leg. Figure 5 is actual output of the HHI PTS tool which illustrates the two deepest steam entries and

the top of the water column at 6300'. The 17 rps increase in spinner data from 6070' to 6100' (Figure 5) results from a slight diameter decrease in the open hole at this depth.

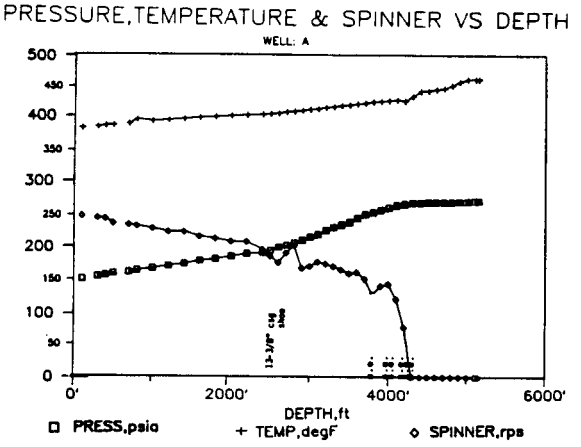


Figure 3

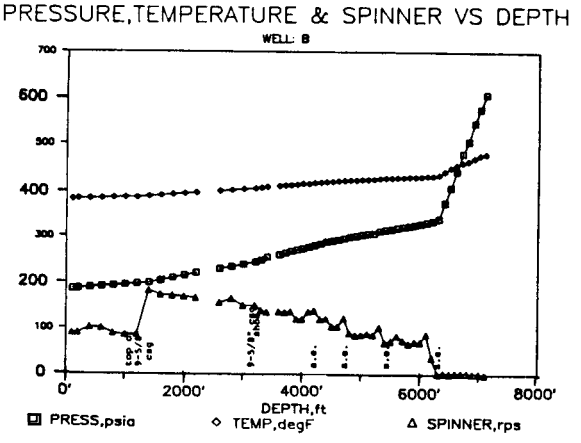


Figure 4

Enthalpy data plotted versus depth is shown in Figure 6 for Wells A, B and C. Note Well A's higher enthalpy values throughout the wellbore compared to Wells B and C. Well A had been on production for over six years at the time it was logged and is located in a more mature, depleted section of the field. Wells B and C had only been on production for eight months and are located in an area of the field more indicative of initial reservoir conditions. Typically wells producing in older portions of The Geysers field exhibit higher enthalpy due to a "drying out" of the reservoir over time. This occurs as the liquid fraction of the reserves is boiled away. All three wells exhibited greater enthalpy decreases in the cased versus open hole sections due to wellbore heat loss (except in Well B's liquid column). The minimum enthalpy value at 6800' in Well B (Figure 6) probably results from cold water entering the wellbore at this depth. Below this water entry, the standing liquid column is heated to 480 °F by conduction from the reservoir rock.

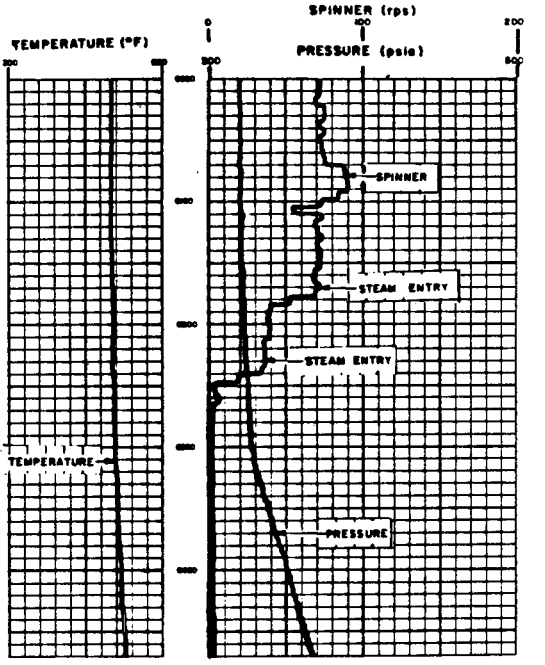


Figure 5
HHI PTS Log of Well B

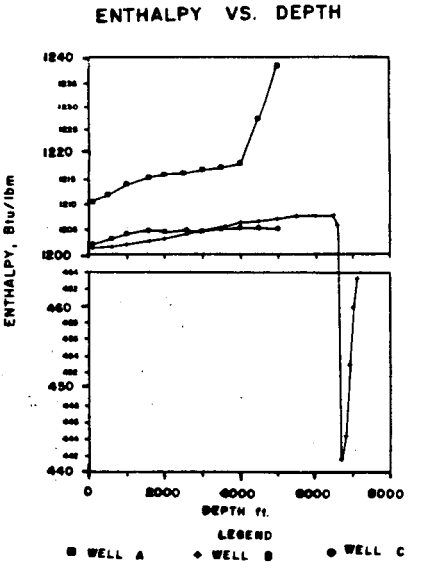


Figure 6

A zone of interwell cross flow/interference between Well C and an offset producer was pinpointed using the PTS tool. Well C was logged at three different flowrates, 190, 216 and 119 klb/hr respectively. During the first and last PTS runs, the offset producer flowed at its normal rate of 178 klb/hr at 173 psia. However, the offset well was throttled back to 40 klb/hr at 313 psia during the second PTS run, causing an increase in flow at Well C. Figure 7 illustrates pressure and spinner data plotted versus depth for the first and second runs (Well C flowing 190 and 216 klb/hr respectively).

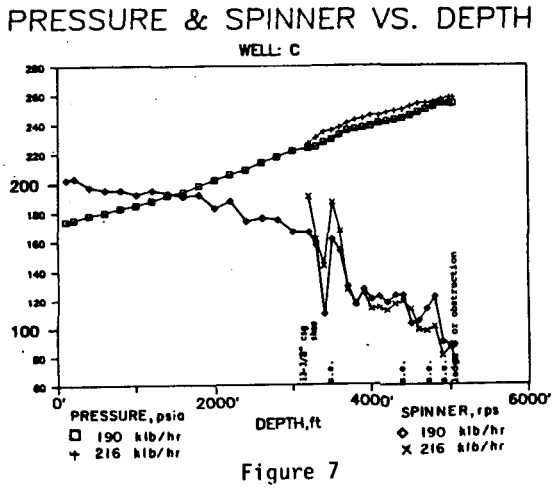


Figure 7

Although the flowrate had increased 26 klb/hr for the second run, the pressure was also greater. The spinner data from the second run exhibited a marked increase in flow at the shallowest steam entry at 3655'. However, contributions from the deeper entries tended to be lower for the second run. From this data it is evident that the 3655' zone is in direct communication with the offset producer and "shares" steam between the two wells.

Figure 8 illustrates Well C's percent of total flow versus steam entry depth for the three PTS runs. An obstruction or ledge at 5050' prohibited logging the entire wellbore. The PTS survey showed that about half of the flow is entering the well below 5000' (Figure 8). This verifies air drilling data which indicated that an additional six steam entries were encountered below 5000'. Also, the cross flow/interference zone at 3655' contributes proportionately more flow at higher flowrates since it "shares" steam with an offset producer. Conversely, a greater percentage of total flow is contributed by deeper entries (below 5000') at lower flowrates.

Apparently the flow from the shallowest entry is very sensitive to slight changes in wellhead pressure and to the flowrate of the offset well.

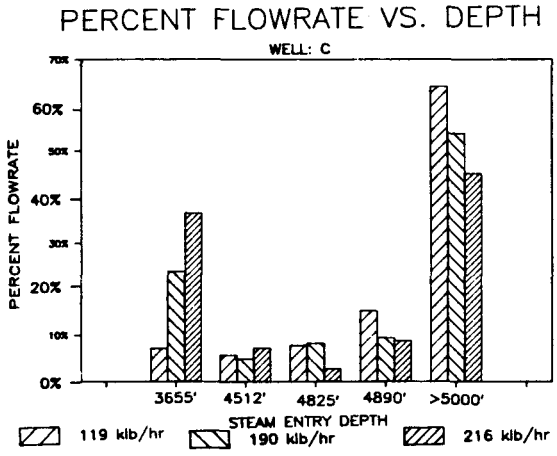


Figure 8

A shallow thief zone was detected by PTS surveys in Well D and is illustrated in Figures 9 and 10. When Well D's surface pressure was increased by only 14 psi (189 to 202 psia) the flowrate dropped 50% (150 to 75 klb/hr). The spinner reversal at 2450' identifies the thief zone in Figure 9.

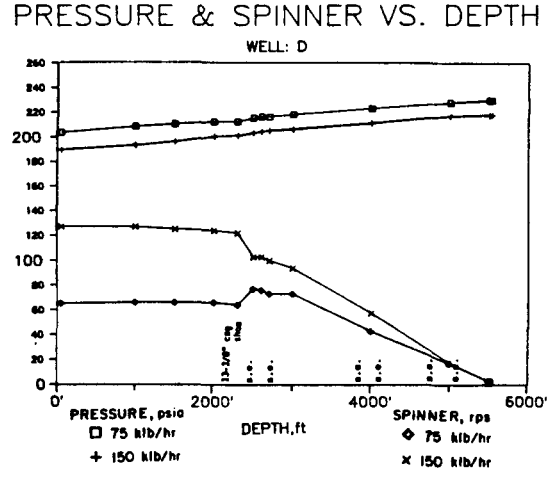


Figure 9

About 14% or 10 klb/hr of the total flow (75 klb/hr) exits the wellbore at 2450' (Figure 10). The detection of the thief zone by PTS data explains the unusual flowrate sensitivity to small changes in wellhead pressure.

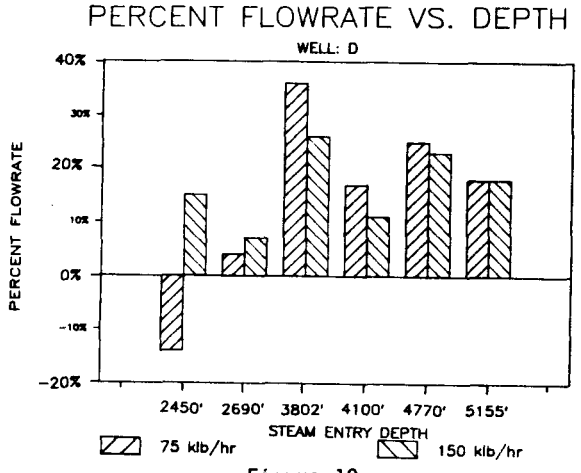


Figure 10

WELLBORE MODEL

Actual downhole flowing pressures were modeled by a single-phase saturated steam wellbore model. This model assumes adiabatic conditions and negligible kinetic energy. The pressure drop solution is based on the Cullender-Smith method. This in-house wellbore model was developed for the PC using a Lotus 123 spreadsheet.

A good match was obtained between the calculated and actual pressures for Well A in Figure 11. Although Well C could not be logged to total depth, reasonable downhole flowing pressures (below 5000') were predicted using the model (Figure 12). Well B's calculated downhole pressures provided an excellent match with measured values throughout the cased and steam producing sections of the wellbore (Figure 13). However, the model did not accurately predict actual pressures in the portion of the wellbore containing the liquid column and two phase flow because it is limited to single-phase steam conditions.

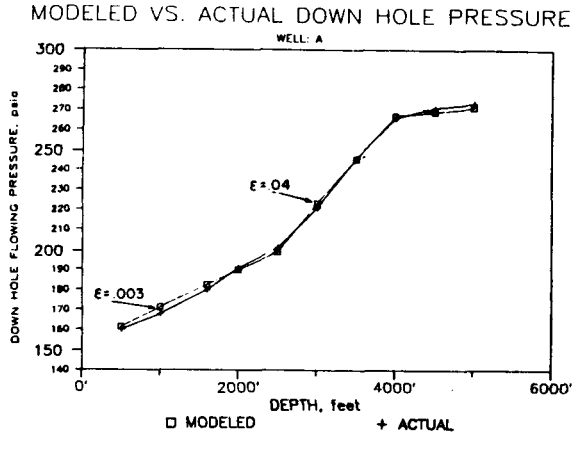


Figure 11

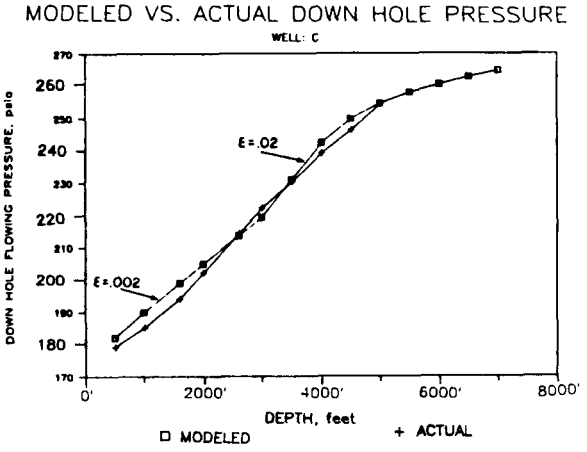


Figure 12

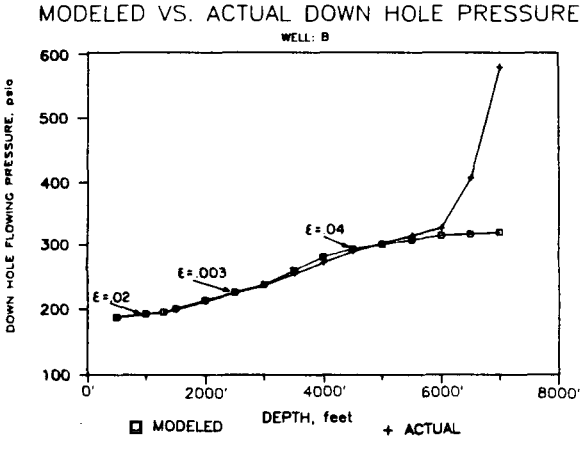


Figure 13

CONCLUSIONS

- PTS surveys provide reliable downhole information such as steam entry location and magnitude, wellbore heat loss, pressure drop due to friction, and maximum rock temperature in geothermal wells at The Geysers.
- Interwell cross flow/interference and thief zones in the wellbore can be detected with the PTS tool.
- PTS information aids the engineer in interpreting characteristics such as interwell behavior, pressure and temperature profiles, pressure decline and location of fluid entry or exit points in the wellbore. This knowledge is essential in order to arrive at practical solutions to production and reservoir problems in addition to reservoir modeling.

PROCEEDINGS, Thirteenth Workshop on Geothermal Reservoir Engineering
Stanford University, Stanford, California, January 19-21, 1988
SGP-TR-113

NEDO'S PROJECT ON GEOTHERMAL RESERVOIR ENGINEERING - A RESERVOIR ENGINEERING STUDY OF THE KIRISHIMA FIELD, JAPAN

H. Kitamura[1], T. Ishido[2], S. Miyazaki[1], I. Abe[3] and R. Nobumoto[4]

[1]New Energy Development Organization, Sunshine 60, 29F 1-1, 3-Chome, Higashi-Ikebukuro, Tokyo 170, Japan
[2]Geological Survey of Japan, Ibaraki, Japan
[3]Nippon Steel Company, Tokyo, Japan
[4]Nittetsu Mining Company, Tokyo, Japan

INTRODUCTION

In order to promote the development of geothermal energy resources, it is important to understand and (to the extent possible) to alleviate potential risks associated with each proposed development project. Further, it is essential to estimate the generation capacity of the reservoir prior to full-scale commitment so that the power plant design may be intelligently formulated. Starting in 1984, the New Energy Development Organization (NEDO) in Japan undertook a four-year program to develop technical methods for the evaluation of potential geothermal resources and for the prediction of production capacity and the appropriate level of electrical generation to be anticipated.

EVALUATION OF GEOTHERMAL RESERVOIRS

Figure 1 outlines NEDO's general approach to theoretical reservoir evaluation. For fields in which long-term fluid discharge tests have taken place and in which several survey wells have been drilled, NEDO is carrying out studies of the following types:

(1) *Well Tests:* In each field, single-well pressure transient tests (as well as some interference tests) are performed to obtain information concerning the reservoir permeability distribution and the locations and types of reservoir boundaries.

(2) *Natural-State Reservoir Simulation:* Numerical reservoir simulations are carried out, based upon available analyses of well-test measurements, geophysical survey results, geological data, and other relevant information. These simulations are carried out in an iterative manner, varying the various unknown parameters in the mathematical model to maximize agreement between measurements (for example, pressure and temperature distributions) and computed results. These calculations are time-dependent in character, but are carried forward for long periods of time so that a nearly steady natural-state representation is obtained. The unknown parameters are adjusted until a consistent model of the reservoir's natural condition results which is in adequate agreement with the available field measurements.

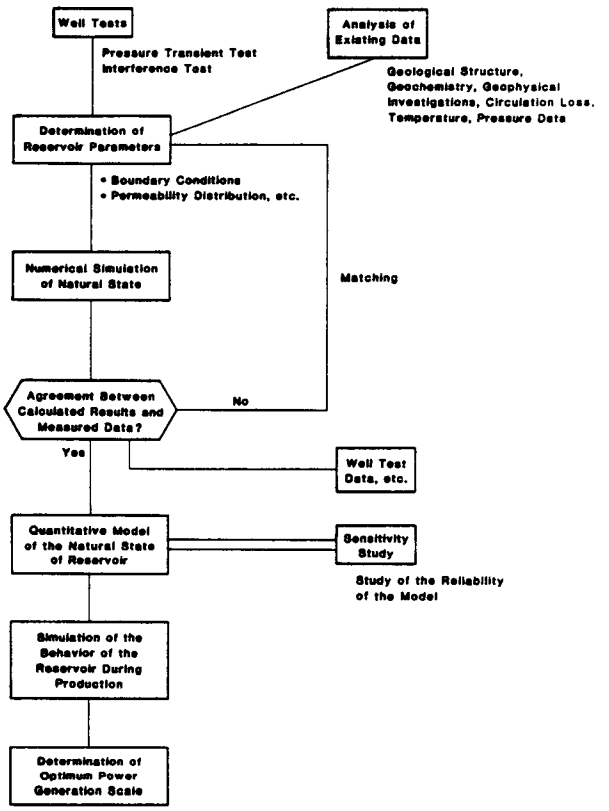


Figure 1. Pre-exploitation evaluation procedure for geothermal reservoirs.

(3) *Simulation of Reservoir Response to Production:* Once an internally consistent natural-state model is obtained which is in adequate agreement with measurements, changes in reservoir conditions (pressure, temperature, steam saturation, etc.) with time are computed based on a variety of scenarios concerning various reservoir development strategies (principally locations and flow rates of fluid production and reinjection). Sensitivity studies are carried out to estimate the reliability of the resulting predictions, and an optimum reservoir development plan is devised.

NEDO'S PROGRAM FOR EVALUATION TECHNOLOGY DEVELOPMENT

Table 1 indicates the schedule of NEDO's four-year project. Four main goals are identified, as indicated: the development of numerical reservoir simulators, the drilling of observation wells, the performance of pressure-transient and flow tests in wells, and reservoir simulation studies. Progress along these lines to date is as follows.

(1) *Development of Reservoir Simulators:* NEDO is developing two general-purpose three-dimensional unsteady geothermal reservoir simulators ("SING-I", restricted to single-phase flow; and "SING-II", also capable of treating two-phase water/steam systems). In addition, NEDO has developed the "WENG" code, which treats the steady flow of single-phase and two-phase (water/steam) mixtures up a borehole (including such effects as heat transfer through the casing, frictional effects, and slip between liquid and gaseous phases), permitting the prediction of wellhead conditions based on downhole conditions.

(2) *Drilling of Observation Wells:* Two model fields have been selected for study. At each of these two fields (the Sumikawa field in northern Honshu and the Kirishima field in Kyushu), two deep (1500 m - 1700 m) observation wells were drilled by NEDO. Both fields are also under development by private companies, so that several other wells are also present in each case. Temperature and pressure logs during heat-up as well as short-term injection tests were carried out in each NEDO well to gather basic information. The NEDO wells were also used as monitor wells during subsequent pressure interference testing.

(3) *Well Tests:* Pressure transient tests (both single-well tests and pressure interference tests) were carried out in each of the model fields (Kirishima and Sumikawa) using both existing wells drilled by the private developers and the new NEDO wells. For these tests, downhole pressures were measured using gauges of the capillary-tube type.

(4) *Reservoir Simulation:* Reservoir simulation studies of the type outlined above (involving both natural-state and production calculations) were carried out for each field, using the SING-I and SING-II numerical reservoir simulation programs developed by NEDO (described above).

THE KIRISHIMA GEOTHERMAL FIELD

In the remainder of this paper, we will describe some results obtained from the NEDO well-testing program in the Kirishima field. Kirishima lies in the southern part of Kyushu, the southernmost of the main islands of the Japanese archipelago. Starting in 1972, the Nippon Steel Company and the Nittetsu Mining Company have been jointly engaged in survey work in the area with the ultimate objective of constructing a geothermal power plant. These companies have carried out a variety of geological and geophysical surveys in the Kirishima area, and have also drilled a number of fairly deep wells (the 400 m to 2000 m "KE" series wells).

TABLE 1

NEDO PROJECT SCHEDULE

	1984	1985	1986	1987	comment
1. Development of reservoir simulators					• I-phase, II-phase reservoir simulator (SING-I, SING-II) and wellbore simulator(WENG).
2. Drilling of observation wells	(Kirishima field) 1500m×1	(Kirishima field) 1500m×1			
		(Sumikawa field) 1800m × 1	1700m × 1		
3. Well tests		(Kirishima field)			• Injection test • Interference test
		(Sumikawa field)			
4. Reservoir simulation					• Reservoir simulation of Kirishima and Sumikawa field

Figure 2 is a general map of the Kirishima field, showing many of the wells and natural hot springs in the area. Kirishima lies at an elevation between 800 meters and 1000 meters above sea level, and several hot springs are present (notably Ginyu and Kinyu, as indicated in Figure 2). The Kirishima volcanos are located about five kilometers to the northeast of the explored geothermal area. Figure 3 shows the distribution of mapped faults and surface lineaments as established by geological surveys and aerial photography. The trend of these faults is mainly northeast – southwest. The most important faults in the area are the "Ginyu fault" and the "Shiramizugoe fault"; many wells were drilled along these faults in an attempt to find permeable horizons.

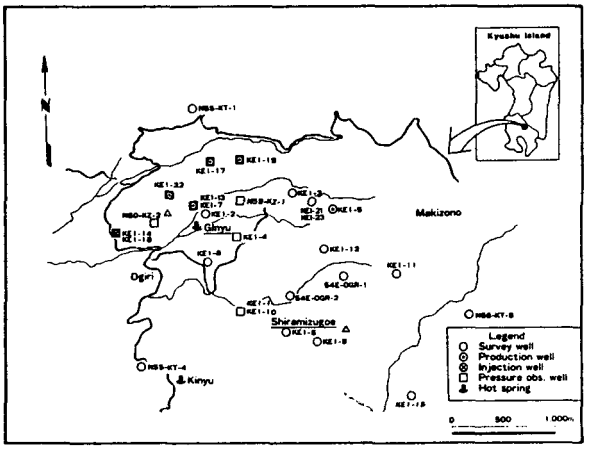


Figure 2. Map of Kirishima geothermal area.

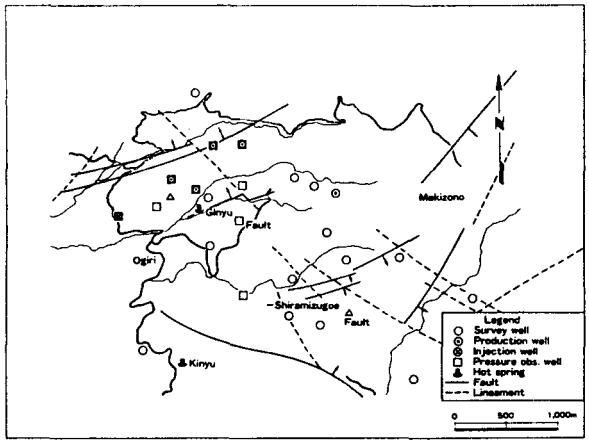


Figure 3. Locations of faults and lineaments.

TEMPERATURE AND PRESSURE DISTRIBUTIONS AT KIRISHIMA

In most of the Kirishima wells, repetitive surveys of downhole temperature and standing water level were carried out for at least several days after cold-water circulation was terminated. These heat-up surveys permit the estimation of reservoir pressure and temperature. Figure 4 shows the estimated natural-state temperature distribution in a horizontal plane 500 meters below sea level (approximately 1.4 kilometers depth) in the study area. Two major features are evident. First, there is a general tendency for temperatures to decrease from east to west; this implies that the thermal anomaly is associated with the volcanos located northeast of the field. Second, a local high-temperature (over 220°C) feature is found at this level in the center of the study area. Based on these isotherm shapes, we conclude that the Ginyu fault is responsible for the local geothermal feature located in this part of the Kirishima field.

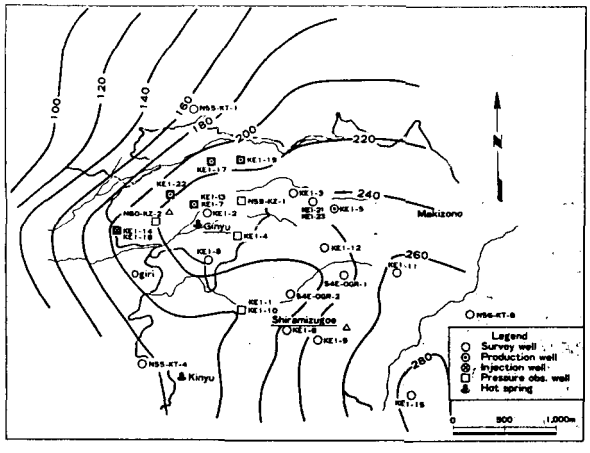


Figure 4. Distribution of temperature (°C) 500 meters below sea level.

As discussed above, simultaneous downhole temperature surveys and measurements of standing shut-in water level were carried out during heat-up for most of the wells in the area. These measurements permit the determination of the stable feedpoint pressures for the various wells. These results indicate that underground pressures are significantly different between the Ginyu part of the Kirishima field (to the north) and the Shiramizugoe area (farther south). This suggests, in turn, that an impermeable boundary is present separating these two parts of the field, and that little communication between these two areas should be expected.

INTERFERENCE TESTING AT KIRISHIMA

Table 2 shows the two-year test program which was carried out at Kirishima starting in April 1985. A total of five production wells, two reinjection wells, and nine shut-in observation wells were involved at one time or another during the test period.

TABLE 2

INTERFERENCE TEST SCHEDULE

Year	1985												1986												1987		
Month	4	5	6	7	8	9	10	11	12	1	2	3	4	5	6	7	8	9	10	11	12	1	2	3
Discharge Well																								
KE1-5																								
KE1-7																								
KE1-17																								
KE1-19S																								
KE1-22																								
Reinjection Well																								
KE1-14																								
KE1-18																								
Pressure Measurement Well																								
KE1-4																								
KE1-13S																								
KE1-10																								
NSS-KZ-1																								
NSO-KZ-2																								
KE1-14																								
KE1-18																								
KE1-19S																								
KE1-22																								

Figure 5 illustrates the capillary-tube type downhole pressure monitoring system used in these tests. The chamber and the capillary tube are filled with helium gas, and the pressure within the downhole chamber is transmitted to the surface equipment by means of the capillary tube. A quartz transducer transforms the pressure fluctuations in the tube to an electrical signal which is digitized and recorded on a hardcopy printer and stored on magnetic disk by an on-site microcomputer. The transducer accuracy is very good (± 0.01 psi, or about one millibar).

Figure 6 shows the total discharge rate from the flowing wells (KE1-7, 17, 19S, and 22) as a function of time during the test period. Also shown is the recorded downhole pressure history in observation well KE1-13S. The total discharge rate was about 170 tons per hour (on the average) for the first eighteen months of the test; thereafter, however, the discharge increased gradually, reaching 670 tons per hour in March 1987. As Figure 6 clearly shows, this increase

in discharge rate resulted in a significant pressure decrease in observation well KE1-13S, amounting to about 0.2 MPa (~ 2 bars). The correlation between discharge rate changes and downhole pressure changes is seen to be very good, both on the overall time-scale and shorter time-scales (1-2 months; associated with short-term fluctuations in discharge rate). Similarly, Figure 7 shows the pressure histories recorded in wells KE1-13S, KE1-19S and KE1-22 from April 1986 to March 1987. The signal recorded in well KE1-13S shows a very clear response to the changes in discharge from the various flowing wells. These pressure signals were analyzed to try to establish the permeability distribution and other relevant properties of the reservoir. Analyses of these signals are still continuing. In the following, preliminary results are presented.

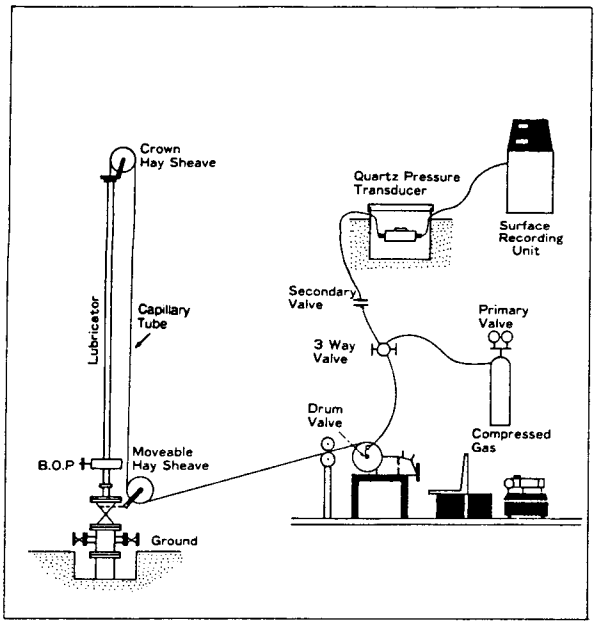


Figure 5. Capillary-tube downhole pressure observation system.

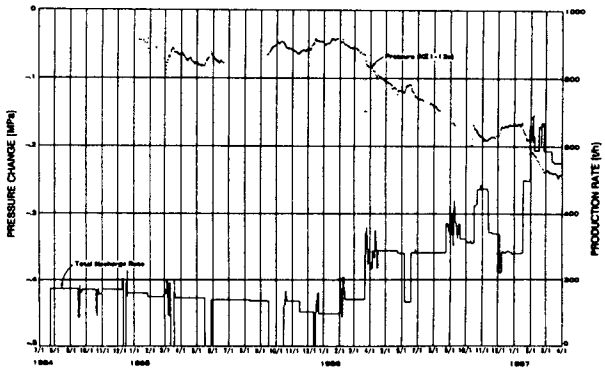


Figure 6. Total field discharge rate, and pressure history in Well KE1-13S.

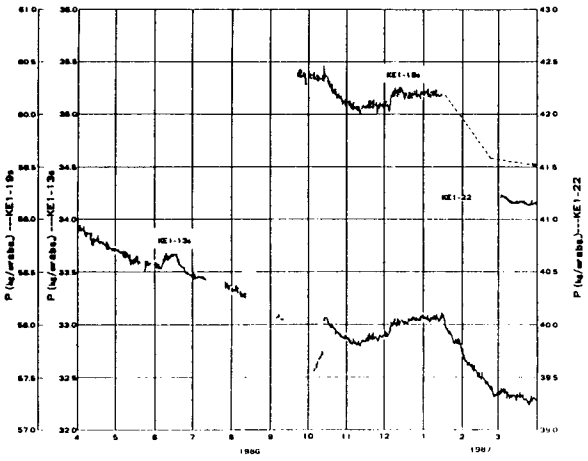


Figure 7. Pressure histories in Wells KE1-13S, KE1-19S and KE1-22 from April 1986 to March 1987.

PERMEABILITY DISTRIBUTION AT KIRISHIMA

The classical radial-flow model was used for the preliminary interpretation of the pressure-transient test pressure measurements. Figure 8 shows a typical result in graphical form. (Figure 9 indicates the geometry assumed for the interference test interpretation.) The scatter in Figure 8 is due mainly to uncorrected effects of atmospheric temperature fluctuations on the quartz transducer. In Figure 8, downhole pressures recorded every two hours are plotted against a reduced time which is derived from the discharge rate history. The value of the permeability-thickness product (kh) obtained from the slope of the best-fit straight line in Figure 8 is 4.19×10^{-11} m^3 (41.9 darcy-meters).

The wells which were employed in this study apparently penetrate the Ginyu reservoir (as contrasted to the Shiramizugoe reservoir farther south), so that the values of kh (permeability-thickness) obtained are presumably representative of that system. Table 3 summarizes the results of these analyses. A total of fourteen sets of data were analyzed, including those listed in Table 3. Permeability-thickness values ranging from 11 to 185 darcy-meters were obtained from these analyses; the average value was about 63 darcy-meters. Owing to the relatively short durations of the test periods considered in these analyses (about one month), these values are considered to represent mainly the permeabilities in the neighborhoods of the individual wells. To examine larger-scale permeability structures, long-term (January 1985 to April 1987) analyses were also conducted. These yielded the following average values for the permeability-thickness (kh) and porosity-compressibility-thickness (ϕch) products:

kh = 40.5 darcy-meters
ϕch = 5.0×10^{-8} meters per Pascal.

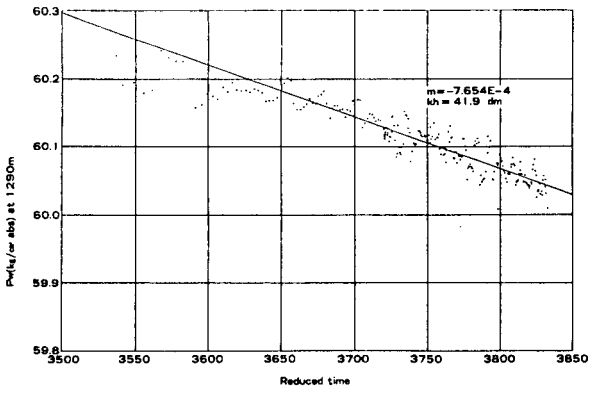


Figure 8. Interference test analysis (Well KE1-19S).

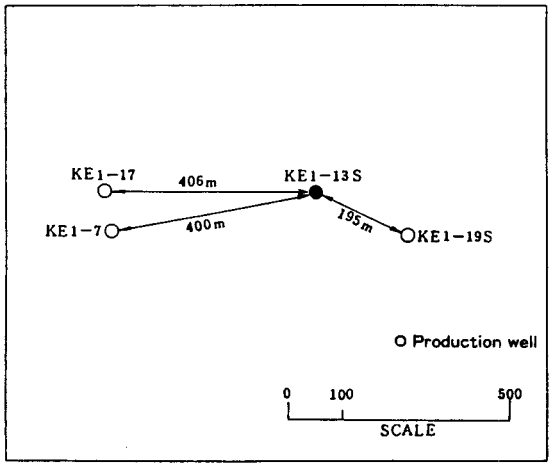


Figure 9. Bottomhole locations for wells involved in interference test.

TABLE 3

RESULTS OF WELL TEST ANALYSES

Period of Observation	Observation Well	Active Well	KH Value (darcy·m)
1986-4-17 ~6-5	KE1-13S	KE1-7,KE1-17	25.5
1986-6-18 ~7-12	KE1-13S	KE1-17,KE1-7	53.7
1986-10-23 ~11-11	KE1-19S	KE1-7,KE1-17	41.9
1987-3-3 ~3-13	KE1-22	KE1-7,KE1-17, KE1-19S	11.4

ONGOING STUDIES OF THE KIRISHIMA FIELD

Further analyses of the pressure-transient test results are now being carried out using numerical simulation techniques to take into account more complicated phenomena such as two-phase flow effects. Based on the available results from the well-test experiments, large-scale reservoir simulation studies are also being performed to try to estimate the productive capacity of the Kirishima field.

ACKNOWLEDGMENTS

This research was performed as a part of the NEDO's program *Survey to Promote Geothermal Development*, which is supported by the Electric Power Generation Division, the Agency of Natural Resources and Energy of the Ministry of International Trade and Industry.

PROCEEDINGS, Thirteenth Workshop on Geothermal Reservoir Engineering
Stanford University, Stanford, California, January 19-21, 1988
SGP-TR-113

Well-Test Analysis for a Well in a Finite, Circular Reservoir

Anil K. Ambastha and Henry J. Ramey, Jr.

Stanford Geothermal Program

ABSTRACT

This study presents drawdown and buildup pressure derivative type-curves for a well producing at a constant rate from the center of a finite, circular reservoir. Early time response (wellbore storage and skin effects) is correlated by C_De^{2s}, and late time response (outer boundary effects) by r_{eD}^2/C_D. The outer boundary may be closed, or at a constant pressure. Design relations are developed for the time to the beginning and the end of infinite-acting radial flow. Producing time effects on buildup responses are also discussed.

INTRODUCTION

Transient pressure response for a well producing from a finite reservoir of circular, square, and rectangular drainage shapes has been studied by *van Everdingen* and *Hurst* (1949); *Miller et al.* (1954); *Aziz* and *Flock* (1963); *Earlougher et al.* (1968); *Ramey* and *Cobb* (1971); *Kumar* and *Ramey* (1974); *Cobb* and *Smith* (1975); and *Chen* and *Brigham* (1978) among others. *Mishra* and *Ramey* (1987) presented a buildup derivative type-curve for a well with storage and skin, and producing from the center of a closed, circular reservoir. Their type-curve applies for large producing times such that $t_{pD} > t_{DPss}$. This work presents drawdown and buildup pressure derivative type-curves for a well producing at a constant rate from the center of a finite, circular reservoir. The outer boundary may be closed, or at a constant pressure. The differences between the responses for a well in a closed, circular reservoir (fully developed field), and a well in a circular reservoir with a constant-pressure outer boundary (active edgewater drive system, or developed five-spot fluid-injection pattern) are discussed. Design relations are developed to estimate the time period which corresponds to infinite-acting radial flow, or to a semi-log straight line on a pressure vs. logarithm of time graph. Producing time effects on buildup responses are studied using the slope of a dimensionless *Agarwal* (1980) buildup graph.

THEORY

The dimensionless wellbore pressure drop for a constant-rate well with storage and skin may be expressed as (*van Everdingen* and *Hurst*, 1949):

$$p_{wD}(t_D) = \frac{2\pi kh\,(p_i - p_{wf})}{qB\mu}$$

$$= L^{-1}\left[\frac{1}{C_D l^2 + \dfrac{l}{s + l\bar{p}_D}}\right], \qquad (1)$$

where L^{-1} is the inverse Laplace transform operator. In Eq. (1), $\bar{p}_D$ refers to the dimensionless wellbore pressure drop in Laplace space without storage or skin. For the case of a constant-rate well producing from the center of a closed circle, the expression for $\bar{p}_D$ is (*van Everdingen* and *Hurst*, 1949):

$$\bar{p}_D = \frac{1}{l^{3/2}}\left[\frac{K_0(\sqrt{l})\,I_1(r_{eD}\sqrt{l}) + I_0(\sqrt{l})\,K_1(r_{eD}\sqrt{l})}{K_1(\sqrt{l})\,I_1(r_{eD}\sqrt{l}) - I_1(\sqrt{l})\,K_1(r_{eD}\sqrt{l})}\right] \qquad (2)$$

For the case of a constant-rate well producing from the center of a circular reservoir with a constant-pressure outer boundary, the expression for $\bar{p}_D$ is (*van Everdingen* and *Hurst*, 1949):

$$\bar{p}_D = \frac{1}{l^{3/2}}\left[\frac{K_0(\sqrt{l})\,I_0(r_{eD}\sqrt{l}) - I_0(\sqrt{l})\,K_0(r_{eD}\sqrt{l})}{K_1(\sqrt{l})\,I_0(r_{eD}\sqrt{l}) + I_1(\sqrt{l})\,K_0(r_{eD}\sqrt{l})}\right]. \qquad (3)$$

The dimensionless wellbore pressure drop from Eq. (1) was obtained by inverting the Laplace space solution numerically with the *Stehfest* (1970) algorithm.

DRAWDOWN RESPONSE

Table 1 shows the dimensionless wellbore pressure drop and the semi-log pressure derivative expressions for a well in a finite, circular reservoir during specific flow periods. All expressions in Table 1 may be written as combinations of t_D/C_D, C_De^{2s}, and r_{eD}^2/C_D. For example,

$$\ln(r_{eD}) + s = \frac{1}{2}\ln\left[\frac{r_{eD}^2}{C_D}\,C_De^{2s}\right], \text{ and} \qquad (4)$$

$$C_2 = \frac{1}{2}\ln\left[\frac{2.2458\,A}{C_A r_w^2}\right] + s = \frac{1}{2}\ln\left[\frac{2.2458\,\pi}{C_A}\,\frac{r_{eD}^2}{C_D}\,C_De^{2s}\right] \qquad (5)$$

Thus, if the dimensionless drawdown pressure and the pressure derivative responses are graphed against t_D/C_D, the parameters C_De^{2s} and r_{eD}^2/C_D may be selected as the correlating parameters. The verification of C_De^{2s} and r_{eD}^2/C_D as the

Table 1 - Dimensionless wellbore drawdown pressure and derivative expressions for a well in a finite, circular reservoir

Flow period	p_{wD}	$p'_{wD} = dp_{wD}/d \ln t_D$
Wellbore storage	t_D/C_D	t_D/C_D
Infinite-acting radial flow	$0.5\ [\ln (t_D/C_D) + C_1]$	0.5
Pseudosteady state (No wellbore storage, and closed reservoir)	$2\pi\ t_{DA} + C_2$	$2\pi\ t_{DA}$
Steady state (Constant-pressure outer boundary)	$\ln (r_{eD}) + s$	0

$$C_1 = \ln (C_D e^{2s}) + 0.80907 \quad \text{, and} \qquad C_2 = 0.5 \ln \left[\frac{2.2458\ A}{C_A r_w^2}\right] + s$$

correlating parameters is also shown in Fig. 1 for both closed and constant-pressure outer boundary cases. The individual values of C_D, s, and r_{eD} used to generate the pressure derivative responses are shown on Fig. 1.

Figure 2 shows the drawdown pressure derivative type-curve developed in this study. Both closed and constant-pressure outer boundary cases are shown. The dimensionless times by which the semi-log pressure derivative is within 2% of 0.5 are:

$$\left.\frac{t_D}{C_D}\right]_{begin} \approx 150 + 200 \log (C_D e^{2s}) \quad \text{, and} \tag{6}$$

$$\left.\frac{t_D}{C_D}\right]_{end} \approx \frac{0.175\ r_{eD}^2}{C_D} \quad . \tag{7}$$

Design Eqs. (6) and (7) apply for both closed and constant-pressure outer boundaries. Equations (6) and (7) yield the condition for the development of at least half a log cycle of semi-log straight line as:

$$r_{eD}^2/C_D > 2710 + 3600 \log (C_D e^{2s}) \quad . \tag{8}$$

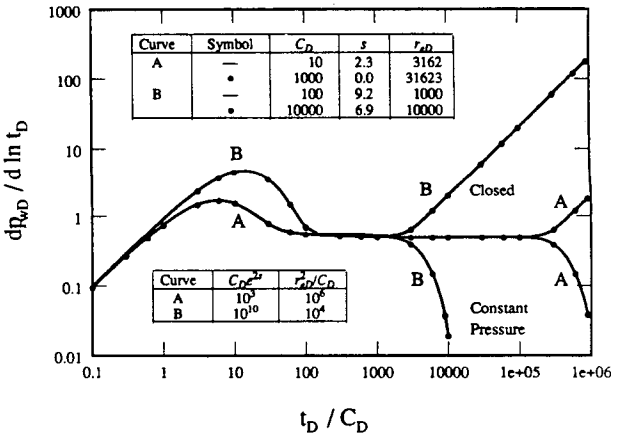


Fig. 1: Verification of C_De^{2s} and r_{eD}^2/C_D as the correlating parameters for the drawdown responses.

BUILDUP RESPONSE

The dimensionless buildup pressure is:

$$p_{wDs}(\Delta t_D) = \frac{2\pi kh\ (p_{ws} - p_{wf})}{qB\mu}$$

$$= p_{wD}(t_{pD}) + p_{wD}(\Delta t_D) - p_{wD}(t_{pD} + \Delta t_D) \tag{9}$$

and the slope of a dimensionless *MDH* (*Miller, Dyes,* and *Hutchinson,* 1950) buildup graph is:

$$MDH\ Slope = \frac{dp_{wDs}}{d \ln (\Delta t_D)} = \Delta t_D \frac{dp_{wDs}(\Delta t_D)}{d(\Delta t_D)} \quad . \tag{10}$$

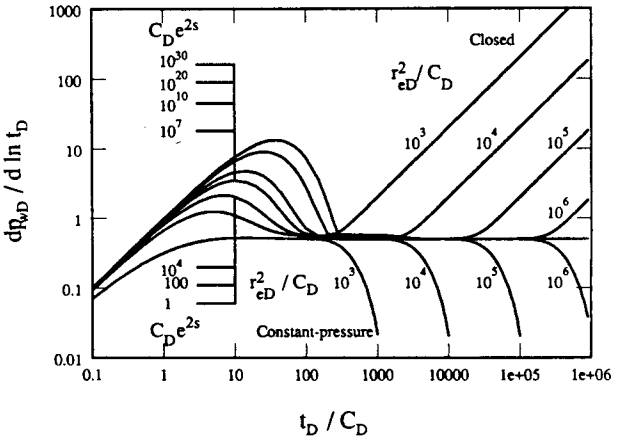


Fig. 2: Drawdown pressure derivative type-curve.

For large producing times such that $t_{pD} > t_{Dpss}$, *Mishra* and *Ramey* (1987) presented a type-curve as a log-log graph of *MDH* slope vs. $\Delta t_D/C_D$ with the correlating parameters as C_De^{2s} and r_{eD}^2/C_D. Their type-curve applies for a well in the center of a closed, circular reservoir. For large producing times such that $t_{pD} > t_{Dss}$, Fig. 3 shows the verification of the correlating parameters C_De^{2s} and r_{eD}^2/C_D for the buildup pressure derivative responses of a well in the center of a circular reservoir with a constant-pressure outer boundary. Figure 4 presents a buildup derivative type-curve for a well in the center of a circular reservoir with a constant-pressure outer boundary. The dimensionless times by which the semi-log buildup pressure derivative is within 2% of 0.5 on Fig. 4 are:

$$\left.\frac{\Delta t_D}{C_D}\right]_{begin} \approx 150 + 200 \log (C_De^{2s}) \quad \text{, and} \qquad (11)$$

$$\left.\frac{\Delta t_D}{C_D}\right]_{end} \approx \frac{0.175\, r_{eD}^2}{C_D} \quad . \qquad (12)$$

Equations (11) and (12) yield the condition for the development of at least half a log cycle of semi-log straight line as:

$$r_{eD}^2/C_D > 2710 + 3600 \log (C_De^{2s}) \quad . \qquad (13)$$

which is the same as Eq. (8).

Figure 5 shows the buildup derivative responses for a well in a circular reservoir with two different outer boundary conditions: closed and constant-pressure. Figure 5 applies for $C_De^{2s} = 1000$ and $r_{eD}^2/C_D = 10^6$. Figure 5 shows that for the same values of C_De^{2s} and r_{eD}^2/C_D, the semi-log straight line is longer for a well in a circular reservoir with a constant-pressure outer boundary than for a closed outer boundary.

The dimensionless times by which the slope of a dimensionless *MDH* buildup graph for a well in a closed reservoir is within 2% of 0.5 are:

$$\left.\frac{\Delta t_D}{C_D}\right]_{begin} \approx 150 + 200 \log (C_De^{2s}) \quad , \qquad (14)$$

$$\left.\frac{\Delta t_D}{C_D}\right]_{end} \approx \frac{0.01\, r_{eD}^2}{C_D} \quad \text{for } r_{eD}^2/C_D < 10^5 \quad \text{, and}$$

$$\approx \frac{0.005\, r_{eD}^2}{C_D} \quad \text{for } r_{eD}^2/C_D \geq 10^5 \quad . \qquad (15)$$

Equation (14) is the same as Eq. (11). The criterion for $\Delta t_D/C_D\big]_{begin}$ presented by *Mishra* and *Ramey* (1987) corresponds to the dimensionless time by which the slope of a dimensionless *MDH* buildup graph is approximately within 14% of 0.5. A comparison of Eqs. (12) and (15) shows that a semi-log straight line on a *MDH* buildup graph for a constant-pressure outer boundary is about one to one-and-a-half log cycles longer than a semi-log straight line on a *MDH* buildup graph for a closed reservoir, with all other conditions being same. Thus, if the buildup pressure derivative data for a well in a circular reservoir with a constant-pressure outer boundary is matched on a type-curve for a closed reservoir (Fig. 2 of *Mishra* and *Ramey*, 1987), the value for r_{eD}^2/C_D may be overestimated. Similarly, if the buildup pressure derivative data for a well in a closed reservoir is matched on a type-curve shown in Fig. 4, r_{eD}^2/C_D may be underestimated.

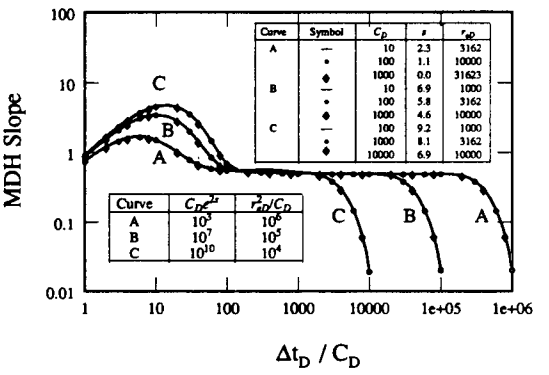


Fig. 3: Verification of C_De^{2s} and r_{eD}^2/C_D as the correlating parameters for the buildup responses (Constant-pressure outer boundary).

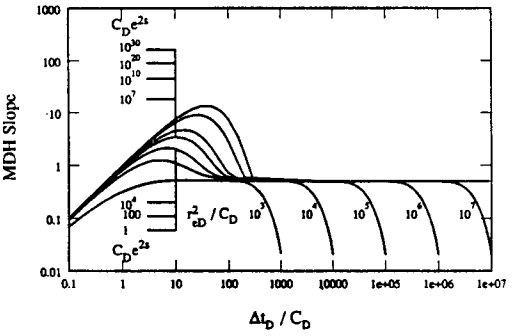


Fig. 4: Buildup pressure derivative type-curve (Constant-pressure outer boundary).

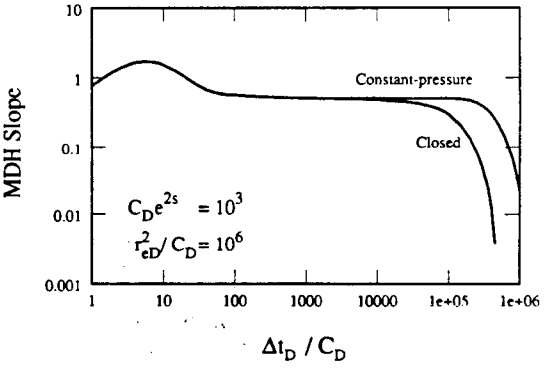


Fig. 5: Comparison of buildup derivative responses.

PRODUCING TIME EFFECTS ON BUILDUP RESPONSE

The *Horner* (1951) method has been recommended in the literature to analyze buildup data obtained after short producing times. The slope of a dimensionless *Horner* (1951) graph is:

$$Horner\ Slope = \frac{dp_{wDs}}{d \ln\left[\frac{t_{pD} + \Delta t_D}{\Delta t_D}\right]}$$

$$= -\frac{(t_{pD} + \Delta t_D)\Delta t_D}{t_{pD}} \cdot \frac{dp_{wDs}\,(\Delta t_D)}{d\,(\Delta t_D)} \quad (16)$$

Agarwal (1980) developed the concept of an equivalent drawdown time to analyze buildup data using drawdown type-curves for a well in an infinite reservoir. The dimensionless equivalent drawdown time is:

$$\Delta t_{eD} = \frac{t_{pD}\,\Delta t_D}{t_{pD} + \Delta t_D} \quad . \quad (17)$$

Agarwal (1980) showed that a graph of p_{wDs} vs. Δt_{eD} correlated buildup responses of a well in an infinite reservoir with the drawdown response. The correlation was good for all producing times larger than the time for storage effects to become negligible. For producing times less than the time for storage effects to become negligible, early time buildup responses did not correlate well. Also, the slope of a dimensionless *Agarwal* (1980) buildup graph is:

$$Agarwal\ Slope = \frac{dp_{wDs}}{d \ln (\Delta t_{eD})}$$

$$= \frac{(t_{pD} + \Delta t_D)\Delta t_D}{t_{pD}} \cdot \frac{dp_{wDs}\,(\Delta t_D)}{d\,(\Delta t_D)} \quad (18)$$

Equations (16) and (18) show that the *Horner* slope is equal, but opposite in sign to the *Agarwal* slope. Thus, producing time effects on buildup responses may be studied by using either the *Agarwal* or the *Horner* slope.

Aarstad (1987) presents the *Agarwal* (1980) slope as a function of the dimensionless shut-in time, Δt_{DA}, for several producing times, t_{pDA}, for wells without storage or skin, and located in a square or a rectangle. *Aarstad* (1987) shows that a graph of the *Agarwal* slope vs. Δt_{DA} does not result in a single curve for all producing times, if a well is located in a square or a rectangle. Therefore, *Aarstad* (1987) used t_{pDA} as a parameter to present the producing time effects on buildup responses for a well in a square or a rectangle.

Figure 6 shows an investigation of t_{pDA} as a correlating parameter for the buildup behavior of a well in the center of a closed, circular reservoir. Figure 6 applies for $C_De^{2s} = 10^4$ and $r_{eD}^2/C_D = 10^6$. The values of C_D, s, t_{pD}, and r_{eD} used for various responses are shown on Fig. 6. Figure 6 shows that the early time responses for $t_{pDA} \le 10^{-5}$ do not form a single curve with the responses for $t_{pDA} \ge 10^{-4}$. For $t_{pDA} \le 10^{-5}$, the producing time is less than the time for storage effects to become negligible. Thus, the lack of correlation at early times is consistent with *Agarwal's* (1980) finding. At late times, the buildup responses for all producing times do not form a single curve which is consistent with the work by *Aarstad* (1987). The lack of correlation at late times is due to the finite reservoir size.

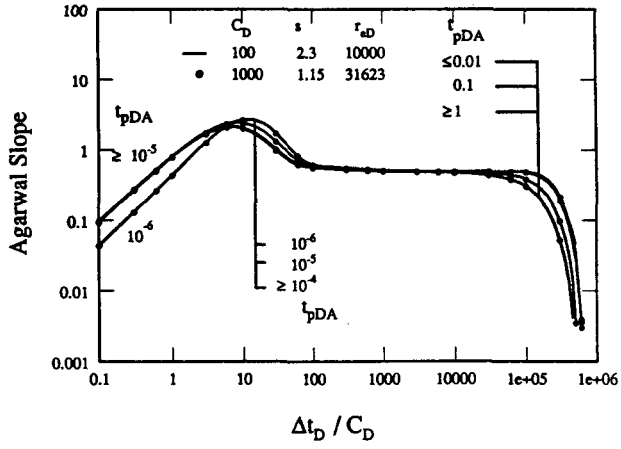


Fig. 6: Producing time effects on the buildup responses for a well in a closed reservoir ($C_De^{2s} = 10^4$, and $r_{eD}^2/C_D = 10^6$).

For buildup derivative data analysis, a log-log graph of $d\,(p_{ws} - p_{wf})/d \ln (\Delta t_e)$ vs. Δt may be matched with a type-curve such as Fig. 2 of *Mishra* and *Ramey* (1987). But Fig. 6 shows that a type-curve matching without considering producing time effects may yield an overestimated r_{eD}^2/C_D for smaller producing times.

Figure 7 shows an investigation of t_{pDA} as a correlating parameter for the buildup behavior of a well in the center of a circular reservoir with a constant-pressure outer boundary. Figure 7 applies for $C_De^{2s} = 10^4$ and $r_{eD}^2/C_D = 10^6$. The remarks for Fig. 6 also apply to Fig. 7. Thus, producing time effects may not be ignored in a type-curve matching analysis of buildup derivative data obtained from a well in a finite, circular reservoir.

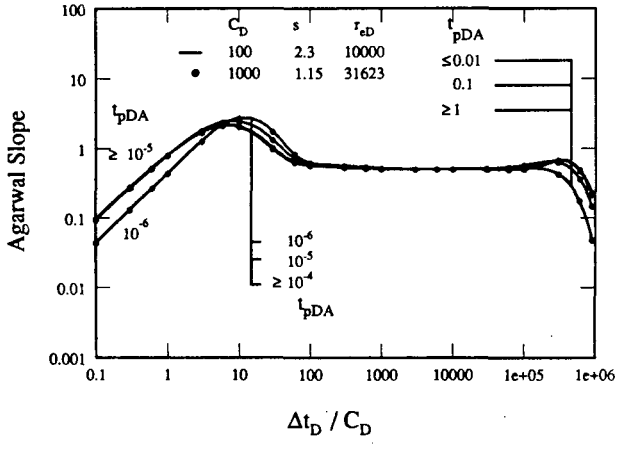


Fig. 7: Producing time effects on the buildup responses for a well in a reservoir with a constant-pressure outer boundary ($C_De^{2s} = 10^4$, and $r_{eD}^2/C_D = 10^6$).

SUMMARY

New drawdown and buildup derivative type-curves for a well with storage and skin, and located in the center of a finite, circular reservoir have been presented. Design equations for the time to the beginning and the end of the semi-log straight line have been developed. The drawdown and the buildup responses for a well in a closed reservoir are compared with the responses for a well in a reservoir with a constant-pressure outer boundary. Producing time effects and outer boundary condition should be considered for a proper type-curve matching analysis of buildup derivative data obtained from a well in a finite, circular reservoir.

ACKNOWLEDGMENTS

Financial support was provided by the Stanford Geothermal Program, DOE Contract No. DE-AT02-80SF11459; SUPRI A, DOE Contract No. AC03-81SF-11564; SUPRI A Industrial Affiliates; and by Stanford University.

NOMENCLATURE

A	Area
B	Formation volume factor
C	Wellbore storage coefficient
C_A	Shape factor
C_D	Dimensionless wellbore storage coefficient = $C/2\pi\phi c_t h r_w^2$
c_t	Total system compressibility
h	Thickness
I_n	Modified Bessel function of first kind of order n
K_n	Modified Bessel function of second kind of order n
k	Permeability
l	Laplace transform variable
p	Pressure
$\bar{p}_D$	Dimensionless pressure drop in the Laplace space
q	Well flow rate
r	Radius
r_{eD}	Dimensionless exterior radius = r_e/r_w
s	Skin = $2\pi kh(\Delta p_s)/qB\mu$
t	Time
t_D	Dimensionless time = $kt/\phi\mu c_t r_w^2$
t_{Dpss}	Dimensionless time to reach pseudosteady state = $kt_{pss}/\phi\mu c_t r_w^2$
t_{Dss}	Dimensionless time to reach steady state = $kt_{ss}/\phi\mu c_t r_w^2$
t_{pD}	Dimensionless producing time = $kt_p/\phi\mu c_t r_w^2$
t_{pDA}	Dimensionless producing time based on area = $kt_p/\phi\mu c_t A$
Δp_s	Pressure drop due to skin
Δt	Shut-in time
Δt_D	Dimensionless shut-in time = $k\,\Delta t/\phi\mu c_t r_w^2$
Δt_{DA}	Dimensionless shut-in time based on area = $k\,\Delta t/\phi\mu c_t A$
Δt_e	Equivalent drawdown time = $t_p\,\Delta t/(t_p + \Delta t)$
Δt_{eD}	Dimensionless equivalent drawdown time [Eq. (17)]

Greek symbols

ϕ	Porosity
μ	Viscosity

Subscripts

D	Dimensionless
e	Exterior, or equivalent
f	Flowing
i	Initial
p	Producing
pss	Pseudosteady state
s	Shut-in
ss	Steady state
t	Total
w	Wellbore

REFERENCES

Aarstad, K: "*Criteria for Determining Times for End of Transient Flow and Start of Pseudosteady State Flow*," Engineer Thesis, Stanford University, Stanford, CA (Aug. 1987) 162 pp.

Agarwal, R.G.: "A New Method to Account for Producing Time Effects when Drawdown Type Curves are Used to Analyze Pressure Buildup and Other Test Data," paper SPE 9289 presented at the 55th Annual Meeting of SPE of AIME in Dallas, TX (Sept. 21-24, 1980).

Aziz, K. and Flock, D.L.: "Unsteady State Gas Flow - Use of Drawdown Data in the Prediction of Gas Well Behavior," *J. Can. Pet. Tech.*, 2 (1), (1963) 9-15.

Chen, H.K. and Brigham, W.E.: "Pressure Buildup for a Well with Storage and Skin in a Closed Square," *J. Pet. Tech.* (Jan. 1978) 141-146.

Cobb, W.M. and Smith, J.T.: "An Investigation of Pressure Buildup Tests in Bounded Reservoirs," *J. Pet. Tech.* (Aug. 1975) 991-996; *Trans.*, AIME, **259**.

Earlougher, R.C., Jr., Ramey, H.J., Jr., Miller, F.G., and Mueller, T.D.: "Pressure Distributions in Rectangular Reservoirs," *J. Pet. Tech.* (Feb. 1968) 199-208.

Horner, D.R.: "Pressure Buildup in Wells," *Proc.*, Third World Pet. Cong., The Hague, II, (1951) 503-523.

Kumar, A. and Ramey, H.J., Jr.: "Well-Test Analysis for a Well in a Constant-Pressure Square," *Soc. Pet. Eng. J.* (April 1974) 107-116.

Matthews, C.S., Brons, F., and Hazebroek, P.: "A Method for Determination of Average Pressure in a Bounded Reservoir," *Trans.*, AIME (1954) **201**, 182-191.

Miller, C.C., Dyes, A.B., and Hutchinson, C.A., Jr.: "The Estimation of Permeability and Reservoir Pressure From Bottom-Hole Pressure Build-Up Characteristics," *Trans.*, AIME (1950) **189**, 91-104.

Mishra, S. and Ramey, H.J., Jr.: "A New Derivative Type-Curve for Pressure Buildup Analysis with Boundary Effects," *Proc.*, 12th Workshop on Geothermal Reservoir Engineering at Stanford Univ., Stanford, CA (Jan. 20-22, 1987) 45-47.

Ramey, H.J., Jr. and Cobb, W.M.: "A General Pressure Buildup Theory for a Well in a Closed Drainage Area," *J. Pet. Tech.* (Dec. 1971) 1493-1505.

Stehfest, H.: "Algorithm 368, Numerical Inversion of Laplace Transforms," D-5, *Comm. of ACM*, 13, No. 1 (Jan. 1970) 49.

van Everdingen, A.F. and Hurst, W.: "The Application of the Laplace Transformation to Flow Problems in Reservoirs," *Trans.*, AIME (1949) Vol. 186, 305-324.

PROCEEDINGS, Thirteenth Workshop on Geothermal Reservoir Engineering
Stanford University, Stanford, California, January 19-21, 1988
SGP-TR-113

THE DEPTH OF FEED WATER INFLUENCES MAXIMUM DISCHARGE-PRESSURE OF HOT WATER GEOTHERMAL WELLS

Russell James

Geothermal Research Centre, Wairakei,
D.S.I.R., Private Bag, Taupo, New Zealand

ABSTRACT

The maximum wellhead pressure at which hot water wells discharge is an important parameter for geothermal power and as it slowly declines with years of exploitation presents a moving target for project designers.

It can also decrease rapidly for newly closed-in wells (within days or even hours) to a point at which auto-discharge is impossible and tedious techniques have to be employed to restart flow.

The common cause of this phenomenon is reduction in the temperature of the hot water feeding the well; in the former case is the result of a general decline in the reservoir water enthalpy, and in the latter is due to cooler denser water from higher in the uncased part of the well percolating down and flooding the lower more permeable levels from which a discharging well mainly draws its fluids.

The inter-relationship of feed water temperature, depth and maximum discharging-pressure is determined in this study with illustrated examples demonstrating application.

INTRODUCTION

The highest well head pressure which can be attained by a hot water geothermal well is related to the feed water temperature and in the particular case where the subterranean reservoir is at Boiling Point with Depth (BPD), the relevant relationships have been deduced James (1980). These are as follows, with notation given later in metric units.

$$C = 99.75\ P_m^{0.283} \quad \text{for } 8 < P_m < 80 \qquad (1)$$

$$C = 69.56\ L_m^{0.2085} \quad \text{for } 30 < L_m < 3000 \qquad (2)$$

Although the BPD condition is common for hot water reservoirs, it is not unusual to find fields where displacement of this zone is downwards, or even upwards, by an amount which formerly could only be determined by careful downhole measurements under discharge. Such measurements have now been accomplished and indicate that the following equation is applicable:

$$P_m\ L_m^{0.574} = P_x\ L_x^{0.574} \qquad (3)$$

As an example of the use of this equation we can consider a well whose feed water temperature was measured at 247°C and from equations (1) and (2) with BPD prevailing, P_m = 24.63 and L_m = 436. The actual value of MDP was P_x = 19.24. When these values are substituted in equation (3), it is found that L_x = 670.7 which represents a displacement downwards of the BPD by 670.7 - 436 equaling 234.7 m.

Another well with feed water temperature of 320°C gave an actual MDP of P_x = 67 while from equations (1) and (2), P_m = 61.5 and L_m = 1509.6. Using these values in equation (3) gives L_x = 1300 which represents a displacement of the BPD upwards by 1300 -1509.6 equaling - 209.6 metres. Downhole measurements confirmed these figures.

It should be noted that the discharge at the highest operating wellhead pressure (MDP) is usually quite large being of the order of 100 t/h for a 0.2032 diameter well with a feed water temperature of 250°C. This condition is not the same where a well is discharging through a small "bleed" pipe of about 20 mm diameter as in this case flows are of the order of 1 t/h as studied previously, James (1987). The bleed condition is a long-term small discharge whose purpose is to retard corrosion in a well and to avoid differential expansion of the steel casing with possible rupture when full flow is required. Some wells if fully closed can also gradually increase in well head pressure due to the presence of non-condensible gas (mainly carbon dioxide) up to a point at which they exceed the safe working pressure of surface equipment; bleeding retards this gas pressure build-up to acceptable values and is mandatory where gas generation is suspected.

DECLINE IN MDP (SLOWLY)

Under production discharge, flow rate and MDP decline with time and in fact these parameters are roughly proportional to each other (so long as factors such as mineral deposition within the well does not intrude). The cause of this decline is sympathetic fall in the feed water temperature entering the well, and this is usually found to be precisely at the boiling point for the pressure.

For example, one of the most powerful of the Wairakei wells, WK30, originally derived its flow from a permeable horizon at a depth of 564. Flashing of the 254°C water took place at a depth of 499 giving a MDP of about 27.2. After 25 years of production, the MDP has fallen to 12.3 with flashing over the whole depth of 564 now taking place. To determine the associated feed temperature from these data in place of actual downhole measurements, which would require taking the well off production (not an attractive idea to the power station engineers) requires re-arranging the equations, as follows:

Substituting C for both P_m and L_m from equations (1) and (2) in (3), we have:

$$C = 85.1835\ P_x^{0.1591}\ L_x^{0.0913} \qquad (4)$$

Hence for $P_x = 12.3$ and $L_x = 564$, C = 226.4°C.

Downhole measurements made while bleeding the well in 1986 gave a Bottom Hole Temperature (BHT) of 226.5°C which is in good agreement with this result and for most other wells of that area for approximately the same depth.

DECLINE IN MDP (RAPIDLY)

Compared with the slow decline of MDP under production, some wells when fully closed or even when bleeding, decrease in wellhead pressure to a point at which they are difficult or impossible to start, without employing pressurising techniques or other means of starting discharge. When this is likely, engineers are hesitant about closing such wells - even for important measurements -because of the chance of losing flow completely. The cause of such relatively rapid decline in MDP (a matter of weeks rather than the years of production) is almost certainly due to fall in the water temperature within the well. And this is likely to be due to "cooler" water percolating down from minute fissures higher up the well in the uncased region. These fissures make a negligible contribution to flow when commercial discharges are taking place but when the well is closed (or bleeding) even a relatively small seepage of 1 litre/sec at say 150°C would flood the well bottom with over 600 m^3 of water in a week. It appears probable that flows much less than 1 litre/sec would also exert a considerable effect on the MDP and thus the ability of a well to autodischarge.

For closed wells which have long lengths of casing, it is possible that heat loss to cooler zones of the reservoir will result in cooling of internal fluids with the same overall effect but this is not so certain as for an uncased length.

For autodischarge to be possible, it would appear reasonable that the value of MDP should always exceed atmospheric pressure which we can assume at roughly 1 bar. If, for example, we take this figure together with a depth of $L_x = 564$ as for well WK30 at Wairakei, then equation (4) gives a water temperature of 152°C. For water of this temperature percolating downwards in the well, the MDP would not exceed atmospheric pressure and hence the well should not be capable of spontaneous discharge when the wellhead valve is open.

Although the accuracy of equation (1) is reduced where P_m is less than 8 ba and hence equation (4) cannot be accepted as exact, the relationship is considered reasonably correct. This is somewhat confirmed by results on Wairakei well WK107 which declined in output until it could not be discharged when the wellhead pressure had fallen to near atmospheric. Downhole measurements with the "Spinner" showed the existance of a downflow of cooler water at 140°C at 300 metres depth within the uncased portion of the well. When this horizon was sealed off, the well head pressure increased, and it was resurrected as a production well again.

Boiling point temperatures which are insufficient to give a wellhead pressure exceeding atmospheric (at 1 bar) are tabled below at various depths and have been calculated from equation (4).

TABLE 1: Boiling water temperatures at depth whose vertical flow develops a well head pressure of 1.0 bar abs.

Depth	230	500	1000	1500	2000	2500	3000
Temp	140	150	160	166	171	174	177

Illustrated Example 1

The Maximum Discharge Pressure (MDP) is 31 bar for a well which boiling water enters at a depth of 1500 m. Estimate the water temperature and likely displacement of the BPD zone. From equation (4),

$$C = 85.1835\ 31^{0.1591}\ 1500^{0.0913}$$
$$= 286.8°C \text{ water temperature}$$

From equation (2),

$$286.8°C = 69.56\ L_m^{0.2085}, \text{ hence } L_m = 893$$

Displacement of the BPD downwards = 1500 - 893
= 607 metres.

Illustrated Example 2

At Wairakei, production wellhead pressures are about 7 bar. What temperature of boiling water entering wells at 564 metres will give Maximum Discharging Pressures of 10, 9, 8, and 7 bar? From equation (4), for L_x = 564.

$$C = 85.1835\ P_x^{0.1591}\ 564^{0.0913}$$
$$= 151.9\ P_x^{0.1591}$$

For values of P_x = 10, 9, 8, and 7, boiling water feed temperatures are respectively 219.1°C, 215.5°C, 211.5°C and 207°C.

These temperatures may be close to the minimum which is acceptable to give reasonably stable flows when MDP approaches the production well-head pressure.

CONCLUSIONS

Geothermal wells which derive their flow from subterranean hot water have hitherto been considered as more complex than wells which discharge only dry steam. The use of the MDP can however give vital data on downhole conditions in the former and bring it more in line with the simplicities of the latter.

Its plot versus time for power production wells may be a useful aid in predicting the terminal condition where MDP approaches or coincides with the production well-head pressure.

NOTATION

C boiling water temperature, degree celcius

P maximum discharging pressure (MDP), bar

L depth in well from ground surface, metre

Suffixes

m for reservoir at boiling point with depth (BPD) where top is 100°C at ground surface

x condition which may diverge from ideal BPD

REFERENCES

James, R. (1980): Significance of the Maximum Discharging Pressure ofGeothermal Wells. Proc. 6th Workshop, Geothermal Reservoir Engineering, Stanford University, Stanford, California, U.S.A.

James, R. (1987): Bleeding Characteristics of Geothermal Wells. Proc. 12th Workshop, Geothermal Reservoir Engineering, Stanford University, Stanford, California, U.S.A.

PROCEEDINGS, Thirteenth Workshop on Geothermal Reservoir Engineering
Stanford University, Stanford, California, January 19-21, 1988
SGP-TR-113

RESERVOIR MANAGEMENT - AS CONCEIVED AND APPLIED ON THE PALINPINON RESERVOIR, PHILIPPINES

Zosimo F. Sarmiento and Arthur E. Amistoso

PNOC-Energy Development Corporation
PNPC Complex, Merritt Road, Ft. Bonifacio, Makati
Metro Manila, Philippines

ABSTRACT

The present exploitation of Palinpinon reservoir has revealed valuable information on the subsurface characteristics of the reservoir under large scale production. The initial behavior of the field has given signals that there is a need to implement appropriate strategies to optimise its capacity without jeopardizing the supply of adequate steam to the power plant.

Some of the problems encountered such as reinjection returns, mineral deposition, ingress of acid fluid and other phenomena indicated the need to pursue an agressive monitoring capability and timely appraisal of the field response to design an approach which will best suit the optimum management of the reservoir. The results of reservoir monitoring are discussed as well as the policies applied in operating the field.

INTRODUCTION

With only a few years of experience in exploring for and developing geothermal energy, PNOC-EDC and NPC were able to install two 112.5 MW power plants in 1983 in Tongonan and Palinpinon. In both fields, the formulation of reservoir management policies were instituted, especially in Palinpinon where the reservoir properties are considered complicated. The development of the field was conceptualized with over a few wells drilled to support a 112.5 MW power plant. Several constraints (also discussed in Tolentino (1986)) like the commitment to meet the plant commissioning schedule, the rugged terrain, ecomomic cost and the lack of sufficient long term well test data have substantially affected the total development plan of the field. It is in this field where we applied the first compact development plan by drilling more directional wells in a multiwellpad system. The multiwell-pads were compressed on the surface resulting to a tightness in spacing within the upper portions of the wells. Identifying the reinjection sectors, the main production sectors and determining the distances between wells, the casing design, the targets of the directional wells and the intersection of the different faults with the wells had been based on the field model inferred from initial drilling results. More data have become available after the initial stage of exploitation showing indications on how the field would behave under long term exploitation. Some uncertainties were recognized especially on the effects of injection fluid to the production wells.

An intensive monitoring program was embarked since the plant was commissioned in 1983. The results have been used in formulating reservoir management strategies which are modified and changed during the period, with the main objective of (1) optimizing the field capacity based on available wells and installations (2) minimizing adverse effects of reinjection fluids (3) ensuring that adequate steam is supplied to the power plant and (4) operating the field with minor expenditures.

The present paper describes the exploitation of Palinpinon reservoir with respect to the results of the monitoring and management schemes implemented up to the present period.

THE PALINPINON RESERVOIR

The Palinpinon geothermal field is located on the island of Negros in the Central Visayan region within a reservation encompassing 133,000 hec-

tares. The first geoscientific surveys in the area were conducted in 1973 followed by drilling the first three shallow exploratory wells N-1, N-2, and N-3 in 1977. This led to the successful discharge of N-3 and the drilling of deep exploratory wells Okoy-2, Okoy-3, Okoy-4 and Okoy-5 with the intention of probing the drainage source of the initial shallow wells. Positive results in the latter wells also led to the development of Puhagan sector for Palinpinon I and the Nasuji-Sogongon sector for Palinpinon II.

Todate, 21 wells have been hooked up to supply steam for Pal I, 18 directional, 3 vertical and 10 RI wells, most of them directional. The results of well drilling and discharge testing indicated that Palinpinon reservoir is a typical liquid dominated system discharging mainly from single-phase liquid feed zones. There exists boiling in the upper part of the reservoir as the pre-exploitation data indicated two-phase zone at shallow levels in OK-2 (at -200 m RL) and in OK-2 (at -750 to -950 m RL) and in PN-31D. A two phase zone also exists in the shallow level of the reservoir in the Sogongon sector. This two-phase zone has been observed in PN-30D and OK-9D as a result of exploitation.

During shut condition, internal flows in the well persist with strong inflows of 260-280 C liquid from -600m to -800m MSL downflowing and exiting at -1600m to -2000m MSL. In the eastern part of the field, temperature inversions are noted, e.g. at PN-15D, PN-17D, Okoy-10D and PN-21D (not continous to bottomhole) indicating outflow features and/or lateral incursion of relatively colder fluids. Fig. 1 shows the temperature contour distribution in the field, depicting the upwelling zone in Puhagan sector beneath Okoy-9, PN-27D and PN-23D. Two major outflow regions are distinguished by (1) long but narrow temperature lobe flowing to the NE across the NE part of the field and (2) broad temperature lobe to the west across the southwestern part of the field. This agrees very well with the chemistry data although these indicate more dilute fluid in Nasuji-Sogongon sectors in contrast to the NE wells which are highly mineralized.

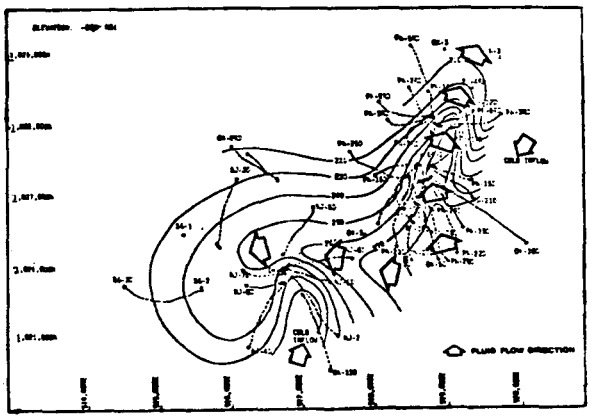


Fig. 1. Temperature Contours at -500 m MSL and Inferred Hydrological Flow

It is inferred that permeability controls have largely affected the flows between the two outflow regions, with the Ticala fault as the most probable channel of fluid to the NE. Fig. 2 shows other faults crisscrossing the field, e.g., Puhagan fault and its splays, Odlumon fault, Lagunao fault and Ticala fault splays which comprise the Puhagan fault system (Alcaraz, 1985). These faults are similarly inferred to have been responsible for the permeability encountered at depths aside from the stratigraphic contacts between formation. Recent data also indicate that these faults are acting as channels of communication among wells and are now causing more problems than were expected before.

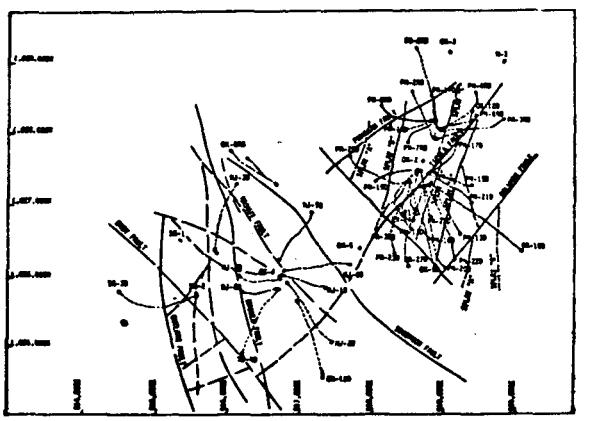


Fig. 2: Geologic Structures Across Palinpinon Field

RESERVOIR MONITORING & MANAGEMENT PARAMETERS

In the middle of 1983, the 112.5 MW power plant was commissioned to generate power for the whole Negros Island. The plant is a variable load power plant which handles load fluctuations by using blow-off system and control valves in the steam gathering system. A typical 31 MW (average) plant load is shown in Fig. 3. Inspite of the plant capacity and the availability of full power potential on the wellhead, only 30-50 MW are currently generated due to low power demand. This situation allows ample flexibility in the utilization of production and reinjection wells, which become beneficial to the management of the resource in terms of providing reasonable time for the field to be observed. It also allows management policies to be changed without introducing immediate and radical solutions to some major problems.

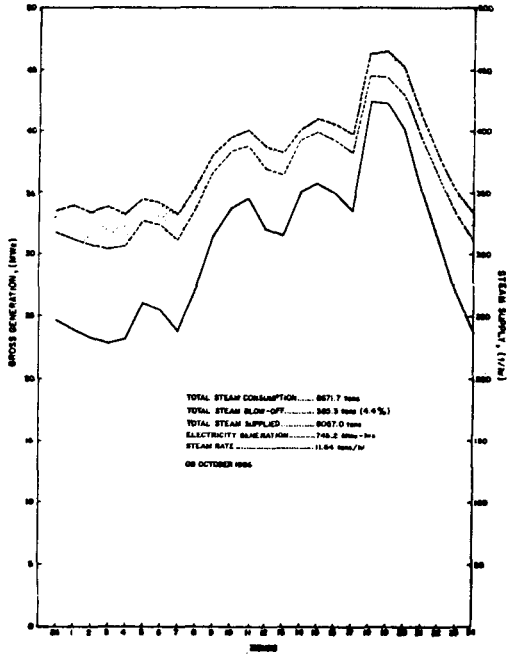


Fig. 3: Typical Power Generation Curve in Palinpinon I Power Plant

In formulating the reservoir management strategy, focus was given to the implications of the folllowing parameters to the prudent management and lenghtening of the deliverability of the field:

Pressure Drawdown

Downhole pressure measurements are conducted on a regular basis in order to determine pressure changes with time. These enable the reservoir engineers to determine which sector of the field is highly affected by production and/or influenced by natural recharge or reinjection fluid returns. As a start, we minimized the creation of large pressure drawdowns which may be localized or confined in a small sector by initially distributing production on a large part of the field. We considered it a first step countermeasure in order to avoid premature incursion of surface meteoric water or lateral flow of relatively colder fluids from the edges of the field. This is attained by throttling the well discharges such that two phase zone is also minimized in the upper zone and contribution from the high temperature bottom zone is enhanced. As a consequence, high volume of waste water were produced necessitating a bigger reinjection capacity as compared to when production is coming from the created two-phase region in the upper zone. Neverthless, this is offsetted by the fact that the two-phase zone easily collapses and condenses upon cooling of reinjection fluid returns and invasion of cold meteoric water.

In the first year of operation, wells in the eastern borefield were utilized (PN-15D, PN-21D, PN-17D, PN-22D, PN-26, Okoy-7 and Okoy-10D) reinjecting into Okoy-12RD, PN-6RD, PN-1RD, PN-2RD, PN-5RD and PN-7RD. These wells were drilled closer to the production wells. While on line, pressure drawdowns were noted but when production was shifted to the western borefield, pressure recoveries were observed. The upper zones in some wells like Okoy-7, Okoy-9D, PN-20D and Okoy-10D, which were going two phase gradually went back to single phase because of the effect of reinjection fluid returns. But in the case of Okoy-10D, it is believed that natural recharge occurs as no RI fluids are detected in this well.

In wells PN-1RD, PN-7RD and PN-9RD, pressure declines were noted although they were under reinjection. This similarly indicates that these wells are connected to the production sector and should be used only minimaly as much as possible. Pressure declines were also noted in Okoy-1, N-1, N-2, and N-3; all

drilled further and shallower from the outflow region - hinting connection with the production sector. This connection is inferred to be via the upper zone. On the other hand, Okoy-3, which is also located in the northern outflow region of the field, exhibited a pressure increase of 0.8 MPa during the same period in 1983-1984. We interpreted this to be connected to the main reinjection sector. Fig. 4 shows the pressure changes of the different wells. To date, the average pressure decline after 4 years of exploitation has reached 1.56 MPa with maximum drawdown of 2.6 MPa in PN-24D. PN-14, a vertical well close to the RI sector has had pressure fluctuations highly dependent on production and reinjection wells utilized.

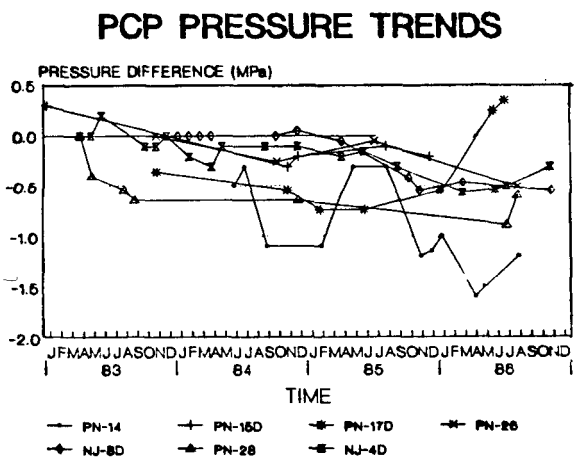


Fig. 4: Pressure Drawdown of Palinpinon I Wells During Exploitation

From 1983-1987, pressure declines were similarly noted in Nasuji-Sogongon sector although with some preference on the eastern wells like Okoy-11D, NJ-8D, NJ-4D and NJ-7D. The decline appears to have been propagated through the faults crisscrossing Pal-I and Pal II wells, most probably from Ticala fault. This observation is being investigated to see its implications on the development of the sector.

Thermal Drawdown

Since reinjection is a main component of the strategy, temperature deterioration due to fluid returns has been the primary concern. Influx of cold meteoric water and lateral flows from the edges of the field are also watched out. It has been our policy to keep reinjection fluid return as minimum as possible if not avoidable.

The most significant observation on the changes in temperature associated with reinjection returns was the decline in temperature at Okoy-7 at the bottomhole from 310°C to 290 in 1985. During the period PN-9RD was on line from about 4 months and fluids were leaving the well @ -2200 m, almost in the same elevation as in Okoy-7 feed zone @ -2000 m. The distance between the two zones is about 800 m. When PN-9RD was shut, the temperature recovered to its original temperature indicating that the temperature decline is a reversible process (see Fig. 5). This may also mean that the cooling in the well is only localized and confined mainly within the walls and vicinities of the fluid channel. Later in 1987, the decline in temperature at the upper zone in Okoy-7 was also noted from 282°C to 268°C. The two phase condition earlier observed has gradually turned single phase also. It is inferred that this phenomenon is due to the reinjection at PN-1RD and PN-6RD, which are both accepting at the upper zone.

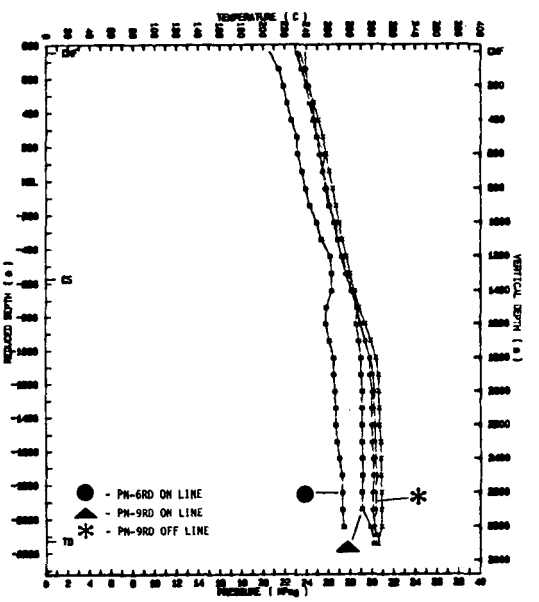


Fig. 5: Well Okoy-7 Temperature Changes With Reinjection Well Utilization

Another well which has suffered from the effects of reinjection return is well PN-26. It has since decline in temperature from 270 C to 238 C. This well is believed to be communicating with PN-9RD,PN-1RD, and PN-6RD. Its silica temperature also substantiated this temperature deterioration and in February 1986, a silica breakthrough was confirmed. The temperature of 258 C was measured while the calculated silica temperature was 267 C.

Some temperature changes have also occured in other wells due to increased reinjection returns but many of them disappear as soon as changes in the dominant zones occur. For example, downflows were initiated when shut but these are suppressed upon discharge from the lower zone.

To make use of the observed temperature decline in the field, a correlation has been established to predict deterioration of temperature in wells due to reinjection returns. The parameter used was the cumulative reinjection return produced from a well as against time. Based on Okoy-7 and PN-26, temperature decline in the wells is expected to be observed after producing a mass flow of 1.5 x 10 tonnes (produced reinjection fluid). This is clearly demonstrated in Fig. 6. Based on the figure, it is expected that thermal decline in many wells is expected to occur in 1987- 1988.

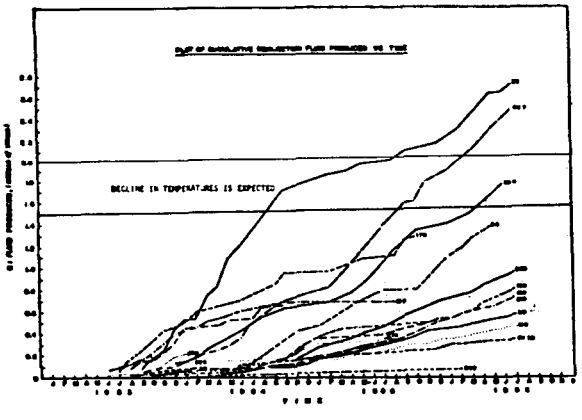


Fig. 6: Plot of Cumulative Reinjection Fluid Produced for Palinpinon I Wells

In view of the above observations and the continuos rapid return of reinjection fluid to majority of the wells, a long term plan is drawn to move the reinjection sector further to the area of Okoy-3, N-3 and northwards. With the full operation of 112.5 MW, it is expected that 75% of the reinjection fluid will be reinjected into this region.

Chemical Changes

Harper and Jordan (1985) have reported the chemical changes in the reservoir in response to production and reinjection at the Palinpinon Field. Not long after the commissioning of the plant, reservoir chloride has already increased despite the absence of highly mineralized source from within the reservoir. This led to the conclusion that RI returns were the principal cause of the increased mineralization. Continuos monitoring of calcium, sulfate, silica, gas and acidity are conducted in order to assess the major implications of reinjection returns to the performance of the reservoir. Fig. 7 shows the reservoir chloride increases calculated from individual wells PN-15D, PN-21D PN-26, PN-28 and Okoy-7. Most of these wells exhibited significant increases while RI wells PN-1RD, PN-6RD and Okoy-12RD were on line. When PN-1RD was put off line, reservoir chloride for Okoy-7, PN-26 and PN-28 decreased, and when PN-9RD was put on line in the middle of 1985, chloride values increased again. These imply good communication between these production wells and reinjection wells. As a result, the production wells were put on reserve and production were shifted to the western sector.

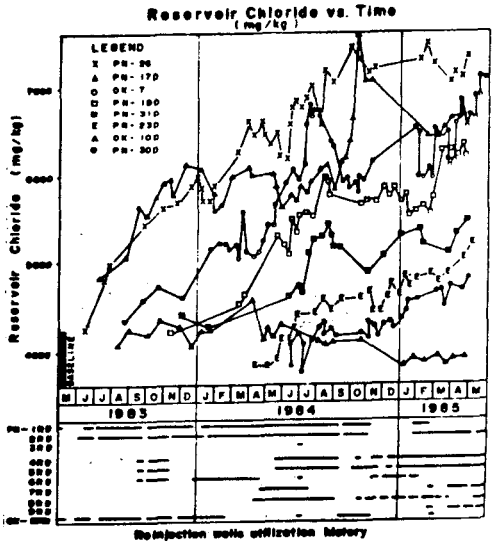


Fig. 7: Reservoir Chloride Changes of Palinpinon I Wells During Exploitation (from Harper & Jordan, 1985)

Tracer Test

To further understand the fluid movements in the reservoir, tracer tests were programmed at certain periods. Urbino et al (1986) discussed in detail the result of the iodine and sodium fluorescein tracer tests conducted in Palinpinon. The results are consistent with the observations from the pressure changes and chloride increases.

In the eastern part of the production borefield, wells PN-15D, PN-17D and PN-28 were found to have communicated rapidly with Okoy- 12RD, with less than a day detection at PN-17D. The mean transit time was from 3.9 to 7 days on the three wells. Based on the sodium fluorescein tracer tests, Okoy-7 also communicates rapidly with PN-9RD, with a breakthrough time of only 1.08 days. The average mean transit time detected from the Iodine tracer gave an average mean transit time of 5.7 days. Breakthrough velocities are calculated to be from 35 m/hr for PN-9RD to Okoy-7 and from 4.7 to 8 m/hr to other production wells. On the basis of the results shown in Table 1, production and reinjection showing rapid communication were given less priorities in the utilization.

TABLE 1 - PN-9RD TRACER TEST RESULTS

Well	% Return	I-131 TRACER Ave. Transit Time DAYS	SODIUM FLUORESCEIN Breakthrough Time DAYS
OK-7	29.2	5.7	1.08
PN-29D	6.8	14.0	6.00
PN-26 *	3.9	11.0	5.50
PN-28 *	1.1	10.3	6.00
PN-18D	0.8	15.6	Not Monitored
PN-30D	0.8	15.7	8.30
PN-23D	0.4	15.8	7.50
PN-31D	0.4	16.0	5.50
PN-16D	Tracer found in samples after 8-19 days		9.80
PN-19D	Tracer found in samples after 8-19 days		6.00
PN-17D	No response		6.00
OK-9D	No response		No response detected

* Wells on heavy bleed. Tracer return values believed to be erroneous to inaccurate mass flowrates used.

Attempts were made to correlate this tracer arrival data to thermal breakthroughs but they were not successful. However, the results were found to be very valuable during the initial exploitation of the field, especially in tracing the preferential flowpath of the reinjection returns and prioritizing well for utilization.

Well Output Changes

Corollary to the above parameters, the performance of the production wells were monitored to detect output decline caused by thermal decline and pressure draw down. From June 1984 - Sept 1985, well PN-26 output characteristics had started changing significantly with its operating WHP declining from 2.4 to 1.82 MPag. As of November 1986, WHP dropped to 1.07 MPag, with a corresponding drop in enthalpy from 1230-1120 kJ/kg. This feature was later observed at Okoy-7 reinforcing the initial concern on the adverse effects of rapid reinjection returns. Since then, well PN-26 and Okoy-7 were given low priority and utilized sparingly during peak hours.

Reinjection Well Capacities

Like the production wells, the performance of the reinjection wells is critical to the performance of the system. Waste water cannot be dumped to the river because of environmental constraints. Regular measurements were conducted to accurately determine changes in the wells' injectivity and capacity.

In general, an increase in capacity has been observed after 1 or 2 years of reinjection, probably resulting from improvement in permeability caused by the contraction of the reservoir rocks as they are cooled by reinjected fluid.

Well PN-2RD had initially suffered a decline in capacity attributed to silica deposition and formation of blockage. In this particular well, fluid residence time has been considered responsible for the silica polymerization since it is tapping from the farthest end of the reinjection header making it insusceptible to the preferential flow of liquid.

To ensure that all wells have short fluid residence time, steps were taken to use all the RI wells at/or near full capacity, e.g. with water level at the CHF. No extra wells are put on line that can cause excess capacity than required.

Accumulation of debris, cuttings and solid materials were also noted

to have been responsible for the reduction of well capacities. As a countermeasure, solid traps and strainers were installed to trap and screen out the debris and solid materials transported with the reinjection fluid.

Slugging of hot reinjection fluids are also carried after cutting reinjection wells from the system in order to displace and push the supersaturated silica fluid into the formation with undersaturated liquid.

In view of the general increase in the reinjection capacity, it is difficult to determine any decline in reinjection well capacity caused by an increase in reservoir pressure.

Acidity and Anhydrite Deposition

Prior to exploitation, no signs of acidity were detected in the discharge tests of the wells. However, some acid indications were recognized in the field which is now a cause of concern vis-a-vis the field management. Well PN-22D became acidic after 2 months of discharge to the SGS and was shut merely after 4 months. This was the first well to have shown acid discharge. Another well which has a tendency to become acidic is Okoy-10D, also in the eastern borefield. The discharge of OK-10D indicated higher sulphate concentration com pared to the other production wells, although its discharge has not become acidic as in PN-22D. An adjacent well (PN-20D) is currently showing acidity after having been used sparingly in the last 4 years.

As a result of the ingress of acid fluids, anhydrite blockage were formed as the acid fluid mixed with calcium-rich neutral liquid. This results to a reduction in well output.

Work-over were conducted in PN-22D and Okoy-10D in 1987 to clean the anhydrite blockage and hopefully suppress the acid fluids during production. But this was not successful. Contribution from the acid feeds in the upper zone persists, even under injection condition and during the post work-over discharge. Formation of anhydrite blockage reoccured although Okoy-10D is still supplies the system. Experiments are being undertaken to seal-off these acid feeds and hopefully eliminate this problem.

Calcite Deposition

Only wells PN-13D, PN-15D and PN-21D had suffered calcite deposition so far. This may be attributed to the relatively colder fluid produced from these wells which are aggravated by the contribution from the zones of temperature inversion at the bottom.

After 6 months of discharge, calcite deposits grew up in PN-13D requiring a work-over prior to commissioning of the plant. It was put to operation in 1984 but again suffered calcite problem after 6 months. This well has since been shut and put on low utilization priority.

Pipeline Scaling

Deposition in the SGS pipeline also affects the utilization and program of the production and reinjection wells. From experience, silica deposition accumulates from strategic points in the system which requires inspection and cleaning at regular periods. Collapse of compensator liners, cuttings and commissioning debris left in the pipeline during the construction stage have also promoted silica deposition. To minimize deposition, wells which are exhibiting low silica saturation were put on high utilization also prioritized. Efforts are also made to avoid backflow of reinjection fluid in order to minimize damage to the compensators.

Heat Utilization Efficiency

Since the plant is a variable load plant, the main SGS was designed in such a way that fluctuations in the power would be absorbed immediately by the SGS. Its operation requires installing control valves and blow-off valves. These take into account extra steam which are immediately required to supply steam when demand is increasing and to bypass steam when load is decreasing. Because of this, over protection in the ability of the system to respond load fluctuations had been resorted to. During the initial stage of exploitation, approximately 50-70 TPH of steam are blown-off to the atmosphere. However, with the installation of sufficient control valves and subsequent gain in operating experience, blow-off has been reduced to 20 TPH.

All efforts are also being made to ensure that power generation company utilizes their Mechanical Gas Extractor (MGE) instead of the Steam Gas Extractor (SGE) which consumes 10% to 12% of the total steam supply to the power station. This is intended to minimize wastage and improve the heat utilization of the field.

Other parameters like fluid mass and heat withdrawal/injected, load forecast, microseismic activities, environmental constraints and quality of steam fed to the turbines are also considered in the planning and utilization of wells.

RESERVOIR MANAGEMENT POLICIES

Based on the preceding discussions, management policies have evolved on how to utilize the wells and promote the optimization of the resource.

a. Those wells in the eastern part of the production borefield should be used only as reserve wells considering that they are communicating rapidly with the reinjection wells. In lieu of this, wells located in the western and southwestern part of the field are given higher utilization priorities.

b. Wells PN-1RD, PN-6RD, Okoy-12RD and PN-9RD were proven to be responsible for the rapid returns of reinjection fluid to the production wells. They are also put on low priority.

c. RI wells which have shown minimal effects to the production wells are given high priorities and are always put on line, i.e. PN-2RD, PN-3RD, PN-4RD and PN-5RD.

d. In view of the deteriorating temperature in wells Okoy-7 and PN-26, the wells are also put on reserve. Okoy-7 is to be used only to supply the 1.5 MW power plant.

e. Monthly measurements of well output and RI well capacities are conducted to ascertain flow changes.

f. Wells are throttled such that production in the field are distributed to spread pressure drawdown and avoid creation of localized two phase fluids prematurely.

g. Wells which are acidic are also put on reserve, and studies are being undertaken to combat entry of acid fluids to the well during production.

h. Wells which have calcite deposition tendencies are heavily throttled to raise the flashing point higher up in the wells (i.e. in the production casing). They are also put on low priority.

i. Efforts are being made to minimize blow-off in the atmosphere but ensure prompt response of the system to absorb power fluctuations. The use of Mechanical Gas Extractors (MGE) instead of the Steam Gas Extractor (SGE) in the power plant is being pursued.

j. As much as possible, wells are operated to give lower silica saturation index to minimize scaling in the well, separator and the pipeline.

k. Reinjection wells are operated at full capacity to lessen residence time thus reducing silica polymerization.

l. As a long term strategy, replacement reinjection wells will be drilled to the northern sector of the field collared from Okoy-3 or N-3 and targetted farther away from the field. This has been contemplated earlier but flexibility attained in operating the field because of initial low utilization level allow us to delay this plan. Similarly, thermal breakthrough and output decline were much delayed than chemical and tracer arrivals. Activities are now under way for the construction of a pipeline that can accomodate 150-450 kg/s of fluids to these sectors. Once this happens, many of the wells drilled will be fully utilized and production will be thoroughly distributed throughout the field.

CONCLUSION

The present exploitation of the Palinpinon field emphasises the need for a prudent reservoir management in order to fully optimize the full utilization of the resource Pressure drawdown, ingress of acidic fluids, mineral deposition and others have been encountered which put a challenge on the ability of the developer to operate the field properly. The initial operating policies and guidelines have been laid out to minimize these risks associated with reinjection returns. Additional studies are also undetaken in order to accurately predict field performance and to be used in formulating the over-all management strategy for the field.

ACKNOWLEDGEMENT

The authors wish to thank the management of PNOC-EDC for their permission to present and publish this paper. We would like to particularly thank B.S. Tolentino for his review and comments which significantly improved this paper.

REFERENCES

1. Alcaraz, A. P. (1985), "Geothermal Plumbing System of Puhagan, Southern Negros Geothermal Field, Philippines". Proceedings of the 1985 International Symposium on Geothermal Energy, Geothermal Resources Council, Kailua-Kona, Hawaii.

2. Harper, R. T. and Jordan, O. T. (1985). "Geochemical Changes In Response to Production and Reinjection for Palinpinon I Geothermal Field, Negros Oriental, Philippines." Proceedings 7th New Zealand Geothermal Workshop Auckland University, New Zealand

3. Maunder, B. R., Brodie, A. J. and Tolentino, B. S. (1982) - "The Palinpinon Geothermal Resource, Negros, Republic of the Philippines - Exploration Case History". Proceedings of Pacific Geothermal Conference 1982. Fourth New Zealand Geothermal Workshop Part I. University of Auckland Geothermal Institute.

4. Tolentino, B. S. (1986) - Lectures on Geothermal Energy in the Philippines, Geothermal Training Programme. UNU Iceland Report No. 12. 1986.

5. Urbino, M. E. G., Zaide, M. C., Malate, R. C. and Bueza, E. L. (1986), Structural Flowpaths of Reinjected Fluids Based on Tracer Tests - Palinpinon I, Philippines". Proceedings of the 8th New Zealand Geothermal Workshop 1986. Auckland University, New Zealand.

PROCEEDINGS, Thirteenth Workshop on Geothermal Reservoir Engineering
Stanford University, Stanford, California, January 19-21, 1988
SGP-TR-113

A VAPOR-DOMINATED RESERVOIR EXCEEDING 600°F AT THE GEYSERS SONOMA COUNTY, CALIFORNIA

M. A. Walters, J. N. Sternfeld, J. R. Haizlip, A. F. Drenick, and Jim Combs

GEO Operator Corporation
1330 N. Dutton Ave., Santa Rosa, CA 95401

ABSTRACT

A high-temperature vapor-dominated reservoir underlies a portion of the Northwest Geysers area, Sonoma County, California. The high-temperature reservoir (HTR) is defined by flowing fluid temperatures exceeding 500°F, rock temperatures apparently exceeding 600°F and steam enthalpies of about 1320 BTU/lb. Steam from existing wells drilled in the Northwest Geysers is produced from both a "typical" Geysers reservoir and the HTR. In all cases, the HTR is in the lower portion of the wells and is overlain by a "typical" Geysers reservoir. Depth to the high-temperature reservoir is relatively uniform at about -5900 ft subsea. There are no identified lithologic or mineralogic conditions that separate the HTR from the "typical" reservoir, although the two reservoirs are vertically distinct and can be located in most wells to within about 200 ft by the use of downhole temperature-depth measurements. Gas concentrations in steam from the HTR are higher (6 to 9 wt %) than from the "typical" Geysers reservoir (0.85 to 2.6 wt %). Steam from the HTR is enriched in chloride and the heavy isotopes of water relative to the "typical" reservoir. Available static and dynamic measurements show pressures are subhydrostatic in both reservoirs with no anomalous differences between the two; the HTR pressure being near 520 psia at sea level datum. The small observed differences in pressure between the reservoirs appear to vary along a steam density gradient. It is postulated that the Northwest Geysers area evolved more slowly toward vapor-dominated conditions than other parts of The Geysers field because of its poor connection with the surface. In this paper, a model is presented in which the boundary between the HTR and "typical" reservoir is a thermodynamic feature only, resulting from recent deep venting of a liquid-dominated system in which conduction is still an important component of heat transfer.

INTRODUCTION

The presence of high temperatures (>600°F) in wells drilled by GEO Operator Corporation (GEOOC), a wholly owned subsidiary of Geothermal Resources International, Inc. (GEO), in the Northwest Geysers (Figure 1) was first recognized in 1982 from temperatures measured during downhole directional well surveys. With the availability of high-temperature logging tools, the presence of flowing high-temperature (>656°F) steam was recorded in January 1984.

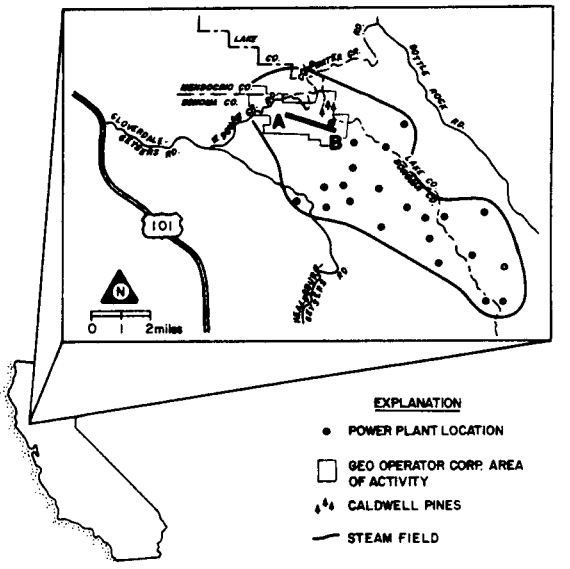


Figure 1: Map of The Geysers with location of geologic cross section (A-B) of Figure 2.

Wells in leases offsetting the Northwest Geysers area of GEOOC also penetrate (a) high-temperature reservoir(s) (Sternfeld and others, 1983 and Beall, 1985). Because there are at least two deep (±10,000 ft) wells that do not encounter high temperatures between the GEOOC and high-temperature wells on other leases, the HTR in the GEOOC area is treated in this paper as if it were a separate reservoir not related to others.

Wells penetrating the Northwest Geysers HTR, referred to as high-temperature wells later in this paper, are the subject of previous papers. Drenick (1986) discussed the logging and interpretation of a single high-temperature well and Haizlip (1985) described enriched isotope composition in steam from Northwest Geysers wells.

The primary purpose of this paper is to document the existence of a HTR by describing the areal extent and characteristics of the HTR penetrated by GEOOC wells. In this paper, it will be shown that the temperature and enthalpy of steam in the HTR are significantly different from the "typical" Geysers reservoir steam. It will also be shown that rock type, secondary mineralogy and pressure do not appear to be diagnostic of the HTR. Finally, a conceptual model is presented to explain the presence of the HTR in the Northwest Geysers.

GEOLOGIC SETTING

Lithology and Secondary Mineralogy

Most wells drilled by GEOOC in the Northwest Geysers are drilled from the surface to total depth in Franciscan graywacke (Figure 2). The only interruptions of the graywacke are occasional, thin (usually less than 100 ft) units of greenstone and chert, and tectonic-related melanges which include serpentinite, blueschist and clay. No significant changes in primary Franciscan formation metamorphic grade or detrital composition are observable between the graywackes of the unfractured rock overlying the top of steam, the "typical" reservoir and the HTR. These weakly metamorphosed metasedimentary rocks are reconstituted to textural grade 1 described by Blake and others (1967).

There is a gradational alteration of the graywacke with depth due to hydrothermal as well as thermal metamorphism. With increasing depth, the graywacke becomes hornfelsic as matrix materials and then framework grains become increasingly recrystallized. Tourmalinized reservoir rock (single hatching on the lithology column of Figure 3) displays weak to moderately developed schistose textures. At greater depths, the reservoir is noticeably hornfelsic (double hatching on the lithology column of Figure 3).

The HTR is most often encountered within hornfelsic graywacke and sometimes within the tourmalinized zone inferring a causal relationship. However, the correlation is fortuitous as "typical" steam reservoir conditions are also found in tourmaline-bearing and hornfelsic altered rocks in other Northwest Geysers wells. The apparent correlation between the hornfels and the HTR is simply a depth relationship.

The hornfels indicates intrusive rocks are relatively near. Publicly available, open-file well records from the California Division of Oil and Gas indicate that hornfels aureoles occur within 1500 ft or more above felsite bodies in the Southeast and Central Geysers areas. The nearly planar distribution of hornfelsic graywacke (Figure 2) indicates that felsite intrusives probably underlie a large extent of the GEOOC portion of the field although only two subsurface occurrences of intrusives are as yet drilled in the Northwest Geysers. Additional indirect evidence for Quaternary intrusion comes from geomorphological studies of the area. Circular anomalies, barbed tributaries and arcuate stream segments are evidence for

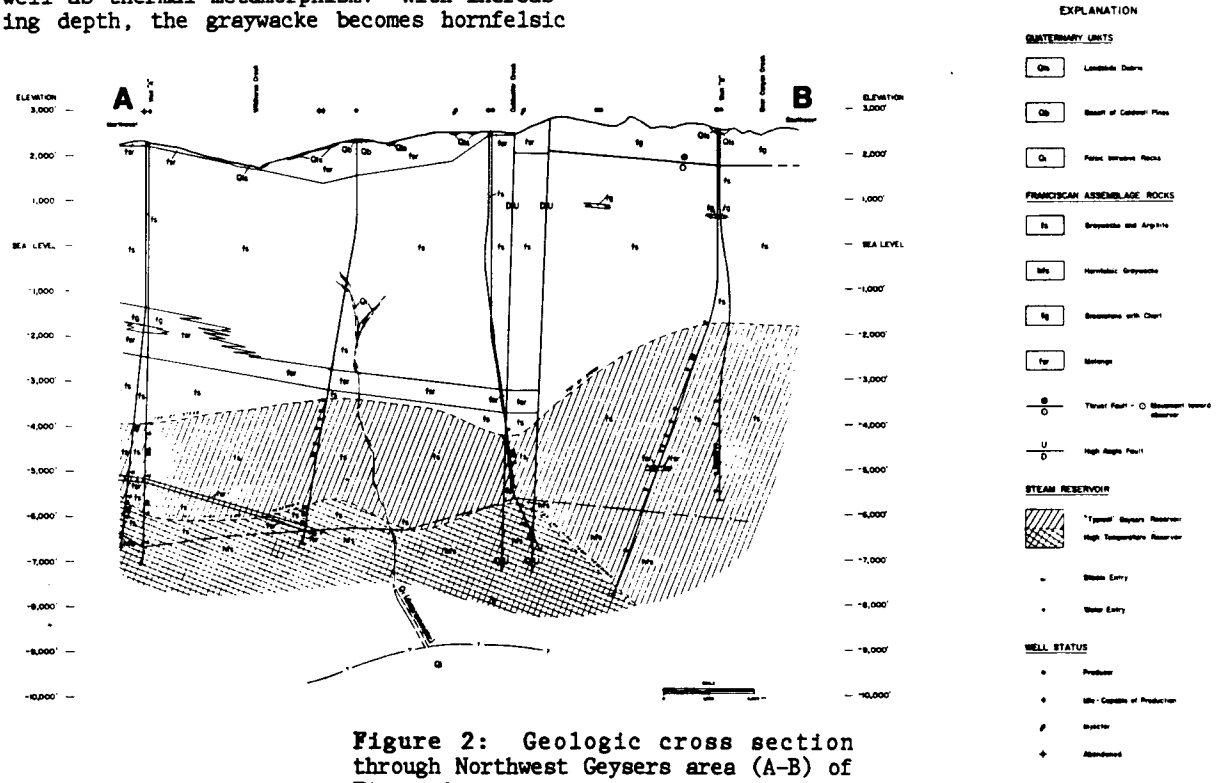


Figure 2: Geologic cross section through Northwest Geysers area (A-B) of Figure 1.

recent uplift and associated tensional faulting related to intrusive activity (Bebber, 1986).

There is no evidence to suggest that secondary minerals form a seal between the HTR and "typical" reservoir. The percentage of vein-filling minerals to total rock in both reservoirs is typically 1 to 3% and there is not a unique assemblage of minerals restricted to either reservoir. At least three generations of secondary minerals are recognized in The Geysers (Figure 3) as determined from petrologic and isotopic studies (Lambert, 1976; Sternfeld, 1981). The dominant secondary mineralization is a strongly zoned succession of Quaternary mineral assemblages deposited by a liquid-dominated hydrothermal system induced by felsite intrusion. A later Quaternary set of retrograde minerals superimposed over the first, occurs sporadically throughout the steam reservoir and tends to correlate with steam entries in well bores. This later Quaternary mineral assemblage, characterized by prehnite and axinite, probably represents the last forming minerals precipitated from liquid during the vaporization process that transformed The Geysers from a liquid-dominated to a vapor-dominated system. The temperature of formation for prehnite in active geothermal systems, 460 to 680°F (Bird and others, 1984), corresponds with the range of observed temperatures in both reservoirs.

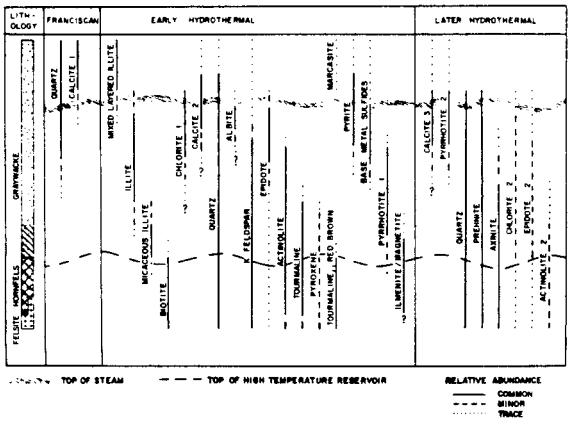


Figure 3: Generalized secondary mineralogy at The Geysers.

Surface Geothermal Manifestations

Unlike the Central and Southeast Geysers, relatively few surficial hydrothermal manifestations, i.e., vent areas, occur in the Northwest Geysers as shown in Figure 4. Presently, the only known venting of noncondensible gases in the portion of the Northwest Geysers developed by GEOOC are confined along the traces of two faults. These gases are from dry gas vents and cold springs which have anomalous concentrations of sulfate, carbon dioxide, boron and carbonate. Because hydrothermal alteration is often evidence for past geothermal activity, it is concluded that the surficial geothermal manifestations in the Northwest Geysers were also of limited extent in the past as in the present. The spatial relationship of noncondensible gas in steam from geothermal wells to surficial geothermal manifestations is also shown in Figure 4. As discussed later in this paper, the high gas content in the steam from wells of the Northwest Geysers and the relatively few surface manifestations are believed to be directly related.

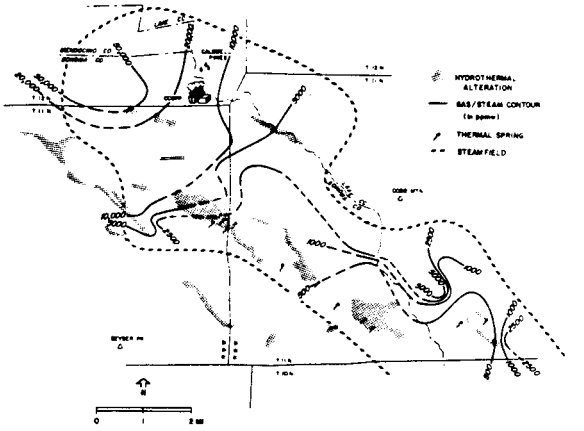


Figure 4: Relationship of gas/steam ratios from wells to vent areas in The Geysers.

RESERVOIR DATA

Temperature Measurements

The HTR is recognized primarily by downhole temperature measurements. Wellhead data are also useful in the recognition of wells penetrating the HTR but are not diagnostic in some cases where the relative steam contribution from the HTR to the total flow rate of the well is low (Table 1).

TABLE 1
Northwest Geysers
Sonoma County, California

WELLHEAD DATA

WELLS PENETRATING "TYPICAL" GEYSERS RESERVOIR (≤480°F)

Enthalpy (BTU/lb)	Total N/C Gas (ppmw)	H_2S (ppmw)	Isotopes vs. SMOW** $\delta^{18}O$(°/oo)	δD(°/oo)	Chloride (ppmw)
1195-1211	8500-25700	250-870	-0.2	-50	<1

WELLS PENETRATING HIGH TEMPERATURE RESERVOIR (≥500°F)

Enthalpy* (BTU/lb.)	Total N/C* Gas (ppmw)	H_2S* (ppmw)	Isotopes vs. SMOW** $\delta^{18}O$(°/oo)*	δD(°/oo)*	Chloride (ppmw)
1200-1242	26,000 - 76,700	750-1660	+1.4	-44	15-150

* Note: Values represent combined steam flow from both the HTR and "typical" Geysers reservoir. The relative contribution from the HTR at the wellhead ranges from >5 to 69% of the total flow. The highest values are from wells with the greatest steam contribution from the HTR.

** Isotope values are weighted averages.

Publicly available temperature-depth data for wells in the Central Geysers (Lipman and others, 1978 and Thomas and others, 1981) and proprietary temperature-pressure-spinner (TPS) data obtained by GEOOC are the bases of the following conclusions about temperatures in the "typical" Geysers reservoir:

1. Temperature logs from flowing wells consistently indicate temperatures in the range of 440 to 490°F within the reservoir. Where TPS logs are available, enthalpy values range from approximately 1220 to 1250 BTU/lb.
2. Temperature-depth plots of maximum-reading thermometer (MRT) measurements made on bottom during directional surveys while drilling in the "typical" reservoir usually range from 400 to 450°F with maximum values near 480°F. MRT temperatures exceeding 600°F are the first indication of a high temperature reservoir.
3. Flow line temperatures (FLT) of the circulating drilling medium (air) measured while drilling the "typical" reservoir are normally in the range of 210 to 230°F but may approach 320°F in some cases.

Using the data developed from wells in the "typical" Geysers reservoir, criteria were established to determine whether or not the HTR is penetrated. These criteria are as follows and are ranked by importance:

1. MRT values exceeding 500°F.
2. Downhole flowing steam temperatures exceeding 500°F.
3. FLT measurements of more than 300 to 320°F.

Taken together, these criteria were used to estimate the depth to the HTR for each well drilled by GEOOC. Examples of these criteria and the resulting estimate of depth to the HTR are graphically presented as individual temperature-depth plots for both a "typical" well and a high-temperature well (Figures 5 and 6). Accuracy of the depth estimates to the HTR is about 200 ft for most wells.

The temperature logs of flowing steam from completed wells often do not accurately show the boundary between the "typical" and high-temperature reservoirs. The reason for this is that high-temperature steam flowing up the wellbore masks the cooler entries in the "typical" reservoir (Drenick, 1986). Consequently, MRT values collected while drilling wells serve as a better criteria for delineating the top of the HTR and are ranked accordingly. However, it is acknowledged that MRT values from unequilibrated boreholes are not accurate temperature measurements of the reservoir rock temperatures (Pruess and others, 1987).

Although the maximum temperature of the HTR is not known, a flowing steam temperature of

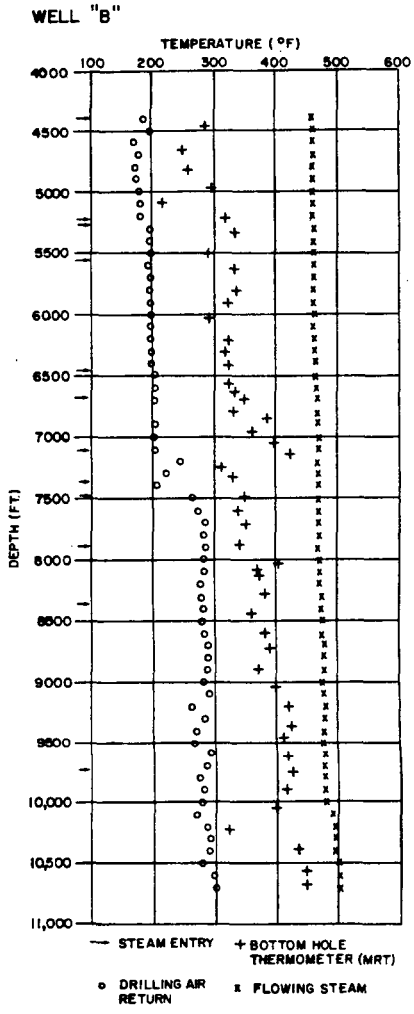


Figure 5: Temperature-depth plot for well penetrating only the "typical" Geysers reservoir.

656°F was measured prior to the failure of one temperature tool. The upper limit is not known because neither thermometers nor electric logging tools are available which exceed about 650°F. Where TPS logs are available, the enthalpies measured in the HTR range from 1300 to 1320 BTU/lb.

The depth to, and areal extent of, the HTR in the area of GEOOC's operation in the Northwest Geysers is shown on Figure 7. High-temperature wells are also known to the northeast (e.g., Occidental Wilson 1 well) but because several deep wells between these two areas encounter only the "typical" reservoir, it is unknown whether or not the two areas tap the same HTR. It is unknown how far the HTR may extend to the northeast, but it could extend across the Clearlake volcanic field (Beall, 1985). Similarly, it is unknown whether or not the HTR is present below the greater Geysers production area and has not yet been detected (Drenick, 1986) because wells and/or temperature measurements may not be deep enough.

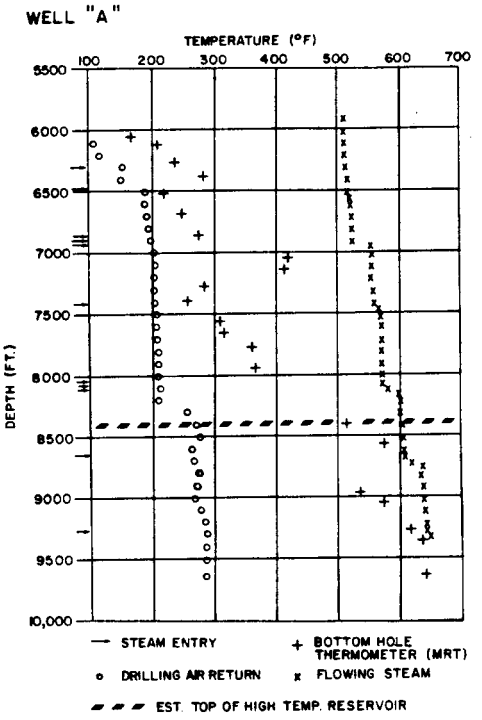


Figure 6: Temperature-depth plot for well penetrating HTR and overlying "typical" Geysers reservoir.

The thickness of the "typical" Geysers reservoir overlying the HTR is shown on the geologic cross section of Figure 2. This section is indicative of the relative contribution that the "typical" reservoir makes to wells penetrating the HTR. The thinnest part of the "typical" reservoir is also where the enthalpy and gas concentration of the steam, as measured at the wellhead, are highest.

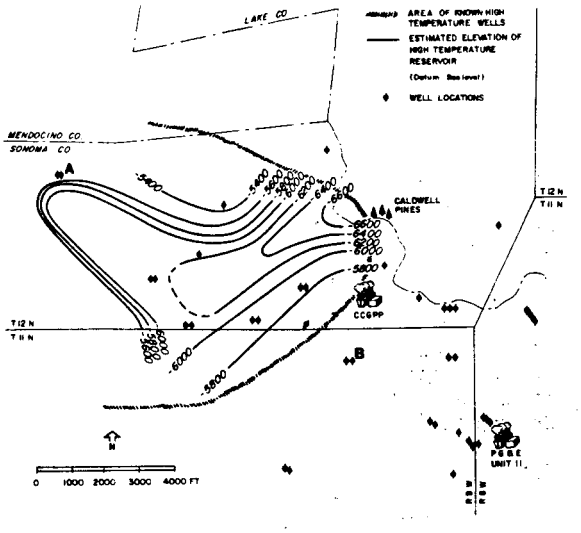


Figure 7: Depth to HTR in GEO portion of Northwest Geysers.

Heat transport from the "typical" reservoir to the surface is largely by conduction (Urban and others, 1975). Within the "typical" reservoir, heat transport is largely by convection (White and others, 1971) as evidenced by almost isothermal temperature-depth relationships. In Figure 5, an illustration of this phenomenon is presented. Heat transport in the HTR appears to have a large conductive component. Although the bottom-hole measurements made while drilling are not equilibrated, there are definite increases in temperature with depth in the HTR with apparent gradients ranging from approximately 5 to 10°F/100 ft. An illustration of an apparently high temperature gradient in the HTR is provided in Figure 6.

For any given heat flux, the temperature gradient is a function of thermal conductivity. Thermal conductivity measurements on 19 samples of hornfelsic graywacke were made using a method described by Sass and others (1971) to determine if the apparent higher temperature gradients observed in the HTR were related to the thermal alteration of the graywacke. Thermal conductivity values of the hornfelsic graywacke samples ranged from 6.1 to 7.6 TCU (mcal/cm-sec-°C) with a median value of 6.8 TCU. These values are very similar to graywacke which has a mean value of 7.6 TCU (Thomas, 1986). Therefore, the apparent high-temperature gradients in the HTR cannot be attributed primarily to contrasting thermal conductivity values.

Pressure Measurements

Pressure profiles were obtained in flowing wells, idle wells on small "bleeds", and completely static wells. The profiles are from wells both inside and outside the HTR shown in Figure 7. Approximately 50 profiles are available from the various wells, with the measurements having been performed from 1 to 600 days after completion of drilling. In all cases, steam is the pressure controlling medium with the maximum pressure measured being approximately 520 psia at sea level datum. All pressure gradients conform to expected steam densities; higher gradients which would be expected for a liquid-dominated section or a boiling, vapor-dominated to liquid-dominated interface have not been encountered. Further, there do not appear to be significant pressure differences between the two reservoirs. Thus, the HTR is not a liquid-dominated region at this time, nor does it appear to have substantial pressure differences from the "typical" reservoir which overlies it. Analysis of pressure buildup data, and other pressure transient measurements is underway to clarify the interpretation of the pressure behavior of the HTR.

Geochemistry of Fluids

Samples of steam were collected at the wellhead or steam line during drilling and flow

testing. Drilling samples were collected during trips and directional surveys. The drilling samples represent cumulative samples; i.e., the steam of each succeeding or deeper entry is mixed with the previous entries. Flow test samples represent combined production from all entries. Data from the analyses of noncondensible gas, chloride, oxygen-18 (O-18) and deuterium (D) data can be used to distinguish the HTR and "typical" reservoir.

Samples collected during drilling reflect changes of concentration with depth. A "typical" Geysers well has relatively constant fluid chemistry concentrations in the reservoir (see Figure 8), except for a possible gassy upper layer due to condensation. Gas concentrations in a high-temperature well increase significantly near the top of the HTR (see Figure 9).

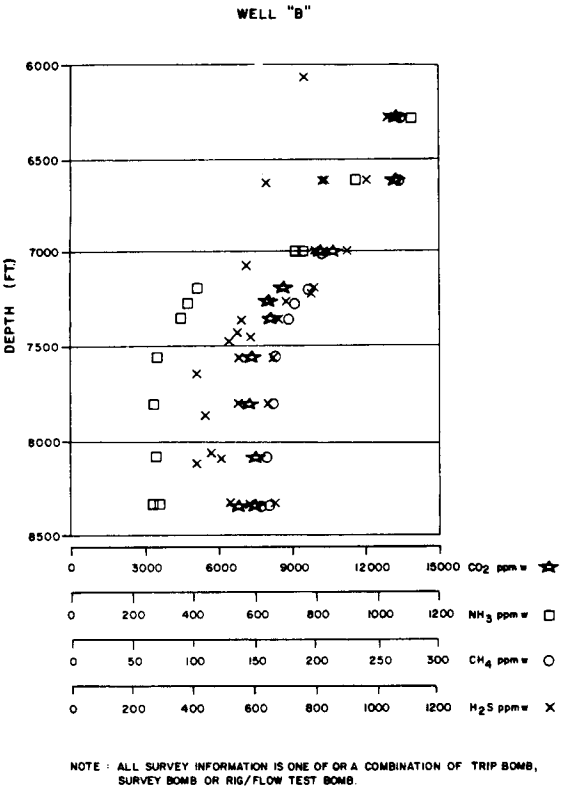


Figure 8: Wellhead gas concentrations of a well penetrating only the "typical" Geysers reservoir.

Flow test results from high-temperature wells representing the combined production of the "typical" and HTR reservoirs are compared with "typical" wells in Table 1. Wells penetrating the HTR contain higher concentrations of noncondensible gas, chloride and to a lesser extent O-18 and D than "typical" wells. When the gas results are compared to the proportional contribution of the HTR to the total flow, the HTR appears to produce steam with 6 to 9% by weight noncondensible gas and 1900 to 2600 ppmw hydrogen sulfide (H_2S) contrasted to 0.85 to 2.6% and 150 to 800 ppmw, respectively, in the "typical" reservoir. Chloride concentrations in steam at the wellhead from the high-temperature wells range from 15 to 150 ppmw; chloride in HTR steam is estimated to be about 200 ppmw. O-18 and D are enriched in high-temperature wells relative to the "typical" reservoir but the data are not sufficiently consistent to calculate the isotopic composition of the HTR steam.

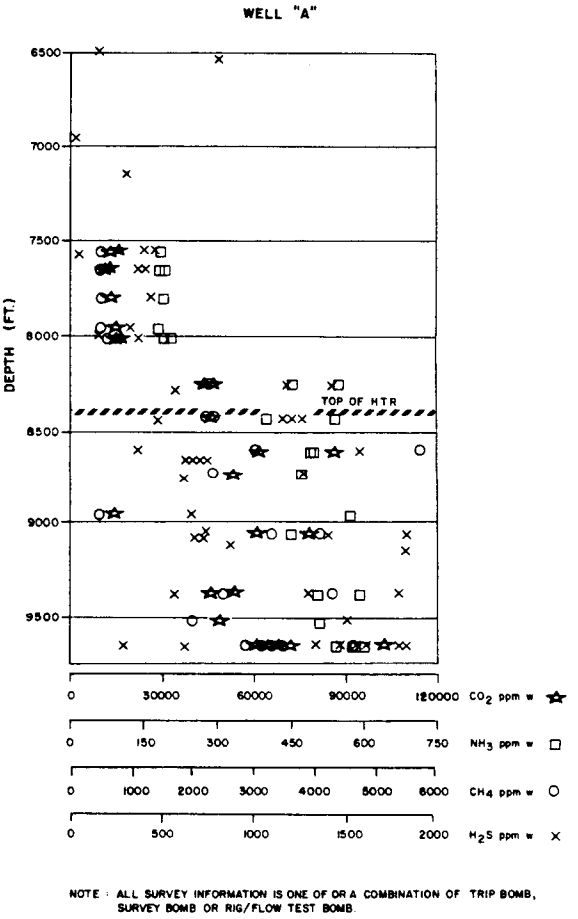


Figure 9: Wellhead gas concentrations of a well penetrating the HTR.

The composition of gas from the HTR is distinguished by enrichment in methane (CH_4) and carbon dioxide (CO_2) and depletion in ammonia (NH_3) and H_2S relative to the "typical" reservoir. However, these differences are small compared to the fieldwide variations in the noncondensible gases across The Geysers (see Figure 4) where noncondensible gas values are almost two orders of magnitude higher in the Northwest than the Southeast (Truesdell and others, 1987).

Similar gas composition and gas concentrations on the same order of magnitude in the HTR and "typical" Northwest Geysers reservoir are consistent with the similar mineralogy between the two reservoirs given that water/rock reactions are the primary control on reservoir fluid chemistry. Variations can

be explained by differences in source fluid and temperature. The presence of connate water as suggested previously (Haizlip, 1986), would increase the concentrations of chloride, D and O-18 in the steam. Higher concentrations of chloride and noncondensible gases (CO_2 and CH_4, in particular), and relatively lower NH_3 can be generated in steam by boiling at higher temperatures. The high gas concentrations in the HTR produce significant partial pressures, possibly over 10 bars (Mahon and others, 1980). This has the effect of lowering and flattening the boiling point to depth curve, partially explaining the change in temperature gradient in the HTR.

EVOLUTION OF THE GEYSERS RESERVOIR

Quaternary felsic intrusives, probably related to the Clearlake volcanics, intruded the Franciscan graywacke and associated rocks (Schriener and Suemnicht, 1980) and are found throughout the subsurface in The Geysers (Hebein, 1986). The intrusions caused heating, uplift, and are a likely cause of fractures in the overlying steam reservoir (Jerome and Cook, 1958; Koide and Bhattacharji, 1975). Uplift in The Geysers initiated deep erosion and landsliding and gave the area a geomorphic signature different from the surrounding areas (Bebber, 1986).

Intrusion probably caused extensive fracture enhancement as well as thermal metamorphism of the graywacke close to the intrusives. Consequently, the five discrete convection cells controlled by fracturing in The Geysers (Thomas and others, 1981) may be a result of localized fracture enhancement by intrusion rather than regional tectonics. Heating of the formation water in the fracture system around the intrusives also initiated (a) hydrothermal system(s). Mineral isotope and other data indicate that a liquid-dominated, high-temperature reservoir pre-dated the present vapor-dominated Geysers reservoir (Sternfeld, 1981). The Quaternary mercury deposits once mined at the periphery of The Geysers (Bailey, 1946) may be the halo around this earlier hydrothermal system.

Where the felsites were intruded sufficiently shallow as in the Southeast Geysers (Hebein, 1986), the associated fracture system reached the surface allowing venting and decompression of the hydrothermal system, beginning boiling and convection. The large, surficially altered, areas in the Southeast and Central Geysers are a record of both past and present degassing of the system.

Compared to other areas in The Geysers, relatively little CO_2 (500± ppmw) and H_2S (50 to 100 ppmw) are presently found in the steam from wells nearest these vent areas (Truesdell and others, 1986). This near-surface fracture enhancement also allowed the entry of meteoric water into the system(s).

The present steam reservoir found in the Southeast and Central Geysers is from a vented liquid system that has lost most of its original gas and formation water and is now flushed by meteoric water (Truesdell and others, 1986). The Northwest Geysers is believed to be following the same, but slower, evolutionary development as in the Southeast and Central Geysers. The HTR is a recently vented liquid-dominated reservoir. A "brine" or liquid-dominated system below the HTR cannot be ruled out.

Evolution of the Northwest Geysers reservoir is believed to be slower because the intrusions are deeper; only a few thin felsic dikes are encountered by wells and the hornfels development is deep (below -5900 ft subsea). The fracture system associated with the intrusive(s) therefore is also deeper; consequently, the top of steam is deeper in the Northwest Geysers than other parts of The Geysers where the felsite intrusives are known to be shallow. The top of steam is -2500 ft to -4500 ft in the Northwest Geysers, compared to 2000 ft to -2500 ft in the Central and Southeast Geysers (Thomas and others, 1981). Venting of the deep Northwest Geysers system to the surface may therefore depend upon faults related to regional tectonism and interconnection with other fracture systems in the Central Geysers. The few, relatively insignificant, vent areas in the Northwest Geysers are all associated with faults. Static pressure declines in unproduced GEOOC wells in the "typical" reservoir suggest connection with the fracture system(s) of wells now being produced in the Central Geysers. Because current Central Geysers production may be an artificial vent of the Northwest Geysers, it is reasonable to assume that the area of extensive alteration near Geysers Resort and along Big Sulphur Creek may also naturally vent the Northwest Geysers.

The consequences of a poorer surface connection with the steam reservoir than the Central and Southeastern Geysers areas includes less venting of noncondensible gas and less dilution by meteoric water. The high-temperature reservoir underlying the "typical" reservoir is believed to be simply a fossil of the liquid-dominated system in which the onset of convection is recent, leaving an important conductive element in the transfer of heat from the evolving hydrothermal system.

CONCLUSIONS AND CONCEPTUAL MODEL

1. The enrichment of O-18 and D in steam from the Northwest Geysers wells previously described by Haizlip (1986) is probably from a connate water component in the high-temperature reservoir (HTR).
2. The single high-temperature well previously described by Drenick (1986) in the Northwest Geysers penetrated a large HTR that may extend beyond the Northwest Geysers.

3. The HTR described in this paper is a transient phenomenon caused by the recent transition from liquid-dominated to vapor-dominated conditions. This is the same conclusion as that suggested by Pruess and others (1987) for high-temperature wells at Lardarello.

The HTR in the Northwest Geysers is probably a deep, evolving system in contrast to the shallower, leaky and mature steam reservoir(s) in the central and southeastern portions of the field. Before natural venting and nearby production caused pressure to decline, the HTR was a liquid-dominated system with some connate water; the connate water being the source of the high gas contents, chloride, and unique isotopic composition relative to steam from a "typical" Geysers reservoir. Therefore, the present boundary between the "typical" reservoir and HTR is a transient, thermodynamic condition due to the recent evolution of a vapor-dominated zone from a liquid-dominated zone which has yet to cool down. It also demarks a previous liquid to vapor interface. Pressure in the two reservoirs is essentially the same because they are in communication with each other. In other words, the temperature change in the HTR is lagging the pressure change.

ACKNOWLEDGEMENTS

We thank Geothermal Resources International, Inc. for financial support for this work and permission to publish. We also thank Dr. Walter Randall for his critical review and ideas on the evolution of geothermal systems, J. Schmidt for technical assistance, and S. Mason, L. Johnson, and B. Kahoonei for manuscript preparation.

REFERENCES

Bailey, E. H., 1946, Quicksilver Deposits of the Western Mayacamas Dist., Sonoma Co., CA, Report 42 of the State Mineralogist, Calif. Mineral Bureau, pp. 220-230.

Beall, J. J., 1985, Exploration of a High Temperature, Fault Localized, Non-meteoric Geothermal System at the Sulphur Bank Mine, California, Geothermal Resources Council Transactions, v.9, part 1, pp. 395-401.

Bebber, C. F., 1986, A Photogeological Interpretation of the Northwest Geysers Region, Unpublished GEOOC Report, 40 pp. + maps.

Bird, D. K., and others, 1984, Calc-Silicate Mineralization in Active Geothermal Systems, Econ. Geol, v. 79, pp. 671-695.

Blake, M. C., and others, 1967, Upside-down metamorphic zonation, blueschist facies, along a regional thrust in California and Oregon, U.S.G.S. Prof. Paper 575-C, pp. 1-9.

Drenick, A. F., 1986, Pressure-Temperature-Spinner Survey in a Well at The Geysers, Proceedings of the Eleventh Stanford Workshop on Geothermal Reservoir Engineering, Stanford University, January 21-23, 1986, pp. 197-206.

Haizlip, J. R., 1985, Stable Isotopic Composition of Steam from Wells in the Northwest Geysers, The Geysers, Sonoma County, California, Geothermal Resources Council Transactions, v. 9, part 1, pp. 311-316.

Hebein, J. J., 1986, Conceptual Schematic Geologic Cross-Sections of The Geysers Steam Field, Proceedings of the Eleventh Workshop on Geothermal Reservoir Engineering, Stanford University, January 21-23, 1986, pp. 251-257.

Jerome, S. E. and Cook, D. R., 1958, Relation of Some Metal Mining Districts in the Western United States to Regional Tectonic Environments and Igneous Activity, Nevada Bureau of Mines Bulletin 69, 35 pp.

Koide, H. and Bhattacharji, S., 1975, Formation of Fractures Around Magmatic Intrusions and their Role in Ore Localization, Econ. Geol., v. 70, pp. 781-799.

Lambert, S. J., 1976, Stable Isotope Studies of Some Active Hydrothermal Systems, Unpublished Calif. Inst. of Tech., Ph.D Thesis, 362 pp.

Lipman, S. C., and others, 1978, Reservoir Performance of The Geysers Field, Geothermics, v. 7, pp. 209-219.

Mahon, W. A. J., and others, 1980, Carbon Dioxide: Its Role in Geothermal Systems, New Zealand Journal of Science, v. 23, pp. 133-148.

ruess, K., 1985, A Quantitative Model of Vapor-Dominated Geothermal Reservoirs as Heat Pipes in Fractured Porous Rock, Geothermal Resources Council Transactions, v. 9, part 2, pp. 353-361.

Pruess, K., and others, 1987, On Fluid and Heat Transfer in Deep Zones of Vapor-Dominated Geothermal Reservoirs, Proceedings of Twelfth Workshop on Geothermal Reservoir Engineering, Stanford University, Jan. 20-22, 1987, (in press).

Sass, J. H., and others, 1971, Thermal Conductivity of Rocks from Measurements on Fragments and its Application to Heat Flow Determinations, Jour. of Geophys. Research, v. 76, n. 14, pp. 3391-3400.

Schriener, A. and Suemnicht, G., 1980, Subsurface Intrusive Rocks at The Geysers Geothermal Area, CA, Geol. Soc. of Amer., Abstracts with Programs, v. 12, n. 3, p. 152.

Sternfeld, J. N., 1981, The Hydrothermal Petrology and Stable Isotope Geochemistry of Two Wells in The Geysers Geothermal Field, Sonoma Co., CA, M.S. Thesis, U.C. Riverside, 202 pp.

Sternfeld, and others, 1983, Hydrothermal Mineralization of a Clear Lake Geothermal Well, Geothermal Resources Council Transactions, v. 7, pp. 193-197.

Thomas, R. P., and others, 1981, A Reservoir Assessment of The Geysers Geothermal Field, Calif. Division of Oil and Gas, Publication No. TR27, 60 pp. + maps.

Thomas, R. P., 1986, Heat-flow Mapping at The Geysers Geothermal Field, Calif. Division of Oil and Gas, Publication No. TR 37, 58 pp.

Truesdell, A. H., and others, 1987, Fieldwide Chemical and Isotopic Gradients in Steam from The Geysers, Proceedings of Twelfth Workshop on Geothermal Reservoir Engineering, Stanford University, Jan. 20-22, 1987, (in press).

Urban, T. C., and others, 1975, Heat Flow at The Geysers, California USA, Second U.N. Symposium on the Development and Use of Geothermal Resources, v. 2, pp. 1241-1246.

White, D. E., and others, 1971, Vapor-Dominated Hydrothermal Systems Compared with Hot Water Systems, Econ. Geol., v. 66, pp. 75-96.

PROCEEDINGS, Thirteenth Workshop on Geothermal Reservoir Engineering
Stanford University, Stanford, California, January 19-21, 1988
SGP-TR-113

A SUMMARY OF MODELING STUDIES OF THE NESJAVELLIR GEOTHERMAL FIELD, ICELAND

G.S. Bodvarsson,[1] *S. Bjornsson,*[2] *A. Gunnarsson,*[3] *E. Gunnlaugsson,*[3]
O. Sigurdsson,[4] V. Stefansson,[5] and B. Steingrimsson[4]

[1]Earth Sciences Division, Lawrence Berkeley Laboratory,
Berkeley, California 94720
[2]The University of Iceland, Reykjavik, Iceland
[3]The Reykjavik Municipal District Heating Service,
Reykjavik, Iceland
[4]The Icelandic National Energy Authority, Reykjavik, Iceland
[5]Braedraborgarstigur 23, Reykjavik, Iceland

ABSTRACT

The Nesjavellir geothermal field in Iceland is being developed to provide the capital city of Reykjavik and surrounding areas with hot water for space heating. In the last few years, many wells have been drilled at the site and various geothermal studies have been conducted. The main upflow to the system is underneath the nearby Hengill volcano, and the natural recharge rate and enthalpy are estimated to be 65 kg/s and 1850 kJ/kg, respectively. An extensive vapor zone is believed to be present in the upflow region. Permeabilities and porosities of the system range between 1 and 50 md and 1 and 10 percent, respectively. In this paper, the characteristics of the Nesjavellir field are described and a three-dimensional numerical model of the resource is discussed.

INTRODUCTION

The Nesjavellir geothermal field in southwest Iceland is being developed for production of hot fluids for space heating purposes in the capital city of Reykjavik and surrounding areas. The hot geothermal fluids will be used to heat up fresh water to a temperature of about 90 °C using heat exchangers. The hot fresh water will then be piped about 30 km to the capital, and distributed. After use, most of the spent water is discharged into the sea at a disposal temperature of some 40 °C.

The Nesjavellir geothermal field has been under intermittent development for over 20 years, with the first well being drilled in the mid-1960s. At present, 18 wells have been drilled, identifying the presence of a high temperature (>300 °C) geothermal system. Most of these wells were drilled after 1982, as a result of the need for identifying a longterm solution to the approaching shortage of hot fluids from the geothermal fields in the vicinity of Reykjavik.

Concurrent with the drilling activities in recent years, various studies have been conducted in order to better understand the geothermal system. This includes a thorough geological and geophysical investigation (Arnason et al., 1986, 1987), extensive reservoir studies and flow testing of the wells, fluid sampling and analysis and the development of a three-dimensional numerical model of the system. All of these studies aim toward a proper assessment of the characteristics of each well and the overall generating capacity of the resource.

In this paper the available field data from Nesjavellir are briefly described and a conceptual model of the field presented. Then we describe the development of the three-dimensional reservoir model and the results obtained in terms of the characteristics and properties of the system.

THE NESJAVELLIR FIELD

The Nesjavellir geothermal field is a part of the Hengill geothermal area, which extends over some 70 to 100 km^2 (Bodvarsson, 1951).

The Hengill area is densely faulted, with the primary fault direction being SW-NE. Locations of extinct and active surface manifestations are controlled by the fault patterns, as is the flow of fluids and heat within the geothermal system. In general, the faults enhance N-S trending fluid flow, but probably retard E-W trending flow.

Drilling in the Nesjavellir area started in the mid-1960s; five wells were drilled during the period 1965 through 1972 (wells 1 through 5; Stefansson, 1985). These wells identified the presence of a high temperature resource, with higher temperatures at shallow depth found towards the south (Tomasson et al., 1974). Data from these wells also indicated that part of the system is two-phase, the remainder being a subcooled liquid system (Steingrimsson and Stefansson, 1979). Since the early 1980s 13 additional wells have been drilled at Nesjavellir (Fig. 1). All of these wells are commercial producers with the exception of well 8, which was abandoned at a depth of 400 m because of high shallow pressures (Franzson and Sigvaldason, 1985).

The Nesjavellir wells encounter vastly different thermodynamic conditions as evidenced by their pressure and temperature profiles and the enthalpy transients during production.

Figure 2 shows the estimated temperature distributions in a vertical cross sections extending W-E. The figure shows high temperatures near the Kyrdalshryggur fracture zone (wells 11 and 3), and rapidly declining temperatures away from it in both directions (east and west). Temperatures in excess of 380 °C were measured deep in well 11, perhaps related to a magmatic intrusion. In order to control the high pressure, high temperature feed near the bottom of this well, the well was filled with gravel at depths between 1700-1900 m (Steingrimsson et al., 1986).

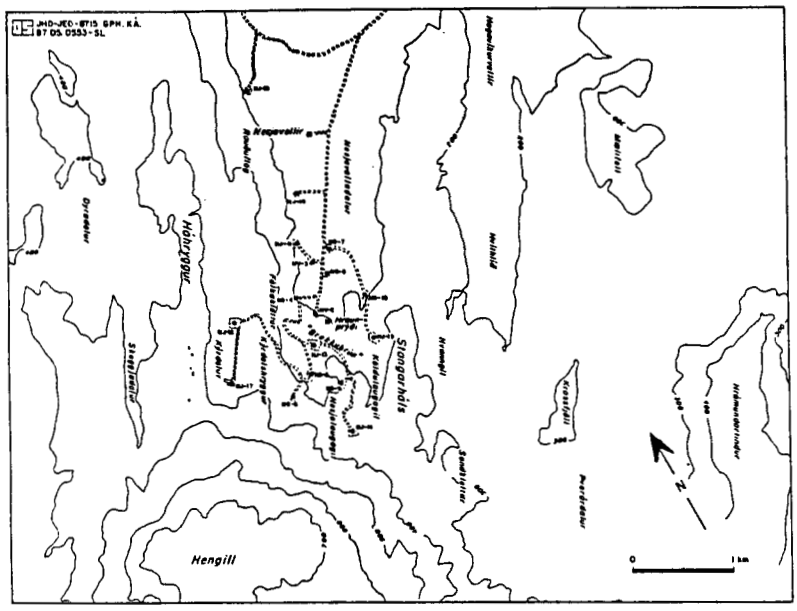


Figure 1. The Nesjavellir wellfield (after Arnasson et al., 1986).

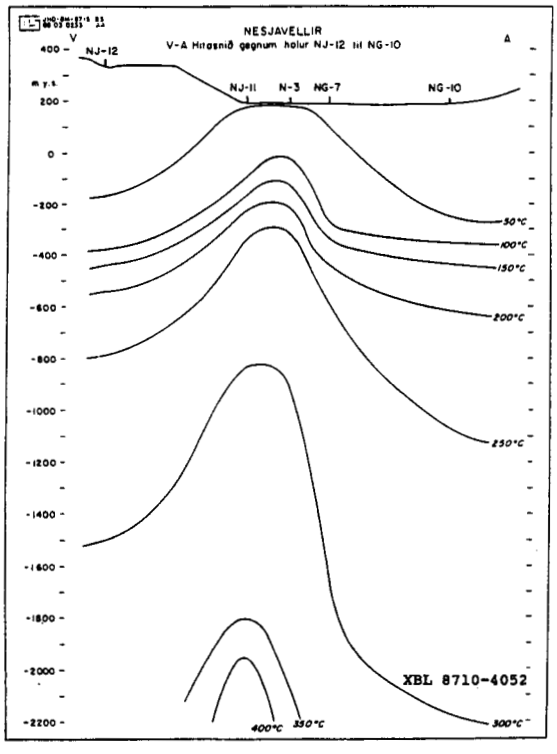


Figure 2. A W-E cross section through the northern wellfield showing the estimated temperature distribution.

The pressure conditions at feed zones in the various wells, shown in Figure 3, illustrate the complex thermodynamic state of the resource. The data suggest the presence of several aquifers with different pressure potential (Stefansson, 1985). Pressures are very high in shallow aquifers in the southern part of the reservoir system with two-phase conditions prevailing in the region around wells 6, 8 and 9. In the northern part of the wellfield the shallow aquifers do not contain high temperature fluids and the pressure potential is much lower. At intermediate depths high pressures prevail, but the temperatures are rather low, indicating subcooled liquid aquifers. Wells 12, 17 and 18 have anomalously high pressures at depth, about 5 bars higher than those in other wells at Nesjavellir.

The geological formations encountered at Nesjavellir consist primarily of hyaloclastites and basalt lavas. (Figure 4; Franzson et al., 1986). Basaltic hyaloclastite formations are dominant in the top 600 m, with basaltic lava series becoming more abundant below 600 m. Intrusions also increase drastically with depth and exceed 50% at depths below 1500 m (Franzson et al., 1986). The geological cross section shows two major fault structures delineating a central graben. The hydrothermal alteration indicates that in most of the reservoir system the mineral assemblages are in equilibrium with the prevailing temperatures (Franzson et al., 1986).

Franzson et al. (1986) discuss the fracture characteristics of the Nesjavellir system in light of fluid production. They believe that horizontal permeability is predominant in the upper 800 m of the system, perhaps due to contact permeability between layers. This agrees well with the observed pressure discontinuities between aquifers in the shallow parts of the field. For the main reservoir section below 800 m depth, Franzson and coworkers believe that vertical permeability becomes more dominant as fracture and fault permeability becomes important as well as contact permeability at the boundaries of the intrusions.

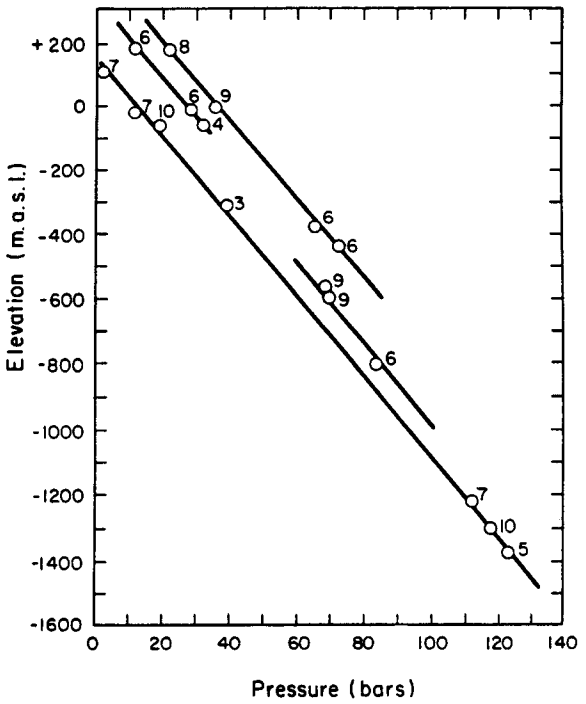


Figure 3. Pressures at feed zones in some of the wells (after Stefansson, 1985).

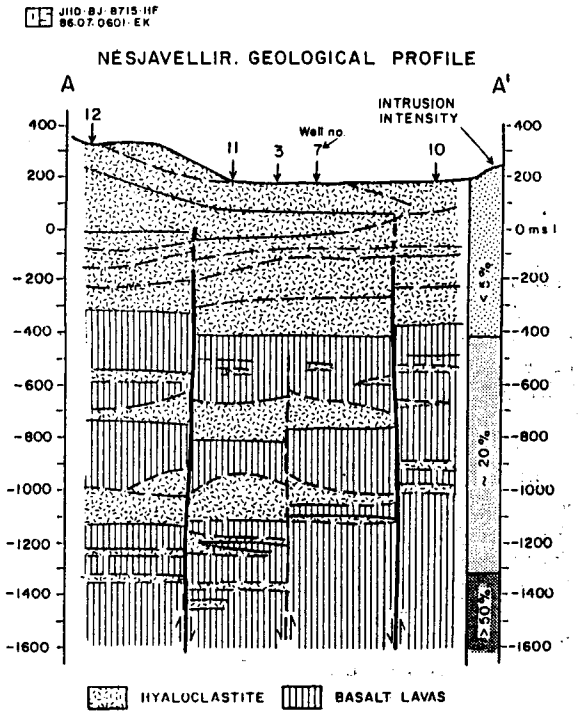


Figure 4. Geological cross section extending W-E through the Nesjavellir field (after Franzson et al., 1986).

Almost all of the Nesjavellir wells are good producers. Table 1 lists typical flow rates, enthalpies and energy outputs (in MW_t) for each of the commercial wells. The table shows that on the average the thermal output of the wells is about 60 MW_t. The average electrical generating capacity of the wells is about 8 MW_e.

The Nesjavellir wells vary greatly in the enthalpy of the produced fluids (see Table 1), which is mostly due to the different thermodynamic conditions in the vicinity of the wells. The two-phase wells produce fluids with enthalpy varying from 2000 to 2500 kJ/kg, whereas the wells completed in the subcooled part of the reservoir produce fluids with enthalpies below 1500 kJ/kg.

Monitoring of chemical concentrations of gases and dissolved solids in the produced fluids shows that concentrations of these chemicals are relatively low in comparison with other high temperature geothermal fields. In general, the chemical characteristics of the fluids from individual wells are so similar that it is difficult to infer fluid flow directions from the data. Recent isotope studies have shown that the fluids feeding well 12 have undergone less interaction with the rock than those feeding the other Nesjavellir wells.

CONCEPTUAL MODEL

A conceptual model of the field was proposed by Stefansson (1985) before the drilling of the last eight wells (wells 11 through 18). Most of the ideas proposed in the conceptual model developed by Stefansson are consistent with the results of wells drilled after the model was presented.

All evidence collected to date suggests that the main upflow zone to the system is located southwest of the wellfield under the Hengill volcano. In addition to the Nesjavellir anomaly, this upflow zone probably also

Table 1. Productivity of Nesjavellir wells.

Well	Flow rate (kg/s)	Enthalpy (kJ/kg)	Steam at 7 bars (kg/s)	Thermal output (MW_t)
5	10	1600	5.3	18
6	22	2500	19.0	55
7	36	1300	10.9	48
9	28	2200	20.4	62
10	52	1350	16.4	70
11	37	2500	32.7	93
12	57	1300	17.2	75
13	36	2500	31.4	90
14	28	1300	8.6	37
15	47	1450	16.5	67
16	27	2300	21.0	62
17	45	950	5.5	43
18	36	930	4.1	33

feeds fluids to other geothermal anomalies in the Hengill area (e.g., Kolvidarholl, Innstidalur, etc.). We believe that vapor-dominated conditions exist in the upper part of the upflow region, which helps to explain the high pressures in shallow aquifers in the southern part of Nesjavellir and the vastly different pressure potential at different depths in the wells. Well 8, in the southern part of the wellfield, identified a shallow two-phase aquifer ($\approx$ 120 m depth) with very high pressure (20-23 bars); this aquifer is also present in well 6, but has lower pressure (H. Franzson, personal communication, 1986). At depths between 400 and 800 m a single-phase aquifer with a high pressure potential can be found in many of the wells. The presence of an upflow zone with a small vertical pressure gradient (vapor-dominated zone), located beneath a high topography anomaly (i.e., the Hengill volcano) can explain the high shallow pressures and vastly different pressure potentials.

It is hypothesized that this vapor zone will have pressure on the order of 70 bars to be consistent with the large pressure potential of the aquifers between 400 and 800 m depth. The vapor zone would have to extend down to an elevation of about 600 mbsl to create the lower pressure potential in the deeper reservoir.

The temperature and pressure data obtained from the wells suggest that the fault zone near Kyrdalshryggur has higher permeability than the surrounding rocks. The extent of this high permeability zone (discharge channel) to the north is not well known, but it extends past well 16 and perhaps as far as well 18, which is located about 1 km north of well 12. Depths to the hot fluids become greater towards the north. The high temperature and pressure zone found deep in well 11 is located within the discharge channel, and perhaps some localized upflow occurs along it. The last eruption at Nesjavellir some 2000 years ago was a fissure eruption in the Kyrdalshryggur area (see Figure 1).

The anomalously high pressures deep in well 12 in Kyrdalur necessitate the presence of low permeability rocks between well 12 and the other wells to the east. Recent data from wells 17 and 18 also indicate high pressures in these wells, suggesting that they may be hydrologically connected to the aquifers feeding well 12. The impermeable barriers between well 12 (and perhaps wells 17 and 18) and the other wells can be readily explained because of the numerous eruptive fissures (dikes) extending NE-SW in the Kyrdalshryggur area.

The heat loss from the Nesjavellir system occurs through conductive heat transfer to the ground surface and laterally to the sides, and steam and hot water loss to surface manifestations. Most of the present active surface springs are located in the Koldulaugargil (see Figure 1) or in Nesjalaugargil between wells 6 and 9. Temperature data from the Nesjavellir wells generally show that the conductive shallow temperature gradient varies between 0.4 and 0.7 °C/m. There is a S-N flow of cooler fluids at depths of about 150-400 m over most of the northern parts of the wellfield. This fluid flow enhances the heat losses of the system.

THREE-DIMENSIONAL NUMERICAL MODEL

Because of the complex thermodynamic and geologic conditions of the Nesjavellir field it was decided to develop a fully three-dimensional model of the field. The model had to consider all relevant field data and be consistent with observed field conditions and behavior, including:

1. The pressure and temperature conditions;
2. The presence of two-phase zones;
3. The flow rates and enthalpies of wells;
4. The observed pressure interference effects.

After the model development was completed, performance predictions of the generating capacity of the field were made.

The Numerical Grid

The three-dimensional model consisted of four layers, three of which were 400 m in thickness, while the bottom layer was 800 m thick. The choice of the number of layers and their respective thicknesses was made based on the observed thermodynamic conditions in the field and the locations of major feed zones in the wells.

The grid used extends 12 km in all directions from the wellfield; constant pressure boundaries were used as external conditions to the model. In most of the simulations the outer boundary conditions did not affect the results.

The upflow zone was assumed to be located in grid block 53, which geographically represents a part of the Hengill volcano (Fig. 5). This location was chosen rather arbitrarily, but it places the upflow zone under the Hengill volcano, which we believe is necessary to explain the vast differences in pressure potential shallow in the wellfield.

Various reservoir parameters were adjusted during the natural state and history match simulations, including permeabilities and porosities, the production indices for the wells and the mass recharge rate and the enthalpy of the upflow zone. Most other parameters used are well known for geothermal systems or did not affect any of the simulation results significantly. The computer code MULKOM (Pruess, 1982) was used in this work.

Natural State Modeling

Over most of the Nesjavellir area the conductive heat losses amount to some 0.9 - 1.5 W/m^2, as indicated by the "static" temperature profiles in some of the wells. This conductive heat loss will decrease away from the main thermal plume. Convective heat losses to surface springs are estimated to be about 10 MW_t in Koldulaugargil and 5 MW_t Nesjalaugagili. In addition to these, we also include in our model mass flow to warm springs located close to Sandkletter on the eastern flanks of the Hengill volcano, where about 5 kg/s of 80 °C water are discharged in the area (S.P. Snorrason and K. Saemundsson, personal communication, 1986; see also Arnason et al., 1986).

As mentioned earlier, a basic four-layer model was used for all of the modeling work. The four layers will be referred to as layers U, M, L and R. Uppermost layer U averages 400 m in thickness, as do layers M and L beneath it. Bottom layer R is 800 m thick and resides at

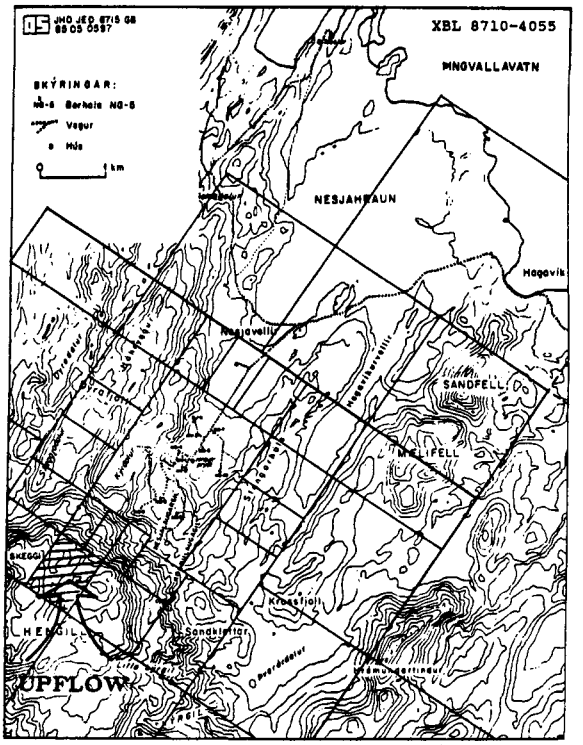


Figure 5. The basic grid superimposed on a topographic map of the Nesjavellir area.

elevations between 1000 and 1800 mbsl. Depending upon the specifics of the topography, layer U varies in thickness from about 300 m to about 550 m. Additional shallow layers are used in the vicinity of the upflow zone in the Hengill area to represent the topographic high of the central volcano.

The basic grid shown in Figure 5 was used for the main reservoir layers (layers L and R). Because of predominant conductive heat transfer to the ground surface for many regions in the two "shallow" layers (layers U and M), many of the elements (gridblocks) shown in Figure 5 were not needed in those layers. The conductive heat losses were computed by an algorithm developed by Vinsome and Westerfeld (1980).

In the "conductive" regions the conductive heat losses are computed for different areas based on the observed temperature data from the wells with proper interpolation and extrapolation where needed. Thus, the conductive heat losses vary areally to the degree the observed data demand. An average annual surface temperature of 5 ° C was assumed in the simulations.

Many simulation runs were necessary until a coarse match with the observed thermodynamic conditions in the field was obtained. Each run simulated several hundred thousand years until near steady-state conditions were reached, after which temperatures would change by less than 1 ° C anywhere in the system. As the model has about 300 gridblocks and 950 connections, the computations needed to reach steady state for each run were rather intensive.

History Match Simulations

For the history match simulations of the flow rate and enthalpy data from the wells, a finer grid than that used in the natural state simulations was required around each well.

A subgrid was placed in the well elements containing the major feed zones, using the approach developed in the Krafla (Pruess et al., 1984) and Olkaria (Bodvarsson et al., 1985) simulations. Concentric cylinders of radii 20 and 60 m were used as subgridblocks in the elements, which are typically equivalent in size to a cylinder 100 m in radius. The subgrid allowed for the simulation of the early time response of the wells.

In order to obtain a reasonable match with observed flow rates and enthalpies of the wells, numerous iterations were necessary. The main parameters controlling flow rate decline and enthalpy changes of the wells are productivity indices, permeabilities and porosities.

The method we used in the iterations was to determine the productivity indices of the wells based on the initial flow rate history, before well interference is seen. Then the enthalpy rise was matched by adjusting porosities, while the permeabilities were adjusted until the flow rate decline was approximately represented. It should be noted that any change made in porosity and permeability anywhere in the wellfield will have an affect on all nearby wells. Consequently, many iterations were required before a reasonable match was obtained. In addition to the flow rate and enthalpy data from the wells the model was also calibrated against pressure interference effects observed during the well production period.

As mentioned earlier, the calibration of the model against flow rates and enthalpies of wells and the observed pressure decline started after a coarse match was obtained with the natural thermodynamic conditions of the field. The calibration with the production history required many changes in the permeability distribution, especially in the production layers (layers L and R). This in turn required recalibration of the natural state calculations and vice versa.

Best Model

Natural State Results

In the best model 65 kg/s of steam-water mixture with an enthalpy of 1850 kJ/kg feed the Nesjavellir system through the upflow zone underneath the Hengill volcano. This energy input corresponds to about 120 MW_t, which is a similar value to that estimated from the two-dimensional natural state model (Bodvarsson and Pruess, 1986).

In the model some of this energy is lost through steam flow to surface springs in Koldulaugargil ($\approx$10 MW_t), Nesjalaugagil ($\approx$ 5 MW_t), and to warm springs near Sandklettar ($\approx$1.5 MW_t). However, most of the energy is lost through conductive heat transfer to the surface, or to shallow groundwater aquifers.

Figures 6 and 7 show the computed temperature distributions in the U and R layers, with observed temperatures of wells given in parentheses. The solid hatched lines indicate the presence of impermeable barriers retarding fluid flow and significantly reducing the

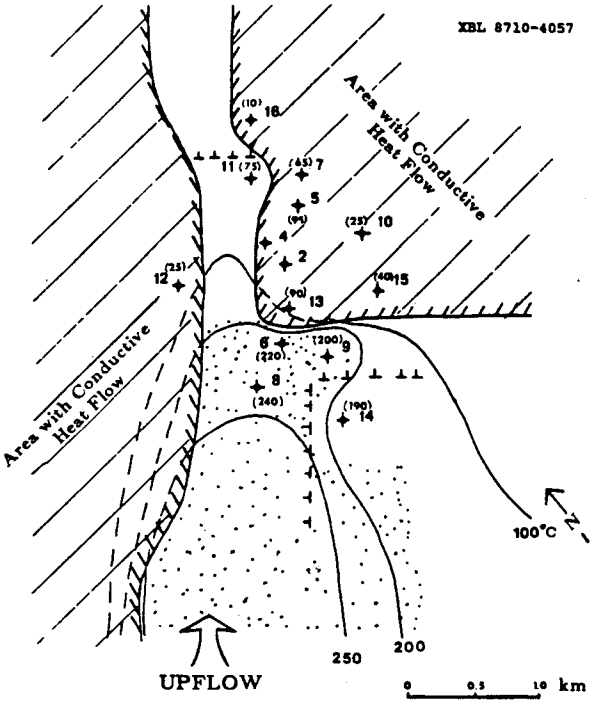


Figure 6. The computed temperature distribution for layer U. Observed values for each well are given in parentheses; dotted area represents two-phase zone.

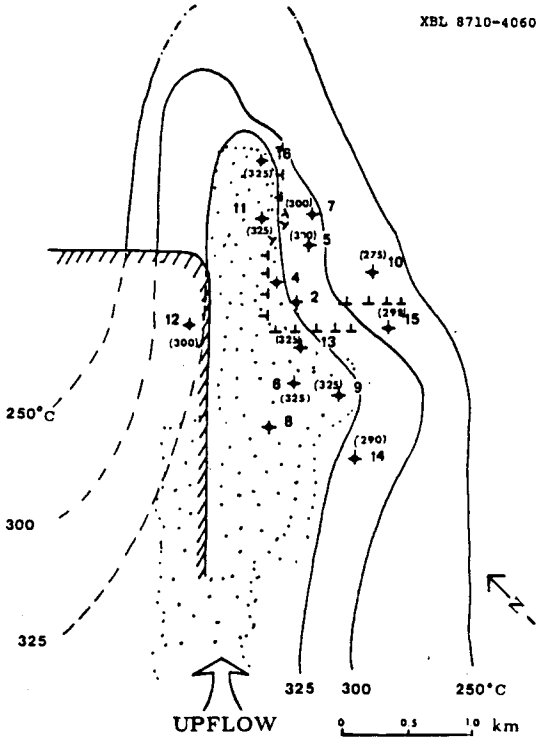


Figure 7. The computed temperature distribution for layer R. Observed values for each well are given in parentheses; dotted area represents two-phase zone.

total flow areas in layers U and M. The locations of these barriers are inferred from the shallow temperature distributions in the wells, indicating conductive heat flow for areas surrounding most of the low enthalpy wells. The impermeable barriers shown in layer R are inferred from the high pressure in well 12 in Kyrdalur in comparison with pressures in other wells. In the present model it is hypothesized that the high pressure in well 12 is due to separate high permeability flow paths from the upflow zone to the well. The broken lines shown in Figures 6 and 7 represent "imperfect" barriers, that is, lower permeability connections between various regions of the system. These are inferred from various observations during the calibration process with the temperature and pressure data, the production history and the observed pressure decline as will be described later. It should be emphasized that there is considerable uncertainty involved with these permeability barriers, and their locations and permeabilities are subject to various non-uniqueness problems.

As shown in Figures 6 and 7 the Nesjavellir model matches the temperature distributions in layers U and R reasonably well. In the U layer the match is good and the computed two-phase zone extends around wells 6, 8 and 9, which is in good agreement with observed data. The vapor saturation in this zone is fairly high and varies between 20 and 60%, which is consistent with the observation that mostly steam (and gas) was produced out of well 8 from the high pressure fracture zone at a depth of 120 m. Similar temperature matches were obtained for layers M and L, and also the computed three-dimensional pressure distribution agrees well with observed values. The high pressure potential in layer M and relatively low temperatures were not easy to simulate. This was finally achieved using a model with rather complex interaction between the various layers, as shown in Figure 8. As mentioned earlier we hypothesize that there is a vapor-dominated zone approximately 800 - 1000 m thick underneath the Hengill volcano. In the vapor-dominated zone steam is the pressure-controlling fluid with a near vaporstatic heat pipe transferring the energy upward towards the caprock. The average pressure in the vapor-dominated zone is grossly estimated to be about 70 bars. Below the vapor-dominated layer in the upflow zone there is a liquid-dominated two-phase zone that extends to unknown depths. The near-uniform pressure in the vapor-dominated zone causes the different pressure potential in the various aquifers in the drilled region of the geothermal field. According to this model, most of the fluids recharging the U layer consist of steam and gases ascending from the deeper M layer. The high vertical permeability needed for this mass exchange is provided by a series of faults cutting through the Hengill volcano just northeast of the proposed upflow zone, and then continuing towards the north near the Kyrdalshyggur area and providing high permeability for fluid flow towards the north. The vertical steam flow from the M layer to the U layer accomplishes two things consistent with the observed data. First, the steam loss cools down the fluids and rocks in the M layer, yielding single-phase liquid conditions with high pressure potential. Second, it produces a gas-rich, two-phase mixture in the U layer, without the excessively high pressures that would result if the U layer were in good lateral communication with the vapor-dominated upflow zone. It is possible that

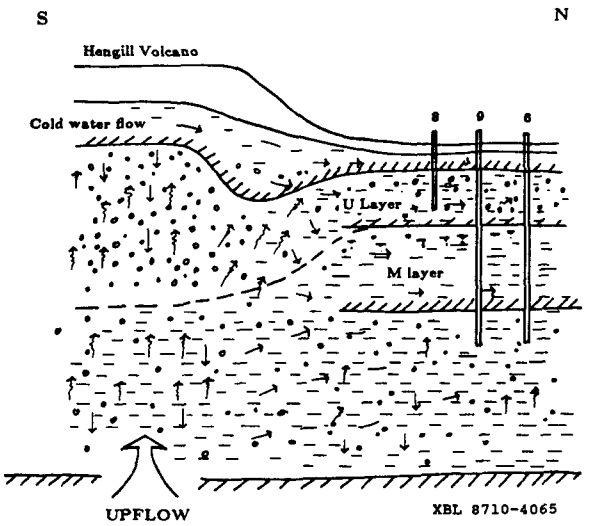


Figure 8. A model of the upflow zone and flow patterns for the various layers. Straight arrows indicate liquid flow and wriggled arrows vapor flow.

some of the degassed waters recharge certain regions of the L layer and provide fluids to well 14, which has anomalously low gas content and low fluid enthalpy.

History Match Results

All of the wells were modeled individually and their flow rate and enthalpy histories matched. The main parameters that were adjusted to obtain matches with the flow rate and enthalpy data of the wells were the productivity indices, permeabilities and porosities.

As an example, Figure 9 shows the match between observed and calculated flow rates and enthalpies for well 6. This well shows considerable variations in flow rate and enthalpy caused by mobility effects; i.e., when low enthalpy fluids recharge the well the flow rate increases and vice versa, but the thermal output of the well remains near constant. During the early flow period of the well the enthalpy decreases and the flow rate rises, which could be partly due to the large water losses during drilling (Stefansson et al., 1983). However, since the low enthalpy period lasts for more than a year it cannot be explained solely by the drilling fluid losses. It is probable that the low enthalpy fluids recharge the well from the region around well 9 and perhaps even further to the east. There is undoubtedly a very good permeability connection between wells 6 and 9, as evidenced by the rise in fluid enthalpy in well 6 in late 1984, when well 9 starts to flow. In our model, we find that very high permeabilities ($\approx$ 50 md) connect these wells, and that this high permeability zone extends considerably further to the east. The model results show good agreement with the flow rate history of well 6, especially the gradual decline that starts soon after well 9 starts producing. The rise in enthalpy due to the interference from well 9 is somewhat more gradual than what has been observed.

Some pressure decline has been observed at Nesjavellir due to fluid production. In June 1986 the low enthalpy wells were shut in and the pressure recovery was observed. The results suggest a 3 - 4 bar pressure

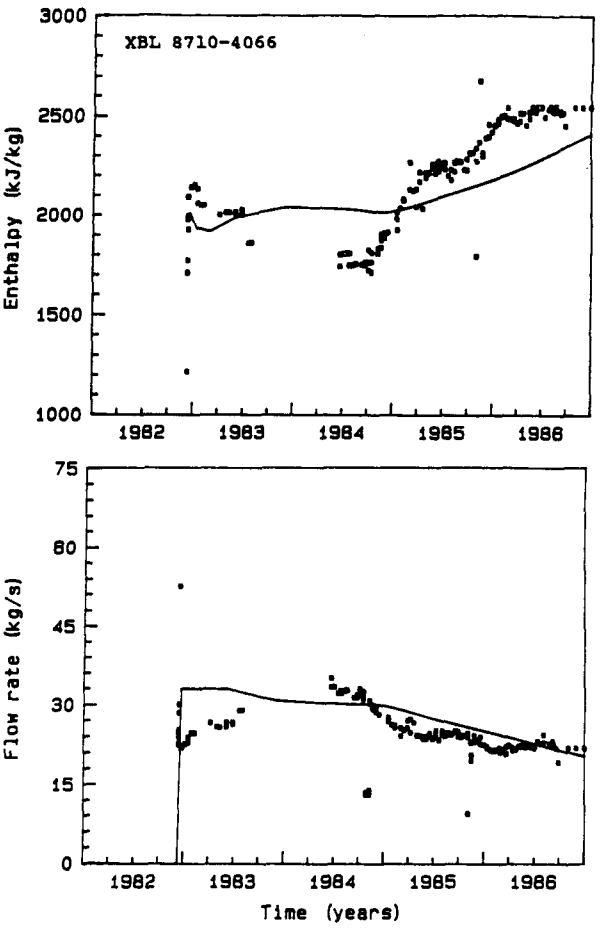


Figure 9. Comparison between computed and observed flow rates and enthalpies for well 6.

decline in well 7, a 1 - 2 bar decline in well 10, and no decline in wells 12 and 14.

Figure 10 shows the computed downhole pressure versus time for well 7, and suggests that well 7 is in reasonable hydrologic communication with wells 10 and 15. Total pressure decline in well 7 is about 3 - 4 bars, which agrees very well with the observed data. As an example, the inferred permeability distribution in the main reservoir layer, layer R, is shown in Figure 11. The high permeabilities in the discharge channel are most pronounced. The permeability of this zone is estimated to be about 30 md. Other high permeability areas include the region north and east of wells 16 and 7 that enhance recharge from these directions and the high permeability zone extending from the upflow zone north towards well 12. The background permeability is estimated to be about 10 md, primarily from the matches with the pressure decline data. It should be noted that the area of influence from fluid production to date only extends a few kilometers in each direction, so that permeabilities outside this area are completely unknown.

The transmissivities deduced from this modeling work suggest that the overall average transmissivity of the Nesjavellir reservoir is about 10 Dm. This value is somewhat higher than those inferred from injection test

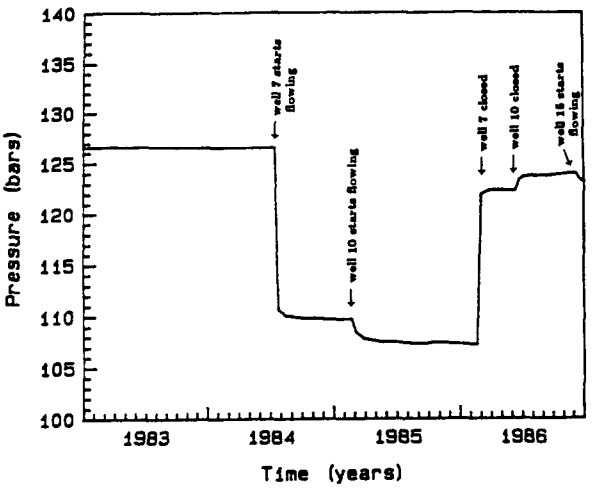


Figure 10. Computed downhole pressure changes in well 7.

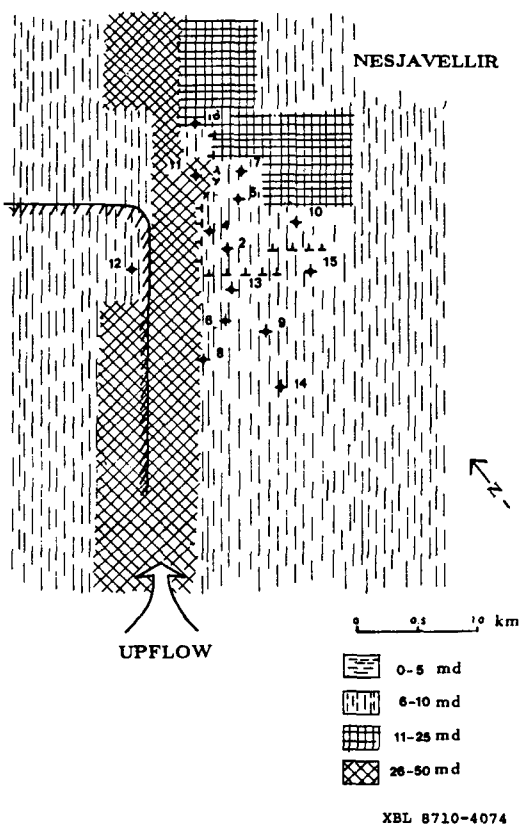


Figure 11. The permeability distribution in the R layer, inferred from the model.

data, which range from 2 - 8 Dm. The reservoir porosity values inferred from this model study were generally in the range of 3.5 to 5 percent, which is somewhat lower than those measured on cores.

CONCLUSIONS

A three-dimensional numerical model of the Nesjavellir field has been developed. The model is consistent with the observed thermodynamic conditions of the reservoir system and matches reasonably well the production histories of the wells and the observed pressure interference effects. The model has been used to study various exploitation cases for Nesjavellir in order to determine the generating capacity of the system, and the effects of reinjection and different well spacings. Many approximations and assumptions have been used in this work, including the use of a porous medium model for a fractured reservoir, and the assumption of constant bottomhole pressure in producing wells. The reader should evaluate the following conclusions in light of the approximations made:

1. It is hypothesized that the main upflow zone to the system is under the Hengill volcano. The recharge rate in the upflow zone is estimated to be 65 kg/s with an enthalpy of 1850 kJ/kg. An extensive vapor zone with high pressure ($\approx$ 70 bars) is hypothesized to reside underneath the Hengill volcano.
2. Most of the energy losses in the Nesjavellir area are due to conductive losses to the ground surface as well as lateral conductive and convective heat losses. Mass and heat losses to surface springs only amount to some 20 MW_t, compared to the total energy input of 120 MW_t.
3. The permeabilities of the system are very heterogeneous, and vary between 1 and 50 md. The permeabilty in shallow parts of the system are estimated to be in the range of 1 to 10 md. In the upper reservoir layer the average permeability is around 5 md, but about 10 md in the lower part of the reservoir. In the upper reservoir layer a high permeability fracture zone is believed to intersect wells 6 and 9; this fault zone is believed to extend a considerable distance east of well 9. In the lower reservoir layer the permeabilities are highest in the discharge channel extending to the north from the upflow zone. Various permeability barriers are believed to be present in the reservoir, isolating some of the wells from the others.
4. The "porous medium" porosities of the system vary between 1 and 10%. The "effective" porosity in the upper part of the reservoir is estimated to be 5% and 3.5% in the lower part. These values appear reasonable given the measured porosity of 8 - 15% in cores and the fact that only portions of the fluids may be recoverable from the tight matrix blocks.

ACKNOWLEDGMENTS

The authors acknowledge valuable work on this project by G. Bjornsson, M. Bodvarsson, K Pruess, M. Ripperda, and S. Suresh. The authors also appreciate technical discussions with K. Arnason, G. Bodvarsson, H.

Franzson, A. Gudmundsson, G. P. Hersir, S. P. Snorrason, and K. Saemundsson. Thanks are also due to the Reykjavik Municipal District Heating Service (RMDHS), for allowing publication of this paper. This work was supported by RMDHS and The Assistant Secretary for Conservation and Renewable Energy, Office of Renewable Technology, Division of Geothermal Technology through U.S. Department of Energy Contract No. DE-AC03-76SF00098.

REFERENCES

Arnason, K., Haraldsson, G.I., Johnsen, G.V., Thorbergsson, G., Hersir, G.P., Saemundsson, K., Georgsson, L.S. and Snorrason, S.P., 1986, Nesjavellir - Geological and geophysical study in 1985, Icelandic National Energy Authority report OS-86014/JHD-02 (in Icelandic), 125 pp.

Arnason, K., Haraldsson, G.I., Johnsen, G.V., Thorbergsson, G., Hersir, G.P., Saemundsson, K., Georgsson, L.S., Rognvaldsson, S.Th. and Snorrason, S.P., 1987, Nesjavellir - Olkelduhals - Geological and geophysical study in 1986, Icelandic National Energy Authority report OS-87018/JHD-02 (in Icelandic), 112 pp.

Bodvarsson, Gunnar, 1951, Report on geothermal research in Hengill, Hveragerdi and surroundings, 1947-1949, Journal Engineering Society of Iceland, pp. 1-48.

Bodvarsson, G.S., Pruess, K., Stefansson, V., Bjornsson, S. and Ojiambo, S.B., 1985, A summary of modeling studies of the East Olkaria geothermal field, Kenya, LBL-19367, Geothermal Resources Council 1985 International Volume, pp. 295-301.

Bodvarsson, G.S. and Pruess, K., 1986, The Nesjavellir geothermal field, Iceland - A two-dimensional natural state model, report prepared for the Reykjavik Municipal District Heating Service, 38 pp.

Franzson, H., Gudmundsson, A., Fridleifsson, O. and Tomasson, J., 1986, Nesjavellir high-temperature field, SW-Iceland - Reservoir Geology, Proc. 5th International Symposium on Water-Rock Interaction, Reykjavik, Iceland, pp. 23-27.

Franzson, H. and Sigvaldason, H., 1985, Nesjavellir well NG-8, Icelandic National Energy Authority report OS-85120/JHD-16 (in Icelandic), 55 pp.

Pruess, K., 1982, Development of the general purpose simulator MULKOM, 1982 Annual Report, Earth Sciences Division, Lawrence Berkeley Laboratory, Berkeley, California, LBL-15500, pp 133-134.

Pruess, K., Bodvarsson, G.S., Stefansson, V. and Eliasson, E.T., 1984, The Krafla geothermal field, Iceland, 4. History match and prediction of individual well performance, Water Resources Research, vol. 20, no. 11, pp. 1561-1584.

Stefansson, V., 1985, The Nesjavellir high temperature geothermal field in Iceland, Proc. 10th Workshop on Geothermal Reservoir Engineering, Stanford University, report SGP-TR-84, pp. 23-30.

Stefansson, V., Tomasson, J., Gunnlaugsson, E., Sigvaldason, H., Franzson, H and Sigurdsson,O., 1983, Nesjavellir - well NG-6, Icelandic National Energy Authority report OS-86023/JHD-04 (in Icelandic), 100 pp.

Steingrimsson, B. and Stefansson, V., 1979, Nesjavellir - Temperature and pressure in the reservoir, Icelandic National Energy Authority report OS-79032/JHD-15 (in Icelandic), 31 pp.

Steingrimsson, B., Gudmundsson, A., Sigurdsson, O. and Gunnlaugsson, E., 1986, Nesjavellir - well NJ-11, Icelandic National Energy Authority report OS-86025/JHD-05 (in Icelandic), 164 pp.

Tomasson, J., Gronvold, K., Kristmannsdottir, H. and Thorsteinsson, T., 1974, Nesjavellir well 5, Icelandic National Energy Authority report, 40 pp.

Vinsome, P.K.W. and Westerfeld, J., 1980, A simple method for predicting cap and baserock heat losses in thermal reservoir simulations, Journal of Canadian Petroleum Technology, July-September 1980.

PROCEEDINGS, Thirteenth Workshop on Geothermal Reservoir Engineering
Stanford University, Stanford, California, January 19-21, 1988
SGP-TR-113

HYDROGEN CHLORIDE IN SUPERHEATED STEAM AND CHLORIDE IN DEEP BRINE AT THE GEYSERS GEOTHERMAL FIELD, CALIFORNIA

J. R. Haizlip[1] and A. H. Truesdell[2]

[1]GEO Operator Corp., Santa Rosa, CA 95401
[2]U.S. Geological Survey, Menlo Park, CA 94025

ABSTRACT

Chloride (Cl) concentrations of 10-120 ppm_w have been measured in superheated steam produced by wells at The Geysers, a vapor-dominated geothermal field in northern California. Corrosion of the well casing and steam-gathering system has been recognized in some parts of The Geysers, and is apparently related to the presence of Cl. Cl in the steam is in a volatile form, generated with the steam at reservoir temperatures, and probably travels to the wellhead as HCl gas. Published experimental data for partial pressures of HCl in steam over aqueous HCl solutions and for dissociation constants of HCl were used to calculate distribution coefficients for HCl. Reservoir liquid Cl concentrations capable of generating steam with the observed Cl concentrations were then calculated as a function of pH and temperatures from 250 to 350°C. Equilibrium mineral/liquid reactions with the K-mica and K-feldspar assemblage found in the wells limit the reservoir liquid pH values at various Cl concentrations to about 5 to 6 (near neutral at 250 to 350°C). Within this pH range, liquid at 250°C could not produce steam containing the high Cl concentrations observed. However, liquid at higher temperatures (300 to 350°C) with chloride concentrations greater than 10,000 ppm_w could generate steam with 10 to over 200 ppm_w Cl. There is a positive correlation between pH and the chloride concentrations required to generate a given Cl concentration in steam. The concentration of Cl in superheated steam constrains not only the reservoir liquid composition, but the temperature at which the steam last equilibrated with liquid.

INTRODUCTION

The Geysers is a vapor-dominated geothermal field in northern California which has been producing steam for generation of electricity since 1960. The Geysers reservoir has been modeled from geochemical, geological, and reservoir engineering viewpoints (e.g., White et al., 1971; Truesdell and White, 1973; D'Amore and Truesdell, 1979; Pruess, 1985; Ingebritsen, 1986, 1987; Truesdell et al., 1987 and Walters et al., 1988). Although the estimated amount of liquid saturation varies widely, most workers agree that the vast majority of reserves in The Geysers are liquid, but little is known about the character or location of this liquid.

Although liquid samples have been collected from The Geysers reservoir (Table 1), these samples appear to be primarily steam condensate either from condensation in the wellbore or from the reservoir itself. Current models of The Geysers (cited above) emphasize the heat-pipe mechanism in which a deep boiling liquid produces steam that moves upward through major fractures in an otherwise predominantly liquid-saturated reservoir (as in the cracked sponge model, Weres et al., 1977). Steam condenses and transfers heat to the upper part of the system. Steam condensate then moves down to replenish the deep boiling zone. Thus, fluids in The Geysers system consist of steam, condensate, the liquid (probably condensate) in saturated blocks within the reservoir, and probably a deep boiling liquid (brine), which may be of varying degrees of salinity (Haizlip, 1985; Truesdell et al., 1987) and temperature (Drenick, 1986; Walters et al., 1988). Although required by the postulated convection in the reservoir, the deep liquids have never been sampled directly.

It is probable that The Geysers reservoir liquids cannot be sampled with conventional methods, but some characteristics may be calculated from the compositions of steam produced. Until now, most of the components recognized in steam were those which partitioned preferentially into the vapor phase, i.e., noncondensible gases. Recently, however, significant concentrations of chloride (written here as Cl with valence omitted except in chemical equations) have been observed in superheated steam produced in several different areas of The Geysers. Concentrations from 10-120 ppm_w have been measured in deep wells producing highly superheated steam (Table 1, analyses 3-6). Some of these wells have produced for several years; others are at the edge of present development, and have not yet been produced.

Corrosion problems in the steam-gathering system connected to these wells appear to be related to the Cl production.

The purpose of this paper is to evaluate the physiochemical conditions that would produce these Cl concentrations, and thus provide some chemical constraints on the composition and chemical environment in the reservoir. Two-phase or "wet" wells that produce Cl are not discussed here.

Because Cl production appears to be related to corrosion problems, and because the chemical characteristics of the reservoir liquid (salinity in particular) strongly affect the boiling characteristics of a liquid, it is hoped that this paper will assist field operations and physical modeling of The Geysers reservoir.

BACKGROUND

The relation of Cl to corrosion of the production equipment associated with some wells has drawn attention to the concentration of Cl in the steam produced at The Geysers, and to the differences between Cl-producing wells (Table 1, analyses 3-6) and wells that produce low or zero amounts of Cl. Cl analyses in steam from some Geysers wells are available from the past several years. Most results indicated a few to 25 ppm_w Cl in steam samples (e.g., Table 1, analyses 13, 14), but the accuracy of these analyses may be doubtful. These levels were not previously considered significant, but it is now realized that such concentrations in steam can cause corrosion. Because such corrosion was generally not found, it appears that these measurements may have been in error. Recent analyses indicate <1 ppm_w Cl in steam from most wells (Table 1, analyses 1, 17-19), even some for which as much as 25 ppm_w Cl had been reported. Analytical methods used now are designed for the detection of low concentrations rather than accuracy at high concentrations.

THE FORM OF CHLORIDE TRANSPORT

Cl concentrations in steam at the wellhead in high-Cl Geysers wells have been reliably measured between 10 and 120 ppm_w (Table 1, analyses 3-6). Some of this steam is probably a mixture of high-Cl and low-Cl (<1 ppm_w) steam, so Cl concentrations in the high-Cl steam as generated in the reservoir could be 200 ppm_w or higher before mixing (Walters et al., 1988). In order to evaluate the chemistry of Cl in steam and reservoir liquid, the chemical form in which the Cl is transported in the vapor phase must be determined. If Cl was present in steam as an alkali salt (NaCl, KCl, etc.), it would have to move as aerosols or in water droplets, because the volatility of these compounds under reservoir conditions is negligible (Strykyovich, 1957).

Liquid samples from the steam-gathering system contain condensed steam and any materials soluble in liquid at line temperature (about 175°C) and pressure (about 10 bars; see Table 1 for a representative sample), such as chloride, boron, and silica compounds. The condensate collected downstream from a Cl-producing well contains Cl, B, NH4, and minor amounts of SO_4, HCO_3, Fe, Mn, and other heavy metals, with little or no alkali metals. The absence of alkalis indicates that Cl is not being transported from the reservoir as an alkali metal salt. Another possible Cl compound is ammonium chloride. Ammonia is a gas in steam, reacting with CO_2 in condensate to form NH_4 and HCO_3 ions. There is no indication that NH_4Cl exists as a gas or has appreciable volatility (except when it dissociates at 300°C to NH_3 and HCl) under reservoir or pipeline conditions (Cotton and Wilkinson, 1972, p. 349).

The most probable form in which Cl is carried in steam is as HCl gas. HCl is a gas at normal and high temperatures (condensing at -84°C) and is moderately soluble in water as HCl (Cotton and Wilkinson, 1972, p. 178; Ellis and Mahon, 1977, p. 288). Its apparent solubility is high at low and moderate temperatures (<250°C) because HCl in solution is a strong acid and dissociates almost completely into H^+ and Cl^-. HCl becomes a weak acid at high temperatures (>300°C) so that un-ionized HCl exists in solution and HCl gas will partition into vapor. HCl is thus found in superheated steam that does not equilibrate with dilute water at moderate (<300°C) temperatures. It is a well-known component of volcanic gases from lavas and high-temperature (>400°C) fumaroles.

Analyses of water from condensate traps of high-Cl wells give clear indications of the presence of HCl in steam (Table 1). The more concentrated of these waters consist almost entirely of Fe^{+3} and Cl with much lower concentrations of B and NH_4. Analysis 3 in Table 1 has 185 milliequivalents (meq) of Cl, 215 meq of Fe^{+3}, 7 meq of Mn^{++}, 48 meq of B (H_3BO_3), and 41 meq of NH_4. SO_4 and HCO_3 were probably present but not analyzed, so exact charge balance is not possible, but the solution is predominantly Cl and Fe^{+3}. $FeCl_3$ is not volatile and Fe and Mn are constituents of steel pipes, so it appears most probable that Fe and Mn are dissolved by the action of H^+ formed by dissociation of HCl when it dissolved in condensate.

Although there are many studies on the dissociation of HCl in solution, there appears to be little data on the solubility of gaseous HCl at high temperatures. In the following section we use the available data to estimate the solubility of HCl and then, using dissociation constant data, estimate the chemical character of waters in equilibrium with high-Cl steam.

CALCULATIONS

A two-part calculation constrains the temperature and composition of liquids that could generate high-Cl Geysers steam. First, the distribution coefficient for HCl is calculated, then this data and the dissociation constants of HCl are used to calculate the concentrations of Cl in liquid in equilibrium with high-Cl (10-200 ppm_w) steam. Second, the pH of the reservoir liquid at various Cl concentrations is calculated from the reaction between K-mica and K-feldspar.

The Distribution Coefficient of HCl

The concentration of associated HCl in aqueous solution is determined by the dissociation reaction:

$$HCl = Cl^- + H^+, \quad (1)$$

$$\text{Therefore, } Kd = [Cl^-]\,[H^+]/[HCl] \quad (2)$$

where Kd = the dissociation constant for HCl. The log of the concentration of HCl in the liquid phase is thus:

$$\log m_{HCl,l} = \log m_{Cl-} + \log \gamma_{Cl-} - pH - \log Kd - \log \gamma_{HCl} \quad (3)$$

where, $m_{HCl,l}$ = moles/kg HCl in solution; m_{Cl^-} = moles/kg Cl in solution; and γ_{Cl^-} and γ_{HCl} = the activity coefficients of Cl^- and HCl, respectively. The concentration of HCl in equilibrium with the liquid phase is determined by the distribution coefficient, B_{HCl}, where,

$$B_{HCl} = m_{HCl,v}/m_{HCl,l} \text{ and thus} \quad (4)$$

$$\log m_{HCl,l} = \log m_{HCl,v} - \log B_{HCl}, \quad (5)$$

where $m_{HCl,v}$ = moles/kg HCl in the vapor phase. Since γ_{Cl^-} and γ_{HCl} can be estimated at a given temperature using the Debye-Huckel theory, if Kd and B_{HCl} are known then m_{Cl}, representing the reservoir liquid chloride composition, can be calculated as a function of pH and T using the following equation:

$$\log m_{Cl-} = \log m_{HCl,v} - \log B_{HCl} - \log \gamma_{Cl-} + pH + \log Kd + \log \gamma_{HCl} \quad (6)$$

Perry and Chilton (1973) obtained experimental data on the partial pressure of HCl over various concentrated HCl solutions for the temperature range 0 to 110°C. The concentrations of undissociated HCl in solution were calculated using Kd values from Helgeson (1969) and equation (2). From HCl concentrations in the vapor phase (calculated from the partial pressure of HCl), and the liquid phase (HCl in solution, above), B_{HCl} was calculated as a function of temperature (Figure 1). B_{HCl} values lie between those of B_{H2S} and B_{NH3}, indicating that HCl partitions into the liquid phase slightly more readily than H_2S but not as easily as NH_3. These results are consistent with the suggestion of Ellis and Mahon (1977, p. 288) that the distribution of HCl gas between liquid and vapor is similar to H_2S. The results were extrapolated to higher temperatures, using B equals 1 at 374°C (true for all gases) and making the curve similar to those of H_2S and NH_3 (Figure 1). A linear regression on the data gives:

$$\log B_{HCl} = 3.5597 - 0.00974\ t\ (R^2 = .958), \quad (7)$$

where t = temperature in °C.

Cl in Reservoir Liquid

The Cl concentration of the reservoir liquid can be calculated using equation (6). We used the HCl dissociation constant data of Ruaya and Seward (1987), and calculated activity coefficients of Cl and HCl from the extended Debye-Huckel equation (Henley et al., 1984). Using B_{HCl} values calculated from (7), the Cl concentrations in reservoir liquid as a function of HCl concentrations in vapor were calculated at 250°C, 300°C, and 350°C, and at pH values from 2 to 7 (Figures 2-4). The results indicate that at 250°C (Figure 2), even with 100,000 ppm_w Cl in the liquid, the pH would have to be less than or equal to 3.5 to generate 100 ppm_w Cl in steam. However, at 350°C (Figure 4) vapor with 100 ppm_w Cl or greater can be in equilibrium with liquids of pH from 5 to 6 and chloride concentrations of 10,000 to 80,000 ppm_w. Liquids at 300°C (Figure 3) are intermediate. Thus, the calculations indicate that there is a positive correlation between liquid pH and the chlorinity values required to generate steam with a given Cl concentration. The higher the pH, the higher Cl concentration required to volatilize the same amount of HCl. There is also a positive correlation between pH and the temperature required to generate steam with a given Cl concentration. At lower temperatures, a lower pH is required to volatilize HCl. The activity coefficients used are probably not acceptably accurate for solutions with Cl >35,000 ppm_w (1 m), although such hypersaline brines could be generated in the reservoir by evaporation.

pH Buffered by Mineral/Water Reactions

Potassium mica and potassium feldspar are present as hydrothermal alteration minerals in The Geysers reservoir at all temperatures encountered (Walters et al., 1988). If it is assumed that the pH of the liquid is buffered by the reaction between potassium mica and potassium feldspar in the presence of quartz, then

$$3\ KAlSi_3O_8 + 2\ H^+ = KAl_3Si_3O_{10}(OH)_2 + 6\ SiO_2 + 2\ K^+, \quad (8)$$

and the activity ratio of K^+ to H^+ is a function of temperature. Using this ratio, electrical neutrality, and the Na/K ratio from the empirical Na-K geothermometer, a

relation between chlorinity (Cl) and pH can be derived at various temperatures (Henley et al., 1984). The results (Figure 5) indicate that at Cl concentrations less than 50,000 ppm_w Cl, the pH of the reservoir liquid is greater than 6.25.

The pH required at 250°C to generate significant Cl in steam cannot exist in the reservoir in equilibrium with K-feldspar and K-mica; therefore it is unlikely that steam generated (boiled) at this temperature would contain Cl. If Cl concentrations in reservoir liquid are between 10,000 and 25,000 ppm_w, and the temperature is 300°C or 350°C at a pH of 6, steam with Cl concentrations between 10 and 200 ppm_w could easily be generated.

DISCUSSION AND CONCLUSIONS

Steam with negligible (<1 ppm_w) Cl has probably been generated by boiling from liquid in parts of The Geysers reservoir at less than 250°C, or has passed through zones of liquid saturation at those temperatures. Condensate contains little Cl (Table 1) and can be in equilibrium with 10 ppm_w Cl steam only at very low pH (<1?; Figure 2). Waters of this acidity would alter aluminosilicate minerals to kaolinite or other aluminum oxides according to temperature (Henley et al., 1984). Since feldspars and mica, rather than kaolinite or other Al oxides, are found in The Geysers reservoir (Sternfeld, 1981; Walters et al., 1988), it is unlikely that such acid reservoir waters exist. Mineral-liquid equilibrium for the reaction of potassium mica and potassium feldspar indicate that pH values for reservoir waters with reasonable chloride concentrations are near neutral (neutral pH = 5.6 at 250°C; 5.7 at 350°C). Thus, steam and steam condensate at typical Geysers reservoir temperatures (220-250°C) probably contain negligible Cl. Because steam condensate is nearly ubiquitous, Cl would be absorbed in the liquid before reaching a well.

Steam that contains significant (greater than 10 ppm_w) Cl must have been generated at temperatures above typical Geysers reservoir temperatures and must have followed a dry or high-temperature path to the wellhead. Specifically, at 350°C, steam with greater than 100 ppm_w Cl can be generated (boiled) from liquid at pH 5 with greater than 10,000 ppm_w Cl and at pH 6, greater than 90,000 ppm_w Cl. At this temperature and range of pH, liquid with greater than 10,000 ppm_w Cl would generate steam with greater than 10 ppm_w Cl. At 300°C, liquid with pH less than 5 and Cl greater than 70,000 ppm_w is required to generate steam with 100 ppm_w Cl (Figures 3 and 4). For the high-temperature (350°C) steam with 200 ppm_w Cl suggested by Walters et al. (1988) to exist in the high-temperature reservoir of the Northwest Geysers, liquid Cl concentrations must be greater than 25,000 ppm_w.

From the limits on pH from reservoir mineralogy, temperatures, and the inferred concentration of Cl in the reservoir liquid, we reach the following conclusions:

1. Reservoir pH is around neutral at The Geysers at 250 to 350°C.

2. Steam containing significant (>1 ppm_w) Cl concentration is not generated at typical Geysers temperatures.

3. Steam boiled at higher temperatures can contain the observed concentrations of Cl if near-neutral reservoir liquid has chlorinity between 10,000 and 80,000 ppm_w.

Thus, the source of the chloride is a hot (>300°C) saline (10,000-80,000 ppm_w) brine. Wells at The Geysers that produce chloride must have some steam derived from this brine. The existence of such a deep boiling brine is proposed by many models of The Geysers (e.g., White et al., 1971; Pruess, 1985) but without direct evidence. These conclusions also support the results of isotopic and noncondensible-gas studies, which have proposed that The Geysers contains reservoir liquids of a variety of salinities, with saline, possibly connate, water in parts of The Geysers and meteoric water in others (Haizlip, 1985; Truesdell et al., 1987). Water from hot springs to the east (Table 1) may be similar in composition to the saline reservoir water, as suggested from isotopic evidence.

Evidence presented by Drenick (1986) and Walters et al. (1988) suggests that Cl-bearing steam is produced from higher temperature reservoirs at The Geysers and that some wells produce mixed steam from both the high-temperature and typical reservoirs. Our work shows that steam passing through a two-phase zone containing condensate at around 250°C would be scrubbed of chloride. Therefore, the suggested mixing must occur in the well; or else the conduit through the typical reservoir must be dry. In newly developed areas like the Northwest Geysers, the former is probably true. In wells that have produced for a long time, the shallower typical reservoir may have become dry due to production.

Our results are in agreement with observations of corrosion from HCl-bearing superheated steam at well 12 of the Krafla, Iceland field (Haldur Armannsson, pers. commun., 1987) and with the occurrence of acid, high-Cl condensate from steam at Tatun, Taiwan (Ellis and Mahon, 1977, p. 289), although liquids in these systems may be much more acid than those at The Geysers. The appearance of Cl in steam at Larderello in the 1960s (D'Amore and Truesdell, 1979) probably resulted from the drying out of the 240°C reservoir rather than from a sudden shift to production from deep brine.

ACKNOWLEDGMENTS

Thanks are given to Geothermal Resources International, Inc. allowing for the release of data included in this paper. The support in preparation by Debbie Darling, Mark Morgan, and Chris Dunkle, and critical reviews by Jim Combs, Andy Drenick, Tom MacPhee, Chan Swanberg, Mark Walters, Bob Fournier, and especially Steve Ingebritsen are greatly appreciated.

REFERENCES

Beall, J.J., 1985, "Exploration of a High Temperature, Fault Localized, Nonmeteoric Geothermal System at the Sulphur Bank Mine, California," Geothermal Resources Council Trans., v. 9, pt. 1, p. 395-401.

Cotton, F.A., and Wilkinson, G., 1972, "Advanced Inorganic Chemistry," John Wiley-Interscience, New York, 1145 p.

D'Amore, F., and Truesdell, A.H., 1979, "Models for Steam Chemistry at Larderello and The Geysers," Proceedings, 5th Workshop on Geothermal Reservoir Eng., Stanford, Calif., p. 283-297.

Drenick, A.F., 1986, "Pressure-Temperature-Spinner Survey in a Well at The Geysers," Proceedings, 11th Workshop on Geothermal Reservoir Eng., Stanford, Calif., p. 197-206.

Ellis, A.J., and Mahon, W.A.J., 1977, "Volatility of Chemicals in Steam," Ch. 8.1 in Chemistry and Geothermal Systems, Academic Press, p. 285-289.

Frye, G.A., 1975, "Water Entry in a Steam Well at The Geysers," Proceedings, 1st Workshop on Geothermal Reservoir Eng., Stanford, Calif., p. 89-92.

Giggenbach, W.F., 1980, "Geothermal Gas Equilibria," Geochim. Cosmochim. Acta, 44, p. 2021-2032.

Haizlip, J.R., 1985, "Stable Isotopic Composition of Steam from Wells in the Northwest Geysers, The Geysers, Sonoma County, California," Geothermal Resources Council Trans., v. 9, pt. 1, p. 311-316.

Helgeson, H.C., 1969, "Thermodynamics of Hydrothermal Systems at Elevated Temperatures and Pressures," American Journal of Science, v. 267, p. 729-804.

Henley, R.W., Truesdell, A.H., and Barton, P.B., 1984, "Hydrolysis Reactors in Hydrothermal Fluids" and "pH Calculations in Hydrothermal Fluids," Ch. 6 and 7, Fluid-Mineral Equilibria in Hydrothermal Systems, Reviews in Economic Geology, v. 1, Soc. of Econ. Geol., El Paso, TX, p. 65-98.

Ingebritsen, S.E., 1986, "Evolution and Natural State of Large-Scale Vapor-Dominated Zones in Geothermal Systems," Proceedings, 11th Workshop on Geothermal Reservoir Eng., Stanford, Calif., p. 117-126.

Ingebritsen, S.E., 1987, "Vapor-Dominated Zones within Hydrothermal Convection Systems," Proc., 12th Workshop on Geothermal Reservoir Eng., Stanford, Calif. (in press).

Perry, R.H., and Chilton, C.H., 1973, eds., "Chemical Engineers Handbook," 5th ed., McGraw-Hill, p. 3-62, 3-63

Pruess, Karsten, 1985, "A Quantitative Model of Vapor-Dominated Geothermal Reservoirs as Heat Pipes in Fractured Porous Rock," Geoth. Res. Council Trans., 9, 2, p. 353-361.

Ruaya, J.R., and Seward, T. M., 1987, "The Ion Pair Constant and Other Thermodynamic Properties of HCl up to 350°C," Geochim. Cosmochim. Acta, v. 51, p. 121-130.

Smith, C.L., Ficklinand, W.H., and Thompson, J.M., 1987, "Concentrations of Arsenic, Antimony, and Boron in Steam and Steam Condensate at The Geysers," Jour. Vol. Geoth. Res., 32, p. 329-341.

Sternfeld, J.N., 1981, "The Hydrothermal Petrology and Stable Isotope Geochemistry of Two Wells in The Geysers Geothermal Field," M.S. Thesis, UC Riverside, 202 p.

Strykyovich, M.A., 1957, "Investigation of the Solubility of Low-Volatility Substances in High-Pressure Steam by Radio Isotopes," in Scien. Res., Radioisotopes, 1, p. 411-425.

Truesdell, A.H., Nathenson, M., and Frye, G.A., 1981, "Downhole Measurements and Fluid Chemistry of a Castle Rock Steam Well, The Geysers, California" Geothermics, 10, p. 103-114.

Truesdell, A.H., Haizlip, J.R., Box, W.T., and D'Amore, F., 1987, "Fieldwide Chemical and Isotopic Gradients in Steam from The Geysers," Proceedings, 12th Workshop on Geothermal Reservoir Eng.", Stanford, Calif., January 20-22, 1987.

Truesdell, A.H., and White, D.E., 1973, "Production of Superheated Steam from Vapor-Dominated Geothermal Systems," Geothermics 2, v. 3-4, p. 154-173.

Walters, M.A., Sternfeld, J.F., Haizlip, J.R., Drenick, A.F., and Combs, J.B., 1988, "A Vapor-Dominated Reservoir Exceeding 600°F at The Geysers, Sonoma County, California," Proceedings, Stanford Geothermal Reservoir Engineering Workshop, this volume.

Weres, O., Tsao, K., and Wood, B., 1977, "Resource Technology and Environment at The Geysers," Lawrence Berkeley Lab. LBL-5231.

White, D.E., Hern, J.D., and Waring, G.A., 1963, "Chemical Compositions of Subsurface Waters, in Data of Geochemistry," U.S. Geol. Survey Prof. Paper 440-F, 67 p.

White, D.E., Barnes, I., and O'Neil, J.R., 1973, "Thermal and Mineral Waters of Nonmeteoric Origin, California Coast Ranges," Geological Society America Bulletin, 84, p. 547-560.

White, D.E., Muffler, L.J.P., and Truesdell, A.H., 1971, "Vapor-Dominated Hydrothermal Systems Compared with Hot-Water Systems," Economic Geology, 66-1, p. 75-97.

Table 1. Chemical Analyses of Water and Steam Condensate from The Geysers and Surrounding Areas
[in mg/L, except $\delta^{18}O$ in °/oo]

No.	Fluids from Wells	pH	SiO_2	Ca	Mg	Na	K	Li	HCO_3	SO_4	Cl	F	B	Fe	Mn	NH_4	$\delta^{18}O$
	CENTRAL GEYSERS																
1	Condensed steam typical well[1]	~6.3	0.8	-	-	-	-	-	*	*	≤1.0	*	21	-	-	*	-4.7
2	Water from condensate trap - typical well[1]	~5.9	4.1	1.29	-	-	-	-	*	*	6.0	*	521.5	-	-	*	*
3	Condensed steam Cl well[1]	*	-	-	-	-	-	-	*	*	13.0	*	34	-	-	*	-2.7
4	Water from condensate	*	14.7	-	-	-	-	-	*	*	4900	*	11	1901	67	*	*
5	trap - Cl wells[1]	4.3	48.0	47.3	27.7	21.1	*	-	*	*	3885	*	664	3011	180	313	*
6		3.1	88.6	34.0	20.2	16.8	*	-	*	*	6575	*	520	4006	186	748	*
	NORTHWEST GEYSERS																
7	Condensed steam	~5.9	-	-	-	0.08	-	-	*	*	46	*	58	-	-	*	+3.0
8	Cl wells[1]	*	-	-	-	0.15	-	-	*	*	120	*	106	-	-	*	+2.0
9		*	0.8	-	-	0.3	-	-	*	*	88	*	80	-	-	*	+1.2
	SOUTHEAST GEYSERS																
10	Water entry original hole[2]	*	*	<10	*	146	110	*	*	*	41	*	82.8	*	*	*	*
11	Water entry redrill[2]	*	400	10	37	117	86	*	12.2	414	10	8	24.1	*	*	43.1	*
12	Steam condensates[2]	*	1.2	<0.1	0.005	<0.1	<0.1	*	80	10	2	<0.01	2.4	1.0	*	25.2	*
13	Steam condensates[3]	6.1	4.3	0.1	0.04	<0.5	<0.5	<0.01	95	4	7.1	<0.1	0.1	-	-	5	-6.3
14		5.7	4.3	<0.1	0.04	<0.5	<0.5	<0.01	46	7.3	10	<0.1	1.2	-	-	9	-4.8
15	Ejected waters[3]	8.9	42	1.8	1.0	18	7.8	0.12	64	9	7.1	0.5	42	-	-	-	-1.3
16		7.8	80	2.9	0.7	71	12	0.6	162	40	18	3.7	-	-	-	-	+0.8
	GEYSERS																
17	Condensed steam Well 1[4]	5.3	<1.0	*	*	<0.1	<0.1	*	*	*	<0.01	<0.04	0.47	*	*	*	*
18	Water from condensate trap - Well 1[4]	5.5	27.0	*	*	4.5	0.5	*	*	*	0.08	0.4	150	*	*	*	*
19	Condensed steam Well 2[4]	*	<1.0	*	*	<0.1	<0.1	*	*	*	0.09	<0.04	2.8	*	*	*	*
20	Water from condensate trap - Well 2[4]	*	15.0	*	*	0.2	0.2	*	*	*	0.14	0.1	150	*	*	*	*
	NATURAL WATERS																
21	Witches' Cauldron, The Geysers[5]	7.0	66	58	108	18	6	*	176	776	1.5	*	15	*	*	111	*
22	Devil's Kitchen, The Geysers[5]	1.8+	225	47	281	12	5	*	0	5710	0.5	*	3.1	63	1.4	1400	*
23	"Geyser" Spring Sulfur Bank Mercury Mine[6]	6.8	42	20	55	1190	23	4.4	3290	598	644	1.0	620	0.0	0.1	464	+5.41
24	Wilbur Hot Springs	6.9	200	28	38	8500	440	*	7310	390	9700	2.5	310	0.04	*	280	+3.24

NOTES
-, Not detected
*, Not analyzed
[1], Data available courtesy of Geothermal Resources International, Inc.
[2], Frye, 1975
[3], Truesdell et al., 1981
[4], Smith et al., 1987
[5], White et al., 1963
[6], White et al., 1973

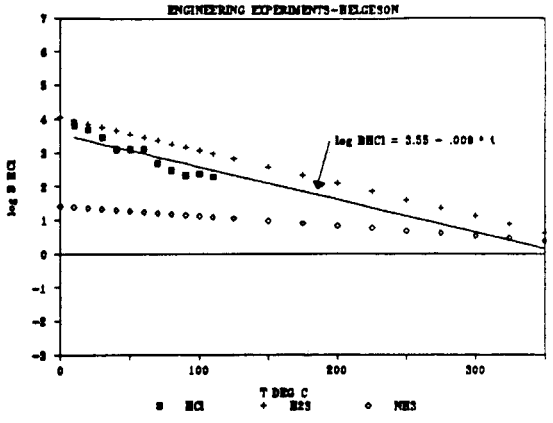


Figure 1. Log of the distribution coefficients of HCl, B_{HCl}, calculated from vapor pressure data (Perry and Chilton, 1973), and the Kd of Helgeson (1969). B_{H2S} and B_{NH3} added for reference are from Giggenbach (1980). Linear regression line calculates to be: log B_{HCl} = 3.56 - .0097 (t in °C).

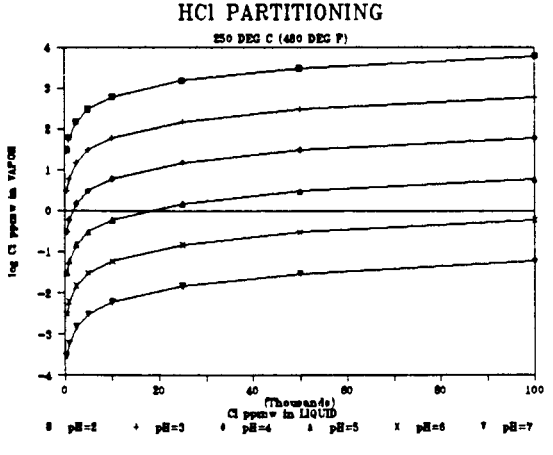


Figure 2. Cl in reservoir liquid versus Cl in reservoir vapor, in ppm_w. Calculated using B_{HCl} derived from experimental data and Kd of Ruaya and Seward (1987) at 250°C.

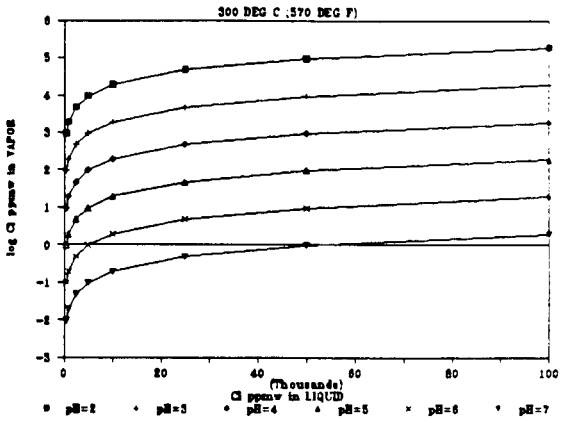


Figure 3. Cl in reservoir liquid versus Cl in reservoir vapor, in ppm_w. Calculated using B_{HCl} derived from experimental data and Kd of Ruaya and Seward (1987) at 300°C.

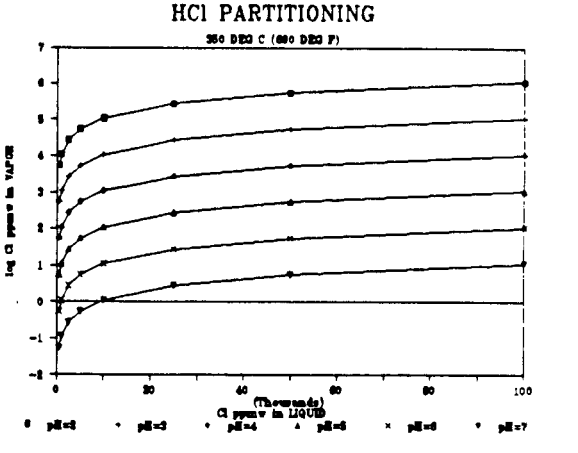


Figure 4. Cl in reservoir liquid versus Cl in reservoir vapor, in ppm_w. Calculated using B_{HCl} derived from experimental data and Kd of Ruaya and Seward (1978) at 350°C.

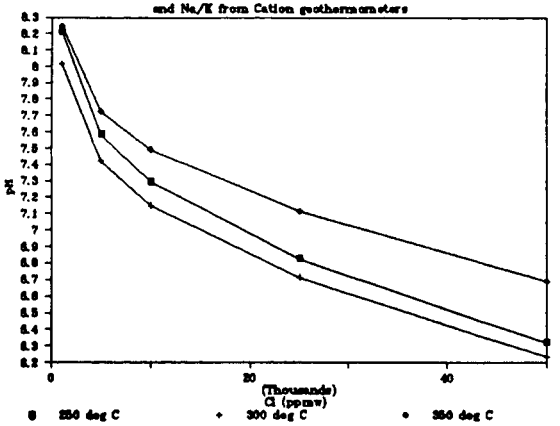


Figure 5. pH versus Cl in reservoir liquid in equilibrium with potassium feldspar and potassium mica. Equilibrium constants from Henley et al., (1984).

PROCEEDINGS, Thirteenth Workshop on Geothermal Reservoir Engineering
Stanford University, Stanford, California, January 19-21, 1988
SGP-TR-113

DOUBLE-DIFFUSIVE CONVECTION AS A MECHANISM FOR TRANSFERRING HEAT AND MASS WITHIN THE SALTON SEA GEOTHERMAL BRINE

Robert O. Fournier

U.S. Geological Survey, Menlo Park, CA 94025

ABSTRACT

H. C. Helgeson noted in 1968 that the salinity of the brine in the geothermal reservoir within the Salton Sea geothermal system generally increases from the top to the bottom and from the center to the sides. He also noted that pressure measurements at perforations in cased wells seemed to indicate that the formation fluids at the depths of production have a specific density about equal to 1, and that hot concentrated brines apparently exist in pressure equilibrium with comparatively cold dilute pore waters in the surrounding rocks. Since 1968 there have been no published reports that dispute these observations. However, a very high heat flux through the top of the system seems to require a substantial component of convective transfer of heat beneath an impermeable cap, whereas the apparent salinity gradient with depth seems to require little or no free convection of brine. This paradox may be resolved if double-diffusive convection is the main process that controls the depth-temperature-salinity relations. Such convection provides a mechanism for transfering heat from the bottom to the top of the hydrothermal system while maintaining vertical and horizontal salinity gradients--densities remaining close to unity.

In 1981, Griffiths showed experimentally that layered double-diffusive convection cells may develop in porous media when hot saline waters underlie more dilute cooler waters. However, nagging questions remain about whether fluid densities within the Salton Sea geothermal system really adjust to unity in response to changing temperature and salinity at depths greater than about 1 km. The State 2-14 well, the Salton Sea Scientific Drill Hole, has provided one high-quality data point for a depth interval of 1,865-1,877 m, where the temperature is about 305°C. The calculated density of the pre-flashed reservoir fluid sampled from that depth is 1.0008 ± 0.0023.

INTRODUCTION

The geologic and thermodynamic characteristics of the Salton Sea geothermal system were described in great detail by Helgeson [1968]. He showed plots of depth versus temperature, pore-fluid pressure, and total dissolved solids for many of the wells that had been drilled at that time. A characteristic of the system is that fluids with different salinities are produced from different wells. The data strongly suggested that within the hydrothermal system the salinity increases from the sides toward the central part of the field, and from the top toward the bottom. The thermal gradients in wells in the central part of the field generally are nearly linear from the surface to a depth of about 0.5 to 1 km and range from about 250° to 380°C km^{-1}. Below about 1 km, thermal gradients generally are nearly linear, but at much lower values (commonly about 40°C km^{-1}). The gradient measured within the State 2-14 Salton Sea Scientific Drill Hole (SSSDH) from a depth of 1,890 to 3,170 m is about 39°C km^{-1} [Sass et al., 1987]. According to Helgeson [1968], pressures measured at perforations in various wells under static conditions fall on a curve with a 0.0295 atmosphere ft^{-1} gradient--a pressure gradient which requires the brines to have virtually unit specific density at all depths (to at least 7,000 ft, the deepest measurement at that time). Since then there have been no published papers that dispute these observations. Rex [1985] agreed that temperature and salinity achieve a balance with specific density of the fluid equal to unity, and stated that according to his study this phenomenon is an intrinsic property of the reservoir.

The observed thermal profile within the Salton Sea geothermal system is typical of geothermal systems that are capped by impermeable rock through which heat is transferred mainly by conduction, and are underlain by relatively permeable rock through which heat is trans-

ferred mainly by convection. Helgeson [1968] recognized that this interpretation of the data presented a paradox: the high heat flow through the top part of the system and the relatively low thermal gradient below the impermeable cap required convective transfer of thermal energy within the hydrothermal system, while a hydrostatic gradient exactly consistent with unit density and systematically increasing salinity with depth precluded free convection in the geothermal reservoir. In view of this paradox, Helgeson [1968] suggested that below about 0.9 to 1.2 km (3,000-4,000 ft) the salinity of the reservoir fluids in a given well may be constant with increasing depth, and that the uncertainty in the pore-fluid pressure measurements was too great to distinguish between isosalinity and isodensity conditions. Helgeson [1968] did note, however, that the model that he proposed was only one of several possible convective mechanisms of heat transfer that might be operating in the reservoir. As an example of other mechanisms, he called attention to the paper by Turner and Stommel [1964] on double-diffusive convection. It is the intent of this paper to again call attention to double-diffusive convection and to suggest that this process be given more consideration as a possible way to explain the variations in pressure, temperature, heat flow, and salinity observed throughout the hydrothermal system.

PREVIOUS MODELS OF THE HYDROTHERMAL SYSTEM

White [1968] and Dutcher et al. [1972] suggested that vertical heat transport in the Salton Sea field is by large-scale convection cells encompassing the entire section of permeable reservoir rocks. However, this suggestion does not account for the reported variations in composition of the brine from bottom to top and center to sides. In the Helgeson [1968] model localized free convection of the brine is favored--uniform salinity occurring within a given well but different salinities in adjacent wells.

Yonker et al. [1982] suggested that vertical convective motion in the reservoir beneath the thermal cap is confined to small units within permeable sand horizons interbedded with and separated by thin shale beds. They further suggest that large-scale horizontal flow could be superimposed on the small-scale convection to transfer heat from the area of the buttes, which is close to the southern shore of the Salton Sea, to the margins of the field. This lateral-flow model was expanded upon by Kasameyer et al. [1984], who shows the heat source as a region of dike intrusion at the side of the region of horizontal fluid convection.

Rex [1985] concluded that the main reservoir is not undergoing significant convection but rather owes its condition to a balance of osmotic and thermo-osmotic effects combined with water-rock interactions. He further concluded that the geothermal reservoir does not need a cap rock but is hydrostatically stable, capped by a ground-water circulation system. In this model, diffusion of water downward plays a major role in the development of the salinity gradient, and the decrease in thermal gradient below about 1 km appears to reflect changes in bulk conductivity of the rock-brine system with depth. Michels [1987] also discussed a model in which salinity gradients develop in non-convecting brine in response to a temperature gradient.

DOUBLE-DIFFUSIVE CONVECTION

The processes involved in double-diffusive convection have been described and reviewed by many investigators, including Stommel et al. [1956], Turner and Stommel [1964], Turner [1974, 1979, 1981], Huppert and Turner [1981], Huppert and Sparks [1984], and Vitagliano et al. [1984]. Double-diffusive convection resulting in layered cells has been applied in geologic environments to explain temperature-salinity profiles in some ocean environments [Strommel et al., 1956; Huppert and Turner, 1981] and to account for stratified chemical variations and mineral banding in some magma chambers [Huppert and Turner, 1981; Huppert and Sparks, 1984]. However, Griffiths [1981] suggested that it might occur in geothermal systems. The two requirements for the occurrence of double-diffusive convection are that the fluid contain two or more components with different molecular diffusivities, and that these components make opposing contributions to the vertical density gradient [Huppert and Turner, 1981]. Within the Salton Sea hydrothermal system the important parameters are the contrasting rates of transport of heat and salt across a boundary layer separating cooler less saline water above from hotter more saline water below. Both heat and salt are transported through the interface solely by molecular diffusion. The fluid mechanical behavior for this situation was first studied experimentally by Stommel in 1962 and described by Turner and Stommel in 1964.

Thermal input from below into the deeper more saline water causes it to become less dense than the overlying less saline water and convection is initiated. Upward movement of the more saline water continues until a slight cooling increases its density to the point where buoyancy is no longer a driving force. Huppert and Turner [1981] describe the process as follows: "After the initial oscillatory instability, the thermal boundary layer breaks down to form a shallow convecting layer that grows by incorporating fluid from the gradient region above it. When the thermal boundary layer ahead of the convecting region reaches

a critical Rayleigh number, it too becomes unstable, and a second layer forms above the first. Convection is sustained by a more rapid vertical transport of heat relative to salt, and eventually many such layers form." For the situation in which there are horizontal as well as vertical temperature and salinity gradients, individual double-diffusive convection cells should be bounded on the sides by other convection cells that have slightly different salinities and temperatures.

Within the Salton Sea hydrothermal system, the situation is greatly complicated by the heat stored in the surrounding rock and by convective flow of fluids, mainly within relatively permeable sands toward the top of the system, and mainly within interconnecting fractures where rock has been indurated by metamorphic processes. However, Griffiths [1981] has demonstrated experimentally that layered double-diffusive convection cells can form in porous media, and has suggested that some chemical variations at Wairakei may be due to this effect. If double-diffusive convection does occur in porous media or in open fractures within the Salton Sea geothermal system, it is likely that the temperatures of the wall rocks would adjust to the temperatures of the many-layered convection cells. Thus, on a gross scale the thermal gradient might be relatively uniform at about 40°C km^{-1}, but on a fine scale the thermal profile would have a staircase structure (Figure 1). Future temperature logging, after the SSSDH has had casing cemented in place to near the bottom and after the well has returned to thermal equilibrium, may provide critical information with which to evaluate the possibility of double-diffusive convection within the system.

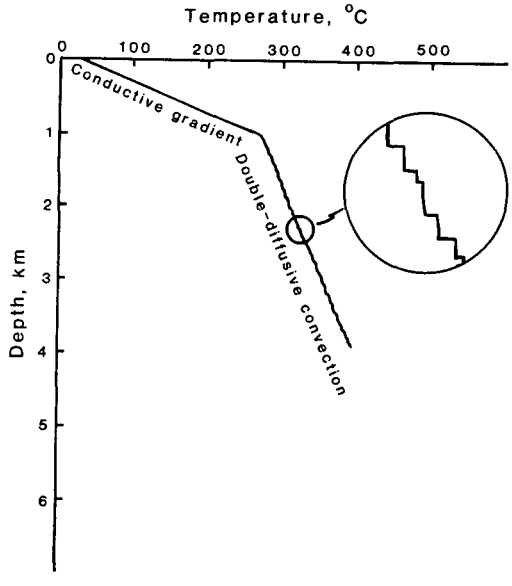


Figure 1. Idealized temperature-depth profile within the Salton Sea geothermal system showing details of effects of double-diffusive convection.

THE FLUID COMPOSITION-DENSITY PROFILE

It is essential that reliable and accurate fluid composition and density profiles be established for the Salton Sea hydrothermal system at several localities in order to choose among possible hydrologic models of the system. Rex [1985] implies that the available data (apparently mostly residing in company files) are sufficient to do this. The basic data, however, have not been published for scrutiny by the scientific community. Much of the available information is difficult to evaluate, because commercial production wells generally are completed with long sections of slotted liners so that fluids sampled at the wellhead may be mixtures of brines from different depths where slightly different initial temperatures prevail.

If it can be shown that salinities really do systematically increase with depth and that fluid densities really do remain close to unity at all depths within the hydrothermal system, free convection would be eliminated as a mechanism of heat transfer, and double-diffusive convection would become a more attractive, though not the only, model to account for the thermal and chemical structure of that system. A major objective of the SSSDH was to address this problem by sampling and analyzing uncontaminated fluid samples from isolated regions at different depths in the well. To date, an uncontaminated fluid sample has been obtained from that well only from a depth interval of 1,865 to 1,877 m and an initial temperature of 305°C [Michels, 1986; Sass et al., 1987; Thompson and Fournier, in press]. The calculated pre-flashed composition of that fluid is shown in Table 1. Although the results provide information about only one point on the depth-composition curve, that point is well constrained, and it can be used as a basis for estimating what the properties of pore fluids should be at shallower and deeper levels in the well.

Table 1. Pre-flashed concentrations of selected elements and total dissolved solids in brine from a depth of 1,865-1,877 m in the State 2-14 well, December 1985 flow test.

Weight %	12/29*	12/29**	12/30**
Na	5.01	5.28	5.27
K	1.72	1.67	1.65
Ca	3.32	2.71	2.65
Cl	15.15	15.34	15.37
Sum	25.20	25.00	24.94
Total dissolved solids	25.2-25.7	25.54	25.46

* Thompson and Fournier [in press]
** Michels [1986]

During drilling, the mud weight required to just balance the pore-fluid pressure at a depth of 1,879 m indicated a pore-fluid density very close to 1 g cm^{-3} (Sass, pers. commun., 1986). No down-hole pressure measurements were made at that depth, and down-hole fluid sampling was unsuccessful. Consequently, the only available check on the pore-fluid density is by calculation, using the pre-flashed composition of the brine sampled at the surface (Table 1). The fluid produced from a depth of about 1,870 m is composed predominantly of NaCl, $CaCl_2$, and KCl, and the total dissolved solids are about 25.5±0.3 weight percent. For this type of brine, the density at high temperature and high pressure can be calculated by using a model published by Potter and Haas [1978]. In that model the density of the brine, d_b, is related to the composition of the brine as follows:

$$d_b = d_N + (d_K - d_N)f_K + (d_C - d_N)f_C, \qquad (1)$$

where d_N, d_K, and d_C are the densities of pure solutions of NaCl, KCl, and $CaCl_2$, respectively, at the given temperature and molality of the total chloride in solution; and f_K and f_C are the mole fractions of chloride present in the brine as KCl and $CaCl_2$, respectively.

Densities of the pure chloride solutions of the three salts were taken from Potter and Brown [1976, 1977] and Potter and Clynne [1976]. Density data for KCl at temperatures in the 200° to 400°C range extend only to about 4-m solutions, so densities of a more concentrated solution ranging from 4.0 to 5.8 m were obtained by extrapolation, using a plot of molality chloride versus the difference in density of KCl and NaCl for solutions of the same molality in respect to chloride. That plot and a similar plot with $CaCl_2$ instead of KCl give straight lines (Figure 2). Density data for both KCl and $CaCl_2$ are available only at the vapor pressures of the solutions, and density data for $CaCl_2$ are not available above 300°C. Therefore, densities of the predominantly NaCl-$CaCl_2$-KCl pre-flashed reservoir fluid [Michels, 1986; Thompson and Fournier, in press] were calculated at 300°C and the vapor pressure of the solution, and then those results were multiplied by factors to correct for the slightly increased temperature and pressure actually present in the reservoir. The correction factors were obtained by assuming that the changes in density caused by increased temperature and pressure were proportional to the changes in density caused by similar increases in temperature and pressure in the pure NaCl system. The temperature-correction factor that was used required multiplication of the density (calculated at 300°C) and the vapor pressure of the solution by 0.995. The pressure-correction factor required multiplication by 1.019. These corrections for temperature and pressure act in opposite directions, and the combined correction factor requires multiplication by 1.014. The exclusion of iron and

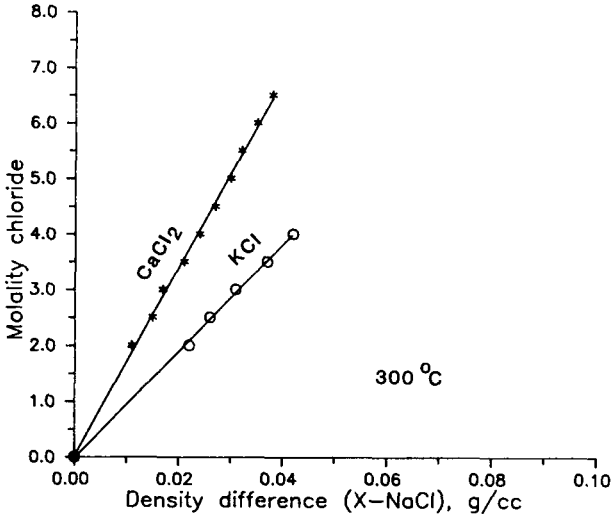


Figure 2. Chloride molality versus the density difference between the indicated salt and NaCl at 300°C. The symbols show data obtained from tables of densities.

other dissolved constituents from the density model is not likely to have made a significant difference, even though they constitute about 2 weight percent of the total dissolved solids, because the model is based mainly on the total chloride in the system. In the Thompson and Fournier data shown in Table 1, all the anionic charges were assumed to be balanced by sodium, calcium, and potassium, thereby compensating in great part for the absence of other dissolved constituents in the density calculation [Thompson and Fournier, in press].

Calculated densities of pre-flashed reservoir fluids produced from the SSSDH at a depth of 1,865 to 1,877 m and a temperature of 305°C are shown in Table 2. The three different sets of analytical information yield a calculated average density of 1.0008 ± 0.0023. This result is in agreement with a double-diffusive model in which hot brines are in approximate pressure equilibrium with cold water at the sides of the hydrothermal system. The errors caused by not taking account of small amounts of other constituents in the brines, such as iron and manganese, and assuming a model based on pure NaCl to correct for pressures greater than the vapor pressure of the solution and a temperature of 305°C instead of 300°C, will cause the calculated density to be slightly on the low side. Therefore, the chemical data favor reservoir fluid densities of about 1 g cm^{-3} or greater at a depth of 1,870 m. The free convection model of Helgeson [1968] requires a fluid density of less than 1 g cm^{-3} (about 0.97-0.98 g cm^{-3}) at a depth of 1.8 km. Conversely, for isochemical conditions in a freely convecting system, brine of the composition found at 1.8 km would have a density of about 1.02 to 1.03 g cm^{-3} at a depth of 1 km and a temperature of 275°C. That high a fluid density

TABLE 2. Calculation of specific density of pre-flashed brine at 305°C at a depth of 1,865-1,877 m in the State 2-14 well. (The notation is given in the text.)

	Dec. 29*	Dec. 29**	Dec. 30**
$d_K - d_N$	0.0604	0.0603	0.0602
$d_C - d_N$	0.0336	0.335	0.335
f_K	0.1029	0.0987	0.0973
f_C	0.3877	0.3125	0.3050
d_{Na}	0.9702	0.9698	0.9696
$(d_K - d_N) f_K$	0.0062	0.0058	0.0059
$(d_C - d_N) f_C$	0.0130	0.0105	0.0102
Sum	0.9894	0.9862	0.9857
P-T correction	x 1.0139	x 1.0139	x 1.0139
Density at 305°C	1.0031	0.9999	0.9994

* Thompson and Fournier [in press]
** Michels [1986]

in the shallow part of the system is not consistent with the observed pressures or with free convection driven by the influx of cold dilute water at the sides of the system.

DISCUSSION AND CONCLUSIONS

The suggestion made by Helgeson [1986] that the salinity of the reservoir fluid in a given well may be constant with increasing depth below about 0.9 to 1.2 km still seems to be a possibility, although a remote one. The critical experiment, in which fluids would be sampled and analyzed from significantly different depths within a given well, has not yet been carried out. Another flow test of the SSSDH from an isolated zone at a depth of about 3,000 m could provide critical information with regard to the possibility of free convection occurring in the 1,800 to 3,000 m depth range.

The models proposed by Rex [1985] and Michels [1987] assume that salinity increases with depth and that little convective flow occurs. However, Rex [1985] would have very slow horizontal flow of the brine southward from the Salton Sink as far as the town of Imperial, a distance of approximately 50 km. Neither Rex [1985] nor Michels [1987] addresses the problem of how to supply large quantities of heat from the base of the system to the top without a significant component of convective heat transport. Rex [1985] simply states that the observed decrease in temperature gradient with depth does not indicate convection in the reservoir, but rather a change in bulk conductivity of the rock-brine system with depth.

The model proposed by Yonker et al. [1982] and Kasameyer et al. [1984] can account for the thermal structure and lack of large-scale vertical convection that would homogenize fluids in the upper part of the hydrothermal system where permeability is controlled by horizontally bedded alternating sands and shales. However, the model does not address the apparent lack of vertical convection in the deeper parts of the system, where fluids may flow through fractures in highly altered and indurated rocks. This model seems to require stagnant conditions where fracture permeability predominates, but could be compatible with slow free convection of an isochemical fluid or double-diffusive convection of fluids with increasing salinity at depth. In addition, this model does not address recharge of highly saline brines of different compositions into the different permeable sandstones in the upper part of the hydrothermal system, where horizontal flow is occurring beneath the thermal cap; nor does it explain why temperature-salinity relations in the pore waters appear to adjust to a specific density of unity in each of the cells. The model also seems to imply that salinities should remain constant within any given sand horizon from the center of the system to near the margin, where mixing with cold dilute water occurs.

The calculated density of the brine sampled from the SSSDH at a depth of 1,865 to 1,877 m is close to unity at 305°C and 18.7 MPa. This result is in agreement with a hydrologic model in which hot brines are in hydrostatic equilibrium with cold dilute water surrounding the hydrothermal system. It also is in agreement with a model in which salinity gradients and heat flux are controlled by double-diffusive convection within the hydrothermal system. A depth-temperature-salinity profile in which specific densities of fluids are everywhere close to unity does not in itself prove that double-diffusive convection is occurring. However, double-diffusive convection has been demonstrated experimentally in porous media [Griffiths, 1981], and it should be given additional consideration as a mechanism for explaining the vertical and horizontal chemical gradients and the high heat flux from the Salton Sea geothermal system. It may offer a plausible alternative or an important adjunct to the models of Yonker et al. [1982] and Kasameyer et al. [1984].

REFERENCES

Dutcher, L.C., W.F. Hart, and W.R. Moyle, Jr. (1972), Preliminary appraisal of ground water storage with reference to geothermal resources in the Imperial Valley Area, California, U.S. Geological Survey Circ. 649, 57 pp.

Griffiths, R.W. (1981), Layered double-diffusive convection in porous media: J. Fluid Mech., 102, 221-248.

Helgeson, H.C. (1968), Geologic and thermodynamic characteristics of the Salton Sea geothermal system, Amer. J. Science, 266, 129-166.

Huppert, H.E., and R.S.J. Sparks (1984), Double-diffusive convection due to crystallization in magmas, Ann. Rev. Earth and Planetary Sci., 12, 11-37.

Huppert, H.E., and J.S. Turner (1981), Double-diffusive convection: J. Fluid Mechanics, 106, 299-329.

Kasameyer, P.W., L.W. Yonker, and J.M. Hanson (1984), Development of a hydrothermal model for the Salton Sea geothermal field, California, Geol. Soc. Amer. Bull., 95, 1242-1252.

Michels, D.E. (1986), SSSDP fluid compositions at first flow test of State 2-14, Geothermal Resources Council Trans., 10, 461-465.

Michels, D.E. (1987), Salinity stabilization for non-convecting brine in a temperature gradient [abs.], EOS, 68, 439.

Potter, R.W., II, and D.L. Brown (1976), The volumetric properties of vapor-saturated aqueous potassium chloride solutions from 0° to 400°C based on a regression of the available data, U.S. Geological Survey Open-File Rept. 76-243, 5 pp.

Potter, R.W., II, and D.L. Brown (1977), The volumetric properties of aqueous sodium chloride solutions from 0° to 500°C at pressures up to 2000 bars based on a regression of the available data, U.S. Geological Survey Bull. 1421-C, 36 pp.

Potter, R.W., II, and M.A. Clynne (1976), The volumetric properties of vapor-saturated aqueous calcium chloride solutions from 0° to 300°C based on a regression of the available data, U.S. Geological Survey Open-File Rept. 76-365, 5 pp.

Potter, R.W., II, and J.L. Haas (1978), Models for calculating density and vapor pressure of geothermal brines, J. Research U.S. Geological Survey, 6, 247-257.

Rex, R.W. (1985), Temperature-chlorinity balance in the hypersaline brines of the Imperial Valley, California, International Symposium on Geothermal Energy, Geothermal Resources Council, Hawaii, 1985, International Volume, 351-356.

Sass, J.H., J.D. Hendricks, S.S. Priest, and L.C. Robison (1987), Temperatures and heat flow in the State 2-14 well, Salton Sea Scientific Drilling Program, [abs.], EOS, 68, 454.

Stommel, H. (1962), Examples of mixing and self-stimulated convection on the S, T diagram (in Russian), Okeanologiya, 2, 205-209.

Stommel, H., A.B. Arons, and D. Blanchard (1956), An oceanographical curiosity: the perpetual salt fountain, Deep-Sea Res., 3, 152-153.

Thompson, J.M., and R.O. Fournier, in press, Chemistry and geothermometry of brine produced from the Salton Sea Scientific Drill Hole, Imperial Valley, California, J. Geophys. Research.

Turner, J.S. (1974), Double-diffusive phenomena, Ann. Rev. Fluid Mech., 6, 37-56.

Turner, J.S. (1979), Buoyancy effects in fluids, Cambridge University Press, 350 pp.

Turner, J.S. (1981), The influence of molecular processes on turbulence and mixing in the ocean, Proc. 2nd Conference on Turbulence in the Ocean, J.D. Woods, ed., Springer.

Turner, J.S. and H. Stommel (1964), A new case of convection in the presence of combined vertical salinity and temperature gradients, Proc. Nat. Acad. Sci. U.S.A., 52, 49-53.

Vitagliano, P.L., C. Della Volpe, and V. Vitagliano (1984), Gravitational instabilities in free diffusion boundaries, J. Solution Chem., 13, 549-562.

White, D.E. (1968), Environments of generation of some base metal ore deposits, Econ. Geol. 63, 301-335.

Yonker, L.W., P.W. Kasameyer, and J.D. Twehey (1982), Geological, geophysical, and thermal characteristics of the Salton Sea geothermal field, California, J. Volcanology and Geothermal Research, 12, 221-258.

PROCEEDINGS, Thirteenth Workshop on Geothermal Reservoir Engineering
Stanford University, Stanford, California, January 19-21, 1988
SGP-TR-113

Evolution Of The Thermal Cap In Two Wells From The Salton Sea Geothermal System, California

Joseph N. Moore and Michael C. Adams

University of Utah Research Institute
Salt Lake City, Utah

ABSTRACT

The Salton Sea geothermal system is overlain by a thermal cap of low permeability rocks that restricts the upward movement of the high-temperature reservoir brines. Petrographic and fluid inclusion data from two wells show that the thermal cap in the southern part of the field consists of an upper layer of lacustrine and evaporite deposits with low initial permeabilities and a lower layer of deltaic sandstones. The sandstones were incorporated into the thermal cap as downward percolating fluids deposited anhydrite and calcite in the pore space of the rocks, reducing their permeabilities. During development of the thermal cap, base-metal sulfides, potassium feldspar and quartz veins were deposited by brines from higher temperature portions of the system.

INTRODUCTION

The Salton Sea geothermal system is located near the center of the sediment filled Salton Trough of southern California and Mexico. Mineral assemblages and textures formed in response to geothermal activity can be categorized as diagenetic or metamorphic (McKibben and Elders, 1985). Diagenetic processes occur at temperatures of less than about 250°C and have resulted in the recrystallization of the sheet silicates, and the deposition of anhydrite, carbonates, and sulfides in the pore space of the sediments. The reduction in the permeabilities of the shallow sediments caused by the deposition of these pore filling minerals has led to the development of a thick thermal cap, or zone of conductive heating, over the reservoir (Younker et al., 1982). Metamorphic processes occurring in the reservoir, where temperatures range from 250° to 365°C, have led to the development of hornfelsic textures and mineral assemblages typical of the greenschist facies (Muffler and White, 1969). Fluids encountered at the depths where these metamorphic processes are occurring have salinities of up to 25 weight percent (Helgeson, 1968).

In contrast to the deep portions of the Salton Sea geothermal system, little data has been presented on the temperatures and salinites of the brines that have characterized the upper parts of the geothermal field. Furthermore, because there is evidence that conditions within the geothermal system have changed with time (Skinner et al., 1967; Huang, 1977; Andes and McKibben, 1987), the present borehole temperatures and fluids may not accurately reflect the conditions associated with the alteration of the shallow sediments. Alternatively, this data can be obtained from fluid inclusions contained within the authigenic minerals. In this paper we describe the results of fluid inclusion and petrographic studies of two boreholes drilled in the southern part of the field (Fig. 1). The samples were provided by Unocal.

LITHOLOGIC AND MINERALOGIC RELATIONSHIPS

The rocks within the Salton Sea geothermal system can be divided into an upper sequence of lacustrine claystone and evaporite deposits and a lower sequence of deltaic sandstones, siltstones and shales (Randall, 1974). Figure 2 details the lithologies and mineral assemblages found in the upper parts of the wells studied by us. These lithologic columns are based on an examination of drill chip samples collected at 6 or 9 m (20 or 30 foot) intervals.

The primary and secondary minerals we observed (Fig. 2) are similar to those found in other parts of the field (e. g. Muffler and White, 1969; McDowell and Elders, 1979, 1980, 1983). With increasing depth, the secondary assemblages are characterized by: 1) anhydrite, calcite, interlayered illite/smectite, and interlayered chlorite/-smectite (interlayered illite/smectite zone: 0-222 m, Well A; 0-241 m, Well B); 2) chlorite, illite, interlayered chlorite-/smectite, calcite, anhydrite, potassium feldspar, quartz, sphene, and base-metal sulfides (chlorite-calcite zone: 222-616 m, Well A; 241-789 m, Well B); and 3) epidote, calcite, chlorite, quartz, potassium feldspar, albitic plagioclase, anhydrite, illite, and sphene (chlorite-epidote-calcite zone: 616-1646 m, well A; 789-1292 m, Well B). Traces of pyrite and hematite occur throughout these zones.

FLUID INCLUSION DATA

Fluid inclusions in anhydrite, sphalerite and vein quartz were studied. In the lacustrine deposits, anhydrite occurs as rosettes in the claystones and as aggregates associated with calcite in the evaporite beds. In the deltaic deposits, anhydrite and calcite cement the sandstones above 387 m in well A and 351 m in well B. At greater depths, anhydrite-rich zones are restricted to a few narrow intervals.

Sphalerite occurs in significant amounts (up to several percent) as a cement in the sandstones between 341 and 387 m in well A and from 277 to 360 m and 424 to 433 m in well B. In places, the sphalerite contains inclusions of anhydrite, suggesting that it has replaced preexisting anhydrite cement. Rocks between depths of 300 and 600 m also commonly contain secondary potassium feldspar after detrital plagioclase. The significance of these mineral assemblages is discussed below.

Quartz veins containing minor barite, chlorite, hematite, and traces of galena, sphalerite, calcite and anhydrite occur between depths of 305 and 378 m in well B (Fig. 2). Barite, in particular, is an uncommon mineral in the Salton Sea geothermal system. In these veins, it is found as embayed crystals surrounded by quartz.

The petrographic relationships suggest that the deposition of anhydrite began prior to both sphalerite cementation and quartz veining. Thus, fluid inclusions in anhydrite can potentially provide information on the temperatures and compositions of the brines since the early evolution of the thermal system. As discussed below, inclusions in sphalerite and vein quartz provide information associated with the episodic upwelling of brines from deeper parts of the system. Most of the fluid inclusion data from the Salton Sea geothermal system is of this latter type (Huang, 1977; Freckman, 1978; Andes and McKibben, 1987; Roedder and Howard, 1987).

All the fluid inclusions examined in this study were liquid-rich and contained a small vapor bubble that occupied about 20 percent of the inclusion volume at room temperature. Most had maximum dimensions in the range of 2 to 10 microns. No evidence of a separate gas phase was observed in these inclusions and, with the exception of anhydrite from 168-177 m in well B, none of the inclusions found contained any solid phases. In order to assure the validity of our data, fluid inclusions in anhydrite from three depth intervals were systematically overheated to determine their stretching characteristics. These experiments demonstrated that stretching caused by laboratory heating is not likely to have affected the results reported in this study.

In addition, the gas contents of inclusions in ten samples were analyzed by mass spectrometry using the techniques described by Sommer et al. (1985). Methane, ethane, propane and carbon dioxide were detected in primary inclusions in sphalerite and quartz. Inclusions in anhydrite contained mainly carbon dioxide and methane.

Anhydrite suitable for fluid inclusion measurements typically occurs as cleavage fragments up to 2 mm across. Typically several generations of secondary or pseudosecondary inclusions are present. Primary inclusions containing a small (<1 micron), unidentified birefringent daughter mineral were observed in samples from 168-177 m in well B. These inclusions form three dimensional arrays that define growth zones in the cleavage fragments.

The homogenization temperatures of fluid inclusions in anhydrite are plotted against depth in Figure 3A. The data show that irrespective of the origin of the inclusions in these samples, homogenization temperatures vary little within each depth interval, and that the two wells record similar thermal profiles. No pressure correction has been applied to these data because of the shallow depths.

Ice melting temperatures of fluid inclusions in anhydrite (Fig. 3B) range from -21.4^{o} to $-4.7^{o}C$. Liquid was observed in some of the larger inclusions at temperatures near $-50^{o}C$ (first melting), indicating that the inclusion fluids are enriched in $CaCl_2$. For reference, melting point depressions ranging from 4.7^{o} to $20.8^{o}C$ correspond to salinities of 7.4 to 23.2 equivalent weight percent NaCl (Potter et al., 1978).

Fluid inclusions in sphalerite suitable for freezing and heating measurements were found in a few crystals from two depth intervals in well B. These inclusions are primary, forming small isolated groups or three-dimensional arrays that parallel color banding. The inclusions yielded homogenization temperatures ranging from 179^{o} to $223^{o}C$ (Fig. 3A), and ice melting temperatures (Fig. 3B) ranging from -12.0 to $-10.0^{o}C$ (16.0 to 14.0 equivalent weight percent NaCl).

Data were obtained on primary (refer to Figs. 3A and B) and secondary inclusions of vein quartz. The primary inclusions occur in three dimensional arrays that define growth zones. Homogenization temperatures of these inclusions range from 194^{o} to $242^{o}C$ (Fig. 3A). Because of their small size (1 to 3 microns) only a few freezing point depressions were measured. The ice melting temperatures ranged from -13.9^{o} to $-9.2^{o}C$ (17.8 to 13.1 equivalent weight percent NaCl).

Secondary inclusions have homogenization temperatures ranging from 189^{o} to $210^{o}C$ and ice melting temperatures that vary from -16.5^{o} to $-0.7^{o}C$ (20.0 to 1.2 equivalent weight percent NaCl). The high-salinity inclusions have freezing point depressions similar to the brines trapped in anhydrite at these depths and thus may represent locally

derived fluids. The low-salinity fluids may represent condensate mixed with a small amount of the higher salinity brines.

DISCUSSION

The data described above suggest that the evolution of the rocks in the shallow portions of the of the two wells studied involved four distinct processes. These include: 1) the formation of secondary minerals through low- to moderate-temperature isochemical reactions; 2) the progressive downward cementation of the sandstones by anhydrite and calcite; 3) the influx of metal-bearing brines; and 4) the development of fracture permeability. The initial heating of the sediments is reflected in the formation of anhydrite after gypsum and the recrystallization of the sheet silicates as discussed by Muffler and White (1969). In contrast, the anhydrite + calcite cement in the deltaic sandstones could not have formed from the fluids or detrital components originally present in these rocks. However, the fluids in the overlying lacustrine rocks would have been enriched in both sulfate and bicarbonate. Because calcite and anhydrite display retrograde solubilities, heating of downward moving sulfate and carbonate ions would have resulted in the depositon of these minerals in the sandstones immediately underlying the lacustrine deposits. With time, continued diffusion of sulfate and carbonate would have led to a progressive thickening of the anhydrite + calcite cemented sandstones.

The fluid inclusions in anhydrite record temperature profiles characterized by high gradients through the upper 323 m in well A and 341 m in well B. Using the average homogenization temperature of 247°C for samples from a depth of 332-341 m in well B, and a mean annual air temperature of 22.5°C (Imperial Irrigation District, 1982), the calculated average gradient to this depth is 0.66°C/m. Younker et al. (1982) have shown that such high gradients are indicative of heat transfer by conduction through rocks of low permeability. This calculated gradient and the mineralogic relationships suggest that the thermal cap extends to the base of the anhydrite + calcite cemented sandstones. In contrast, homogenization temperatures of inclusions in well A between 460 and 622 m are nearly constant with depth, implying that heat is transferred through these rocks by convection (Younker et al., 1982).

The secondary potassium feldspar and sphalerite cement found in the lower part of the thermal cap could not have been formed by the fluids that deposited the anhydrite in the sandstones. The replacement of plagioclase by potassium feldspar involved the addition of K and removal of Na from the rocks. Because the K/Na ratio of geothermal waters increases with increasing temperature (Fournier and Truesdell, 1973), the formation of potassium feldspar in the shallow deltaic rocks must have resulted from the influx of brines derived from higher-temperature portions of the geothermal system. These fluids would also have been a likely source of zinc, lead, and copper.

As discussed above, our observations suggest that the sphalerite cement found in the deltaic sandstones has replaced pre-existing anhydrite cement. Reduction of the sulfate to sulfide could have occurred by several different mechanisms. However, reduction by pre-existing sulfides or anerobic bacteria is not likely in this case. Alternatively, the sulfate could have been reduced by hydrocarbons carried in solution by the upwelling brines according to the reaction (Anderson, 1983):

$$\text{anhydrite} + CH_4 + Zn^{+2} = \text{sphalerite} + Ca^{+2} + CO_2 + 2\,H_2O$$

We infer from the widespread occurrence of sphalerite cement that matrix permeabilities were relatively high during its deposition. In contrast, the formation of veins implies lower matrix permeabilities and fracture-dominated fluid flow (Elders, 1979). The occurrance of barite in these veins suggests that some mixing of the pore and vein fluids occurred. As noted by Barnes (1983) in his discussion of Mississippi Valley lead-zinc deposits, the deposition of barite would most likely occur where barium-bearing solutions encountered a sulfate-rich groundwater or where oxidation of sulfide to sulfate in solution can occur. As discussed above, sulphate-bearing pore fluids must have been present in the sandstones in the upper part of the deltaic section and could have mixed with the rising vein fluids. Later, these fluids would have been purged from the veins as upward flow continued, causing dissolution of early barite and deposition of sulfides, hematite and additional quartz from further cooling.

SUMMARY AND CONCLUSIONS

Fluid inclusion data and petrographic studies have been used to reconstruct the evolution of the rocks in the shallow portions of two wells drilled in the southern part of the Salton Sea geothermal system. The initial heating of these rocks resulted in the formation of anhydrite after gypsum and the formation of secondary phyllosilicates. Anhydrite and calcite were also deposited directly from the pore fluids as a cement in the underlying deltaic sandstones. Cementation of the sandstones progressed downward, reducing their permeabilities and leading to a thickening of the thermal cap with time. Fluid inclusion homogenization temperatures in anhydrite increase systematically with depth through the thermal cap. Variations in the salinities of these fluid inclusions demonstrate

that some mixing of downward-percolating brines and reservoir fluid took place. However, the velocities of the descending waters were apparantly not high enough to disturb the thermal gradient.

The influx of brines from higher temperature portions of the geothermal system occurred episodically during development of the thermal cap. Movement of these brines through the thermal cap resulted in the deposition of potassium feldspar and sphalerite cement and in the formation of quartz veins.

ACKNOWLEDGEMENTS

Funding for this project was provided by the Department of Energy under Contract Number DE-AC03-84SF12196. We would like to thank R. Dondanville and G. Suemnicht of Unocal for providing the samples. M. Sommer performed the gas analyses.

REFERENCES

Anderson, G. M. (1983) Some geochemical aspects of sulfide precipitation in carbonate rocks. In: International Conference on Mississippi Valley Type Lead-Zinc Deposits. Proc. Vol. (Edited by Kisvarsanyi, G., Grant, S. K., Pratt, W. P. and Koenig, J. W.), pp. 61 -76. University of Missouri-Rolla, Rolla, MO.

Andes, J. P., Jr., and McKibben, M. A. (1987) Thermal and chemical history of mineralized fractures in cores from the Salton Sea scientific drilling project (abstract). Eos Trans. AGU. 68, 439.

Barnes, H. L. (1983) Ore-depositing reactions in Mississippi Valley-type deposits. In: International Conference on Mississippi Valley Type Lead-Zinc Deposits. Proc. Vol. (Edited by Kisvarsanyi, G., Grant, S. K., Pratt, W. P. and Koenig, J. W.), pp. 77 - 85. University of Missouri-Rolla, Rolla, MO.

Elders, W. A. (1979) The geological background of the geothermal fields of the Salton Trough. In: Geology and Geothermics of the Salton Trough (Edited by Elders, W. A,), Campus Museum Contribution, University of California, Riverside, Ca. 5, pp. 1 - 19.

Fournier, R. O., and Truesdell, A. H. (1973) An empirical Na-K-Ca geothermometer for natural waters. Geochim. Cosmochim. Acta. 37, 1255 - 1275.

Freckman, J. T. (1978) Fluid inclusion and oxygen isotope geothermometry of rock samples from Sinclair No. 4 and Elmore No. 1 boreholes, Salton Sea geothermal field, Imperial Valley, California, U.S.A. M.S. Thesis, University of California, Riverside, CA. 66 pp.

Haas, J. L., Jr. (1971) The effect of salinity on the maximum thermal gradient of a hydrothermal system at hydrostatic pressure. Econ. Geol. 66, 940 - 946.

Huang, C. I. (1977) Fluid inclusion study of well cuttings from Magmamax No. 2 drillhole, Salton Sea geothermal area, California (abstract). Econ. Geol. 72, 730.

Helgeson, H. C. (1968) Geologic and thermodynamic characteristics of the Salton Sea geothermal system. Am. J. Sci. 266, 3, 129-166.

Imperial Irrigation District, Imperial Valley Annual Weather Summary (1982) Monthly high, low, and mean temperatures and rainfall, 1914-1982. Community and Special Services, Imperial Irrigation District, El Centro, CA. 19 pp.

McDowell, S. D., and Elders, W. A. (1979) Geothermal metamorphism of sandstone in the Salton Sea geothermal system. In: Geology and Geothermics of the Salton Trough (Edited by Elders, W. A.), Campus Museum Contribution, University of California, Riverside, CA. 5, pp. 70 - 76.

McDowell, S. D., and Elders, W. A. (1980) Authigenic layer silicate minerals in borehole Elmore 1, Salton Sea geothermal field, California, U.S.A. Cont. Mineral. Pet. 74, 293 - 310.

McDowell, S. D., and Elders, W. A. (1983) Allogenic layer silicate minerals in borehole Elmore No. 1, Salton Sea geothermal systems. Am. Mineral. 68, 1146 - 1159.

McKibben, M. A., and Elders, W. A. (1985) Fe-Zn-Cu-Pb mineralization in the Salton Sea geothermal system, Imperial Valley, California. Econ. Geol. 80, 539 - 559.

Muffler, L. J. P., and White, D. E. (1969) Active metamorphism of upper Cenozoic sediments in the Salton sea geothermal field and the Salton Trough, southeastern California. Geol. Soc. Am. Bull. 80, 157 - 182.

Potter, R. W., II, Clynne, M. A., and Brown, D. L. (1978) Freezing point depression of aqueous sodium chloride solutions. Econ. Geol. 73, 284 - 285.

Randall, W. (1974) An analysis of the subsurface structure and stratigraphy of the Salton Sea geothermal anomaly, Imperial Valley, California. Ph.D. thesis University of California, Riverside, CA. 92 pp.

Skinner, B. J., White, D. E., Rose, H. J., and Mays, R. E. (1967) Sulfides associated with the Salton Sea geothermal brine. Econ. Geol. 62, 316 - 330.

Sommer, M. A., II, Yanover, R. N., Bourcier, W. L., and Gibson, E. K. (1985) Determination of H_2O and CO_2 concentrations in fluid inclusions in minerals using laser decrepitation and capacitance manometer analysis. Anal. Chem. 57, 449 - 453.

Younker, L. W., Kasameyer, P. W., and Tewhey, J. D. (1982) Geological, geophysical, and thermal characteristics of the Salton Sea geothermal field, California. J. of Volcan. and Geothermal Res. 12, 221 - 258.

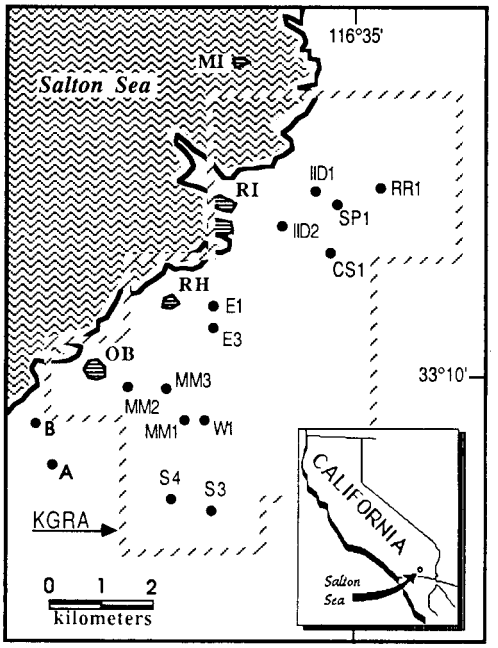


Fig. 1.

Well locations in the Salton Sea geothermal field. Wells: CS = California State; E = Elmore; MM = Magmamax; S = Sinclair; SP = Sportsman; W = Woolsey. A and B are the locations of the wells described in this study. Rhyolite domes: MI = Mullet Island; OB = Obsidian Butte; RH = Rock Hill; RI = Rock Island. The hachured line shows the boundary of the original Salton Sea Known Geothermal Resource Area (KGRA). Modified from McDowell and Elders (1980).

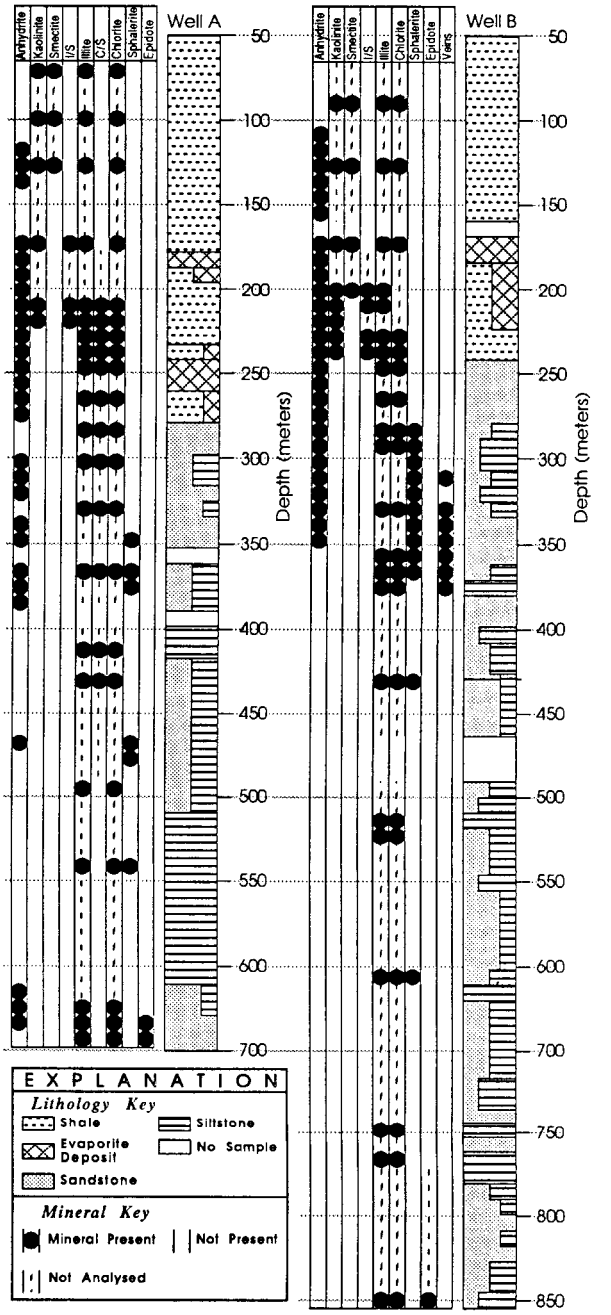


Fig. 2.

Lithologies and mineral distributions in the interlayered illite/smectite and chlorite - calcite zones of the two wells studied. I/S and C/S refer to interlayered illite/smectite and chlorite/smectite respectively.

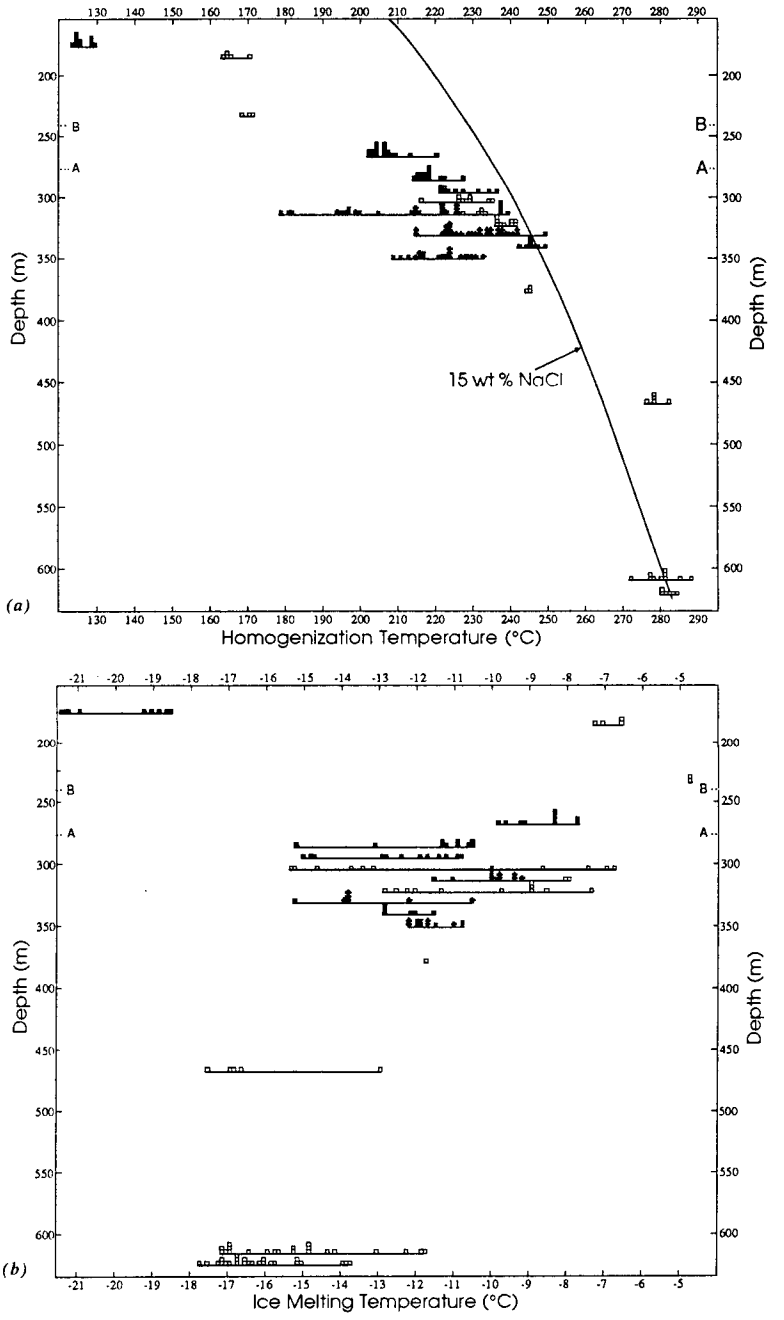


Fig. 3A.

Homogenization temperature vs. depth of fluid inclusions in anhydrite, sphalerite, and quartz. Symbols: anhydrite = open squares, Well A; filled squares, Well B; + = quartz, Well B; X = sphalerite, Well B. The baselines of the histograms are located at the lowermost limit of the sample interval. Tick marks labeled A and B indicate the depth to the base of the lacustrine deposits in the two wells. The boiling point curve for a 15 weight percent NaCl solution (Haas, 1971) is also shown for reference. B. Freezing point depression vs. depth for fluid inclusions in anhydrite. Refer to Fig. 3A for an explanation of the symbols.

A Comparison of Two Heat Transfer Models for Estimating Thermal Drawdown in Hot Dry Rock Reservoirs

Bruce A. Robinson
Paul Kruger*

Los Alamos National Laboratory, Los Alamos, NM
Stanford Geothermal Program, Stanford University, Stanford, CA*

Abstract

Estimates of thermal drawdown in Hot Dry Rock geothermal systems have been made with two different models of heat transfer from hydraulically fractured reservoir rock blocks to water circulated through the fracture permeability. One model is based on deconvolution of experimental tracer response curves into a network of flowpaths connected in parallel with heat transfer calculated individually in each flowpath. The second model is based on one-dimensional flow through the rock with a block size distribution described as a group of equivalent-radius spheres for which the heat transfer equations can be solved analytically. The two models were applied to the planned Phase II long-term thermal drawdown experiment at Fenton Hill, NM. The results show good agreement between the two models, with estimates of temperature cooldown from 240°C to 150°C in a few years depending on selected operation parameters, but with somewhat differing cooldown curve characteristic shapes. Data from the long-term experiment will be helpful in improving the two models.

Introduction

The long-term success of hydrothermal and hot dry rock geothermal resources depends on a high efficiency of thermal energy extraction with reinjected or circulated fluids. Adequate reservoir management of hydrothermal systems includes the need for predicting thermal effect of reinjected separator brine and turbine condensate on production with respect to reinjection well location and estimated production rates. Similarly, reservoir management of hydraulically fractured hot dry rock reservoirs includes the need to predict reservoir size, thermal capacity, and long-term sustainable rates of energy extraction.

Several models have been developed for estimating heat extraction from fractured geothermal reservoirs (e.g., Gringarten et al. (1975), Hunsbedt et al. (1978, 1983), Bodvarsson and Tsang (1982), Pruess (1983), Zyvoloski (1983), Dyadkin and Gendler (1985), and Robinson and Jones (1987)). These models differ in assumptions about fluid flow geometry in thermal contact with the reservoir rock blocks and the physics of the heat transfer processes. Two simple one-dimensional heat extraction models are described in this paper for application to the planned Phase II reservoir long-term thermal drawdown experiment at Fenton Hill, NM. One is the 1-D Heat Sweep Model developed at the Stanford Geothermal Program (SGP), the other is the tracer-based model developed at the Los Alamos National Laboratory (LANL). The upcoming Phase II long-term thermal drawdown experiment will test the usefulness of these models and provide additional field data on the behavior of HDR reservoirs.

Model Descriptions

SGP 1-D Linear Heat Sweep Model

The linear heat sweep model, suitable for evaluation of heat extraction from fractured geothermal reservoirs by artificially circulated fluids, was developed by Kuo et al. (1977), Hunsbedt et al. (1978), and Iregui et al. (1978). Kuo showed experimentally that an irregularly-shaped rock block with aspect ratio as large as 8:1 could, for heat transfer purposes, be described as a sphere with an equivalent radius based on its surface to volume ratio. Analytical methods for solving the time dependent heat transfer equations for spherical solids are given in Carslaw and Jaeger (1973). Iregui showed that a distribution of rock block sizes and shapes could, also for heat transfer purposes, be described as a single size spherical rock block with mean equivalent radius. Hunsbedt showed that the difference in temperature between the equivalent radius rock block at a lumped mean temperature T_r and the surrounding fracture volume fluid at a temperature T_f could be expressed as

$$T_r - T_f = \mu\tau(1-e^{-t/\tau}) \qquad (1)$$

where μ = cooldown rate (°C/s)
τ = time constant for the rock (s).

Hunsbedt, Kruger, and London (1978) showed that the time constant for spherical rock

blocks can be expressed as

$$\tau = \frac{R^2}{3\alpha}(0.2 + 1/N_{Bi}) \qquad (2)$$

where R = equivalent rock radius (m)
α = thermal diffusivity (m^2/s)
N_{Bi} = Biot number of the rock.

The thermal diffusivity is given by

$$\alpha = k/\rho C \qquad (3)$$

where k = thermal conductivity W/m°C
ρ = density (kg/m^3)
C = specific heat capacity (J/kg°C).

The Biot number is given by

$$N_{Bi} = hR/k \qquad (4)$$

where h = heat transfer coefficient (W/m^2°C)

The differential equation which describes heat transfer from the equivalent spherical rock block to the circulating fluid under linear heat sweep was given in Hunsbedt et al. (1983). The solution for the given linear sweep boundary and initial conditions is initiated by conversion to a Laplace transform equation and the inversion is accomplished numerically with the algorithm reported by Stehfest (1970). Application of the model to a low temperature hydraulically fractured petrogeothermal system in the USSR was described by Dyadkin and Kruger (1987).

LANL Tracer-Based Heat Transfer Model

For an HDR reservoir with flow connections established between injection and production wells, tracer experiments, in which a pulse of tracer is injected at the inlet and the concentration-time curve is measured in the production fluid, are useful for characterizing the nature of fluid flow in the reservoir. The tracer response curve provides information on the existence of short circuit flow paths via the measurement of the first arriving tracer, as well as the amount of flow through long-residence-time paths.

The tracer-based heat transfer model uses the tracer response curve to approximate the extent of flow channeling, thus accounting for the effect of nonuniform flow on the heat extraction performance. The model, first proposed in Robinson and Jones (1987), assumes multiple flow paths of different size and flow rate adjusted to match the observed tracer response. The thermal response of each path is calculated individually, then the composite outlet behavior is calculated as the weighted mean of the individual responses. The model, using only inlet-outlet tracer data, assumes that there is no thermal or hydraulic interaction between the flow paths.

The thermal model used to estimate the Phase II experiment cooldown has been modified from the model developed in Robinson and Jones (1987), which assumed highly fractured rock, so that the fluid in the reservoir was everywhere in thermal equilibium with the rock. In that model, heat extraction results in a sharp temperature front which travels from inlet well to outlet well. An ad-hoc parameter was included to simulate dispersion of the front based on an analogy to the convective-dispersion equation, but this parameter had little physical significance. In the revised model (Jones, 1987), each path is assumed to consist of a set of equally-spaced fractures, each accepting equal flow, as shown in Figure 1a. The energy balance equation in the rock in dimensionless form is

$$\frac{\partial T}{\partial \theta} = \frac{\partial^2 T}{\partial \eta^2} \qquad (5)$$

while in the fluid, the energy balance equates convection in the fluid to conduction in the rock at the interface:

$$\left.\frac{\partial T}{\partial \eta}\right|_{\text{interface}} = Bi_m \frac{\partial T}{\partial \xi} \qquad (6)$$

where the following dimensionless variables are defined:

$$\eta = \frac{2x}{S}, \quad \xi = \frac{y}{L}, \quad \theta = \frac{4\alpha t}{S^2},$$

$$Bi_m = \frac{(\dot{m}C)_f}{2k\, A_{ht}/S} = \frac{S^2(\dot{m}C)_f}{4k\, V_r} \qquad (7)$$

where S = the rock spacing (m)
L = the flow path length (m)
α = the rock thermal diffusivity (m^2/s)
t = time (s)
$\dot{m}$ = the fluid mass flow rate (kg/s)
C = the fluid heat capacity (J/kg°C)
k = the rock thermal conductivity (W/m°C)
V_r = the total rock volume of the flow path (m^3)
A_{ht} = heat transfer area (m^2)

The quantity Bi_m, a modified Biot number, governs the nature of heat extraction from the rock mass. For low Biot numbers, associated with closely-spaced fractures, low flow rates, and large rock volumes, heat extraction produces a sharp thermal front as described by Robinson and Jones (1987). At Biot numbers of order 1 or higher, the behavior deviates from a sharp thermal front, and significant temperature gradients remain in the rock in the x direction.

Equations (5) and (6) were solved by finite difference techniques. Equation (5) was approximated with centered differences for the spatial derivative and a Crank-Nicholson scheme for the time derivative. At the interface, the equation for the rock temperature is written as a finite difference form of Eqn. (6). At each time step the code starts at the entrance of the flow path and marches forward in the y direction, sequentially calculating the fluid and rock temperatures.

In the tracer response model, Robinson and Tester (1984, 1986) showed, for a nonadsorbing tracer, that a parallel plug flow path model could be used to match the measured tracer response curve or residence time distribution (RTD). The RTD f(t) is defined as follows: f(t)dt = the fraction of fluid leaving the system with residence times between t and t+dt. The RTD is calculated from experimental data using the following equation:

$$f(t) = \frac{QC(t)}{m_p} \qquad (8)$$

where Q is the volumetric flow rate, and m_p is the mass of tracer injected. For a large number of flow paths, the flow path of residence time t has a fluid flow rate of Qf(t)dt and a fluid volume of Qtf(t)dt. For modeling purposes, a finite number of paths is needed. To set the fluid volumes and flow rates of these paths, the tracer response curve is divided into time intervals 0 to t_1, t_1 to t_2, t_2 to t_3, etc., and the flow rate and fluid volume of each path are given by the following expressions:

$$Q_i = Q \int_{t_{i-1}}^{t_i} f(t)dt \qquad (9)$$

$$V_i = Q \int_{t_{i-1}}^{t_i} tf(t)dt \qquad (10)$$

Two adjustable parameters are required, the fracture half-spacing R and the rock volume V_r. Since the tracer response provides values for the fluid volumes of each path, the rock volumes are calculated as V_r/ϕ, where ϕ is the fracture porosity. Robinson and Jones (1987) outline methods for estimating fracture porosity, but the range of values obtained spans over an order of magnitude, implying that fracture porosity is essentially an adjustable parameter. The fracture spacing is also considered adjustable, since data are usually difficult to obtain in fractured geothermal reservoirs.

The Fenton Hill Phase II Reservoir

The Fenton Hill HDR program is designed to demonstrate the feasibility of creating and operating a prototype hot dry rock geothermal reservoir. In Phase I of the program, conducted in the 1970s, the feasibility of the concept was demonstrated in a series of hydraulic fracturing and flow tests (Dash et al., 1981). In the longest flow experiment, lasting 286 days, energy was extracted at an average rate of 3 MW thermal at a temperature of about 140°C.

Phase II of the program is designed to demonstrate the technology for long-term energy extraction on a larger scale at higher temperatures. In May and June of 1986, a 30-day flow test of the deeper Phase II reservoir was performed to test the hydraulic and thermal performance and to provide design input for a longer flow test. One purpose of this longer test is to operate the reservoir long enough to achieve a decrease in the temperature of the production fluid, which is needed to estimate reservoir size. This paper summarizes the predictions of thermal drawdown by the two models. A third model, which uses finite element techniques to solve the heat and mass transport equations in three dimensions, is developed in Birdsell and Robinson (1988).

Model Results

SGP 1-D Heat Sweep Model Simulation

Figure 1 shows the equivalent flow geometry for the Phase II cooldown simulation. The input data for the simulations, listed in Table 1, were matched as close as possible for the models. Runs were made for an injection temperature of 50°C, with estimated reservoir thickness of 150 and 250 m. A sensitivity analysis was made for rock block sizes with mean fracture spacings from 20 to 60 m and for varying flow rates from half to twice the anticipated flow rate.

The results of the SGP simulations for the injection temperature of 50°C are given in Figure 2. Part (a) shows the cooldown curves as a function of mean fracture spacing for a reservoir thickness of 150 (m) and part (b) for a reservoir thickness of 250 m. Part (c) shows the overlapping cooldown curves for the three values of porosity chosen for the study, and part (d) shows the cooldown curves for various values of flow rate.

The family of cooldown curves indicates that rock blocks of about 40 m mean fracture spacing (MFS) is the optimum mean size for a steady rate of temperature decline. For large block sizes, the rate of heat conduction from the interior of the block to its surface is too small for the given residence time, whereas for smaller sizes, the residence times are sufficient for effective heat extraction. The total heat extracted is given by the area under the

TABLE 1

Input Parameters

Fixed Parameters	SGP	LANL
T (initial) (°C)	240	240
T (injection) (°C)	50	50
α (m^2/s)	1.048×10^{-6}	1.048×10^{-6}
C (J/kg°C)	4756	4756
k (W/m°C)	2.7	2.7
Variable Parameters		
ϕ_1	0.0084	0.0084
ϕ_2	0.003	0.003
ϕ_3	0.00048	0.00048
ϕ_4	0.000197	0.000197
MFS (m)	20-60	1-20

Flowrates	Path	Tracer Curve Deconvolution No	$\dot{m}$(kg/s)	V_f (m^3)	
1/2 x Q (base)	10.6	1	1.395	23.0	
2/3 x Q (base)	15.9	2	1.446	37.0	
Q (base)	21.2	3	1.397	51.3	
3/2 x Q (base)	31.8	4	1.357	73.9	
2 x Q (base)	42.4	5	1.410	121.7	
		6	14.196	10040.7	
		total	21.2	10347	

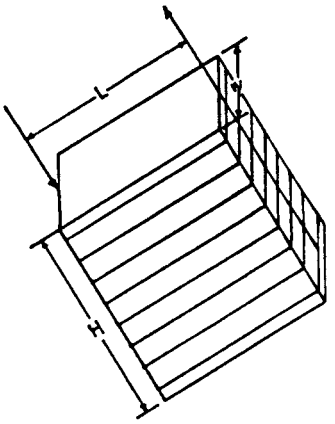
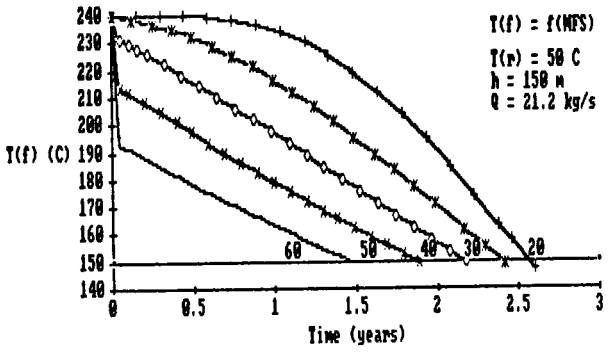
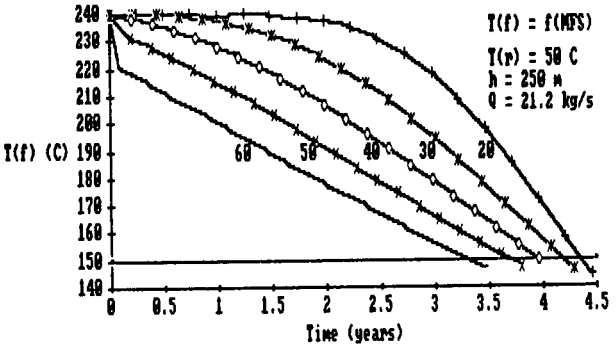


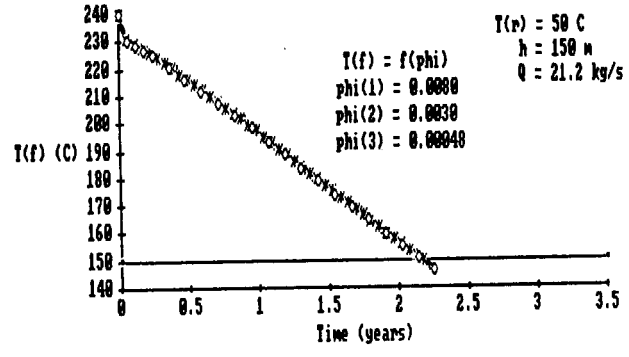
Figure 1. Equivalent Flow Geometry for the 1-D SGP Model.



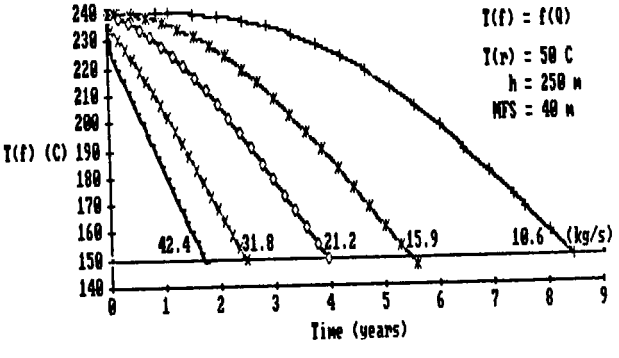
(a)



(b)



(c)



(d)

Figure 2. Results of the 1-D Heat Sweep Simulations of Cooldown to an Abandonment Temperature of 150°C for: (a)different values of mean fracture spacing for a fractured reservoir of 150 m thickness; (b) for 250 m thickness; (c) as a function of fracture porosity; and (d) as a function of flowrate.

cooldown curve relative to the total heat content above the injection temperature. At a mean fracture spacing of 20 m, the fracture of heat content extracted exceeds 90% after about 80 residence times (2.6 years). The ratio of cooldown times of 3 to 5 years to the abandonment temperature of 150°C varies linearly with the ratio of reservoir thickness of 150 to 250 m.

The apparent independence of cooldown time from fracture porosity is indicative of the small mean residence time compared to the rock time constant, so that the number of heat transfer units is small for all values of small porosity. The heat extraction is essentially limited for a constant production rate by the rate of heat conduction from the rock blocks. The dependence of heat extraction on flow rate appears to follow a relationship given by $t_a = f(1/Q^n)$, for which $n = 1.15$ compared to the value $n = 1.3$ for the low-temperature parallel fractured petrogeothermal reservoir described by Dyadkin and Kruger (1987).

Tracer-Based Heat Transfer Model

The tracer response used to perform the heat transfer calculations, shown in Figure 3, was measured near the end of the Phase II 30-day flow test. The curve, normalized by Eqn. (8), shows both an early response due to channeling flow between the two wells and the long tail caused by dispersed flow through a large volume of rock. A large fraction of the tracer (67%) had not been recovered at the end of the tracer test, and extrapolation techniques developed in Robinson and Tester (1986) were used to estimate the tracer response for long times. The tracer response curve was divided into six paths, the first five with approximately the same flow rate, and the sixth representing the extrapolated tail of the tracer response curve.

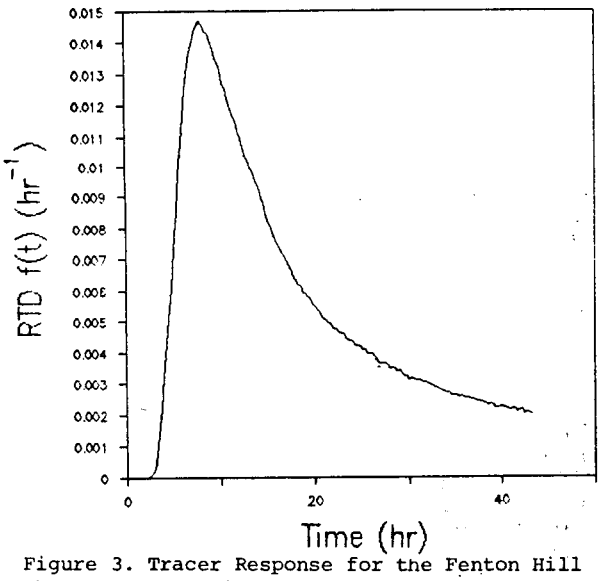


Figure 3. Tracer Response for the Fenton Hill Phase II Reservoir.

The input data for the tracer-based heat transfer model are also listed in Table 1. The range of values for ϕ (determining the rock volume heat content) were selected from various estimates by others. The values of 0.0084, 0.003, and 0.00048 were obtained from Robinson and Jones (1987) based on various assumptions. The value of 0.000197 was obtained from Birdsell and Robinson (1988) based on their finite element model. Figure 4 shows the model results for different values of fracture spacing. All of the curves exhibit an early drop in production temperature within the first 200 days due to cooldown of the short-residence-time, channeling flow paths. Fracture spacing controls the time at which the thermal drawdown occurs and the shape of the cooldown curve. Smaller fracture spacings lead to more efficient heat extraction from the rock mass. However, since in each case the same quantity of heat is potentially available, the long term behavior is similar.

Figure 5 shows the cooldown curves for different values of porosity. As seen in Figure 5 and Table 2, the largest values of ϕ, 0.0084, results in a small rock volume and rapid thermal drawdown. The low value, 0.000197, leads to the prediction of a large, long-lasting energy source. This 40-fold difference in predicted reservoir rock volume points out the need to develop better field experimental techniques for estimating fracture porosity, or more fundamentally, the reservoir rock volume exposed to fluid flow. Simple reservoir geometrical considerations can be used to place these porosity estimates in perspective. Table 2 lists the calculated reservoir rock volumes and dimensions assuming a cubic rock block in each case. The smaller sized reservoirs correspond to flow confined to a region of rock defined by the separation distance between the wellbores, roughly 100-150 m. The larger reservoirs require a flow model of potential-like flow which sweeps through a much larger rock volume. The upcoming long term flow test will determine which estimates of porosity and rock volume are closest to reality.

Comparison of Model Results

The two models used in this study represent different approaches for estimating thermal cooldown of fractured geothermal reservoirs. The 1-D SGP model assumes uniform flow, in a single path, through a volume of rock of given dimensions with assumed rock block size distribution. The LANL tracer-based model uses an observed tracer response curve to obtain the degree of flow nonuniformity and

TABLE 2

Predicted Phase II Cooldown Times to T_a=150°C

SGP 1-D Heat Sweep Model

Mean Fracture Spacing (MFS) (m)	Time (yr) to T_a=150°C for Reservoir Thickness (m) 150	250
20	2.57	4.35
30	2.4	4.17
40	2.15	3.94
50	1.86	3.71
60	1.47	3.30

Flowrate (kg/s)	Time (yr) to T_a = 150°C for MFS = 40 (m), H = 250 m
10.6	8.44
15.9	5.45
21.2	3.94
31.8	2.46
42.4	1.71

LANL Tracer-Based Model

Fracture Spacing (m)	Time (yr) to T_a = 150°C for ϕ = 0.003
1	3.41
5	3.20
10	2.73
20	1.73

Porosity	Time (Yr) to T_a=150°C for 5 m spacing	Total Rock Volume (m^3)	Calculated Cubic Volume Dimension (m)
0.0084	1.04	1.23×10^6	107
0.003	3.20	3.45×10^6	151
0.00048	21.8	2.16×10^7	278
0.000197	>27	5.25×10^7	374

the total fluid volume. The rock volume is determined by the choice of fracture porosity. Thus, the apparent dependence on ϕ for the LANL model is due to the way the rock volume is defined, and not due to any major differences in the fundamental physics of the model. In the SGP model the rock volume was chosen to be consistent in size with the LANL estimates for the base case of ϕ = 0.003.

The shapes of the output cooldown curves at short times are somewhat different for the two models due to different assumptions about the flow field. The LANL model assumes nonuniform flow as determined by the tracer response. Thus, an initial rapid cooldown is predicted for the short-residence-time, channeling flow paths. These paths are mixed with larger flow paths which cool more slowly, and the overall thermal cooldown is more gradual than that of the channeling paths. The SGP model on the other hand assumes a uniform rate of heat transfer based solely are the mean rock temperature and surrounding fluid temperature.

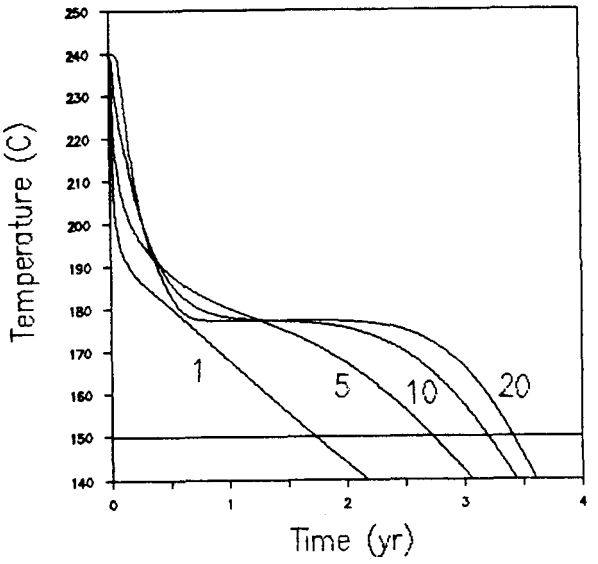


Figure 4. Predicted Cooldown Curves Using the LANL Tracer-Based Model for Different Values of the Fracture Spacing S.

For the base case input data with similar rock volumes, the two models predict similar times for cooldown to the abandonment temperature of 150°C. For this case, the SGP simulations for reservoir thickness of 150 m based on the LANL values of ϕ = 0.003 results in the same values for the rock volume. The time to reach 150°C ranges from 1.5 to 2.6 years for the SGP model and 1.7 to 3.4 years for the LANL model. The agreement is close; the differences can be attributed to differences in fracture spacing and model assumptions about the nature of the flow field. The greatest uncertainty in using either model is in the choice of the adjustable parameters which control the reservoir rock volume available for heat transfer to the circulating fluid.

Conclusions

Two heat transfer models have been used to predict thermal cooldown in the Fenton Hill HDR reservoir. The SGP model assumes uniform flow through the fracture network, while the LANL tracer-based model adopts a nonuniform flow field for heat extraction based on observed tracer test data. The differences in predicted thermal cooldown occur at early

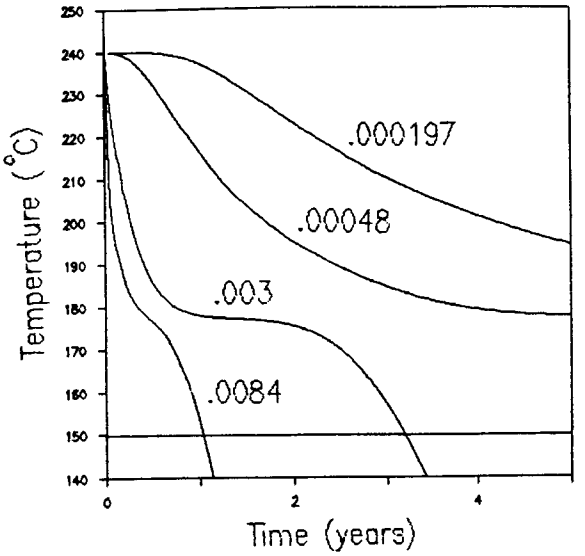


Figure 5. Predicted Cooldown Curves Using the LANL Tracer-Based Model for Different Values of the Fracture Porosity ϕ.

times, with the LANL model predicting a sharp cooldown initially, but a slower decline at later times, whereas the SGP model predicts a smooth temperature-time curve. Nonetheless, when parameters are chosen which result in similar values of the rock volume, the two models predict similar times to reach the abandonment temperature, assumed to be 150°C. Conservative estimates for this time are 1.5 - 3.2 years at the expected flow rate of the upcoming long term flow test. The comparison of the two models emphasizes the uncertainly over the appropriate value for the rock volume. New field techniques are needed to estimate this parameter. Future tests will allow the model predictions made in this study to be evaluated as well as providing additional information on the nature of fluid flow and energy transport in HDR geothermal reservoirs.

Acknowledgements

This work was performed under the auspices of the U.S. Department of Energy, Geothermal Technology Division. The authors thank Hugh Murphy for his editorial and technical comments in reviewing this work and Cheryl Straub for typing the manuscript.

Nomenclature

A_{ht}	heat transfer area (m^2)
Bi_m	modified Biot number (Eqn. 7)
C	fluid heat capacity (J/kg°C)
C(t)	tracer concentration-time response curve (kg/m^3)
f(t)	tracer residence time distribution (s^{-1})
h	heat transfer coefficient ($W/m^2°C$)
H	reservoir thickness (m)
k	rock thermal conductivity (W/m°C)
$\dot{m}$	fluid mass flow rate (kg/s)
m_p	tracer pulse mass (kg)
N_{Bi}	Biot number (Eqn. 4)
Q	fluid volumetric flow rate (m^3/s)
Q_i	fluid volumetric flow rate for path i (m^3/s)
R	equivalent rock radius (m)
S	fracture spacing (m)
t	time (s)
T	temperature (°C)
t_a	reservoir abandonment time (y)
T_a	reservoir abondonment temperature (°C)
T_f	fluid volume (m^3)
T_r	rock temperature (°C)
V_f	fluid volume (m^3)
V_i	fluid volume of path i (m^3)
x	direction perpendicular to flow (m)
y	direction of flow (m)
α	rock thermal diffusivity (m^2/s)
η	dimensionless variable (Eqn. 7)
ρ	rock density (kg/m^3)
ϕ	fracture porosity
μ	cooldown rate (°C/s)
θ	dimensionless variable (Eqn. 7)
τ	time constant for the rock (s)
ξ	dimensionless variable (Eqn. 7)

References

Birdsell, S. A. and B. A. Robinson, A Three-Dimensional Model of Fluid, Heat, and Tracer Transport in the Fenton Hill Hot Dry Rock Reservoir, to be presented at the 13th SGP Workshop on Geothermal Reservoir Engineering, January, 1988.

Bodvarsson, G. S. and C. F. Tsang, Injection and Thermal Breakthrough in Fractured Geothermal Reservoirs, J. Geophys. Res. 87, 1031-1048, 1982.

Carslaw, H. S. and J. C. Jaeger, Conduction of Heat in Solids, Oxford University Press, 1973.

Dash, Z. V. et al., Hot Dry Rock Geothermal Reservoir Testing: 1978-1980, J. Volcanology and Geothermal Res, 15, 59-99, 1981.

Dyadkin, Y. D. and S. G. Gendler, Processes of Heat-Mass Transfer in Geothermal Energy Extraction (Leningrad Mining Institute Press, Leningrad, 1985) in Russian.

Dyadkin, Y. D. and P. Kruger, Estimates of Thermal Cooldown in Fractured Petrogeothermal Resources, presented at 12th SGP Workshop on Geothermal Reservoir Engineering, January 1987.

Gringarten, A. C., P. A. Witherspoon, and Y. Ohnishi, Theory of Heat Extraction from Hot Dry Rock, J. Geophys. Res., 80, 1120-1124, 1975.

Hunsbedt, A., P. Kruger, and A. L. London, Energy Extraction from a Laboratory Model Fractured Geothermal Reservoir, J. Petrol. Tech., 712-718, 1987.

Iregui, R., A. Hunsbeldt, P. Kruger, and A. L. London, Analysis of Heat Transfer and Energy Recovery in Fractured Geothermal Reservoir, Stanford Report SPG-TR-31, Stanford Geothermal Program, Stanford University, 1978.

Jones, G. F., Recent Heat Transfer Modeling, Los Alamos National Laboratory Internal Memorandum, Number ESS-4-87-202.

Kuo, M. C. T., P. Kruger, W. E. Brigham, Shape-Factor Correlations for Transient Heat Conduction from Irregular-Shaped Rock Fragments to Surrounding Fluid, ASME paper 77-HT-57, American Society of Mechanical Engineers, New York, 1977.

Pruess, K., Development of the General Purpose Simulator MULKOM, Technical Report LBL-15500, Lawrence Berkeley Lab., Earth Sciences Div., 1983.

Robinson, B. A. and G. F. Jones, A Tracer-Based Model for Heat Transfer in a Hot Dry Rock Reservoir, Proc. Geothermal Resources Council 1987 Annual Meeting, Sparks, NV, 1987.

Robinson, B. A., and J. W. Tester, Dispersed Fluid Flow in Fractured Reservoirs: An Analysis of Tracer-Determined Residence Time Distributions, J. Geophys. Res., 89, B12, 10374-10384, 1984.

Stehfest, H., Numerical Inversion of Laplace Transforms. Algorithm No. 368, Comm. ACM 13, No. 1, 47-49, January, 1970.

Zyvoloski, G., Finite Element Methods for Geothermal Reservoir Simulation, Int. J. for Num. and Anal. Meth. in Geomechanics, 75-86, 1983.

PROCEEDINGS, Thirteenth Workshop on Geothermal Reservoir Engineering
Stanford University, Stanford, California, January 19-21, 1988
SGP-TR-113

A HYDROLOGIC MONITORING PROGRAM TO DETECT POTENTIAL IMPACTS OF GEOTHERMAL DEVELOPMENT IN LONG VALLEY CALDERA, CALIFORNIA

Michael L. Sorey

U.S. Geological Survey
Menlo Park, California

ABSTRACT

Long Valley caldera is a tectonically active area in east-central California that contains a high-temperature geothermal system currently being explored and developed for electric power production. Concerns expressed by public agencies and private citizens over the potential impacts of geothermal development on thermal springs at the Hot Creek Fish Hatchery and Hot Creek gorge have resulted in the establishment of a Hydrologic Advisory Committee. The committee includes representatives from development projects and regulatory agencies. Its role is to formulate and oversee a hydrologic monitoring program capable of detecting such impacts before they become significant. The advisory committee and the monitoring program provide effective mechanisms with which to proceed with geothermal development in areas such as Long Valley, where the level of environmental risk cannot be determined a-priori because the relavent geo-hydrologic parameters are not adequately delineated.

INTRODUCTION

The ground water and geothermal resources of the Long Valley caldera, in east-central California, are currently being explored and developed by commercial and municipal interests. At present there are four production wells supplying hot water to a 10 MWe binary-electric power plant at Casa Diablo and one well producing cold ground water for municipal consumption in Mammoth Lakes (fig. 1). Permits are being sought for four additional 10 MWe geothermal plants on both private and public land. Additional cold-water wells will also needed in the near future to supply water to Mammoth Lakes and to a proposed expansion project at the Mammoth/June Lakes Airport.

Recent studies of the ground water system in Long Valley caldera have indicated that both the hot and cold-water aquifers involved in these developments are in hydrologic connection with thermal springs at the Hot Creek Fish Hatchery and Hot Creek gorge (Sorey, 1976, 1985: ESA, 1987: Westec, 1987). However, fluid flow paths and hydrologic parameters are not well enough understood at this point to adequately assess the potential risks to the thermal springs or to specify mitigation measures to prevent such impacts. This uncertainty has given rise to considerable public debate, which has resulted in permitting delays and has raised the possibility of costly litigation to resolve the issue.

In an effort to overcome these difficulties, a Hydrologic Advisory Committee (HAC) has been formed to formulate and oversee a hydrologic monitoring program capable of detecting impacts to the ground water system before the springs are significantly affected. Representatives of each development project and and the appropriate regulatory agencies participate in the HAC, and technical guidance is provided by the U.S. Geological Survey. The Geological Survey has conducted similar hydrologic monitoring in the Long Valley area since 1982 (Farrar et al., 1987).

MONITORING PROGRAM

The monitoring network includes surface water sites, springs, wells, and precipitation gages (fig. 2). Data collection includes measurements of stream flows and spring discharge, well production rates and temperatures, ground water levels, and chemical and isotopic characterization of water from wells, springs, and streams. Data collected under this program will be collated into three quarterly reports and an annual summary report each year. The reports will be reviewed by the HAC and significant hydrologic trends at variance with natural background conditions will be discussed by committee members. The committee will provide these data to interested parties and will advise appropriate regulatory agencies of their findings. The monitoring program is dynamic and will change as needed if and when future ground water development or geothermal projects come into fruition.

A key feature of the monitoring program is the completion of observation wells at depths and locations such that any changes induced in production or injection aquifers can be detected before they migrate to the thermal springs. Although the technical and financial obligations for completing these wells rests with the developers, their adequacy for the

intended purpose must be reviewed by the HAC and certified by the appropriate regulatory agency. Initially, one obervation well located near each development would be required. If induced pressure or temperature changes are detected in an observation well, additional wells may be needed at locations closer to the thermal springs. It is also anticipated that use permit conditions will include requirements that aquifer tests be carried out prior to production at each development project to better delineate aquifer characteristics and the potential for hydrologic impacts on the thermal springs.

CURRENT STATUS

As of January 1988, the HAC has been functioning for about six months. Details of the initial monitoring program have been worked out and one observation well has been completed at Casa Diablo. Arrangements for funding the program are not yet finalized; some combination of funding from each developer who obtains a use permit and from a grant to Mono County by the State Energy Commission is anticipated. Data collection and reporting activities will most likely be carried out by the U.S. Geological Survey.

A use permit application by Mammoth Pacific for a 10 MWe power plant (MP-II on private land at Casa Diablo) was approved by the Mono County Planning Commission in October 1987. This decision was appealed by the Sierra Club, and a hearing on the appeal before the Board of Supervisors is scheduled for late February 1988. A decision by the U.S. Bureau of Land Management on a 10 MWe power plant (PLES-I on federal land at Casa Diablo) proposed by Pacific Lighting Energy Systems is expected in the near future. A use permit application by Bonneville Pacific Corporation for a 10 MWe power plant on private land northwest of the Hot Creek Fish Hatchery (BP in fig. 1) was rejected by the Planning Commission in September 1987. That decision was appealed by Bonneville Pacific and a final decision by the Board of Supervisors is set for February 2, 1988. If each proposed geothermal project is approved, a total generating capacity of 40 MWe could be on line by 1989.

A permit for ground water production to supply the airport expansion project, which is to include a hotel and golf course, has not yet been applied for. The anticipated water requirement for this project is 662 acre-feet per year, or 410 gpm. A potential impact of development is a decrease in the nonthermal component of flow in the hatchery springs, whose total discharge is currently about 60 gpm. The hatchery springs could also be affected by future ground-water production from wells recently completed and tested by the Mammoth County Water District south of Mammoth Lakes (fig. 1). Consequently, the hydrologic monitoring program will eventually include observation wells associated with each of these developments.

REFERENCES

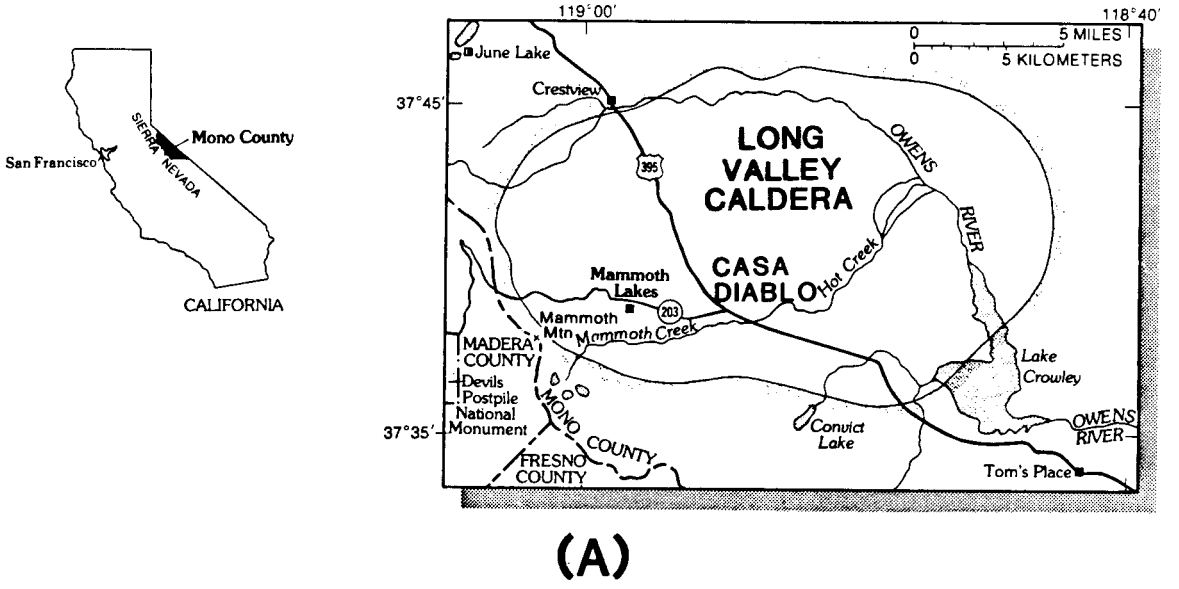
ESA, 1987, Mammoth Pacific Geothermal Development Project: Units II and III Environmental Impact Report and Environmental Assessment: Report prepared for the County of Mono Energy Management Department and Bureau of Land Management, July 1987 (three parts)

Farrar, D., Sorey, M.L., Rojstaczer, S.A., Janik, C.J., Winnett, T.L., and Clark, M.D., 1987, Hydrologic and geochemical monitoring in Long Valley caldera, Mono County, California, 1985: U.S. Geological Survey Water-Resources Investigations Report 87-4090, 71 p.

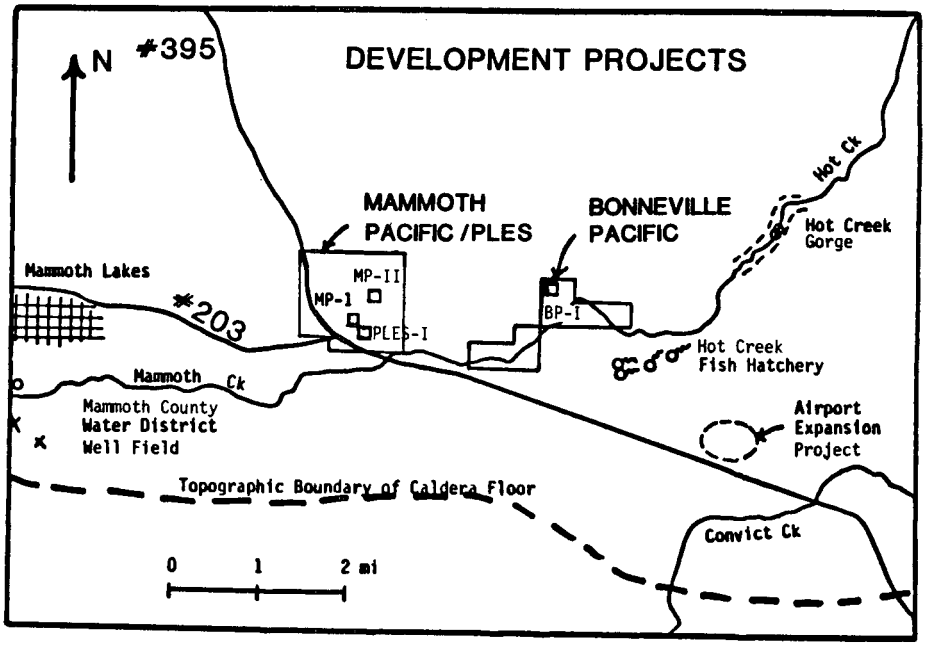
Sorey, M.L., 1976, Potential effects of geothermal development on springs at the Hot Creek Fish Hatchery in Long Valley, Mono County, California: U.S. Geological Survey Open-File Report 75-637, 8 p.

Sorey, M.L., 1985, Evolution and present state of the hydrothermal system in Long Valley calera: Journal of Geophysical Research, v. 90, p. 11219-11228.

WESTEC Services, Inc., 1987, Bonneville Pacific Corporations's Mammoth/Chance Geothermal Development Project Final Environmental Impact Report: Report prepared for County of Mono Energy Management Department, September 1987.



(A)



(B)

Figure 1(A). Maps of Long Valley caldera and Mono County, California.

1(B). Map of southern part of Long Valley caldera showing locations of proposed and existing (MP-I) development projects that would utilize ground water and geothermal resources, and thermal springs at the Hot Creek Fish Hatchery and Hot Creek gorge.

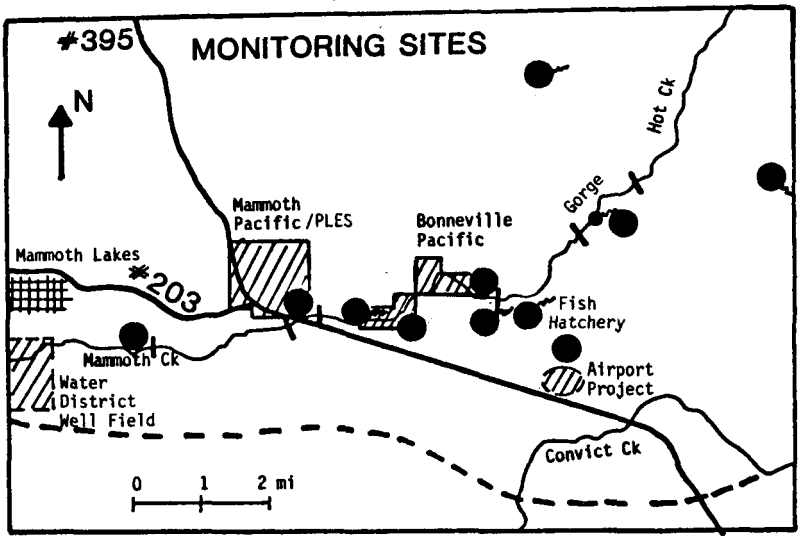


Figure 2. Map of the southern part of Long Valley caldera showing locations of data collection sites in hydrologic monitoring program. Dots represent observation wells, dots with tails are springs, and bars are stream gaging and sampling sections.

PROCEEDINGS, Thirteenth Workshop on Geothermal Reservoir Engineering
Stanford University, Stanford, California, January 19-21, 1988
SGP-TR-113

VAPLIQ HYDROTHERMAL SYSTEMS, AND THE VERTICAL PERMEABILITY OF LOS AZUFRES, MEXICO, GEOTHERMAL RESERVOIR

Eduardo R. Iglesias and Victor M. Arellano
Instituto de Investigaciones Electricas
Apartado Postal 475, C.P.62000, Cuernavaca, Mor., Mexico

ABSTRACT

We identify a new category of natural hydrothermal systems intermediate between liquid- and vapor-dominated. This category is characterized by a "vapliq" vertical pressure profile, which is nearly vaporstatic in the shallower portion of the system, and nearly boiling-point-for-depth at depth. The prototype of these systems is the geothermal field of Los Azufres, Mexico. To explore the thermohydrological conditions conducent to this type of system, we propose a 1-D vertical scenario based on generally accepted conceptual models of liquid- and vapor-dominated geothermal reservoirs. We use the corresponding mass and thermal energy transport equations to establish that a necessary condition for the existence of 2-phase hydrothermal systems is that the absolute value of the vertical thermal flux must exceed Q_{min}, a parameter that depends only on the values of the pressure and of the thermal conductivity at the boiling point of the system. The values of Q_{min} are typically 1-4 times the average terrestrial flux. We also find that geothermal systems in which convective heat transport is accomplished by the well-known heat-pipe mechanism can exist only if the corresponding heat flux exceeds Q_{min} and the permeability at the boiling point of the system is smaller than k_{Bmax}, a parameter that depends only on the values of the pressure and of the thermal conductivity at the boiling point. Typical values of k_{Bmax} are $1\text{-}3\times10^{-18}$ m^2, suggesting a reason for the fact that all vapor-dominated systems are associated with very-low matrix permeability formations. Applying these insights, and the mass and heat transport equations to Los Azufres, we conclude that a contrast of 1-3 orders of magnitude exists between the vertical permeability at the boiling point and that corresponding to the vapor-dominated portion of the system. We propose that similar permeability contrasts may be responsible for the characteristic composite pressure profiles observed in other vapliq systems.

INTRODUCTION

The Los Azufres, Mexico, geothermal field presented in its natural state (Iglesias et al., 1985a; 1985b) an unusual pressure profile (Fig. 1) revealing a transition between a vapor- and a liquid-dominated hydrothermal system. Traditionally, geothermal reservoirs unperturbed by exploitation have been classified as either liquid-dominated or vapor-dominated. Thus, it seems relevant to ask whether similar hydrothermal systems exist, and to investigate the thermohydrological conditions conducent to their existence. Furthermore, the profile of Fig. 1 offered an oportunity to obtain insights on the vertical permeability and on other parameters of the system, that we attempted to exploit.

The thermohydrologic conditions for the existence of both liquid- and vapor-dominated systems have been addressed by several authors (e.g., Martin et al., 1976; Grant et al., 1982; Pruess, 1985). In the first part of this paper we explore the particular conditions conducting to the formation of vapliq systems. Then, we apply the results to obtain insights on the distribution of the vertical permeability and on other parameters of Los Azufres.

VAPLIQ SYSTEMS

The existence of a third type of geothermal reservoir, in which a transition between the traditionally recognized types is observable, has been demonstrated in Los Azufres, Mexico (Iglesias et al., 1985a; 1985b). We propose the name "vapliq" for these systems.

Vapliq systems are characterized by a vertical pressure profile which is

nearly vaporstatic in the shallower portion of the system, and nearly boiling-point-for-depth at depth. The geothermal field of Los Azufres, Mexico, displays the prototype profile (Fig. 1).

We are aware of at least two more examples of vapliq systems, both in Italy. Pruess et al. (1987) persuasively argued that in its natural state the Larderello geothermal field also showed a transition between liquid- and vapor- dominated. And in Poggio Nibbio the pressure profile (Celati et al., 1976) offers clear evidence of the existence of another vapliq system.

ON CONDITIONS FOR THE EXISTENCE OF VAPLIQ SYSTEMS.

To explore the conditions for the existence of vapliq systems we consider the following 1-D vertical scenario, based on generally accepted conceptual models of liquid- and vapor-dominated geothermal systems. The unperturbed reservoir is in steady state. In the central part of the system, where there is a net wpward mass flow, the mass and heat transfer only have vertical components. We assume that at the base of the system there is hot compressed liquid that flows upwards nearly isoenthalpically (e.g., White, 1967). The fluid pressure decreases as it ascends, until the saturation pressure is reached. At this so called boiling point of the system ($p=p_B$, elevation $z=z_B$), the flow becames 2-phase. At this point, the liquid saturation $S_L=1$. As the flow proceeds to shallower horizons, pressure and liquid saturation decrease. Eventually, S_L reaches a value small enough for the vapor to become the pressure-controlling phase. At this transition point $p=p_{trans}$, $z=z_{trans}$. For $p<p_{trans}$ $(z>z_{trans})$ the pressure gradient is comparable with a vaporstatic gradient.

In this scenario conservation of mass can be represented by

$$F = F_L + F_V \qquad (1)$$

where F, the net mass flux, is constant, and F_L and F_V, the liquid and vapor fluxes respectively, are, with z pointing upwards,

$$F_L = -(kk_L/\mu_L)\,\rho_L\,[\nabla p + \rho_L g] \qquad (2)$$

$$F_V = -(kk_V/\mu_V)\,\rho_V\,[\nabla p + \rho_V g] \qquad (3)$$

where k stands for absolute permeability, k_α, μ_α, ρ_α, for relative permeability, viscosity, and density of phase α, respectively, and g is gravity acceleration.

Similarly, energy conservation can be expressed as

$$Q = Q_{cond} + Q_{conv} \qquad (4)$$

where Q, the thermal flux, is constant, and the conductive and convective fluxes are

$$Q_{cond} = -K\gamma\nabla p, \qquad (5)$$

$$Q_{conv} = h_L F_L + h_V F_V, \qquad (6)$$

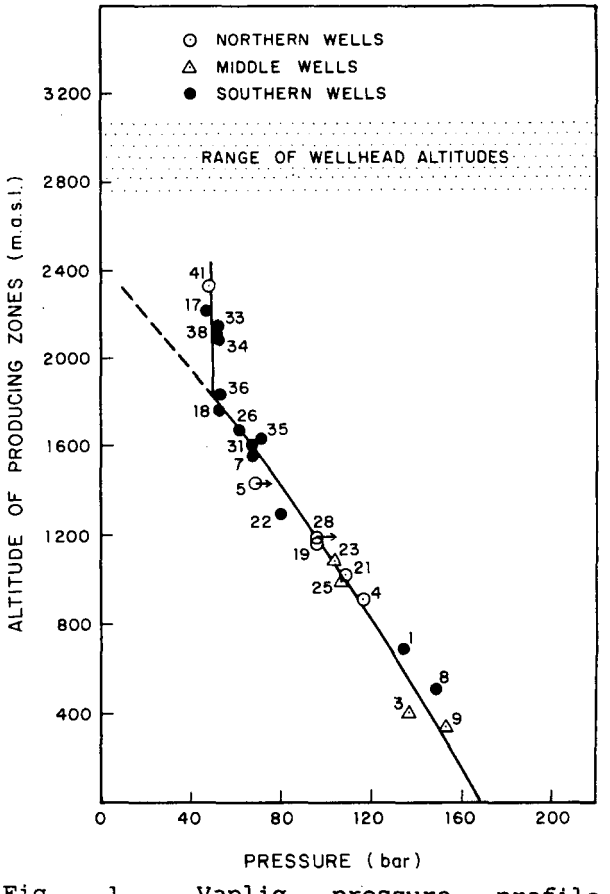


Fig. 1. Vapliq pressure profile observed at Los Azufres (after Iglesias et al., 1985b).

respectively. Here K is thermal conductivity, and $\gamma=(dT/dp)$.

At $p=p_B$, $k_L=1$, $k_V=0$, and from (1) and (6) the (constant) net mass flux is

$$F = [Q-K\gamma g\rho_L]_B/[h_L+(K\gamma\mu_L/k\rho_L)]_B \qquad (7)$$

In the compressed-liquid region FL>0 for the fluid to ascend. Thus, since in that region $F=F_L$ and F is constant in the system,

$$F > 0 \qquad (8)$$

It follows from (7) and (8) that in the central ascending part of 2-phase hydrothermal systems

$$Q > (K\gamma g\rho_L)_B \qquad (9)$$

Note that Q_{min} only depends on K_B and p_B (or T_B, the temperature at the boiling point). Fig. 2 illustrates this dependence for some typical values of both variables. Considering that the average normal thermal flux at the surface of the Earth is approximattely 0.060 W m^{-2} (e.g., Elder, 1976; Jessop et al., 1976), we conclude that typical values of Qmin are about 1-3 times the average value of the normal terrestrial flux.

The heat-pipe mechanism is responsible for convective heat transfer in vapor-dominated hydrothermal systems (White et al., 1971; Martin et al., 1976; Pritchett, 1979; Strauss and Schubert, 1981; Pruess, 1985; Pruess et al., 1987). In these systems steam flows upward, condensates in the cooler upper regions, and results in liquid condensate flowing downwrad. A characteristic of this mechanism is that high heat fluxes are possible with negligibly small net mass fluxes. Heat pipes can also occur in liquid-dominated systems (e.g. Martin et al., 1976). Thus, in our scenario we assume that vapor-liquid counterflow occurs somewhere in the 2-phase region. For this to happen, F_L, which is positive for $p> p_B$ ($z< z_B$), must change sign at some point characterized by $p=p*$ ($z=z*$), with $p* < p_B$. From (2), and (6) we get

$$Q - (K\gamma\rho_L g)_* - h_{V*}F = 0 \qquad (10)$$

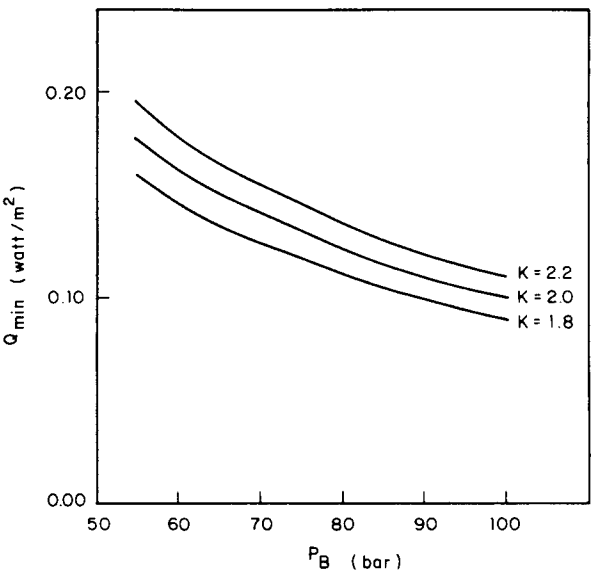


Fig. 2. Typical values of Q_{min}.

an expression that can be inverted to obtain $p*$, if Q, p_B, k_B and $K*$ are known. In Fig. 3 we present results for p_B = 86 bar Tthe boiling point at Los Azufres), and $K_B=K*=2$ $Wm^{-1}{}^0C$. This figure demostrates that in this case, for $p*$ to be smaller than p_B, k_B must be smaller than a certain value that we call k_{Bmax}. In other words, if the vertical distribution of thermal conductivity is uniform, a necesary condition for the existence of liquid-vapor counterflow (i.e. $p*p_B$) is that the vertical permeability at the boiling point of the system must be smaller than k_{Bmax}. Fig. 3 also shows that k_{Bmax} corresponds to $p*=p_B$. From this last condition and (10) we find

$$k_{Bmax} = [K\gamma\mu_L/\rho_L)/(h_V - h_L)]_B \qquad (11)$$

that only depends on K_B and p_B. Fig. 4 illustrates some typical values of k_{Bmax} for this case. These results indicate that the vertical permeability at the boiling point of hydrothermal systems with vapor-liquid couterflow, such as vapliq and vapor-dominated systems, must be relatively small, about $1\text{-}3\times10^{-18}$ m^2 for p_B in the range 50-100 bar, if the vertical distribution of thermal conductivity is approximately uniform. These results are compatible with the small matrix permeabilities measured in the Los Azufres andesites (Iglesias et al., 1987).

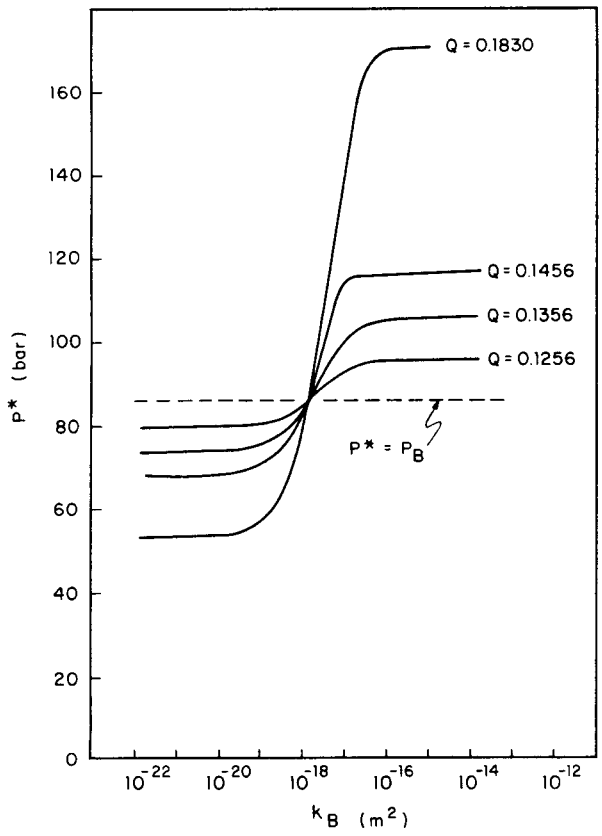


Fig. 3. The pressure at which F_L changes sign as a function of the vertical permeability at the boiling point and the thermal flux.

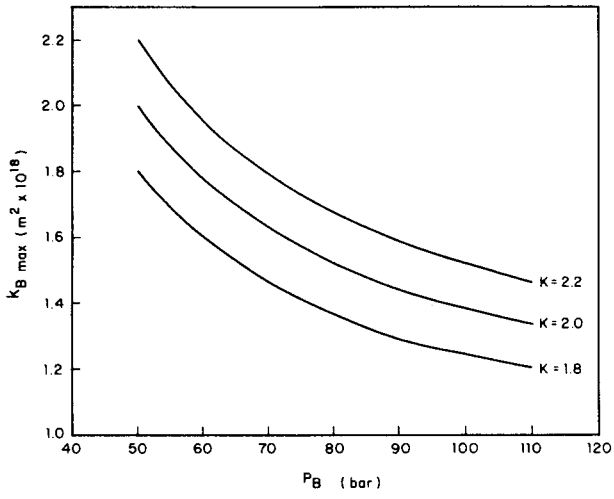


Fig. 4. Typical values of k_{Bmax}.

If the distribution of thermal conductivity deviates significantly from uniformity, i.e. $K_B \neq K^*$, K_B can be greater than indicated in Fig. 4. In the few cases we have already explored, the maximum values obtained for K_B exceeded those of Fig. 4 by about one order of magnitude.

We belive these results are related to the fact (e.g., Pruess and Narashiman, 1982) that all known vapor-dominated systems are associated with low matrix permeability formations. Research is in progress to confirm or deny this suggestion.

THE VERTICAL PERMEABILITY DISTRIBUTION AT LOS AZUFRES

The observed pressure profile at Los Azufres is shown in Fig. 1. The boiling point of the system is approximately at p_B=86 bar, z_B=1300 m.a.s.n. (Iglesias et al., 1985b). Knowing p_B, one can estimate Q_{min} and k_{Bmax} for the systems, from (9) and (11). The thermal conductivity of the andesites (the predominant rocks) in Los Azufres ranges between 1.0 and 2.4 $Wm^{-1}{}^{o}C^{-1}$, with a mean equal to 1.72 $Wm^{-1}{}^{o}C^{-1}$ (Iglesias et al., 1987). The mean effective porosity of these rocks is about 10 % (Iglesias et al., 1987), and therefore the effects of the fluid conductivity on K are negligible. Taking the extreme measured value of K we find.

$$Q_{min} \sim 0.06\text{-}0.14 \text{ W m}^{-2}, \quad (12)$$

$$k_{Bmax} \sim (0.74\text{-}1.76) \times 10^{-18} \text{ m}^2, \quad (13)$$

The values estimated for k_B in (13) lie within the typical range of matrix permeabilities (smaller than 2.3×10^{-18} m^2) found for the Los Azufres andesites (Iglesias et al., 1987). This suggests that near the boiling point of the system the vertical flow proceeds predominantly through the rock matrix, not through fractures. More information about the vertical permeability at Los Azufres can be obtained from the profile in Fig. 1. One way to do this is to rearrange (1) and (4) to obtain

$$kk_L = \mu_L \, (Q+K\gamma\nabla p-h_V F)/[h_{LV}\rho_L(\nabla p+\rho_L g)] \quad (14)$$

$$kk_V = -\mu_V \, (Q+K\gamma\nabla p-h_L F)/[h_{LV}\rho_V(\nabla p+\rho_V g)] \quad (15)$$

In the liquid-dominated zone the pressure gradient is negative, and its absolute value is very close to hydrostatic (i.e., $\rho_L g$). Thus, even small errors in ∇p translate into great uncertainties for estimates of the effective vertical permeability. This approach is therefore impractical for liquid-dominated zones. In vapor-dominated zones the differences between ∇p and the vaporstatic term tends to be much greater, and practical estimates of effective permeability are possible. To apply this method we estimated Q via temperature gradients from stabilized temperatures in the caprock, obtained while drilling. Data from wells Az-9 , Az-23 and Az-28 (Alfonso Aragón, personnal communication) indicate $0.045<Q<0.380$ Wm^{-2}, with a mean value equal to 0.180 Wm^{-2}. Having estimates of Q, p_B, k_{Bmax} and K (and therefore of F), and considering the constraints

$$0 \leq k_V \leq 1.0 \leq k_L \leq 1 \qquad (16)$$

we obtain

$$k_{V\text{-dom}} > 1.5\times10^{-17} \quad m^2 \qquad (17)$$

for the vertical permeability in the vapor-dominated zone at Los Azufres.

A second approach to obtain permeability information from the profile in Fig. 1 is based on an expression for the pressure gradient

$$\frac{dp}{dz} = -g\left[\frac{k_V \rho_V^2 \mu_L + k_L \rho_L^2 \mu_V + F\frac{\mu_L \mu_V}{k g}}{k_V \rho_V \mu_L + k_L \rho_L \mu_V}\right] \qquad (18)$$

and a constitutive constraints equation

$$k_V\left[\left[\frac{Q}{k g}\right]\left[\frac{\mu_L}{\rho_L^2 h_V}\right] - \left[\frac{F}{k g}\right]\left[\frac{\mu_L}{\rho_L^2}\right] - \left[\frac{k}{k}\right]\left[\frac{\gamma \rho_V \mu_L}{\rho_L^2 h_V}\right]\right] + k_L\left[\left[\frac{Q}{k g}\right]\left[\frac{\mu_V}{\rho_L \rho_V h_V}\right] - \left[\frac{F}{k g}\right]\left[\frac{\mu_V h_L}{\rho_L \rho_V h_V}\right] - \left[\frac{k}{k}\right]\left[\frac{\gamma \mu_V}{\rho_V h_V}\right]\right] - k_L k_V\left[1-\frac{\rho_V}{\rho_L}\right]\left[1-\frac{h_L}{h_V}\right] = \left[\frac{F}{k g}\right]\left[\frac{k}{k}\right]\left[\frac{\mu_L}{\rho_L^2}\right]\left[\frac{\gamma \mu_V}{\rho_V h_V}\right] \qquad (19)$$

obtained manipulating equations (1)-(6) (e.g., Pritchett, 1979). In this approach one integrates (18) subject to the constraints (16) and (19), assuming values for Q, F, the vertical distributions of permeability and thermal conductivity, and relative permeability functions in terms of liquid or vapor saturations. One advantage of this approach is that, given p_B and z_B, it provides self-consistent estimates of Q, F, K, k_B and $k_{V\text{-dom}}$.

We first tried a simple model in which k and K were constant. Numerous integrations were performed for reasonable values of K and trial functions for the relative permeabilities, including Corey-type curves, "fracture permeabilities" ($k_L+k_B=1$), and others. The synthetic pressure profiles so generated could not satisfactorily fit the observed profile. The greatest discrepancy was in the profile's "knee" marking the transition between the liquid- and vapor-dominated regimes. To obtain acceptable fits it was necessary to adopt permeability values drastically greater than the estimates of k_{Bmax}, for the vapor-dominated zone. The two-permeability model ($k=k_B$ in the liquid-dominated zone, $k=k_{V\text{-dom}}$= constant in the vapor-dominated zone) was able to generate acceptable fits. More complex models, with permeability monotonically increasing from k_B to $k_{V\text{-dom}}$ in a variety of ways, resulted unsatisfactory.

Our best fit is shown in Fig. 5. its parameters are $Q=0.0128$ Wm^{-2}, $F=8.26\times10^{-10}$ $kgm^{-2}s^{-1}$, $k_B=1.5\times10^{-19}$ m^2, $k_{V\text{-dom}}=1.0\times10^{-16}$ m^2 and $K=2$ Wm^{-1}. The value indicated for Q is consistent with that inferred from stabilized temperatures. The value obtained for k_B lies in the typical range found for matrix permeability in andesites from Los Azufres. The value indicated for K is close to the mean thermal conductivity found from measurements in drill cores for these rocks.

The two approachs indicate that in Los Azufres there is a vertical permeability contrast between the liquid dominated- and the vapor-dominated zone, with the deeper zone significantly less permeable. The permeability contrast is 1-3 orders of magnitude. These results suggest that similar permeability contrasts may underlie the characteristics pressure profiles of other vapliq systems.

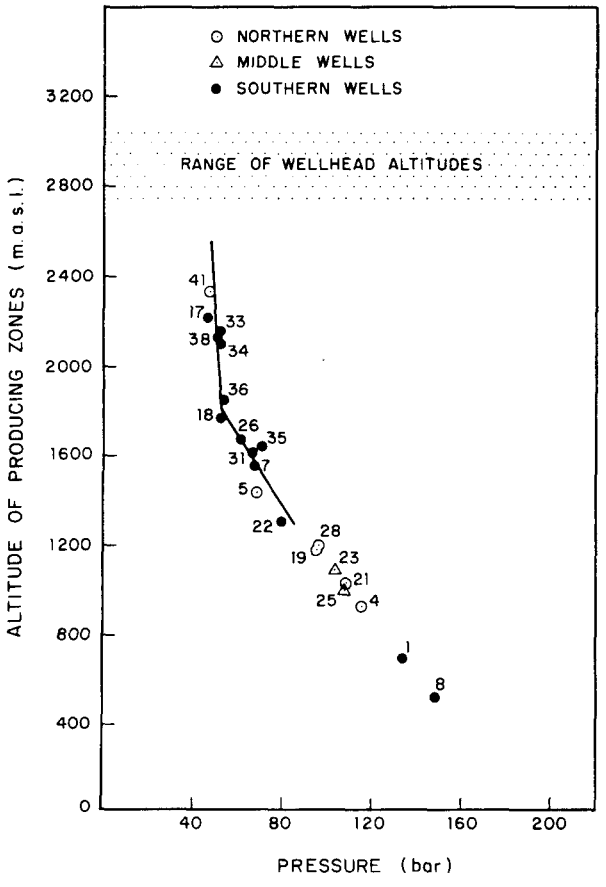


Fig. 5. Best fit to the observed profile.

CONCLUSIONS

We identified a new category of hydrothermal systems, that we call vapliq, which are intermediate between the traditionally recognized liquid- and vapor-dominated systems. Vapliq systems are characterized by a composite pressure profile which is nearly vaporstatic in the shallower zone, and nearly boiling-point-for-depth at depth.

A necessary condition for the existence of 2-phase hydrothermal systems is that the vertical thermal flux must exceed Q_{min}, a parameter that only depends on the values of the pressure and of the thermal conductivity at the boiling point of the system. Typical values of Q_{min} are 1-4 times the average terrestrial flux.

Our results indicate that the existence of hydrothermal systems with vapor-liquid counterflow is conditioned to having low (e.g., < 3×10^{-18} m^2) boiling-point permeabilities. This is consistent with the observation that all vapor-dominated and vapliq systems are associated with low matrix permeability formations.

Finally, in Los Azufres there is a vertical permeability contrast between the liquid dominated- and the vapor-dominated zone, with the deeper zone significantly less permeable. The permeability contrast is 1-3 orders of magnitud. These results suggest that similar permeability contrasts may underlie the characteristic pressure profiles of other vapliq systems.

REFERENCES

Celati, R., P. Squarci, L. Taffi and G.C. Stefani, (1976), Analysis of Water Levels and Reservoir Pressure Measurements in Geothermal Wells, United Nations Symposium, 3, 1583-1590.

Elder, J., (1976), The Bowels of the Earth, Oxford University Press.

Grant, M.A., I. Donaldson and P. Bixley, (1982), Geothermal Reservoir Engineering, Academic Press.

Iglesias, E.R., V.M. Arellano and A. Garfias, (1985a), The Natural Thermodynamic State of the Fluids in the Los Azufres Geothermal Reservoir, Proc. 10th Stanford Workshop Geoth. Res. Eng., 241-246.

Iglesias, E.R., V.M. Arellano, A. Garfias, C. Miranda and A. Aragon, (1985b), A One-dimensional Vertical Model of the Los Azufres, México, Geothermal Reservoir in its Natural State, Geothermal Resources Council Transactions, 9(II), 331-336.

Iglesias, E.R., E. Contreras y A. Garcia, (1987), Propiedades Físicas de Andesitas del Campo Geotérmico de Los Azufres, Instituto de Investigaciones Eléctricas, Informe IIE/11/2014/I 03/F, Cuernavaca, Mor.

Jessop, A.M., M.A. Hobart and G. Sclater, The World Heat Flow Data Collection 1975, Geothermal Service of Canada, 5, 175.

Martin, J.C., R. Wegner and F.J. Kelsey, 1976, One-dimensional Convective and Conductive Geothermal Heat Flow, Proc. 2nd. Stanford Workshop Geoth. Res. Eng., 251-262.

Pritchett, J.W., (1979), Vertical Two-phase Flow in Geothermal Reservoirs, Systems Science and Software Report SSS-R-80-4341.

Pruess, K., T.N. Narashiman, (1982), On Fluid Reserves and the Production of Superheated Steam from Fractured Vapor-dominated Geothermal Reservoirs, J. Geophys. Res. 87(B11), 9329-9339.

Pruess, K., (1985), A Quantitative Model of Vapor-dominated Geothermal Reservoirs as Heat Pipes in Fractured Porous Rock, Geothermal Resources Council Transactions, 9(II), 353-361.

Pruess, K., R. Celati, C. Calore and G. Capetti, (1987), On Fluid and Heat Transfer in Deep Zones of Vapor-dominated Geothermal Reservoirs, Proc. 12th Stanford Workshop Geoth. Res. Eng.

Strauss, J.M. and G. Schubert, (1981), One-dimensional Model of Vapor-dominated Geothermal Systems, J. Geophys. Res., 86(b10), 9433-9438.

White, D.E., (1967), Some Principles of Geyser Activity, Mainly from Steambot Springs, Nevada, Am. J. Sci. 265, 641-684.

White, D.E., L. Miffler and A. Truesdell, (1971), Vapor-dominated Hydrothermal Systems Compared With Hot-water Systems, Economic Geology, 66(1), 75-97.

PROCEEDINGS, Thirteenth Workshop on Geothermal Reservoir Engineering
Stanford University, Stanford, California, January 19-21, 1988
SGP-TR-113

NATURAL FLOW AND VERTICAL HETEROGENEITIES IN A SEDIMENTARY GEOTHERMAL RESERVOIR (PARIS BASIN, FRANCE) : GEOCHEMICAL INVESTIGATIONS

Annie Criaud, Philippe Fouassier, Christian Fouillac and Michel Brach

Institut Mixte de Recherches Géothermiques
BRGM - BP 6009 - 45060 ORLEANS CEDEX

ABSTRACT

Three geothermal wells tapping the Dogger aquifer were studied in detail for their variations in chemical composition with time or conditions of exploitation. Analytical improvements for the determination of Cl, SO_4, Ca, Mg, Na and K make it possible to detect variations respectively of 0.15, 0.8, 0.6, 1.8, 1.8 and 1.4 %. Despite the fact that the natural flow may be important in some parts of the basin aquifer, we conclude that this factor is not responsible for the small variations noticed in mineralization within the one year survey period. The results concerning reactive and nonreactive species are best explained if a vertical heterogeneity of the chemistry of the fluid is assumed. A number of calcareous sub-layers, already demonstrated by geological studies, contribute to varying degrees to the production of the hot water. The changes in pumping rates, which are fixed according to external requirements, play a major role in the hydrodynamic and chemical disequilibrium of the wells. The consequences for the geothermal exploitations are emphasized.

INTRODUCTION

Intensive exploitation of the Dogger limestone aquifer for geothermal purposes has drawn attention to the need for detailed knowledge of the characteristics of the reservoir in order to manage and protect the resource (Rojas et al., 1987). Fluid velocity and chemical heterogeneity of the productive layers may have a marked influence on the lifetime of the installations if the location and orientation of the doublets do not take these parameters into account or if the change in composition of the fluid with time increases corrosion and scaling in the well casing, heat exchangers and surface network. In the Val de Marne Department (south of Paris), the increasing number of wells has brought to light hydraulic contacts between adjacent exploitations. So far, a few tracer experiments (131-I) on single wells for two doublets located south of Paris, at Fontainebleau and Cachan, suggest relatively important natural flow towards the north-west in the south of the basin (De Marsily et al. 1986). This may be linked to an actual recharge of the aquifer which consist in this area of a dilute but warm water, evidenced by isotopic and chemical indications (Criaud et al., 1986 ; Fouillac et al., 1986 ; Marty et al., 1988). On the other hand, unpublished work by the Institut Mixte de Recherches Géothermiques shows that the chemistry of a fluid collected at the wellhead for a given site may change with the working conditions (pumping rate) and/or the period of sampling. However the range of variation in chemistry was of the same order of magnitude as the relative precision of standard analytical procedures.

We present here the results of a detailed survey for three case studies, in the south and east of the basin, where minimum and maximum salinities respectively of the geothermal fluid are encountered (figure 1). The needs were to improve the analytical methods and quantify the precise variations in chemical composition with time and conditions of exploitation (these consist mainly of variable pumping rates causing differing pressure conditions at wellheads). The aim was to develop a geochemical tool useful for hydrodynamic studies. Because downhole sampling at different depths could not be carried out (due to the presence of immersed pumps), all samples were collected at the wellheads. Sampling at three sites has been carried out over a year or more and at various pumping rates. Total dissolved solids and dowhole temperatures for the wells are respectively 6.5 g/l and 74°C (Fontainebleau), 23.5 g/l and 79°C (Créteil) and 35 g/l and 85°C (Coulommiers). Only a limited number of chemical parameters was selected for this survey. We have included highly soluble ions such as Cl or SO_4, concentrations of which are not controlled by fluid-mineral equilibria in this aquifer (Bastide, 1985), and reactive cations such as Na, Ca, Mg and K which can be affected by water-rock interactions. The former are expected to result from mixing phenomena, while the latter would reflect

different extents of water-rock interaction. We assume that no reequilibration of the fluid happens during ascent in the well, i.e. the concentrations of these species do not vary between the aquifer and the surface. This is supported by the fact that only the deposition of iron sulfide has been reported in the casing (Honegger et al., 1986).

SAMPLING AND ANALYTICAL PROCEDURES

Sampling

For the three wells concerned, samples were collected at different times of year, under different conditions of exploitation of the geothermal installation. The pumping rates consequently vary approximately between 80 m^3/h (summer) and 250 m^3/h (winter). A special survey was undertaken in Coulommiers in May 1987, with five steps at different pumping rates. Six hours were allowed for stabilization before new pumping rate conditions were fixed. The first sampling was carried out after 3 hours and a second one after 6 hours. In all cases, water samples were collected at the wellheads. The sampling period spread over more than one year but all the determinations were carried out at the same time in the laboratory, in order to avoid time drifts due to the devices.

pH, temperature, alkalinity and sulfide concentration were measured on site following the procedure already described in Criaud et al. (1986). In the case of Fontainebleau, where the sulfide content reaches 30 mg/l, a special sample was collected for sulfate determination in order to avoid the oxidation of sulfide and subsequent artificial increase of sulfate concentration before analysis. This method was also used for the Coulommiers samples, where sulfide content may reach 0.5 % of the sulfate content but this was unnecessary in Créteil because the sulfide content is negligible compared to sulfate. Two procedures were tested : in the first, a known amount of cadmium acetate was added to the sample immediately after sampling. In the second mercuric nitrate was used. All reagents and samples were weighed to improve the precision.

Analytical methods

Chloride: The method involves potentiometric titration with silver nitrate, an Ag/AgCl electrode and a reference electrode. Because the aim of the study was to quantify precise and tiny relative variations rather than very exact determinations, no attempt was made to correct for the bromide and other halogenides which are titrated along with chloride.

The reproducibility of the method is 0.12 % for 10 determinations of the chloride content of Coulommiers water, which is the most saline fluid. This result was found to be satisfactory for the main objectives of the study. Duplicate analysis were performed routinely.

Calcium: Complexation of alkaline earths by EDTA offers a very suitable method for the determination of calcium. The use of a titration device under control of a specific optical fiber which transmits a light beam (λ = 660 nm) considerably improves the reproducibility of end point determination, giving a reproducibility of 0.6 % for 10 determinations. It is affected mainly by the quantity of indicator, the time for stabilization and the large variation of the photometric signal after each drop of the EDTA reagent. Ba and Sr are titrated together with Ca but again it was assumed that the concentrations of Sr (30 to 70 mg/l) and Ba (approx. 0.1 mg/l) and their relative variations are of little importance compared respectively to the concentrations of calcium and their variations in these fluids.

Magnesium: The Mg concentration was calculated from the difference between the results of the titration of calcium on the one hand and the sum of Ca + Mg on the other hand. Ca + Mg was also determined by complexometric titration using black eriochrome as indicator and the 660 nm phototrode. The concentrations of Sr and Ba and their variations were neglected as compared to the magnesium content for the reasons mentioned above. Reproducibility was 0.15 % for 10 determinations of Ca + Mg. Depending on the Ca/Mg ratio, the reproducibility for Mg alone is thus 1.4 % for Fontainebleau, 2.3 % for Créteil and 2.4 for Coulommiers.

Sulfate: The method is based on the determination of barium in excess after removal of the cations of the sample with ion exchange cationic resin, and addition of barium chloride with precipitation of barium sulfate. The complexometric titration with EDTA and the use of the 550 nm phototrode for the determination of the end point provide an accurate method if the excess of barium is kept small. The reproducibilities for the indirect determination of sulfate in the samples were respectively 0.8 % for Fontainebleau and 1.1 % for Coulommiers. For the fluids containing dissolved hydrogen sulfide and treated on site, the addition of cadmium acetate did not give satisfactory results for the more saline fluids because of the low pH and the consequent inefficient removal of cations by the resin, but mercuric nitrate was found suitable for both Fontainebleau and Coulommiers.

Sodium and potassium: Na and K were determined by flame emission spectrophotometry. All samples were diluted and the emission measured at 589 and 766.5 nm respectively. The standard solutions were prepared with chemical composition and Na/K ratios close to those of the samples. The reproducibility is 1.3 % for K and 1.8 % for sodium.

RESULTS

The variation of the chemical components displays variable relative trends in different wells. Table 1 summarizes the maximum deviations compared to the reproducibility of the analytical methods.

	Maximum deviations %			Analytical reproducibility %
	1	2	3	
Cl	1,7	0,6	0,6	0,1
Ca	1,1	1,2	0,6	0,6
SO_4	7,1	0,5	1,6	0,8
Na	3	1,5	1,3	1,8
Mg	12,9	2,6	0,5	1,8
K	5,7	2,8	2,1	1,4
Ca + Mg	4,5	0,9	0,6	0,15

1: Fontainebleau ; 2: Créteil ; 3: Coulommiers

Table 1: Maximum deviations of the chemical parameters during the one year survey and analytical reproducibility

Fontainebleau

The most important variations with time were observed in the fluid from Fontainebleau which is the most dilute in the basin. Unfortunately the pumping rates could not be monitored for this well. If the results are interpreted as a function of time, then the concentrations of chloride, potassium and sodium tend to increase within the one year survey period, while those of calcium and magnesium decrease. This would favor the assumption of a natural "horizontal" flow of the fluid within the aquifer. This circulation should be quite important to be consistent with the extent of chemical changes evident on the very small time-scale of one year. The main objection to this assumption is that the natural flow (Rojas et al., 1987) and the isosalinity curves (Criaud et al., 1986) in this part of the basin imply rather that the salinity of the fluid decreases with distance (figure 1). On the other hand the exploitation of the aquifer with various pumping regimes is unlikely to provoke such movements of the fluid near the well.

Another approach is to compare the variations of the chemical components relative to each other. From table 1, it appears that Cl, Na, Ca and K vary significantly and can be used as indicators of geochemical phenomena. Although Cl would be preferable, we have also taken Na into account to illustrate the main variations of the other elements. It can be seen in figure 2 that the mineralization of the geothermal fluid shows no regular variations according to chronological order of the samples, thus confirming that the "horizontal" circulation of the water is not responsible for the observed variations. The behavior of Cl, Na, K and HCO_3 are best explained if we assume that the water collected at the wellhead results from the mixing of slightly different fluids. Flow rate measurements after the end of drilling had shown the existence of at least three productive geological facies, each of them subdivided into several productive layers which could be interconnected (Rojas et al., 1987). Since some samples deviate significantly from the trend observed for Na versus Cl (both of which are considered here as non-reactive) on figure 2a, it may be concluded that more than two different fluids cause the changes in chemical composition. The results for K lead to the same conclusion.

In contrast, the Mg content clearly decreases with the Cl (figure 2d). Since dissolved Mg is controlled by the solubility of dolomite in the Dogger fluids (Bastide, 1985), the different Mg/Cl ratios in the various sub-aquifers can be related to different temperatures. Another consequence of this would be the positive correlation of salinity with temperature for these sub-layers.

Créteil

The operating conditions of the geothermal wells vary according to the hot water requirements and the main factor that could be responsible for the variations observed is the variable pumping rate. This is not accurately known for the Fontainebleau samples, but Créteil is very suitable for examining the effects of both time and pumping rates on the chemistry of the fluid. The available data are for discharge rates between 96 and 220 m^3/h and were measured over ten months. Figures 3a, b, c and d show that the samples taken at lower and upper regimes are respectively the least and the most mineralized, the two other points being very close to each other with respect to both analytical determinations and pumping rate measurements. It must be emphasized that the relative variations (table 1) are close to the standard deviation of analytical methods for Na, Ca and SO_4, but despite this, the variations are remarkably consistent on figure 3. A mixing model involving two or more fluids could account for these correlations. So far the importance of the circulation of the fluid within the aquifer is not known in this area, but vertical variations in the chemistry are likely to occur at Créteil, which would satisfactorily explain the geochemical results.

The calcium is in this case much more reactive than at Fontainebleau, its concentration decreases as sodium (or chloride) increases. This may be linked to a slight rise of temperature, and to the solubility of calcite.

There is no evidence in Créteil for time variations on the chemistry of the fluid.

Coulommiers

This fluid is the most mineralized of any in the basin, and very little modification of the chemical composition was observed within the one year survey period (table 1). The greatest variations were obtained for sulfate and potassium. On figures 4a and 4b the concentrations in K versus SO_4 and Cl are plotted. The points display a rough positive correlation which is not linked to the order of collection. No systematic relation is found between the discharge rate or composition but this again may be due to imprecise knowledge of the exploitation parameters during the first part of the survey. Mixing of fluids from separate layers of the main aquifer with constant Cl/K and SO_4/K ratios would explain these patterns.

The pumping conditions were carefully controlled for the second part of the study at Coulommiers. The changes were made in 5 stages of 6 hours of fixed pumping rates. The deviations for most of the elements determined are hardly noticeable with regard to analytical error. SO_4, Cl and K only show significant variations (figure 4). Other considerations based on iron contents (Ouzounian et al., 1987 and unpublished results by IMRG) tend to indicate that hydrodynamic equilibration of the well is still not attained after 6 hours of pumping at a constant rate. When the second set of samples (collected after 6 hours) is considered, a fair correlation between K and SO_4 is observed (figure 4d). Na and SO_4 concentrations also display a positive correlation when all the points are plotted. This is consistent with the hypothesis of mixing of two or more fluids. The influence of several producing layers is assumed, in view of geological considerations. So far, no information concerning the circulation rate of the fluid within the aquifer in the east of the basin is available. With regard to the results of the two parts of the chemical survey, we believe that the main influence demonstrated is in modifications of the pumping conditions. The relative percentages of water produced by the Dogger sub-aquifers seem to vary in a complex manner, according to the equilibration time required and the relations between mineralization and pumping rates, which are not simple (as far as the analytical precision is sufficient).

DISCUSSION

Previous geochemical investigations came to the conclusion that the origin of the fluid collected at the wellheads of about a hundred wells is complex. Local trends make it possible to distinguish at least three different mixing phenomena, according to specific ratios such as Cl/SO_4 or Cl/B, but Cl/Br or Cl/Na, which are rather homogeneous at the basin scale, arguing for a common origin and a global mixing model. The very precise determinations made for this study can be used to compare the ratios between Cl, SO_4 and Na obtained for the three wells of Fontainebleau, Créteil and Coulommiers, each belonging to a different group (Criaud et al., 1986), with those obtained at local or regional scale. The Dogger aquifer pattern for Cl versus Na defines a correlation according to the equation: (n = 55 wells) (Cl) = 1.917 (Na) - 774.9 with r = 0.9898, while for Fontainebleau and Créteil significantly lower slopes were found for the mixing lines calculated from figures 2 and 3. The variations of the chemistry at Coulommiers are too small to allow such confident interpretation. Differences in Na/SO_4 ratios confirm the local trends previously pointed out (Criaud et al., 1986). We thus emphasize the fact that three degrees of mixing could account for the complex evolution of the Dogger fluids:

- At the regional scale (200 km), the natural flow is responsible for a variety of mineralizations and temperature distributions. Certain chemical indications favor the hypothesis of a common parent for these waters (Cl/Br and Cl/Na ratios).
- At the local scale (10 km or less), certain groups of fluids are clearly characterized by their Cl/B and Cl/SO_4 ratios as well as isotopic properties (Seine St Denis, Val de Marne, Fontainebleau, eastern and western wells) (Fouillac et al., 1986).
- Any particular producing well taps a number of sub-strata which constitute the Dogger aquifer and are obviously not homogeneous in chemistry. Because most of the wells are exploited at different pumping rates, with a consequent hydrodynamic disequilibrium, the relative contribution of each layer to the chemical composition at the wellhead varies depending on the sampling period.

The variations of chemical composition demonstrated by this work result mainly, or entirely, from the varying contributions of the vertical sub-systems constituting the Dogger aquifer. The relative proportions involved depend on site, pumping rate and equilibration time. The other influences (regional or local "horizontal" flow) could possibly be displayed by geochemical methods if longer experiments could be undertaken, especially for the wells of moderate salinity, because analytical problems could be solved more easily.

CONCLUSIONS

The variations of the chemical composition of three geothermal wells were monitored carefully over a year or more and if we except Fontainebleau, the variations are very small (< 3%). This study has been possible because analytical methods for the determination of Cl, SO_4, Mg, Ca, Na and K

have been improved. The techniques involved are independent, i.e. chemical interferences can hardly explain the observed correlations between the concentrations of some elements, and consequently we believe that they are significant. Despite the fact that greater precision is needed for Na and K, it is remarkable that their variations often correlate well with those of other species (SO_4, Cl, Mg or Ca).

Several mechanisms can account for the modification of the chemistry of the fluids at Fontainebleau, Créteil and Coulommiers. A complex and permanent disequilibrium of the hydrodynamics of the wells is probably due to changing conditions of exploitation, which are adapted to the external requirements for heating. Examination of the chemical data permits to conclude that the variations of the pumping rate play a major role. Slight differences in the chemistry of the fluids produced by the association of several strata are assumed. In contrast the gradual evolution of chemistry with time (on a one year scale) is unnoticeable. Though evidence exists for a "rapid" horizontal circulation of the fluid in some parts of the basin, the chemical changes induced on the human scale are negligible compared to analytical uncertainties. Other experiments, such as the use of tracers, are required to monitor this kind of circulation. Nevertheless, the vertical zonation of the wells that is observed for chemistry as well as for lithology, is expected to have a marked influence on the concentrations of highly reactive species (iron and sulfide, e.g.).

This kind of geochemical method, based on wellhead sampling can be useful for the knowledge of the geothermal reservoir and to detect vertical heterogeneities, even when downhole sampling cannot be carried out.

BIBLIOGRAPHY

Bastide J.P. (1985). Etude géochimique de la nappe du Dogger du Bassin Parisien. 3rd cycle thesis, University of Paris VII, 152 p.

Criaud A., Fouillac C. and Brach M. (1986). Chemical evolution of the fluids from the Dogger aquifer. Workshop on geochemistry. EC contractors meeting, Antwerp, Nov. 1986.

De Marsily G. (1985). Détermination expérimentale de la vitesse d'écoulement de la nappe géothermique du Dogger en région parisienne. CEC report, EUR 140281 FR.

Fouillac C., Fouillac A.M., Criaud A., Iundt F., and Rojas J. (1986). Isotopic studies of oxygen, hydrogen and sulfur in the Dogger aquifer from Paris Basin. Proceedings of the 5th Intern. Symposium on Water Rock Interaction, Reykjavik, p. 201-205.

Honegger J.L., Criaud A., Menjoz A. and Proust E. (1986). Résultats des opérations récentes de reprise de puits en région parisienne. Workshop Corrosion et entartrage dans les systèmes géothermaux, Commission of the European Communities, Orléans, Nov. 1986, 11 p.

Iundt F., Fouillac C., Ouzounian G. (1984). Etude géochimique des fluides du Dogger. In "Le réservoir géothermique du Dogger en région parisienne. Exploitation, gestion. Hydrogéologie de l'ingénieur, 1, p. 57-85.

Marty B., Criaud A. and Fouillac C. (1988). Low enthalpy geothermal fluids from the Paris sedimentary basin. 1: Characteristics and origin of gases. Geothermics (in press).

Ouzounian G., Castagné S., Fouillac C. and Criaud A. (1987). L'origine du fer dans les eaux géothermales exploitées au Dogger (Bassin Parisien). Géothermie Actualités, 4(3), p. 31-34.

Rojas J., Menjoz A., Martin J.C., Criaud A. and Fouillac C. (1987). Development and exploitation of low enthalpy geothermal systems: example of the Dogger in the Paris basin, France. Proceedings of the 12th Workshop on Geothermal Reservoir Engineering, Stanford 1/87.

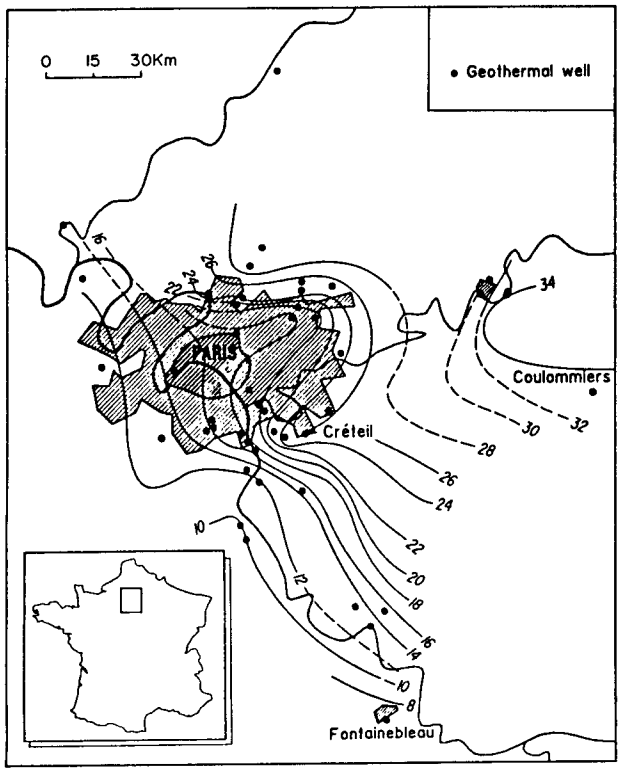


Figure 1 : Location map of the geothermal wells in the Paris basin.
-12- : isosalinity Curves obtained after geothermal and oil wells data.

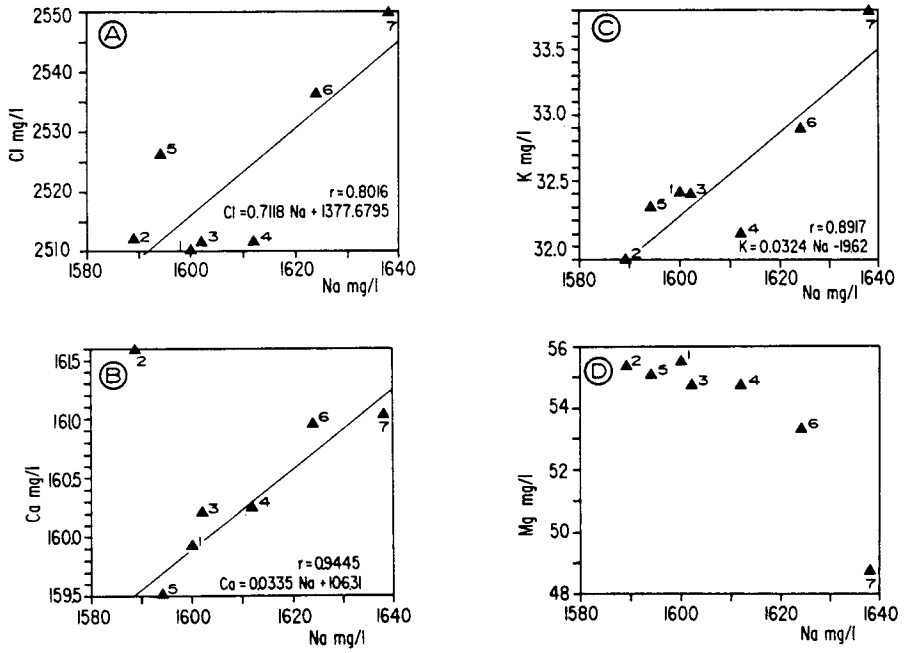


Figure 2 : Fontainebleau. Variation diagrams for Cl, K, Ca and Mg relative to Na during one year - Results are consistent with a mixing model - Numbers represent sampling dates : 1=June 1986 2=Aug 1986 3=Oct 1986 4=Nov 1986 5=Nov 1986 6=Feb 1987 7=Apr 1987 8=May 1987.

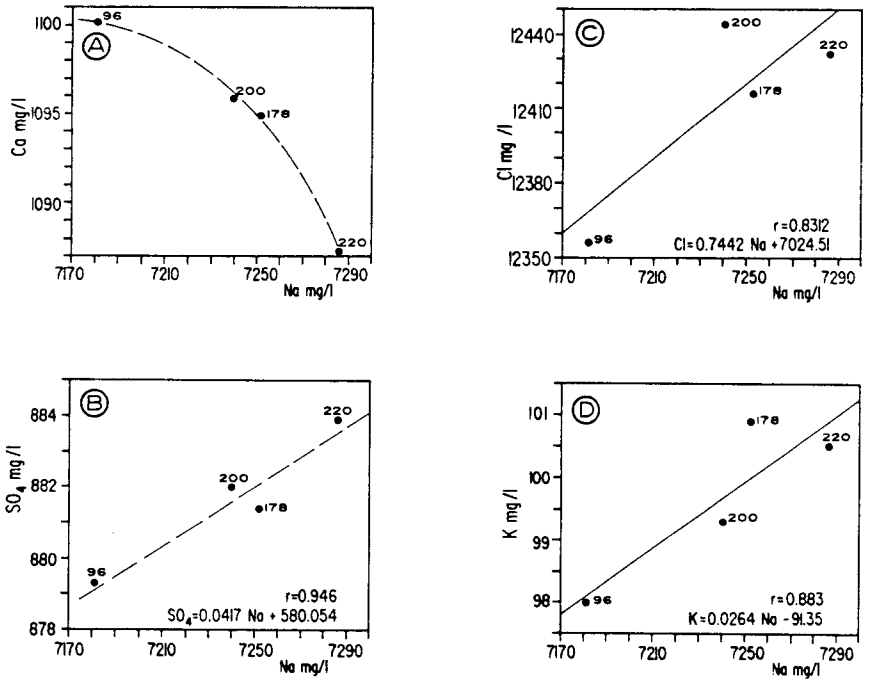


Figure 3 : Créteil. Effects of variable pumping rates (m^3/h) on Ca, Cl, SO_4 and K versus Na content.

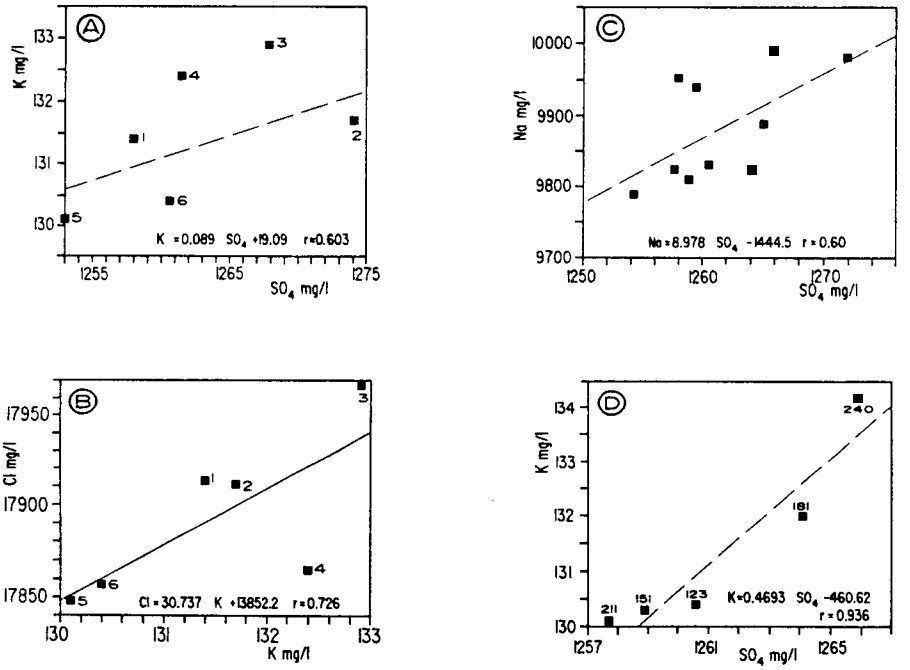


Figure 4 : Coulommiers.

Ⓐ and Ⓑ Effects of time on the variations of K and Cl relative to SO_4 and K

1=Aug 1985 2=Aug 1986 3=Dec 1986 4=Dec 1986
5=Apr 1987 6=May 1987

Ⓒ Correlation between Na and SO_4 - All results are from May 1987 with various pumping rates.

Ⓓ Effects of pumping rates on K versus SO_4 contents (May 1987) - Numbers represent pumping rates.

PROCEEDINGS, Thirteenth Workshop on Geothermal Reservoir Engineering
Stanford University, Stanford, California, January 19-21, 1988
SGP-TR-113

GEOCHEMICAL MUD LOGGING OF GEOTHERMAL DRILLING

F. B. Tonani[1], M. Guidi[2], S. D. Johnson[3]

1 Univeristy of Palermo, via Archirafi 36, Palermo, Italy
2 Geotermica Italiana, via Lungarno Mediceo 16, Pisa, Italy
3 Chevron Resources, San Ramon, CA

ABSTRACT

The experience and results described in the present paper were developed over nearly two decades, with a major R&D project around 1980.

The expression Geochemical Mud Logging (GML) has ill defined meaning in the geothermal industry, and ought to be specified. We refer here to GML as featuring mud and formation fluid tracer(s) and temperature as the bare essentials and with specified accuracies. Air and water logging are expected to be less demanding with regard to analysis accuracy, but are not discussed in this report.

During application of GML to several drill holes with low formation permeabilities and under conditions of high temperature and high mud weight, GML as specified, revealed unexpected influx of formation brine. Such influx was a recurring feature that has been referenced to individual fractures and reflects both fracture size and permeability. As a consequence, continuous or subcontinuous sampling of mud systems appears more cost effective than trying to keep up with cumulative changes of bulk mud composition; although, the latter approach is more sensitive to extremely low rate, steady, inflow of formation fluid into the mud system. It appears, that based on this influx of formation fluid, permeability can be estimated well before mud losses are detected and/or drill strings are stuck.

The main advantages of GML are: (1) the capability to assess formation temperature and permeability in nearly real time, resulting in (a) assessments of undisturbed formation and (b) having data in hand for holes lost during drilling operations and (2) being effective under conditions of very high temperatures where electcrical logs are very costly and less reliable.

Estimated cost for GML is $1500 per day (1982) based on assessments of R&D operations. However, extrapolating to larger scale services and to different operating conditions is indeed difficult. GML cost is probably the only significant point of controversy with regard to GML being a viable evaluation tool.

INTRODUCTION

The experience with geothermal logging outlined in this report began to build up in occasional observations in the Geysers area in the mid to late 1960's; limited geochemical logging of some drill holes followed on Basin and Range projects in the mid 1970's; a full scale project was developed during exploration geothermal drilling in the Campi Flegrei, Italy, in the late 1970's to early 1980's, with some parallel application going on in California exploration drilling marginal to the Geysers area.

The project in the Campi Flegrei was partly mud logging services, and to a major extent, research and development of new techniques. In respect to the latter, the senior author as the consultant, and the involved service and consulting company, Aquater (a ENI company) were on equal footing.

The present report furnishes an outline of: (1) definitional specifications of the developed Geochemical Mud Logging (GML) method; (2) facts established throughout the early applications outlined above; (3) techniques that were used; and (4) points that became the subject of scientific and technical controversy among the involved professionals.

A formal presentation and discussion of the GML topic took place for the first time in 1985, at a workshop held in Tirrenia, near Pisa, Italy. It was presented as part of discussions regarding means to detect and assess permeability based on data other than well testing. The workshop was set up by ENEL, and the Proceedings (available in Italian from ENEL) give a very extensive report based on tape records of discussions. The procedure and results have also been briefly outlined in lectures by Tonani, given in Strassburg, Germany in 1980.

BACKGROUND

2.1 Defining terms

Geochemical logging can be any of a great variety of procedures. Contrary to geochemical mud logging in the petroleum industry, where a well established tradition makes this a fairly specific term, such terms as geochemical logging (GL) and geochemical mud logging (GML) have hardly any specific meaning with reference to geothermal drilling. Of course, GL of air drilling (GAL), water drilling (GWL) and so forth, are entirely different from each other and from GML in specific application and techniques. Here, we shall concentrate on GML which constitutes the bulk of our work in this area.

To begin with, not any chemical monitoring of drilling air, water, or mud is to be considered a Geochemical Logging technique. Referring to chemical monitoring

for, e.g., environmental purposes, the use of the term (GL) would be misleading. We shall reserve the term Geochemical Logging (GL) when referring to chemical logging aimed at gathering information on the properties of, and conditions prevailing in, the formation being being drilled through. Moreover, we shall do it with reference to properties and conditions relevant to formation and reservoir evaluation; in our case, it shall relate specifically to geothermal exploration and development drilling aimed at formation and reservoir evaluation. Requirements, hence specifications, resulting from these circumstances shall define such terms as Geochemical Logging, GML and related terminology.

Whereas specifics will be reported in the following sections, one consequence of this report is aptly stated here: As long as consistant GML terms and methods are not established, such statements as, "GML is, or is not, effective." will be meaningless. This is of considerable consequence in regard to the commercial contracting of GML services and also has been a center of controversy in discussing even the technical success of GML.

For our GML analysis, "tracer" refers to a substance, usually a mobile one, whose concentration relates to a process; in the present case, a mixing process.

In our context, "mobility of" or "mobile" refer to the ability of the considered chemical substance (tracer) to move around some specified physical setting. It is empirically related to the chemcial ability of the considered species to concentrate in a physically mobile phase, such as in the present connection, the filterable waters of drilling muds.

2.2. Defining the specific GML method referenced in this report

GML as investigated and implemented in experimental work referred to in the introduction is defined by the following specifications. These specifications are both of a general nature and in practice may become site and project specific.

General specifications are: (1) recording temperature to within 0.1° C; (2) determining at least one mud tracer substance to within a few 0.1 percent precision; (3) determining at least one of the nonvolatile and mobile formation fluid tracers (chloride) within a few percent precision; (4) taking samples at a rate in excess of one sample every fifteenth minute.

Project specific downgrading of general specifications can be used to scale down cost as dictated by information objectives of the individual drilling projects. Site and project specific tracers must be selected according to the chemistries of the drilling target (expected formation target and formation fluids) and the drilling mud system. Specifications must be carefully tailored to the known geochemistry of the target geothermal system.

Although effective GML can be carried on with the general specification of one sample per fifteen minutes or more, recommended frequency based on presently obtain results should be increased to sampling at five minute intervals. Actual specifications for the most significant experimental work to date as reported in the referenced ENEL proceedings are listed in the next section.

OUTLINE OF PROCEDURES AND RESULTS OF GML EXPERIMENT

3.1 Procedures

Temperature. Temperature was continuously recorded to within 1° C as is usual in mud logging practice. Although this limited the quality of the results and decreased the number of cases where results were actually attainable, it did not prevent the demonstration that GML methods can estimate formation fluid enthalpy during drilling. Measurement of temperature to within 0.1 C is recommended since it is operationally feasible and hence, it is definitional in respect to the considered general GML procedure.

Frequency of sampling. Discrete sampling intervals were deemed appropriate for experimental work. Four samples per hour were used as a compromise sampling interval. This still required pumping mud samples continuously to the drill-site laboratory for efficient operations. The significance of selecting the sampling interval follows from the consideration, that the mixing of downhole drilling mud with formation fluids controls the minimum volumetric width of point like events (tracer anomolous spikes) in the mud circulation system. At mud circulation rates prevailing during these experiments (1.0 to 1.5 m^3/min), the corresponding time width of instant events resulting from formation fluid influx to the mud system was measured at approximately five minutes; e.g.; it entails a maximum frequency of sampling on the order of one sample per five minutes for detection of these instantaneous events.

Continuous sampling is recommended in principle, but is obviously not feasible, nor is as high a sampling frequency as one sample per five minutes practical with discrete sampling. Thus, sampling is not yet definitional on a practical general basis as applied to GML, in contrast to, for example, reading temperature to within 0.1° C.

Mud tracer. Nitrite ion was used as a mud tracer for the purposes of measuring formation water inflow based on mud dilution. A combination of monitoring nitrite and controlling its concentration in mud was used: nitrite would be determined in input mud, and some would be aptly added to the mud mixing system whenever appropriate.

Formation fluid tracer. Chloride was used throughout these studies to trace brine inflow into the drilling mud system. Chloride monitoring is easier and more sensitive than the use of nitrite as the mud tracer, however, to use chloride as a formation fluid tracer requires previous knowlege of brine composition (chloride concentration). In principle, by using GML procedures, an evaluation of the behavior of both mud tracer and formation fluid tracer should allow determination of the brine chemistry.

3.2 Obtained results

Observed facts. The rate of change of mud

composition resulting from drilling mud-formation fluid exchange can, at times, be directly observed as the difference in composition of output and input mud in the circulating mud system. However, only comparatively high rates of exchange or mixing can in fact be determined by directly comparing output and input mud composition. Instead, monitoring the cumulative change of bulk mud composition utilizing longer time intervals in the system analysis, results in increasing sensitivity for detection of formation fluids. However, the trade off, is that as longer time intervals are considered in the analysis, there are larger errors resulting from mud processing operations and the consequential adjustments to the mud system.

Correcting for mud processing operations has proved difficult and depends on many factors. It is costly, in as much as it required much professional time under the conditions prevailing in the presently reported central project of consideration. Measuring steady and very low rate changes was, however, accomplished and it led to an accurate material balance sheet of bulk mud. This result was of limited direct use, however, it did provide the ground work for detecting short term input-output variations.

Transients of higher rate of change in mud composition were also observed; detecting and measuring them required increasing the frequency of sampling. Broad peaks lasting on the order of one hour as well as peaks that might be as brief as five minutes or less in duration were observed regularly. The latter features appear as individual anomalous samples in a series of samples 15 minutes or more apart. Their significance depends on how accurately the composition of the bulk mud system has been determined.

The occurrence of high amplitude peaks of mud compositional change is a persistant feature and could be definitely proved to exist. These peaks demonstrate that an influx of formation fluids does occur. This was an unexpected result based on the previously prevailing opinion regarding mud behavior and the formation of mud cake in drill holes using balanced mud systems.

By and large, rapid (spike) changes are easier to measure in many respects. Providing the baseline mud composition that is then required to detect these spikes has proved a great deal easier than monitoring the effect of mud processing and adjustment operations on absolute mud composition.

Inferred processes. Some inferences regarding the process responsible for the observed changes could be made based upon information collected during GML of several production drill holes in the Campi Flegrei. Steady, low rate, change in mud composition brought about by incorporation of formation fluids in the drill mud system as the country rock was ground by the drill bit was observed. The fairly accurate material balance sheet that was obtained in this monitoring formed the basis for further observations.

Individual anomalous change of output mud composition relative to input mud has been interpreted as the effect of short duration events lasting less than the time interval betwen discrete samples. Many of these peaks are so large amplitude compared to the admissible size of voids produced by the penetration of the drill bit (based on hole size and drill rate records), that some influx of information fluid had to be assumed in as much as these anomalies would result in estimated porosities in excess of 100%. A number of cases where such calculation was feasible indicated that formation water invades the wellbore from fractures and that this inflow must be in excess of at least several wellbore radii of influence. It seems only reasonable that the volume of each formation water influx be related to permeability.

Other, broader peaks seem referrable to washouts of the bore wall. The association of these broad peaks with compositional changes attributed to ion exchange in the mobile phase tracers was taken as evidence supporting such interpretation.

Correlation of Temperature with Chemical Change. In some cases the observed chemical peaks were accompanied by a concurrent observation of a temperature anomaly in the return mud system. These temperature anomalies were detected not withstanding the previously discussed generally below specification sensitivity of the temperature measurements. When such temperature anomalies were detected, an estimate of the enthalpy of the formation fluid influx couild also be made. Namely, the formation temperature at several points during the drilling of the San Vito #1 well were estimated. A bottomhole temperature of about 400° C and a constant temperature gradient could be inferred from GML.

SAMPLING, SAMPLE PROCESSING, AND CHEMICAL ANALYSIS TECHNIQUES USED IN EXPERIMENTAL GML

4.1 Sampling

Mud outlet samples were taken just downstream of the shaker screen and mud inlet samples were taken downstream of the mud pumps. At early stages, sample collection was essentially manual, however at later stages in the drilling, the mud samples were pumped directly to the drill-site laboratory, resulting in increased efficiency of the GML operations.

4.2 Sample processing

Throughout most of the project, plain mud filtrates were analyzed and obtained results refer to filtrate, i.e., mobile phase composition. The expression "mud composition" is used, but as discussed earlier is not definitionally quite exact.

One of the research teams involved in this experimental GML used acidified mud samples which is expedient to efficient mud filtration. The obtained filtrate obviously does not represent the mobile phase in the actual drilling mud system; as a consequence, although the technique may well work and deserved testing, it cannot be taken for granted without adequate further study. The negative results reported from this type of sample processing is not conclusive, in that the followed GML procedure did not meet the same specifications reported in this paper in section 2.2 under GML specifications. Necessary information

on bulk mud composition for interpreting widely spaced samples was missing. Techniques of broadly similar approach deserve further, but adequate study.

4.3 Chemical analyses

A large variety of components were tested as candidates for GML. Metal ions were determined by flame emission and atomic absorption ; anions were mostly determined by automatic colorimetry (Auto-Analyzer); chloride was determined by back-titration following a variant of the Volhard method.

Experimental work with ion specific electrodes was carried out with regard to chloride and sulphide; the former technique revealed itself to be satisfactory, and does indeed work best with untreated mud. It was developed at a late stage in the program, in preparation for continuous monitoring, and was never applied extensively. Sulphide ion determinations were abandoned after preliminary tests pointed out the lack of mobility of sulphide in the drilling mud.

The same group of scientists that carried out work with acid treated samples used ICP to determine a large array of metal ions. Although, in general, metals are less mobile than anions, they did deserve attention; however, the same comments as give in Section 4.2 above apply.

DISCUSSION AND CONTROVERSY

Thus far, according to our understanding of the viewpoints that have been expressed either formally or informally, the only meaningful controversy regards whether or not full scale GML as defined in the present report is cost-effective. There is no simple answer to such a question, as (1) there is no simple way to extrapolate from the present research and development efforts to a service company cost basis, and (2) there is no simple way to determine the potential value or worth of the information that is obtained from the cost of GML.

Some guess can be made based on the main project referred to in the present report, inasmuch as this work consisted of actually logging exploratory drilling in the then new area of Mofete (Campi Flegrei, Italy). Discussion can hardly be conclusive, however, as further controversy remains on the future of prospects in that area. Pending definitive verification of subsurface conditions in this area where our work was concentrated, the following can be concluded. The results of GML demonstrate that it can deliver decisive data regarding formation permeability (or at least its relative distribution) and temperature; that permeability information complements in essential ways the lost circulation data that usually go with commercial potential of a production well. The specific project area is likely to furnish an exemplary pattern in this respect; however, the project could not be fully developed as yet, hence it cannot be discussed in full in this report.

The main argument in favor of discontinuing the GML project was its cost. Those costs, however, were the unadjusted cost to the Research and Development project; moreover, it does not take an accountant to realize that transactions between closely related companies such as were involved in that project are hardly representative of conditions in the marketplace.

Some cost estimates were attempted based on analysis of the procedure, and on costs of partial services, personnel and so forth. This resulted in some $1500/day (1982 $) for full scale GML as defined. Such a cost compares well with similar services such as traditional mud logging and electrical logging and in our opinion, the obtained results are worth the costs.

The consideration is, that no other method gives comparable assessment of permeability, let alone in nearly real drilling time, and results reflect the undisturbed formation. A similar assessment applies to formation temperatures. In addition to such essential information, GML potentially results in a fallout of other useful information (such as fluid losses and changes of fluid chemistry with depth). An expansion on this fallout data is beyond the scope of this report, and perhaps would distort the basic contentions that GML is an effective stand alone tool within the specifications already discussed.

The fact that GML information remains available for lost drill holes and/or sections of drill holes and the entailed saving of redrilling costs, also contributes considerably to the worth of GML as defined in this report, especially, in connection with wildcats and early exploratory wells.

The above arguements are not meant to question any company's specific decisions regarding GML, as these decisions are also project specific, and possibly depend on subjective risk assessment. What is a meaningful subject of controversy is the assessment of GML's cost effectiveness as referenced to averaged conditions in the geothermal industry. The arguments presented above have, in the present case study, resulted in confusing specific company policies with general exploration strategies. Defending or refuting management decisions in this project is not an issue, (it may even lead to incorrect scientific conclusions). Such a conclusion was the case when the failure of GML was reported for the Mofete project; but, the fact that the GML program did not meet the minimum specifications as outlined above was not mentioned in the operators assessment of the GML method.

PROCEEDINGS, Thirteenth Workshop on Geothermal Reservoir Engineering
Stanford University, Stanford, California, January 19-21, 1988
SGP-TR-113

A NEW ILLITE GEOTHERMOMETER

JUDITH M. BALLANTYNE and JOSEPH N. MOORE

UNIVERSITY OF UTAH RESEARCH INSTITUTE
SALT LAKE CITY, UTAH

ABSTRACT

Sericite, either as illite or illite/smectite, is ubiquitous in geothermal systems. Theoretical Ca- and Na-smectite contents of non-expanding geothermal sericites have been calculated from published electron microprobe analyses. Geothermal sericites can be modeled as solid solutions of muscovite and smectite. For those sericites that fit the model, the amount of smectite in solid solution is related to temperature by the expression:

$T°C = 1000/(0.45\mathrm{Log}X_{smectite} + 2.38) - 273$

The temperature dependence of illite interlayer chemistry suggests a related temperature dependence of the K, Na and Ca content of geothermal fluids. The original data used by Fournier and Truesdell (1973) to derive the empirical Na-K-Ca geothermometer for geothermal fluids can be modeled equally well by an equation incorporating the equilibrium constant for the reaction of smectite to illite:

$T\ °C = 1.145*10^3/(\{[0.35\mathrm{Log}Na+0.175\mathrm{Log}Ca-0.75\mathrm{Log}K] +1.51\} - 273$

where the concentration units are molalities. This supports the hypothesis that illite and illite/smectite are important controls on the concentrations of Na, K and Ca in geothermal fluids.

INTRODUCTION

Fine grained white micas, including muscovite, illite and interstratified illite/smectite, and collectively termed sericite, are ubiquitous in geothermal systems (Browne, 1978). These minerals differ chemically primarily in the amount of K^+ in the interlayer site (Fig. 1). Interstratified illite/smectite contains <0.75 K^+ per $O_{10}(OH)_2$ (Srodon et al., 1986), illite contains 0.75 to 1.0, and muscovite (or its Fe-rich analog, phengite) contains 1.0 K^+ per $O_{10}(OH)_2$. The interlayer site can also contain minor amounts of Na^+ and Ca^{++}, and occasionally Mg^{++} and NH_4^+. Published studies of sericites from geothermal systems (McDowell and Elders, 1980, Ballantyne, 1981, Parry et al., 1984, Bishop and Bird, 1987) show that the interlayer site is incompletely filled in sericites formed at low temperatures, and becomes increasingly filled at higher temperatures.

The smectite general formula chosen for use in this study is:
$(0.5Ca,Na)_{0.35}(Al,Mg,Fe)_2[(Si,Al)_4O_{10}](OH)_2.n\text{-}H_2O$ (Deer et al., 1966). Exchangeable K^+ and Mg^{++} can also substitute for Ca^{++} and Na^+. The maximum interlayer site occupancy for a smectite is thus between 0.18 and 0.35 cations, compared to the maximum of 1.0 for an ideal muscovite.

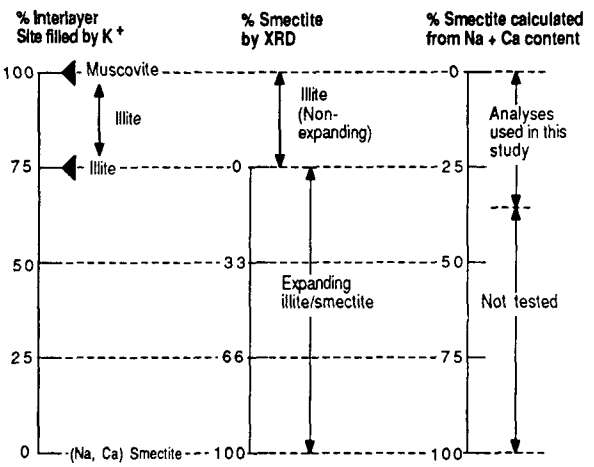


Figure 1. Comparison of models for illite and illite/smectite determined by XRD and from chemical analyses.

The percentage of smectite interstratified with illite in illite/smectite is normally determined by X-ray diffraction (XRD), not by chemical analysis. The amount of expansion of glycolated samples relative to non-glycolated equivalents is converted to percent smectite. Numerous studies of expanding illite/smectite have shown decreasing expandability with increasing temperature. The temperature dependence of non-expanding sericites has been modeled assuming solid solution between muscovite ($KAl_2[AlSi_3O_{10}](OH,F)_2$), paragonite ($NaAl_2[AlSi_3O_{10}](OH,F)_2$), and pyrophyllite ($Al_2[Si_4O_{10}](OH,F)_2$) to account for the K, Na and incomplete site occupancy (1-(K+Na+Ca)), respectively (Bird and Norton, 1981, Capuano and Cole, 1982, Parry et al., 1984, Bishop and Bird, 1987). While this method has shown correlations between temperature and the

activities of these solid solution components, it does not account for Ca, and it cannot readily be extended to interlayered illite/smectites formed at lower temperatures. In this paper we describe an alternative hypothesis, that illite is actually a muscovite-smectite solid solution. We then use this data to establish a relationship between temperature and sericite chemistry. Finally, we discuss a possible relationship between illite/smectite and the Na-K-Ca geothermometer of Fournier and Truesdell (1973).

SMECTITE SOLID SOLUTION IN NON-EXPANDING ILLITE

Geothermal sericites range from illite/smectite to muscovite (or phengite), and from <0.75 to 1.0 K^+ per $O_{10}(OH)_2$ (McDowell and Elders, 1980, Ballantyne, 1981, Parry et al., 1984, Bishop and Bird, 1987). Table 1 shows sericite analyses calculated as muscovite, Ca-, and Na-smectite components. Averages of analyses for each depth are listed because individual grain analyses are reported only for Roosevelt Hot Springs samples (Ballantyne, 1981). Small differences in analysed Ca and Na content make large differences in calculated smectite content. A step of 0.01 cations per $O_{10}(OH)_2$ represents 6% Ca-smectite, 3% Na-smectite, but only 1% muscovite or paragonite.

The sum of the smectite and muscovite components for the majority of samples in Table 1 is surprisingly close to 100%, given the uncertainties in the method of calculation described above. Totals close to 100% in Table 1 support the hypothesis that most sericites can be considered as muscovite either interstratified or in solid solution with Ca- and Na-smectite. High temperature samples from the Salton Sea have totals much higher than would be expected if Na were present as smectite. These four samples are better described as muscovite in solid solution with paragonite. One Coso sample with an exceptionally high Ca content may be intergrown with another Ca-bearing mineral (Table 1), and a total of 100% is assumed for this sample.

Some samples from each system, particularly low temperature samples, have unaccounted-for vacancies in the interlayer site. We suspect that this is due to cations that were not determined, such as NH_4^+ and Sr^{++}, or to inaccuracies inherent in methods of chemical analysis and structural formula computation. Some volatilization of K and Na can occur under the microprobe beam. In addition, a small amount of K^+ can be present as K-smectite. K-smectite is not detectable by XRD analysis because it does not swell (Drever, 1982), and analytical techniques yield only total K. We assume that all K^+ is present as muscovite.

Table 1. Calculated smectite and muscovite components in geothermal sericites.

Depth (m)	T °C	Interlayer Cations K[1]	Ca[1]	Na[1]	% K-Musc	% Ca-Smect	% Na-	% Total
Coso well 16-8[2]								
190		0.630	0.145	0.017	63	83[5]	5	152[5]
215		0.755	0.025	0.006	76	14	2	92
236		0.831	0.013	0.016	83	7	5	95
250		0.861	0.004	0.035	86	2	10	98
Salton Sea well Elmore #1[3]								
439	190	0.56	0.03	0.06	56	17	17	90
622	251	0.65	0.03	0.05	65	17	14	96
675	264	0.68	0.01	0.04	68	6	11	85
845	295	0.83	0.01	0.08	83	6	23[6]	112[7]
924	306	0.90	0.00	0.08	90	0	23[6]	113[7]
991	315	0.91	0.01	0.09	91	6	26[6]	122[7]
1064	322	0.93	0.00	0.07	93	0	20[6]	113[7]
Roosevelt Hot Springs well 14-2[4]								
503	215	0.675	0.004	0.014	68	3	4	75
518	215	0.795	0.009	0.020	80	6	6	91
610	220	0.760	0.007	0.018	76	3	6	85
854	230	0.805	0.010	0.025	81	6	7	93
869	230	0.870	0.007	0.020	87	3	6	96
896[8]	250	0.860	0.010	0.015	86	6	4	96
1341	250	0.740	0.020	0.015	74	11	4	90
1524	255	0.900	0.010	0.015	90	6	4	100

[1]Calculated on the basis of 22 negative charges, equivalent to $O_{10}(OH)_2$. Smectite is considered to contain $(0.5Ca, Na)_{0.35}$ per unit formula. Averages of analyses for each depth are listed. [2]Bishop and Bird (1987). [3]McDowell and Elders (1980). [4]Ballantyne (1981). Temperatures are estimated to nearest 5°C from static log (Glenn and Hulen, 1979). [5]The anomalously high Ca content of this sample is believed to be due to an intergrown Ca-rich mineral. A total of 100% is assumed in later calculations, and a Ca-smectite content of 32% used. [6]The Na in these samples is believed to be in paragonite, not smectite. [7]Totals with Na as paragonite instead of smectite would be (from top to bottom) 97, 98, 106 and 100%, respectively. [8]One anomalously Na-rich analysis was omitted from the average.

A few samples may contain Mg-smectite. The three shallow samples from Roosevelt Hot Springs, 503m, 518m and 610m, have octahedral site occupancies of 2.07, 2.01 and 2.04 respectively, while all other samples from the same well contain less than the ideal 2.00 cations in the octahedral site (Ballantyne, 1981). If the excess (>2.00) site occupancy is calculated as Mg-smectite, Mg-smectite contents of 39%, 6% and 22%, respectively, are obtained for the three samples. These amounts are more than enough to account for the low totals (Table 1) of 75%, 92% and 85%, respectively. Two Coso samples with

octahedral site occupancies >2.00 correspond to downhole measured temperatures of 190° and 236°C. Octahedral site occupancies of 2.018 and 2.005 for these samples (Bishop and Bird, 1987), can be converted as above to 10% and 3% Mg-smectite, respectively. No estimates of octahedral site occupancy can be made for the Salton Sea samples because structural formulas were calculated assuming the ideal 2.00, with all Mg in the octahedral site (McDowell and Elders, 1980).

A comparison of chemically-calculated and XRD-determined smectite contents can be made for the one expandable Salton Sea sample, from 439 m depth. The XRD data shows 10-12% expandable layers (McDowell and Elders, 1980). The smectite content calculated from chemical analyses is 34% (Table 1). According to our model, non-expandable illite containing 0.75 K^+ per $O_{10}(OH)_2$ can contain up to 25% non-expandable smectite. Thus a chemically-calculated smectite content of 34% is equivalent to [1.33(34-25) = 12]% expandable smectite. The conversion factor of 1.33 is required to convert chemically-calculated % smectite to % expandable smectite (see Fig. 1). Thus, for this Salton Sea sample, the two methods give identical results.

TEMPERATURE DEPENDENCE OF INTERLAYER SITE CHEMISTRY

Figure 2 shows the relationship of calculated smectite content to the sum of muscovite and paragonite components. The closer to the line on the figure that a sample lies, the more fully its interlayer site occupancy is accounted for.

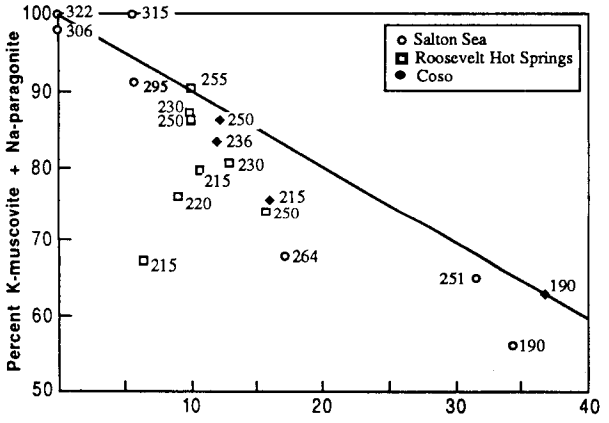


Figure 2. Components accounting for interlayer cations in geothermal sericites, calculated from microprobe analyses. The diagonal line represents interlayer site occupancy fully accounted for by the four components, equivalent to 100% totals in Table 1. Points are labelled with measured downhole temperatures in °C. Data are from Table 1.

The labels on data points in Fig. 2 are measured downhole temperatures. The distribution of the temperatures relative to compositions suggests an equilibrium reaction between muscovite and smectite. If such an equilibrium occurs, then a relationship of the type:

$$\hat{-}G°_{f(reaction)} = -2.303RT\log K$$

is expected, where K is the equilibrium constant, and a plot of smectite activity vs 1/T should be linear. Only samples close to the line on Fig. 2 (those with totals >90% in Table 1) are used in determining temperature dependence (Fig. 3). In addition, the Salton Sea sample from 622 m is excluded because the associated temperature is much higher than for other samples in this range of smectite content. With smectite activity approximated by mole fraction, X, the data in Fig. 3 are linearly distributed, with a correlation coefficient of 0.86. The regression equation for this line is given by the equivalent expressions:

$$1000/T = 0.45\log X_{smectite} + 2.38 \quad (1)$$

and:

$$T\ (°C) = \frac{1000}{(0.45*\log X_{smectite} + 2.38)} - 273 \quad (2)$$

where T is in degrees Kelvin.

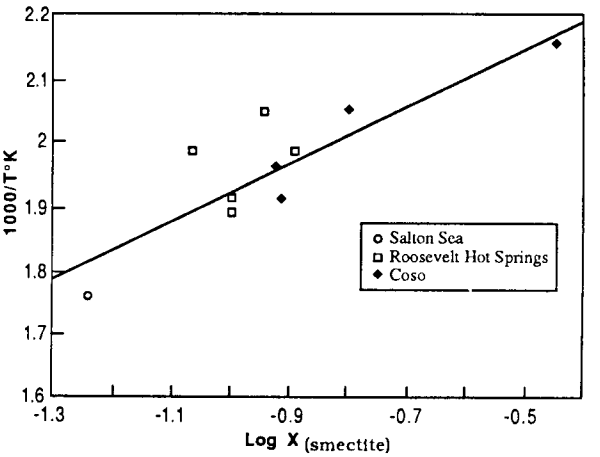


Figure 3. Relationship of temperature (°K) to calculated smectite content of sericite (NOT XRD-determined expandability). Data are from Table 1.

Table 2 compares downhole measured temperatures to the temperatures calculated using the illite geothermometer, for all samples. Two methods are used to calculate $X_{smectite}$. The first converts Ca and Na content to smectite. The second assumes that all interlayer sites not filled by K (and Na in paragonite) are filled by smectite. The lower temperature samples from Coso and Roosevelt Hot Springs give a much closer fit to measured temperatures using this second method. One reason is that cations other than Na and Ca may occur in smectite interlayer sites, as discussed above, and therefore a smectite component calculated using only Ca and Na data would be too low.

Table 2. Comparison of measured temperatures with those predicted from the illite geothermometer.

Depth (m)	Meas[1] Temp °C	Smect[2] Temp °C	Vac[3] Temp °C
Coso well 16-8[4]			
	190	185	185
	215	222	202
	236	236	219
	250	235	228
Salton Sea well Elmore #1[5]			
439	190	188	178
622	251	191	187
675	264	218	191
845	295	276	251
924	306	346	346
991	315	276	NA
1064	322	NA	NA
Roosevelt Hot Springs well 14-2[6]			
503	215	263	190
518	215	238	210
610	220	253	203
854	230	232	212
869	230	253	232
896	250	245	228
1341	250	222	199
1524	255	245	245

[1]Measured downhole temperature. [2]Temperature predicted from calculated Ca- and Na-smectite content. [3]Temperature predicted assuming all interlayer site vacancies are due to smectite. [4]Bishop and Bird (1987). [5]McDowell and Elders (1980). [6]Ballantyne (1981). Temperatures estimated to nearest 5°C from static log (Glenn and Hulen, 1979).

The high smectite contents of the Salton Sea samples from depths of 622 and 675 m, relative to the Roosevelt Hot Springs and Coso samples may be due to differences in the fluid chemistries between the systems. The rate of illitization in hydrothermal experiments is slowed by the presence of Ca, Mg and Na (Eberl and Hower, 1976; Roberson and Lahann, 1981). The K/Ca ratio in Salton Sea fluids (Helgeson, 1968) is 2 to 3 orders of magnitude lower than in fluids from Coso (Bishop, 1985) or Roosevelt Hot Springs (Capuano and Cole 1982). K/Na and K/Mg are of similar orders of magnitude in all three systems.

Analytical and/or mathematical limitations may also cause uncertainties in temperatures calculated from compositions. Smectite contents of 5, 4, 3, 2 and 1% respectively correspond to temperatures of 284°, 298°, 317°, 346° and 403°C. Because of the detection limits for Ca and Na it seems that 300°C is a practical limit above which the interlayer site can be considered completely filled, i.e. that illite becomes muscovite. The lower temperature limit for the geothermometer is about 200°C. "Pure" non-expanding illite containing 0.75 K^+ per $O_{10}(OH)_2$ (Srodon et al., 1986) corresponds to 25% calculated smectite, and has a calculated geothermometer temperature of 202°C.

We have limited our discussion to non-expanding illites because of lack of good analytical data on expandable illite/smectite from geothermal systems. Extrapolation of the geothermometer into the expandable range (Fig. 4), shows that 100% smectite yields a temperature of 147°C. Smectite persists in many geothermal systems to higher temperatures than this, and mixed-layer illite/smectite can occur at lower temperatures (Hulen and Nielson, 1986). Figure 4 also compares XRD data for samples from two Salton Sea wells (Moore and Adams, 1988) to the predicted geothermometer. Temperatures shown were obtained from fluid inclusions in anhydrite from the same or adjacent samples. The smectite content estimated by XRD is increased by 25% non-expandable smectite as discussed above. The predicted temperatures are better for those samples having intermediate expandabilities than those at either end of the range. This relationship suggests that expanding interstratified illite/smectite may behave differently from non-expanding illite.

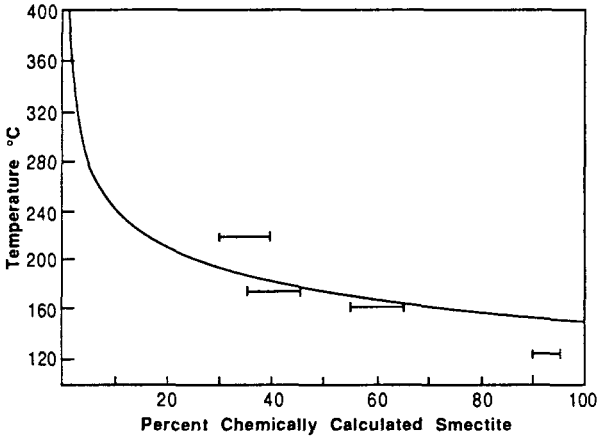


Figure 4. Geothermometer curve extrapolated to 100% smectite. Shown for comparison are expandable illite/smectites from two Salton Sea wells (Moore and Adams, 1988, this volume). An assumed 25% non-expandable smectite is added to XRD-determined expandabilities. Temperatures are from fluid inclusions.

For comparison with the temperature dependence of smectite content (Fig. 3), the relationship between temperature and the mole fraction of muscovite + paragonite is shown in Fig. 5. All samples in Table 1 are included

in Fig. 5. Sericites from the saline Salton Sea system appear to behave differently from the dilute system samples.

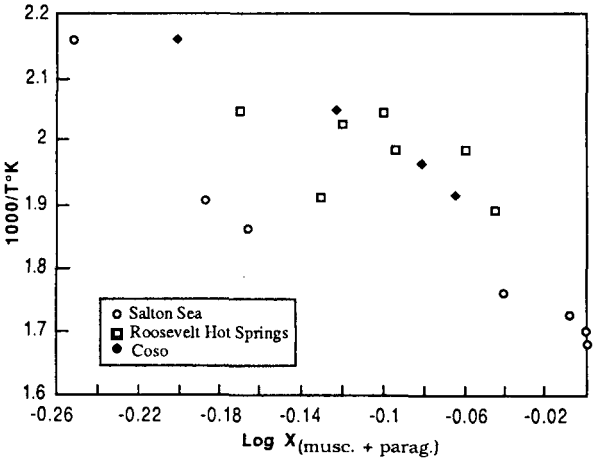


Figure 5. Relationship of temperature (°K) to calculated muscovite plus paragonite content of sericite. Data are from Table 1.

ILLITE/SMECTITE AND THE NA-K-CA GEOTHERMOMETER

Because illite and interstratified illite/smectite are so common in geothermal systems, these minerals are expected to exert some control on fluid chemistry. The relationship between Na, K and Ca in geothermal fluids should therefore be consistent with equilibria involving illite/smectite. Possible reactions include:

$$Ca_{smectite} + Na_{smectite} + 1.0K^{+} = K_{muscovite} + 0.175Ca^{++} + 0.35Na^{+} \quad (3)$$

for non-expanding illite, and:

$$Ca_{smectite} + Na_{smectite} + 0.75K^{+} = K_{illite} + 0.175Ca^{++} + 0.35Na^{+} \quad (4)$$

for expanding illite/smectite.

The equilibrium constants for these reactions are:

$$K = (Ca^{++})^{0.175}(Na^{+})^{0.35} / (K^{+})^{1.0} \quad (5)$$

and:

$$K = (Ca^{++})^{0.175}(Na^{+})^{0.35} / (K^{+})^{0.75} \quad (6)$$

A test for such a relationship can be made using the data that Fournier and Truesdell (1973) used to derive the empirical Na-K-Ca geothermometer. Only those samples with measured temperatures ≥100°C are used in this figure. Figure 6 shows the data plotted in logarithmic form according to Eqn. 6. The correlation coefficient, r, for a regression of this data is 0.95. Similar regressions can be calculated using the logarithmic form of Eqn. 5 (r=0.92), and the empirical geothermometer (r=0.96) as the dependent variables. In the case of the empirical geothermometer, the expression used is: Log(Na/K) + (1/3)Log((Ca)$^{0.5}$/Na). Nearly identical correlation coefficients of 0.96 and 0.95 are obtained for the empirical geothermometer and for the equilibrium constant expression for illite/smectite. This suggests that the relationship of Na, K and Ca in geothermal fluids is controlled by reactions involving illite/smectite.

An alternative expression for the Na-K-Ca geothermometer, based on illite/smectite equilibrium, is given by:

$$T\ °C = 1.145*10^{3}/\{[0.35LogNa+0.175LogCa-0.75LogK] +1.51\} - 273.$$

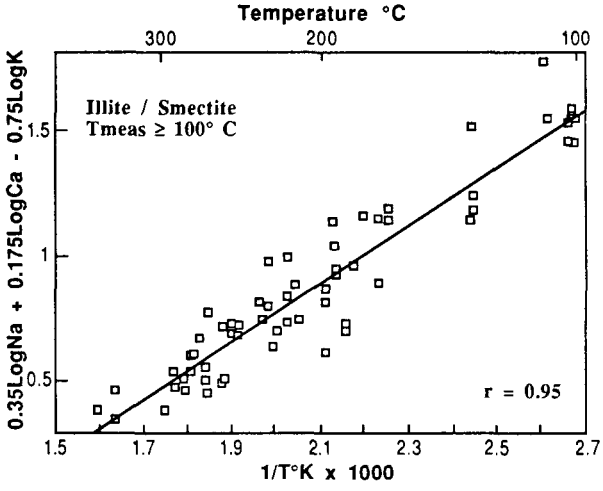


Figure 6. Fit of fluid chemistry to the equilibrium constant expression for illite/smectite equilibrium, Eqn. 6. Data are those with measured temperatures ≥100°C, from Fournier and Truesdell (1973).

CONCLUSIONS

The data discussed above challenge the conventional belief that illite does not contain smectite. The calculated smectite content of illite appears to be a reasonable predictor of temperature, at least for the published data available. More studies are necessary to test the geothermometer derived here.

Aqueous concentrations of Na, K and Ca are consistent with equilibria involving illite/smectite. Testing of the illite/smectite equilibrium form of the equation for the Na-K-Ca geothermometer is recommended.

Because of the exchangeability of interlayer cations in smectite and the general non-reversibilty of the smectite to illite reaction, use of the illite geothermometer derived here may be restricted to systems in which the associated aqueous chemistry conforms to the Na-K-Ca geothermometer. Thus illites in sedimentary basin systems, and in waning or fossil hydrothermal systems subjected to subsequent, non-illitizing fluids, may not fit the model described here.

ACKNOWLEDGEMENTS

Funding for this investigation was provided by the Department of Energy under contract numbers DE-AC03-84F12196 and DE-AC07-85ID12489. Discussions with J. B. Hulen provided information about temperature ranges of geothermal illite/smectite. P. Daubner drafted the illustrations.

REFERENCES

BALLANTYNE, J. M. (1981), Geochemistry of hydrothermal sericite and chlorite. Ph.D. dissertation, University of Utah, 134 p.

BIRD, D. K. and NORTON, D. L. (1981), Theoretical prediction of phase relations among aqueous solutions and minerals: Salton Sea geothermal system. Geochim. Cosmochim. Acta, 45, 1479-1493.

BISHOP, B. P. (1985), Correlation of hydrothermal sericite composition with temperature and permeability, Coso Hot Springs geothermal field, Inyo County, California. M.S. thesis, Stanford University, 45 p.

BISHOP, B. P. and BIRD, D. K. (1987), Variation in sericite compositions from fracture zones within the Coso Hot Springs geothermal system. Geochim. Cosmochim. Acta 51, 1245-1256.

BROWN, P. R. L. (1978), Hydrothermal alteration in active geothermal fields. Ann. Rev. Earth Planet. Sci., 6, 229-250.

CAPUANO, R. M. and COLE, D. R. (1982), Fluid-mineral equilibria in a hydrothermal system, Roosevelt Hot Springs, Utah: Geochim. Cosmochim. Acta, 46, 1353-1364.

DEER, W. A., HOWIE, R. A, and ZUSSMAN, J. (1966), An introduction to the rock-forming minerals. John Wiley and Sons, 528 p.

DREVER, I. (1982), The geochemistry of natural waters. Prentice-Hall, 388 p.

EBERL, D. and HOWER, J. (1976), Kinetics of illite formation. Geol. Soc. Am. Bull. 87, 1326-1330.

GLENN, W. E. and HULEN, J. B. (1979), Interpretation of well log data from 4 drillholes at Roosevelt Hot Springs KGRA: Earth Science Laboratory, University of Utah Research Institute Report 28, DOE/DGE contract EG-78-0-07-1701. 74 p.

HELGESON, H. C. (1968), Geologic and thermodynamic characteristics of the Salton Sea geothermal system. Am. Jour. Sci., 266, 129-166.

HULEN, J. B. and NIELSON, D. L. (1986), Hydrothermal alteration in the Baca geothermal system, Redondo Dome, Valles caldera, New Mexico. J. Geophys. Res. 91, No. B2, 1867-1886.

FOURNIER, R. O. and TRUESDELL, A. H. (1973), An empirical Na-K-Ca geothermometer for natural waters. Geochim. Cosmochim. Acta, 37, 1255-1275.

McDOWELL, S. D. and ELDERS, W. A. (1980), Authigenic layer silicate minerals in borehole Elmore 1, Salton Sea geothermal field, California, USA. Contrib. Mineral. Petrol., 74, 293-310.

MOORE, J. N. and ADAMS, M. C. (1988), Evolution of the thermal cap in two wells from the Salton Sea geothermal system, California. Thirteenth Workshop on Geothermal Reservoir Engineering (this volume).

PARRY, W. T., BALLANTYNE, J. M., and JACOBS, D. C. (1984), Geochemistry of hydrothermal sericite from Roosevelt Hot Springs and the Tintic and Santa Rita porphyry copper systems. Econ. Geol., 79, 72-86.

ROBERSON, H. E. and LAHANN, R. W. (1981), Smectite to illite conversion rates: effects of solution chemistry. Clays and Clay Minerals, 29, 129-135.

SRODON, J., MORGAN, D. J., ESLINGER, E. V., EBERL, D. D., and KARLINGER, M. R. (1986), Chemistry of illite/smectite and end-member illite. Clays and Clay Minerals, 34, 368-378.

PROCEEDINGS, Thirteenth Workshop on Geothermal Reservoir Engineering
Stanford University, Stanford, California, January 19-21, 1988
SGP-TR-113

A WELLBORE FLOW MODEL IN THE PRESENCE OF CO_2 GAS

Masahiro Takahashi

Japan Metals & Chemicals Co., Ltd. (JMC)
24-Ukai, Takizawa-mura, Iwate 020-01 Japan

ABSTRACT

The fluid produced by the geothermal wells in the Nigorikawa field which is located in southern Hokkaido, Japan's northern island, is rich in carbon dioxide(CO_2). The dissolved CO_2 causes a scale deposition problem of calcium carbonate($CaCO_3$).

Japan Metals & Chemicals Co., Ltd.(JMC) has already solved the $CaCO_3$ scale deposition problem by injecting a scale inhibiting chemical fluid directly and continuously through a injection tube extending into the production well.

The $CaCO_3$ scale deposition occurs at the flash point. It is important, therefore, to estimate the flash depth correctly so that the depth of the chemical injection point can be determined.

However, the boiling point curve of the geothermal fluid with dissolved CO_2 is different from that of pure water(H_2O). So, a wellbore flow model in the presence of CO_2 gas has been developed.

This model was tested by comparing the temperature and pressure values calculated by the computer to depth profiles drawn the Nigorikawa field data. As a result of the comparison, a satisfactory fitting has been obtained.

A brief explanation of this model and a few examples of analysis by this model are presented.

INTRODUCTION

Japan Metals & Chemicals Co., Ltd.(JMC) has been producing steam and supplying it to three geothermal power stations in Japan. The locations of these power stations are shown in Fig. 1.

The Nigorikawa (Mori) geothermal field located in southern Hokkaido is a hot water dominated area. The Mori geothermal power station began to generate electricity (50MWe) in 1982. The fluid produced in the Nigorikawa field is rich in carbon dioxide(CO_2). The average concentration in 1982 was about 8 weight %. The present average concentration is about 1 weight %.

Output of the 50MWe power station decreased soon after the plant began operating in November, 1982. This is due to the plugging effect by the deposition of $CaCO_3$ scale formed in the production wells.

The problem of $CaCO_3$ scale deposition has been solved by injecting a scale inhibiting chemical fluid directly and continuously through a chemical injection tube extending into the production well. $CaCO_3$ scale deposition occurs at the flash point in each production well. Therefore,

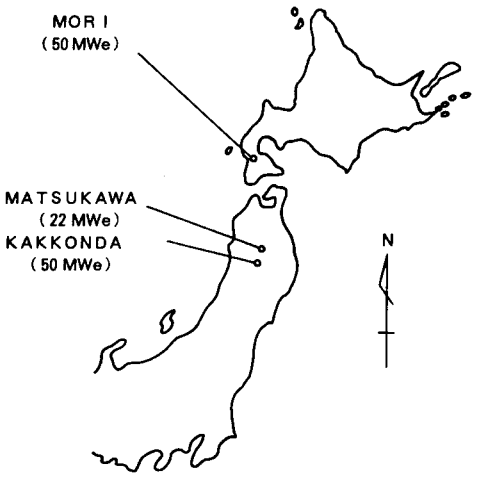


Fig.1 Locations of geothermal power stations where JMC supplies steam

to adopt this prevention system, it is necessary to estimate the flash depth of each production well so that a depth of the chemical injection point can be determined.

The wellbore flow model in the presence of CO_2 gas developed by JMC is useful for the following items.

- Calculation of the flash depth
- Estimation of the various reservoir conditions (kh, reservoir temperature and/or pressure)
- Prediction of the steam productivity from a production well making use of the predictions of the reservoir behavior made with a reservoir simulator.

GOVERNING EQUATIONS

A wellbore flow model in the presence of CO_2 gas has been developed under the following assumptions.

1. The geothermal fluid has steady-state flow.
2. The flash point is in the wellbore.
3. The CO_2 concentration in the incoming compressed water to the production well is constant even if the flow rate varies.
4. The heat exchanged between the geothermal fluid and surrouding rocks can be ignored.
5. Henry's law is valid.

This model is constructed from three calculation parts as shown Fig. 2.

(a) Calculation of bottom hole conditions

The single phase water flow in the formation in the vicinity of the production well can be expressed as Darcy's law.

$$G=2\pi kh\gamma/\mu/\ln(re/rw)\cdot(Pe-Pw) \qquad (1)$$

In this equation, viscosity and specific weight

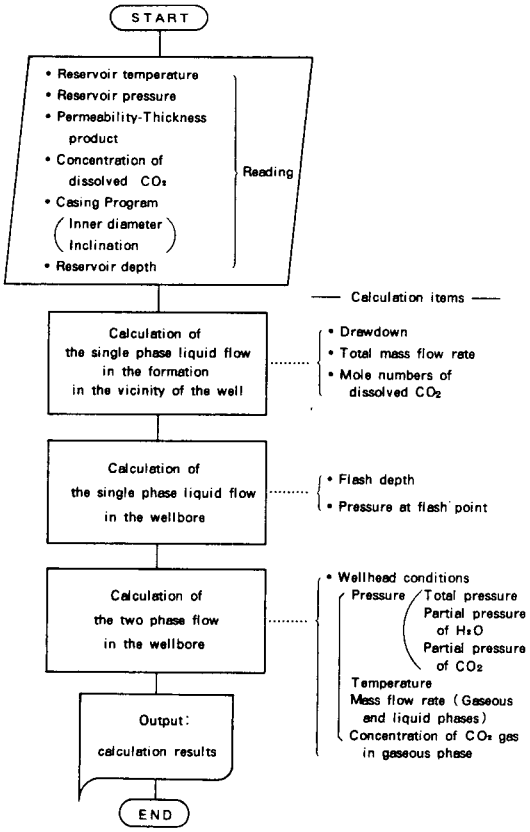


Fig. 2 Computer code flow diagram

values are assumed equal to those of pure water. Mole numbers of CO_2 in the incoming compressed water to the production well, furthermore, are calculated from

$$Mco_2=1000G\cdot Cco_2/44 \quad (2)$$

(b) Calculation of flash point

The flash point can be calculated from total pressure as the sum of partial pressure of CO_2 and vapor pressure of pure water at reservoir temperature. The partial pressure of CO_2 can be evaluated by Henry's law. Henry's constant is used in a function of temperature proposed by S.D.Malinin(1963).

$$Kco_2=39.66+67.7403\cdot T-0.17884\cdot T^2 \quad (3)$$

The flash depth corresponding to this total pressure can be calculated from the upward flow equations of the single phase water. Thus

$$Ph=\gamma\cdot dl\cdot\cos(\theta) \quad (4)$$
$$Pf=\lambda/2/g/D\cdot\omega^2\cdot\gamma\cdot dl \quad (5)$$

(c) Calculation of two phase flow through the wellbore

The two phase upward flow through the wellbore is accompanied by a decrease in pressure and temperature. For the numerical approach to calculate the conditions in two phase flow, therefore, the secant method is used. That is, total pressure corresponding to an arbitrary drop of fluid temperature is calculated first. Secondly, the depth corresponding to this total pressure is calculated.

(c-1) Calculation of total pressure

The steam quality in the H_2O component can be calculated from

$$\chi=(h-h')/r \quad (6)$$

Mole numbers of water and steam can be calculated from

$$H_2OL=(1000G-44Mco_2)\cdot(1-\chi)/18 \quad (7)$$
$$H_2OV=(1000G-44Mco_2)\cdot\chi/18 \quad (8)$$

The mole ratio between gaseous and dissolved CO_2 is expressed by W.F.Giggenbach(1980). Thus

$$Bco_2=10^{(4.7593-0.01092\cdot T)} \quad (9)$$

Mole numbers of dissolved CO_2, furthermore, can be also calculated from the definition equation of the vapor-liquid gas distribution coefficient(Bco_2) as follows.

$$CO_2L=Mco_2\cdot H_2OL/(H_2OV\cdot Bco_2+H_2OL) \quad (10)$$

Total pressure can be obtained as the sum of partial pressure of CO_2 calculated from (3) equation and vapor pressure of pure water corresponding to an arbitrary temperature.

(c-2) Calculation of a corresponding depth to the total pressure

The pressure drop per unit pass length can be expressed as the sum of head, acceleration and friction losses. A depth corresponding to the total pressure, therefore, is calculated from these losses.

•Head loss

The head loss can be evaluated from the definition equation of the void fraction. Thus

$$Ph=[fg/\upsilon v+(1-fg)\cdot\upsilon L]\cdot dl\cdot\cos(\theta) \quad (11)$$

where the specific weight of the gaseous phase is calculated from the state equation of an ideal gas as

$$\upsilon v=(H_2OV/PH_2O+CO_2V/Pco_2)\cdot 0.8478\cdot(T+273.15)/(H_2OV\cdot 18+CO_2V\cdot 44) \quad (12)$$

The void fraction, furthermore, is evaluated by an experimental equation obtained from a matching with the field data from the Takinoue.

•Acceleration loss

The acceleration loss can be evaluated from the definition equation of momentum as

$$Pa=(G/F)^2/g\cdot(\upsilon me-\upsilon min) \quad (13)$$

where

$$\upsilon me=[1+\chi\cdot(S-1.0)]\cdot[1+\chi\cdot(\upsilon v/\upsilon L/S-1)]\cdot\upsilon L \quad (14)$$

$$\chi=(H_2OV\cdot 18+CO_2V\cdot 44)/G \quad (15)$$

•Friction loss

The friction loss is evaluated from the following equations depending upon the flow regimes.

[Bubble flow]

An equation proposed by Inoue and Aoki(1965) is adopted. Thus

$$Pf=(B/BL)\cdot[(1-fg)+fg\cdot\upsilon L/\upsilon v]^{3/4}/[1-fg/K\cdot(1-\upsilon L/\upsilon v)]^{7/4}\cdot\Delta PLO \quad (16)$$

[Slug flow]

An adopted equation is proposed by D.Chisholm et al.(1969-70).

$$Pf=\upsilon m/(1-\chi)^2/\upsilon L\cdot\Delta PLO \quad (17)$$

[Mist flow]

The pressure loss under the condition of mist flow is calculated from the following equation proposed by Akagawa(1974) as the sums of head, acceleration and friction losses. Thus

$$PT=Ph+Pa+Pf=(4\cdot\tau L/D+\gamma m)\cdot dl\cdot\cos(\theta) \quad (18)$$

[Discrimination of flow regime]

Two discriminating criteria proposed by P. Griffith et al.(1961) and L.P.Golan et al. (1969-70) are adopted to determine the flow pattern.

COMPARISON WITH FIELD DATA

The model described above was tested by comparing the values calculated by the computer with temperature and pressure profiles drawn from the Nigorikawa field data measured during production.

JMC measures temperature and pressure profiles during production with the Kuster gauge. The Kuster gauge's error gradually changes owing to the change of the coefficient of elasticity of its mechanical sensor (bimetal or bourdon tube). So, to maintain the accuracy, JMC calibrates the Kuster gauge with a calibration machine developed in house.

Fig. 3 shows the comparison between temperature and pressure profiles calculated by the computer and field profiles. As is evident from Fig. 3, the calculated values gives good agreement with the Nigorikawa field data. It seems, hence, that this model is accurate enough for practical use.

EXAMPLES OF USE

(a) Estimation of the reservoir conditions

The $CaCO_3$ scale deposition in the production wells in the Nigorikawa field has been prevented by a scale inhibiting chemical fluid injected directly and continuously through a chemical injection tube extending into the well to the geothermal fluid. A production logging in order to measure the historical changes of reservoir temperature and pressure of the production well cannot be carried out while the chemical injection tube is in place.

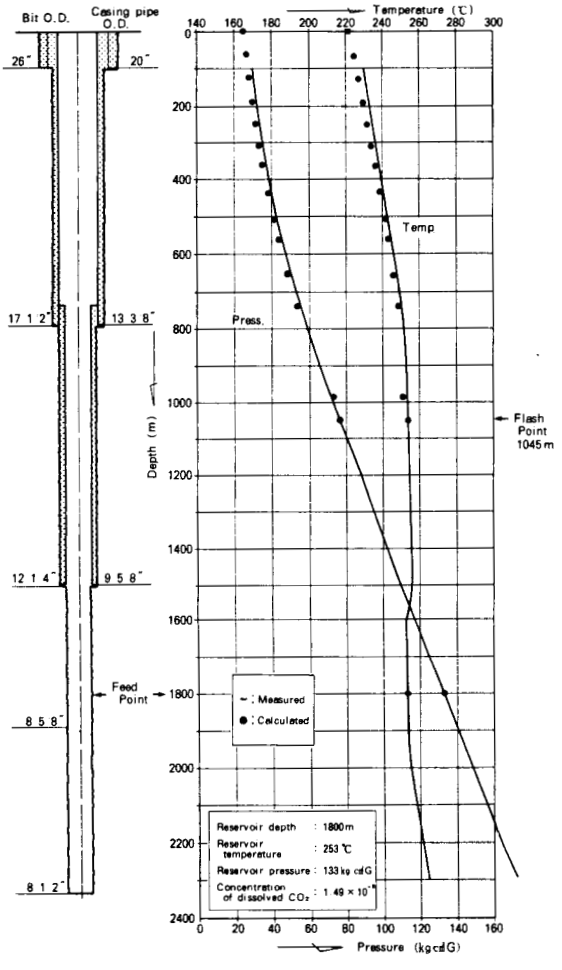


Fig. 3 Comparison between temperature and pressure profiles calculated by the computer and field profiles during production

So, we estimate the reservoir conditions through matching with a flow characteristic (flow rate versus wellhead pressure) obtained by the surface equipment only as shown Fig. 4.

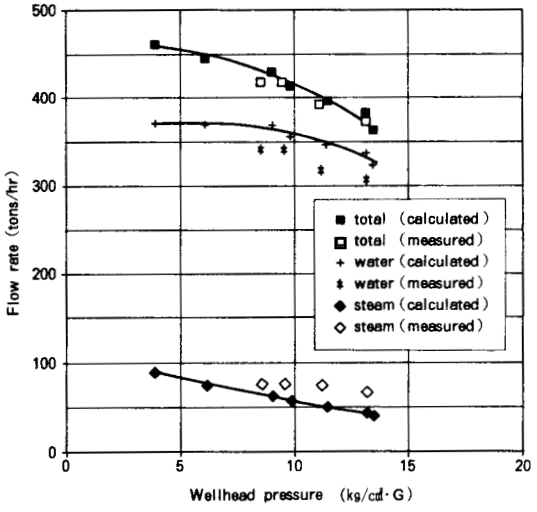


Fig.4 Matching result between measured and calculated characteristic production curves

(b) Determination of the depth of the chemical injection point

In order to prevent $CaCO_3$ scale deposition, the location of the chemical injection point in the production well must be lower than the flash depth. Hence, we evaluate the flash depth as shown in Fig. 5 and determine the chemical injection point.

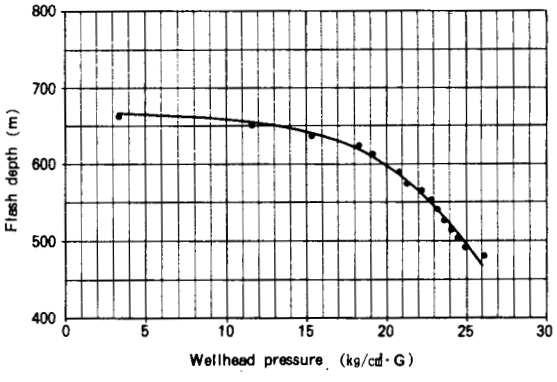


Fig.5 Correlation between flash depth and wellhead pressure

(c) Prediction

Presently, we are evaluating the Nigorikawa field through the historical matching by the reservoir simulator. In predicting the reservoir behavior, it will be important that the steam productivity from each production well at an arbitrary time is predicted accurately. So, this model will play an important part in obtaining an accurate prediction.

CONCLUSIONS

1. A wellbore flow model in the presence of CO_2 gas has been developed.
2. Comparison of the results of the computer program and the experimental temperature and pressure profiles shows that these are in satisfactory agreement.
3. The wellbore flow model can be applied to estimate the reservoir conditions in the vicinity of a production well through the matching between a measured characteristic production curve and a calculated one.
4. The model can be also used in evaluating the depth of $CaCO_3$ scale deposition. The $CaCO_3$ scale problem in the production wells can be, hence, prevented by a chemical injection tube inserted deeper than the calculated flash depth in the well, wherein scale inhibiting chemical fluid is injected through the tube directly and continuously to the geothermal fluid.
5. A good example of use will be in predicting the steam production rate from each well with the prediction results by reservoir simulator.

NOMENCLATURE

B =function of void fraction, specific weight, velocity, and viscosity
B_{CO_2}=vapor-liquid gas distribution coefficient
BL =constant
C_{CO_2}=CO_2 concentration in the incoming compressed fluid to the well
CO_2L=mole numbers of dissolved CO_2 (mole)
CO_2V=mole numbers of gaseous CO_2 (mole)
D =inner pipe diameter (m)
dl =unit pass length (m)
F =cross-sectional area of pipe (m^2)
fg =void fraction
G =total mass flow rate (kgf/s)
g =gravity acceleration (m/s^2)
h =specific enthalpy of the incoming compressed fluid to the well (kcal/kgf)
h' =specific enthalpy of water (kcal/kgf)
H_2OL=mole numbers of water (mole)
H_2OV=mole numbers of steam (mole)
K =flow parameter
K_{CO_2}=Henry's constant
kh =permeability•thickness product (m^3)
M_{CO_2}=mole numbers of CO_2 in the incoming compressed fluid to the well (mole)
Pa =acceleration loss (kgf/m^2)
P_{CO_2}=partial pressure of CO_2 (kgf/m^2)
Pe =reservoir pressure (kgf/m^2)
Pf =friction loss (kgf/m^2)
P_{H2O}=vapor pressure of pure water (kgf/m^2)
Ph =head loss (kgf/m^2)
PT =total pressure loss (kgf/m^2)
Pw =wellbottom flowing pressure (kgf/m^2)
r =heat of vaporization (kcal/kgf)
re =reservoir radius (m)
rw =wellbore radius (m)
T =temperature (°C)
γ =specific weight of fluid (kgf/m^3)
γm =specific weight of the liquid-gas mixture (kgf/m^3)
θ =inclination (deg.)
λ =friction factor
μ =viscosity ($kgf \cdot s/m^2$)
τL =shearing stress on the pipe (kgf/m^2)
υL =specific volume of liquid phase (m^3/kgf)

υ_m =specific volume of the liquid-gas mixture (m^3/kgf)

υ_{me} =specific volume of the liquid-gas mixture at the outlet of interval (m^3/kgf)

υ_{min}=specific volume of the liquid-gas mixture at the inlet of interval (m^3/kgf)

υ_v =specific volume of gaseous phase (m^3/kgf)

χ =quality

ω =velocity (m/s)

ΔP_{LO}=friction loss under the single phase liquid flow (kgf/m^2)

REFERENCES

Akagawa,K.(1974),"Gas-liquid two-phase flow', Corona publishing Co., Ltd. (in Japanese)

Barelli,A.,Corsi,R.,Pizzo,G.D.,Scali,C.(1982), "A two-phase flow model for geothermal wells in the presence of non-condensable gas", Geothermics,Vol.11,No.3,175-191

Chisholm,D.(1969-70),L.A.Sutherland, Inst. of Mech. Engrs. Proceeding, 184, Pt. 3c, 24

Giggenbach,W.F.(1980),"Geothermal gas equilibrium", Geochimica et cosmochimica acta, Vol.44 2021-2032

Golan,L.P.,Stenning,A.H.(1969-70), Proc. Ind. Mech. Engrs., 184, Pt. 3c, 108

Griffith,P.,Wallis,G.B.(1961),"Two-phase slug flow", Trans. ASME, Ser. C, Vol.83, No.3

Inoue,Aoki(1965), Collection of thesis in the Japanese society of mechanical engineers, 31-224, 588 (in Japanese)

JMC(1975),"Know-how book:The control technology of the production wells", Japan Metals & Chemicals Co., Ltd. Report (in Japanese)

Malinin,S.D.(1963),"An experimental investigation of the solubility of calcite and witherite under hydrothermal conditions", Geochemistry, No.7, 650-667

The Japan society of mechanical engineers (1968), Steam tables

PROCEEDINGS, Thirteenth Workshop on Geothermal Reservoir Engineering
Stanford University, Stanford, California, January 19-21, 1988
SGP-TR-113

COMPUTER CODE OF TWO-PHASE FLOW IN GEOTHERMAL WELLS PRODUCING WATER AND/OR WATER-CARBON DIOXIDE MIXTURES

Shouichi Tanaka and Kosuke Nishi

The University of Tokyo, Faculty of Engineering
Hongou, Bunkyouku, Tokyo 113, Japan

ABSTRACT

Mathematical well models are developed for pure water and for water-carbon dioxide mixtures. For the slug flow regime, three correlations (Orkiszewski's, Nicklin's and modified Nicklin's) are compared. An equation-of-state package for water-carbon dioxide mixtures is proposed as a function of pressure and temperature. The predicted values are compared with sixteen field cases, in which the maximum carbon dioxide content is 2.8 %.

INTRODUCTION

A wellbore configuration shown in Fig. 1 is used for a computer code of the two-phase flow in geothermal wells. Well inclination, diameter of conduit and heat loss to surrounding formations are included in the code. Two sets of computer codes, a GSW code and a GCW code, are developed. The GSW code is applicable to a pure water system. The GCW code is an extended version of the GSW code, and has a routine to calculate the phase behavior and properties of a water-carbon dioxide system. The GSW code is described here and the GCW code is described in the next section.

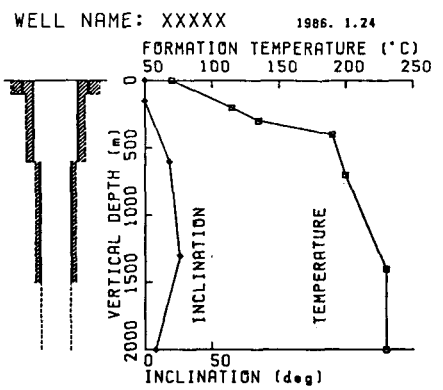


Fig. 1. Model of well configuration.

A flow diagram of the GSW code is shown in Fig. 2. Thermodynamic properties of water and steam are estimated by the formulas in JSME STEAM TABLES. The GSW code can calculate a flashing point and profiles of pressure, temperature, enthalpy, steam quality, density and flow regime. An example output of the GSW code is show in Fig. 3 for a hypothetical well.

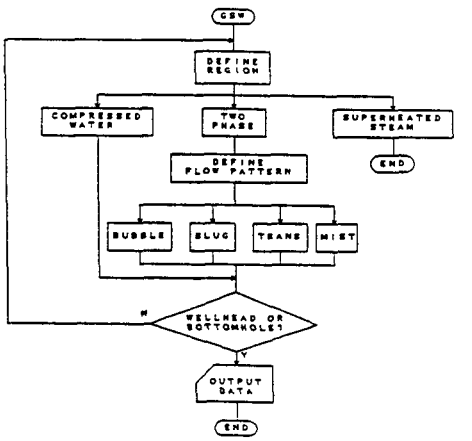


Fig. 2. Flow diagram of a GSW code

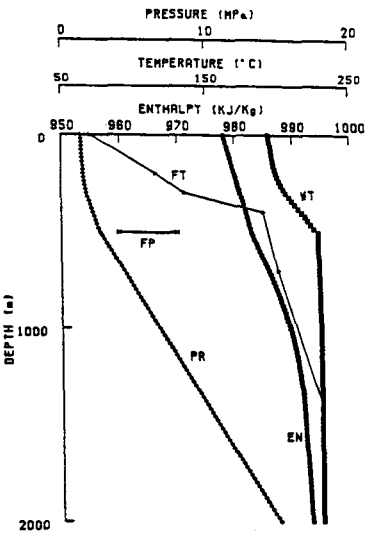


Fig. 3. An example output of the GSW code, PR:Pressure, WT:Temperature of wellbore, EN:Enthalpy, FP:Flashing point and FT:Formation temperature.

Griffith and Wallis correlation is used for bubble flow, and Duns and Ros correlations are used for transition and mist flows. For the slug flow regime, the following correlations are compared in this study:
(1) Orkiszewski correlation.
The mixture density and bubble rise velocity are evaluated by Orkiszewski correlation. A proposal by Gudmundsson et al. is employed to evaluate the liquid distribution factor Γ.
(2) Nicklin correlation.
The mixture density is evaluated by Griffith and Wallis correlation. The bubble rise velocity is calculated by a following equation obtained by Nicklin et al.:

$$V_b = \Lambda V_m + 0.35\sqrt{gd} \qquad (1)$$

where $\Lambda = 0.2$ when $N_{Re} > 8000$.

(3) Modified Nicklin correlation.
The Λ value of equation (1) is assumed to 0.1. The mixture density is evaluated by Griffith and Wallis correlation.
A comparison of these methods is shown in MODEL EVALUATION section.

MODEL FOR WATER-CARBON DIOXIDE MIXTURE

A flow diagram of the GCW code is shown in Fig. 4. An equation-of-state package for water-carbon dioxide mixture is constructed. The dew point pressure of the system is estimated by Dalton's law of partial pressures and Rault's law for solvent, but the mole fraction is replaced by the mass fraction according to Sutton:

$$P_d = P_w/(1-n_c) \qquad (2)$$

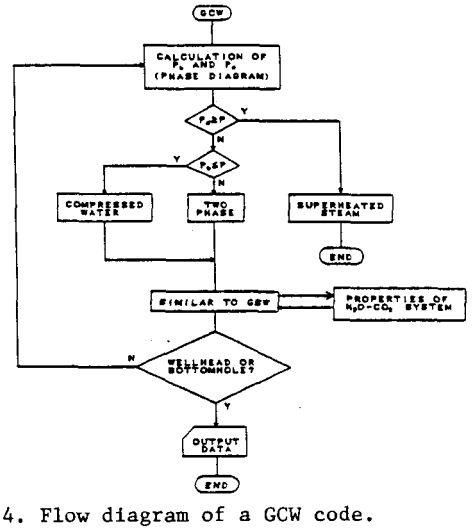


Fig. 4. Flow diagram of a GCW code.

The modified Henry's coefficient proposed by Sutton has been used so far to estimate the solubility of carbon dioxide in water, but this method considers only the effect of temperature. We propose a new approach to estimate the solubility of carbon dioxide in water as a function of temperature and pressure. Experimental solubility data of carbon dioxide in water are collected as shown in Fig. 5 from Dodds et al., Ellis et al. and Takenouchi et al. Polynominal fittings are employed in the several pressure levels from 0.1 MPa to 30 MPa. The intermediate value is interpolated.

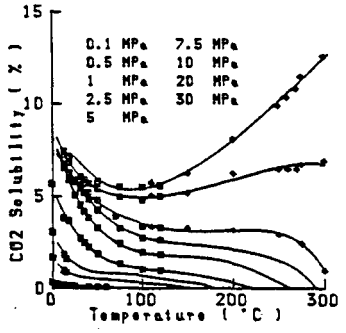


Fig. 5. Compiled solubility data of carbon dioxide in water.

The following matters are estimated from Fig. 5:
(1) Bubble point pressure.
When the concentration of carbon dioxide in the system is known, the bubble point is able to be calculated as a function of temperature. If a calculated pressure is greater than the bubble point, the system is in the compressed water region. If the pressure is less than the bubble point, the system is in the two-phase region. If the pressure is equal to the bubble point, this depth is a "Flashing Point".

(2) Distribution of carbon dioxide in liquid phase.
In the two-phase region, mass fraction of carbon dioxide in liquid phase is equal to the solubility of carbon dioxide in water at the calculated temperature and pressure.

(3) Distribution of carbon dioxide in gas phase.
In the two-phase region, mass fraction of carbon dioxide in gas phase is calculated by the following modified Dalton's law according to Sutton:

$$n_{gc} = P_c/P \qquad (3)$$

$$P_c = P-P_w \qquad (4)$$

(4) Mass fraction of gas phase(quality).
In the two-phase region, mass fraction of gas phase is calculated by the following equation:

$$n_g = (n_c-n_{lc})/(n_{gc}-n_{lc}) \qquad (5)$$

A calculated phase diagram of the water-carbon dioxide system is shown in Fig. 6 about four concentrations of carbon dioxide in system from 0.5 % to 3 %. Dew point curves are not plotted since they are located so closely to the pure water curve. Bubble point curves are affected significantly by the concentration of carbon dioxide.

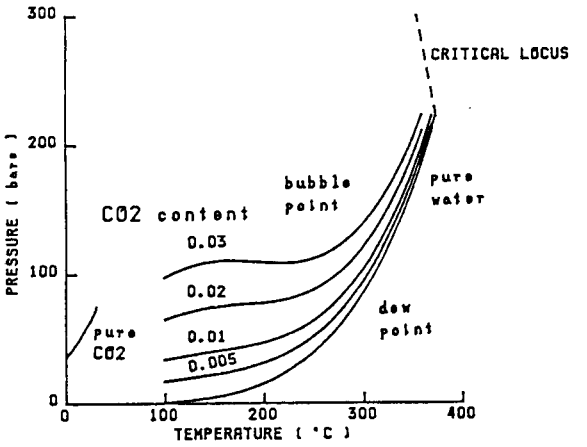


Fig. 6. Phase diagram of water-carbon dioxide system.

Thermodynamic properties of carbon dioxide are interpolated from the tables of Vargaftik. The properties of water-carbon dioxide system are calculated by the following equations for each region:

(1) Compressed water region.

The specific volume, viscosity and thermal conductivity of the solution are assumed to be the same as those of pure water. The specific enthalpy of the solution is calculated from

$$h(P,T,n_c) = (1-n_c)h_w(P,T) + n_c\{h_c(P,T) + h_{soln}(P,T)\} \quad (6)$$

The heat of solution is given by Ellis et al.

(2) Two-phase region.

The specific volume, viscosity and thermal conductivity of the liquid phase are assumed to be the same as those of pure water. The specific enthalpy of the liquid phase is calculated from

$$h_l(P,T,n_{lc}) = (1-n_{lc})h_w(P,T) + n_{lc}\{h_c(P,T) + h_{soln}(P,T)\} \quad (7)$$

The specific volume, specific enthalpy, viscisity and thermal conductivity of the gas phase are calculated from

$$v_g(P,T,n_{gc}) = (1-n_{gc})v_w(P_w,T) + n_{gc}v_c(P_c,T) \quad (8)$$

$$h_g(P,T,n_{gc}) = (1-n_{gc})h_w(P_w,T) + n_{gc}h_c(P_c,T) \quad (9)$$

$$\mu_g(P,T,n_{gc}) = (1-n_{gc})\mu_w(P_w,T) + n_{gc}\mu_c(P_c,T) \quad (10)$$

$$\lambda_g(P,T,n_{gc}) = (1-n_{gc})\lambda_w(P_w,T) + n_{gc}\lambda_c(P_c,T) \quad (11)$$

The properties of the system are weighted by mass fractions.

MODEL EVALUATION

Field data are summarized in Table 1. Case Nos. 1, 2 and 3 are for pure water and other thirteen cases for water-carbon dioxide mixtures. The maximum mass fraction of carbon dioxide is 2.8 %. The range of mass flow rate is from 10.8 t/h to 290.0 t/h.

(1) Pure water system, prediction by the GSW code.

Parameters at the wellhead of case No. 3 are summarized in Table 2 to evaluate bubble rise velocity formulas. Liquid Reynolds number is 19.0 million, and total superficial velocity is 8.22 m/s. The bubble rise velocities given by Orkiszewski, Nicklin and modified Nicklin correlations are 295.6 m/s, 2.26 m/s and 1.44 m/s respectively. The bubble rise velocity obtained by Orkiszewski correlation is an unreasonable big value, which shows that its correlation is not suitable for such a huge liquid Reynolds number. On the other hand, the bubble rise velocities given by Nicklin and modified Nicklin correlations seem to be reasonable.

Measured and calculated profiles of the case No.3 are shown in Fig. 7. In this case,

Table 1. Summary of field data.

Case No.	Well name	Mass fraction of CO_2 %	Wellhead Mass flow rate t/h total	liquid	gas	pressure MPa	Bottom hole depth m	pressure MPa	temperature °C
1	W-1	0.0	67.9	47.0	20.9	1.54	945	6.25	246
2	W-1	0.0	114.5	79.0	35.5	1.51	945	5.25	250
3	W-2	0.0	131.0	97.7	33.5	2.96	998	5.21	264
4	C-2	1.0	158.0	148.0	10.0	2.11	1500	8.42	252
5	C-3	0.14	52.0	48.7	3.3	1.44	544	4.18	221
6	C-3	0.13	260.1	245.0	15.1	1.51	544	4.04	221
7	C-4	0.61	290.0	281.0	9.0	1.92	500	4.55	227
8	C-4	0.61	177.0	172.0	5.0	2.01	500	4.81	228
9	C-4	0.61	64.5	60.3	4.2	2.06	500	4.99	230
10	C-5	1.0	206.2	200.0	6.2	1.18	1300	9.25	210
11	C-5	1.0	117.4	114.0	3.4	1.38	1300	10.3	210
12	C-8	2.8	10.8	7.2	3.6	2.34	1500	12.4	265
13	C-8	2.8	15.6	10.4	5.2	2.78	1500	12.4	267
14	C-8	2.8	20.4	13.6	6.8	3.17	1500	12.4	266
15	C-10	1.0	172.0	163.0	9.0	2.89	1500	10.8	255
16	C-10	1.0	76.0	73.0	3.0	2.99	1500	11.8	254

Table 2. Summary of parameters at the wellhead of case No. 3.

Temperature,	°C	:	233
Pressure,	MPa	:	2.96
Quality,		:	0.256
Mass flow rate,	t/h	:	131.0
Well diameter,	m	:	0.3204
Surface tension,	N/m	:	0.0300
Specific volume of water,	m^3/kg	:	0.0012
Specific volume of steam,	m^3/kg	:	0.0676
Viscosity of water,	mPa·s	:	0.114
Viscosity of steam,	mPa·s	:	0.017
Superficial velocity of liquid phase,	m/s	:	0.41
Superficial velocity of gas phase,	m/s	:	7.81
Total superficial velocity,	m/s	:	8.22
Liquid Reynolds number,	$\times 10^6$	:	19.0
Bubble rise velocity by Orkiszewski,	m/s	:	295.6
Bubble rise velocity by Nicklin,	m/s	:	2.26
Bubble rise velocity by this work,	m/s	:	1.44

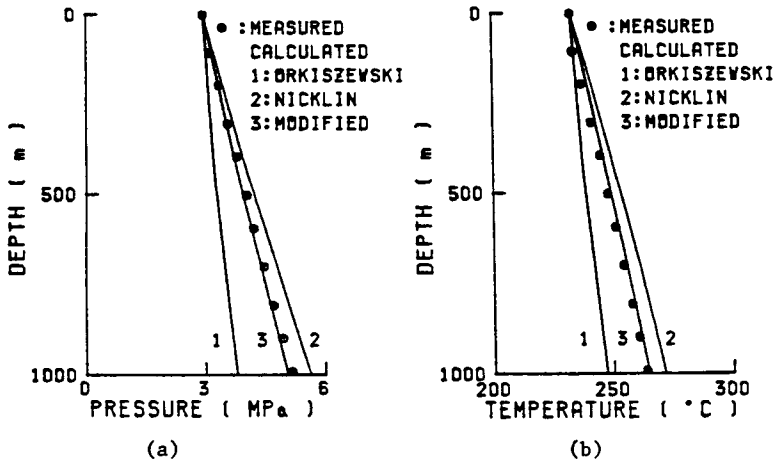


Fig. 7.
Measured and calculated profiles of the case No. 3.

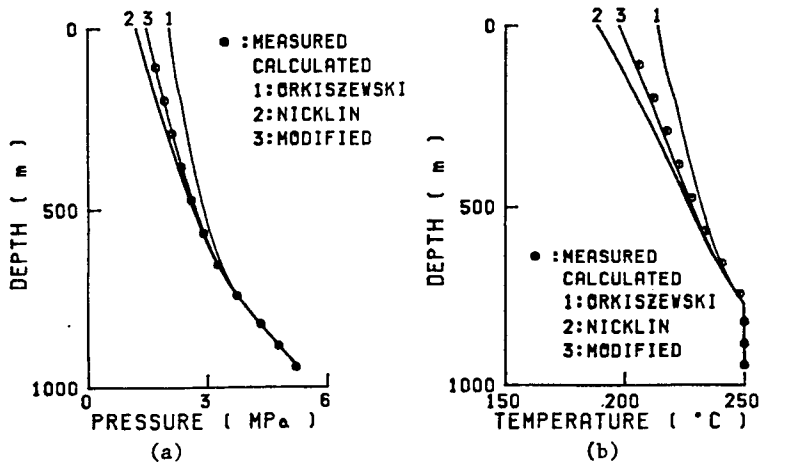


Fig. 8.
Measured and calculated profiles of the case No. 2.

calculation begins from the wellhead condition, because the two-phase state occurs at the bottom hole and the steam quality is not given there. The calculated profiles by the modified Nicklin correlation make an accurate prediction of the field data. The Orkiszewski correlation underestimates, and the Nicklin correlation overestimates in this case. Measured and calculated profiles of the case No. 2 are shown in Fig. 8. In this case, the calculation begins from the bottom hole. The calculated flashing point agrees very well with the observed position. The modified Nicklin correlation satisfactorily predicts the field data.

Calculated results at the wellhead by the modified Nicklin correlation are summarized in the upper part of Table 3.

(2) Water-carbon dioxide system, prediction by the GCW code.

Calculated profiles of 1 % carbon dioxide content and pure water (0 %) are compared with measured data in Fig. 9, in which the effect of carbon dioxide content is obvious. The calculated flashing point deepens from 594 m to 911 m with increasing carbon dioxide content to 1 %.

Distributions of carbon dioxide between both phases are calculated for the case No. 15 as shown in Fig. 10. The gas phase contains much more carbon dioxide than the liquid phase.

Table 3. Summary of calculated results by modified Nicklin.

Case No.	Mass fraction of CO_2	Wellhead					Flow* regime
		Quality	Mass fraction of CO_2		pressure	temperature	
			liquid	gas			
	%	%	%	%	MPa	°C	
1	0.0	11.0			1.48	198	C,B,S
2	0.0	12.1			1.49	198	C,B,S
3**	0.0	19.3***			5.07***	265***	S
4	1.0	10.0	0.06	9.47	2.20	212	C,B,S
5	0.14	7.4	0.01	1.81	1.21	181	C,B,S
6	0.13	6.1	0.01	2.00	1.43	195	C,B,S
7	0.61	4.4	0.08	11.9	2.18	210	C,B,S
8	0.61	4.3	0.08	12.4	2.25	212	C,B,S
9	0.61	4.7	0.08	11.4	2.18	211	C,B,S
10	1.0	5.7	0.08	16.3	1.40	187	C,B,S
11	1.0	4.8	0.10	19.0	1.56	190	C,B,S
12	2.8	8.1	0.44	29.7	4.11	232	C,B
13	2.8	7.8	0.49	30.2	4.57	237	C,B
14	2.8	8.7	0.42	27.7	4.20	234	C,B,S
15	1.0	8.2	0.11	10.9	2.79	224	C,B,S
16	1.0	8.0	0.11	11.2	2.76	223	C,B,S

* C = compressed water
B = bubble
S = slug
T = transition
M = mist

** Calculation begins from wellhead.

*** At bottom hole.

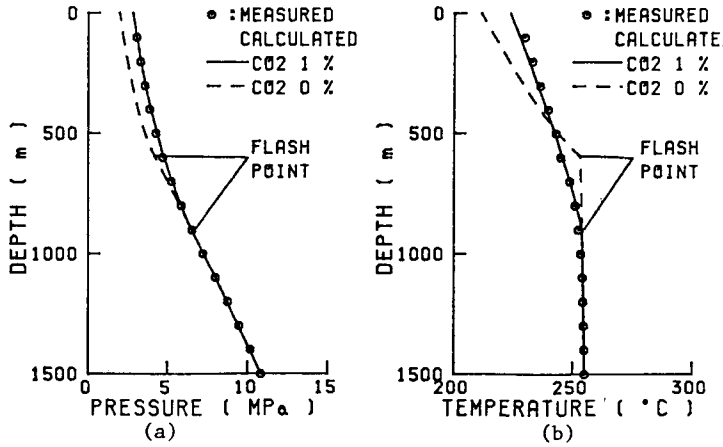


Fig. 9.
Measured and calculated profiles of the case No. 15.

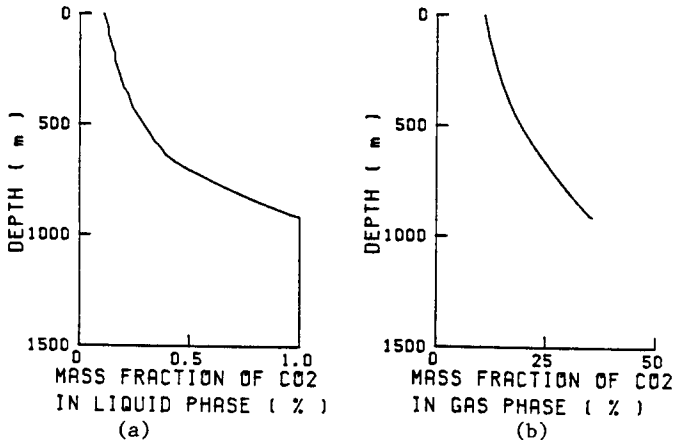


Fig. 10.
Distributions of carbon dioxide between liquid and gas phases for the case No. 15.

Calculated results at the wellhead by the modified Nicklin correlation are summarized in the lower part of Table 3.

(3) Comparison of calculated results with field data.

The predicted pressure losses are compared with measured data in Table 4. For the pure water system, the case No. 1, 2 and 3, the modified Nicklin correlation is better than the others in this study. For the water-carbon dioxide system, following comments are obtained. At low mass flow rate in the well C-8(case Nos. 12, 13 and 14), calculated data are primarily located in compressed water region and bubble flow regime, and the prediction of pressure losses does not agree with field data. For the other cases, the slug flow regime appears in a considerable length of the two-phase region. In ten cases from No. 4 to No. 16 except Nos. 12, 13 and 14, calculated pressure losses fall in ten-percent deviation range in most cases with the Nicklin and/or modified Nicklin correlations. Standard deviations for all cases are 15.57 %, 9.78 % and 7.26 % for Orkiszewski, Nicklin and modified Nicklin correlations, respectively.

One of sources introducing errors is supposed to be the measuring method of carbon dioxide content. The content is usually calculated from the analysis of carbon dioxide in the wellhead steam.

Table 4. Comparison of calculated pressure losses with field data.

Case No.	Pressure loss between bottom hole and wellhead MPa				Percentage error* between calculated and measured ΔP		
	measured	calculated					
		Orkiszewski	Nicklin	modified	Orkiszewski	Nicklin	modified
1	4.71	4.63	4.91	4.76	-1.69	4.24	1.06
2	3.74	3.20	4.04	3.78	-14.44	8.02	1.07
3**	2.25	0.85	2.69	2.12	-62.22	19.56	-5.78
4	6.31	5.44	6.52	6.22	-13.79	3.33	-1.43
5	2.74	3.05	3.02	2.96	11.31	10.22	8.03
6	2.53	2.31	2.74	2.61	-8.70	8.30	3.16
7	2.63	2.10	2.49	2.38	-20.15	-5.32	-9.51
8	2.80	2.24	2.64	2.55	-20.00	-5.71	-8.93
9	2.93	2.88	2.86	2.81	-1.71	-2.39	-4.10
10	8.07	7.37	8.02	7.85	-8.67	-0.62	-2.72
11	8.92	8.60	8.82	8.73	-3.59	-1.12	-2.13
12	10.06	8.26	8.26	8.26	-17.89	-17.89	-17.89
13	9.62	7.84	7.84	7.84	-18.50	-18.50	-18.50
14	9.23	8.46	8.21	8.19	-8.34	-11.05	-11.27
15	7.91	7.44	8.23	8.04	-5.94	4.04	1.64
16	8.81	9.13	9.11	9.00	3.63	3.41	2.16
Average deviation,				%	-11.92	-0.01	-4.07
Average absolute deviation,				%	13.79	7.73	6.21
Standard deviation,				%	15.57	9.78	7.26

* Percentage error = $\frac{100(P_{calc} - P_{meas})}{P_{meas}}$

** Calculation begins from wellhead.

CONCLUSIONS

1. Mathematical well models are developed for pure water and for water-carbon dioxide mixtures.
2. For the slug flow regime, three correlations for bubble rise velocity are compared. The Orkiszewski correlation estimates the velocity too large. The Nicklin correlation or modified one estimates the reasonable velocity.
3. An equation-of-state package for water-carbon dioxide mixtures is proposed as a function of pressure and temperature.
4. The predicted values are compared with sixteen field cases, in which maximum carbon dioxide content is 2.8 %. Standard deviations are 15.57 %, 9.78 % and 7.26 % for Orkiszewski, Nicklin and modified Nicklin correlations, respectively.
5. Following problems seem to remain still in this study:

(1) Determination between bubble and slug flow regimes at a low mass flow rate in a large diameter wellbore.
(2) Assumption of a constant slip velocity of 0.24 m/s at the bubble flow regime.
(3) Limiting number of experiments available to estimate solubility of carbon dioxide in water.

NOMENCLATURE

d = diameter
g = acceleration of gravity
h = specific enthalpy
n = mass fraction
N_{Re} = Reynolds number
P = pressure
T = temperature
v = specific volume
V_b = bubble rise velocity
V_m = total superficial velocity
λ = thermal conductivity
μ = viscosity

subscripts
c = carbon dioxide
d = dew point
g = gas phase
l = liquid phase
w = water

ACKNOWLEDGEMENTS

This work is performed with support provided by the Grant-in-Aid of Scientific Research of the Ministry of Education, Science and Culture, Japan. We wish to thank Japan Metals & Chemicals Co., Ltd. for providing field data.

REFERENCES

Dodds, W.S. et al. (1963), Industrial and Engineering Chemistry, Chemical and Engineering Data series, 1, 92.

Duns, H., Jr. and Ros, N.C.J. (1963), "Vertical Flow of Gas and Liquid Mixtures in Wells", Proc. 6th World Pet. Cong., Section 2, Paper 22-PD6, 451-465.

Ellis, A.J. and Golding, R.M. (1963), "The Solubility of Carbon Dioxide above 100 °C in Water and in Sodium Chloride Solutions", American J. of Science, 261, Jan, 47-60.

Griffith, P. and Wallis, G.B. (1961), "Two-Phase Slug Flow", J. of Heat Transfer, Aug, 307-320.

Gudmundsson, J.S., Ortiz-R., J. and Granados-G., E. (1984), "Two-Phase Flow and Calcite Deposition in Geothermal Wells", Paper SPE 12741, 145-152.

JSME STEAM TABLES (1980).

Nicklin, D.J., Wilkes, J.O. and Davidson, J.F. (1962), "Two-Phase Flow in Vertical Tubes", Trans. Instn. Chem. Engrs., 40, 61-68.

Orkiszewski, J. (1967), "Predicting Two-Phase Pressure Drops in Vertical Pipe", J. of Petroleum Technology, Jun, 829-838.

Sutton, F.M. (1976), "Pressure-Temperature Curves for a Two-Phase Mixture of Water and Carbon Dioxide", N.Z. J. of Science, 19, 297-301.

Takenouchi, S. and Kennedy, G.C. (1964), "The Binary System H_2O-CO_2 at High Temperatures and Pressures", American J. of Science, 262, Nov, 1055-1074.

Vargaftik, N.B. (1975), "Tables on the Thermophysical Propertoes of Liquids and Gases", second edition, John Willey & sons, Inc., New York.

PROCEEDINGS, Thirteenth Workshop on Geothermal Reservoir Engineering
Stanford University, Stanford, California, January 19-21, 1988
SGP-TR-113

SOME EFFECTS OF NON-CONDENSIBLE GAS IN GEOTHERMAL RESERVOIRS WITH STEAM-WATER COUNTERFLOW

Robert McKibbin* and Karsten Pruess

Earth Sciences Division, Lawrence Berkeley Laboratory,
University of California, Berkeley, California 94720

ABSTRACT

A mathematical model is developed for fluid and heat flow in two-phase geothermal reservoirs containing non-condensible gas (CO_2). Vertical profiles of temperature, pressures and phase saturations in steady-state conditions are obtained by numerically integrating the coupled ordinary differential equations describing conservation of water, CO_2, and energy. Solutions including binary diffusion effects in the gas phase are generated for cases with net mass throughflow as well as for balanced liquid-vapor counterflow. Calculated examples illustrate some fundamental characteristics of two-phase heat transmission systems with non-condensible gas.

INTRODUCTION

It is well established that a mechanism of gas-liquid counterflow, also known as a "heat pipe," provides the main heat transfer in two-phase reservoirs of vapor- and liquid-dominated type (White et al., 1971; Martin et al., 1976; Straus and Schubert, 1981; Pruess, 1985; Iglesias et al., 1986; Pruess et al., 1987; McGuiness and Pruess, 1987; and others).

A heat pipe is here supposed to be a steady-state mechanism established in a porous medium where heat is transferred by a process of vapor rising vertically from depth to condense near the top with the liquid condensate moving under gravity downwards in counterflow to the rising gas. Additional heat transfer also occurs by conduction. There may be a net flow of mass through the system, although many of the previous studies assume this is negligible, or zero.

Previous work on heat pipe conditions in geothermal reservoirs has been restricted to the consideration of two-phase single-component flow of liquid water and vapor. However, many two-phase reservoirs contain considerable amounts of non-condensible gases, chiefly CO_2. The CO_2 content of the produced geofluids is often in the range of 0.1 - 10% and in some cases is much higher. The initial composition of the produced fluid in the Bagnore field in Italy was greater than 80% by weight CO_2 (Atkinson et al., 1980). The Broadlands geothermal field in New Zealand contained about 4% by mass CO_2 in the fluid before exploitation (Sutton and McNab, 1977). During initial production from such fields, the CO_2 content of the produced fluid is much higher than *in situ* values, and the reservoir appears to degas quickly (O'Sullivan et al., 1985). Surface manifestations in geothermal fields are also often rich in CO_2.

Studies in the heat transfer literature have indicated that the presence of non-condensible gas can have strong effects on heat pipes. The non-condensible gas tends to accumulate near the cold (condensing) end of the heat pipe, where molecular diffusion is balanced by mass convection; this accumulation reduces the effective heat pipe length (Udell and Fitch, 1985). The quantitative details of non-condensible gas concentration near the cold end of a heat pipe depend on the strength of binary diffusion between the non-condensible gas and the vapor. This strength is, apart from pressure and temperature, a function of formation tortuosity and volumetric gas phase content. Thus, from observed profiles of CO_2 concentrations versus depth it should be possible, at least in principle, to obtain some insight into gas phase saturation in a geothermal reservoir.

In this paper a model for steady-state vertical gravity-driven heat pipes containing water and CO_2 is developed. Mathematically, the model is represented by three coupled ordinary differential equations which express conservation of mass of water, mass of CO_2 and energy, respectively. Numerical integration of these equations gives vertical profiles for temperature, pressures, phase saturations and phase compositions for heat pipes with and without net mass throughflow. The profiles are compared with those calculated by numerical simulation of transient heat pipe conditions using the program MULKOM (Pruess, 1983).

The results indicate that, with or without a net mass throughflow, the partial pressure of any non-condensible gas present in the heat pipe forms a characteristic "wedge" at the top. Within this "wedge," there is very little fluid movement, with the main condensation region for the heat-pipe counterflow occurring at the bottom, or tip, of the "wedge." Above this condensing zone, temperature gradients are close to conductive. The gas zone therefore appears to act as a transition region between the heat pipe and a conduction zone of low permeability above.

For a net CO_2 mass flow through the system, partial pressures of non-condensible gas are non-zero at depth, and there is a simple relationship between the partial pressure and net mass flowrate per unit area of CO_2. For a zero net throughflow, the partial pressure of CO_2 is negligible at depth.

*On leave from Geothermal Institute, University of Auckland, Private Bag, Auckland, New Zealand

The inverse problem of trying to determine relative permeabilities and phase saturations from observed pressure and temperature profiles in a reservoir is also studied. The accuracy needed in temperature and pressure measurements to provide good estimates of the flow parameters is estimated.

MATHEMATICAL MODEL

The heat pipe is supposed to consist of steady vertical flows or a counterflow of liquid and gas, with two components, namely water and CO_2, within a porous matrix. Binary diffusion may occur in the gas phase of vapor and gaseous CO_2. The liquid phase consists of water and dissolved CO_2. Thermal equilibrium at each point is assumed, i.e., the temperature of liquid, gas and matrix are the same at each point in the system. Capillary pressure is neglected, i.e. $p_l = p_g = p_v + p_c = p$. The partial pressure of CO_2 gas and the mass fraction of dissolved CO_2 in the liquid phase are related by Henry's law.

Using conservation of momentum (Darcy's law), the mass flow rates per unit area in the z-direction (the z-axis is positive vertically upwards) can be written as follows:

(i) for water:

$$F_l^w = -(1-X)\frac{k k_{rl}}{\nu_l}\left(\frac{dp}{dz} + \rho_l g\right), \tag{1}$$

$$F_g^w = -(1-Y)\frac{k k_{rg}}{\nu_g}\left(\frac{dp}{dz} + \rho_g g\right) - \rho_g \tau \phi S_g D_{vc}\frac{d(1-Y)}{dz}; \tag{2}$$

(ii) for CO_2:

$$F_l^c = -X\frac{k k_{rl}}{\nu_l}\left(\frac{dp}{dz} + \rho_l g\right), \tag{3}$$

$$F_g^c = -Y\frac{k k_{rg}}{\nu_g}\left(\frac{dp}{dz} + \rho_g g\right) - \rho_g \tau \phi S_g D_{vc}\frac{dY}{dz}, \tag{4}$$

where X and Y are the mass fractions of CO_2 in the liquid and gas phases, respectively. The liquid and total gas pressures are equal, i.e., $p = p_v + p_c$, where $p_v = p_{sat}(T)$ is the saturation pressure corresponding to the local temperature and p_c, the partial pressure of the CO_2 gas, is related to the CO_2 liquid mass fraction X by Henry's law. Since X is small, this relationship can be written, to good accuracy, as

$$p_c = K_H X \frac{M_{H_2O}}{M_{CO_2}}$$

where K_H, a function of temperature, is Henry's constant. The binary diffusion coefficient D_{vc} is written as (Perry, 1963)

$$D_{vc} = D_{vc}^0 \frac{p_0}{p}\left(\frac{T + 273.15}{273.15}\right)^{\theta}$$

where $D_{vc}^0 = 1.38 \times 10^{-5}$ m^2/s (for standard conditions of $p_0 = 1$ bar, $T = 0\,^\circ$C) and $\theta = 1.91$.

Application of the principles of conservation of mass of water, mass of CO_2, and heat flow in the z-direction lead to the equations

$$F_l^w + F_g^w = m_w \tag{5}$$

$$F_l^c + F_g^c = m_c \tag{6}$$

$$F_l^w h_l^w + F_g^w h_g^w + F_l^c h_l^c + F_g^c h_g^c - K\frac{dT}{dz} = q \tag{7}$$

where m_w, m_c and q are constant water mass flow rate, CO_2 mass flow rate and heat flux, respectively, all per unit cross-sectional area.

By substituting the expressions (1) - (4) for the mass flow rates into (5) - (7), writing $p = p_v + p_c$ and using the Clapeyron equation, the Equations (5) - (7) become a set of three coupled first-order ordinary differential equations for T and p_c, with coefficients that depend on T, p_c and S_g (the volumetric gas saturation). The thermodynamic properties of water and CO_2 are calculated from correlations as used by O'Sullivan et al. (1985). Thus (5) - (7) are of the form

$$a_{i1}\frac{dT}{dz} + a_{i2}\frac{dp_c}{dz} = b_i, \quad i = 1, 2, 3,$$

where the a_{ij} and b_i are functions of T, p_c and S_g. For given values of T and p_c, the condition that this set of equations be consistent is

$$\det\begin{bmatrix} a_{11} & a_{12} & b_1 \\ a_{21} & a_{22} & b_2 \\ a_{31} & a_{32} & b_3 \end{bmatrix} = 0$$

which gives an equation to be solved for S_g. Once S_g is determined, dT/dz and dp_c/dz can be found.

The coefficients a_{ij} and b_i also depend on the parameters K, k, τ, ϕ, q, m_w and m_c, as well as on some functional relationship between gas saturation and the relative permeabilities k_{rl}, k_{rg}.

The mathematical problem of integration of the system of differential equations is a boundary value problem; the boundary conditions are just values of T and p_c. The system turns out to be stiff with respect to integration in the positive z-direction; most solutions are obtained by integration downwards. A fourth-order Runge-Kutta method was used, with a stepsize between 0.5 and 1 m providing stability and accuracy.

Some consideration was given to how the mass fluxes m_w and m_c might be determined. Four methods seemed possible:

(i) choose m_w and m_c independently (perhaps basing each on measured field values);

(ii) set a total mass flow $m_t = m_w + m_c$, and apportion m_w and m_c according to their total mobilities at the top of the heat pipe;

(iii) set a total mass flow m_t, and apportion m_w and m_c according to the total mass fraction of each at the top of the pipe;

(iv) set a total mass flow m_t, and apportion m_w and m_c according to the mass fraction of each in the gas phase only at the top of the pipe.

Each alternative has merit, depending on what mechanism is favored as a discharge condition at the top of the heat pipe. The results given below are calculated using (ii) but any of (i) - (iv) is easily implemented.

After all parameters are determined, or chosen, and relative permeability dependence on S_g is decided, integration of the equations proceeds. For given starting values of T and p_c, a solution for S_g and hence dT/dz and dp_c/dz is possible only provided q, m_w and m_c lie within a certain envelope. If so, there may be one or two solutions for S_g; if two, these correspond to the so-called vapor (gas)-dominated (larger S_g) or liquid-dominated (smaller S_g) heat pipes. In many cases, integration proceeds satisfactorily until a point is reached where there is suddenly no solution for S_g; this indicates a limit to the vertical extent of the heat pipe.

As can be seen, there are many parameters "to play with." Nevertheless, there are several characteristics that are common to most configurations studied so far; these are demonstrated in the examples chosen for illustration below.

RESULTS

The behavior of the two-component systems is best illustrated by considering some typical examples, and then making comparisons with them for other parameter values.

The most significant feature of most of the cases studied is the presence of a "wedge" of CO_2 partial pressure at the top of the system. This is demonstrated in Figure 1, where the variation with depth of total pressure, p, and CO_2 partial pressure, p_c, are plotted. At the top, T = 110 °C and p_c = 10 bar, with a net heat flux of 1 W/m^2 and various net total mass throughflows $m_t = 0$, 10^{-8} and 10^{-7} kg/m^2 s. The mass flows are apportioned to m_w and m_c according to the total mobilities at the top of the system. The relative permeability functions are chosen to be the Corey curves with residual liquid gas saturations $S_{lr} = 0.3$, $S_{gr} = 0.05$ respectively, while K = 2 W/m °C and k = 10^{-15} m^2 (1 md).

From the top of these systems, arbitrarily designated z = 0, the CO_2 partial pressure decreases while total pressure increases, albeit slowly in the case $m_t = 0$. For

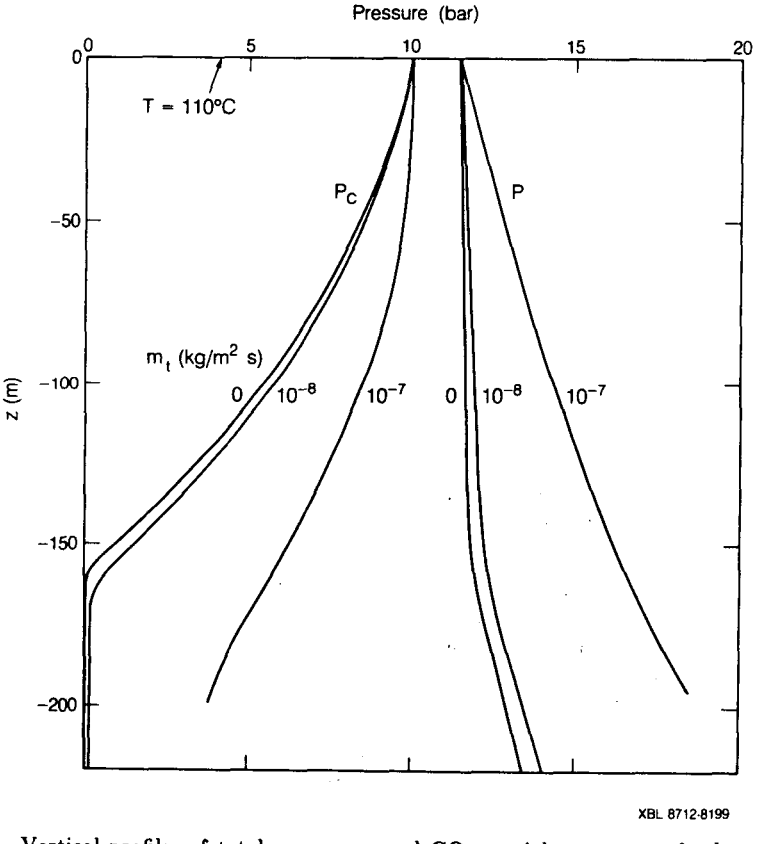


Figure 1. Vertical profiles of total pressure p and CO_2 partial pressure p_c for heat flow q = 1 W/m^2 and total mass throughflows $m_t = 0$, 10^{-8} and 10^{-7} kg/m^{2}s. Boundary conditions at the top are T = 110 °C and p_c = 10 bar. (K = 2W/m °C, k = 10^{-15} m^2, Corey relative permeabilities with $S_{lr} = 0.3$, $S_{gr} = 0.05$.)

that case ($m_t = 0$), p_c becomes almost zero at a depth of 160 m, and decays quickly below that point. For $m_t = 10^{-8}$, behavior is similar, but p_c does not become zero at depth because of the finite throughflow. For $m_t = 10^{-7}$, decrease of p_c is slower, and indeed there is no solution below 196 m, which corresponds to the limit of this two-phase heat transport mechanism. A system with single-phase water and dissolved CO_2 could be found to match the heat and mass flux requirements below this depth.

It should also be noted that it is possible, with suitable selection of q and m_t, to obtain pressure profiles where p_c increases significantly with depth. An example of such a profile was obtained as part of a simulation of Ohaaki by O'Sullivan et al. (1985). Such results are investigated further in McKibbin and Pruess (1988).

The three different pressure profiles in Figure 1 do not correspond to the same temperature profiles, although $T = 110\,^\circ C$ at the top of each. This and other such differences are also demonstrated in Figures 2 and 3, where a comparison between a vapor-dominated and a liquid-dominated heat and mass transfer mechanism is made. The top temperature is now $200\,^\circ C$, and the total mass throughflow is 10^{-8} kg/m^{2}s; otherwise parameters and relative permeability functions are as for Figure 1.

The profiles for temperature T, pressures p and p_c, gas saturation S_g, liquid flow rate $F_l = F_l^w + F_l^c$ and condensation rate (in kg/m^{3}s) are shown in Figures 2 and 3 for the vapor-dominated and liquid-dominated systems respectively. Both have a CO_2 partial pressure profile that decreases in a wedge shape to a very small value. Below this pressure transition point, the total pressure changes gradient slightly, increasing for the vapor-dominated, and decreasing for the liquid-dominated systems respectively. This opposite behavior is also reflected by the corresponding smooth but distinct changes in gas saturation at the base of the CO_2 gas wedge.

The liquid flow rate profiles indicate a very small value of F_l in the gas wedge region, with a significant condensation region at the base of the wedge. There is consequently very little mass counterflow taking place above the transition, with the main heat flow being conductive, as reflected by the temperature profiles: there is a nearly conductive gradient in the gas wedge region.

The overall effect of the gas wedge seems to be to provide a transition between the counterflow, or heat pipe, below and a conductive region above, with a short but significant condensation zone to accomplish this. Such provision of a condensation zone has not been noted before; most assumptions are based on condensation at an impermeable caprock.

The possibility of a mixed vapor-dominated/liquid-dominated heat transfer system is demonstrated in Figure 2, where dashed lines indicate the calculated profiles found by assuming that, below depths of 30 m, 60 m or 100 m, the system is liquid-dominated.

Comparison with MULKOM

Some comparisons were made between profiles calculated using Equations (1) - (7) as described above and results found by numerically running transient heat pipe conditions to steady state with the program MULKOM (Pruess, 1983). Over a simulated depth of 400 m, temperatures agreed to within $0.5\,^\circ C$ over a range of $100\,^\circ C$ and pressures to within 0.15 bars over a range of 6 bars with discretizations of both 20 blocks and 400 blocks for the MULKOM program. Since the correlations for the properties of water and CO_2, and the equation formulation are the same for both calculations, the small difference in results may be due to the consistent upstream weighting technique used in the transient calculations. Further investigation is proceeding.

Pressure/Throughflow Relationship at Great Depth

Substitution of Equations (1) - (4) into Equations (5) - (7) and subsequent elimination of k_{rl} and k_{rg} gives the following equation:

$$\rho_g \tau \phi S_g D_{vc} \frac{dY}{dz} = m_w Y + m_c (1 - Y)$$

$$+ (Y - X) \left[\frac{q + KT' - m_w h_g^w - m_c h_g^c}{(1 - X)(h_g^w - h_l^w) + X (h_g^c - h_l^c)} \right] \quad (8)$$

where $T' = dT/dz$. Provided m_w and m_c are not too large, calculations indicate that, below any gas wedge, Y does not vary much with depth; binary diffusion is therefore negligible in deeper regions, and can be neglected. Also, the assumption that the ideal gas law is satisfied closely, leads to a relationship between Y and p_c, namely

$$Y \approx \frac{p_c}{p_c + \rho_v R (T + 273.15)} \quad (9)$$

where $R = R_0/M_{CO_2} \approx 189$. Neglecting X, the very small mass fraction of CO_2 in the liquid flow, and substituting (9) into (8) with the LHS = 0 gives, upon rearrangement,

$$p_c \approx \frac{\rho_v R (T + 273.15) h_{lv}}{q + KT' - m_w h_l^w - m_c h_g^c} m_c \ .$$

For small mass fluxes, this reduces further to

$$p_c \approx \frac{\rho_v R (T + 273.15) h_{lv}}{q + KT'} m_c \quad (10)$$

which gives a simple approximate relationship between CO_2 partial pressure, p_c, and CO_2 mass flux per unit area, m_c. The proportionality coefficient depends only on the measured temperature and its gradient at a point (and, of course, an estimate of K and total heat transfer q, perhaps measured at the surface). Equation (10) may be useful in determining CO_2 mass fluxes from deep temperature and pressure profiles.

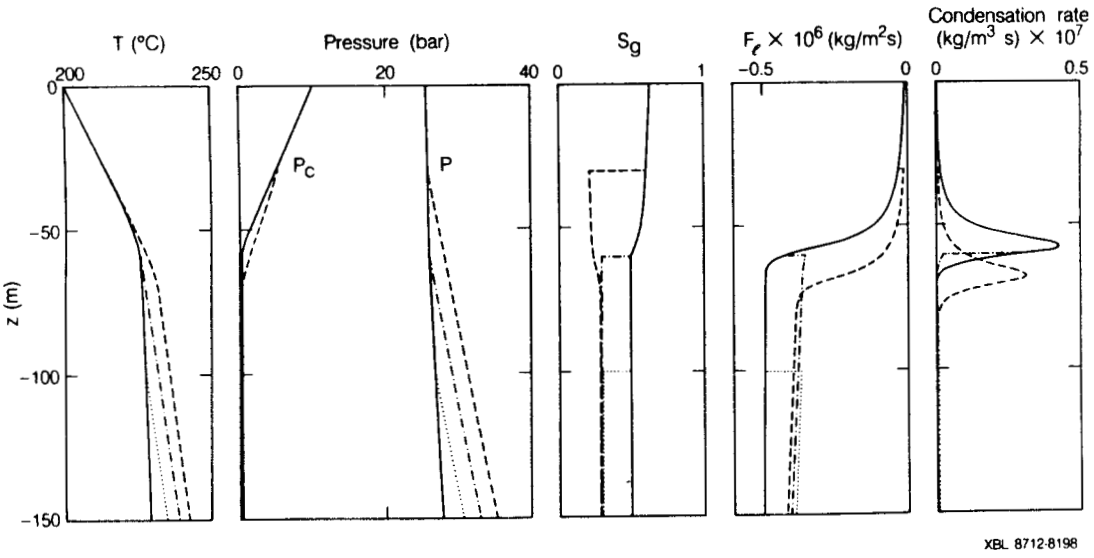


Figure 2. Vertical profiles of temperature T, pressures p and p_c, gas saturation S_g, liquid flow rate F_l and condensation rate for a vapor-dominated system with top conditions T = 200 °C and p_c = 10 bar. Total mass throughflow is 10^{-8} kg/m^{2}s. Other parameters are as for Figure 1. Broken lines correspond to liquid-dominated systems beneath the vapor-dominated system at depths of 30 m, 60 m or 100 m.

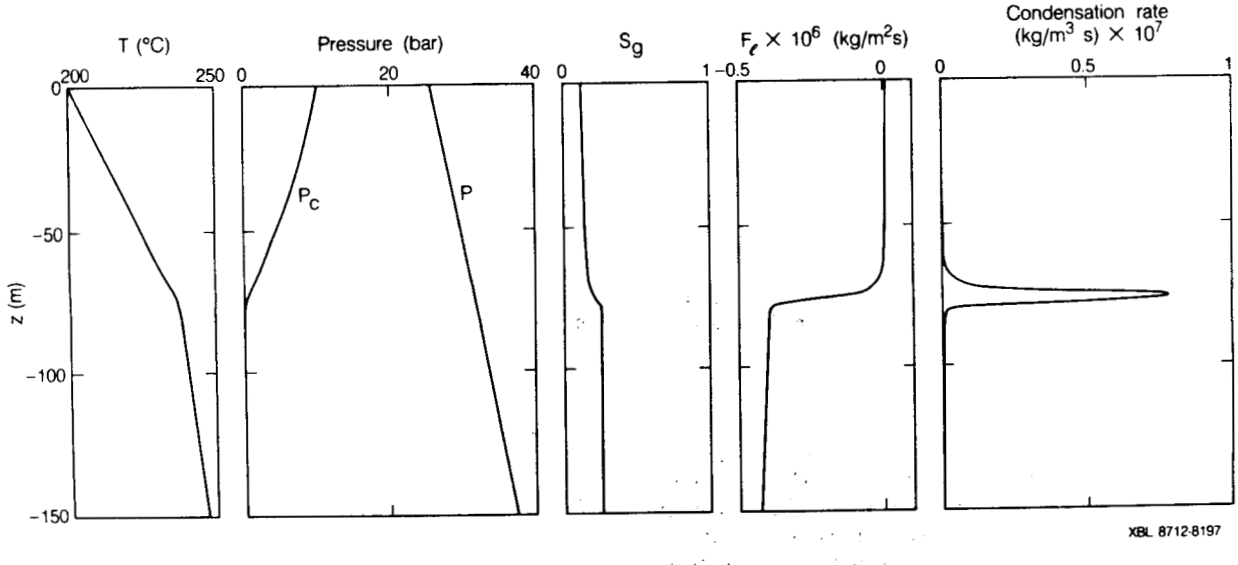


Figure 3. Vertical profiles of temperature T, pressures p and p_c, gas saturation S_g, liquid flow rate F_l and condensation rate for a liquid-dominated system. Parameters are as for Figure 2.

Inverse Problem

Writing

$$\overline{m} = \frac{q + KT' - m_w h_g^w - m_c h_g^c}{(1 - X)(h_g^w - h_l^w) + X(h_g^c - h_l^c)},$$

equation (8) may be rearranged to give an expression for $S_g \tau \phi$:

$$S_g \tau \phi = \frac{m_w Y + m_c (1 - Y) + \overline{m} (Y - X)}{\rho_g D_{vc} Y'}. \quad (11)$$

Use of (1) - (4) also gives expressions for kk_{rl} and kk_{rg} as follows:

$$kk_{rl} = \frac{\overline{m}}{(p' + \rho_l g)/\nu_l}, \quad (12)$$

$$kk_{rg} = \frac{(1 - X)\overline{m} + m_w - \rho_g S_g \tau \phi D_{vc} Y'}{-(1 - Y)(p' + \rho_g g)/\nu_g} \quad (13)$$

Theoretically, at least, expressions (11) - (13) enable values of $S_g \tau \phi$, kk_{rl} and kk_{rg} to be deduced from known (measured) values of q, m_w and m_c, an estimate of K, and measured values of temperature, pressure and their gradients at some depth in a reservoir (through correlations, all values of water and CO_2 properties and therefore X, Y and Y' can be subsequently calculated and substituted into (11) - (13)).

Preliminary investigations show that parameters can be estimated to within 10% from synthetic heat pipe data generated using the numerical solutions of the Equations (1) - (7) provided T, p are known to within 0.01 ° C and 0.01 bar respectively. These requirements are rather more stringent than current instrumentation would allow. Investigation is continuing to try to separate out the effects of accuracy of estimating absolute values of T and p from those of estimating the gradients. Results will be reported later (see McKibbin and Pruess, 1988). If reliable estimates can be made from Equations (11) - (13), then it should be possible to determine some relationship between phase saturations and relative permeabilities from field data. In any case, results to date show much better estimates coming from data within the gas wedge than from below it.

SUMMARY AND CONCLUSIONS

A model for steady-state vertical gravity-driven flows of two-phase mixtures of water and CO_2 has been presented. Numerical integration of the resulting differential equations gives vertical profiles of temperature, pressures, phase saturations and phase compositions.

In systems with relatively small mass throughflow the presence of CO_2 results in a "wedge" of CO_2 partial pressure at the top of the system. This decays to small, but finite pressures at depth for a non-zero CO_2 mass throughflow, and to zero pressure at depth for zero net throughflow. Within the gas pressure wedge, counterflow is small, and the counterflow (or coflow) heat transfer mechanism operating at depth is replaced by an almost conductive temperature profile. Between the two regions i.e. at the base of the wedge, a very active condensation zone controls the transition from heat pipe to conduction. Systems with significant throughflow of CO_2 display a different profile, with CO_2 partial pressure largest at depth.

From accurate observations of vertical pressure and temperature profiles the rate of CO_2 discharge may be estimated. Determination of in-place gas saturation, as well as effective liquid and gas phase permeabilities, is possible in principle; however the accuracy requirements for temperature and pressure measurements may be so stringent as to be impractical.

ACKNOWLEDGMENT

Robert McKibbin is grateful for the hospitality of the Earth Science Division, LBL, while taking part in this work during a period of sabbatical leave from the University of Auckland.

This work was supported through U.S. Department of Energy Contract No. DE-AC03-76SF00098.

NOMENCLATURE

a_{ij}, b_i	coefficients, functions of T, p_c, S_g
D_{vc}	binary diffusion coefficient (m^2/s)
F	mass flux per unit area (kg/m^2s)
g	gravitational constant (m/s^2)
h	specific enthalpy (J/kg)
h_{lv}	vaporization enthalpy for water (J/kg)
k	permeability (m^2)
k_{rl}, k_{rg}	relative permeabilities for liquid and gas phases
K	thermal conductivity of saturated formation (W/m ° C)
K_H	Henry's constant (Pa)
m	(constant) mass flux per unit area (kg/m^2s)
M_{H_2O}, M_{CO_2}	molecular weights of water and CO_2
p	pressure (Pa)
q	heat flux per unit area (W/m^2)
R	gas constant
S	saturation (volume fraction)
T	temperature (° C)
X	mass fraction of CO_2 in liquid phase
Y	mass fraction of CO_2 in gas phase
z	vertical coordinate (m)

Greek

ν	kinematic viscosity (m^2/s)
ρ	density (kg/m^3)
τ	tortuosity
ϕ	porosity

Super- and Subscripts

c	CO_2
g	gas
l	liquid
r	residual
t	total
v	vapor
w	water
0	standard value

REFERENCES

Atkinson, P. G., Celati, R., Corsi, R., and Kucuk, F., (1980), "Behavior of the Bagnore Steam/CO_2 Geothermal Reservoir, Italy," Soc. Petroleum Engineers J. (Aug. 1980), 228-238.

Iglesias, E. R., Arellano, V. M., and Ortiz-Ramirez, J., (1986), "Natural Vertical Flow in the Los Azufres, Mexico, Geothermal Reservoir," Proc. Eleventh Workshop on Geothermal Reservoir Engineering, Report SGP-TR-93, Stanford University, January 1986, 237-342.

Martin, J. C., Wegner, R. E., and Kelsey, F. J., (1976), "One-Dimensional Convective and Conductive Geothermal Heat Flow," Proc. Second Workshop on Geothermal Reservoir Engineering, Stanford University, 1976, 251-262.

McGuiness, M. J., and Pruess, K., (1987), "Unstable Heat Pipes," Proc. Ninth New Zealand Geothermal Workshop, University of Auckland, New Zealand, 1987.

McKibbin, R., and Pruess, K., (1988), "On Non-Condensible Gas Concentrations and Relative Permeabilities in Geothermal Reservoirs with Gas-Liquid Co- or Counterflows," in preparation.

O'Sullivan, M. J., Bodvarsson, G. S., Pruess, K., and Blakely, M. R., (1985), "Fluid and Heat Flow in Gas-Rich Geothermal Reservoirs," Soc. Petroleum Engineers J. (April 1985), 215-226.

Perry, J. H., (1963), "Chemical Engineers Handbook," McGraw-Hill, New York, Section 14, 19-23.

Pruess, K., (1983), "Development of the General Purpose Simulator MULKOM," Earth Sciences Division 1982 Annual Report, LBL-15500, Lawrence Berkeley Laboratory, Berkeley, CA, 133-135.

Pruess, K., (1985), "A Quantitative Model of Vapor-Dominated Geothermal Reservoirs as Heat Pipes in Fractured Porous Rock," Geothermal Resources Council Transactions 9 (August 1985), 353-361.

Pruess, K., Celati, R., Calore, C., and Cappetti, G., (1987), "On Fluid and Heat Flow in Deep Zones of Vapor-Dominated Geothermal Reservoirs," Proc. Twelfth Workshop on Geothermal Reservoir Engineering, Stanford University, 1987.

Straus, J. M., and Schubert, G., (1981), "One-Dimensional Model of Vapor-Dominated Geothermal Systems," J. Geophys. Res., 86, 9433-9438.

Sutton, F. M., and McNab, A., (1977), "Boiling Curves at Broadlands Geothermal Field, New Zealand," New Zealand J. Science, 20, 333-337.

Udell, K. S., and Fitch, J. S., (1985), "Heat and Mass Transfer in Capillary Porous Media Considering Evaporation, Condensation and Non-Condensible Gas Effects," Paper presented at 23rd ASME/AIChE National Heat Transfer Conference, Denver, CO, August 1985.

White, D. E., Muffler, L. J. P., and Truesdell, A. H., (1971), "Vapor-Dominated Hydrothermal Systems Compared with Water Systems," Economic Geology, 66, 75-97.

PROCEEDINGS, Thirteenth Workshop on Geothermal Reservoir Engineering
Stanford University, Stanford, California, January 19-21, 1988
SGP-TR-113

MATHEMATICAL MODELING OF NEAR-CRITICAL CONVECTION

B. L. Cox, K. Pruess, and R. McKibbin*

Earth Sciences Division, Lawrence Berkeley Laboratory
University of California, Berkeley, California 94720

*On leave from Geothermal Institute, University
of Auckland, Private Bag, Auckland, New Zealand

ABSTRACT

Fluid and heat flow at temperatures approaching or exceeding that at the critical point (374°C for pure water, higher for saline fluids) may be encountered in deep zones of geothermal systems and above cooling intrusives. Laboratory experiments have demonstrated strong enhancements in heat transfer at near-critical conditions (Dunn and Hardee, 1981).

We have developed special numerical techniques for modeling porous flow at near-critical conditions, which can handle the extreme non-linearities in water properties near the critical point. Our numerical experiments show strong enhancements of convective heat transfer at near-critical conditions; however, the heat transfer rates obtained in the numerical simulations are considerably smaller than those seen in the laboratory experiments by Dunn and Hardee. We discuss possible reasons for this discrepancy and develop suggestions for additional laboratory experiments.

INTRODUCTION

Fluid conditions approaching or exceeding the critical point (374°C, 221 bars for pure water; higher temperatures and pressures for saline brines) may be reached in the deep ends of geothermal systems such as Mofete (Facca, 1985) and Larderello (Cappetti et al., 1985), as well as above crustal magma bodies. Yet, little is known about how heat and fluid flows are affected by critical conditions. In order to better evaluate geothermal reservoirs with critical conditions at depth, and to estimate heat and fluid flows in critical zones above magma bodies, we need to better understand the behavior of geothermal fluids near the critical point.

Previous studies include one by Cathles (1977) who used a finite difference model to study cooling igneous intrusives and the formation of liquid- and vapor-dominated geothermal systems, as well as the formation of porphyry-type ore deposits. He concluded that fluids circulate around the critical point of water to become gaseous without boiling, and that these zones are potentially exploitable. Norton and Knight (1977) also performed finite difference simulations of cooling plutons; they found that the style of circulation was controlled by the critical fluids and that the total heat flow calculations can be significantly in error if these convecting zones are not considered.

Laboratory experiments of natural convection of critical fluids in a porous medium were performed by Dunn and Hardee (1981) for water, and by Hadley (1982) for carbon dioxide. Dunn and Hardee found that heat transfer rates increased by factors of up to 70 when compared to conductive heat flow near the critical point of water, and attributed this enhancement to the extreme behavior of fluid properties (especially density and heat capacity) in the critical region. Hadley (1982) found substantial heat transfer enhancement (Nusselt number of 12) for carbon dioxide, and concluded that thermal dispersion was very important because of high fluid velocities generated near the critical point.

Above critical temperatures and pressures, there are no longer distinct liquid and gas phases, but instead a continuous variation from liquid-like fluid to gas-like fluid. This supercritical fluid has an enhanced ability to transport heat by convection because of the extreme behavior of fluid properties such as density and heat capacity. Contours of density and of internal energy at near-critical temperatures and pressures are plotted in Figures 1a and 1b. These plots were made by using a table generated from the Haar equation of state for water (Haar et al., 1984). The rapid changes in values indicated by the bands of compression of contours show one of the many problems occurring when trying to model a system with such non-linear behavior.

NUMERICAL MODELING OF NEAR–CRITICAL FLOW

Simulations were performed with the geothermal reservoir simulator MULKOM (Pruess, 1983), utilizing the Haar equation of state for water (Haar et al., 1984). Non-linearities in the water properties near the critical point create problems for numerical models, necessitating the development of new techniques. One of the modifications made in MULKOM was the use of a table of densities and internal energies as functions of temperature and pressure in the critical region. For every time step, these values are called, and used as starting values for the energy and mass flow calculations. A bi-linear interpolation scheme is used to estimate values between table values.

A second problem resulted from large pressures near the critical point (of the order 10^7 Pa) which are accompanied by very small pressure differences (of the order 10 Pa) between neighboring volume elements in a finite difference grid. This problem was overcome by using a floating reference pressure (average pressure in the flow system at each time step) so that more significant figures could be retained.

A third problem was encountered when a thermal convection problem was initialized with uniform temperature everywhere except at the heat source. This method of initializa-

tion gave rise to many transient flow reversals and was very slow and costly in computer time. In the present work we are only interested in the steady state attained after all transient changes have disappeared. To speed up the approach to steady state, we initialized the simulations by generating a set of temperatures corresponding to pure conduction between the heat source and the outer constant temperature boundary. This conductive steady state initialization greatly improved the efficiency of the simulations.

There is still a need to incorporate further modifications into MULKOM for near-critical convection. Thermal dispersion, flow channeling, and near-critical phase transitions may all be important, depending on the type of problem studied.

CODE VALIDATION AND NUMERICAL EXPERIMENTS

Before the simulator can be used to model geologic systems, it needs to be validated against some experimental data. The only available experimental work on near-critical porous convection of water is the one performed at Sandia National Laboratories (Dunn and Hardee, 1981). A conceptual sketch of the experimental setup is shown in Figure 2. A 1 liter cylindrical vessel filled with a fine silica sand was heated with electrical tape heaters on the cylinder mantle, and along a thin platinum wire in the center of the vessel. The outside of the cylinder was kept at a somewhat lower temperature than the wire, and the top and bottom of the cylinder were insulated. The steady-state temperatures were measured with embedded thermocouples, and a measure of the total heat transfer divided by conductive heat transfer (Nusselt number, Nu) was estimated. The experimenters found an enhancement in heat transfer over a broad temperature range from 360 to 400°C, which near the critical point reached a peak of about 70 times that for pure conduction.

Dunn and Hardee (1981) presented calculations of Rayleigh numbers (Ra) for parameters representative of their experiment, using a hypothetical temperature difference of 2°C between the wire and the cylinder mantle. They found a narrow peak centered at 374°C with maximum Rayleigh number of Ra = 700. The experimental measurements, when plotted as rate of heat transfer per unit temperature drop between two measurement points in the vessel, showed a temperature dependence similar to that of the calculated Rayleigh numbers. This correspondence led Dunn and Hardee to suggest that the enhanced heat transfer near the critical point was in fact brought about by the enhanced convective heat transport. However, this correspondence (Ra-Nu) should be viewed in a qualitative rather than quantitative sense because the calculated Ra are much too small to explain the observed heat transfer enhancements by factors up to 70 (Prasad et al., 1985; Reda, 1986).

Furthermore, a Rayleigh number based on temperature differences between hot and cold boundaries is not a very meaningful measure of convective heat transfer in a flow system with cylindrical symmetry, because temperature behaves in a singular fashion near the symmetry axis. We believe that fairly large temperature differences (substantially larger than 2°C) must have been present in the experiments. The precise location of the temperature sensors is not given by Dunn and Hardee, but from the sketch in the paper, it appears that the temperature measurements were made at the mid-height of the vessel, and none were made next to the wire. When convection occurs, a thin boundary layer would form next to the wire, and the pattern of convection would be asymmetrical in the vertical, so that measuring temperature differences at mid-height and away from the wire would not give quantitatively accurate estimates of the Nusselt number. A second reason for believing that temperature differences in the experiment must have been substantially larger than 2°C is that measured heat transfer is strongly enhanced over a rather broad temperature interval (from 360 to 400°C), while the peak in the Rayleigh numbers (for a 2°C temperature difference) is very narrow and steep right at the critical temperature.

We conclude that the Sandia experiment does not provide a sufficiently detailed definition of thermodynamic conditions to permit a careful code validation. Using the flow geometry shown in Figure 2, we performed a series of numerical experiments (Tables 1 and 2) to study various issues relating to near-critical heat transfer, such as the effects of boundary conditions, aspect ratio of convecting cells, discretization, and size of temperature interval. Our initial simulations gave rather weak enhancements in overall heat transfer, and specific efforts were made to obtain a more enhanced heat transfer, using flow geometry and parameters similar to those of the experiment. The two-dimensional axisymmetric computational grid is shown in Figure 3. The convection flow directions were similar in all simulations and an example is given in Figure 4.

Boundary Conditions

For most of the simulations the following boundary conditions were imposed: all boundaries are impervious, with constant temperature along the innermost elements and on the cylinder mantle, and insulated (no heat flow) boundaries on top and bottom of the vessel. Typical isotherm patterns for conduction only, and for convection, are shown in Figures 5a and 5b, respectively. We also examined the case of constant temperature at the top and bottom boundaries, and although the isotherms are different (Figures 5c and 5d), the average heat flow is not very much changed (Table 2, Figure 6). Another variation in boundary conditions was the use of uniform heat flux at the wire heater instead of constant temperature. We found no significant difference compared to constant temperature boundary conditions.

Aspect Ratio

We ran some cases with a different aspect ratio, since the actual geometry of the convecting cells is unknown. These results are shown in Figure 6 and Table 2. For a permeability of 40 darcies, the Nusselt number for a radius to height ratio of 1:6 (that of the experiment) was 2.2, while for a ratio of 2:1, the Nusselt number was 4.8, over twice as large. Thus heat transfer increases considerably with aspect ratio, especially for small aspect ratios (Figure 7).

Size of Temperature Interval

Another variation which we tried was to use a 10°C temperature difference rather than 2°C. The Nusselt number resulting from this case for a permeability of 40 darcies, was only 1.5, considerably less than had been obtained with the smaller temperature difference. This seems logical, since for

a larger temperature interval across the system the region with strongest convective enhancement near the critical point is reduced in volume.

Discretization Effects

Discretization effects result from two sources: from the spacing of the grid points, and from the interpolation of densities and internal energies from tabular data for discrete pressure and temperature values. We found that the first type of discretization effects were not a problem for our simulation. Cases 1 and 2 (Table 2) were identical, except that case 2 had an extra grid point next to the hot wire, to provide improved spatial resolution in the region where discretization effects are strongest. The addition of the extra grid point actually decreased the Nusselt number slightly (Table 2).

Discretization effects resulting from table interpolations were not very great either, but could be significant for a small temperature interval at the critical point. For most of the cases, a table with 1 bar pressure intervals and 0.05°C temperature intervals was used. Another table was constructed with 0.1 bar pressure intervals and 0.1°C temperature intervals, and case 3 (see Table 2) was rerun with this table. For a permeability of 40 darcies, the Nusselt number was 2.2 instead of 2.1. For the case with the 10℃ temperature difference, use of the higher resolution table gave nearly identical results.

DISCUSSION

We have developed special numerical techniques to model convective heat transfer at near-critical conditions. Stable steady states were achieved for model systems with linear dimensions of the order of 10 cm, with spatial resolutions better than 1 mm and pressure differences of order 10 Pa between neighboring finite difference grid points.

No validation of the numerical model was possible because the only available experiment on near-critical flow of water in a porous medium (Dunn and Hardee, 1981) lacks sufficiently detailed definition of thermodynamic conditions. Numerical experiments for a flow system similar to that studied by Dunn and Hardee showed significantly enhanced heat transfer near the critical point. However, the enhancements seen in the simulations (up to a factor 5 over pure conduction) are substantially smaller than what was reported from the experiments (up to a factor 70). While we did not expect detailed agreement, a discrepancy that large is surprising and unexplained at the present time. Possible mechanisms for enhanced heat transfer not included in the simulations are thermal dispersion, and flow in channels of high permeability near the wire heater (perhaps generated by dissolution of quartz). In particular, transverse dispersion (Kvernvold and Tyvand, 1980; Hadley, 1982) might have very significant effects for the cylindrical flow geometry considered here, because it produces a component of velocity in the direction of heat transfer (radial).

We suggest that additional carefully controlled and instrumented laboratory experiments should be undertaken to better define the physical conditions and mechanisms for near-critical heat transfer. The cylindrical geometry employed by Dunn and Hardee (1981) is complicated by singular behavior at small radius, and has the undesirable feature that flow behavior may be strongly influenced by conditions (heterogeneities, etc.) on a very small spatial scale. From the standpoint of ease of interpretation a linear flow geometry would be most desirable, but this appears difficult to realize experimentally. The best geometric configuration for experimental studies may be a porous annulus (Prasad et al., 1985; Reda, 1986), where the inner radius is not very much smaller than the outer radius, so that the flow geometry is non-singular and approximately linear. After validation of the numerical model has been achieved, we can look at natural hydrothermal and magma systems and incorporate additional effects such as salinity, fluid-rock interaction, and non-condensible gases.

ACKNOWLEDGEMENT

This work was supported by the Geothermal Technology Division, U.S. Department of Energy, under Contract No. DE-AC03-76SF00098. Robert McKibbin is grateful for the hospitality of the Earth Sciences Division, Lawrence Berkeley Laboratory, while taking part in this work during a period of sabbatical leave from the University of Auckland. The authors are indebted to M. Lippmann for a critical review of the manuscript. Thanks are due to J. Dunn of Sandia National Laboratories for providing us with additional parameters of his laboratory experiments.

REFERENCES

Cappetti, G., Celati, R., Cigni, U., Squarci, P., Stefani, G., and Taffi, L., 1985, Development of Deep Exploration in the Geothermal Areas of Tuscany, Italy, 1985 International Symposium on Geothermal Energy, International Volume, Geothermal Resources Council, 303-309.

Cathles, L. M., 1977, An Analysis of the Cooling of Intrusives by Groundwater Convection which Includes Boiling, *Econ. Geol., 72,* 804-826.

Dunn, J. C. and Hardee, H. C., 1981, Superconvecting Geothermal Zones, *J. Volcanol. and Geotherm. Res., 11,* 189-201.

Facca, G., 1985, Geothermal Activity in Italy, *Geothermal Resources Council Bulletin,* January 1985, 10-14.

Haar, L., Gallagher, J. S., Kell, G. S., 1984, NBS/NRC Steam Tables, Hemisphere Publishing Corp.

Hadley, G. R., 1982, Natural Convection of a Near Critical Fluid through a Porous Medium, Sandia Report SAND82-1072J.

Kvernvold, O., and Tyvand, P., 1980, Dispersion Effects on Thermal Convection in Porous Media, *J. Fluid Mech., 99,* part 4, 673-686.

Norton, D. and Knight, J., 1977, Transport Phenomena in Hydrothermal Systems and Cooling Plutons, *Am. J. Sci., 77,* 937-981.

Prasad, V., Kulacki, F. A. and Keyhani, M., 1985, Natural Convection in Porous Media, *J. Fluid Mech., 150,* 89-119.

Pruess, K., 1983, Development of the General Purpose Simulator MULKOM, Annual Report 1982, Earth Sciences Division, report LBL-15500, Lawrence Berkeley Laboratory.

Reda, D. C., 1986, Natural Convection Experiments with a Finite-Length, Vertical Cylindrical Heat Source in a Water-Saturated Porous Medium, *Nuclear and Chemical Waste Management, 6,* 3-14.

Table 1. Parameters used in Simulations

Parameter	Value
porosity	0.25
permeability	1 to 40 darcies
thermal conductivity	3.35 W/m°C
temperature of wire	377°C
temperature of outer wall	375°C
average pressure	225 bar
cylinder radius	0.0381 m
cylinder height	0.2286 m
aspect ratio (radius : height)	1:6
computational grid (see Fig. 3)	21 x 15
top and bottom boundaries insulating	

Table 2. Results of Critical Convection Simulations

Case	Modifications	Permeability, darcies	Nusselt number Nu
1	coarser mesh*	1	1.039
	average pressure = 230 bars	10	1.211
	temperature interval: 377-379°C	20	1.399
		40	1.694
2	finer mesh (21 x 15)	40	1.493
	average pressure = 230 bars		
	temperature interval: 377-379°C		
3	Average pressure = 225 bars	20	1.854
	temperature interval: 375-377°C	40	2.056
	finer resolution (T,P) table	40	2.227
4	top and bottom boundaries at	20	1.738
	constant temperature	40	2.077
5	aspect ratio 1:3	10	1.795
		20	2.182
		40	2.742
6	aspect ratio 1:2	10	1.945
		20	2.428
		40	3.150
7	aspect ratio 1:1	10	2.198
		20	2.895
		40	3.956
8	aspect ratio 2:1	10	2.313
		20	3.227
		40	4.794
9	temperature interval: 370-380°C	1	1.007
		10	1.150
		20	1.290
		40	1.537
	finer resolution (T,P) table	40	1.531

*the two columns of grid blocks closest to the heater wire were combined

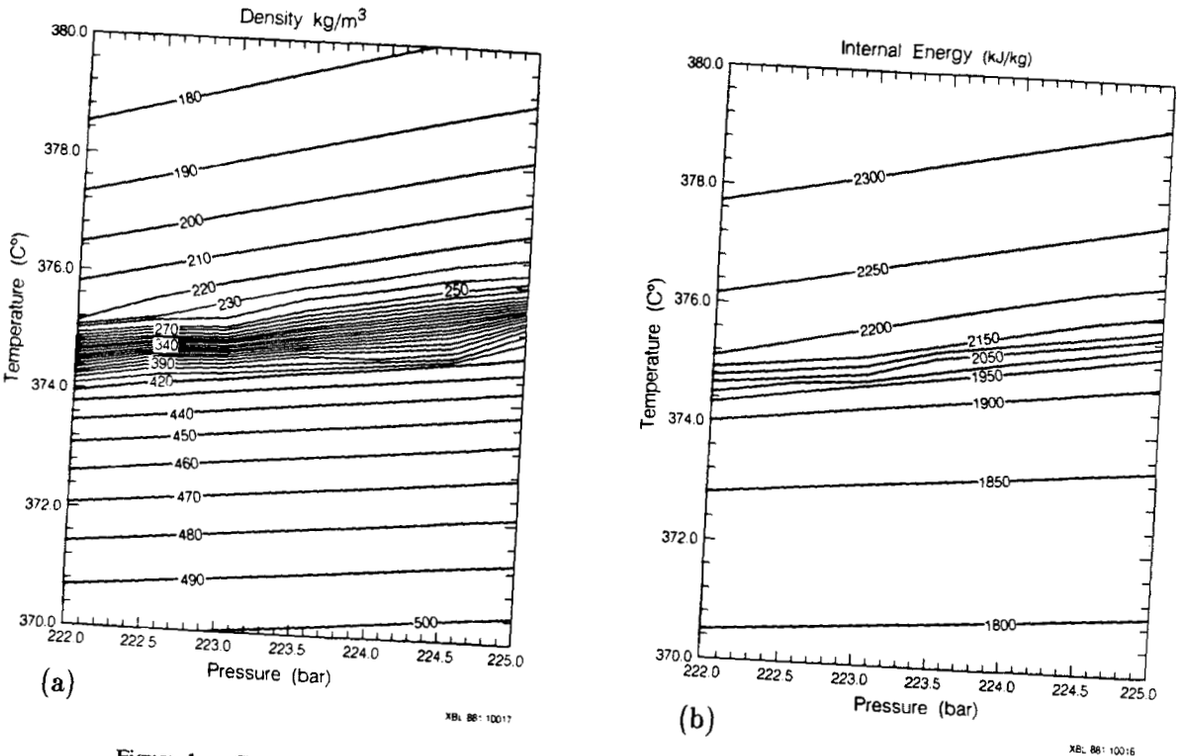


Figure 1. Contours of (a) density (kg/m^3) and (b) internal energy (kJ/kg) for pure water in the critical region.

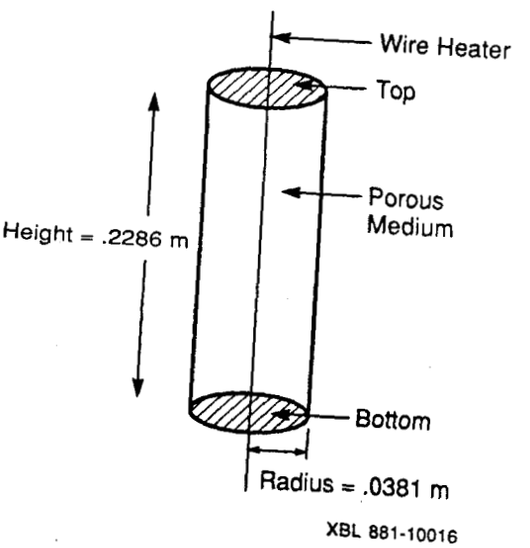


Figure 2. Cylindrical geometry for heat transfer study.

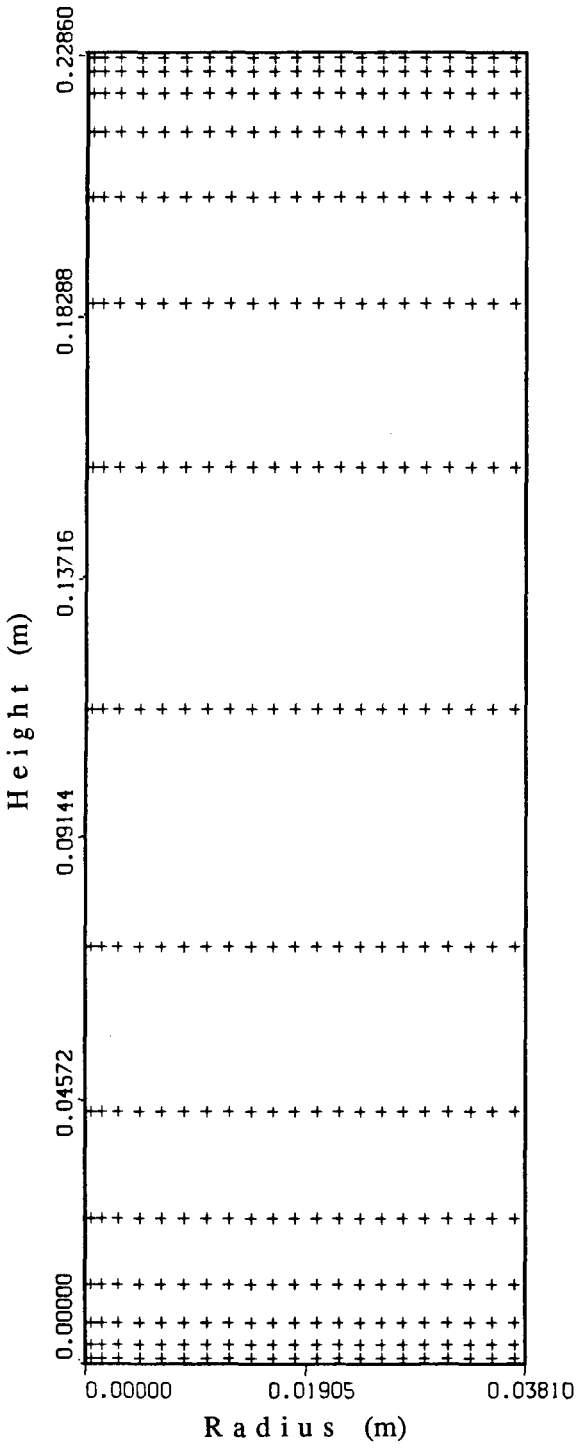


Figure 3. Radial mesh geometry used in simulations. Left hand side of figure is axis of symmetry.

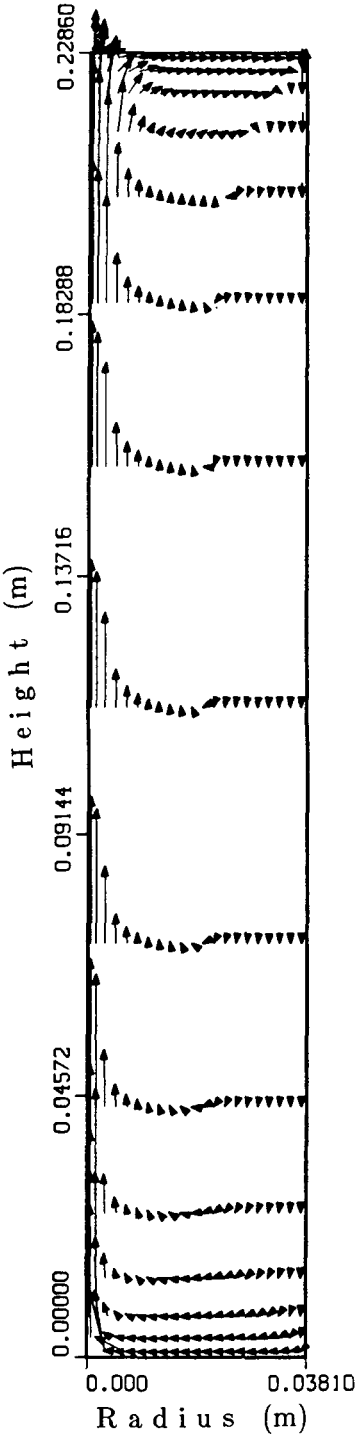


Figure 4. Typical fluid flow vectors (case 3) resulting from simulations of natural convection near the critical point.

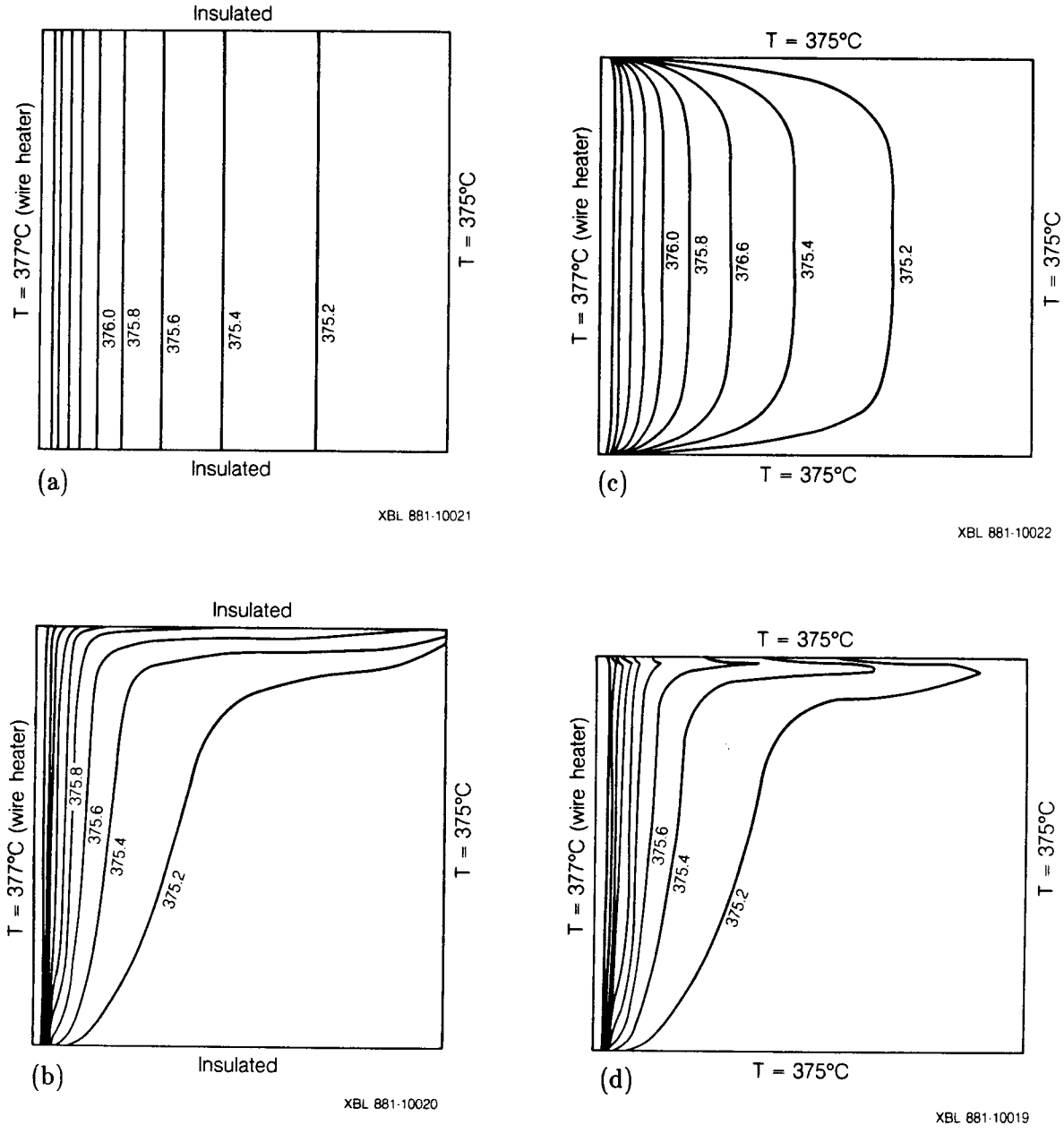


Figure 5. Isotherms for (a) case 2, conduction only (b) case 2, convection, (c) case 4, conduction only and (d) case 4, convection. The radial dimension is exaggerated 6 times.

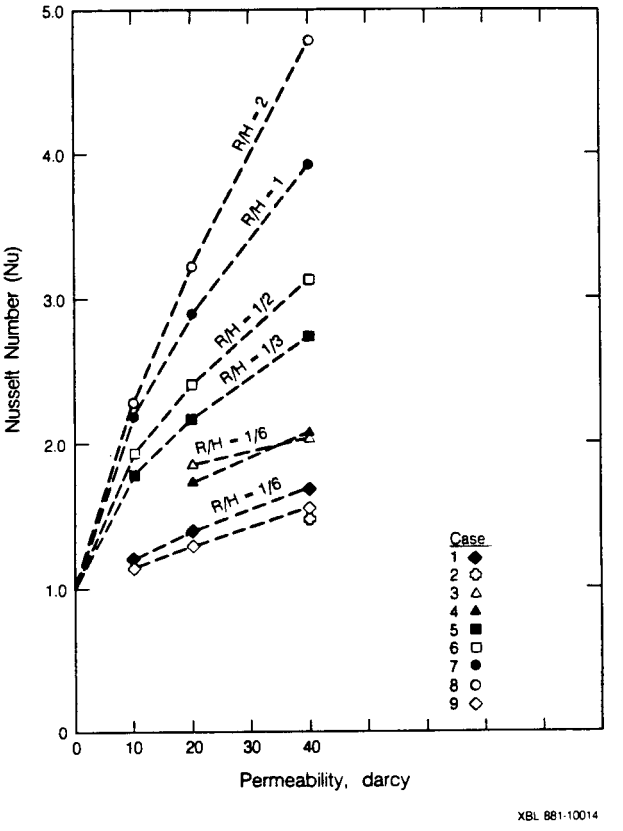


Figure 6. Results of critical convection simulations, plotted in terms of Nusselt number versus permeability (cases described in Table 2).

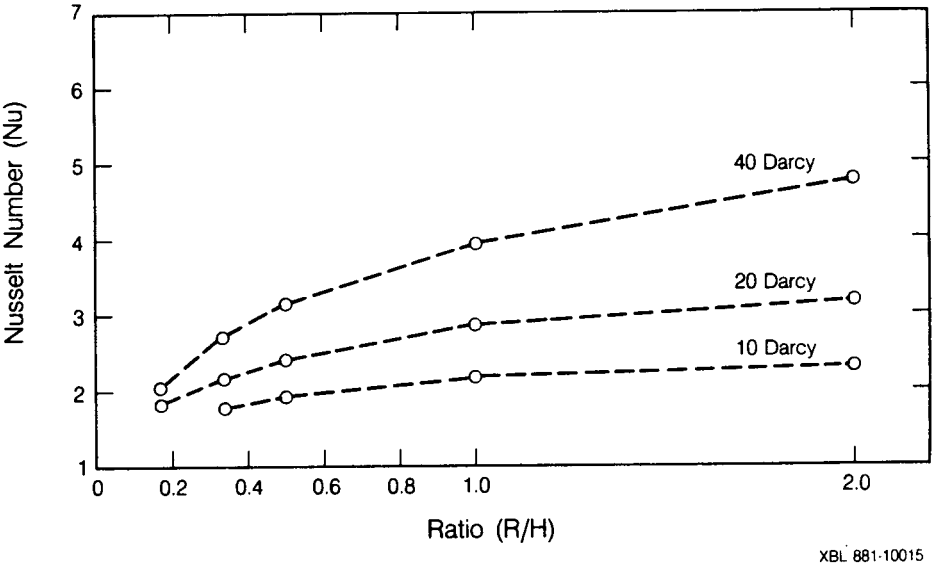


Figure 7. Results of critical convection simulations, plotted in terms of Nusselt number versus aspect ratio (r/H).

PROCEEDINGS, Thirteenth Workshop on Geothermal Reservoir Engineering
Stanford University, Stanford, California, January 19-21, 1988
SGP-TR-113

FLOW RATE DECLINE AND PRESSSURE TRANSIENT IN THE LARDERELLO GEOTHERMAL FIELD

Guiseppe Neri

ENEL - UNG
Pisa, Italy - 56100

ABSTRACT

The production history of most of the Larderello wells, both the older ones and the recent ones, that we have produced at constant pressure, is characterised by a rapid initial decline.
In this study such a decline is interpreted as the consequence of on original flow regime of the "depletion" type being followed by a "diffusion" type regime. Such an interpretation, which does prove consistent with the phenomenology of the geothermal field, was suggested by the results of the analyses of the well-closure tests carried out in the North zone of Larderello and in the Travale field.

THE DECLINE IN PRODUCTION

The production of steam in the Larderello geothermal field depends for over one third of the total on a group of ninety wells located in the northern part, near the township the field is named after.
The analisys of the decline in production as described in this study is mainly based on measurements taken on these particular wells, for the reason that their number has remained constant over two long and quite distinct time-periods; the decline has therefore depended solely on the physical processes regulating the production of the reservoir.
This feature is not true for the other areas of Larderello.
The history of production (Fig.1) is characterised by two peaks corresponding to the years 52-56 and 65-67 due to the contribution of the wells built in those years in the areas known as Valle Secolo and Gabbro (Gennai, 1964; Celati, 1976),

Other features of the production history are:
- a uniformity of supply pressure (~ 5 bar) in the wells (1), steady over long time-spans;
- the contribution made by the reinjection of condensate waters, as of the year 1979;
- the limitations put on the flow from 1980 onwards, with the aim of increasing the pressure in the reservoir.

The fall in production has already been analysed by various authors with methods based on Arps [6] correlations and other kinds (Atkinson, 1978; Celati, 1976; Gennai, 1964). Gennai and Sestini come to the conclusion in their study that the law of decline is of a harmonic type, but such a conclusion is not very convincing due to the poor resolution of the method of graphic smoothing used.
Atkinson et al. found that the whole family of curves proposed by Arps have to be used to describe the drop in flow of some Larderello wells situated in the Serrazzano area, thus failing to come to any conclusions about the type of decline.
However in that study little consideration was given to the effects of interference between wells, which can modify the typology of the decline when they come into play.
In this analysis we are therefore considering wells or groups of wells which can be considered isolated. One example of the decline in the flow of an "isolated" well, which has produced at a more or less

(1) An exception to this is the group in the Gabbro area which produce at pressures a few bar higher.

constant pressure, is provided by Well VC 10. The law of decline turns out to be of an exponential type over the first ten years or so of production (Fig. 2). Thereafter the flow remains almost constant, with the same type of decline as the older wells have.
The entire decline can be described in a single analytical function of the type:

$$G-G_\infty = (G_o - G_\infty) \cdot \mathrm{Exp}(-t/\tau) \quad (1)$$

which however does not satisfy the condition of zero flow at $t \to \infty$, which we would expect on the strength of plausible physical considerations.
To check if the decline of Well VC 10 were characteristic of the wells of Larderello North too, it was decided to subdivide those wells into homogeneous groups, according to their topographical location and their year of construction; this was done with the aim of overcoming difficulties of interpretation caused by interference phenomena. In this way two groups of wells selected in Larderello North, the first being a group of seventy wells mostly in the Valle Secolo area, and built before 1956, and the second being the five wells located in the Gabbro area.
For both of wells the decline in flow is characterised initially by a law of exponential type (Fig. 3,4).
Such behaviour could to some extent be influenced by the fact that the wells under consideration began producing over a time-span which is not negligible in respect of the time constant of the decline. Noting however that the time-constants of the single wells have similar readings, we must conclude that the exponential nature of the decline is real, and not the result of a manipulation of data.
Once again we find that a function like the (1) interpolates excellently the experimental data.
Considering that an exponential decline is typical of a reservoir in depletion, the period of decline successive to it might be the manifestation of a new production phase of the reservoir. The levelling-out of the curves showing declining flow could indicate the presence of a recharging of the reservoir, manifesting when the depletion has brought about some drop in the pressure. Such a recharge could be caused by a deep water table feeding the upper part of the reservoir, (Truesdell, 1973) or by meteoric surface waters located on the outer edges of the geothermal field, as has been proposed by various authors (Celati, [7], 1976; Petracco, 1975).
But some indications provided recently by the drilling of wells more than 3000 m. deep (Cappetti, 1985) go against the previous hypotheses, whereas the results of some closure tests carried out simultaneously on groups of wells (see Ch.3 and Neri, 1985) indicate the existence of a diffusive flow regime in the pressure transients.
For this reason we have looked for the existence of such a flow regime in the history of production, plotting the flows as a function of $t^{-1/2}$.
One can recognise in the decline of production illustrated in Fig. 5 that at the end of the depletion phase the flow falls linearly as a function of $t^{-1/2}$, and that the line interpolating the graph of Fig.5 satisfies the condition $G = 0$ for $t \to \infty$, as considerations of a physical nature would demand. This means that a diffusive flow regime is set up within the reservoir.
This interpretation of the decline in flow leads to a conception of a reservoir behaving firstly with a more or less constant volume (depletion phase) and then continually variable (diffusion phase).
The diffusive condition seems moreover to manifest in a vertical direction, for the second group of wells under consideration - the one which started up production a few years later than the first group - possesses the same features.
But over and beyond these considerations, which may have a great importance in the elaboration of a conceptual model, we are also interested in

making forecasts for production based on past records.
With this aim in mind it may be useful to describe the decline with a single analytical function that nevertheless satisfies the conditions

$$G \equiv \mathrm{Exp}(-t/\tau) = 1-t/\tau \quad \text{for } t \ll \tau$$

$$G \equiv 1/\sqrt{t} \quad \text{for } t \gg \tau$$

The most simple function to satisfy these conditions is

$$G \equiv \sqrt{\emptyset} \,/\, \sqrt{(1 + t/\emptyset)} \qquad \emptyset = \tau/2$$

which is up to describing the entire decline in production of the wells being considered and has been put forward by A. Barelli (2) as a solution to a flow problem in which the reservoir and the production pressures are constant, but the resistance to flow increases in linear fashion with the mass produced.
An analytical funcion describing the decline in flow, and with the correct boundary conditions, can acquire the significance of an influence function, at constant pressure, of the linear flow equation - if one exists - governing production.
If we admit the existence of an equation of this kind, at least in that period of production with a diffusive condition, then the function

$$Fp(t) \equiv \beta/\sqrt{t}$$

can be considered an influence function of the reservoir.
We shall therefore write that the flow G(t), at constant supply pressure P_f, is rendered by

$$G(t) = (P_o^2 - P_f^2) * \beta/\sqrt{t}$$

where P_o is the initial static pressure.
From the slope of the line in Fig. 5 we have

$$(P_o^2-P_f^2)*\beta \simeq 3 \cdot 10^8 \ (\mathrm{tons}/\sqrt{h})$$

Along with the influence function at constant pressure, can be considered the analogous function $F_o(t)$ at constant flow defined as

$$(P_o^2-P_f^2(t)) = G \cdot F_o(t)$$

From the theory

$$F_o(t) = \alpha\sqrt{t} \ ; \ \alpha = 2/(\pi*\beta)$$

Knowing about the two influence functions allows us to describe the evolution of the reservoir in the two possible management scenarios of imposed flow or pressure. Assuming that $P_o^2-P_f^2$ is in the order of 10^3 bar^2 we can calculate

$$\alpha \simeq 2 \cdot 10^{-3} \ (\mathrm{bar}^2 \cdot \sqrt{h}/\mathrm{tons})$$

and the response function at constant flow turn out to be

$$P_o^2-P_f^2(t) = 2 \cdot 10^{-3} G\sqrt{t}$$

This result can be used to forecast the recovery of pressure in the reservoir, caused by a closure of the wells for a time δt, small with respect to the production time preceding the closure, and during which the flow can be held to be constant.
Applying the principle of superposition, and indicating with t^* the time the closure occured in, measured as from the start-up of production, the reservoir pressure P(t) for $t>t^*$ is given by

$$P^2(t)-P^2(t^*) = 2 \cdot 10^{-3} G(t^*) \sqrt{(t-t^*)}$$

Putting

$$G(t^*) = 950 \ \mathrm{t/h}, \ P(t^*)=6.5 \ \mathrm{bar}$$

we get approximately

$$\delta P = P(t)-P(t^*) \simeq -15\sqrt{(t-t^*)}$$

THE FLOW REGIME AND PRESSURE TRANSIENTS

From the year 1980 onwards, closure tests have been carried out for entire groups of wells. The first of such testings concerned the Travale field (Neri, 1985), and the second the Larderello North field - this carried out with the aim of assessing the possibility of managing the reservoir at a

(2) Private communication.

pressure higher than the one at present.

The Larderello North Well-Closure Test

The test involved the closure, within the span of two hours, of 51 wells which were producing 950 t/h of steam.
During the closure period, which had a duration of 20 days, the pressure at the head of all the closed wells was measured daily, and then measurements continued intermittently at the 19 control wells after the reopening of the producing wells.
At the reopening phase the flow was regulated at the level pertaining before closure; in some cases the well-head valves were throattled.
The pressure build-up curves of the 70 wells involved in the test (Fig. 6,7) reveal a homogeneous behaviour, with just a few exceptions due to phenomena of condensation or such.
The homogeneity of behaviour indicates the existence of a single law of pressure build-up one which has turned out to be of a diffusive type, as can be seen in Fig. 7, in which the pressures are plotted as a function of the square root of closure time.
The majority of the closure curves lie between 6 and 7 bar, with a slope of 0.05 bar/(h)$^{1/2}$, three times less of that calculated. A limited number of 12 wells lie outside these margins, with slopes of a similar value.
These are wells located further out from those with lower pressure, and a few hundred metres deeper.
The test did not point to phenomena of radial flow between the edges of the reservoir and its centre, neither did the storage capacity of the reservoir turn out to be very significant.
The test results demonstrate rather that there is a flow regime of a diffusive nature throughout the reservoir, with negligible storage, and that it is developping in a vertical direction.

Compressibility and Diffusivity

During the drilling of new wells in the Larderello North Zone, it has recently been found that there exists, in the most heavily drilled area,a vertical pressure gradient of 0.01 bar/m.
Given that the reservoir produces in a semistationary state, this gradient determines the current flow of vapour according to Darcy's law

$$q = \frac{K}{\mu} \cdot \text{grad}\,(P)$$

Assuming a linear flow model, the increase δP of pressure during the closure of the wells, is rendered by

$$\delta P = 2q \frac{\mu}{K} \sqrt{\frac{\eta \delta t}{\pi}}$$

Combining the two equations we see that the diffusivity depends only on the pressure gradient (3) and on th slope of the build-up curves.
The value of $5 \cdot 10^{-3}$ m^2/s, coming from the calculation, is two scales lower than the previous estimates made by analyzing the build-up of single wells.
The estimation of $\underline{\varepsilon}c$ does not come as readily as that of the diffusivity. We need to postulate a flow surface, that we will suppose equal to the topographical one (5 km^2) over which the wells are located. So we get

$$\frac{K}{\mu} \simeq 10^{-8} \text{ m}^2/\text{Pa} \cdot \text{s})$$

$$\underline{\varepsilon}c \simeq 2 \cdot 10^{-6} \text{ Pa}^{-1}$$

A figure of this kind for $\underline{\varepsilon}c$, is more compatible with a biphase fluid than with superheated steam.

Influence Functions at Constant Flow

The results of the closure tests show that the relationship which exists between increase of

(3) The dependence is quadratic, and so in the calculation of η the uncertainty over the figure for the gradient gets amplified.

pressure and time of closure is of the type

$$\delta(P^2) = G \cdot F_e(\delta t)$$

were $F_e(t)$ is the influence function at constant flow, which is

$$F_e(\delta t) = .65\sqrt{\delta t}\ /G$$

The influence function can be used to simulate reservoir manegement scenarios, with variable flow regimes; in particular it can be used to calculate the fall in pressure during the period following the reopening of wells. Given the invariance of the flows we shall write

$$\delta(P^2)=.65[\sqrt{\delta t} - \sqrt{(\delta t-T^*)}]\ ;$$
$$;\ \delta t > T^*$$

T^* = Closure time

The theoretical variation in pressure which is calculated with the above equation is shown in diagramatic form in Fig. 8, together with the pressures of the control wells.
The similarity between the theoretical curves and the measurement graphs is considerable and shows the validity of the theoretical approach used.
A more detailed analysis of the various curves shows (Fig. 9) that the measured decline of pressure is not, initially, of a diffusive type, nor is it from storage. It might rather be caused by a phenomenon of evaporation of the steam condensed during the closure.
This consideration would explain also the difference between the coefficient α as mesasured, and that as estimated from the production decline.

CONCLUDING CONSIDERATIONS

The decline in production of the Larderello reservoir is interpreted is this study as the consequence of two production regimes, defined as the depletion and the diffusion regimes. The diffusive vertical-flow regime has been experimentally confirmed by the simultaneous closure tests of some fifty wells. The results of that testing, along with the measurements of the vertical pressure gradient made possible by the recent drilling of deeper wells then those currently in production, have enabled us to establish figures for the diffusivity and compressibility of the reservoir fluid.
Regimes of depletion and diffusion had already been considered by W. Brigham and the author (1980) to elaborate a production model for one part of the Larderello reservoir, getting some excellent concordance between calculations and measurements. Hovever, in that study the major factor contributing to the depressurization at the top of the reservoir was seen to be mainly due to a diffusion process ongoing since the start-up of production. In this present analysis, on the other hand, the initial depressurization is held to due to a depletion production regime.
The studies that we have described were motivated by needs of an industrial nature.
If we consider from this point of view the results which have been obtained, some useful indications can be extracted for the management of the geothermal field's exploitation.
First of all, as far as the practical problem of production forecasts is concerned, the Arps family of analytical equations is of limited use. A family of equations of this kind bears upon the exponential decline wich occurs during the depletion production regime, but cannot describe the decline that occurs once the regime becomes a diffusive one.
The equations that we have proposed do have a more general utility.
As far as the implications involved in a diffusive flow regime are concerned, one of the main ones is the existence of a vertical pressure gradient, as has indeed been experimentally verified.
It follows that a considerable increase of production pressures might be obtained by deepening the present wells.

Another feature of a diffusive production regime with a biphase fluid is the existence of an evaporation surface which is steadily receding from the top of the reservoir with the passing of time.
Therefore the upper part of the reservoir is no longer contributing to production now, since the reserve of liquid water which was initially there has run out. And so there should be large volumes of dry rock still at high temperatures (Cappetti, 1982).
Thus, when a diffusive regime is well under way, conditions exist in the reservoir which are particularly favourable for reinjection. Such conditions do not exist when a reservoir is producing in a depletion phase though, when water exists in a liquid phase in the neighbourhood of the well.

ACKNOWLEDGEMENT

I'm indebted to G. Boni and C. Frati for their contributions to the handling of production data. Discussions held with my colleagues A. Barelli and G. Manetti have proved highly useful.

REFERENCES

[1] TRUESDELL A.H.,WHITE D.E., - Production of Superheated Steam from Vapor Dominated Geothermal Reservoir. Geothermics 2, 3/4, 1973.

[2] BRIGHAM W.E. and NERI G. - A Depletion Model for the Gabbro Zone. - Proc. 2nd DOE-ENEL Workshop for Cooperative Research in Geothermal Energy, Berkeley 1980.

[3] ATKINSON P., MILLER F.G., MARCONCINI R., NERI G., CELATI R. - Analysis of Reservoir Pressure and Decline Curves in Serrazzano Zone. Larderello Geothermal Field. Geothermics 7, 2/4, 133, 1978.

[4] CELATI R., MANETTI G., MARCONCINI R., NERI G. - A Reservoir Engineering Study in Gabbro Zone (Northern part of Larderello Field). Proc. 2nd Workshop on Geothermal Reservoir Engineering. Stanford University, Stanford, 1976.

[5] GENNAI N., SESTINI G. - Studio sulle Cause del Declino della Portata di Vapore Endogeno nel Tempo - Ricerche di Termotecnica 14, 1964.

[6] ARPS J.J. - Analysis of Decline Curves Trans. AIME 160, 228, 194.

[7] CELATI R., SQUARCI P., STEFANI G., TAFFI L. - Study of Water Levels in Larderello Region Geothermal Wells for Reconstruction of Reservoir Pressure Trend. - Atti del "Simposio Internacional sobre Energia Geotermica en America Latina. Guatemala 1976. Edito da Istituto Italo Latino Americano, Roma.

[8] PETRACCO C., SQUARCI P. - Hydrological Balance of Larderello Geothermal Region. Proc. 2nd U.N. Symposium on the Development and Use of Geothermal Resources S. Francisco 1975.

[9] CAPPETTI G., CELATI R., CIGNI U., SQUARCI P., STEFANI G., TAFFI L. - Development of Deep Exploration in the Geothermal Areas of Tuscany. Geothermal Resources Council Trans. Int. Volume, 1985.

[10] NERI G. - Recent Development and Tests in Travale Field. Geothermal Resources Council Trans. 9/II, 1985.

[11] CAPPETTI G., GIOVANNONI A., RUFFILLI C., CALORE C., CELATI B.. - Reinjection in the Larderello Geothermal Field. Proc. Int. Conf. on Geoth. Energy. BHRA, Florence, 1982.

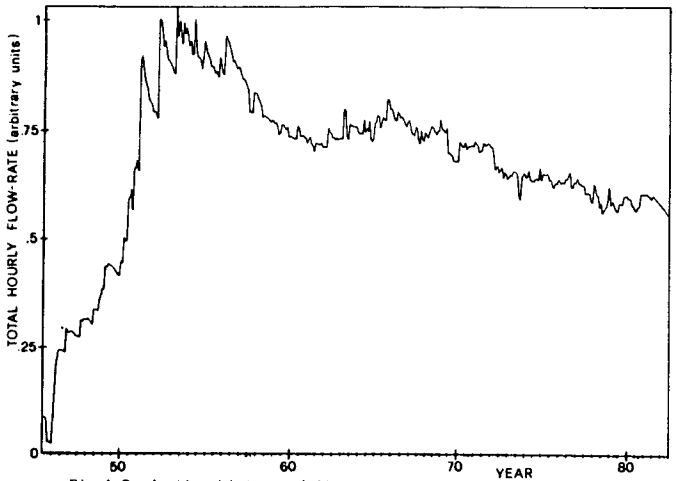


Fig.1 Production history of 89 Larderello wells

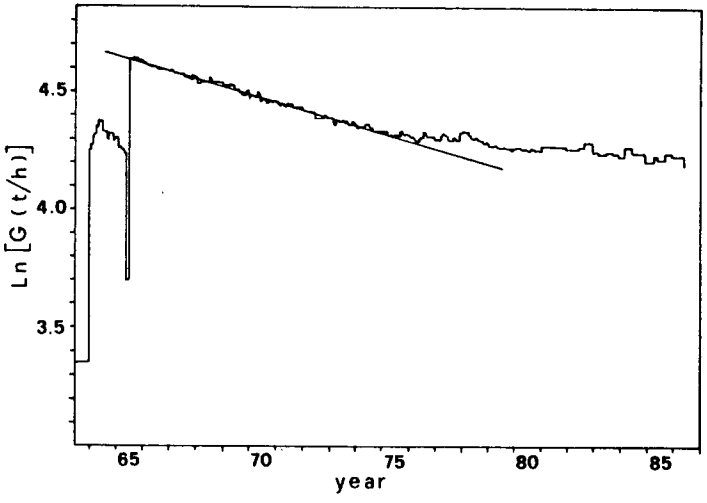


Fig.2 Production history of well VC10 represented by the natural logarithm of flow.

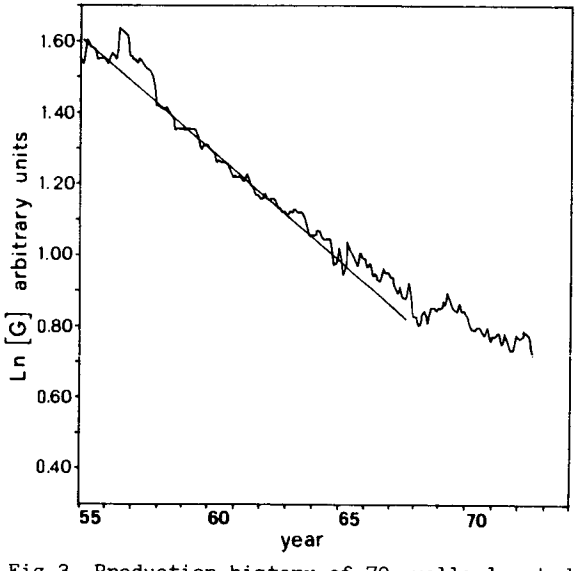


Fig.3 Production history of 70 wells located mostly in the Val di Secolo area.The se gment drawn in on the figure does not represent any interpolation.

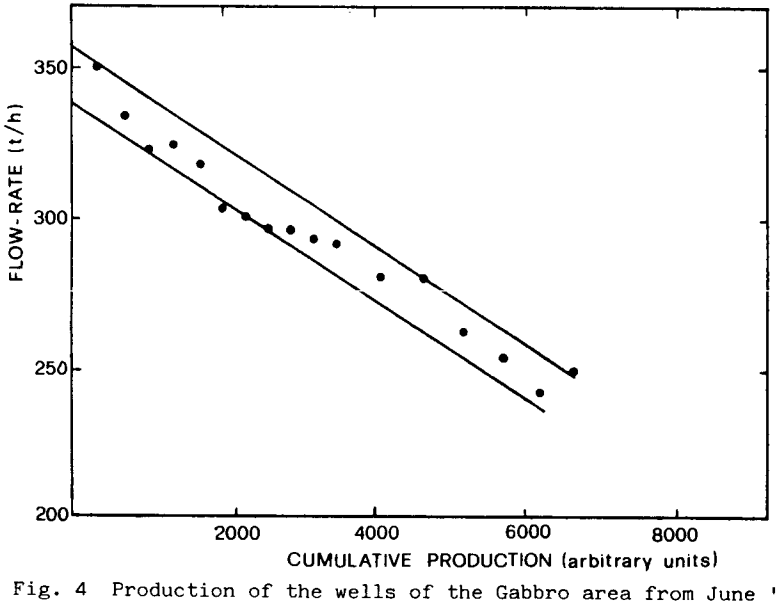


Fig. 4 Production of the wells of the Gabbro area from June '69.

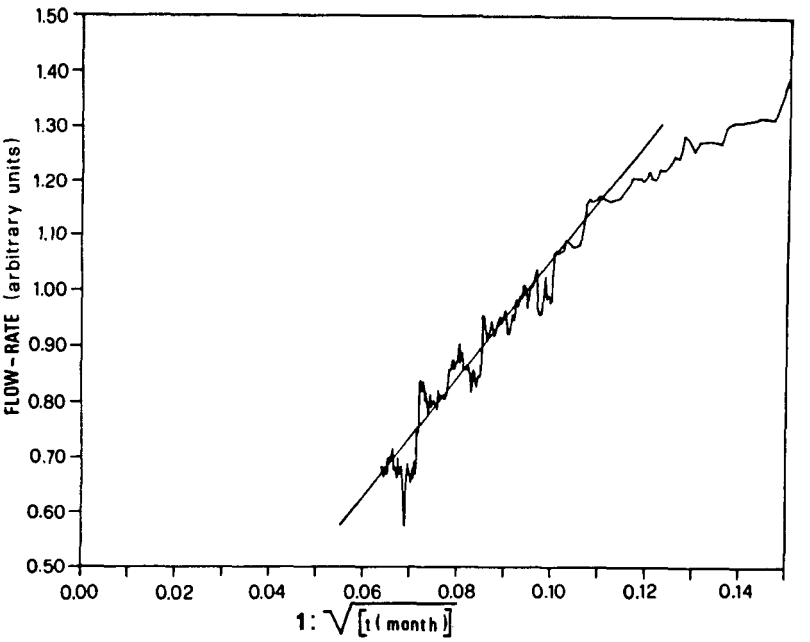


Fig. 5 Graph of the flow of the Fig. 3 wells as an inverse function of the square root of production time, measured as of Aug. 1956.

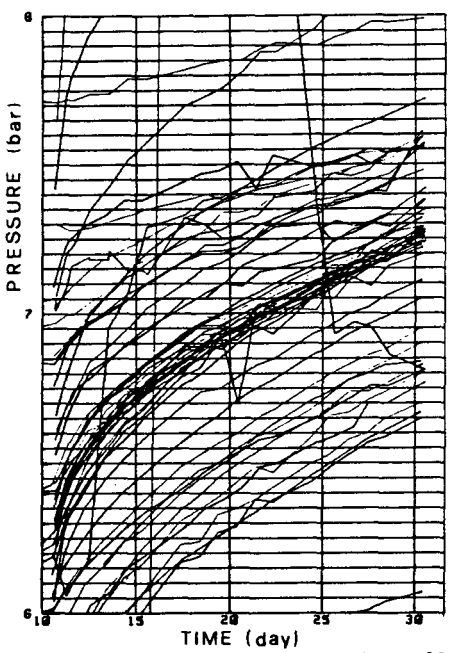


Fig. 6 Pressure graphs for the wells closed during the June '85.

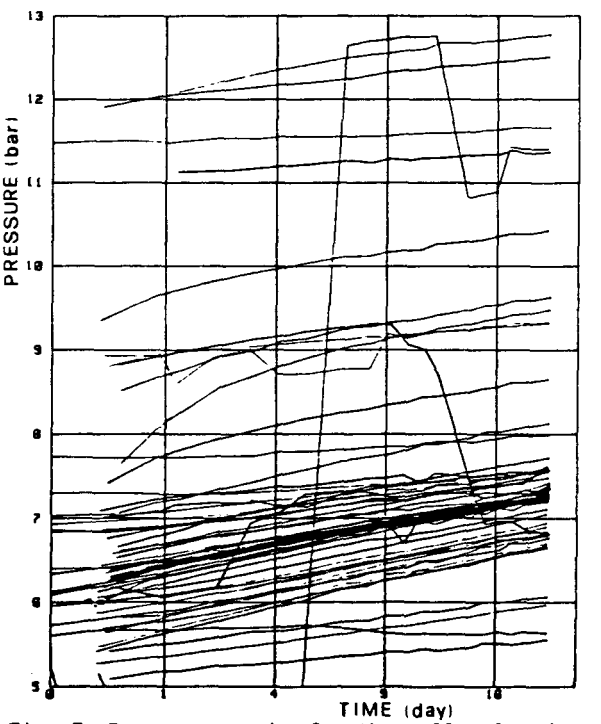


Fig. 7 Pressure graphs for the wells closed during the June '85 tests, as a function of the square root of closure time.

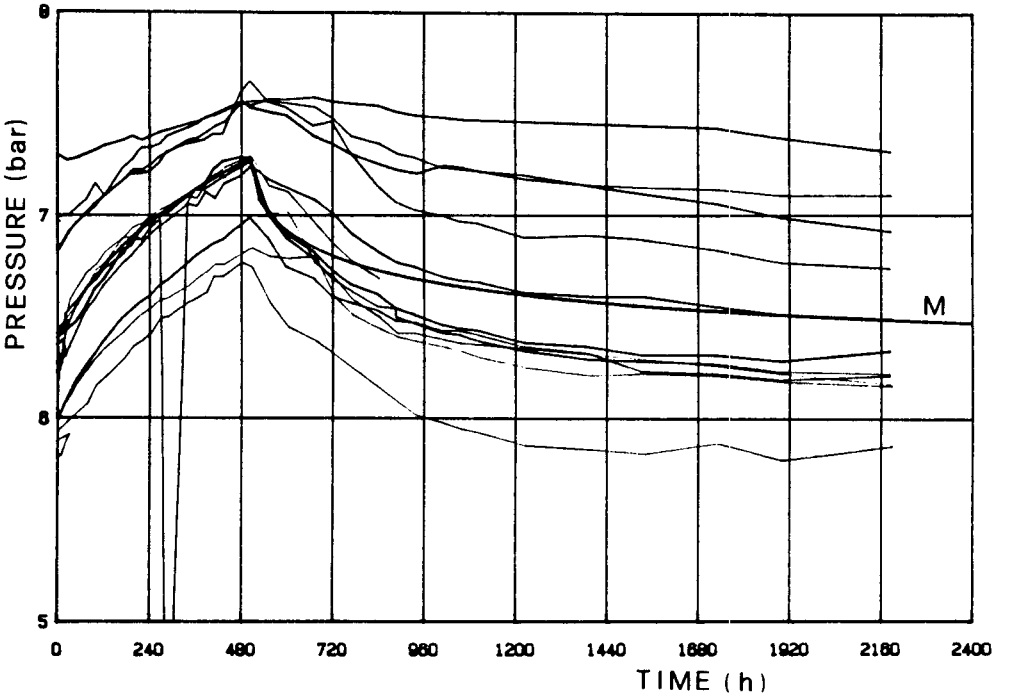


Fig. 8 Pressure graphs of the control wells during the June '85 closure of the production wells and in the period following their reopening. The curve marked M was calculated using the influence function of Well 85.

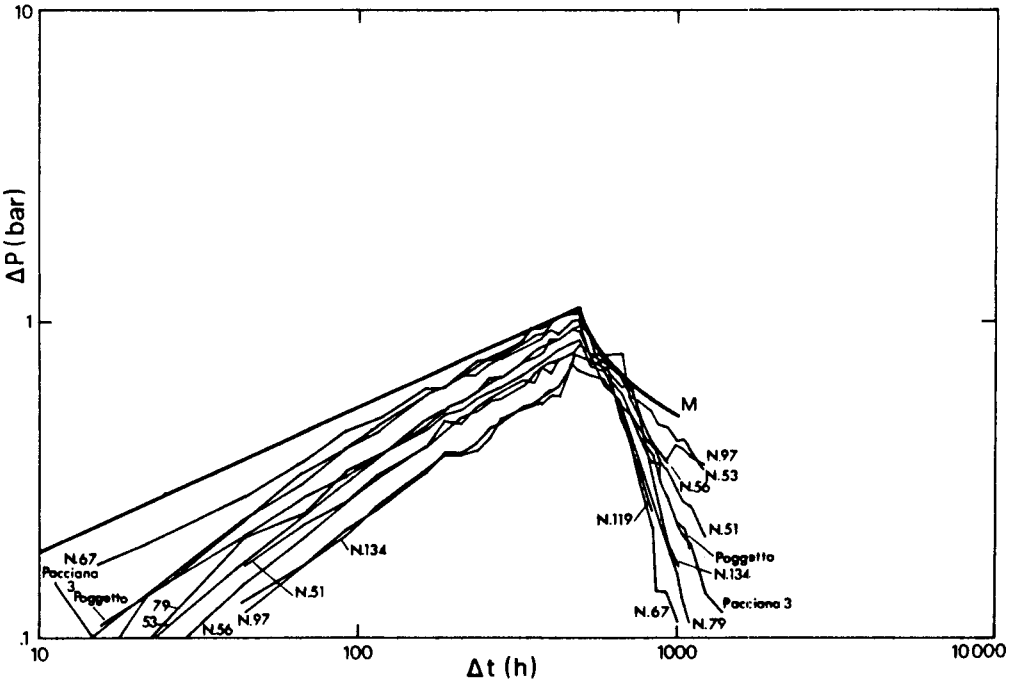


Fig. 9 Bilogarithmic pressure graph of some of the control wells. The curve M was calculated as in Fig. 8.

RESERVOIR ENGINEERING OF WAIRAKEI GEOTHERMAL FIELD

MALCOLM A GRANT

Department of Scientific and Industrial Research
New Zealand

1 INTRODUCTION

Wairakei was the first liquid dominated geothermal field exploited for major power production. As such many decisions were taken on an ad-hoc or experimental basis. In retrospect the choice of Wairakei was fortunate : with extensive shallow high permeability and major recharge it is an easy field to exploit.

This lecture describes the history of the field and the contribution of reservoir engineering to field management, and describes the reservoir as it is now understood.

2 THE FIELD

This section describes the reservoir as it is now understood. Figure 1 shows a map of Wairakei field and its link to the adjacent Tauhara field.

A line of section is shown on the map. Figure 2 shows geological structure along this section line. Figures 3 and 4 show isotherms in the undisturbed state of the field and in the early 1080's.

Significant geological units are:

- Huka Falls formation, impermeable except where fractured, and so forming a partial cap to the reservoir.
- Waiora Breccia, generally permeable, and extremely permeable at its contacts with the Huka Falls formation, and the underlying.
- Wairakei Ignimbrite and Karapiti Rhyolite.

The principal permeability from which wells derive fluid is the contact between the breccia and the ignimbrite. Some shallow wells also draw on the mudstone-breccia contacts, and outlying wells (not in current use) on the breccia-rhyolite contact. On the reservoir scale, the uniformity of drawdown across the field shows that good permeability is horizontally continuous across Wairakei and Tauhara. A

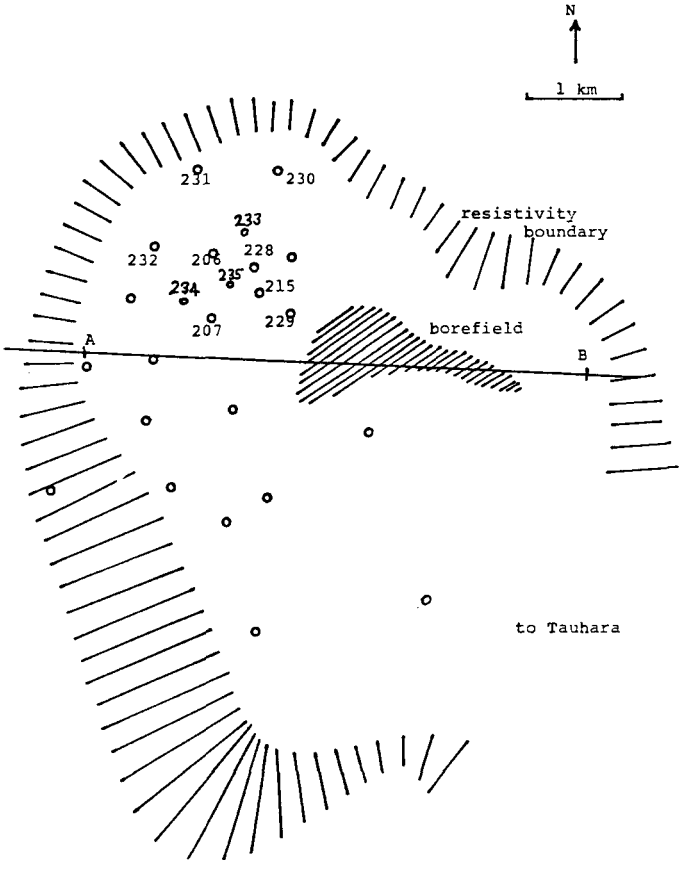


FIGURE 1. WAIRAKEI GEOTHERMAL FIELD, after Risk et al. 1984
Open circles denote '200 series' wells.

representative kh value is 30-300 darcy-metres, although production wells intercept local regions of markedly higher or lower permeability.

The faults constitute the principal vertical permeability of the field, giving an average k_v for Wairakei of about 5 md. Compared with the k_h value for the formation contacts and a reservoir of h of say 1 km, this indicates that one the gross scale the reservoir is anisotropic, with $k_h >> k_v$. As the principal vertical flow channels, the

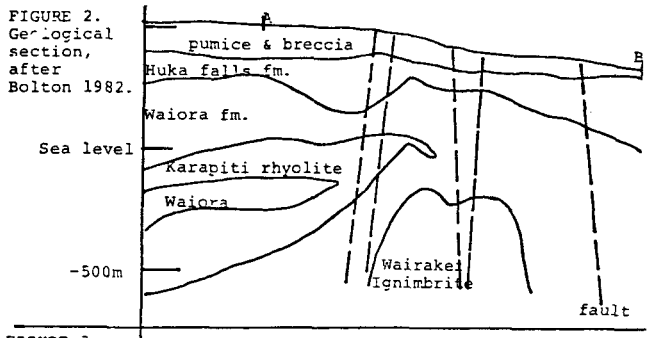


FIGURE 2. Geological section, after Bolton 1982.

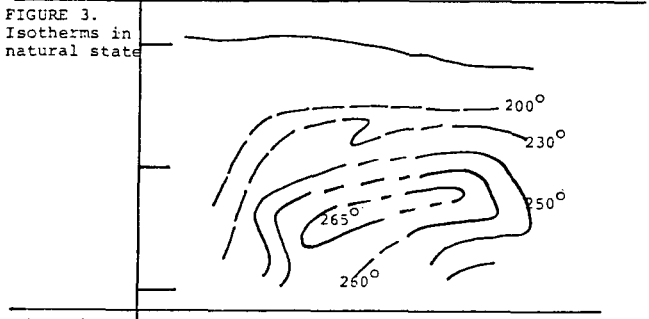


FIGURE 3. Isotherms in natural state

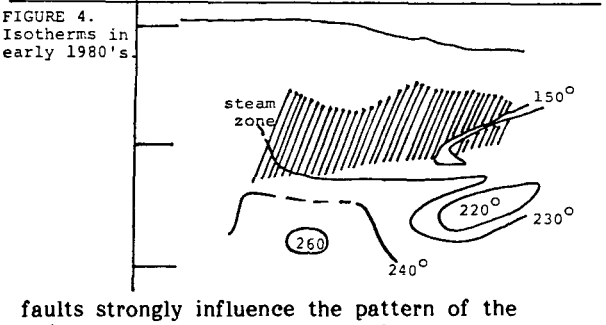


FIGURE 4. Isotherms in early 1980's.

faults strongly influence the pattern of the upflow in the natural state, and the downflow of surface waters induced by exploitation.

Figure 3 shows an isothermal section in the undisturbed state of the reservoir. The isotherms show that the natural flow originates as an upflow in the west of the field (to the north of the section). From this upflow there is an outflow almost due east, which, beyond the end of the section, manifests itself in the surface discharge at Geyser Valley.

The maximum temperature attained within the reservoir depths is about 265°C. In the natural state, this rising water boiled at 260-230°C, forming a liquid-dominated two-phase zone in much of the shallower parts of the reservoir.

Pressures in the natural state were those of a liquid-dominated reservoir. Reservoir pressures at feedpoints of early wells define a gradient some 7% above hydrostatic. This pressure excess is the gradient needed to drive the natural flow up through the reservoir, and it is from this that k_V = 5md is computed. No break in gradient or discontinuity is apparent so that there is, on the reservoir scale, no confining layer.

The changes in the reservoir following exploitation are conveniently discussed under three categories: pressure, fluid type, and temperature. Traditionally, pressure changes have been of greatest interest, but they do not fully characterise a geothermal reservoir. Figure 5 shows pressure and temperature profiles in one section of the field at different times in field history. (After Allis & Hunt, 1986)

There is now a shallow liquid-dominated region, not greatly disturbed by exploitation, and a deep liquid-dominated region in which pressures have fallen below the original trend. Between the two is a region of low gradient and somewhat variable pressures. The pressure drop in the lower "water" zone is fairly uniform across the field. Figure 6 shows pressure profiles along the section and it is this pressure that is referred to as the "field pressure", "reservoir pressure" or "deep liquid pressure". The history of this field pressure has been analysed in a number of simple and elaborate models of the reservoir from the first by Whiting & Romey (1969) to the elaborations of Frudkin et al (1982). In general good matches have been obtained by quite a wide range of models. Figure 7 shows the field history, with the changes in deep liquid pressure, discharge enthalpy, and the mass flow from the production wells.

The changes in fluid type correspond to the changes in pressure. In the undisturbed reservoir, there was a shallow two-phase zone. Mass withdrawal and pressure drop caused the two-phase zone to increase in depth and dryness. By 1962, enough water had drained for a vapour-dominated interval to form between two liquid-dominated zones.

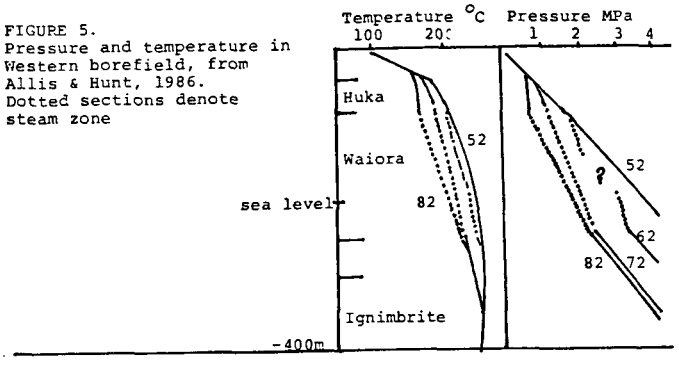


FIGURE 5. Pressure and temperature in Western borefield, from Allis & Hunt, 1986. Dotted sections denote steam zone

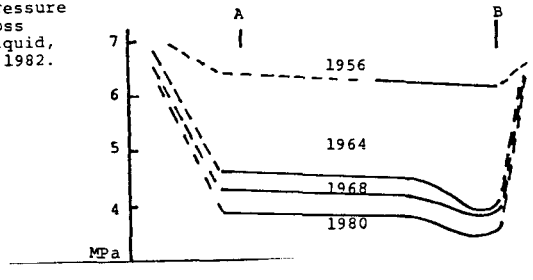
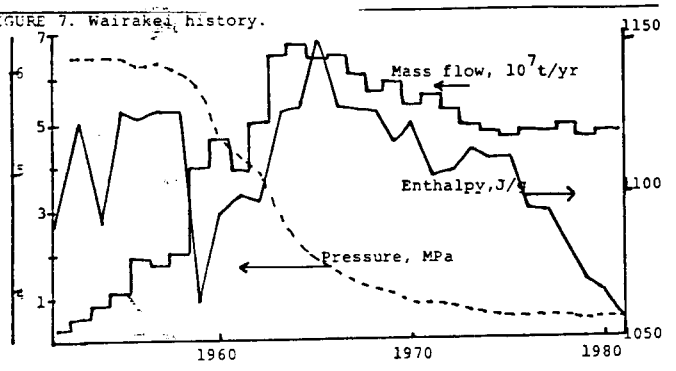


FIGURE 6. Pressure profile across field, in liquid, from Bolton 1982.

FIGURE 7. Wairakei history.



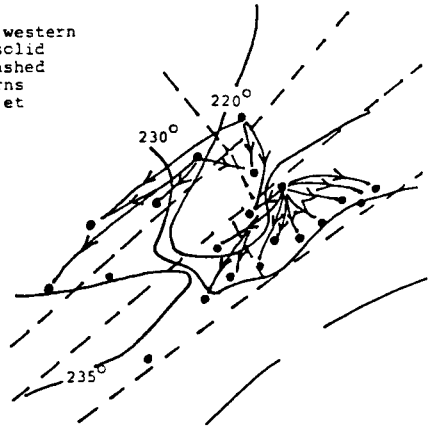
This is the region of reduced gradient in Figure 5. Feedpooints in this steam zone generally supply high-enthalpy fluid, or "dry" steam (saturated, not superheated). Two-phase fluid may also be discharged from the upper liquid-dominated zone, and from the top of the lower; but the bulk of production derives from liquid water further down.

The previous paragraph assumed that all temperature changes are caused by boiling: that two-phase conditions occur everywhere pressure has fallen below saturation corresponding to the original temperature. In general this is true, but there has also been some cooling of the reservoir by the entry of cooler water. Figure 4 shows the 1981 conditions for the same section as Figure 3. In the west, the extent of 260°C water is unclear. Internal flows are now so frequent in wells that it is very difficult to construct isotherms, and 260°C water may occur extensively, disguised by downflows. The temperatures in the west reflect the changes caused by boiling. In the production field intrusions of colder water are present. One shallow intrusion (<150°C) is very localised, but carries several hundred tonnes per hour of water, and was responsible for downflows or temperature inversions in WK 31, 107 and 57. A more extensive area of cooling at greater depth is shown by inversions in WK 48 and 121. It is possible that this zone of cooler water derives from the upper intrusion, by downflows in wells.

Figure 8 shows a plan view of the western production area. Isotherms at RL-200 m are shown, as are faults and the pattern of returns in a number of tracer tests. There is a strong correlation between the pattern of the isotherms, the pattern of flow as indicated by radioactive tracer (McCabe et al., 1981), and the predominant SW-NE fault direction. Colder water is entering the reservoir from the New Zealand, along the paths where there was once outflow to surface discharge. The connection to surface is further confirmed by the fall in groundwater level in this area of the field. Figures 4 and 8 also show hot inflow to the production area, slanting upward and flowing almost due east from the west of the field.

It should be stressed that the area affected by cold inflow is, so far, fairly small - about 1 km^2 of the reservoir. A heat balance shows that cold inflow does not yet form the dominant part of the Wairakei recharge and most of the reservoir is little affected by it. However the production area is so affected, and this has had significant effects on the performance of wells. Despite this deterioration, there remains a very large heat store at Wairakei, in a reservoir of proven permeability. Production, possibly through replacement wells further west, can be maintained for a long time to come.

FIGURE 8. Isotherms in western borefield at RL-200m (sclid lines) major faults (dashed lines) and tracer returns (arrows). After McCabe et al 1981.



3 HISTORY 1953-1980

The preceding summary contains much relatively recent data and interpretation. Actual decisions were made in the light of the available data and concepts.

Major drilling began in 1953, after some preliminary shallow wells. Wells were drilled at sites determined on geology. If successful, they were left to discharge. Lacking any other basis, the proven potential was taken as the total output of the wells. The extent of the field was not known and in fact drilling covered only a fraction of the field.

Banwell (195) made stored heat calculations, and demonstrated that the heat reserve was large. Interference was measured between two wells, and a downhole pressure transient measured by gas purge, but these results were not pursued.

Wellhead pressures were measured and downhole temperature profiles. After 1960 downhole pressures were also measured. The wellhead pressure data show drawdown began in 1952-53. For political reasons (denial of effect on surface activity) this observation was ignored. Generation and full production began in 1958 and with it major pressure drops.

The station was designed to include a heavy water separation plant. Although this was

cancelled, design parameters remained set. In particular the operating wellhead pressures was set at what is now regarded as a high value of 15 bar.

After commissioning the first two stages of the station to a total capacity of 192MW, the fall in pressure was so obvious that Stage III was abandoned. Through the first half of the 1960's further exploration wells ('200 series') were drilled that by about 1965 had roughly delineated the field. A first resistivity survey now also gave an indication of field size. Many pressure transients were recorded at this time but nothing was made of them. In retrospect, they are dominated by wellbore thermal and flow effects.

Part of the 200 series were drilled to northwest of the production borefield at Te Mihi. It was thought this might be a separate resource capable of supporting another new station. However the same (draw down) pressures were found and so it was concluded that this area was effectively exploited by the existing borefield. This inference is the first application of reservoir engineering to field management.

In 1965, the first reservoir engineering study of Wairakei was commissioned, later published as Whiting and Ramey (1969). The field was modelled as a sealed reservoir of compressed liquid, and the model validated by a regression fit to pressure-discharge history. The volume of liquid found was enormous, and implied a field capacity of 2000 MW. After some interesting discussion, the conclusions were rejected. However the study permanently influenced the development of concepts of Wairakei, and in particular the later series of simple models fitted by regression.

Uncertainty about the field capacity continued. Through this period and up to the early 1980's decisions about field management were taken by engineers on a practical basis. Estimates of field capacity at this time ranged from 2000 MW down to claims that the field would not sustain the existing plant for more than a few years longer. In the face of this uncertainty it was decided to finally abandon plans to expand the station. The danger of depletion was also guarded against. A sequence of exploration wells were drilled in 1965-66 in a number of other fields. Two were drilled at Rotokawa, the nearest field to Wairakei. Having found steam here, the field was then abandoned. It was in fact being left aside as an informal "reserve" to pipe steam to Wairakei power station if necessary.

Four wells were also drilled at the adjacent Tauhara field, which, like Te Mihi, proved to be linked to Wairakei.

Drilling stopped at Wairakei in 1966. Over the next 15 years field management consisted of a series of engineering improvements and the connection of idle wells. The engineering improvements resulted in doubling the thermal efficiency. Actual output was maintained fairly steady at 140-150MW. Continued drawdown of the reservoir meant that operating wellhead pressures had to fall progressively with time.

Original reservoir engineering contributions began to appear by the mid 1970's. McNabb developed the technique of interpreting reservoir pressure and plotting this against depth to determine reservoir pressure distribution, a technique now standard in New Zealand. From this and the natural flow he deduced the vertical permeability. McNabb also developed the first version of the drainage model as late elaborated by Fradkin et al. (1982). This model idealises the reservoir as an open tank with a free surface, and with pressure-dependent recharge.

This model was used to estimate future pressure drop. Given the stable flow rate, it predicts little change in pressure; a result also obtainable from extrapolating past trends.

Gravity surveys (Allis & Hunt, 1986) were used to determine the amount of recharge and provide major constraints to modelling concepts.

4 HISTORY AFTER 1980 : REDEVELOPMENT PROGRAM

The program of incremental adjustments began to fail in the early 1980's. Larger changes in management are now called for, and reservoir engineering has begun to contribute effectively to decisions.

There are three major pressures on present field management:

1 Existing production is declining, and wells failing. The cause is cold water incursion and falling vapour pressures.
2 An excellent production area remains at Te Mihi, unaffected by cold water, and having generally higher vapour pressures.
3 A commitment has been made to start reinjection.

The response that has evolved is:

1 Abandon attempts to prolong the life of wells in the existing production area.
2 Use a section of the Eastern production area near abandonment for reinjection (thereby accelerating its decline).
3 Develop new production at Te Mihi. This requires drilling and construction of steam lines and, later water lines. The Te Mihi wells will initially be shallow

steam producers, later deepened to normal depths.

The changes in production and injection will cause major changes, locally in reservoir temperature, and field-wide in reservoir pressure.

5 THE PRESENT STATE OF THE BORE FIELD

Wairakei power station's output has been falling significantly in recent years, due to a shortage of steam. (Thain & Stacey 1984). Over much of the field's past history, the field history has been dominated with changes in reservoir liquid pressure. However reservoir liquid pressures are now roughly stable. The continuing fall in output is due to incursion of cold water and falling production temperature. Figure 7 shows the history of field pressure.

As many wells operate close to Maximum Discharging Pressure (MDP) on production, any fall in enthalpy and consequent fall in WHP can be critical. Evidence for the incursion of cooler waters into the borefield comes from a variety of measurements:

(i) downhole temperatures
(ii) production chemistry
(iii) gravity.

For both downhole temperatures and production chemistry, it is the case that changes are sufficiently gradual that they cannot be easily detected over a few years. However over a longer period and using a large number of wells clear trends are detectable, identifying a zone of cold water intrusion from the northeast. Gravity increases in the eastern borefield also require cooler water incursion.

Figure 9 shows the temperature of water entering some representative production wells. There is a clear and continuing fall with time. Chloride contours show much greater detail with fingers of cooler (low silica and chloride) water entering the western borefield. (Brown et al in prep). Isotopic evidence confirms that pattern of groundwater encroachment. The entering cool water is strongly associated with the major faults.

The cold water enters the borefield from above, as a slanting downflow following the path that originally carried upflow to Geyser Valley. The faults provide the passage through the impermeable mudstone. The cold water invasion is getting worse. Several wells have downflows of this water where it enters the well at a shallow feed point and runs down the well.

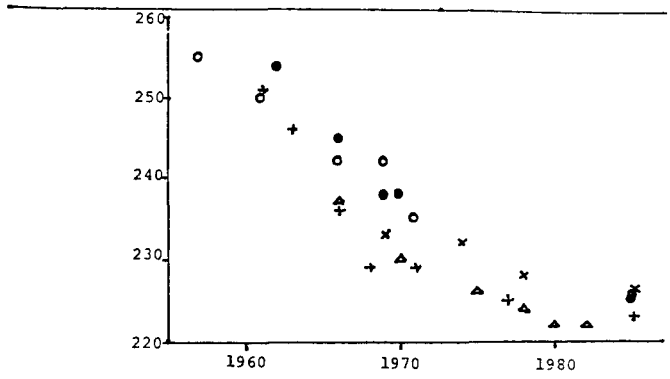


FIGURE 9. Inflow temperatures in five representative wells.

Gravity results also indicate cold water advance. There are areas of gravity increase and decrease. Gravity increase over the western borefield can only be explained by cooling, or by water replacing (Allis & Hunt 1986).

How rapidly production decline will continue if nothing is done is not clear. unpublished reports by Bacon and Grant predict major or steady declines. A better prediction will need an adequate reservoir model, including a good description of the cold water inflow and of well performance.

6 TE MIHI

By contrast to the degraded state of the present production borefield, at Te Mihi the geothermal reservoir has pressures lowered by exploitation but temperatures remain only a few degrees below their original values (except where pressure drop has required cooling by boiling).

As elsewhere in the field, the upper portions of the Wairoa formation contain a steam zone, a vapour-dominated region extending from the base of the overlying Huka Formation to about sea level. At Te Mihi the steam zone has pressures of 20-25 bar. Beneath here liquid water at up to 260°C is found. These temperatures imply far better well performance than from the temperature of 220-230°C available in the existing borefield, although wellheads will be at up to 100 m higher elevation. A region of high pressure extends from Te Mihi and partly into the western borefield. Only in Te Mihi is the zone of high pressure very thick and capable of producing major steam flows.

Given the good production available at Te Mihi, the obvious suggestion is to seek production from here to replace losses in the existing borefield. The exploration wells originally drilled in the 1960's here were production to delineate a new area; they were never used because it was found that they shared a common pressure with the

rest of the field, and hence one might as well use the existing borefield, and pressures were then falling so rapidly no additional withdrawal could be tolerated (Bolton, pers. comm.). This argument is no longer valid because of the temperature difference now present. Given that Te Mihi has better production, issues that need to be addressed are:

(i) economic - is it worth drilling at all at Wairakei
(ii) distance from the power station
(iii) interference between Te Mihi and the existing borefield
(iv) longevity of Te Mihi production

and in general the expected response of the reservoir to what would ultimately be a major shift in production in the field.

The reservoir, and the production drilling, needs to be discriminated into steam and liquid. The steam zone at Te Mihi represents an excellent immediate production prospect. WK228, the first well drilled under the new strategy, initially produced 180 t/h steam with a drilled depth of 393 mm. It is the most productive well ever drilled at Wairakei, and leads to the obvious suggestion of drilling as many such wells as the resource will stand. The obvious question then is:

- what is the production capacity of the Te Mihi steam zone?

7 TE MIHI DEVELOPMENT PROGRAM

Some answers are known already, and in consequence some actions can be planned upon now.

The most obvious example is the drilling of steam wells at Te Mihi. The resource is at present over an area of several square kilometres and hence contains sufficient energy to sustain a steam flow of several hundred t/h for several years. The steam is sufficiently valuable that this justifies drilling and construction of steam mains.

When the steam depletes, deepening such steam wells to water also appears viable. As a competent caprock exists at Te Mihi, the reservoir here is protected from overlying colder water.

Assuming therefore that we are committed to an initial program of steam well drilling at Te Mihi, and steam main construction, what is needed is:

(i) what is the expected rundown of the existing borefield - what is the baseline scenario against which we compare alternatives?

(ii) how long will the Te Mihi steam zone last?

(iii) what will be the effects of water production from Te Mihi?

(iv) what will be the effects of reinjection on the existing and Te Mihi borefields?

These questions will be answered by a coordinated program of exploration drilling and scientific work.

8 TE MIHI EXPLORATION DRILLING

Some exploratory drilling is required to define the Te Mihi resource. The most important aspect is its size, and next its temperature. The existing "200 series" wells define only part of Te Mihi, the northern and western extent is really indicated only by resistivity survey.

In particular, the steam zone, which was created by exploitation, need not coincide with the resistivity. The most important parameter is simply its size, and to determine this we need to find its far edge. This requires drilling wells to the north and west, down 100 to 200 m below sea level, to confirm the presence or absence of steam. As a secondary objective the liquid temperature needs to be defined.

9 REINJECTION

Environmental constraints require Wairakei to reduce waste discharge into the Waikato River. Reinjection is the only practical way to achieve this.

Initial investigations focussed on peripheral reinjection and a trial reinjection well was drilled as WK301. It lies on the resistivity boundary near the power station. Unfortunately it was one of the few wells drilled at Wairakei that did not find good permeability.

Accepting that failure, it is necessary to move into the field to be sure of good permeability. Tracer tests have repeatedly shown rapid movement of tracer over long distances, arguing very strongly that injection wells need to be well separated from procedures. I suggest that a reasonable design is to have injection wells spread over the southern boundary, from the eastern borefield to WK226.

If this is accepted, about one-third of the area lies near the existing eastern borefield. If these wells are now dying, it is an obvious suggestion to use them instead. A reinjection trial is therefore proposed for an initial test of injection 500 t/h into the eastern borefield. This will accelerate the decline of adjacent

wells but their expected lifetime is short anyway.

11 ISSUES

A considerable number of issues need to be described or quantified. They can be roughly grouped under four headings:

(i) Existing trends - what is the baseline against which to evaluate the effects of changes in field management? This essentially requires a good model of the field. The primary contribution is from chemistry and reservoir engineering.

(ii) Te Mihi development - what is the capacity to supply steam, how long will the steam wells last (how many of them?) before they need to be deepened to liquid?

This requires adequate physical definition of the Te Mihi resource by exploratory drilling, well testing, interference testing, geology, geophysics and chemistry; followed by some modelling.

(iii) Eastern injection - what are the effects on existing producers, will thermal decline or pressure increase dominate?

This requires adequate physical and chemical monitoring of the injection, tracer testing and gravity surveys, again followed by modelling.

(iv) Field wide interactions. Injection will raise the liquid pressure. Substituting Te Mihi steam production for liquid borefield production also reduces the withdrawal of liquid. Both will affect reservoir liquid pressure. The addition of 3 "200 series" wells in 1983 added to net total steam flow only half the added capacity, due to the interference effects on existing wells. A rise in liquid pressure will improve well performance but has other long term effects. This is at present substantial hot recharge and raising pressure may reduce this. This will be addressed as part of the modelling required elsewhere.

11 RESERVOIR ENGINEERING CONTRIBUTION

Major changes in field management plans have occurred in the last three years, equivalent to a redevelopment plan for the next ten years. Reservoir engineering studies played a major part, for perhaps the first time in Wairakei's history.

The original decision not to exploit Te Mihi was based on reservoir engineering - the fact that pressures were the same as the borefield. The decision to progressively substitute Te Mihi production was based on two lines of argument:

- initially, economic calculations (Thain) of the cost of additional steam supplies available by connecting existing 200 series wells.
- arguments by reservoir engineers (Bixley, Grant) that long-term production could be maintained only from Te Mihi : and the suggestion of drilling initially shallow wells to exploit the steam zone. Such wells can later be deepened to water producers.

A major reservoir engineering and simulation effort is underway based on both simple models and simulations. Starting injection, and substituting steam for liquid producers will produce major rises in liquid pressure, and falls in temperature. All these effects need to be quantified. In practical terms the major decisions to be made are:

- How much can the Te Mihi steam zone supply before being flooded out?
- Where can injection safely proceed?

12 EXPLORATION RESULTS SO FAR

So far five production wells and three exploration wells have been drilled at Te Mihi since 1985. The first production well, WK228, was drilled in 1985 and was spectacularly successful. An initial flow of 180 t/h of steam made it the best well ever drilled at Wairakei - 35 years after there exploration began.

WK229 was drilled in 1986 to test steam production near the existing borefield. No steam permeability was found and it is a normal Wairakei liquid producer.

WK230-232 are exploration wells drilled to 600 m in 1986-87. WK230 found steam but little permeability, and a temperature reversal. WK231 found low temperatures. WK232 found steam, high permeability and temperature, and produces 50 t/h.

Production wells WK233 and 234 each produce an initial flow of about 270 t/h of dry steam. WK235 did not find permeability and was drilled on to 1400 m.

An additional steam line is under construction.

ACKNOWLEDGEMENTS

I thank the Electricity Corporation of New Zealand for permission to use material commissioned by them, and to quote the results of the recent exploration drilling. I also thank Chris Morris for many helpful comments.

REFERENCES

Allis, R.G., Hunt, T.M., 1986 "Analysis of exploitation-induced gravity changes at Wairakei geothermal field Geophysics, V51, No. 8, pp. 1647-1660.

Bolton, R.S., 1982 "Fracturing in the Wairakei geothermal field" Proc. Geoth. Res. Council Workshop, Hawaii, 27-28 Aug.

Brown, K.L., Henley, R.W., Plum, J., 1986 "Aquifer dilution and boiling in the Wairakei field due to exploitation".

Grant, M.A., Donaldson, I.G., Bixley, P.F., 1982 "Geothermal reservoir engineering" Academic Press, New York.

Risk, G.F., Rayner, H.H., Stagpoole, V.M., Graham, D.J., Dawson, G.B., Bennie, S.L., 1984 "Electrical resistivity survey of the Wairakei geothermal field" report 200, Geophysics Division, NZDSIR.

Thain, J.A., Stacey, R.E., 1984 "Wairakei geothermal power station 25 years operation" NZ Electricity Corporation.

Whiting, R.L., Ramey, H.J. Jr, 1969 "Application of material and energy balances to geothermal steam production". J. Pet. Tech. v 21 pp. 893-900.

PROCEEDINGS, Thirteenth Workshop on Geothermal Reservoir Engineering
Stanford University, Stanford, California, January 19-21, 1988
SGP-TR-113

The Hydraulic Fracturing of Geothermal Formations

K. Ben Naceur and M.J. Economides

Dowell Schlumberger

Abstract

Hydraulic fracturing has been attempted in geothermal formations as a means to stimulate both production and injection wells. Since most geothermal formations contain fissures and on occasion massive natural fissures, the production behavior of the man-made fractures results in certain characteristic trends.

A model is offered that allows the presence of a finite or infinite conductivity fracture intercepting a fissured medium. The method is based on a numerical discretization of the formation allowing transient interporosity flow.

Type curves for pressure drawdown and cumulative production are given for infinite acting and closed reservoirs. Since most of the fissured formations exhibit a degree of anisotropy, the effects of the orientation of the hydraulic fracture with respect to the fissure planes, and of the ratio between the directional permeabilities are then discussed.

Guidelines are offered as to the size of appropriate stimulation treatments based on the observed fissured behavior of the reservoir.

Introduction

Almost all producing geothermal reservoirs are naturally fissured. In certain cases, these reservoirs contain massive natural fractures, and in fact a well may not produce if a fracture is not met. Matrix permeability is usually extremely small (fractions of μ-darcies). As a result, hydraulic fracturing has been attempted to either create artificial injectivity for spent fluids in an injection well or, in the hope of connecting with natural fractures, to improve the production of flowing wells.

The latter may not be successful. Irrespective of the origin and geological history of the fissures and natural fractures, the current state of stresses influences their distribution and orientation. Since stresses are compressive in nature, the maximum stress would preferentially close fissures that are normal to its direction (see Fig. 1). This would result in a permeability anisotropy with a maximum value in the direction of maximum stress. However, an artificially induced fracture will also be in the direction of the maximum stress (Hubbert and Willis [1]). This configuration is the least favorable for the expected production increase from the hydraulic fracture (Ben-Naceur and Economides [2]). Furthermore, the hope of connecting natural fractures, which would also follow the general trend of the manmade fracture, may not be realized.

It is important to define here the deliberate distinction between fissured and naturally fractured systems. Although many authors have used the term interchangeably, we use the term "naturally fractured" only for those wells (usually geothermal steam wells - see Economides and Fehlberg [3]) where a log-log graph of pressure difference against time forms a slope equal to 0.5, indicative of linear flow (Gringarten *et al.* [4]). All other reservoirs are termed "fissured".

Considerations for the Treatment of Fissured Formations

The permeability distribution near a well is the key factor for deciding whether to stimulate it or not. If a massive natural fracture already intersects the plane of the well, then hydraulic fracturing would generally not contribute to a significant productivity or injectivity increase. If damage occurs near the well, within a reservoir having a relative large permeability ($\geq$ 1-5 md), acidizing or creating multiple short fractures will generally restore the production. Hence, the best candidates for stimulation are those wells that have a low matrix permeability.

Stimulating geothermal fissured formations creates unique problems during the treatment, due to the presence of discontinuities that may affect the propagation path of the induced fracture, and high leakoff due to the presence of *thief* fissures. Warpinski and Teufel [5] considered the effect of geological discontinuities on the propagation of a hydraulic fracture, giving criteria for the fracture to alter its direction. If treating pressures are large enough, shear slippage may be induced along joint or fissure sets. Jeffrey *et al.* [6] analyzed the condition

for effective proppant transport in those situations. When there is proppant bridging, the resulting increase in treating pressures may lead to "dendritic" fracturing. Kiel [7] discussed the advantages of the created connected pattern which results in a volume drainage versus a classical areal drainage created by a planar fracture. Murphy and Fehler [8] discussed the conditions for such a dendritic fracture growth to occur as a function of the dilatation behavior of joints, as well as fluid rheological properties. The injection of a high viscosity fluid and high injection rates will favor the creation of a single main hydraulic fracture. Campbell *et al.* [9] described a technique to create dendritic fractures using a staged injection of low viscosity fluids, and discussed a series of treatments performed in Idaho, some of them showing evidence of large increases in productivity subsequent to hydralic fracturing. Several papers have been published on the characterization of fracture extension using acoustic techniques in an attempt to identify shear stimulation when low viscosity fluids are injected: Pine and Batchelor [10] compared the results of an actual treatment with the prediction of a numerical code, while House *et al.* [11] conducted seismic studies using a surface array of seismometers, indicating the creation of such shear features. The propagation of shear fractures is however not desirable, when the hydraulic fracture is to be propped, because of the high probability of screening out due to the accumulation of proppant at the tip of the fracture. Hence, the use of high viscosity fluids is generally recommended for an improved control of proppant transport.

The second important effect of fissures is to induce a significant increase in the volume of fluid lost during the injection. Classically, three mechanisms have been considered to model the fracturing fluid leak-off and the factors controlling it (Settari [12]):

- The first type of control is due to the creation of a *cake* deposited by the fracturing fluid on the fracture walls: the leak-off coefficient for fissured formations has been shown to be two to three times larger than for tight reservoirs (Hall and Houk [13]).
- A second mechanism is due to the viscosity of the filtrate: the corresponding permeability is the fissure permeability, hence the mechanism would not generally be effective to reduce leak-off.
- The third mechanism is due to compressibility effects in the reservoir. For fissured systems, the derivation of the corresponding leak-off coefficient is not straightforward, since the solution is based on the transient solution for a plane source in a double porosity representation. For practical purposes, however, the corresponding resistance may be neglected.

The *combined* leak-off coefficient, which lumps the previous three mechanisms, will hence generally be equal to the wall builiding coefficient. The addition of silica flower or 100-mesh proppant allows a reduction in the amount of leak-off.

Modeling the Production of Stimulated Fissured Systems

If the formation behaves as a homogeneous system, classical models simulating the effect of a vertical fracture can be used (see Cinco [14] for a review of the different models), and such an approach has been used by Glowka [15] to estimate the qualitative effects of the different types of treatments. Geothermal wells, however, generally exhibit a fissured behavior, with distinct properties for the matrix (generally extremely tight), and distributed fissures. The work of Barenblatt [16] provides a framework for modeling the effects of flow in a system characterized by two sets of porosities corresponding to the high permeability fissures, and to the tight matrix. Analytical derivations have been given by Warren and Root [17] to describe the flow of a single fluid in the non-stimulated case. Numerical models have been developed since, some of them based on the analogy between fissured media and multi-layer reservoirs (Kazemi [18], Boulton *et al.* [19], see also Van Golf Racht [20] for a detailed discussion).

The parameters describing the response of the fissured system can be lumped into the following:

- Ratio of storativities: $\omega = \frac{\phi_f}{\phi_f + \phi_m}$
- Interporosity Flow Factor $\lambda_0 = \alpha \frac{k_m}{k_f} r_w^2$

where α is the interporosity flow shape factor [16].

The model used in this study is based on finite-difference discretization of the reservoir, allowing a spatial variation of the permeabilities (see also Ben Naceur and Economides [2] for a detailed presentation). The implicit scheme used, permits accurate modeling of the high contrasts in permeability between the formation and the vertical fracture. Symmetry conditions lead to a discretization of a quarter of the reservoir only.

The new permeability and porosity distribution in the reservoir induced by the vertical fracture is described by (see Fig. 1):

$$k(x,y) = k_F \ , \ r_w \leq x \leq x_F \ , \ 0 \leq y \leq w/2 \quad (1)$$

$$\phi(x,y) = \phi_F \ , \ r_w \leq x \leq x_F \ , \ 0 \leq y \leq w/2 \quad (2)$$

where x_F and w are the fracture half-length and width, and k_F and ϕ_F are respectively the packed proppant permeability and porosity.

Houze *et al.* [21] have presented solutions for the infinite conductivity fracture in a fissured medium. Ben-Naceur and Economides [2] have extended this work to finite conductivity fractures and quantified the effects of anisotropy. Further they correlated the "intensity" of

the natural fissures with the conductivity of the created fracture for constant well cumulative production within a period of time.

Figure 2 is a pressure and pressure derivative type curve from Ben Naceur and Economides [2] for finite conductivity fractures in a fissured medium of known ω and λ. Data from a well test are shown matched on the type curve. To use the type curve it is essential that the values of ω and λ_0 are known from a pretreatment test. The variable λ has been defined for the posttreatment state of the well by Houze *et al.* and is given by:

$$\lambda = \lambda_0 \frac{x_F^2}{r_w^2} \tag{3}$$

A type curve such as the one shown in Fig. 2 is generated for a range of λ. Since the fissure permeability is also known from a pretreatment test, then the dimensionless pressure may be calculated in the usual manner for either oil or gas wells. This allows only one degree of movement (horizontally) for the match. Type curve matching of both pressure and pressure derivative allows the calculation of the fracture half-length, the value of λ as well as the dimensionless fracture conductivity. The procedure is demonstrated in detail in Ben-Naceur and Economides [2].

Figure 3 is a cumulative production type curve for various fracture conductivities (F_{CD}) for a fissured reservoir with typical values of λ and ω (1 and 0.1 respectively). The relationship between the interporosity flow coefficient λ and the fracture conductivity is shown on Fig. 4. For equal cumulative productions, a horizontal line allows the estimation of the desired fracture conductivity for a given value of λ. If λ_0 is known from a pretreatment test, then Fig. 4 is valuable in the design stage of a hydraulic fracture.

Figure 5 is a graph of the dimensionless pressure response for a closed fissured reservoir for various lateral penetration ratios of the fracture. The time to pseudosteady state is given by $t_{DxF} = 0.25\ (x_F/x_e)^2$ where x_e is the drainage radius of the reservoir.

The Effects of Anisotropy

Ben-Naceur and Economides [2] have defined a new equivalent dimensionless pressure:

$$\bar{p}_D = \frac{2\pi \bar{k} h \Delta p}{qB\mu} \tag{4}$$

and fracture time

$$\bar{t}_{DxF} = \frac{\bar{k}t}{\phi \mu c_t \tilde{x}_F^2} \tag{5}$$

where:

$$\bar{k} = \sqrt{k_x k_y} \tag{6}$$

and

$$\tilde{x}_F = x_F \left(\frac{k_y}{k_x}\right)^{\frac{1}{4}} \tag{7}$$

These definitions allow the normalization of all pressure responses for an infinite conductivity fracture into one as shown as shown in Fig. 6. This graph is identical to the Gringarten *et al.* [4] type curve for an infinite conductivity fracture.

The permeability k_x in Eq. 7 is parallel to the fracture and as explained earlier it should be larger than the normal permeability k_y. Since pressure transient analysis would extract the "apparent" value of fracture length $\tilde{x}_F$, then it can be seen from Eq. 7 that the actual fracture length x_F would be larger. If both k_y and k_x have been determined from an interference test, then the actual fracture length may be calculated.

For finite conductivity fractures, the normalization mentionned on Fig. 6 (which is for an infinite conductivity fracture) cannot be done using the variables in Eqs 4 to 7. In the case of geothermal formations, however, the very low matrix permeability would almost always lead to quasi-infinite conductivity fractures.

Conclusions

The following general conclusions can be derived from this study:

1. The effect of a vertical fracture on the productivity of a geothermal (fissured) well can be assessed by using the type curves presented here.
2. Optimization of the treatment requires the determination from a pretreatment test of the flow parameters of the formation. The desired characteristics of the fracture can then be estimated using the new cumulative production type curve.
3. Posttreatment tests allow a determination of the effectiveness of a fracture and its dimensions, with the use of pressures and pressure derivatives.
4. The identification of permeability anisotropy is necessary for an accurate estimation of the potential of hydraulic stimulation. Type curves for isotropic systems can be used to predict the productivity increase, if the introduced normalizing variables are used.

Nomenclature

Roman

- B: Formation volume factor
- b_F: Fracture width
- c_t: Formation total compressibility
- F_{CD}: Dimensionless fracture conductivity ratio
- h: Height (formation and vertical fracture)
- k_f: Fissure permeability
- k_F: Hydraulic fracture (or proppant) permeability
- k_{ma}: Matrix permeability

- k_x: Directional permeability in the x-direction
- k_y: Directional permeability in the y-direction
- $\bar{k}$: Reservoir average permeability
- Δp: Pressure drop
- p_D: Dimensionless pressure drop
- q: Production rate
- q_D: Dimensionless production rate
- Q: Cumulative production rate
- Q_D: Dimensionless cumulative production rate
- r_w: Wellbore radius
- t: Time
- t_{Dx_F}: Dimensionless time
- x_F: Hydraulic fracture length
- $\tilde{x}_F$: Equivalent anisotropic hydraulic fracture length

Greek

- α: Interporosity flow shape factor
- λ_0: Interporosity flow parameter before stimulation
- λ: Interporosity flow parameter after stimulation
- ω: Ratio of storativities
- μ: Reservoir fluid viscosity

References

[1] Hubbert,M.K. and Willis,D.G. "Mechanics of Hydraulic Fracturing". *Trans. AIME*, 210:153–166, 1957.

[2] Ben Naceur,K. and Economides,M.J. "Production from Naturally Fissured Reservoirs Intercepted by a Vertical Fracture". In *SPE California Regional Meeting*, 1988. SPE 17425.

[3] Economides,M.J. and Fehlberg,E.L. "Two Short-time Build-up Tests Analysis for Shell's Geyser Well D-6 a Year Apart". In *Proc. of the 5th Workshop on Geother. Res. Eng.*, pages 139–152, 1979.

[4] Gringarten,A.C., Ramey,H.J. and Raghavan,R. "Unsteady State Pressure Distributions Created by a Single Infinite Conductivity Vertical Fracture". *Soc. Pet. Eng. J.*, 347, 1974.

[5] Warpinski,N. and Teufel,L.W. "Influence of Geological Discontinuities on Hydraulic Fracture Propagation". In *SPE Annual Meeting - Houston*, 1984. SPE 13224.

[6] Jeffrey,R.G. and Vandamme,L. . "Mechanical Interaction in Branched or Subparallel Hydraulic Fractures". In *SPE/DOE Meeting on Low Permeability Reservoirs*, 1987. SPE 16422.

[7] Kiel,O.M. "The Kiel Process - Reservoir Stimulation by Dendritic Fracturing". In *SPE-AIME 52nd Annual Conference, Denver*, 1977. SPE 6984.

[8] Murphy,H.D. and Fehler,M.F. "Hydraulic Fracturing of Jointed Formations". In *SPE International Meeting on Petroleum Engineering - Beijing*, 1986.

[9] Morris,C.M.
Campbell,D.A. and Verity,R.V. "Geothermal Well Stimulation Experiments and Evaluation". In *SPE Annual Fall Meeting, San Antonio*, 1981. SPE 10316.

[10] Pine,R.J. and Batchelor,A.S. "Downward Migration of Shearing in Jointed Rock during Hydraulic Injections" . *Int. J. Rock Mech. Min. Sci. Geomech. Abst.*, 21:249–263, 1984.

[11] Keppler,H. House,L. and Kaieda,H. "Seismic Studies of a Massive Hydraulic Fracturing Experiment". In *Proc. of Geother. Res. Council Annual Meeting*, August 1985.

[12] Settari,A. "A New General Model of Fluid Loss in Hydraulic Fracturing". In *SPE/DOE Symposium on Low Permeability Reservoirs, Denver*, 1983. SPE 11625.

[13] Hall,B.E. and Cook,S.G. "Fluid Loss Control in the Naturally Fractured Buda Formation". In *SPE Annual Fall Meeting, San Francisco*, 1983. SPE 12152.

[14] Cinco,L.H. "Evaluation of Hydraulic Fracturing by Transient Pressure Analysis Methods". In *International Meeting on Petroleum Engineering - Beijing*, 1982. SPE 10043.

[15] Glowka, D.A. "Effects of Artificial Fracture Geometry on Geothermal Well Production". In *Proc. of geother. Res. Council Annual Meeting*, pages 507–512, 1985.

[16] Barenblatt, G.I., Zheltov, Y.P. and Kochina,I.N. "Basic Concepts in the Theory of Seepage of Homogeneous Liquids in Fissured Rocks". *J. Appl. Math. Mech.*, 852–864, 1960.

[17] Warren,J.E. and Root,P.J. "The Behaviour of Naturally Fractured Reservoirs". *Soc. Pet. Eng. J.*, 245–255, 1963.

[18] Kazemi, H. Seth,M.S. Thomas,G.W. "The Interpretation of Interference Tests in Naturally Fractured Reservoirs with Uniform Fracture Description". *Soc. Pet. Eng. J.*, 463–475, 1969.

[19] Boulton,N.S. and Streltsova, T.D. "Unsteady Flow to a Pumped Well in a Fissured Water-Bearing Formation". *J. Hydrol.*, 257–269, 1977.

[20] Van Golf-Racht T.D. *Fundamentals of Fractured Reservoir Engineering.* Elsevier, Amsterdam, 1982.

[21] Houze,O.P., Horne,R. and Ramey, H.J. Jr. "Infinite Conductivity Vertical Fracture in a Reservoir with Double Porosity Behaviour". In *SPE California Regional Meeting*, 1984. SPE 12778.

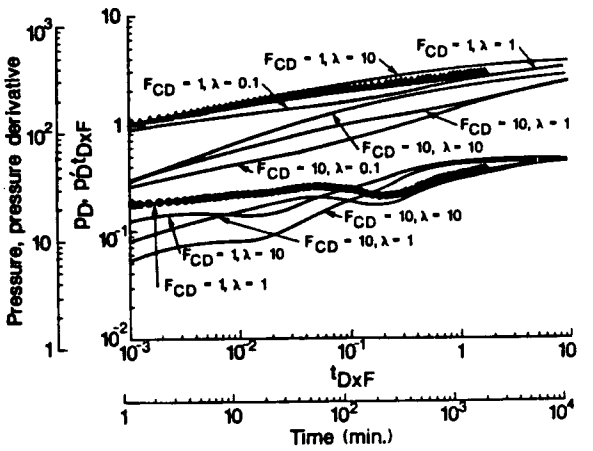


Figure 2: Interpretation of a Well Test in a Fissured Reservoir Intercepted by a Finite Conductivity Fracture

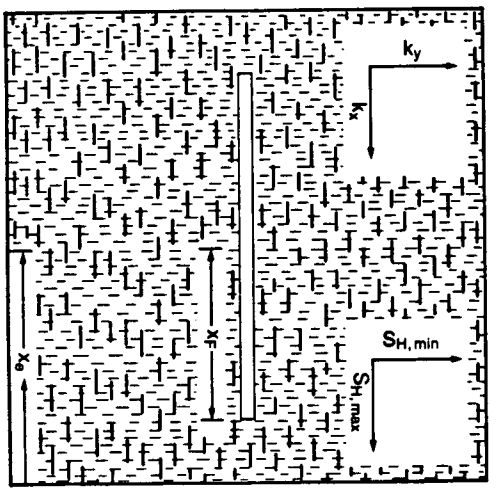


Figure 1: Conceptual Diagram of Open and Closed Fissure Distribution Leading to Permeability Anisotropy as a Result of Stress Anisotropy

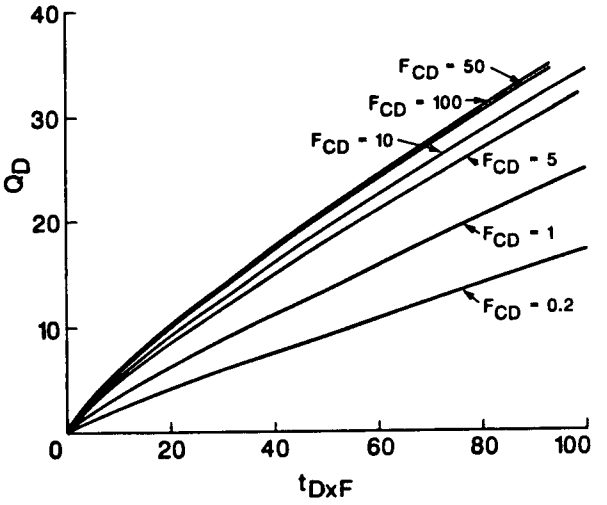


Figure 3: Cumulative Production for a Fissured Reservoir Intercepted by a Finite Conductivity Fracture. (ω =•1, λ = 1)

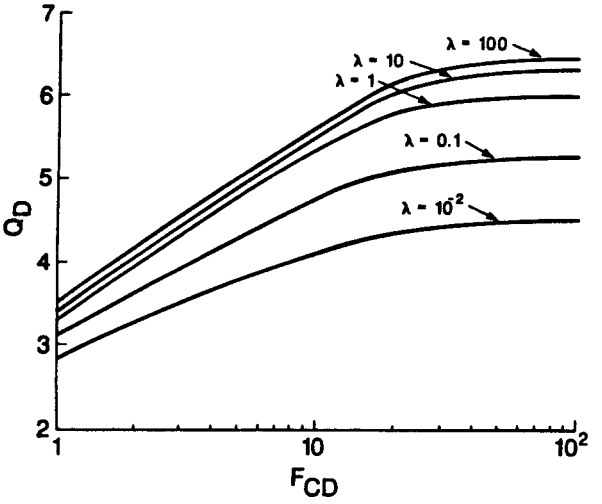


Figure 4: Correlation of Hydraulic Fracture Conductivity and Natural Fissure Intensity (λ) [$t_{DxF} = 10$, $\omega = 0.1$]

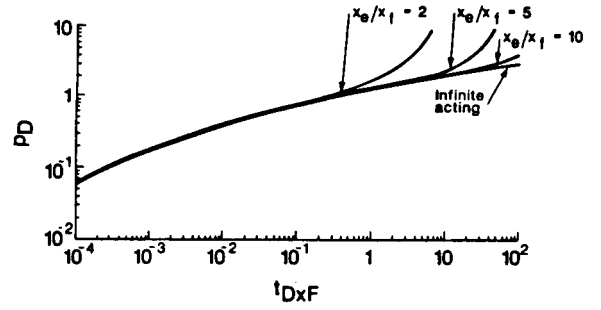


Figure 5: Closed Boundary Effects of the Behavior of an Infinite Conductivity Fracture in a Fissured Medium

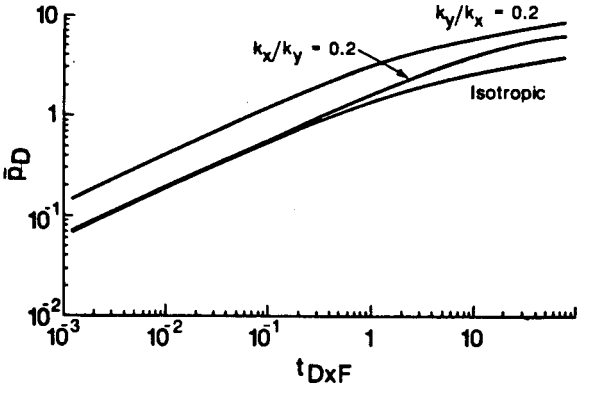


Figure 6: Dimensionless Pressure for an Infinite Conductivity Fracture in an Anisotropic Homogeneous Medium. Effect of Permeability Ratio. When using the normalized variables, all curves will collapse on the isotropic one

PROCEEDINGS, Thirteenth Workshop on Geothermal Reservoir Engineering
Stanford University, Stanford, California, January 19-21, 1988
SGP-TR-113

TRANSIENT BEHAVIOR IN FRACTURED MEDIA WITH ZERO MATRIX PERMEABILITY

E.Okandan, J.Öngen, M.Arpacı

Petroleum Engineering Dept.,METU, TURKEY

ABSTRACT

Pressure transient analysis is one of the powerful tools that provides estimates on in-situ reservoir properties. Development of theory since 1935 from the classic paper of Theis, has provided analysis procedures for different pressure tests in wells. The solutions to respective partial differential equations for dual porosity or fractured systems also found wide application in estimating reservoir properties in geothermal reservoirs.

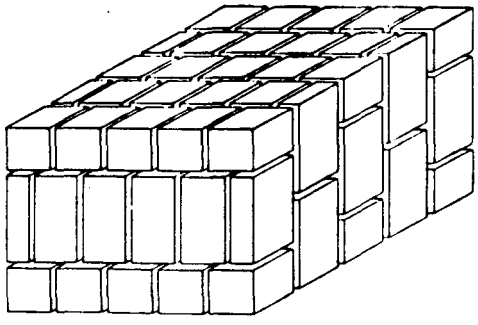
When we analyze the response of a reservoir to pressure disturbances, we assume a model to simulate the system, and properties are estimated from the best fit to this model. The present paper will discuss some experimental results obtained from a fractured medium with zero matrix permeability, where dimensions of blocks, fracture spacing, exact location of production points and reservoir size are known. The pressure transient data obtained from a laboratory geothermal model, were analyzed using conventional analysis techniques. The results imply, even for this fully fractured system, the reservoir behaves as if it has the properties of a dual porosity medium. Several tests conducted at different rates and at different production depths resulted in similar kh and $\phi C_t h$ values, indicating that the parameters affecting the pressure transients were the overall properties of the medium.

In this paper only drawdown tests will be presented.

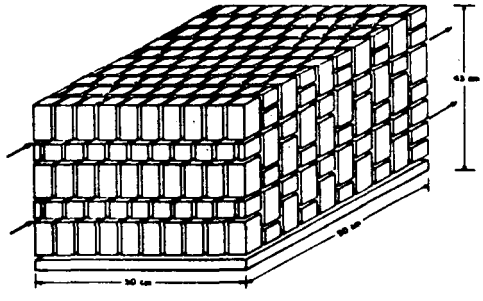
INTRODUCTION

Geothermal reservoirs are generally fractured rocks and their matrix permeabilities may be negligibly small. In such cases the flow will be mainly through fractures and transient behavior will depend on the fracture network and fracture properties.

Laboratory experiments were designed to obtain pressure transient data for a specific fracture geometry where marble matrix blocks had no permeability. The orientation of blocks was such that there was flow connection between all fractures and the injection-production points. Two different block sizes were chosen (Fig.1.a, Fig 1.b). The details of the experimental set up were given elsewhere (1,2).



Model A



Model B

Fig. 1. Packing of marble blocks in the experimental set up.

EXPERIMENTAL CONDITIONS

The reservoir model was heated upto 110 C and to a pressure above boiling pressure, then the selected ports for injection and production were connected to measuring equipment. An initial drawdown test was followed by an interference test where pressure rise at the producing end was recorded while cold water was injected at constant rate. This was followed by another drawdown test. The location of injection and production ports were changed in order to create different flow paths and observe their effect on transient behavior. The flow rates ranged between 20 cc/min to 60 cc/min on both models. The fracture spacing created by the big blocks were 10 cm and it was 5 cm in the pack created by smaller blocks.

RESULTS AND DISCUSSION

In both models due to the packing of marble blocks flow paths are connected and continuous and it was expected to see the effect of fractures intersecting the production ports. The transient behavior should reflect the fracture density as well as the limited volume of the models.

In both models, the shapes of both semi-log and log-log plots characterized a dual porosity system (Fig.2, Fig.3). The late time data were checked if increase in ΔP was due to pseudo steady state flow. For all experiments, the data did not follow a unit slope straight line on log ΔP versus log t plot, where the second semi-log straight line was observed. So the flow behavior is due to the dual porosity effect created in the models.

In the analysis of the data, the $(kh)_f$ value estimated from the semi-log straight line was used to find the pressure match for the log-log type curve. The best fit to $(C_D\, e^{2S})_f$; λe^{2S} and $(C_D\, e^{2S})_{f+m}$ were obtained for each drawdown data obtained from different production ports (3).

Since production was obtained from a point without a wellbore the effect of wellbore storage and skin was absent.

Therefore the match obtained on $(C_D\, e^{2S})$ curves are basically equal to C_D. The flow period which corresponds to first $(C_D)_f$ curve is due to the main preferential fracture path leading to the production point, this main path is fed from auxiliary fractures whose overall affect is reflected in the second C_D curve. The values of λ and w then indicate the relationships between the medium made up of these auxiliary flow paths and main flow path.

From the type curve match, average $(C_D)_f$ values for model A, larger blocks, were 4 while for model B it was 1. Similarly $(C_D)_{f+m}$ for model A was 0.75 and for model B, 0.45 (Table 1). This indicated that the storativity was higher in the large block model. This concluison was also reflected in the w values that were calculated. For model B w was higher than model A.

The storage was determined from the time match. Since there was no wellbore, the storage observed is due to the fissures intersecting the production port.

The fractures created by larger blocks (Model A) exhibited larger storage average being 3.25×10^{-9} m^3/Pa compared to 2.23×10^{-9} m^3/Pa in smaller blocks. Permeability was also high in Model A. In Table 1, only $(k,h)_f$ values are reported since h which is the effective height open to flow was not very easy to define for the models under consideration.

$(\phi c_t\, h)_f$, as determined from the $(C_D)_f$ match and from semi-log analysis had shown some differences. This is due to uncertainly in matching the initial data to the first $(C_D\, e^{2S})$ curve. However order of magnitude values for both models were similar.

The λ values determined from the type curve, assuming skin to be zero was slightly higher for model B. Since geometric shape of blocks and fractures were similar, the slight difference is due to $(kh)_m/(kh)_f$ values which correspond to auxilary flow path conductance to main flow path conductance in the present models.

Drawdown tests conducted before and after an interference test showed very similar behavior exhibiting the reproducibility of data (4,5).

Experimental data obtained at different production depths, expressed as H_p measured from bottom as a fraction of total depth, was not different , (Fig. 4,5) because the geometry of the fractures were the same and their distribution was similar. However, tracer experiments conducted on both models, showed varying dispersions as the injection and production depths were changed (2,5).

Concentration profiles of tracer returns also indicate a main fracture flow path and later auxiliary fractures feeding to it. As the fracture density was increased (model B) the dispersion was higher. (Fig.6,7) and it was reflected in the tracer profiles obtained at different production points.

CONCLUSION

Model experiments on two fractured reservoir models with zero matrix permeability, showed the transient behavior was similar to a double porosity system.

Increased fracture density in small

block model, caused $(kh)_f$ values to be smaller which also affected λ, interporosity flow parameter to become slightly higher as compared to larger blocks.

Storativity of the main fracture flow system was high in the model that had more fractures and smaller block sizes.

Geothermal reservoirs which generally produce fluid through fractures may exhibit dual porosity behavior even the matrix may have very low or effectively zero permeabilities. The minor or auxiliary fractures that contribute to the flow in the main fracture system, will act as the less permeable medium of a dual porosity model.

NOMENCLATURE

$$C_D e^{25} = \frac{0.8936.\ C\ e^{25}}{\phi C_t\ h\ r_w^2}$$

$$\lambda e^{-25} = \alpha r_w^2 .\ \frac{k_m}{k_f}\ e^{-25}$$

$$W = \frac{(C_D\ e^{25})_{f+m}}{(C_D\ e^{25})_f} = \frac{(\phi C_t\ h)_f}{(\phi C_t\ h)_{f+m}}$$

REFERENCES

1. Hosca, H., Okandan, E. (1986), "Reinjection Model Studies in Fractured and Homogeneous Geothermal Systems", Proceedings Eleventh Workshop Geothermal Reservoir Engineering, Jan. 21-23, 1986.
2. Bayar, M., Okandan, E.(1987), "Tracer Flow In a Fractured Geothermal Reservoir Model" Proceedings Twelfth Workshop on Geothermal Reservoir Engineering, Jan. 20-22, 1987.
3. Bourdet, D., Gringarten, A.C. (1982), "Determination of Fissure Volume and Block Size in Fractured Reservoirs by Type-curve Analysis", SPE paper no. 9293, 1982.
4. Öngen, J. (1987), "Interpretation of pressure Data in a Three Dimensional Fractured Reservoir Model", MSc.Thesis 1987, Petroleum Eng.Dept., METU
5. Arpacı, M. (1988), "Transient and Tracer Behavior in Fractured Geothermal Model with Zero Matrix Permeability", MSc.Thesis 1988, Petroleum Eng.Dept., METU

TABLE 1. Semi-log and Log-log Analysis of Some Pressure Transient Data Obtained on Model A and B.

			Semi-log Analysis		Log-log Analysis				
H_p		Test No	kh, md-ft	$(\phi C_t\ h)_f$ m/Pa	λ	w	$(\phi C_t\ h)_f$	$(C_D)_f$	$(C_D)_{f+m}$
0.25	Model A								
		41	4.46	81×10^{-6}	0.1	0.25	55×10^{-6}	2	0.5
		30	5.74	78.7×10^{-6}	0.15	0.3	30×10^{-6}	3	1
	Model B								
		FDW-1	2.75	59.3×10^{-6}	0.14	0.5	56.5×10^{-6}	1	0.5
		FDW-4	2.49	78.7×10^{-6}	0.12	0.34	66.5×10^{-6}	1.5	0.5
		IDW-1	2.45	60.2×10^{-6}	0.14	0.5	44.1×10^{-6}	1.5	0.4
0.75	Model A								
		27	3.24	105×10^{-6}	0.15	0.14	50.8×10^{-6}	5	0.7
		36	2.29	43.7×10^{-6}	0.1	0.1	17.3×10^{-6}	5	0.5
	Model B								
		FDW-2	2.42	64.9×10^{-6}	0.20	0.3	69.3×10^{-6}	1	0.3
		FDW-3	2.16	64.1×10^{-6}	0.16	0.5	68.2×10^{-6}	1	0.5

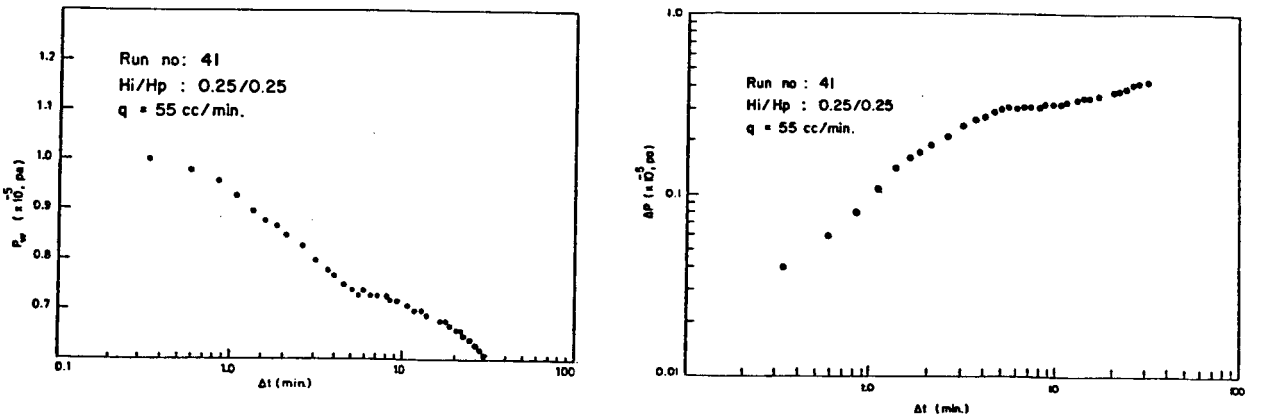


Figure 2. Pressure Drawndown Obtained on Model A at H_p of 0.25 (Test#41)

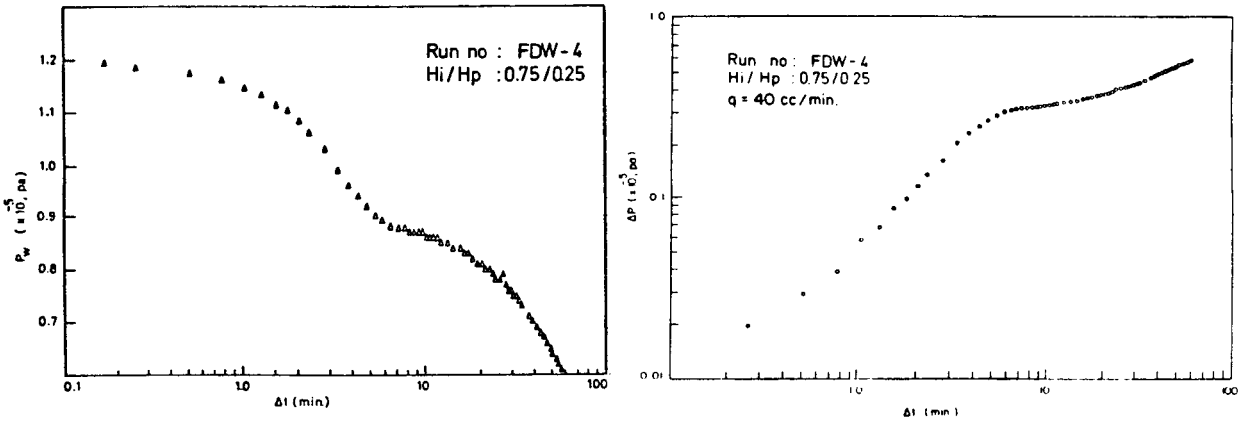


Figure 3. Pressure Drawndown Obtained on Model B at H_p of 0.25 (Test FDW-4)

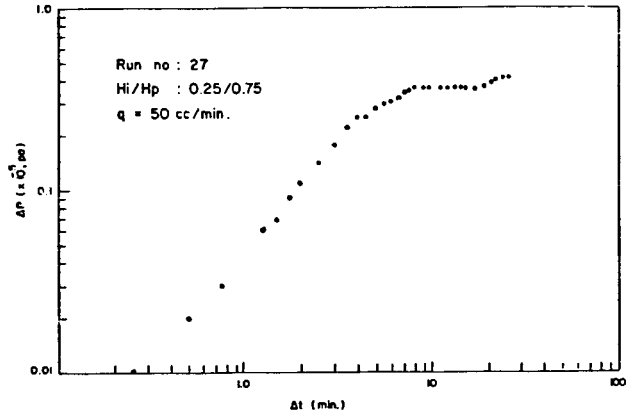


Figure 4. Transient Behavior at H_p of 0,75 for Model A (Test #27)

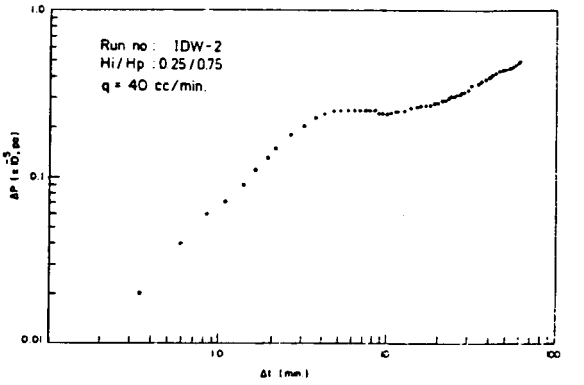


Figure 5. Transient Behavior at H_p of 0.75 for Model B (IDW-2)

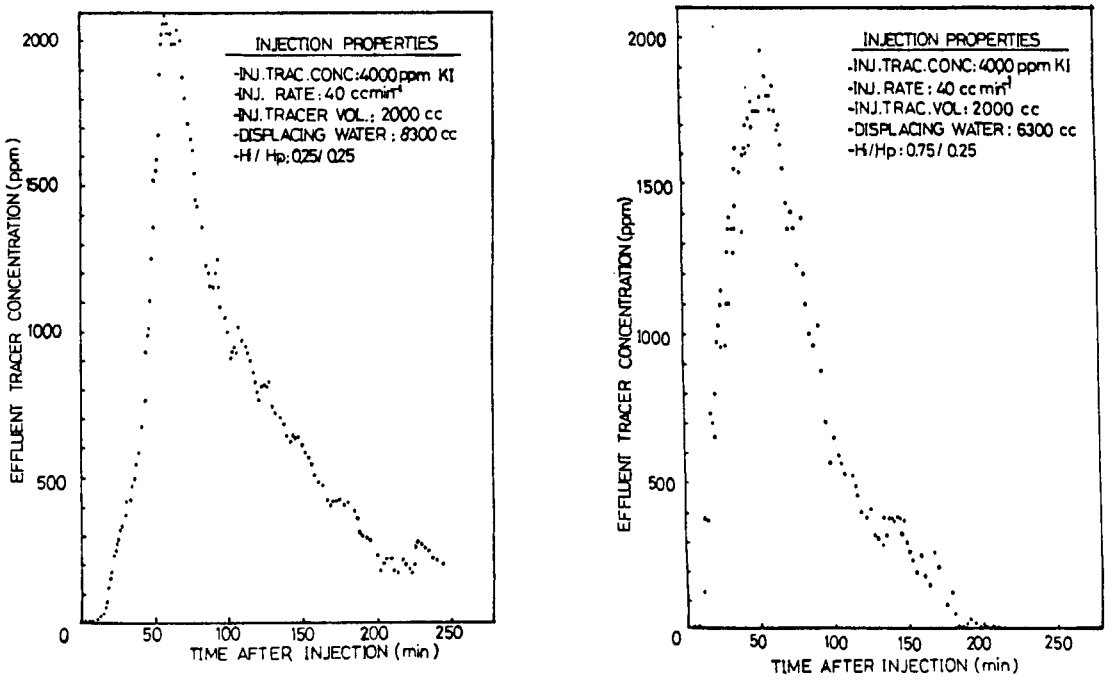


Figure 6. Tracer Production Profile in Model A for H_i/H_p of 0.25/0.25 and 0.75/0.25

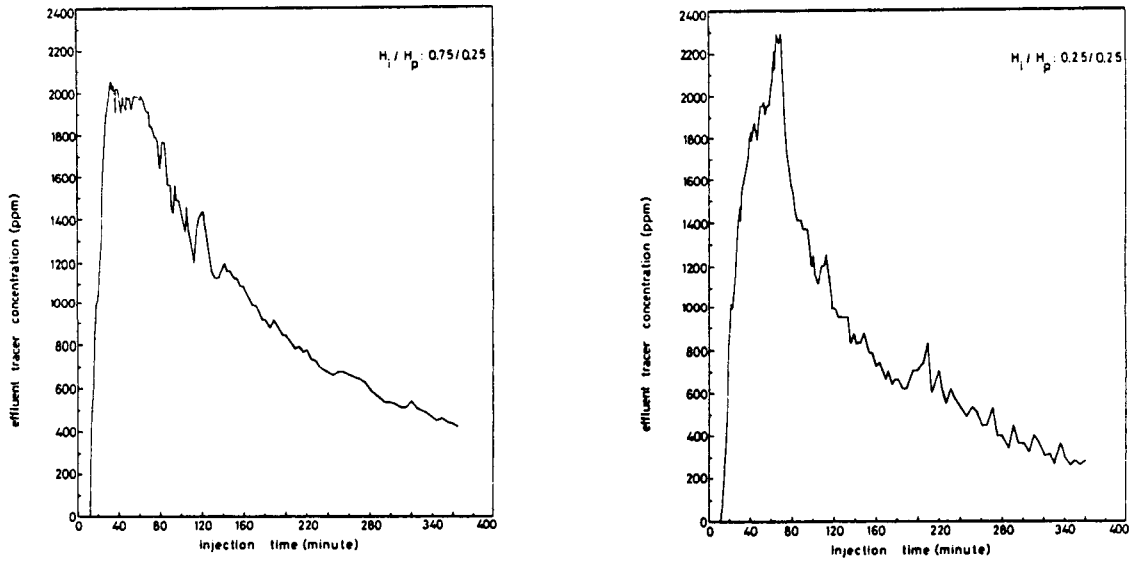


Figure 7. Tracer Production Profile in Model B for H_i/H_p of 0.25/0.25 and 0.75/0.25

PROCEEDINGS, Thirteenth Workshop on Geothermal Reservoir Engineering
Stanford University, Stanford, California, January 19-21, 1988
SGP-TR-113

FRACTURE NETWORK MODELING OF A HOT DRY ROCK GEOTHERMAL RESERVOIR

Bruce A. Robinson

Los Alamos National Laboratory
Los Alamos, New Mexico 87545

ABSTRACT

Fluid flow and tracer transport in a fractured Hot Dry Rock (HDR) geothermal reservoir are modeled using fracture network modeling techniques. The steady state pressure and flow fields are solved for a two-dimensional, interconnected network of fractures with no-flow outer boundaries and constant-pressure source and sink points to simulate wellbore-fracture intersections. The tracer response is simulated by particle tracking, which follows the progress of a representative sample of individual tracer molecules traveling through the network. Solute retardation due to matrix diffusion and sorption is handled easily with these particle tracking methods. Matrix diffusion is shown to have an important effect in many fractured geothermal reservoirs, including those in crystalline formations of relatively low matrix porosity. Pressure drop and tracer behavior are matched for a fractured HDR reservoir tested at Fenton Hill, NM.

INTRODUCTION AND MOTIVATIONS

Reservoir engineers and groundwater hydrologists have long recognized the importance of fractures on fluid flow and solute transport in underground porous media. Many analytical and numerical models exist to predict flow behavior for various fracture geometries ranging from a single fracture to multiple, interconnected fractures. Steady state or pressure transient responses can often be predicted using these models, which provide a macroscopic description of the flow process in terms of parameters suitable for use by hydrologists and engineers.

Solute transport is not so easily simulated using these models, however. The typical approach of employing the convective-dispersion equation with the adjustable parameter of dispersion coefficient usually fails in several important ways. In one dimension, a good match between model and field data is often difficult to achieve, since field data are seldom if ever perfect Gaussian distributions of residence times about a mean value. Multi-dimensional forms of the convective-dispersion equation can provide better fits, but at the expense of more adjustable parameters of questionable physical significance.

Fracture network modeling is a different approach to simulating flow and transport in fractured rock. The flow system is comprised of a network of interconnected fractures. A pressure difference imposed in such a system due to fluid injection or a natural hydraulic gradient results in a flow of water through the fractures. This flow field can be calculated assuming a fracture geometry, appropriate boundary conditions, and a relationship between pressure drop and flow rate within each fracture. Once the flow field is determined, the transport of a conservative, reacting, or adsorbing chemical component can be calculated using particle tracking techniques, which follow the progress of a representative sampling of tracer molecules through the network.

Fracture network modeling has been used extensively to model groundwater flow (see, for example, Castillo et al. (1972), Schwartz (1977), Smith and Schwartz (1980), Schwartz et al. (1983), Long et al. (1982), Andersson and Thunvik (1983), and Hopkirk et al. (1985), Long and Billaux (1987)). The primary focus of most previous work has been to determine the conditions under which a fractured rock could be treated as an equivalent porous medium. With the fracture network approach, one can assess the effect of fracture size, spacing, aperture, and orientation on the fluid flow, permeability distribution, and tracer behavior. Typically, Monte Carlo techniques are used, in which a large number of realizations of different fracture geometries, all with identical fracture statistics, are performed to determine the average and variability of behavior. The latter is a measure of the inherent uncertainty of flow behavior in the fracture network, given the measured statistical parameters. In most cases, these studies have assumed the flow to be within a rectangular grid in two dimensions, with constant-head boundary conditions at opposite ends of the plane and no-flow or linearly-

decreasing head boundaries on the two sides. These boundary conditions simplify the analysis and interpretation of results, and are probably sufficient for modeling large-scale groundwater flow problems.

Unfortunately, interwell flow and tracer tests in HDR geothermal reservoirs cannot be interpreted with these simplified boundary conditions. Wellbores often resemble point sources and sinks for flow, since they are directly connected to only a few fractures. In this study, we develop a code which realistically simulates the wellbore source-sink boundaries in fractured rock. The code is then used to model the fluid flow and transport processes in interwell flow and tracer experiments.

MODEL DEVELOPMENT

Fracture network modeling techniques are capable of handling many different model assumptions, such as regular or random fracture networks, a variety of boundary conditions and fluid flow laws, and various types of tracer transport processes. The model described below takes one set of assumptions which is particularly useful for HDR geothermal reservoir modeling.

Fracture Model Geometry: Figure 1 shows a two-dimensional fracture network containing two orthogonal fracture sets. Fractures are equally-spaced, and the average aperture of each set is known. Wellbores intersect the fracture network at the positions shown, and fluid is injected at constant pressure at one point and withdrawn at a lower pressure at a second point. The positions of the source and sink points and the numbers of each are adjustable. The outer boundaries of the square fracture network are assumed to be impermeable to fluid flow, as are the rock blocks between the fractures. A steady state flow field is set up within the fractures as a result of the constant-pressure and no-flow boundaries.

Fluid Flow Law: Assuming fracture flow can be modeled as laminar flow between parallel plates separated by distance w, the fracture aperture, the fluid velocity is given by

$$u = \frac{-w^2 \Delta P}{12\mu L} \tag{1}$$

The volumetric flow rate per unit depth of fracture is

$$q = wu = \frac{-w^3 \Delta P}{12\mu L} \tag{2}$$

The sign convention is such that flow into a node is positive, and flow from a node is negative.

Flow Equations: As noted by Castillo et al. (1972), the least number of unknowns results when an equation is developed for the pressure P at each node. Assuming steady state fracture flow with no pressure diffusion in the rock blocks,

$$\sum_{i=1}^{n} q_i = \sum_{i=1}^{n} \frac{w_i^3 (P_i - P_o)}{12\mu L_i} = 0 \tag{3}$$

where n can be 2, 3, or 4, depending on the number of fractures connected to the node. Rearranging Eqn. (3):

$$P_o = \frac{\sum_{i=1}^{n} \frac{w_i^3 P_i}{L_i}}{\sum_{i=1}^{n} \frac{w_i^3}{L_i^3}} \tag{4}$$

where subscript o represents the node in question, and the i's refer to the adjacent nodes. Equation (4) is an expression for the pressure at node o in terms of pressures at each of the adjacent nodes.

Solution of Flow Equations: Equation (4) can be written for the pressure at each node, while the pressures of the source and sink nodes are set constant. The outer boundaries automatically simulate the no-flow condition because they are not connected to any points on the other side of the boundary. The resulting equation set is solved using the successive overrelaxation (SOR) method, an iterative solution procedure which offers a considerable improvement over the successive substitutions or Gauss-Seidel techniques. When the numerical parameter ω is optimized, the solution vector more rapidly approaches the correct values for slowly converging equation sets. A value of 1.87 was found to be optimum for a test problem, decreasing the number of iterations by a factor of 8.

Particle Tracking Technique: The assumption underlying the particle tracking technique is that a tracer response can be approximated by passing a large number of individual tracer molecules through the system, measuring the residence time of each, and accumulating the overall response, thus obtaining the residence time distribution of the individual molecules.

To calculate the residence time of an individual molecule traveling from the inlet to the outlet, the residence time within a fracture must be determined, and rules governing tracer transport at a node must be assumed. Within a fracture, tracer transport laws can be developed to account for dispersion, matrix diffusion, and adsorption. In the present study, we assume that dispersion within a fracture is negligible compared to overall dispersion levels measured in the fracture network (Robinson and Tester (1984)). Thus in the absence of

sorption or matrix diffusion, the particle residence time equals the fracture length divided by average fluid velocity, or, in terms of the variables used above:

$$\tau = \frac{-12\mu L^2}{w^2 \Delta P} \quad (5)$$

Sorption and matrix diffusion are included by using the solution developed by Starr et al. (1985) for tracer transport in a single fracture. Tracer is assumed to travel in plug flow in the fracture and is transported by molecular diffusion to and from the stagnant fluid in the matrix. Adsorption can occur either on the face of the fracture or in the rock matrix. Assuming equilibrium adsorption with a linear isotherm in both the fracture and matrix, the tracer response at the outlet to a step change in concentration at the input is (Starr et al., 1985)

$$\frac{C}{C_{in}} = \text{erfc}\left[\frac{Di}{(\theta - R)^{1/2}}\right] \quad (6)$$

where $\theta = t/\tau$ and Di, the diffusion number, is given by

$$Di = \frac{(D_{AB} R' \tau)^{1/2} \phi}{w} \quad (7)$$

In the present study we will consider only conservative, nonadsorbing chemicals for which R and R', the retardation factors in the fracture and matrix, are equal to unity. Figure 2 shows the solution for values of Di ranging from 0.001 to 1. The step tracer response is equivalent to a probability distribution function for an individual tracer molecule. Thus, the residence time of a tracer particle in a single fracture is calculated stochastically by generating a random number between 0 and 1 and calculating the time corresponding to that value for C/C_{in} (see Figure 2). This methodology for simulating tracer transport processes in a single fracture is valid for any linear transport process, those for which the solution is independent of concentration.

At a fracture intersection, we assume complete mixing, whereby the tracer partitions to the different fractures in the same proportion as the flow rate. In the particle tracking formulation, the probability that an individual molecule at a node chooses a given fracture is equal to the flow fraction entering that fracture. A random number generator is used to choose which path a molecule takes. When the particle reaches the outlet port, the total residence time is sum of the residence times in the individual fractures.

When this calculation is repeated, say 10000 times, a distribution of residence times is obtained. To record the tracer response, a group of time blocks (0 to Δt, Δt to $2\Delta t$, $2\Delta t$ to $3\Delta t$ ...) are identified and the number of molecules with residence times falling in each of the time blocks is counted. The resulting histogram is the residence time distribution, equivalent to the response of the system to a short slug of tracer injected at the inlet. The integral of this function, when normalized to unity, is the cumulative residence time distribution F(t).

One additional complication is the effect of fracture roughness on the fluid flow and tracer transport laws. Although the parallel plate law has been used in the derivations given above, in reality the equivalent hydraulic aperture w_h is a weighted average value accounting for the distribution of apertures encountered by fluid passing through the fracture. This parameter is different than equivalent aperture encountered by tracer, w_t, and thus requires a revision of Eqns. (2) and (5). Due to the w^3 dependence on flow rate, the narrow apertures will contribute the most to the pressure drop. On the other hand, tracer molecules sample the entire flow volume and thus w_t is an unweighted average of apertures encountered in the flow path. Thus, the tracer aperture w_t will always be larger than w_h.

Long and Billaux (1987) addressed a similar issue in their study of data from the Fanay-Augeres uranium mine in France. Data were available from over 200 packer tests in which individual fractures were isolated and hydraulic conductivities were measured. In addition, the observed free aperture was measured in each case from examination of cores. Assuming the hydraulic aperture to be proportional to the free opening, Long and Billaux determined the average value for the ratio of hydraulic to free aperture to be 8.6. The free aperture is likely to be nearly equivalent to the tracer aperture w_t, since w_t is an unweighted mean of the true aperture distribution and the free aperture is determined from a core which randomly samples the aperture distribution of a fracture. Thus, we can expect potentially large differences between w_h and w_t. However, given that very little is known about this phenomenon, we will assume that w_h is proportional to w_t, but treat the ratio $f_w = w_t/w_h$ as an adjustable parameter. Thus, Eqns. (2) and (5) become

$$q = \frac{-w_t^3 \Delta P}{12\mu L f_w^3} \quad (8)$$

and

$$\tau = \frac{-12\mu L^2 f_w^3}{w_t^2 \Delta P} \quad (9)$$

In addition, the aperture in the definition of Di (Eqn. (7)) is w_t. Clearly, future theoretical and experimental research should be performed to aid in the understanding of the relationship of hydraulic and tracer apertures.

The computer code FRACNET was developed to solve for the steady state pressure field, flow patterns, and tracer behavior for the model summarized above. In addition, the code computes flow streamlines with a particle tracking technique.

The Fenton Hill Phase I Experiments

The Fenton Hill HDR program is designed to demonstrate the feasibility of creating and operating a prototype hot dry rock geothermal reservoir. In Phase I of the program, conducted in the 1970s, the feasibility of the concept was demonstrated in a series of hydraulic fracturing and flow tests (Dash et al., 1981). In the longest experiment, lasting 286 days, energy was extracted at an average rate of 3 MW thermal at a temperature of about 140°C. The present study focuses on hydraulic and tracer data obtained from this reservoir. Tracer response curves were measured by injecting a short pulse of irradiated NH_4Br^{82} salt dissolved in water and measuring the gamma activity as a function of time in the production fluid. Phase II of the program, which is designed to demonstrate the technology for long-term heat extraction on a larger scale at higher temperatures, is currently being carried out.

Results and Discussion

Table 1 lists the input parameters for the base case. Of these, the parameters which are fully or partially adjustable are f_w, the ratio of tracer aperture to hydraulic aperture, w_1 and w_2, the average tracer apertures for the two fracture sets, σ, the standard deviation of the aperture for the two fracture sets, the fracture spacing S, and the matrix porosity ϕ (used to evaluate tracer matrix diffusion effects). For the base case, agreement was achieved between the model and tracer data by using the measured value of ΔP and known physical property values, assuming the values of S, σ, and ϕ listed in Table 1, and adjusting the values of w_1, w_2, and f_w. To evaluate the "goodness-of-fit" of the simulation, three criteria were used: 1) the first arrival and peak tracer times must be matched; 2) the fraction of tracer recovered at the end of the tracer test (120 hr) should be within about 10% of the measured value of 0.83; and 3) there should be no anomalous behavior in the model results, such as multiple peaks, since the data have no such peaks.

Table 1 Input Parameters for the Base Case

N	40
L	300 m
S	25 m
ϕ	0
w_1	0.4 mm
w_2	0.4 mm
σ	0
f_w	2.36
P	2 MPa
D_{AB}	2.5×10^{-8} m^2/s
R	1
R'	1

A final consistency check on the model results requires the calculation of reservoir thickness. The flow rate per unit depth, q, at the injection or production well is calculated from Eqn. (8). The measured flow rate (6.31×10^{-3} m^3/s in this case) divided by q equals the reservoir thickness. If this thickness is less than the fracture spacing or much greater than the well spacing, then the model is utilizing an unrealistic reservoir geometry, even if the tracer data are reproduced accurately.

Base Case Results: For the base case, the inlet and outlet points were placed along the same fracture, as in Figure 1. Although f_w, w_1, and w_2 were adjustable parameters, it was found that keeping these values constant was adequate for all simulations presented in this paper. The calculated tracer pulse response is compared to the measured data in Figure 3. These curves are residence time distributions, normalized so that the area under the curves are equal to unity. The model results are plotted as a series of straight lines connecting the points in the residence time histogram. The first arrival and peak arrival times match the data reasonably well, and the fraction of tracer recovered at the end of the experiment, as measured by the area under the curves, are nearly equal for the two curves. Finally, although the curve exhibits some jaggedness, there is only one pronounced peak. The simulation meets the criteria established above, and thus is an adequate fit to the data. The integral of the pulse response curve representing the response to a step change in tracer concentration, is shown in Figure 4. The close agreement between model and data is more evident here because the integral smooths out the jaggedness of the pulse response curve.

The calculated reservoir thickness based on the model result and injection flow rate of 6.31×10^{-3} m^3/s is 48 m. Thus, the final consistency check on the model, that the reservoir simulation produce a reasonable 3-dimensional shape for the reservoir, is satisfied. This criterion is also met for the model results presented below.

The flow streamlines plotted in Figure 5 illustrate the nature of fluid flow in the fracture network. Much of the flow travels in a small region of rock near the injection and production points, but a significant fraction also travels in circuitous paths through a much larger region. This behavior gives rise to the observed tracer response consisting of an early, elevated concentration and a very long tail of the residence time distribution.

Effect of Fracture Spacing: In addition to the base case value of S=25 m, simulations were performed varying the fracture spacing while holding other parameter values constant. The flow geometries for these cases were similar to that of Figure 1, except that a larger fracture spacing results in fewer fracture intersections between the inlet and outlet points, and a smaller fracture spacing results in more fracture intersections. The resulting tracer response curves are shown in Figures 6a and b for S=15 m and S=50 m. The S=15 m case fits the data well, but the S=50 m case has too many individual peaks and thus fails to fit the data. With too few fracture intersections between the inlet and outlet, the reservoir with S=50 m does not contain a sufficient number of different possible routes for the fluid and tracer particles. The result is a tracer response curve with multiple peaks, in contrast to the smooth response curve measured. Thus the average fracture spacing of this reservoir is probably no greater than about 25 m.

Distribution of Fracture Apertures: In a fracture network, not all fractures have the same aperture. After extensive examination of fractures in cores, Snov (1970) showed that a lognormal distribution of apertures can be assumed. To simulate a fracture network with a lognormal aperture distribution, we randomly set the aperture value (subject to the lognormal distribution) for each flow segment in the network, treating each as an individual fracture. Figure 7 shows the tracer response for one realization assuming $\sigma = 0.5$ (units of ln(m)) for each fracture set (all other parameter values are those of the base case). The agreement is adequate, although one would have to perform more realizations to prove definitively that these model parameters with a distribution of apertures can be used to represent the Phase I reservoir. The flow streamline contour plot for this realization is shown in Figure 8. Fluid is diverted preferentially to fractures with larger apertures, resulting in distortions of the flow streamlines from the base case result of Figure 5. However, the correlation length for apertures is only 25 m, the fracture spacing. Since this value is much less than the well spacing, only the details of the flow field are affected by the distribution of apertures, while the overall tracer behavior is relatively unchanged. If large or small apertures were assumed to be continuous over longer distances, then the tracer behavior would have depended much more strongly on the distribution of apertures, and greater variability would be observed from one realization to the next.

Effect of Matrix Diffusion: Figure 9 shows the simulated tracer step response curves for different values of matrix porosity ϕ. Matrix diffusion exhibits a strong effect on the long-residence-time tail of the response curve, the effects becoming stronger for higher values of ϕ. The result is a decreased recovery of tracer for larger values of ϕ, as a larger fraction of the tracer is delayed in the stagnant matrix fluid.

Unfortunately, there exists no reliable technique for determining in situ matrix porosity in fractured granitic reservoirs, so a range from 0 to 0.005 was used. At the depths at which HDR reservoirs will typically be found, large earth stresses will compress the rock, lowering its porosity. However, injection of fluid at pressures nearly equivalent to the in situ earth stresses lowers the effective stress on the granite blocks, thus raising the porosity. Laboratory measurements of porosity on core specimens as a function of stress are possible, but in the process of recovering the core, the granite may have undergone additional fracturing as a result of cooling. The simulation just presented illustrates that matrix diffusion may have a significant impact on tracer behavior even in fractured granitic reservoirs, and that reliable techniques for measuring matrix porosity are needed to quantify this phenomenon.

Despite the uncertainties currently impeding progress, fracture network modeling holds great promise for characterizing fractured geothermal reservoirs. The approach used in the present study incorporates pressure drop and tracer data, two of the most common measurements in HDR reservoirs, into a physically realistic reservoir model. Thus, using currently available data, the model provides a better understanding of fluid flow and solute transport in fractured reservoirs. Furthermore, heat transfer can be included in the model to enable predictions of the thermal cooldown behavior to be made. Future work will extend the modeling to include heat transfer predictions.

CONCLUSIONS

1. A two-dimensional fracture network model has been developed to simulate steady state fluid flow and tracer transport in a two-well HDR geothermal reservoir.

2. Particle tracking techniques are used to simulate tracer advection, matrix diffusion,

and adsorption. Particle tracking can be used to model any linear transport process, one which is independent of tracer concentration.

3. Tracer data from the Fenton Hill Phase I reservoir is adequately simulated assuming a regular fracture network with fracture spacings of 25 m, apertures of all fractures equal to 0.4 mm, and f_w, the ratio of tracer to hydraulic aperture, equal to 2.36. Smaller fracture spacings also result in good fits to the data, but it is unlikely that larger values of S are realistic since they produce tracer response curves with multiple peaks not present in the field data. Imposing a distribution of aperture widths changes details of the flow field, but has little effect on the overall tracer behavior. Matrix diffusion can have a significant impact on tracer transport even in fractured granitic reservoirs.

4. Future research is required to constrain the fracture network model. The relationship between the hydraulic aperture, which is dominated by the smallest apertures in a rough fracture, and the tracer aperture, an unweighted mean of the aperture distribution, must be studied. Also, reliable techniques for estimating the in situ matrix porosity in fractured reservoirs are needed to quantify the effect on matrix diffusion on tracer transport.

NOMENCLATURE

C	tracer concentration (kg/m^3)
C_{in}	inlet tracer concentration during step input (kg/m^3)
D_{AB}	molecular diffusion coefficient of tracer (m^2/s)
Di	diffusion number (Eqn. (7))
$f(t)$	residence time distribution (s^{-1})
$F(t)$	cumulative residence time distribution
f_w	w_t/w_h
L	fracture length (m)
L_i	length of fracture i (m)
n	number of nodes connected to node o
N	number of rock blocks in each direction
P	pressure (Pa)
P_i	pressure at node i
P_o	pressure at node o
q	flow rate per unit depth (m^2/s)
q_i	flow rate per unit depth in fracture i (m^2/s)
R	tracer retardation factor in the fracture
R'	tracer retardation factor in the matrix
u	fluid flow velocity (m/s)
S	fracture spacing (m)
t	time (s)
w	fracture aperture (m)
w_1	average tracer aperture of fracture set 1 (m)
w_2	average tracer aperture of fracture set 2 (m)
w_h	hydraulic aperture (m)
w_i	aperture of fracture i (m)
w_t	tracer aperture (m)
ϕ	matrix porosity
θ	dimensionless time t/τ
μ	fluid viscosity (Pa-s)
ω	parameter in SOR solution technique
τ	fluid residence time in fracture (s)
σ	lognormal standard deviation of apertures (ln(m))

ACKNOWLEDGEMENTS

This work was performed under the auspices of the U. S. Department of Energy, Geothermal Technology Division. The author would like to thank Don Brown and Hugh Murphy for many useful discussions during the course of this work, and Cheryl Straub for helping to prepare the manuscript.

REFERENCES

Andersson, J., and R. Thunvik, Predicting Mass Transport in Discrete Fracture Networks With the Aid of Geometrical Field Data, Water Resour. Res., 22, 13, 1941-1950, 1986.

Castillo, E., Karadi, G. M., and R. J. Krizek, Unconfined Flow Through Jointed Rock, Water Res. Bull., 8, 2, 266-281, 1972.

Dash, Z. V. et al., Hot Dry Rock Geothermal Reservoir Testing: 1978 to 1980, J. Volcanology and Geothermal Res., 15, 59-99, 1981.

Hopkirk, R. J., Gilby, D. J, Rybach, L., and J. C. Griesser, Modelling of Heat and Mass Transfer in Deep, Fractured Crystalline Rock, Geothermics, 14, 2, 385-392, 1985.

Long, J. C. S., and D. M. Billaux, From Field Data to Fracture Network Modeling: An Example Incorporating Spatial Structure, Water Resour. Res., 23, 7, 1201-1216, 1987.

Long, J. C. S., Remer, J. S., Wilson, C. R., and P. A. Witherspoon, Porous Media Equivalents for Networks of Discontinuous Fractures, Water Resour. Res., 18, 3, 645-658, 1982.

Robinson, B. A., and J. W. Tester, Dispersed Fluid Flow in Fractured Reservoirs: An Analysis of Tracer-Determined Residence Time Distributions, J. Geophys. Res., 89, B12, 10374-10384, 1984.

Schwartz, F. W., Macroscopic Dispersion in Porous Media: The Controlling Factors, Water Resour. Res., 13, 4, 743-752, 1977.

Schwartz, F. W., Smith, L., and A. S. Crowe, A Stochastic Analysis of Macroscopic Dispersion in Fractured Media, Water Resour. Res., 19, 5, 1253-1265 1983.

Smith, L., and F. W. Schwartz, Mass Transport 1. A Stochastic Analysis of Macroscopic Dispersion, Water Resour. Res., 16, 2, 303-313, 1980.

Snow, D. T., The Frequency and Apertures of Fractures in Rock, Int. J. Rock. Mech. Min. Sci., 7, 23-40, 1970.

Starr, R. C., Gillham, R. W., and E. A. Sudicky, Experimental Investigation of Solute Transport in Stratified Porous Media 2. The Reactive Case, Water Resour. Res., 21, 7, 1043-1050, 1985.

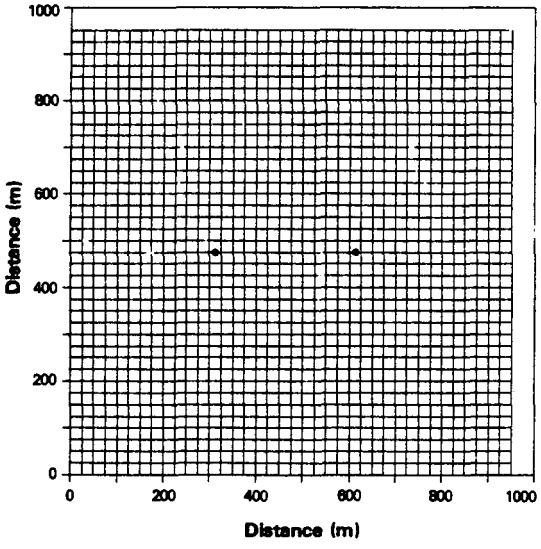


Figure 1. Typical fracture network with two fracture sets, inlet and outlet points, and outer boundary

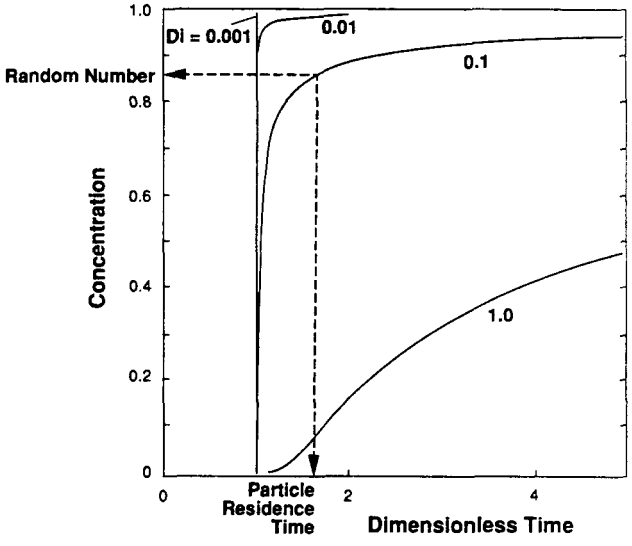


Figure 2. Tracer step response curves for flow through a single fracture with matrix diffusion for different values of the diffusion number Di. Also shown is a calculated value for residence time for a given random number.

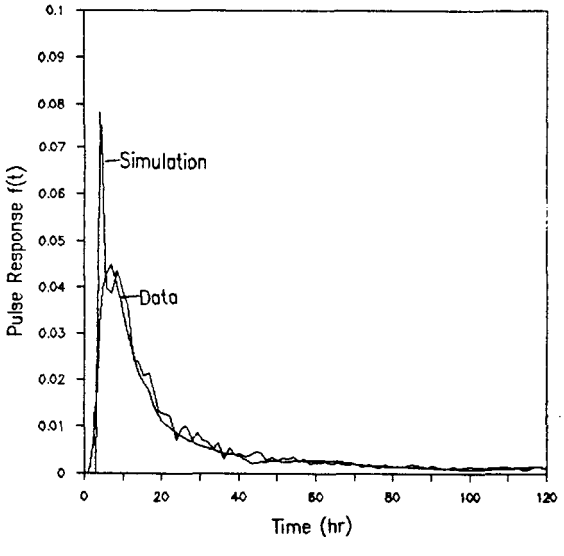


Figure 3. Comparison of measured and simulated pulse response curves for the base case.

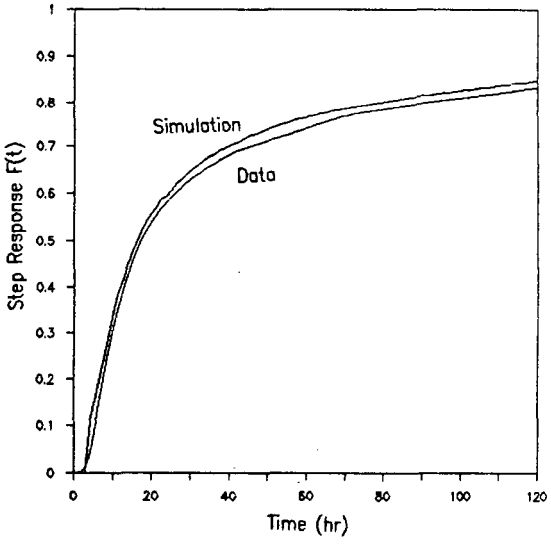


Figure 4. Comparison of measured and simulated step response curves for the base case.

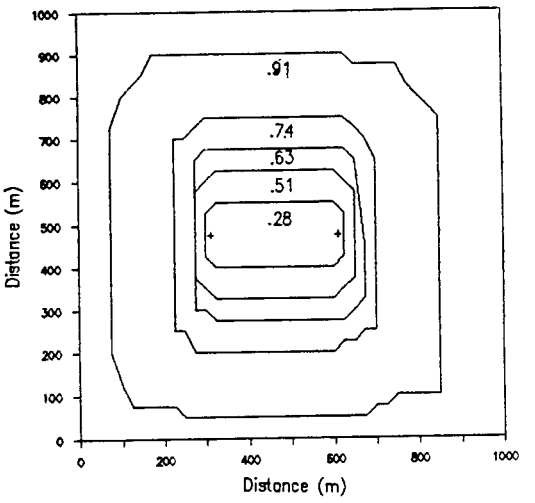
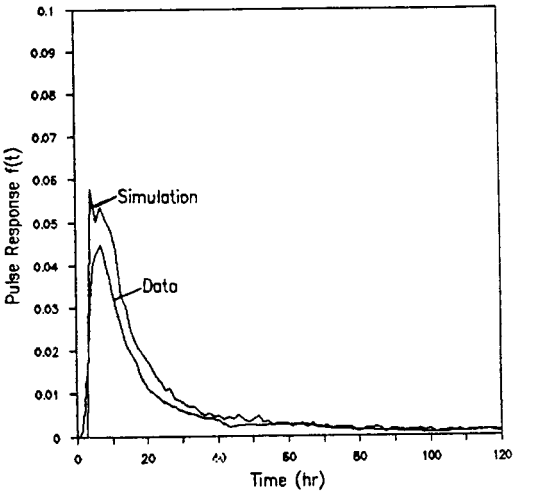


Figure 5. Flow streamlines for the base case.



6(a)

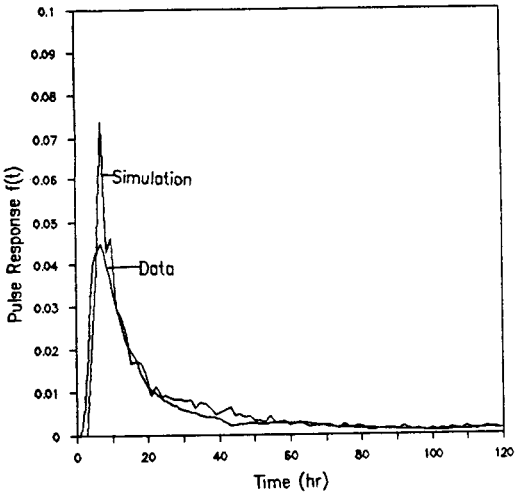
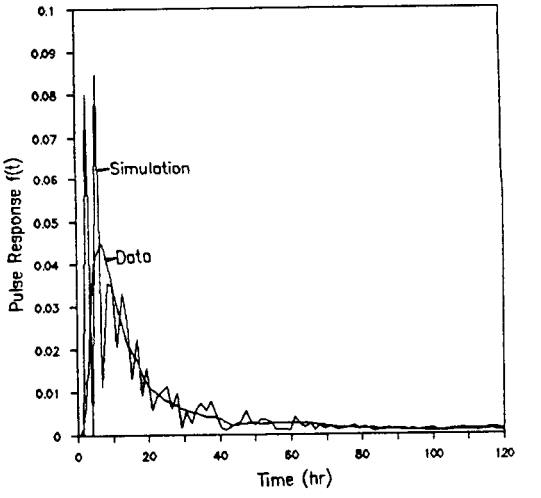


Figure 7. Pulse response for σ=0.5.



6(b)

Figure 6. Pulse response curves for various values of S: (a) S=15 m; (b) S=50 m.

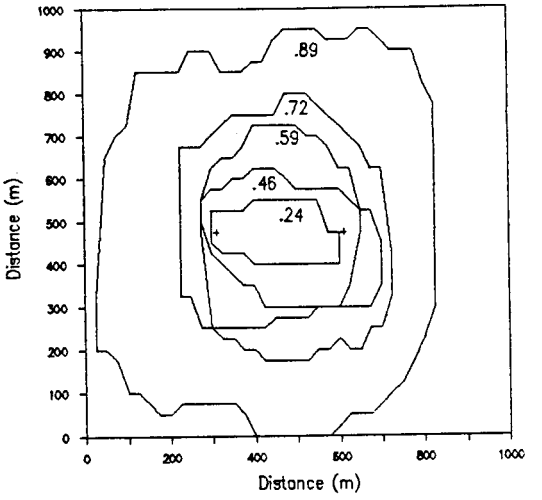


Figure 8. Flow streamlines for the σ=0.5 simulation.

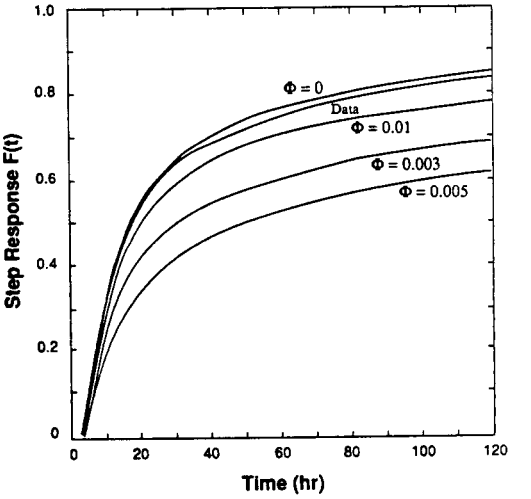


Figure 9. Effect of matrix diffusion: step responses for different values of ϕ.

PROCEEDINGS, Thirteenth Workshop on Geothermal Reservoir Engineering
Stanford University, Stanford, California, January 19-21, 1988
SGP-TR-113

A SEMI-ANALYTICAL METHOD FOR HEAT SWEEP CALCULATIONS IN FRACTURED RESERVOIRS

K. Pruess and Y. S. Wu

Earth Sciences Division, Lawrence Berkeley Laboratory
University of California, Berkeley, California 94720

ABSTRACT

An analytical approximation is developed for purely conductive heat transfer from impermeable blocks of rock to fluids sweeping past the rocks in fractures. The method was incorporated into a multi-phase fluid and heat flow simulator. Comparison with exact analytical solutions and with simulations using a multiple interacting continua approach shows very good accuracy, with no increase in computing time compared to porous medium simulations.

INTRODUCTION

Despite major advances in recent years, the mathematical modeling of fluid and heat flow in fractured geothermal reservoirs remains a difficult problem. Porous medium approximations have been shown to be inadequate for many flow processes in fractured systems (Pruess, 1983), while double- or multiple-porosity techniques may involve excessive amount of numerical work or large discretization errors.

Combining finite-difference and analytical techniques, we have developed a method which can provide an accurate and efficient representation of fluid and heat flow in fractured reservoirs under conditions of strong heat transfer and insignificant fluid exchange between rock matrix and fractures. The method is an adaptation of a technique developed by Vinsome and Westerveld (1980) to describe heat exchange with impermeable confining beds in thermally enhanced oil recovery.

THE METHOD OF VINSOME AND WESTERVELD

An important aspect of thermal oil recovery schemes is the transfer of heat by conduction from the reservoir to adjacent strata of low permeability. In steam and hot waterfloods this represents a heat loss which may have significant effects on process economics. In steam soak operations (huff-and-puff) heat lost to cap and base rock during injection can be partially conducted back to the reservoir during the production cycle, providing beneficial effects. The heat exchange with impermeable strata can be large and must be included in numerical simulations of thermal recovery. At early times the conductive temperature profile has rather steep gradients near the surface of the conductive zone, while at late time it extends to large distance from the boundary. A reasonably accurate representation of heat conduction by numerical methods (e.g. finite differences) therefore requires many grid blocks and can greatly increase the computational work.

A number of semi-analytical and variational approaches have been developed which permit modeling of conductive heat exchange with impermeable strata without requiring these strata to be explicitly included in the domain of a finite difference model (Weinstein, 1972, 1974; Chase and O'Dell, 1973; Vinsome and Westerveld, 1980). Of these the method of Vinsome and Westerveld is the most attractive due to its elegance and simplicity. Observing that the process of heat conduction tends to dampen out temperature variations, Vinsome and Westerveld suggested that cap- and base-rock temperatures would vary smoothly even for strong and rapid temperature changes at the boundary of the conductive zone. Arguing that heat conduction perpendicular to the conductive boundary is more important than parallel to it, they proposed to represent the temperature profile in a conductive layer by means of a simple trial function, as follows:

$$T(x,t) - T_i = (T_f - T_i + px + qx^2)e^{-x/d} \qquad (1)$$

Here x is the distance from the boundary, T_i is initial temperature in cap- or base-rock (assumed uniform), T_f is the time-varying temperature at cap- or base-rock boundary, p and q are time-varying fit-parameters, and d is the penetration depth for heat conduction, defined by

$$d = \frac{\sqrt{\kappa t}}{2} \qquad (2)$$

where $\kappa = K/\rho c$ is the thermal diffusivity, with K the heat conductivity, ρ the density of the medium, and c the specific heat. In connection with a finite-difference simulation of non-isothermal flow, each grid block in the top and bottom layers of the computational grid will have an associated temperature profile in the adjacent impermeable rock as given by Eq. (1). The coefficients p and q will be different for each grid block; they are determined concurrently with the flow simulation from simple physical principles, namely: (1) temperature at the conductive boundary obeys the heat conduction equation for the impermeable stratum, and (2) the rate of change in total cap- or base-rock heat content is equal to the heat flux at the boundary. Vinsome and Wester-

veld presented test calculations which showed that their method was able to accurately represent monotonic as well as non-monotonic temperature profiles. We incorporated their technique into our MULKOM simulator (Pruess, 1983b, 1988) and verified that it gave accurate results (Pruess and Bodvarsson, 1984).

HEAT EXCHANGE WITH BLOCKS OF IMPERMEABLE ROCK

The method of Vinsome and Westerveld treats heat exchange between a surface with time varying temperature and a semi-infinite conductive half-space. It can be easily adapted to the problem of heat exchange between impermeable rock matrix blocks and fluids flowing in fractures or porous materials around these blocks. The required modifications involve the equation of heat conduction and the calculation of total heat content in the blocks, both of which differ from those for a semi-infinite medium.

Following concepts developed in the method of "multiple interacting continua" or "MINC" (see Fig. 1) we approximate heat flow in impermeable blocks of rock as being one-dimensional, with temperatures in the blocks depending only on the distance x from the nearest surface (i.e. from the nearest fracture; Pruess and Narasimhan, 1982, 1985). We use the concept of "proximity function" (Pruess and Karasaki, 1982) to describe one-dimensional flow in blocks of arbitrary shape, as well as flow in stochastic assemblages of matrix blocks which are encountered in fractured reservoirs. For matrix blocks of volume V_m having a volume V(x) within a distance x from the fractures (i.e., from the block surfaces), the proximity function is defined as:

$$\mathrm{PROX}(x) = \frac{V(x)}{V_m} \tag{3}$$

The interface area for flow in the matrix blocks at distance x from the surface is

$$A(x) = \frac{dV}{dx} = V_m \, d\frac{\mathrm{PROX}}{dx} \tag{4}$$

Considering a heat balance for a volume element dV = A(x) dx, we obtain the following equation for one-dimensional heat conduction in the blocks:

$$\frac{\partial T}{\partial t} = \kappa \frac{\partial^2 T}{\partial x^2} + \kappa \frac{\partial T}{\partial x} \frac{\partial \ln A}{\partial x} \tag{5}$$

Choosing the same form Eq. (1) for the temperature profile in the blocks as was used by Vinsome and Westerveld for the semi-infinite solid, the condition that Eq. (5) must be satisfied at the surface of the blocks gives

$$\frac{T_f - T_f^\circ}{\kappa \Delta t} = \frac{\theta}{d^2} - \frac{2p}{d} + 2q + \left.\frac{\partial \ln A}{\partial x}\right|_o \left(p - \frac{\theta}{d}\right) \tag{6}$$

Here we have replaced the time derivative by a first-order forward finite difference, as required for incorporating the method into our numerical simulator MULKOM. T_f° and T_f are temperatures in the fracture at the beginning and end of the time step Δt, respectively. θ is an abbreviation for T_f - T_i. For a semi-infinite solid the derivative term involving A(x) vanishes, so that Eq. (6) then reduces to the form given by Vinsome and Westerveld. Energy conservation in the blocks is expressed as follows.

$$\frac{d}{dt} \int_{V_m} \rho c T dv = -K \left.\frac{\partial T}{\partial x}\right|_o A(x=0) \tag{7}$$

With a slight rearrangement of terms the integral on the left hand side becomes

$$I(t) = \int_0^{D/2} [T(x,t) - T_i] \frac{A(x)}{A(0)} dx \tag{8a}$$

The integration extends to D/2, which for fracture spacing D is the largest distance from the block surfaces. Inserting from Eq. (1) this integral can be written as

$$I(t) = \beta q + \gamma p + \delta \theta \tag{8b}$$

The coefficients β, γ and δ represent a weighting of the x-dependent terms $x^n \exp(-x/d)$ (n = 0, 1, 2) in Eq. (1) with the function A(x)/A(0) characterizing the matrix block shapes. Even for irregular blocks and stochastic assemblages the proximity function and its derivative A(x) can be written as polynomials in x (Pruess and Karasaki, 1982), so that the integral in Eq. (8) can be evaluated by elementary means. Evaluating the spatial derivative from Eq. (1) the finite difference version of Eq. (7) becomes

$$I(t+\Delta t) - I(t) = \kappa \Delta t \left(\frac{\theta}{d} - p\right) \tag{9}$$

Eqs. (6) and (9) (with the definition Eq. 8) represent two linear equations for the two unknown time-dependent parameters p and q. Solution of these is trivial once the coefficients β, γ, and δ in Eq. (8b) have been obtained. The heat flux from the blocks to the fractures is calculated as in Vinsome/Westerveld by

$$Q = K \left.\frac{\partial T}{\partial x}\right|_0 = K \left(\frac{\theta}{d} - p\right) \tag{10}$$

Calculation of the time-dependent coefficients p and q from Eqs. (6) and (9), and of heat exchange between the permeable and the conductive domains from Eq. (10), has to be done at each time step separately for all grid blocks which contain purely conductive material. It is possible to apply the conductive exchange calculation only for certain grid blocks, while others may be treated as homogeneous porous media, or as fractured media with permeable matrix using the MINC method. The temperature T (x=0,t) at the surface of the conductive domain is identified with the temperature in the permeable portion (fractures) of the grid block. In a fully implicit scheme this temperature is evaluated at the new time level t + Δt, and the heat exchange calculation is done in a fully coupled manner as part of the iterative

process to solve the fluid and heat flow equations in the permeable domain.

To incorporate the above scheme into a numerical simulator we partition grid block volumes into a permeable and a purely conductive part.

$$V_n = V_{n,per} + V_{n,cond} \qquad (11)$$

Fluid and heat flow in the permeable portions $V_{n,per}$ of the grid blocks is handled by numerical simulation. Heat transferred by conduction from the impermeable portion $V_{n,cond}$ is represented by including Eq. (10), properly scaled for the total conductive interface area in V_n, as a source term into the heat balance equation for $V_{n,per}$.

EVALUATION

We have implemented the method described in the foregoing section into our general purpose simulator MULKOM, and have performed several tests and comparisons. For simplicity this was done for matrix blocks of cubic shape. For cubes the proximity function can be directly obtained from the definition Eq. (3); it is given by

$$\mathrm{PROX}(x) = \frac{6x}{D} - \frac{12x^2}{D^2} + \frac{8x^3}{D^3} \qquad (12)$$

This leads to a particularly simple form for the expression A(x)/A(0) appearing in the integral Eq. (8), namely,

$$\frac{A(x)}{A(0)} = \left(1 - \frac{2x}{D}\right)^2 \qquad (13)$$

In order to evaluate the accuracy of the semi-analytical approximation we have studied a problem for which exact analytical solutions are available, namely, heat exchange with a cube of initially uniform temperature, which at time $t = 0$ is subjected to a step change in temperature at the surface. The parameters of the problem are given in Table 1.

The heat flow rate at the surface of the cube was computed as function of time using the following four approaches: (1) numerical evaluation of the exact three-dimensional Fourier series solution (Carslaw and Jaeger, 1959); (2) a one-dimensional approximation to heat flow in a cube, for which the exact solution is identical to heat flow in a sphere (Carslaw and Jaeger, 1959); (3) the semi-analytical solution as developed above, incorporated into the MULKOM simulator; and (4) method of multiple interacting continua ("MINC"; Pruess and Narasimhan, 1985). Results are given in Tables 2 and 3.

Table 1. Parameters for test problem (heat exchange with unit cube).

side length of cube	1 m
rock density	2650 kg/m^3
specific heat	1000 J/kg°C
heat conductivity	2.1 W/m°C
initial temperature	300 °C
surface temperature for $t > 0$	100 °C

The "exact 3-D" and the "exact 1-D" results are virtually identical, with the exception of very early and very late times, which have little significance for overall heat transfer. Heat flow rates calculated in the semi-analytical approximation agree very well with the exact results, being typically 1-2 % larger. Cumulative heat transfer in the semi-analytical approximation is underpredicted by typically 10% at most times, but it approaches the correct asymptotic value of 5.3×10^8J at late times. It may appear inconsistent that heat flow rates in the semi-analytical approximation are slightly on the high side at all times while cumulative heat transfer is somewhat low. This effect is caused by the time discretization: In the semi-analytical approach the heat flow rate is constant during each time step; moreover, in our fully implicit scheme it is equal to the heat flow rate at the end of the time step. Because heat flow rates are monotonically declining this leads to some underprediction of cumulative heat transfer. The accuracy of the semi-analytical calculation could be improved by taking smaller time steps (we used 4 time steps per log-cycle), or by using a mid-point weighting in time (Crank-Nicolson equation; Peaceman, 1977) rather than a fully implicit treatment. However, in practical problems one is seldom interested in accurate answers

Table 2. Heat flow rates from unit cube.

Time	Heat Flow Rate (W)			
(s)	exact 3-D	exact 1-D	semi-analytical	MINC
1	1.410E6	1.592E6	1.821E6	1.315E6
10	4.987E5	5.000E5	5.038E5	6.122E5
10^2	1.534E5	1.547E5	1.546E5	1.683E5
10^3	4.429E4	4.547E4	4.514E4	4.913E4
10^4	1.020E4	1.093E4	1.063E4	1.207E4
10^5	6.354E2	4.414E2	9.478E2	8.372E2
10^6	4.275E-7	2.610E-10	1.021E1	5.676E-2

Table 3. Cumulative heat flows from unit cube.

Time	Cumulative Conductive Heat Transfer (MJ)			
(s)	exact 3-D	exact 1-D	semi-analytical	MINC
1	3.285	3.286	2.645	1.22
10	10.04	10.05	9.079	8.52
10^2	31.31	31.44	28.40	30.28
10^3	94.73	95.97	86.09	93.52
10^4	259.6	269.0	235.7	261.8
10^5	503.0	515.9	453.9	503.3
10^6	530.0	530.0	524.9	529.9

over many orders of magnitude in time, so that time steps do not need to grow as fast as in our test case, and better time truncation accuracy will be attainable.

Heat flow rates calculated in the MINC approach, using 50 subcontinua of equal volume, differ by as much as 10 - 20% from the exact values. For rates that change with time by many orders of magnitude this is not a bad approximation. In terms of cumulative heat transfer the MINC approximation does extremely well (Table 3). After a brief period with significant space discretization effects at very early times the MINC results agree to better than 1% with the exact solution.

FIVE-SPOT

We have applied the semi-analytical heat exchange approach to a two-dimensional five-spot production/injection problem similar to that previously studied by Pruess (1983a). Problem parameters are given in Table 4.

The grid used in the numerical simulations represents 1/8 of a five-spot; it has six rows and eleven columns for a total of thirty-six volume elements (see Fig. 2). We assume three sets of equidistant, plane, parallel fractures at right angles, so that the impermeable matrix blocks are cubes. Calculations were done for two different fracture spacings. In addition to using the semi-analytical approach we also performed simulations with the MINC method, and with a uniform porous medium model (with same total void space, i.e., porosity of 1%). The MINC approach uses five subcontinua, with volume fractions of .02, .08, .20, .35, and .35. Results are given in Figure 3 and in Table 5.

Table 4. Specifications of five-spot problem.

Formation	
rock grain density	2650 kg/m^3
specific heat	1000 J/kg°C
heat conductivity	2.1 W/m°C
permeable volume fraction	2%
porosity in permeable domain	50%
impermeable blocks: cubes with side length	50 m, 250 m
effective permeability	6.0×10^{-15}m^2
thickness	305 m
relative permeability: Corey curves with $S_{lr} = 0.30$, $S_{vr} = 0.05$	
initial temperature	300°C
initial liquid saturation	0.99
initial pressure	85.93 bar
production/injection	
pattern area	1 km^2
distance between producers and injectors	707.1 m
production rate (*)	30 kg/s
injection rate (*)	30 kg/s
injection enthalpy	500 kJ/kg

(*) full well basis

Fig. 3 shows temperature profiles along the line connecting a producer and an injector after 36.5 years, corresponding to injection of approximately 12.2 pore volumes. For both fracture spacings the agreement between the semi-analytical and the MINC simulations is excellent. The D = 50 m results are indistinguishable from the porous medium calculation, while at the larger fracture spacing of D = 250 m the thermal sweep is less complete and lower temperatures are obtained. Predicted total heat transfer from the impermeable rocks to the fluids agrees to better than 1% between the semi-analytical and MINC approaches at most times (see Table 5). The semi-analytical approach required the same amount of computing time as the porous medium case, while the MINC calculation was approximately five times slower.

DISCUSSION AND CONCLUSIONS

We have incorporated an analytical heat transfer model into a numerical simulator for fluid and heat flow to calculate heat exchange between impermeable blocks of rock and fluids migrating past these blocks in fractures. For problems in which rock matrix permeability is negligible this offers a means of simulating fluid and heat flow in fractured media with essentially no increase in computing work as compared to porous medium simulations. Detailed analysis of heat flow from a cube suggests that the semi-analytical method should provide acceptable engineering accuracy. We are presently investigating some variations on the form Eq. (1) which might achieve even better accuracy. However, simulations for a two-phase production/injection problem with phase change gave almost perfect agreement with the MINC method for two different fracture spacings, so that there may be little need for further improvement.

There are two reasons why the semi-analytical method performs better on a reservoir problem than might have been expected from the test results for an individual

Table 5. Cumulative heat transfer from rocks to fluids in 1/8 of five-spot.

Time (years)	Cumulative Conductive Heat Transfer (10^{14}J)			
	Fracture Spacing 50 m		Fracture Spacing 250 m	
	MINC	Semi-analytical	MINC	Semi-analytical
1	1.07	1.07	.83	.85
2	2.11	2.10	1.77	1.79
5	5.22	5.18	4.64	4.67
10	10.33	10.29	9.40	9.46
15	15.48	15.44	14.10	14.16
20	20.43	20.38	18.70	18.79
25	25.24	25.19	23.21	23.33
30	30.14	30.10	27.60	27.75
35	35.05	35.00	31.91	32.07

cube. Firstly, time discretization errors are not as severe in the reservoir problem, because time steps can be allowed to settle at $\Delta t = .5$ - 1 year after the initial rapid transient, while in the single-cube problem they were kept growing to cover the large time range from very early transient to late-time temperature equilibrium. Secondly, the aggregate response of many rock blocks in a reservoir problem tends to compensate for whatever inaccuracies may be present in the modeling of individual block response. To see how this comes about, suppose that because of discretization effects the blocks near the injection well do not deliver heat to the fluids as rapidly as they should.(This is what actually happens in the semi-analytical method; see Table 3.) As a consequence fluids will have lower temperatures when at later time they sweep past downstream blocks, and hence they will pick up more heat from those blocks. This compensation of inaccuracies in individual block response from global reservoir mechanisms is completely analogous to what was observed in analysis of waterfloods in fractured hydrocarbon reservoirs (Wu and Pruess, 1986). It indicates that satisfactory accuracy in reservoir flow problems should be attainable with rather modest accuracy requirements for individual blocks.

The semi-analytical method for heat transfer presented here should also be applicable to problems of chemical transport in fractured media, because chemical transport in low-permeability blocks of rock can be described in analogy to heat conduction. Work along these lines is in progress.

ACKNOWLEDGEMENT

This work was supported by the Geothermal Technology Division, U.S. Department of Energy, under Contract No. DE-AC03-76SF00098.

REFERENCES

Carslaw, H. S., and Jaeger, J. C. (1959), *Conduction of Heat in Solids,* Oxford University Press, Oxford, England, Second Edition.

Chase, C. A. and O'Dell, P. M. (1973), "Application of Variational Principles to Cap and Base Rock Heat Losses," *Trans. AIME, 225,* 200-210.

Peaceman, D. W. (1977), *Fundamentals of Numerical Reservoir Simulation,* Elsevier, Amsterdam.

Pruess, K. (1983a), "Heat Transfer in Fractured Geothermal Reservoirs with Boiling," *Water Resources Research, 19,* (1), 201-208, February.

Pruess, K. (1983b), "Development of the General Purpose Simulator MULKOM," Annual Report 1982, Earth Sciences Division, Report LBL-15500, Lawrence Berkeley Laboratory.

Pruess, K. (1988), "SHAFT, MULKOM, TOUGH," Lawrence Berkeley Laboratory Report LBL-24430, Berkeley, Ca., January, (submitted to Geotermia, Rev. Mex. Geoenergia).

Pruess, K. and Bodvarsson, G. S. (1984), "Thermal Effects of Reinjection in Geothermal Reservoirs with Major Vertical Fractures," *Journal of Petroleum Technology, 36,* (10) 1567-1578, September.

Pruess, K. and Karasaki, K. (1982), "Proximity Functions for Modeling Fluid and Heat Flow in Reservoirs with Stochastic Fracture Distributions," presented at Eighth Workshop on Geothermal Reservoir Engineering, Stanford University, Stanford, Ca., December.

Pruess, K. and Narasimhan, T. N. (1982), "On Fluid Reserves and the Production of Superheated Steam from Fractured, Vapor-Dominated Geothermal Reservoirs," *Journal of Geophysical Research, 87,* (B11) 9329-9339.

Pruess, K. and Narasimhan, T. N. (1985), "A Practical Method for Modeling Fluid and Heat Flow in Fractured Porous Media," *Society of Petroleum Engineers Journal, 25,* (1), 14-26, February.

Vinsome, P. K. W., and Westerveld, J. (1980), "A Simple Method for Predicting Cap and Base Rock Heat Losses in Thermal Reservoir Simulators," *J. Canadian Petroleum Technology,* 87-90, July-September.

Weinstein, H. G., (1972), "Semi-Analytic Method for Thermal Coupling of Reservoir and Overburden," *Society Petroleum Engineers Journal,* 439-447, October.

Weinstein, H. G., (1974), "Extended Semi-Analytical Method for Increasing and Decreasing Boundary Temperature," *Society Petroleum Engineers Journal,* 152-164, April.

Wu, Y. S. and Pruess, K. (1986), "A Multiple-Porosity Method for Simulation of Naturally Fractured Petroleum Reservoirs," paper SPE-15129, presented at 56th Annual California Regional Meeting of the SPE, Oakland, Ca., April (to appear in *Society Petroleum Engineers Journal).*

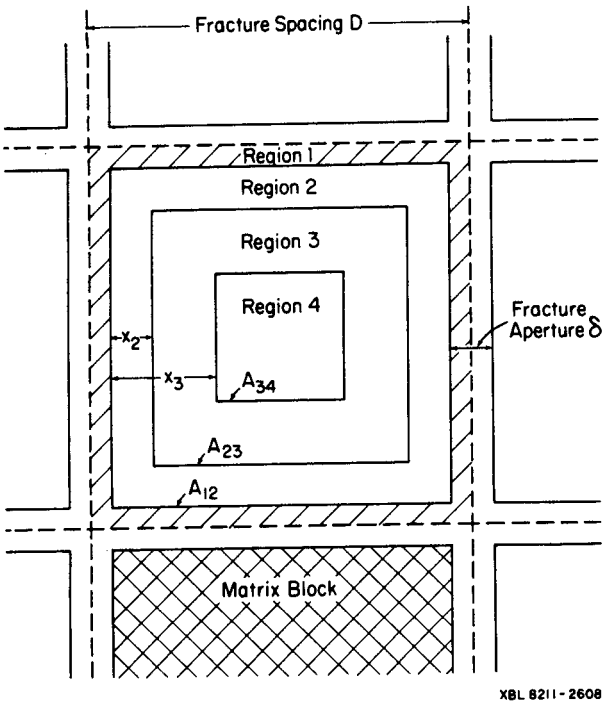


Figure 1. The concept of multiple interacting continua for an idealized fracture system.

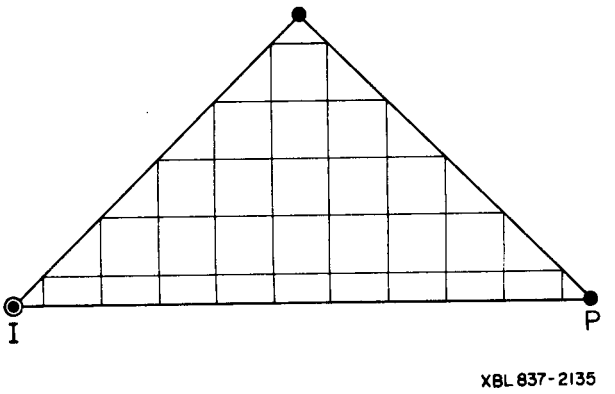


Figure 2. Computational grid for five-spot production/injection problem (I - injector, P - producer).

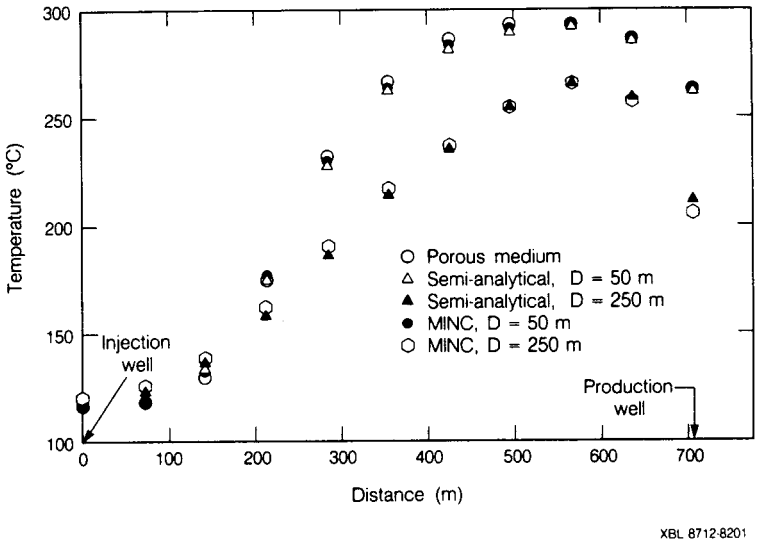


Figure 3. Temperature profiles for five-spot after 36.5 years.

PROCEEDINGS, Thirteenth Workshop on Geothermal Reservoir Engineering
Stanford University, Stanford, California, January 19-21, 1988
SGP-TR-113

A THREE-DIMENSIONAL MODEL OF FLUID, HEAT, AND TRACER TRANSPORT IN THE FENTON HILL HOT DRY ROCK RESERVOIR

Stephen A. Birdsell* and Bruce A. Robinson

Los Alamos National Laboratory
Los Alamos, NM 87545
*Contractor

ABSTRACT

A three-dimensional model of the Fenton Hill Hot Dry Rock reservoir has been developed. The model matches hydraulic, thermal, tracer, and water loss data during a 30-day flow test. Wellbores were placed in the finite element mesh at their relative positions. The data match to this flow test was used to make long-term simulations, and to predict the effect on reservoir performance of redrilling the damaged production wellbore. Increasing the length of producing interval by drilling was found to significantly improve reservoir power production and the temperature of produced fluids, while increasing the wellbore separation distance was found to result in only small improvements.

INTRODUCTION

A 30-day flow test was conducted at the Fenton Hill Hot Dry Rock (HDR) reservoir in May and June, 1986. Although a large quantity of data was recorded, previous attempts to model the test have focused on only portions of the data, such as pressure transient analyses and models for tracer transport. In this study, the computer code Finite Element Heat and Mass Transfer (FEHM) (Zyvoloski et al., 1988) was used to incorporate all of the relevant hydraulic, thermal, tracer, and water loss data into one model.

FEHM is a three-dimensional computer code that was designed for the analysis of geothermal reservoirs. The code solves the conservation of mass and conservation of energy equations subject to the assumption that Darcy's law applies. In addition, tracer tests can be modeled through the solution of the noncoupled solute transport equation. Reservoirs can be modeled as porous media, or discrete fractures can be placed in the mesh. To be practical, a three-dimensional computer code must require little computer memory and execute rapidly. The incomplete factorization method used in FEHM has both of these characteristics.

MODEL DEVELOPMENT

Construction of the model begins with the choice of the outer reservoir boundary and wellbore positions. A cube was chosen for the boundary since it allowed the finite element mesh to be created most easily and could be used to approximate the current limits of the reservoir. The open hole intervals of the injection and production wellbores were placed in the mesh at approximately their known relative positions, thus providing the reservoir fluid source and sink (Figure 1). Wellbores were placed vertically in the cube since excessive computer memory and execution time would be required to mesh in their exact inclined positions. This is a good approximation since the actual injection and production intervals deviated only slightly from the vertical. The injection interval was determined from temperature logs since injection did not appear to be occurring over the entire open hole section of the wellbore. The production interval was taken as the distance from the casing shoe to the sanded-back point (Table 1). North and East locations of the wellbores were determined by the midpoint of the respective injection and production zones. The injection interval, which is longer than the production interval, is centered in the depth direction of the cube, while the wellbore pair is centered in the N-S and the E-W directions, as shown in Figure 1.

For this initial study, the reservoir was assumed to be an equivalent isotropic porous medium. The fluid volume of the reservoir has been estimated to be 8440 m^3 by analysis of a tracer experiment conducted during the flow test (Robinson et al., 1986). Hence, the volume of the reservoir (rock plus fluid) can be calculated by choosing a porosity. For example, the porosity which best matched the 30-day flow test data was $\phi = 0.0002$. Therefore, the length of the sides of the cube are 350 m. To simulate the observed water loss, flow through the faces of the cube was allowed if the local pressure reached a prescribed pressure, roughly equivalent to the fracture extension pressure (i.e., the water loss was assumed to be due to fracture extension).

The following data was input for the simulation of the 30-day test: injection flow rate, production pressure, injection temperature, and the background temperature log. Data that were matched are: production flow rate, water loss flow rate, injection

pressure, production temperature, and the tracer response curve. Temperatures and pressures at the reservoir inlet and outlet were estimated from surface data using the computer code WBHT (Dash and Zyvoloski, 1982). Porosity, permeability, and the water loss pressure were adjusted to obtain the match. The procedure used to match the data is:

1. Using the reservoir fluid volume (calculated from tracer data) and a chosen porosity, calculate the volume of the cube. Center the injection and production zones in the cube. The original background temperature log in the injection well is used to place a temperature gradient on the cube.

2. Set the injection flow rate, injection temperature, production pressure, permeability, and water loss pressure.

3. Run the simulation for 25 days (the day of the tracer experiment). If the injection pressure, production flow rate, water loss flow rate, and production temperature do not match the known values, adjust the permeability and/or water loss pressure. If these values are matched, restart the simulation including a tracer test on day 25. If the simulated peak tracer response matches the experimental peak tracer response, the simulation is completed. If not, adjust the permeability, porosity, and water loss pressure. Then return to 1. and repeat the process.

RESULTS AND DISCUSSION

The Fenton Hill reservoir can be modeled as an equivalent porous medium if the reservoir is highly fractured with many interconnected flow paths linking the source and sink, as is suggested by reservoir data. The tracer data can give a rough estimate of the number of fractures in the reservoir if assumptions are made about the geometry of individual fractures. Assuming that each fracture has an aperture of 1 mm (Dash and Murphy, 1985) and length and width of 100 m (approximately the separation of the wellbores), then the number of fractures is the reservoir fluid volume divided by the volume of each fracture

$$n = 8440 / (0.001 \times 100 \times 100) = 844 \text{ fractures.} \quad (1)$$

Thus, the reservoir appears to be highly fractured. If the fracture network does not channel flow preferentially, then the isotropic porous media assumption appears appropriate for modeling the fluid flow. However, porous media flow may not be appropriate for heat transfer modeling if the fractures are separated by distances such that heat conduction in the rock limits heat transfer to the reservoir fluid. Robinson and Jones (1987) show that for HDR reservoirs, fracture spacing greater than about 3 m will result in heat transfer that is conduction limited. Evenly distributing the number of fractures calculated in eq (1) over all three dimensions of the cube gives a fracture spacing of 1.2 m. Therefore, by assuming that the fractures are roughly evenly distributed throughout the reservoir, the porous flow model will also accurately model heat transfer.

The source and sink in the cube model represent open wellbores separated by a porous medium. If many fractures intersect the wellbores, this is a good approximation. However, if only a few fractures intersect a wellbore, they should be modeled as individual fractures connected to the porous medium. A temperature log conducted in the injection wellbore about 6 days after the flow test showed a fairly constant temperature depression over the injection interval. Therefore, it can be assumed that the injection wellbore was connected to the reservoir by many fractures. A temperature log was not obtainable in the production zone. Given this uncertainty, the porous media assumption was also applied to the production zone.

The mesh used for the simulation of the 30-day flow test is shown in Figure 2. The mesh is composed of 14 x 15 x 14 nodes for a total of 2940 nodes. The fineness of the mesh was checked by adding one node in each direction in the interwell region. Since most of the flow occurs in the interwell region, error due to a coarse mesh should be evident. However, no significant changes in flow, temperature, or tracer responses resulted. Time step size was also checked. The initial time step was changed from 10^{-4} days to 10^{-5} days and the time step multiplier was reduced from 2 to 1.5, resulting in smaller time steps throughout the simulation. No significant changes resulted from this reanalysis.

The matched and observed hydraulic and temperature results are given in Table 2 and the matched and observed tracer responses are shown in Figure 3. These data were matched with a porosity of 0.0002, a permeability of 1.1×10^{-3} darcy, and water loss pressure at the surfaces of the cube of 53 MPa. The peak tracer response was matched and the shape of the simulated tracer response is similar to but higher than that of the experimental tracer response. The tail of the experimental curve cannot be measured accurately, but can be estimated using techniques developed by Robinson and Tester (1986). Since the area under the two curves between zero and infinite time must be the same, the tail of the experimental curve must be much longer than that of the simulation.

Therefore, the porous cube model results in a less disperse estimate of reservoir flow than the tracer data indicates.

During the 30-day flow test, production occurred over only a short depth interval. In order to improve reservoir performance during the upcoming year-long flow test, this wellbore was redrilled. The new wellbore, referred to as the close-in trajectory, was drilled with essentially the same trajectory as the old wellbore, but the length of the producing interval was increased. An alternative redrilling plan that was considered, the step-out trajectory, was to move the production wellbore about 125 m farther away from the injection wellbore in the horizontal plane and increase the producing interval. The locations of the production wellbore for the two cases are shown in Table 1. In order to define a producing interval for each case, fracture planes identified by a statistical treatment of microseismic events in the reservoir were used (Dreesen et al., 1987). Meshes for close-in and step-out were similar to the mesh used for simulation of the 30-day flow test, but the nodes defining the wellbores were moved to their respective positions.

Figure 4 shows the experimental tracer response from the flow test, the matched tracer response from the flow test, and the predicted responses for the close-in and step-out configurations for the production wellbore. The close-in and step-out simulations were performed with the same inputs and matched parameters as those from the 30-day flow test. The close-in prediction has a more disperse tracer response than the flow test match due to the larger flow sink. The step-out tracer response has a more disperse tracer response than the close-in prediction due to the greater wellbore separation.

Figure 5 shows long-term simulations of power output for the 3 cases. The initial power production is greater for close-in and step-out for two reasons. First, the production wellbore is drilled deeper into the reservoir where higher temperatures are encountered. Second, the prediction based on the flow test has a greater water loss. Power production is greatest for the step-out case since flow in the cube is the most uniform for this case, resulting in more efficient energy extraction.

Figure 6 shows the simulated downhole injection pressure out to 20 years for each of the production wellbore configurations. The prediction based on the flow test match has the largest pressures due to its small fluid-flow sink. Injection pressures are predicted to be larger for the step-out case than for the close-in case despite the fact that the sink is the same size in each case. This is because the step-out case has a larger wellbore separation. Figure 7 shows the production flow rates. Water loss increases throughout the simulation of the flow test match due to increasing interwell flow impedance (i.e., flow rate divided by pressure drop). This behavior is caused by the increasing fluid viscosity which results from thermal drawdown between the wellbores. For water, viscosity increases by a factor of 10 when cooled from 260 to 25°C. Therefore, as the interwell region becomes cooled, flow through the leak-off nodes on the surfaces of the cube increases. Since the larger sinks of the close-in and step-out cases result in less interwell pressure drop, no water loss occurs in the close-in case, while water loss just begins in the final year of the simulation for the step-out case.

The trend of increasing interwell impedance may not be observed in long-term operation of HDR reservoirs. This is because thermal contraction of the rock mass may open fractures and, according to the parallel plate law, impedance would decrease as the cube of the fracture aperture. However, fractures need not open uniformly. If the interwell pressure drop is dominated by relatively few asperities, impedance would not be greatly affected by thermal contraction and the effect of increasing viscosity may have a significant effect on the interwell impedance.

Hence, instead of short-circuiting of flow between wellbores due to fracture opening, flow in HDR reservoirs may prefer hot flow paths, resulting in a reservoir in which flow diverges away from the previously cooled paths. Also, the trend of increasing water loss may not be observed in HDR reservoirs. While the cube model has fixed boundaries through which water loss flows, in reality the points of fracture extension will move away from the injection wellbore with time. Therefore, the pressure drop to the points of fracture extension can be expected to increase with the age of the reservoir, and eventually pressures will not be high enough to cause further fracture extension.

Figure 8 shows the predicted downhole production temperatures for the three simulations. The difference in initial temperatures, as mentioned earlier, is due to the deeper wellbores of the close-in and step-out case.

Further development of the model is planned. Elimination of the water loss pressure as an adjustable parameter can be achieved by using values determined from hydraulic stimulation tests (Kelkar, et al., 1986). Temperature and pressure effects on permeability and porosity can be included given appropriate

models. This is desirable since increases in water loss and permeability due to temperature and pressure induced fracture opening could be accounted for. Also, discrete fractures located by a statistical treatment of microseismic events in the reservoir could be placed in the cube (Dreesen et al., 1987). Finally, pressure transients were not matched in the present cube model. Future matches will attempt to use these data.

CONCLUSIONS

1. Hydraulic, thermal, tracer, and water loss data from a 30-day flow test at the Fenton Hill HDR reservoir were matched using a porous medium flow model on the basis of reasonable assumptions regarding reservoir characteristics. Porosity, permeability, and water loss pressure were adjustable.

2. Both power production and water loss were predicted to improve considerably for the close-in and step-out redrilled production wellbores. The small difference in power production between close-in and step-out suggests that the increased risk of not connecting to the fracture network with the step-out target was not justifiable, unless a larger reservoir was a paramount goal of the project.

3. The interwell impedance increases with time due solely to the increase in viscosity with decreasing temperature. This effect may be counteracted by fracture opening, which was not considered in this model.

ACKNOWLEDGEMENTS

This work was performed under the auspices of the U.S. Department of Energy, Geothermal Technology Division. We thank George Zyvoloski for supplying the computer code FEHM and for his many suggestions.

REFERENCES

Dash, Z. V. and H. D. Murphy, "Estimating Fracture Apertures from Hydraulic Data and Comparison with Theory," Geothermal Resources Council 1985 International Symposium on Geothermal Energy, August 26-30, 1985, Kailua-Kona, Hawaii.

Dash, Z. V. and G. Zyvoloski (1982), "Problems Associated with Application of a Wellbore Heat Transmission Computer Code," Eight Workshop On Geothermal Reservoir Engineering, Stanford University.

Dreesen, D. S., Malzahn, M. V., Fehler, M. C. and Z. V. Dash, "Identification Of MHF Fracture Planes And Flow Paths: A Correlation Of Well Log Data With Patterns In Locations Of Induced Seismicity," Geothermal Resources Council, 1987 Annual Meeting, Oct. 11-14, 1987, Sparks, NV.

Kelkar, S., H. D. Murphy and Z. V. Dash, "Earth Stress Measurements in Deep Granitic Rock," 27th US Symposium on Rock Mechanics, University of Alabama, June 23-25, 1986.

Robinson, B. A., R. A. Aguilar, Y. Kanaori, P. E. Trujillo, D. A. Counce, S. A. Birdsell and I. Matsunaga, "Geochemistry and Tracer Behavior During A Thirty Day Flow Test Of The Fenton Hill HDR Reservoir," Twelfth Workshop on Geothermal Reservoir Engineering, Stanford University, January 20-22, 1987.

Robinson B. A. and G. F. Jones, "A Tracer-Based Model For Heat Transfer In A Hot Dry Rock Reservoir," Geothermal Resources Council 1987 Annual Meeting, Sparks, Nevada, October 11-14, 1987.

Robinson, B. A. and J. W. Tester (1986), "Characterization Of Flow Maldistribution Using Inlet-Outlet Tracer Techniques: An Application Of Internal Residence Time Distributions," Chemical Engineering Science, Vol. 41, No. 3, pp.469-483.

Zyvoloski, G., Z. V. Dash and S. Kelkar (1988), "FEHM: Finite Element Heat And Mass Transfer Code," Los Alamos National Laboratory Manuscript, in preparation, Los Alamos, NM.

Table 1. Wellbore locations for the three cases: flow test, close-in, and step out.

Wellbore	Midpoint of Producing Zone (m)	Producing zone (True vertical depth) (m)	North (m)	East (m)
Production	3539	3529-3550	- 218	- 357
Injection	3516	3466-3565	- 334	- 327
		Close-in		
Production	3582	3427-3737	- 197	- 355
Injection	same	same	same	same
		Step-out		
Production	3582	3427-3737	- 97	- 382
Injection	same	same	same	same

Table 2. Modeled hydraulic and temperature data from the 30-day flow test. Input data are: inlet flow rate = 18 Kg/s, inlet temperature* = 47°C, production pressure* = 32 MPa, and the initial temperature profile varied linearly with depth from 230°C at the top of the reservoir to 261°C at the bottom.

	Injection Pressure (MPa)	Production Flow Rate (Kg/s)	% Water - Loss	Production Temperature (°C)
Measured*	65.3	12.6	30%	232
Model	66.9	12.6	30%	242

* Downhole pressure and temperatures were calculated from surface data using the computer code WBHT.

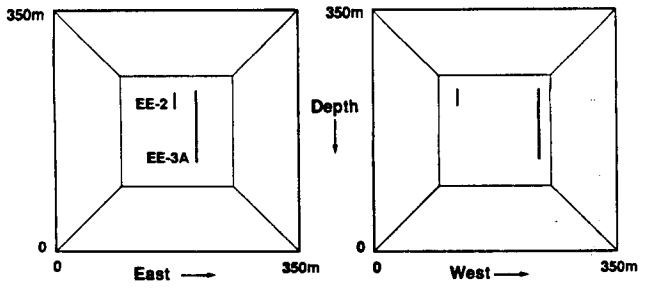


Figure 1. Orientation of the injection and production zones within the cube.

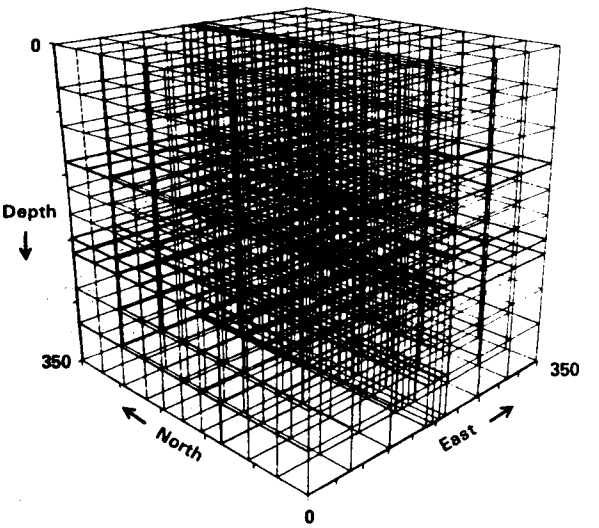


Figure 2. Finite element mesh used for the simulations.

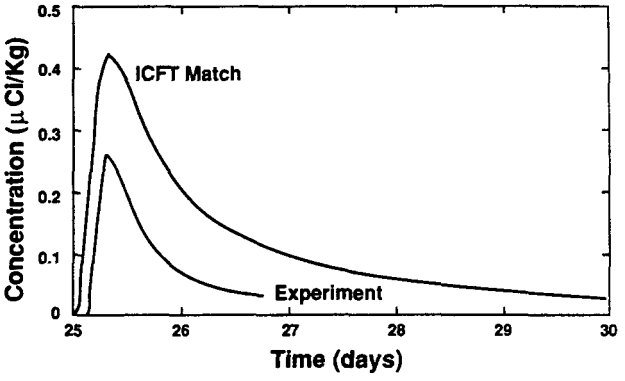


Figure 3. Experimental and matched tracer response for the 30-day flow test.

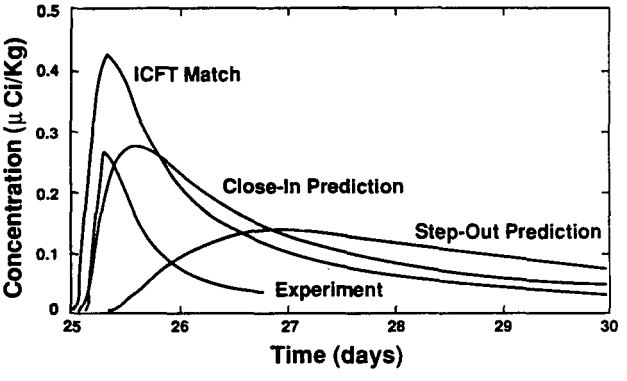


Figure 4. Experimental and matched tracer response for the flow test and predicted tracer response for the close-in and step-out cases.

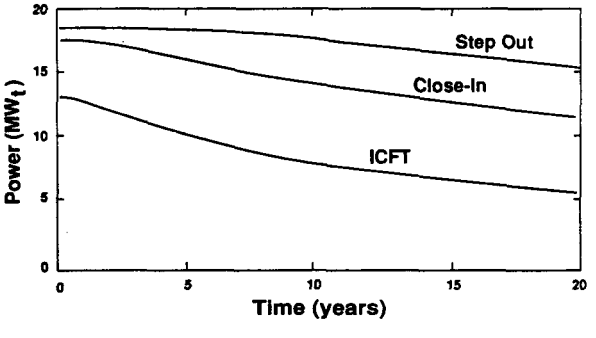


Figure 5. Power production for twenty year simulations of the flow test match, close-in and step-out cases.

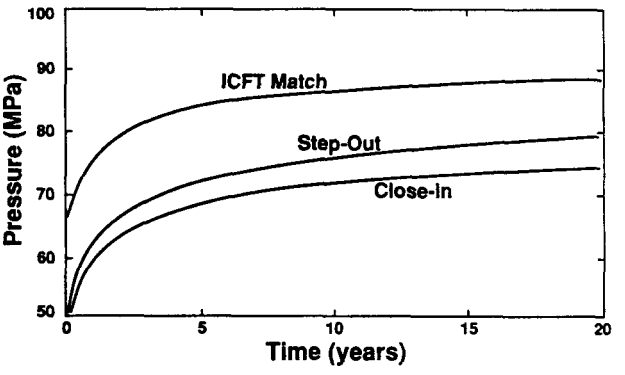


Figure 6. Injection pressure for twenty year simulations of the flow test match, close-in and step-out cases.

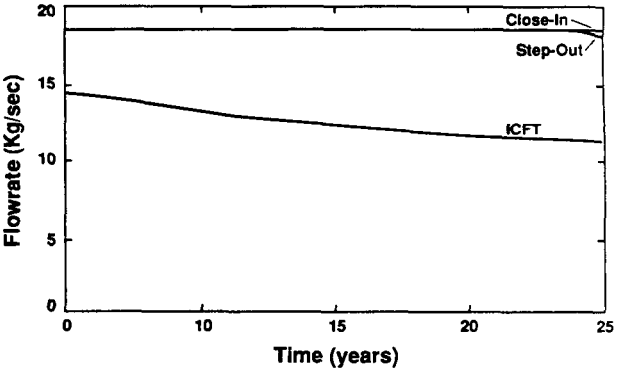


Figure 7. Production flow rate for twenty year simulations of the flow test match, close-in and step-out cases.

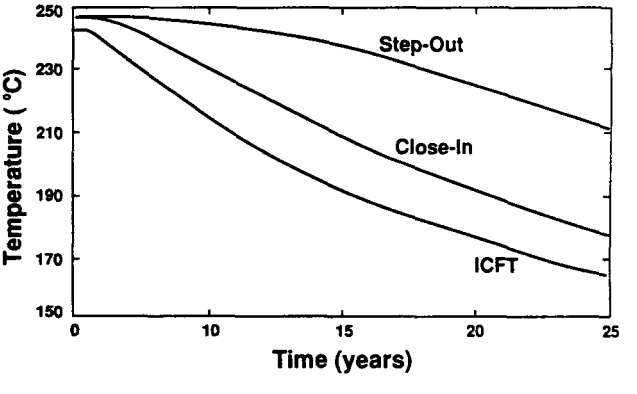


Figure 8. Production temperature for twenty year simulations of the flow test match, close-in and step-out cases.

PROCEEDINGS, Thirteenth Workshop on Geothermal Reservoir Engineering
Stanford University, Stanford, California, January 19-21, 1988
SGP-TR-113

Locating Hydraulically Active Fracture Planes

Mark Malzahn*, Donald Dreesen, and Michael Fehler

Los Alamos National Laboratory, Los Alamos, New Mexico 87545
*Contractor

ABSTRACT

If analysis of the microseismicity accompanying fluid injections is to be of maximum use in predicting hot dry rock (HDR) reservoir performance, it should lead to the determination of both the rock volume and active flowing surface area of the reservoir. In the granitic rock at the HDR geothermal site at Fenton Hill, New Mexico, the microearthquakes located during hydraulic fracturing occur in large three-dimensional volumes called seismic clouds. Cores cut from the region prior to fracturing show numerous planar fractures, some mineral-filled, at virtually random orientations. Evidence supports the hypothesis that only a few of these planes make up the flow path between wells for most of the injected fluid. If this is indeed the case, then it is necessary to be able to distinguish between fractures that accept flow from those which do not. We accomplish this by defining "flow-probable" planes to be those which have seismicity located relatively farther away from lines where other planes intersect. We show that these flow probable planes intercept wellbores at locations where other data confirm the presence of hydraulically active fractures.

INTRODUCTION

The location of planar features in large "clouds" of seismic events is accomplished by a new technique called the three point method (Fehler et al., 1987). Dreesen et al. (1987) showed correlations between well log anomalies (i.e. breakout zones, temperature depressions) and the plane/wellbore intercepts determined by the method. However, not all of the planes discovered by the three point method correlated with well log anomalies. This is because the method cannot distinguish among the following types of features:

1) Hydraulic features, including hydraulically-opened joints and hydraulically-fractured rock;
2) Structural features, including joints or faults, which contribute to fluid loss from the hydraulic features but which do not develop into significant flow paths;
3) Statistical features with no physical significance which result from a large number of microearthquakes coincidentally occurring along a plane.

We will describe the process used to determine whether or not a plane defined by the three-point method is likely to be a hydraulic feature. It does not deal with the distinction between structural and statistical features. Unless the structural features significantly affect the flowing portion of the reservoir, neither of these low-permeability features make much difference when it comes to reservoir modeling or selecting drilling targets for HDR reservoir creation.

IDENTIFICATION OF THE PLANES

The three point method was applied to a dataset consisting of 844 microseismic locations accompanying Experiment 2032 (Dreesen and Nicholson, 1985), a 21,200 m^3 injection which created a 42×10^6 m^3 seismic cloud (House et al., 1985); this resulted in the identification of 10 planar orientations. One feature of the method allows the extraction of the planes to occur in order of declining statistical significance (Fehler et al., 1987). Thus, the first orientation discovered is more likely to be an actual feature than the second, the second more likely than the third, etc. The first five planes all passed a statistical significance test that there be less than a 1 in 10,000 probability of being identified by chance. All 10 orientations were numbered in the order in which they were discovered. In addition, if analysis of the seismic data indicated the presence of two or more independent planes along the same orientation, each of these was labeled alphabetically. Table 1 lists the 21 planes, including strike and dip, associated with the ten most statistically significant orientations extracted from the Experiment 2032 dataset.

DESCRIPTION OF PLANES

The relative uncertainty between any two microseismic locations is roughly 20 meters (House, 1987). Thus, after locating the

planes, a search of the seismic data was conducted which assigned any seismic event occurring within 10 meters of either side of a plane to that plane. As a conservative measure, the 20 meter error was carried through to the spatial location of the planes, although the actual error is certainly much less since many events are used to define each plane.

The projection of all the events within 10 meters of either side of a plane onto that plane generates a unique pattern of seismicity upon each plane called the seismically active area; an example is shown in Figure 1. The seismically active areas are inferred to be the main regions of fluid flow in the planes, since the effective stresses in these areas have changed enough to cause slip to occur. This change in stress is attributed to the effects of pore fluid pressure (Fehler, 1987). The extent of a zone of weakness beyond the seismically active region of a plane is uncertain. However, it is possible that such a zone extends beyond the seismically active portion into the aseismic area, but that microearthquakes did not occur in these regions because of variations in the mechanical properties of the rock, or because the fluid that penetrated beyond the seismically active region was at insufficient pressure to induce seismicity.

The lines where all the other planes intersect a particular plane were also plotted. Two examples of the resulting images are given in Figure 2, which shows orthogonal views of the seismicity defining Plane 1A and Plane 2 along with the lines where other planes intersect these planes. These two planes are used to illustrate the difference between what we define as flow-probable and flow-improbable features.

A plane which is defined as flow-probable is one which has a relatively greater amount of seismicity occurring at a greater distance from lines where other planes intersect it, since such seismicity is more probably associated with only that plane. On Plane 2, virtually all seismicity occurs within 20 meters of a line of planar interception, as opposed to Plane 1A, upon which more than 25% of the seismicity occurs more than 20 meters away from any line of intersection. If a plane has a high percentage of its seismicity occurring near lines of planar interception, such as Plane 2, there is no way of knowing whether the plane is a true hydraulic feature, or is defined simply because of a large conflux of seismicity generated by hydraulic planes.

For each plane found from the Experiment 2032 dataset, Figure 3 shows the cumulative percentage of seismic events associated with a plane as a function of distance from the closest line of planar interception. These are separated into two groups according to their chances of being flowing features, probable or improbable. A flow-probable plane is defined as one having at least 25% of its seismicity occurring at least 15 meters away from any line of planar interception. The flow-improbable group is made up of the remaining planes.

RESULTS

By the above definition, planes 1A, 1B, 4A, 8A, 8B, and 10B make up the group of flow-probables, while the flow-improbable group consists of all the remaining planes. The depths were calculated where all the planes are projected to intercept the three wellbores, EE-2, EE-2A, and EE-3A, as were the minimum and maximum depths where the planes might intercept given the 20 meter error; this information is shown in Table 2. In some cases, as where Plane 1A intercepts EE-3A, there is no projected intercept, but there is a range along the well where an intercept may occur due to the 20 m error.

Temperature logs were then analyzed, superimposing the ranges of intercept depths for all the flow-probable planes along each log, in order to correlate thermal anomalies with the intercept points of these planes. The locations of anomalies, or departures from a constant thermal gradient, indicate either the production or injection of fluids along the well (Murphy, 1982).

Figure 4 shows that the interceptions of EE-2 by flow-probable planes 1A, 1B, and 10B correlate well with the locations of thermal anomalies in a log run on 7/27/82. The temperature log in Figure 4 was made following a smaller stimulation conducted prior to Experiment 2032. Therefore, the correlation of the planes discovered in the 2032 injection data with these anomalies supports the assumption that the flow paths are pre-existing features which are reopened each time the reservoir is pressurized.

Figure 5 shows two temperature logs run in well EE-3A, both taken after Experiment 2032. The log dated 7/10/85 followed a three-day injection into the interval from 3827 m to 4017 m. The two anomalies at 3150 m lie within the error band of flow-probable Plane 1A's location along the well, indicating that this plane might be actively cooling the liner even though it is quite a distance from the injection zone. This may also be the case at 3580 m, where two flow-probable planes, 4A and 8B, correlate with a thermal anomaly. The only flow-probable plane which intercepts the well in the injection interval is Plane 10B, which could be used to explain one of four anomalies.

The log dated 6/23/86 followed a month-long injection into an open-hole interval from 3487 m to 3750 m, and shows a myriad of temperature anomalies occurring both above and throughout the experimental injection zone. The temperature anomalies which are observed above the injection zone indicate flow due to the pressure gradient between the high-pressure injection zone and the low-pressure annular region 200 m above. Even though cement had effectively sealed the annulus, fluid was still able to flow away from the injection zone and cool the outer

casing through the damaged, more permeable rock immediately surrounding the cement. It is interesting to note, however, that most of these anomalies can be correlated with plane intercepts, and that two of the anomalies occur almost exactly where the flow-probable planes 8A and 1B are predicted to intercept the wellbore. If these are indeed flowing planes, then it is logical to assume that they would accept fluid in the region near their points of interception along the wellbore.

The log of the injection region for this experiment shows two minor and three major anomalies. The two minor anomalies, at 3490 m and 3510 m, correlate with the locations of flow-improbable planes 6 and 7B, implicating these planes as possible flowing features. However, the first minor anomaly occurs at precisely the top of the injection interval, and might be more simply explained by the aforementioned transition from cased to open hole. Also, both of these anomalies lie within the error band of flow-probable Plane 1B.

The first major anomaly, at 3550 m, lies within the range of flow-probable Plane 4A, and the second (3600 m) is within the range of both 4A and flow-probable Plane 8B. The last major anomaly at 3650 m does not correlate with any of the planes in this dataset. However, a more thorough examination of the data has shown a planar intersection in this region and is being investigated.

Figure 6 is a temperature log taken on 11/15/87 in the newly drilled well EE-2A during its first production test, showing several clear production points and two minor anomalies. Flow-probable Plane 10B correlates well with the anomaly at 3620 m. Flow-probable Plane 1B can explain the main anomaly at 3660 m or either of the rather less dramatic anomalies at 3670 m and 3680 m, or even the anomaly at 3620 m previously credited to Plane 10B. Flow-probable Plane 8B can also be correlated with the last anomaly at 3680 m. Of the remaining anomalies observed on this log, only the very small one at 3380 m can be correlated with any of the flow-improbable planes; in this case, it is Plane 6, another indication that this may be a flowing plane.

CONCLUSIONS

It has been hypothesized that a seismically active plane is more likely to be a flowing feature when a relatively greater amount of the seismicity by which it is defined lies at a greater distance from the lines of intersection formed by the remaining planes. As a test, a number of planes which were found in a set of microseismic data were classified as flow-probable or flow-improbable according to this hypothesis. We found that all of the planes defined as flow-probable showed a definite correlation with fluid injection or production points as defined by downhole temperature logs. While we could not correlate every temperature anomaly with a flow-probable plane, we could correlate every flow-probable plane with an anomaly. One obvious reason for a flow-probable plane not to show a correlation with a thermal anomaly is that the planes might only be flowing in their seismically active regions, while the wellbore may not intercept this region. While this method does not predict every injection or production point along a well, it can help increase the chances of encountering a flowing feature when confronted with a large choice of potential targets.

ACKNOWLEDGEMENT

We would like to thank Cheryl Straub, Bonita Busse, and Ruth Robichaud for their help with manuscript preparation. This work was supported by the U.S. Department of Energy, Geothermal Technology Division.

REFERENCES

Dreesen, D.S., Malzahn, M.V., Fehler, M.C., and Dash, Z.V. (1987), "Identification of MHF Fracture Planes and Flow Paths: A Correlation of Well Log Data with Patterns in Locations of Induced Seismicity," Geothermal Resources Council Transactions, Vol. 11, pp. 339-348.

Dreesen, D.S. and Nicholson, R.W. (1985), "Well Completion and Operations for MHF of Fenton Hill HDR Well EE-2," Geothermal Resources Council Transactions, Vol. 9, part II, p. 89.

Fehler, M. (1987), "Stress Control of Seismicity Patterns Observed During Hydraulic Fracturing Experiments Carried Out at the Fenton Hill Hot Dry Rock Geothermal Energy Site," Conference on Forced Fluid Flow in Fractured Rock Masses held in Garchy, France, (Proc. published by European Economic Commission in Brussels, Belgium).

Fehler, M., House, L. and Kaieda, H. (1987), "Determining Planes Along Which Earthquakes Occur: Method and Application to Earthquakes Accompanying Hydraulic Fracturing," Journal of Geophysical Research, Vol. 92, pp. 9407-9414.

House, L. (1987), "Locating Microearthquakes Induced by Hydraulic Fracturing in Crystalline Rock," Geophys. Rev. Letters, Vol. 14, pp. 919-921.

House, L., Keppler, H., and Kaieda, H. (1985), "Seismic Studies of a Massive Hydraulic Fracturing Experiment," Geothermal Resources Council Transactions, Vol. 9, part II, pp. 105-110.

Murphy, H.D. (1982), "Enhanced Interpretation of Temperature Surveys Taken During Injection or Production," Journal of Petroleum Technology, June, p. 1313.

TABLE 1

Strike and Dip of All Planes Associated with the 10 Most Likely Orientations Found in the Experiment 2032 Dataset (all angles in degrees)

Plane	Strike	Dip
1A	N29W	76E
1B	N29W	76E
2	N88E	27W
3A	N29W	67W
3B	N29W	67W
4A	N6E	67E
4B	N5E	64E
4C	N8E	67E
5A	N33E	60W
5B	N34E	56E
6	N64W	67W
7A	N84E	32W
7B	N86E	33W
7C	N81E	36W
7D	N86E	34W
8A	N21W	58E
8B	N20W	61E
9A	N79W	74E
9B	N79W	74E
10A	N35W	82W
10B	N32W	81W

TABLE 2

Minimum, Projected, and Maximum Depths of Interception Along Each Wellbore for Each Plane (all measurements in meters along wellbore)

Plane	Well EE-2			Well EE-3A			Well EE-2A		
	minimum	projected	maximum	minimum	projected	maximum	minimum	projected	maximum
1A	3587	3617	3647	3072	--	3186	3691	3759	3765
1B	3527	3557	3587	3205	3349	3417	3569	3627	3694
2	4093	4107	4122	3849	3860	3871	--	--	--
3A	3249	3263	3277	3140	3159	3177	3248	3262	3275
3B	3267	3281	3295	3162	3181	3199	3265	3279	3292
4A	3007 3759	3056 3848	3128 3934	3540	3574	3609	3005	3042	3081
4B	--	--	--	3663	3692	3722	3548	3641	3719
4C	--	--	--	3801	3839	3878	--	--	--
5A	3640	3657	3674	3518	3534	3550	3651	3667	3683
5B	4047	4061	4074	3926	3940	3954	--	--	--
6	3395	3410	3424	3459	3491	3522	3374	3389	3405
7A	2991	3004	3017	3020	3032	3044	2994	3008	3022
7B	3555	3573	3592	3478	3489	3500	3554	3569	3584
7C	3657	3677	3696	3531	3542	3554	3637	3652	3667
7D	4215	4231	4247	3891	3902	3913	--	--	--
8A	3192 4208	3234 4508	3288 4660	3430	3451	3470	3185	3239	3310
8B	--	--	--	3559	3582	3605	3674	3755	3764
9A	--	--	--	--	--	--	--	--	--
9B	--	--	--	4008	--	4016	--	--	--
10A	3402	3419	3437	3296	3334	3380	3392	3410	3429
10B	3578	3593	3608	3906	3955	4001	3603	3622	3641

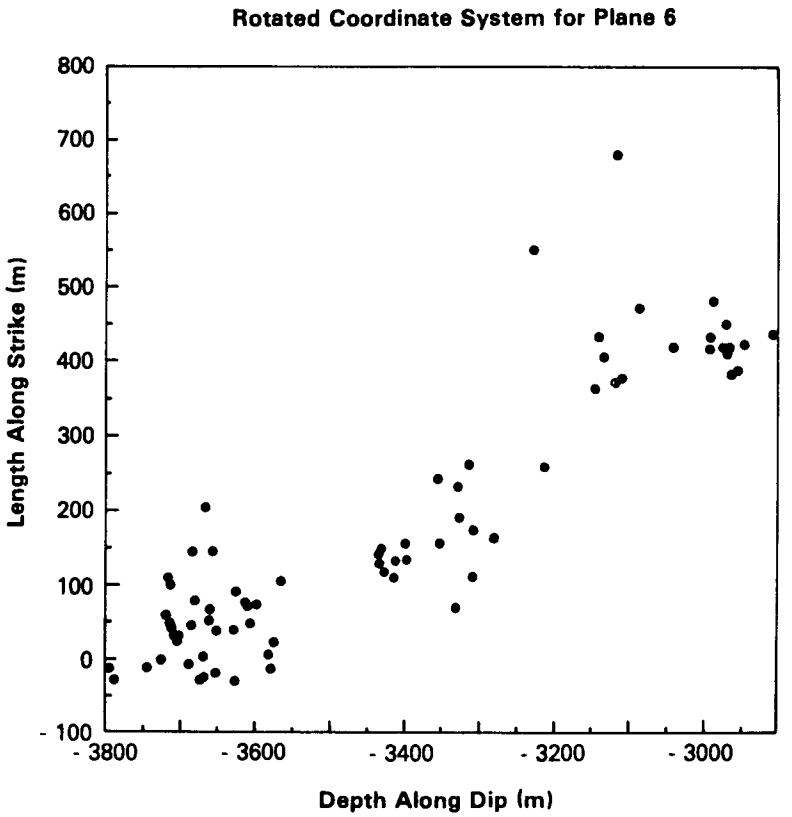


Figure 1: An orthogonal view of Plane 6. The dots mark the locations of all the seismic events associated with this plane, each of which lies within 10 m of either side of the plane.

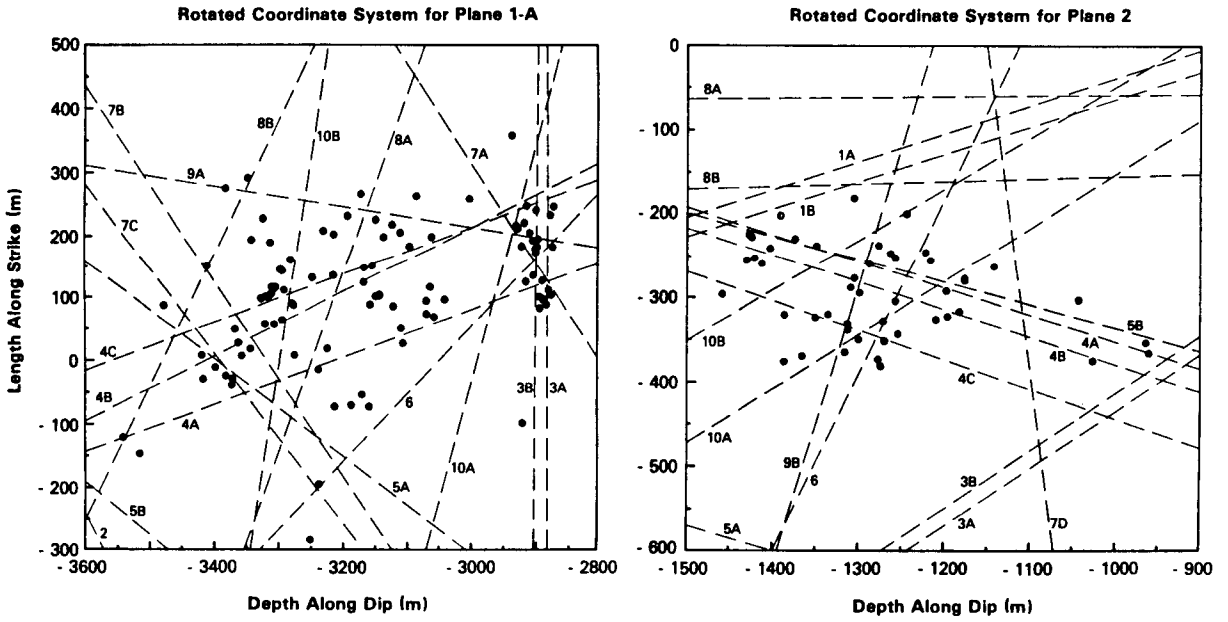


Figure 2: Orthogonal views of planes 1A and 2, including the seismic events which define each plane as well as the lines of intersection made by each of the remaining planes. The seismicity defining Plane 2 generally lies closer to a line of planar intersection than does the seismicity defining Plane 1A; thus, compared to each other, Plane 1A is flow-probable, and Plane 2 is flow-improbable.

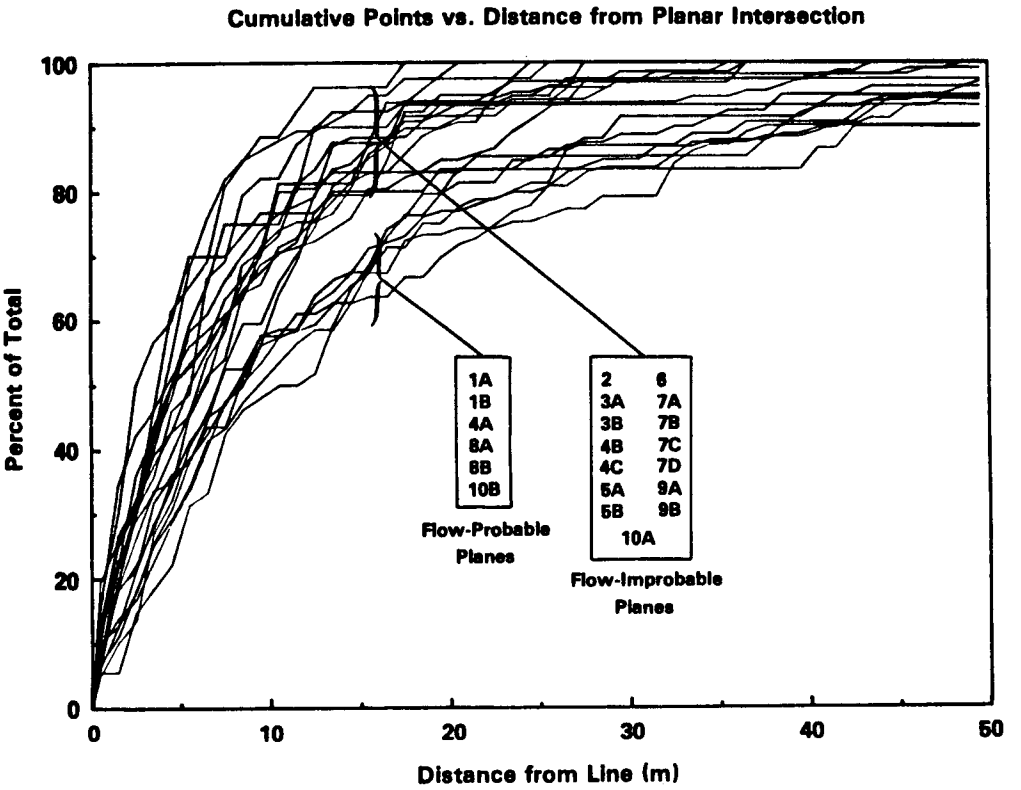


Figure 3: Percent of total seismicity as a function of distance from the nearest line of planar intersection for each plane. Flow-probable planes have at least 25% of their seismicity occurring at least 15 m away from any line of planar intersection.

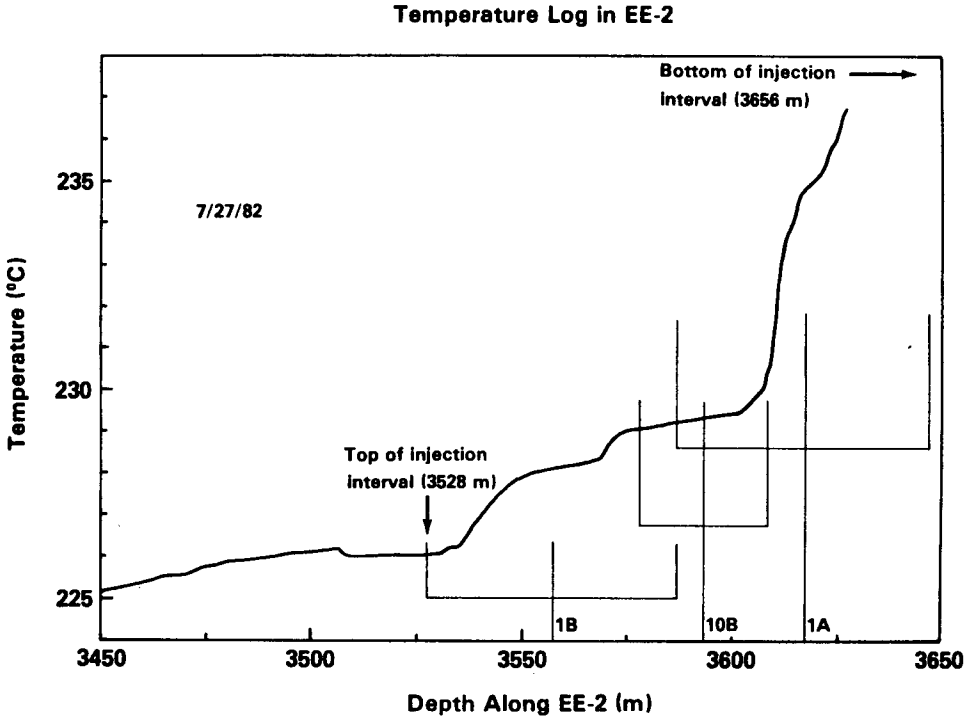


Figure 4: Correlation of thermal anomalies in EE-2 with flow-probable planes.

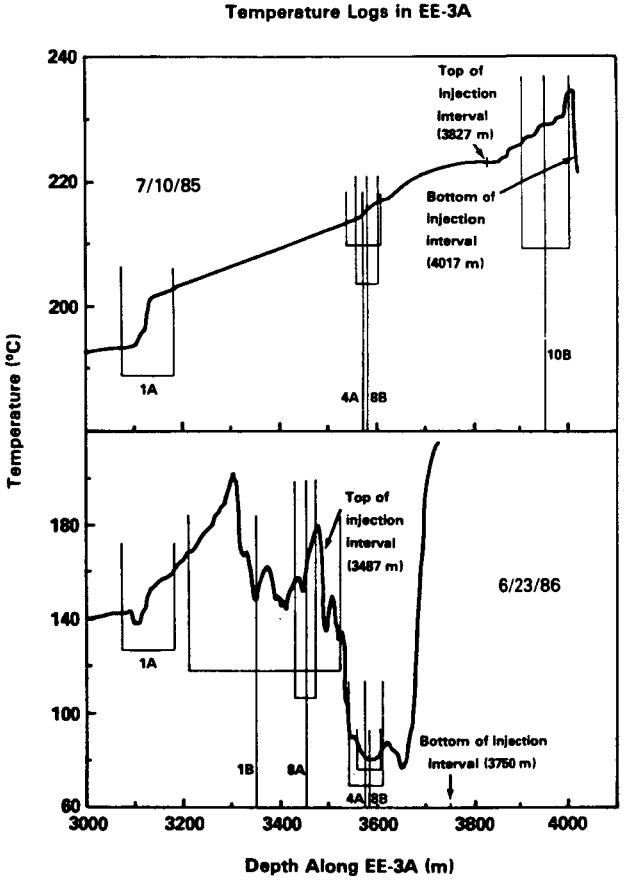


Figure 5: Correlation of thermal anomalies with flow-probable planes in two temperature logs run in EE-3A.

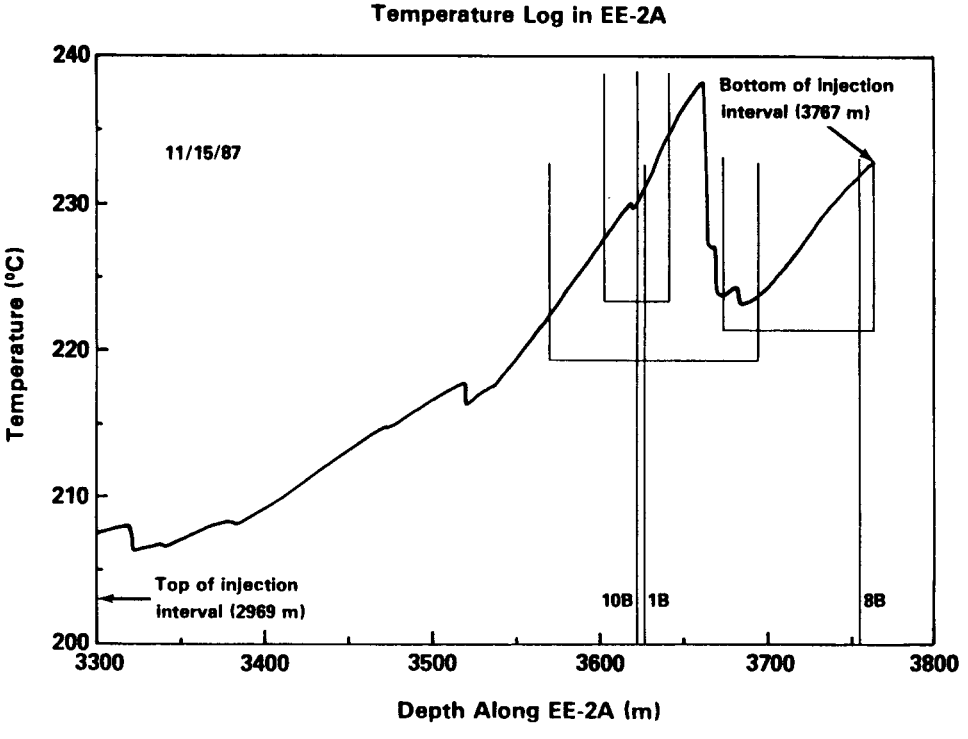


Figure 6: Correlation of thermal anomalies in EE-2A with flow-probable planes.

PROCEEDINGS, Thirteenth Workshop on Geothermal Reservoir Engineering
Stanford University, Stanford, California, January 19-21, 1988
SGP-TR-113

WELLBORE INTERFERENCE IN FRACTURED MEDIA

Mark V. Malzahn*
Hugh D. Murphy

Los Alamos National Laboratory, Los Alamos, New Mexico 87544
*Contractor

ABSTRACT

In order to bypass wellbore casing damage and reaccess productive reservoir regions, it was decided to sidetrack and redrill the bottom 600 m of production well EE-2 at the Hot Dry Rock (HDR) geothermal site at Fenton Hill, New Mexico. The most desirable new trajectory would maximize reservoir size and minimize water diversion to an older abandoned reservoir. Based on a simple model using Muskat's analysis it was determined that the new well should be drilled near the old one since water diversion considerations outweighed the advantages of a larger reservoir.

INTRODUCTION

An uncontrolled vent of production well EE-2 following a three-day, 21,200 m^3 injection into the Phase II HDR reservoir collapsed a portion of the well's casing. The ability to perform logging and stimulation experiments in the producing region of the well was lost. Thus, a sidetracking and redrilling operation was planned in order to bypass the damaged section of the well (Figure 1). While the plan included cement jobs designed to plug the producing region of the old well, only a small probability of success was anticipated due to the difficulty in cementing below the damaged casing.

Previous hydraulic fracturing experiments indicated that one or more fractures that hydraulically communicate with a shallow, now-abandoned reservoir have fracture opening pressures as low as 10 MPa. Thus, there existed the possibility that these low-pressure fractures in the old well would parasitically divert hot water from the newly-drilled well and reduce the energy extraction rate. The question arose as to whether water diversion would be minimized by drilling close to the old well, or farther away. A greater separation would result in the benefit of a larger reservoir, but would have to be balanced against an increase in intrinsic reservoir impedance.

A simple model of the problem was developed and is described below. It showed that while reservoir impedance did not significantly increase with the more distant trajectory, water diversion is minimized by drilling close to the old well.

MODEL ASSUMPTIONS

Because HDR reservoirs are normally operated in a steady-state mode, the model was based on Muskat's relationship between pressure and the log of distance, which assumes steady-state, two-dimensional Darcy flow in a homogeneous reservoir[1]. Since the reservoir at Fenton Hill is so extensively fractured, we treat the rock as a uniformly porous medium. It was assumed that all fluid injected would be recovered at the production well or else be diverted to the low pressure fractures. Also implicit in the analysis were the assumptions that near-wellbore impedance, or skin effect, is independent of wellbore pressure, and that the fractures connecting the abandoned reservoir to the old wellbore would continue to parasitically take water once their opening pressure was exceeded. Finally, as a conservative estimate it was assumed that the cementing operations which were planned to plug the low-pressure fractures would not succeed.

Most of these assumptions represent the worst-case scenario for fluid diversion. For example, if the cement jobs are even partially successful, then less flow will be diverted.

The only non-conservative assumption is that all fluid is either produced or diverted, since there are also losses to the surrounding rock during HDR production. From previous testing[2], we can assume that an average of 30% of the injected fluid will be lost to the field, so an "effective" injection flow rate (in our case, 70% of the actual injection flow rate) may be substituted.

RESULTS

Derivation of the working equations is presented in the appendix. The expression for intrinsic reservoir impedance, I_{RES}, is given by

$$I_{RES} = \frac{\mu}{\pi k h} \ln\left(\frac{d}{a_i}\right) \qquad (1)$$

where μ is the fluid viscosity, d is the interwell spacing, k is the average permeability, and a_i is the effective injection well radius.

If the new well were drilled a distance d_1 from the injection well, the new intrinsic reservoir impedance can be found from equation (1) by substituting d_1 for d. Presumably redrilling has no effect on k or h, so the ratio of new to old reservoir impedances is given by $\ln (d_1/a_i)/\ln (d/a_i)$. Results are given in Table I. Note that halving or doubling the well spacing has little effect on the intrinsic reservoir impedance. In other words, the reservoir impedance would stay nearly the same regardless of whether the new well was drilled near to or far from the existing well. Because reservoir impedance would be nearly unchanged, the only remaining concern about increasing the size of the reservoir was the amount of water diversion.

TABLE I

EFFECT OF INTERWELL DISTANCE UPON INTRINSIC RESERVOIR IMPEDANCE (a_i = 1.0 m)

Ratio of New to Old Inter-Well Spacing	Ratio of New to Old Impedance
0.5	0.86
1.0	1.00
2.0	1.14

In order to determine the well spacing needed to keep the pressure in the old well below the fracture opening pressure of 10 MPa, thereby avoiding a large water diversion to the low-pressure fractures, equation (A2) was employed for a situation with two production wells and one injection well. The distance from the injection well to the new production well is d_1, and a_i and a_p are respectively the effective injection radius and the effective radius of the new production well. The distances from the old well to the injection well and the new production well are given as r_i and r_p. If P_{old}, P_i, and P_p are the pressures at the old well, the injection well, and the new production well, then

$$P_{old} = C + \frac{\mu Q}{2\pi kh} \ln(r_p/r_i) \qquad (2)$$

$$P_i = C + \frac{\mu Q}{2\pi kh} \ln(d_1/a_i) \qquad (3)$$

$$P_p = C + \frac{\mu Q}{2\pi kh} \ln(a_p/d_1) \qquad (4)$$

Combining (2-4) results in

$$\frac{P_{old} - P_p}{P_i - P_p} = \frac{\ln\left(\frac{r_p}{r_i}\frac{d_1}{a_i}\right) + s_p}{2\ln\left(\frac{d_1}{a_i}\right) + s_p} \qquad (5)$$

where s_p is the skin factor at the new well. Notice that P_{old} increases with P_p, which illustrates the effect of high backpressure, and with s_p. When P_p and s_p both equal zero, which provides the most optimistic situation for minimizing P_{old},

$$P_{old} = P_i \frac{\ln\left(\frac{r_p}{r_i}\frac{d_1}{a_i}\right)}{2\ln\left(\frac{d_1}{a_i}\right)} . \qquad (6)$$

Typically, P_i = 30 MPa, so for P_{old} to be less than or equal to 10 MPa in order to minimize fluid diversion to the abandoned reservoir, then

$$r_i/r_p \geq (d_1/a_i)^{1/3} . \qquad (7)$$

This indicates that r_p must be considerably smaller than r_i. For example, if the new well is drilled near the old well so that d_1 is still 150 m, and if a_i can be taken to be 1 m, then the new well can be drilled no greater than 28 m from the old well if the latter's pressure is not to exceed 10 MPa. In other words, the only chance to maintain a pressure lower than 10 MPa at the old well, and thereby avoid a large fluid diversion to the low-pressure fractures, would be to drill quite near it.

However, this result assumes no skin effect around the new well, and no pressure on the new well while it produces. Since neither of these assumptions can be completely assured, some fluid diversion is inevitable. Equations (A9-A12) in the appendix describe how to estimate the of the diversion. The results are graphed in Figure 2, showing four families of curves, each of which assumes a different improvement in the near-production-wellbore impedance. The abscissa, Q_L/Q_i, is the ratio of the flow rate lost or diverted to the old well to the injected flow rate, and is shown as a function of the pressure at the new production well. All cases assume an injection pressure of 30 MPa. The curves labeled "far" simulate the case where the new production well is 100 m farther from the injection well than the old production well; the "near" curves add only 15 m to the distance between the injection and new production wells.

Two trends are immediately obvious. First, high backpressure experiments, where the production well is operated at high pressure, may result in a excessive water diversion to the old reservoir. Most high backpressure tests are run in order to stimulate the producing wellbore and to decrease the overall reservoir impedence. Calculations show, however, that the ratio of flow lost to the old reservoir to flow injected is 50% or more for backpressures above 19 MPa. Nearly all the flow will be diverted to the old well if a backpressure of 25 MPa or more is imposed on the new production well. While it may be possible for these experiments to stimulate the producing regions of the new well and decrease intrinsic reservoir impedance, they would come at a high cost in the form of fluid loss. Unless the old well can be sealed with cement, back-pressures greater than 19 MPa should be avoided.

Secondly, the graphs show that, as stated above, a "far" trajectory will result in some amount of fluid diversion regardless of production pressure, and that at normal producing pressures (i.e. 2.5 MPa), this diversion is greater than that which would result from a closer trajectory. This is due to the increased size of the reservoir which accompanies a more distant trajectory. The larger reservoir allows a higher pressure to exist near the old well, which results in more fluid flowing into the low-pressure fractures.

CONCLUSIONS

A model was developed based on a Muskat analysis which assumed steady-state, two-dimensional flow in a homogeneous reservoir. The model provides quantitative estimates of fluid diversion as a function of production pressure, and shows that for the reservoir at Fenton Hill, a more distant trajectory for a sidetracked well would not result in a very large increase in intrinsic reservoir impedance. However, the model predicts that the new well should be drilled relatively close to the old well in order to minimize water diversion.

POST SCRIPT

As this paper was being prepared, the new well was drilled along a trajectory which maintained a maximum distance of 30 m from the old production zone. Preliminary pump tests indicate that the cement jobs were at least partially, if not completely, successful. Thus, we are expecting only minimal water diversion to the old reservoir.

APPENDIX

Muskat[1] shows that for steady state, two-dimensional, Darcy flow in a homogeneous reservoir with multiple wells, the theory of superposition results in

$$P = C + \frac{\mu}{2\pi k} \Sigma\, q_j \ln(r_j) \qquad (A1)$$

where

- P = pressure at any point in reservoir
- C = arbitrary constant
- μ = fluid viscosity
- k = permeability
- q_j = volumetric flow rate per unit height of reservoir produced from well j, (positive for production, negative for injection)
- r_j = distance from well j to point where P is being evaluated.

For a reservoir of height h, q_j is Q_j/h, where Q_j is the total volumetric flow rate for well j. Hence (A1) becomes

$$P = C + \frac{\mu}{2\pi kh} \Sigma\, Q_j \ln(r_j) \; . \qquad (A2)$$

In a two well system in which the injection flow rate is $-Q$ and the production flow rate is $+Q$, (A2) gives the pressure at a point which is a distance r_i from the injection well and r_p from the production well:

$$P = C + \frac{\mu Q}{2\pi kh} \ln(r_p/r_i) \; . \qquad (A3)$$

If (A3) is evaluated first at the injection well, where r_i then becomes the injection well bore radius a_i, and r_p is the separation distance between the wells d, then

$$P_i = C + \frac{\mu Q}{2\pi kh} \ln(d/a_i) \; . \qquad (A4)$$

Likewise, at the production well,

$$P_p = C + \frac{\mu Q}{2\pi kh} \ln(a_p/d) \qquad (A5)$$

where a_p is the production well radius.

If the production well is fully vented, (i.e. $P_p = 0$) then $C = -\frac{\mu Q}{2\pi kh} \ln(a_p/d)$, and substituting in (A4) yields the injection pressure:

$$P_i = \frac{\mu Q}{2\pi kh} \left[\ln\left(\frac{d}{a_i}\right) + \ln\left(\frac{d}{a_p}\right) \right]$$

or

$$P_i = \frac{\mu Q}{2\pi kh} \left[2\ln\left(\frac{d}{a_r}\right) + \ln\left(\frac{a_r}{a_i}\right) + \ln\left(\frac{a_r}{a_p}\right) \right] \qquad (A6)$$

where a_r is a reference wellbore radius which will be explained below. The second term in the brackets is the skin factor of the injection well s_i, and $\frac{\mu s_i}{2\pi kh}$ is the near-injection wellbore impedance. Likewise, the third term in the brackets is the production well skin factor s_p. Because it is pressurized, the fractures near the injection well are usually more open, so it is nearly always observed that $s_i = 0$. Hence, $a_r = a_i$ and

$$P_i = \frac{\mu Q}{2\pi kh}\left[2\ln\left(\frac{d}{a_i}\right) + \ln\left(\frac{a_i}{a_p}\right)\right] \qquad (A7)$$

and the last term is the production well skin factor. Dividing (A7) by Q results in the familiar impedance concept, based on an electrical resistance analogy:

$$\frac{P_i}{Q} = \frac{\mu}{\pi kh}\ln\left(\frac{d}{a_i}\right) + \frac{\mu}{2\pi kh}\ln\left(\frac{a_i}{a_p}\right). \qquad (A8)$$

The first term on the right hand side is the intrinsic reservoir impedance I_{RES}, and the second term is the near-production well impedance I_p.

A triplet of wells requires the superposition of yet another well and flow rate. P_i and Q_i will continue to indicate injection pressure and flow rate, P_p and Q_p indicate production well conditions, and now P_L and Q_L indicate the "leakage" quantities at the old well. Neglecting permeation losses to the rock surrounding the reservoir, $Q_i = Q_p + Q_L$. Letting $m = \mu/2\pi kh$, the pressures at all three wells are given as:

$$P_i = C + m[-Q_i\ln(a_i) + Q_L\ln(r_i) + Q_p\ln(d_1)] \qquad (A9)$$

$$P_L = C + m[-Q_i\ln(r_i) + Q_L\ln(a_L) + Q_p\ln(r_p)] \qquad (A10)$$

$$P_p = C + m[-Q_i\ln(d_1) + Q_L\ln(r_p) + Q_p\ln(a_p)] \qquad (A11)$$

Combining (A9-A11) and recalling that $Q_i = Q_p + Q_L$, it can be shown that

$$\frac{Q_L}{Q_i} = \frac{\ln\left(\frac{d_1 r_p}{a_i r_i}\right) + s_p - P^*\left[2\ln\left(\frac{d_1}{a_i}\right) + s_p\right]}{2\ln\left(\frac{r_p}{a_i}\right) + s_L + s_p - P^*\left[\ln\left(\frac{r_p d_1}{r_i a_i}\right) + s_p\right]} \qquad (A12)$$

where P* is the pressure ratio $(P_L - P_p)/(P_i - P_p)$, and s_p and s_L are the skin factors at the new and old production wells, respectively.

ACKNOWLEDGMENTS

We would like to thank Ruth Robichaud, Ada DeAguero and Bonita Busse for assisting with the manuscript preparation. This work was supported by the U.S. Department of Energy, Geothermal Technology Division.

REFERENCES

1. Muskat, Morris, Flow of Homogeneous Fluids, J.W. Edwards Inc., 1946, p. 54.

2. Kelkar, S.K., Dash, Z.V., Malzahn, M.V., and Hendron, R.H. (1987), "Hydraulic and Thermal Behavior of a Hot Dry Rock Reservoir During a 30-day Circulation Test," Geothermal Resources Council Transactions, Vol. 11, pp. 547-550.

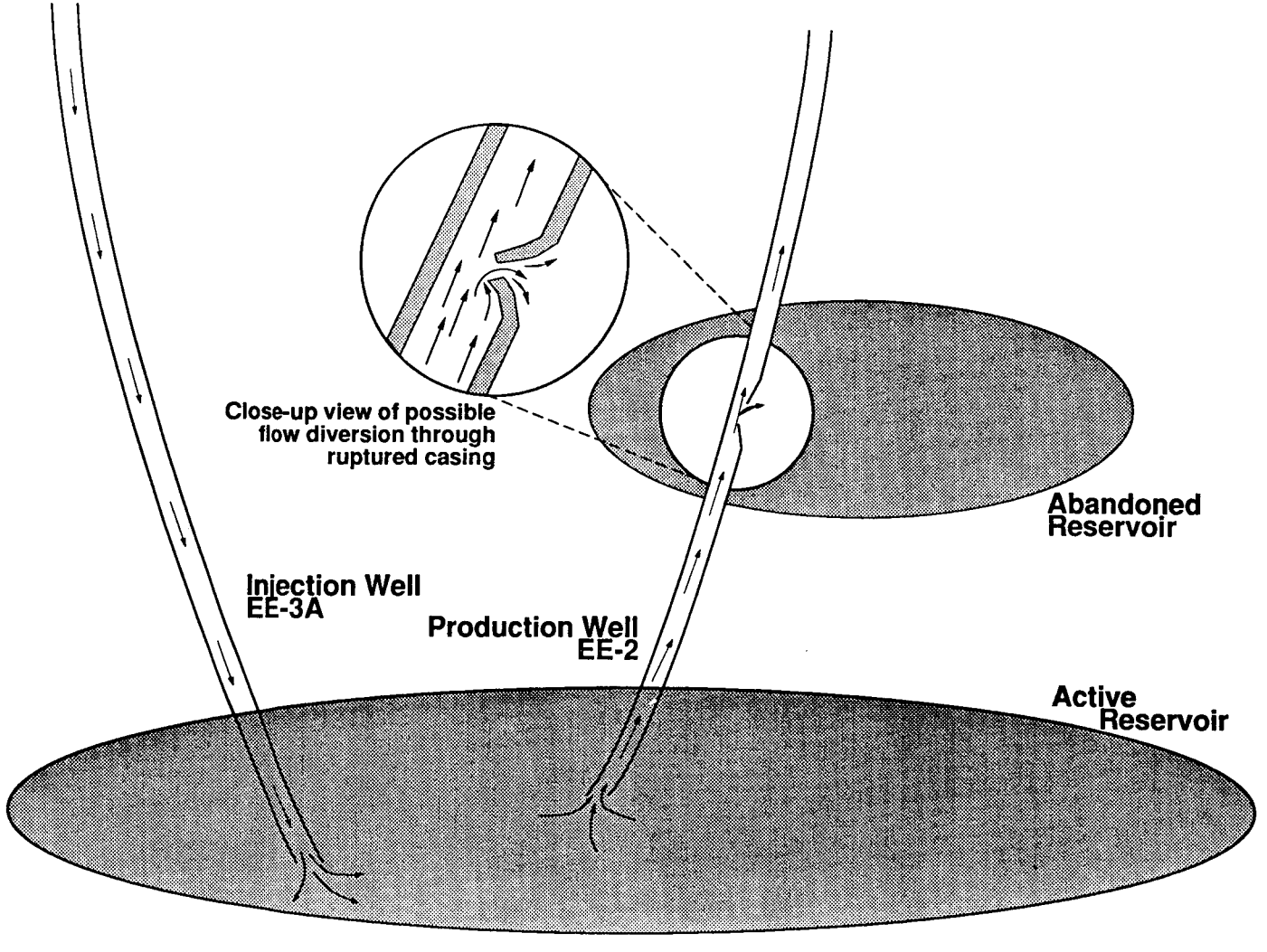


Figure 1: Idealized view of the two reservoirs (not to scale)

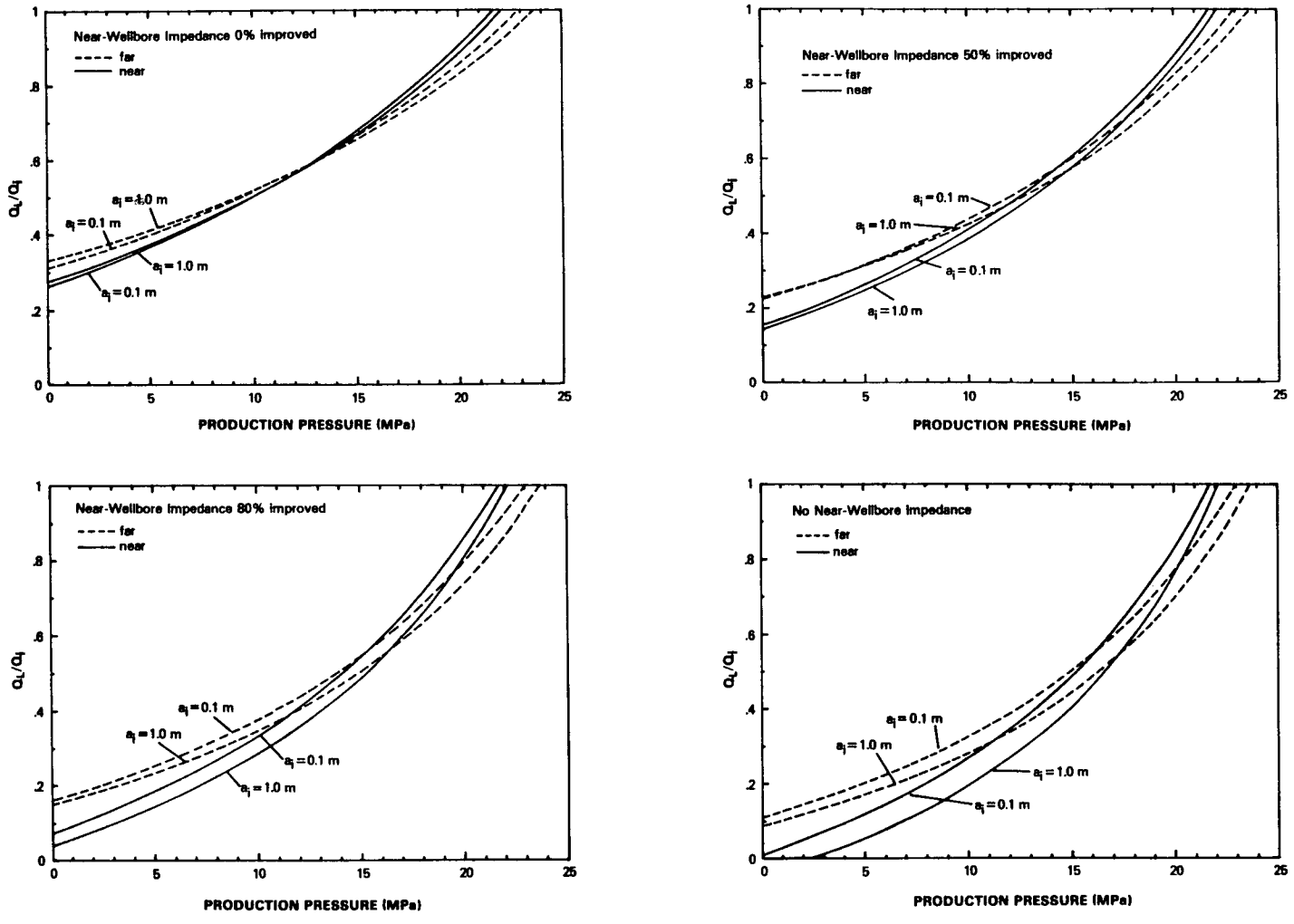


Figure 2: Flow rate diverted to the low pressure fracture, normalized by the injection flow rate, as a function of production pressure at the new well. The "near" curves assume that the producing region of the new well lies 15 m more distant from the injection well than does that of the old well; the "far" curves add 100 m in distance. Two values for a_i, the effective injection well radius, are given for each case. Each family of curves assumes a different degree of improvement in near-production-wellbore impedance, some amount of which is expected due to the regained ability to stimulate producing regions in the new well. The worst case would be 0% improvement; the ideal case would be to have no near-wellbore impedance. An improvement of 50%-80% is expected.

PROCEEDINGS, Thirteenth Workshop on Geothermal Reservoir Engineering
Stanford University, Stanford, California, January 19-21, 1988
SGP-TR-113

TRACER MEASUREMENTS DURING LONG-TERM CIRCULATION OF THE ROSEMANOWES HDR GEOTHERMAL SYSTEM

K A KWAKWA

GeoScience Limited, Falmouth, Cornwall and
Camborne School of Mines Geothermal Energy Project,
Penryn, Cornwall

ABSTRACT

Circulation experiments have been in operation for over two years in the artificially stimulated hot dry rock (HDR) doublet of the Camborne School of Mines (CSM) research facility in Cornwall, England. During that period tracer tests have been run at intervals using inert and reactive compounds.

Initially, the results of the inert tracer investigations showed that the active volume (indicated by modal and median volumes) of the circulating system was dormant. Then, after a period of sustained oscillation, notable increases in active volume were observed which depended on both the subsequent flow rate changes and circulation time. These dynamic changes had almost reached optimum values when a downhole pump was introduced in the production well. The drawdown in the production well caused a reduction of the modal volume, whilst the median volume remained almost the same. Since then, the active volume has remained unchanged and irresponsive to circulation time and flow rate.

The results of the reactive tracer tests confirm increasing chemical reaction with increasing circulation time and correlate qualitatively with the opening of newer and hotter pathways within the reservoir. However, repeated production logs throughout the circulation have identified flow paths that have depleted thermally; a discrepancy that can be explained by the geometry of the system and the preferential downward reservoir growth.

INTRODUCTION

Research into the exploitation of HDR geothermal energy has been in progress at Rosemanowes quarry, the CSM research facility, for several years. A number of published papers describe the location and geology of the area (eg Pine et al, 1983) and progress of the research (eg Batchelor,1983,1984,1986; Pine et al, 1987).

Circulation of the current 2 km-deep system began in August 1985 and tracer testing, involving inert and chemically reactive compounds, has been used to determine the volumetric, flow and thermal characteristics of the reservoir.

The inert tracer, sodium fluorescein (NaFl), was used to determine the residence time distribution (RTD) of the bulk flow. Analysis of the RTD provided the breakthrough, modal and median volumes, and information about tracer dispersion (Johnson, 1984). Comparison of tests at different flow rates and circulation times, also enabled volumetric changes in the reservoir to be monitored.

The concept, theory and application of reactive tracer technology have been well documented (Robinson and Tester, 1984; Tester et al, 1986). It is being developed as a tool for estimating the productive life of a reservoir long before thermal breakthrough occurs at the production well. In the trial at CSM, ethyl acetate (EtAc), an ester sensitive to both temperature and pH, was used repeatedly. Although the material balance did not account for all the recoverable tracer in these experiments, the overall results yielded useful qualitative information.

This paper presents the results of 21 inert and 10 reactive tracer tests carried out during 28 months of continuous circulation of the Rosemanowes HDR reservoir.

BACKGROUND

HDR research at a depth of 2 km started in Phase 2A (1980-1983) with the drilling of wells RH12 (injection) and RH11 (production) in the Carnmenellis granite. The wells were orientated in the north-westerly direction, with RH11 above RH12 in vertical section, and later interlinked by sustained hydraulic stimulation of the naturally occurring joints, creating an artificial reservoir. The growth of the reservoir was predominantly downwards, below the open-hole sections of the two wells, and a diffusive hydraulic connection was achieved between them (CSM, 1984a; Pine and Batchelor, 1984).

In the subsequent circulations only 30% of the injected fluid was returned, and circulation had to be carried out for several weeks before steady conditions could be reached.

Three inert tracer experiments (test nos 1-3) were conducted during Phase 2A. Typically, the test durations were between 600 and 800 hours. The RTDs showed two characteristic peaks (bi-modal) and long diffusive tails. Modelling, using a source and sink in an equivalent uniformly porous medium (Webster et al, 1970), was successful and implied an extremely large, low permeability, system.

In Phase 2B (1983-1986) a third well, RH15, was drilled (to a true vertical depth of 2.6 km) to intersect the already stimulated region below Wells RH11 and RH12. Following a series of hydraulic activities in RH15, including a massive viscous fracturing operation (CSM, 1986a), significant improvement in the interwell connectivity was achieved and a long-term circulation of the RH12-RH15 system began. During this circulation RH11 has continuously produced about 10% of the injection flow, which is ignored in the tracer calculation.

CIRCULATION PROGRAMME

The circulation programme, still continuing in Phase 2C (1986-1988), has involved step changes in injection flow rate varying from 5 l/s to 38 l/s. The tracer tests were carried out between the injection (RH12) and production (RH15) wells, after hydraulically steady conditions had been reached at the wellheads. A summary of the flow rates of both wells, from the start of circulation, is presented in Figure 1. The numbers (4-24) identify the flow conditions at which NaFl tests were carried out. Circled numbers indicate where EtAc tests were also conducted. The Figure also shows that an oscillation experiment was carried out about 3000 hours into the circulation. In the test (CSM, 1986b), the interwell region was cyclically inflated (to pressures in the range 5-6 MPa) and deflated many times, at different periods (by opening and shutting-in RH15, whilst injecting at a steady 10 l/s into RH12).

For reasons to be made apparent, Figure 1 can be broadly divided into three main categories; pre-oscillation, post-oscillation, and the period beginning from the downhole pump test (DHP) as indicated. Apart from the DHP test, during which RH15 was drawn down by a maximum of 5 MPa, the well was fully open to the atmosphere (normal circulation).

INERT TRACER DEFINITIONS

1 The RTD, also known as the exit age distribution function, E(t), is the system response curve derived from the input (C_{in}) and the output (C_{out}) tracer data. These are related by the convolution integral (Levenspiel, 1972) given by:

$$C_{out}(t) = \int_0^t C_{in}(t-t')\, E(t')\, dt' \qquad (1)$$

For convenience each RTD presented in this paper is the response to a pulse injection containing 2 kg of tracer. Where shortage of fresh water necessitated total or partial recirculation of the produced fluid, the above equation was used to determine the RTD.

2 The breakthrough time is the elapsed time between tracer injection at the top of RH12 and first detection at the top of RH15. The breakthrough volume is the total produced volume from the start of the test to breakthrough time. These parameters provide information about the most direct connection in the system.

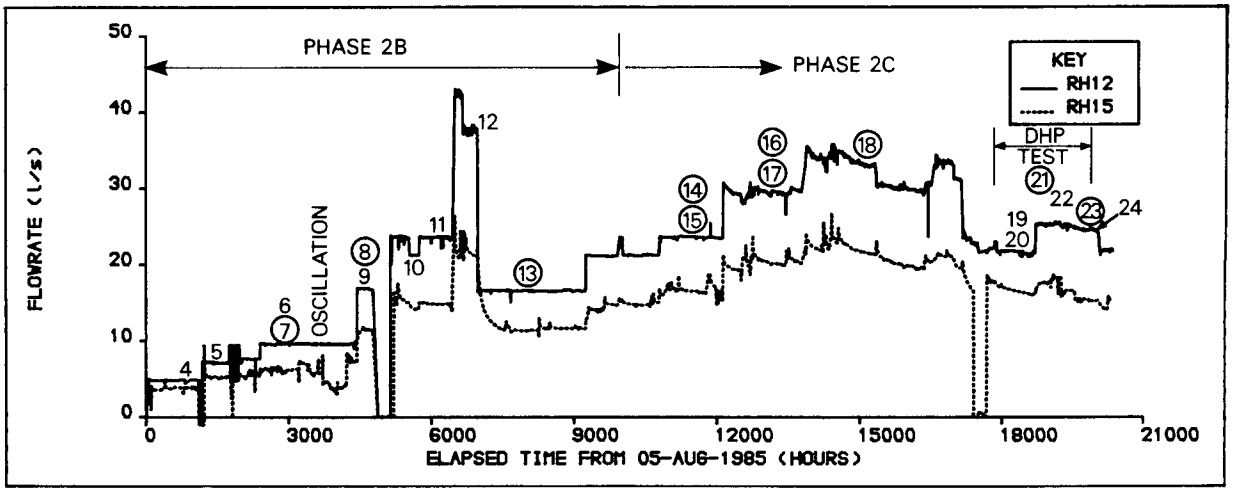


Figure 1. RH12 injection and RH15 production during Phases 2B and 2C circulation.

3 The modal volume is defined as the volume produced from RH15, from the start of the test until peak tracer concentration is reached, less the volumes of RH12 (85 m^3) and RH15 (90 m^3) wellbores. The modal volume is considered to represent the volume of the low impedance connections in the reservoir.

4 The median volume ([V]) is defined by the equation:

$$\int_0^{[V]} C_{out} dV = 0.5 \int_0^{\infty} C_{out} dV \qquad (2)$$

using the RTD (plotted as a concentration versus total produced volume). The median volume is considered as representative of the total volume of the major production paths (Tester et al, 1982).

Since all the tests presented here were carried out at steady state, and the RTDs are based on 2 kg of tracer, [V] can be redefined as the total produced volume containing 50% of the total recoverable tracer. Thus:

$$\int_0^{[V]} C_{out} dV = \text{Circulation Efficiency} \qquad (3)$$

where the circulation efficiency is defined as the percentage of injection fluid returned at RH15 during steady conditions. This definition avoids the extrapolation to infinite volume in equation 2. The median time, t_{50}, is the elapsed time corresponding to [V].

PROCEDURE

Similar experimental procedures were adopted for each of the tests. It was essential to pump each tracer very quickly into the injection stream (at the inlet to RH12) in order to conform to the assumption of pulse injection in the analyses. All the tracers were pumped individually into the injection stream, and at an identical flow rate (12 l/min). Prior to starting each experiment, it was ensured that the background tracer concentration in the reservoir was minimal. Where both inert and reactive tracers were introduced, the inert tracers were introduced first, followed by the reactive tracer. Sodium fluorescein injections lasted about 2.5 min and the times taken to inject the reactive tracers were typically 3-5 minutes.

Fluid samples were abstracted at the wellheads for analysis. The sampling programme was designed to ensure minimal ambiguity in the test results. RH15 samples were taken at 10-15 minute intervals from breakthrough until the peak tracer concentration was completed. Otherwise, the sampling intervals were between 30 minutes and 2 hours. Sampling frequency at RH12 depended on the type of circulation. Typically, samples were taken at 4- to 6-hour intervals on open-loop circulation. During closed-loop circulation, a sampling frequency identical to that for RH15 was used to provide sufficient input data for deconvoluting the system RTD.

A single-sided fluorimeter was used to determine the NaFl concentrations in the samples after they had been cooled to room temperature. A gas chromatograph was used to determine the concentrations of EtAc and ethyl alcohol (EtOH), one of the two reaction products, in the produced fluid. These enabled a mass balance of EtAc to be computed for comparison with NaFl. Laboratory studies showed that these chemicals and NaFl do not interact during analysis (Ferguson, 1985).

RESULTS AND INTERPRETATION

In the text that follows, the pre-qualifiers **total** and **net** are used to distinguish between volumetric parameters. The former refers to the gross volume produced at RH15 from the beginning of a test, and the latter implies that RH12 and RH15 wellbore volumes (estimated at 175 m^3) have been subtracted from the gross volume produced in RH15. Also by definition, the breakthrough and modal volumes are respectively **total** and **net** quantities. Furthermore, selected RTDs have been presented in this paper to illustrate clearly the trends of the volumetric behaviour. The omitted RTDs do not show any deviations from that depicted in this paper.

1 INERT TRACER TESTS

The RTDs are presented on identical horizontal axes in Figures 2 to 4. The steep decay exhibited by the NaFl RTDs after the peak, together with the high percentage tracer recovery (typically over 80%) at the end of

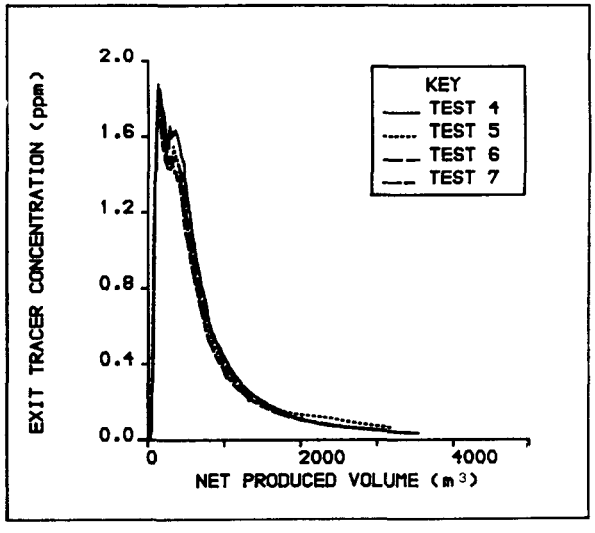


Figure 2. Pre-oscillation NaFl RTDs.

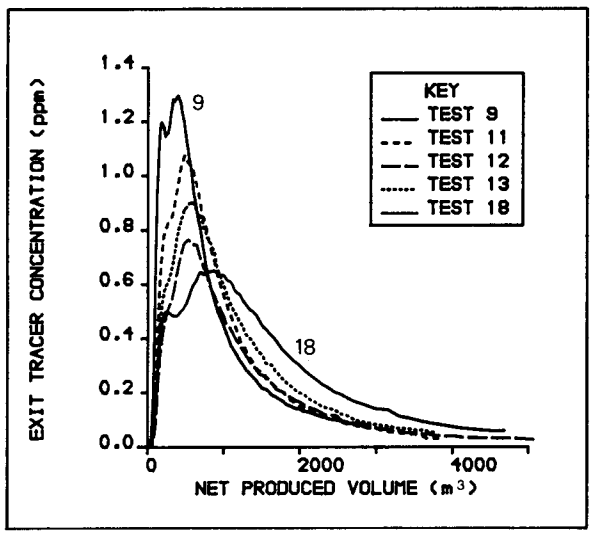


Figure 3. Post-oscillation NaFl RTDs.

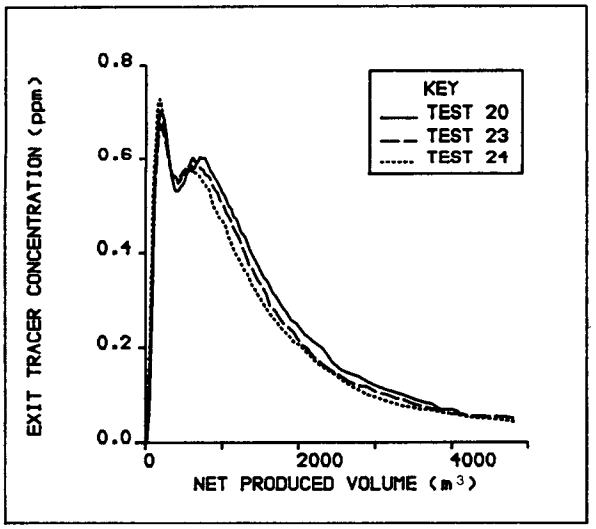


Figure 4. RTDs of NaFl tests during and after DHP.

each test, is indicative of minimal diffusivity and an absence of a 'retention-release' mechanism in the reservoir. These characteristics also imply that the system consists of discrete flow paths/features, and support the suggestion that the principal dispersion mechanism derives from fluid mixing owing to the different path lengths (Gardner, 1984; Breitenbach and Horne, 1982; Capuano et al, 1983). The non-reactive nature of NaFl was confirmed further by the excellent agreement obtained in a simultaneous experiment, using ammonium bromide as an inert tracer, during test 19 (Larkin, 1987).

Bi-modal RTDs, similar to those obtained in these tests, were also observed during Phase 2A. The Phase 2A hydraulic test results show that RH12 was strongly fractured with negligible wellbore impedance (CSM, 1984a). Also the bulk of the injection flow left RH12 near the bottom, and the remaining fluid exit points were almost uniformly distributed along the open section. These characteristics have remained unaltered in Phases 2B and 2C, although RH12 was not directly connected to RH11 in the case of Phase 2A. It was concluded then that the injection fluid left RH12 through large, open fractures and somehow diffused across to RH11.

The drilling of RH15 established a direct connection between RH12 and RH15. After the massive viscous stimulation of RH15, it was found that only the joints which had flowed previously flowed, but at a higher rate (Pine et al, 1987). Therefore, it can be inferred that the similar bi-modal peak displayed by both the current NaFl RTDs and the Phase 2A tests indicates that the dominant connections of the current system derive from the most permeable connections of Phase 2A. This also implies that the open features connected to RH12 continue to dominate behaviour of the current system. Maintenance of the characteristic profiles of the peak concentration regions also suggests that the tortuosity of the paths has not changed significantly.

Excellent linear correlations were obtained by plotting the injection and production flow rates against the reciprocal of the total breakthrough times. The latter indicated that the total volume produced (242 ± 6 m^3) to breakthrough remained constant throughout the circulation. With the wellbore volumes estimated at 175 m^3, the above analyses also suggested that the volume of the breakthrough feature cannot be greater than 67 m^3.

Figure 5 shows a plot of modal volume against time. It is obvious from Figures 2 to 4 that the modal volume depended on which of the two modes showed the highest NaFl concentration. In the pre-oscillation period, the modal volumes were associated with the first mode and remained invariant at about 140 m^3. This was repeated during and after the DHP test, but at a higher modal volume of 210 m^3. Between the two periods (Figure 3), the modal volume was associated with the second mode and increased with increasing flow rate; from about 400 to 710 m^3. Clearly, since the breakthrough feature has remained unchanged throughout the circulation, it can be concluded that the pathways associated with the second mode have been responsible for the changes in modal volume.

A comparison of tests 9 and 13, carried out at similar injection flow rates (but separated by four months of circulation), indicated that the increases in the modal volume were irreversible during normal

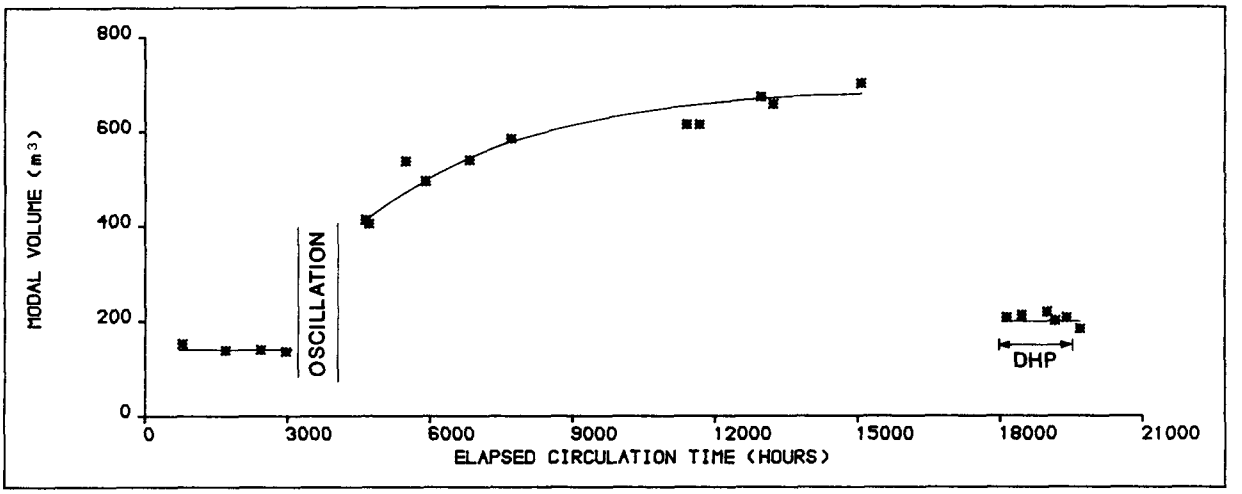


Figure 5. Modal volume trend during Phases 2B and 2C circulation.

circulation. This observation (confirmed by tests 11 and 15) has the implication of a reservoir whose optimum size has not yet been attained. Test 13 showed a slight improvement in the steady state impedance (0.74 compared with 0.77 MPa/l/s), a 44% increase in modal volume, and a 44% increase in median volume. It is believed that the increase in modal volume has not been the consequence of increases in the apertures of the low impedance features alone. (Note that for laminar flow in parallel-sided joints, the impedance reduces in proportion to the cube of the aperture increase). It is likely that the volumetric changes included increases in the swept areas of the original features, and enhancement of the permeabilities of some other, previously high impedance, features.

The median volume derived from the tests showed similar trends to that of modal volume, from the start of circulation to just before the DHP test. It was almost constant (750 m^3) initially, and increased with time/flow rate (from 940 to 1550 m^3) after the intensive oscillation. An even higher median volume of 1810 m^3 was recorded in test 18, during which continuous microseismic activity (indicative of reservoir growth) was recorded. The median volume peaked during the DHP test at 1920 m^3 (probably due to the production of stored fluid) and declined to some 1480 m^3 by the end of the DHP test. The latter value is in good agreement with the optimum value of 1550 m^3 obtained immediately prior to the microseismic activity, and is probably indicative of the end of reservoir development.

Simulation of the NaFl RTDs was carried out successfully with a multiple dipole model consisting of a parallel connection of hydraulically distinct homogeneous media (Webster et al, 1970; CSM, 1986c).

The results showed that a minimum of 3 parallel-connected dipoles could fit each of the NaFl RTDs, with average flow splits of 15%, 80% and 5%. The splits were similar to those used in a simplified thermal model involving three independent parallel plates (CSM, 1986). The derived Peclet numbers ranged between 1 and 5, further confirming that fluid dispersion, due to mixing, is high.

The simulation was not unique. However, it demonstrated clearly that the system was dominated by a finite number of flowing features and could not be simulated with one uniformly diffusive model, as was used in Phase 2A, (CSM, 1984).

2 REACTIVE TRACER TESTS

All the tests were terminated earlier than their corresponding NaFl experiments either due to a malfunction of the gas chromatograph, or because EtAc and EtOH (ethyl alcohol) could not be detected in the production fluid.

Good agreement between the breakthrough and modal volumes of reactive and inert tracer curves implied that the transit characteristics of both types of tracer were similar. A comparison of the quantities of unreacted EtAc recovered from RH15 (Figure 6) indicates that progressively less EtAc was produced as circulation continued. In the Figure, only the first three test results are shown. Subsequent tests followed a similar trend but are not presented, as the quantities were small.

Mass balances showed close agreement with the corresponding NaFl curves at early time only. Deviations after early time suggested loss of EtAc or EtOH. Losses were about 10% or less during the first three tests. In subsequent tests, over 40% of the total recoverable tracer was unaccounted for and there was no

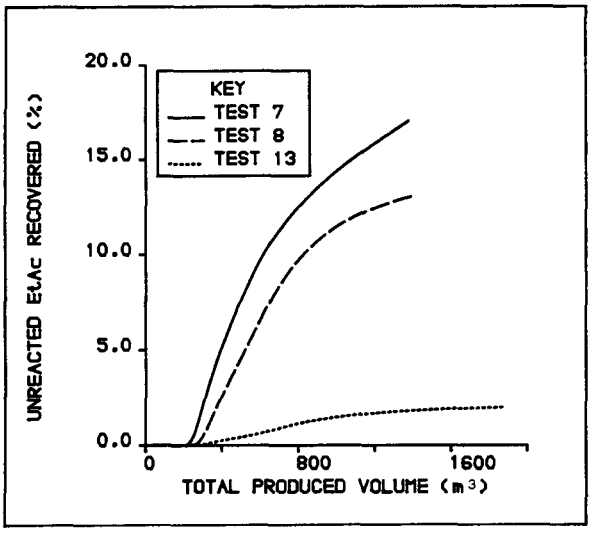


Figure 6. Reactive tracer test results.

detectable reactive tracer in the production fluid by the end of each test. Recent laboratory tests suggest that the losses in the latter tests may be due to the low sensitivity of the gas chromatograph. Further work on the analytical technique is still in progress.

The results of test 13, conducted at a similar flow regime to that of test 8, showed that less ethyl acetate was produced than previously.

These results suggest that the system was progressively more reactive as circulation continued; due to either increased temperature or pH. Since the first three tests were carried out in chemically similar injection conditions, it is believed that an increased temperature is the likely cause.

DISCUSSION

INERT TRACER TESTS

Clearly, the oscillation and DHP experiments have been instrumental in modifying the volumetric and flow behaviour of the current system. In a steady state circulation with RH15 fully venting, the highest system pressure is at RH12 and a steep pressure gradient exists in the reservoir. Hence, any volumetric readjustment is likely to be highest in the vicinity of RH12. An increase in the injection pressure would tend to predominantly stimulate RH12, increase wellbore storage, and probably increase losses.

In the oscillation test, a more gradual pressure gradient was imposed on the reservoir during the inflation half-cycle, causing the average reservoir pressure to increase significantly. However, since the duration was short, the increased pressure was localised (near RH15, and in the low impedance connections) and there was not time for the hydraulic pressure to reach the reservoir boundary to cause further stimulation. Therefore, the high pressure at the 'core' of the reservoir tends to enhance the interwell conductivity without appreciable losses. It appears that the large increases in the volumetric performance (CSM, 1986b) were achieved in this way, probably through joint block re-orientation, relaxation, and mechanical readjustment of flow fractions in the interwell region near RH15. An oscillation test, carried out subsequently at Los Alamos, yielded similar results (Hendron, 1987).

The reverse effect, to the massive oscillation, was probably achieved with the downhole pump. Reduction of the water level in the production well created an even steeper pressure gradient in the reservoir and also increased the effective stresses on the flowing features nearer RH15. These were probably sufficient to reverse some of the changes caused by the oscillation test. The common factor in the two operations is that similar absolute pressures (nominally 5 MPa) were sustained on RH15. This is in good agreement with the onset pressure for shearing along the most favourable joint set in the Rosemanowes granite (Pine and Batchelor, 1984) and is probably not a coincidence. It is likely that such absolute pressures are required to mechanically trigger the volumetric changes. Further work on this tentative interpretation continues.

It has been suggested that the small, unchanging, volume of the breakthrough feature may be responsible for the observed thermal decline in the system. However, routine temperature logs in RH15 show a more complicated distribution, and suggest that the observed effects may be geometry dependent. It is planned to embark on an intensive programme of downhole tracer injection with continuous sampling, at different locations in both wells in order to understand the interwell behaviour and, perhaps, establish the mechanism of the thermal decline.

REACTIVE TRACER TESTS

The reactive tracer results were encouraging. The concept is still in the developmental stage and requires further theoretical, laboratory and field work to improve the confidence in data and its interpretation. Apart from the high losses which are a major source of error, the use of only EtAc requires an estimate of the spatial pH distribution within the reservoir for complete interpretation. This was impossible to determine in these tests. However, the pH complication could perhaps be resolved by the simultaneous introduction of two or more different reactive tracers. Since these

tracers access identical pH and temperature distribution, it should be possible to determine the reservoir temperature as a function of residence time.

The concept of using reactive tracers for predicting the productive life of the HDR system (Tester et al, 1986), was not proven in these tests. Whilst the reactive tracer tests progressively showed more reactivity, production temperature surveys (CSM, 1986d) showed that the temperature of the mixed wellbore fluid at the casing shoe was decreasing. This suggests that the water accesses hotter flow paths as the reservoir grows but on its return to RH15, it either mixes with colder fluid or accesses colder features. Until the reservoir size stabilises, it is unlikely that the reactive tracer would show evidence of thermal drawdown.

CONCEPTUAL RESERVOIR MODEL

A conceptual model which fits the inert tracer and reactive tracer results can be proposed. The open-hole section of RH12 lies along the strike of the dominant joint set (striking in the north-westerly direction). Hence it has a low-impedance access to a limited number of joints with high conductivity. This zone is surrounded by a secondary system of lesser permeability. Injections create pressure, first in the dominant joints, then enhance the conductivity of the secondary zone. By virtue of the high permeability contrast between the two zones, and the increasing stress anisotropy with depth (CSM, 1984b), fluid migration is predominantly downwards (Pine and Batchelor, 1984) to even hotter regions as the reservoir pressure increases. Therefore, the tortuosity of the circulation paths changes and the fluid penetrates deeper into the hotter regions before it rises into the production well through colder features. These zones are coupled to a breakthrough feature, probably located at the top of the structure, which is largely immune to pressure changes.

CONCLUSIONS

The results obtained so far from the long term circulation have demonstrated the importance of tracer testing as a diagnostic tool for characterising the volumetric flow and thermal behaviour of an HDR system early in its productive life. They lead to the following conclusions:

1 The current system derived from an enhancement of the most conductive features of the Phase 2A system, and demonstrates that irrespective of the extent and success of a stimulation, only the natural joints with connectivity would flow.

2 The interconnection is heterogeneous (compared to a uniformly diffusive medium) and the reservoir flow characteristics are dominated by the major features connected to the injection well.

3 Although the limiting breakthrough volume remained constant throughout the tests, all other tracer-determined volumetric parameters were responsive to flow rate changes. The modal volume rose from 140 m^3 to 710 m^3 after the oscillation, and dropped to 210 m^3 during and after the DHP. This has not recovered although the flow distribution in RH15 has not changed significantly since the oscillation.

However, the median volume increased from 750 m^3 to 1550 m^3 after the oscillation and has remained about the same after the DHP. This is consistent with the observed flow distribution in RH15 and suggests that the median volume (rather than the modal volume) is a better measure of gross volumetric and flow changes in the reservoir.

4 The available evidence indicates that substantial improvement in the system was achieved with the oscillation experiment. This, and the downhole pump test, must be further investigated for use as tools for HDR reservoir development.

5 Reactive tracers can be useful tools for diagnosing thermal changes in the interwell region. Their development must be continued.

ACKNOWLEDGEMENTS

During the period of work reported, the author was employed by the Camborne School of Mines and subsequently by GeoScience Limited. This work was carried out at Camborne School of Mines on a programme funded by the UK Department of Energy and the Commission of European Communities. The author wishes to thank the UK Department of Energy through the UK Atomic Energy Authority under contract number E/5A/CON/A37/1593 for permission to publish this paper. The support and encouragement of the staff of these organisations is gratefully acknowledged.

REFERENCES

BATCHELOR A S, 1983. Stimulation of a hot dry rock geothermal reservoir in the Cornubian granite, England. In 8th workshop on geothermal reservoir engineering, Stanford University, California, January 1983.

BATCHELOR A S, BARIA R, HEARN K, 1983. Monitoring the effects of hydraulic stimulation by microseismic event location: a case study. In Inst of Min and Met

conference on rockbursts: prediction and control, October 1983.

BATCHELOR A S, 1984. An overview of hot dry rock technology. In 4th international conference on energy options: the role of alternatives in the world energy scene. IEE, London, Apr. 1984.

BATCHELOR A S, 1986. Reservoir behaviour in a stimulated hot dry rock system. In 11th workshop on geothermal reservoir engineering, Stanford University, California, January 1986.

BREITENBACH K A and HORNE R N, 1982. Evaluation of chemical tracers for geothermal use. Proc Pacific Geothermal Conf, Auckland, New Zealand, November 1982, pp 229-233.

CAMBORNE SCHOOL OF MINES GEOTHERMAL ENERGY PROJECT, 1984a. Hydraulic Results. Internal report, Group II, Part 10, Vol 2, 1984, pp 193.

CAMBORNE SCHOOL OF MINES GEOTHERMAL ENERGY PROJECT, 1984b. In situ stress summary report. Internal report, 1984.

CAMBORNE SCHOOL OF MINES GEOTHERMAL ENERGY PROJECT, 1986a. Viscous stimulation of well RH15. Phase 2B, Internal report, 1986.

CAMBORNE SCHOOL OF MINES GEOTHERMAL ENERGY PROJECT, 1986b. Circulation Results Phase 2B. Internal report, 1986.

CAMBORNE SCHOOL OF MINES GEOTHERMAL ENERGY PROJECT, 1986c. Phase 2B tracer results. Internal report, 1986.

CAMBORNE SCHOOL OF MINES GEOTHERMAL ENERGY PROJECT, 1986d. Production logging report. Phase 2B, internal report, 1986.

CAPUANO R M, ADAMS M C and WRIGHT P M, 1983. Tracer recovery and mixing from two geothermal injection-backflow studies. Proc 9th workshop geothermal reservoir engineering. Stanford Univ, December 1983. SCP-TR-74, pp 299-304.

FERGUSON J, 1985. Personal communications. Chemical Engineering Dept, Massachusetts Institute of Technology, Cambridge, MA 02139, USA, 1985.

GARDNER W W Jr, 1984. Characterisation of retention processes and their effect on the analysis of tracer tests in fractured reservoirs. Interdisciplinary research in Eng and Earth Sciences. Stanford Geothermal Programme, Stanford Univ, Stanford, California, June 1984.

HENDRON R N, 1987. The US hot dry rock project. In Stanford Univ 12th workshop on geothermal reservoir engineering, Stanford Univ, California, January 1987.

JOHNSON S E, 1984. Tracer test analysis of the Klamath falls geothermal resource: A comparison of models. Stanford geothermal programme. Interdisciplinary research in engineering and earth sciences. SGP-TR-81 Stanford University, California. June 1984, pp 108.

LARKIN J P A, 1987. An evaluation of inert tracers for hot dry rock geothermal reservoirs. MSc thesis, University of Birmingham, 1987. pp 114.

LEVENSPIEL O, 1972. Chemical reaction engineering. 2nd edition. John Wiley & Sons. NY, 1972, chap 9.

PINE R J, BARIA R, PEARSON R A, KWAKWA K A, McCARTNEY R, 1987. A technical summary of Phase 2B of the CSM HDR project, 1983-1986. Geothermics, Pergamon Press, Vol 16, No 4, pp 341-353, 1987.

PINE R J and BATCHELOR A S, 1984. Downward migration of shearing in jointed rock during hydraulic injections. Int J Rock Mech, Min and Geomech Abstr, Vol 21, No 5, pp149-263, 1984.

PINE R J, TUNBRIDGE L W and KWAKWA K A, 1983. In situ stress measurement in the Carnmenellis granite: 1 - overcoring tests at South Crofty Mine at a depth of 790 m. Int J Rock Mech Mic Sci and Geomech Abstr, 20, No 2, pp 51-62, 1983.

ROBINSON B A and TESTER J W, 1984. Reservoir sizing using inert and chemically reacting tracers. SPE 13147 pp 7 (plus figures and tables), 1984.

TESTER J W, BIVINS R L and POTTER R M, 1982. Interwell tracer analyses of a hydraulically fractured granitic geothermal reservoir. SPEJ August 1982, pp 537-554.

TESTER J W, ROBINSON B A and FERGUSON J H, 1986. Inert and reacting tracers for sizing in fractured hot dry rock systems. Stanford workshop, 21-23 January, 1986.

WEBSTER D S, PROCTOR J F and MARINE I W, 1970. Two-well tracer test in fractured crystalline rock. Geological survey water-supply, US Dept of Interior, (Paper 1544-1), pp 22, 1970.

PROCEEDINGS, Thirteenth Workshop on Geothermal Reservoir Engineering
Stanford University, Stanford, California, January 19-21, 1988
SGP-TR-113

PRESSURE INTERFERENCE DATA ANALYSIS FOR TWO-PHASE (WATER/STEAM) GEOTHERMAL RESERVOIRS

S. K. Garg and J. W. Pritchett

S-CUBED
P. O. Box 1620
La Jolla, California 92038-1620

ABSTRACT

A previously published approximate solution by Garg is used to develop a practical procedure for analyzing pressure interference (drawdown) data from a hot-water geothermal reservoir which evolves into a two-phase system as a result of fluid production. The observation well is assumed to remain in the single-phase (liquid) part of the reservoir. A numerical geothermal reservoir simulator is employed in a series of calculations to test the limits of applicability of the interpretation procedure. The numerical results suggest that the accuracy of the computed reservoir transmissivity depends somewhat on the size of the induced two-phase region. Even if the two-phase zone is extensive, the method can still be used to provide a good first approximation for the reservoir transmissivity; forward modeling with a numerical reservoir simulator may then be employed to refine the latter estimate for transmissivity. Numerical results also show that the observation well pressure buildup data will obey the superposition principle after the return of the reservoir to single-phase conditions.

INTRODUCTION

A geothermal system may be two-phase before production begins or may evolve into a two-phase system as a result of fluid production. Theoretical analyses of pressure drawdown and pressure buildup data for such systems have been published by Grant (1978), Garg (1980), Garg and Pritchett (1984), Moench and Atkinson (1978) and Sorey, *et al.* (1980); Riney and Garg (1985) applied these theoretical methods to analyze pressure buildup data from several wells which produced two-phase fluids. In contrast with these analyses of pressure drawdown and pressure buildup data from single wells, analysis of pressure interference data observed in nearby shut-in wells for two-phase (water/steam) systems has not yet been treated in the literature.

Pressure interference tests are essential for establishing reservoir connectivity and for computing interwell transmissivity. Planning and executing pressure interference tests in two-phase systems requires special considerations. As discussed by Grant and Sorey (1979), the effective compressibility of a two-phase system can be 100 to 10,000 times greater than the compressibilities of either water or steam alone; conversely, the effective diffusivity for a two-phase system is some 100 to 10,000 times smaller than that for single phase systems. This implies that it will take an inordinately long time to propagate pressure signals through a reservoir which is two-phase everywhere. Consequently, a pressure interference test in a system which is initially two-phase may well be impractical. A more interesting and tractable situation occurs when an initially single-phase reservoir evolves into a two-phase system as a result of fluid production. In the latter case, a boiling front propagates outward (during drawdown) from the producing wellbore; for all practical purposes, the boiling front may be treated as a constant pressure boundary (p = saturation pressure corresponding to the local reservoir temperature). The two-phase region is restricted to the neighborhood of the production well. Provided that the initial reservoir pressure is sufficiently high and that the two-phase region created during the drawdown phase is not too extensive, the entire reservoir will return to single-phase conditions sometime after the cessation of fluid production (see Garg and Pritchett, 1984).

In this paper, we restrict our attention to an initially single phase reservoir which evolves into a two-phase system as a result of fluid production. In addition, it will be assumed that the two-phase region is restricted to the neighborhood of the production well such that the observation well remains in the single-phase part of the reservoir. Our goal is to examine the character of the pressure signal to be expected at the observation well, and to develop practical methods for the analysis of this pressure signal to yield reservoir transmissivity and compressibility.

MATHEMATICAL MODEL

Garg (1980) considered the pressure response of an initially single-phase reservoir which evolves into a two-phase system on production. In this case, the reservoir is two-phase for $r > R$ [$R = R(t)$ denotes the location of the flash front] and is single phase for $r > R$. Consider a fully penetrating well located in an infinite reservoir of thickness h. Assuming that the skin factor is

zero, the pressure response for flow at a constant mass rate of production is given by (Garg, 1980):

$$0 < r < R: \; p = p_s + \frac{M \nu_t}{4\pi h k} \left\{ Ei \left[\frac{-r^2}{4t D_t} \right] - Ei \left[-\lambda^2 \right] \right\} \quad (1)$$

and

$$r > R: \; p = p_i + \frac{p_s - p_i}{Ei \left\{ -\lambda^2 D_t / D_\ell \right\}} \times Ei \left[\frac{-r^2}{4t D_\ell} \right] \quad (2)$$

where

$$R = 2\lambda \left[D_t \; t \right]^{1/2} \quad (3)$$

and λ is the root of

$$\frac{p_s - p_i}{Ei \left[-\lambda^2 D_t / D_\ell \right]} \times \exp \left[-\lambda^2 D_t / D_\ell \right] = \frac{M \nu_\ell}{4\pi h k} \exp \left[-\lambda^2 \right] \quad (4)$$

In Equations (1) to (4), we have employed the following notation:

D_ℓ = diffusivity for the liquid region

D_t = diffusivity for the two-phase region

h = formation thickness

k = absolute permeability

$k_{r\ell}(k_{rg})$ = liquid (gas) relative permeability

M = rate of mass production

p = pressure

p_i = initial formation pressure

p_s = saturation pressure

r = radius

t = time

$\nu_\ell(\nu_g)$ = liquid (gas) kinematic viscosity

ν_t = two-phase kinematic viscosity = $(k_{r\ell}/\nu_\ell + k_{rg}/\nu_g)^{-1}$

The liquid-region diffusivity D_ℓ is given by:

$$D_\ell = \frac{k}{\phi \rho_\ell \nu_\ell C} \quad (5)$$

where

ϕ = porosity

ρ_ℓ = liquid density

$C = C_m/\phi + C_\ell$

C_m = uniaxial formation compressibility

C_ℓ = liquid compressibility.

The effective diffusivity for the two-phase reservoir region can be written as:

$$D_t = \frac{k}{\phi \rho_t \nu_t C_t}, \quad (6)$$

where ρ_t and C_t denote the density of the flowing mixture and the compressibility of the two-phase region respectively. Given the flowing enthalpy H_t, the density of the flowing mixture ρ_t can be evaluated from:

$$\frac{1}{\rho_t} = \frac{H_g - H_t}{L \rho_\ell} + \frac{H_t - H_\ell}{L \rho_g} \quad (7)$$

where

H_g (H_ℓ) = Steam (liquid) enthalpy corresponding to the measured bottomhole pressure, and

L = Heat of vaporization.

For practical purposes, the two-phase compressibility C_t is given sufficiently accurately by the following approximate expression (Grant and Sorey, 1979)

$$\phi C_t = \langle \rho c \rangle \left[\frac{(\rho_\ell - \rho_g)}{L \rho_\ell \rho_g} \right]^2 (T + 273.15) \quad (8)$$

where

$$\langle \rho c \rangle \simeq (1 - \phi) \rho_r c_r + \phi \rho_\ell c_\ell \quad (9)$$

ρ_r = Intrinsic formation density

c_r (c_ℓ) = Specific heat for rock (liquid), and

T = Reservoir temperature.

For $4t D_t/r_w^2 > 100$ (here r_w denotes the well radius), Equation (1) can be approximated to give the following expression for bottomhole pressure, $p_w(t)$:

$$p_w(t) = p_s - \frac{M \nu_t}{4\pi k h} Ei(-\lambda^2)$$

$$- \frac{1.15 M \nu_t}{2\pi k h} \left\{ \log_{10} \frac{D_t t}{r_w^2} + 0.351 \right\} \quad (10)$$

Equation (10) implies that a plot of p_w versus $\log_{10} t$ should be a straight line and that the two-phase kinematic mobility k/ν_t is given by:

$$k/\nu_t = \frac{1.15 M}{2\pi h m} \quad (11)$$

where m denotes the slope of the straight line.

In deriving the above-described solution, Garg (1980) assumed that the two-phase region can be characterized by a constant kinematic mobility k/ν_t and a constant diffusivity D_t. In reality, the situation is much more complex. Both the kinematic mobility and diffusivity vary throughout the two-phase region. After an initial nonlinear period, $|\partial(k/\nu_t)/\partial r|$ and $|\partial D_t/\partial r|$ become small in a region adjoining the wellbore; and the bottomhole pressures are closely approximated by Equation (1). The situation is, however, completely different for large r ($r < R$); $|\partial(k/\nu_t)/\partial r|$ and $|\partial D_t/\partial r|$ remain finite near the flash front. It is thus not *a priori* obvious if Equation (1) provides an accurate solution for all values of r less than R. In that D_t is variable in the two-phase region, Equation (2) gives only an approximate solution for the pressure response in the single-phase region of the reservoir. Finally, it should be noted that Garg's solution is only valid for the drawdown phase. Because of nonlinear effects in two-phase flow, superposition cannot be used to compute the buildup response.

Despite the above-mentioned limitations, Garg's solution serves as a convenient point of departure for analyzing the observed pressure interference signal. In the following, it will be assumed that the reservoir fluid remains single-phase liquid in the vicinity of the observation well, and that *in situ* boiling is limited to a region surrounding the production well. Comparison of Equation (2) with the line source solution for a well producing a single-phase liquid (constant rate of mass production = M) shows that the two solutions become identical if $[p_s - p_i]/Ei\{-\lambda^2 D_t/D_\ell]$ in Equation (2) is replaced by $M \nu_\ell/4\pi kh$. Stated somewhat differently, the pressure response in the single-phase region (Equation 2) can be computed from the single-phase line source solution by replacing the actual flow rate M by an apparent flow rate M_{app}:

$$M_{app} = \frac{p_s - p_i}{Ei\left(-\lambda^2 D_t/D_\ell\right)} \cdot \frac{4\pi k h}{\nu_\ell} . \quad (12)$$

The apparent mass flow rate M_{app} is always less than the actual flow rate M. Because of the vast difference in the single- and two-phase compressibilities, a disproportionate share of the produced fluid comes from the two-phase region of the reservoir. This in turn implies that for identical rates of production the pressure drawdown at the observation well in the presence of *in situ* flashing will be less than that obtained in a liquid reservoir.

The preceding discussion suggests that the observed pressure interference signal may be analyzed in a straightforward manner provided a method was available for estimating the apparent mass flow rate M_{app}. Unfortunately, the calculation of M_{app} requires a knowledge of single-phase and two-phase diffusivities and the formation permeability. In that the latter quantities are the unknown parameters, it is not feasible to estimate M_{app} prior to solving Equations (1) through (11) for D_ℓ, D_t and k.

A perusal of Garg's solution suggests the following procedure for analyzing the pressure interference data:

1. Match the observed pressure interference signal to the line source type curve (see e.g. Earlougher (1977) for a discussion of the matching procedure). The matching procedure essentially involves (1) plotting observed pressure change Δp ($= p_i - p$) versus time t on a log-log scale and (2) overlaying the latter plot on the line source type curve. The type curve is a log-log plot of nondimensional pressure p_D versus a nondimensional similarity variable r_D^2/t_D,

$$p_D = -0.5\ Ei\ [-r_D^2/4\ t_D]. \quad (13)$$

2. Select a match point (p_D, Δp) and (r_D^2/t_D, t), and solve the following equations for X and D_ℓ:

$$-Ei(-X) = \frac{2\ (p_i - p_s)}{\Delta p}\ p_D \quad (14a)$$

$$t_D/r_D^2 = D_\ell\ t/r^2 \quad (14b)$$

where

$$X = \lambda^2\ D_t/D_\ell \quad (14c)$$

and r denotes the distance of the observation well from the production well. Here, it is assumed that the reservoir temperature T (and hence saturation pressure p_s) and initial pressure p_i are known from other measurements.

3. Calculate two-phase kinematic mobility k/ν_t from the observed pressure response in the production well. Compute two-phase diffusivity from Equations (6) through (9). Note that the calculation of D_t requires a knowledge of the enthalpy of the produced fluid in addition to formation porosity and thermal capacity.

4. Given X, D_ℓ and D_t, λ is computed from Equation (14c).

5. Formation transmissivity kh/ν_ℓ is then calculated from

$$kh/\nu_\ell = \frac{M}{4\pi} \exp(-\lambda^2) \cdot \frac{2\, p_D}{\Delta p} \exp(X). \quad (15)$$

An examination of the above-described procedure shows that the analysis of pressure interference data from two-phase reservoirs requires information from both the production and observation wells.

NUMERICAL RESULTS

In order to define the limits of applicability of the preceding theory, the THOR reservoir simulator (Pritchett, 1982) was exercised in one-dimensional radial configuration to generate a series of drawdown/buildup histories. The radially infinite reservoir is simulated using a 100 zone ($\Delta r_1 = \Delta r_2 = \ldots = \Delta r_{10} = 0.1$ m, $\Delta r_{11} = 1.15\ \Delta r_{10}$, $\Delta r_{12} = 1.15\ \Delta r_{11}$, ..., $\Delta r_{100} = 1.15\ \Delta r_{99}$) radial grid. The outer radius of the grid is 222,542 m and is sufficiently large such that no signal reaches this boundary during the time-scale of interest. We consider a fully penetrating well located in a reservoir of thickness h = 100 m. The well is represented as an integral part of the grid by assigning to the well-block (Zone 1) sufficiently high permeability and porosity; fluid production is specified as a mass sink in the well-block. No attempt is made here to treat wellbore storage effects; proper treatment of these effects would require the coupling of transient wellbore flow with the reservoir simulator. The reservoir rock properties selected are given in Table 1. The mixture (rock/fluid) thermal conductivity is approximated by Budiansky's formula (Pritchett, 1982). The initial fluid state for the three cases considered is shown in Table 2. The reservoir is produced at constant rate M (see Table 2 for values of M used) for $t = 10^6$ s and is then shut in for $\Delta t = 2 \times 10^6$ s. In all three cases, the reservoir is assumed initially to contain single-phase fluid at a temperature of 300°C; the initial formation pressure, however, varies from case to case. The saturation pressure corresponding to a temperature of 300°C is 8.5917 MPa. Thus, the initial pressure differs from the saturation pressure by 8.3 kPa, 108.3 kPa, and 408.3 kPa for Cases 1, 2 and 3 respectively. The observation well is assumed to be located at r = 192.202 m (center of grid zone 50).

TABLE 1

ROCK PROPERTIES EMPLOYED IN NUMERICAL SIMULATION

	Wellblock (i = 1)	Rock Matrix 2 ≤ i ≤ 100
Porosity, ϕ	0.9999	0.1000
Permeability k, m^2	5×10^{-11}	5×10^{-14}
Uniaxial Formation Compressibility C_m, MPa^{-1}	0	0
Rock Grain Density ρ_r, kg/m^3	1	2650
Rock Grain Thermal Conductivity K_r, W/m°C	0.00	5.25
Heat Capacity c_r, kJ/kg°C	0.001	1.00
Relative Permeabilities $k_{r\ell}$, k_{rg}	Straight-line*	Straight-line*
Residual Liquid Saturation $S_{\ell r}$	0.00	0.30
Residual Gas Saturation S_{gr}	0.00	0.05

* $K_{r\ell} = (S_\ell - s_{\ell r})/(1 - S_{\ell r})$ for $S_\ell \geq S_{\ell r}$

$K_{rg} = (S_g - S_{gr})/(1 - S_{gr})$ for $S_g \geq S_{gr}$.

TABLE 2

MASS PRODUCTION RATE M AND INITIAL FLUID STATE

Case No.	Production Rate M (kg/s)	Pressure MPa	Temperature °C
1	10	8.600	300
2	10	8.700	300
3	20	9.000	300

Along the saturation line, ASME Steam Tables (ASME, 1967) give the following values for liquid-water and steam density and enthalpy:

Liquid-water density ρ_ℓ = 712.5 kg/m^3

Steam density ρ_g = 46.20 kg/m^3

Liquid-water enthalpy H_ℓ = 1345 kJ/kg

Steam enthalpy H_g = 2749 kJ/kg

Latent heat of vaporization L = 1404 kJ/kg

Assuming that the specific heat for liquid water at initial reservoir conditions is ~ 5.2 kJ/kg°C, and employing the rock properties given in Table 1, we have:

$$<\rho c> = 0.9 \times 2650 \times 10^3 + 0.1 \times 712.5 \times 5.2\ 10^3 \sim 2.76\ 10^6\ J/m^3°C,$$

and

$$\phi C_t = <\rho c> \left[\frac{(\rho_\ell - \rho_g)}{L\ \rho_\ell\ \rho_g}\right]^2 (T + 273.15)$$

$$= 2.76 \left[\frac{712.5 - 46.2}{1404 \times 712.5 \times 46.2}\right]^2 (573.15)$$

$$= 3.29\ 10^{-7}\ Pa^{-1}.$$

Simulated drawdown histories at the production well for the three cases considered are shown in Figures 1 through 3. The drawdown data are seen to closely fit a straight-line in every case. The two-phase kinematic mobilities calculated from the slope of the straight line and Equation (11) are listed in Table 3. The simulated flowing enthalpies H_t were used along with Equations (6) through (8) to compute the flowing fluid densities ρ_t and two-phase diffusivities D_t (see Table 3 for numerical values).

Figures 4 through 6 display the simulated pressure drawdown (i.e. pressure interference) at the observation well; the simulated pressure interference data are seen to match the line-source solution closely. The match point in each case was used to compute the nondimensional parameter X (Equation 14a), the single-phase diffusivity D_ℓ (Equation 14b), and the nondimensional parameter λ (Equation 14c); the calculated values are displayed in Table 3.

Equation (3) implies that the flash-front propagates into the reservoir according to

$$R = At^{0.5},$$

where

$$A = 2\lambda\ D_t^{0.5}. \qquad (16)$$

Figures 7 through 9 show that the flash-front radius is indeed proportional to $t^{0.5}$. Table 3 compares the calculated values of A (Equation 16) with those obtained directly from Figures 7 through 9. The divergence between the computed (cf Equation 16) and actual values for A provides a measure of the adequacy of the theoretical solution. In view of the relatively

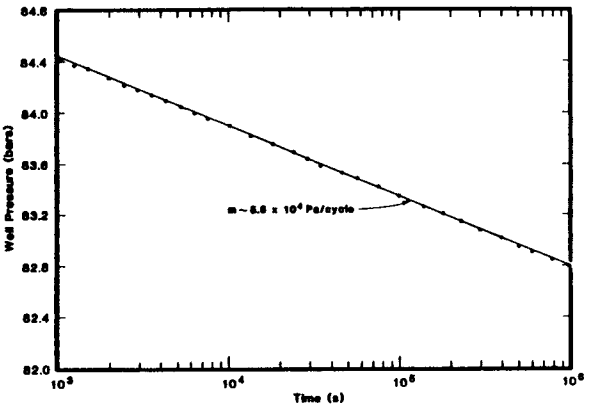


Figure 1. Simulated drawddown history (production well) for Case No. 1. Initial reservoir pressure and mass production rate are 8.600 MPa and 10 kg/s respectively.

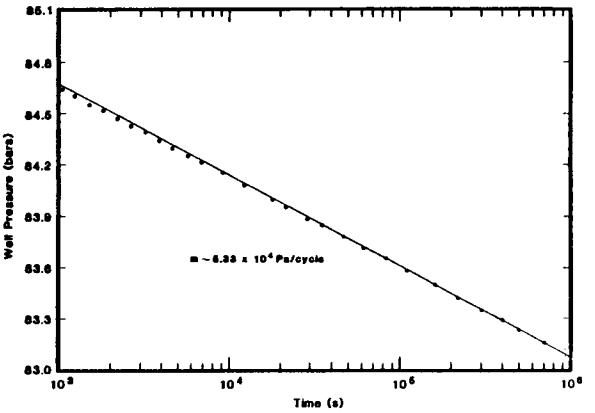


Figure 2. Simulated drawdown history (production well) for Case No. 2. Initial reservoir pressure and mass production rate are 8.700 MPa and 10 kg/s respectively.

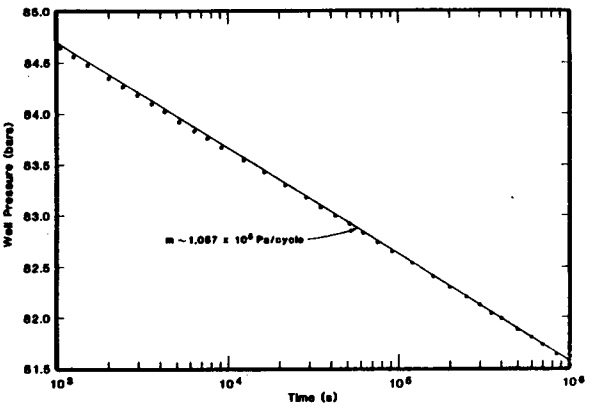


Figure 3. Simulated drawdown history (production well) for Case No. 3. Initial reservoir pressure and mass production rate are 9.000 MPa and 20 kg/s respectively.

TABLE 3

COMPUTATION OF RESERVOIR TRANSMISSIVITY kh/ν_ℓ AND APPARENT MASS FLOW RATE $M_{app.}$

Case No.	Two-Phase Kinematic Mobility k/ν_t (s)	Flowing Enthalpy H_t (kJ/kg)	Flowing Density ρ_t (kg/m^3)	Two-Phase Diffusivity D_t (m^2/s)	Single-Phase Diffusivity D_ℓ (m^2/s)	X $\lambda^2 D_t/D_\ell$ Nondim. *	λ Nondim.	$A_{calc.}$ ($m/s^{0.5}$) **	$A_{act.}$ ($m/s^{0.5}$)	Single-Phase Kinematic Transmissivity kh/ν_ℓ (m-s)	M_{app}/M ***
1	$3.33\ 10^{-7}$	1374.3	547.7	$1.85\ 10^{-3}$	2.364	$0.235\ 10^{-2}$	1.733	0.149	0.140	$2.61\ 10^{-5}$	0.05
2	$3.43\ 10^{-7}$	1360.0	617.4	$1.69\ 10^{-3}$	2.364	$0.356\ 10^{-3}$	0.7057	0.0580	0.0510	$3.29\ 10^{-5}$	0.61
3	$3.46\ 10^{-7}$	1346.5	701.7	$1.50\ 10^{-3}$	2.438	$0.1622\ 10^{-4}$	0.1624	0.0126	0.0114	$3.97\ 10^{-5}$	0.97

* See Equations (14a) and (14c)

** $A_{cal.} = 2\ \lambda\ D_t^{0.5}$

*** Equation (12)

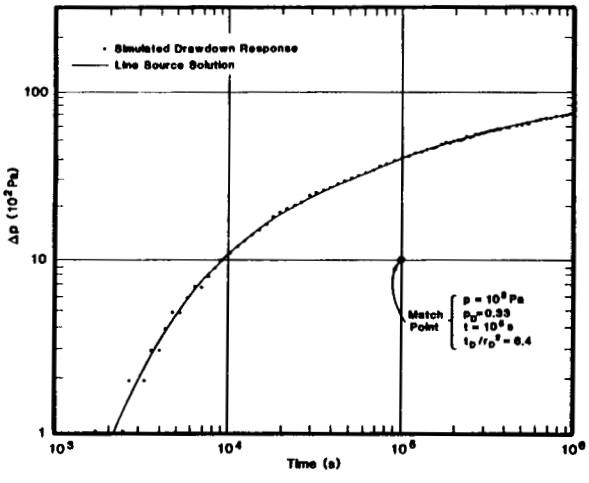


Figure 4. Match of the simulated pressure response at the observation well (r = 192.202 m) to the line-source solution (Case 1).

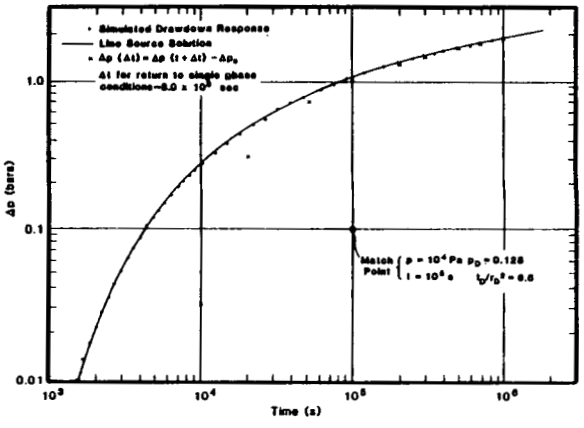


Figure 6. Match of the simulated pressure response at the observation well (r = 192.202 m) to the line-source solution (Case 3).

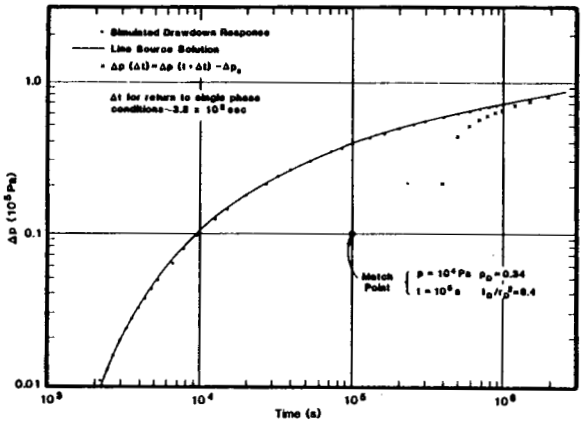


Figure 5. Match of the simulated pressure response at the observation well (r = 192.202 m) to the line-source solution (Case 2).

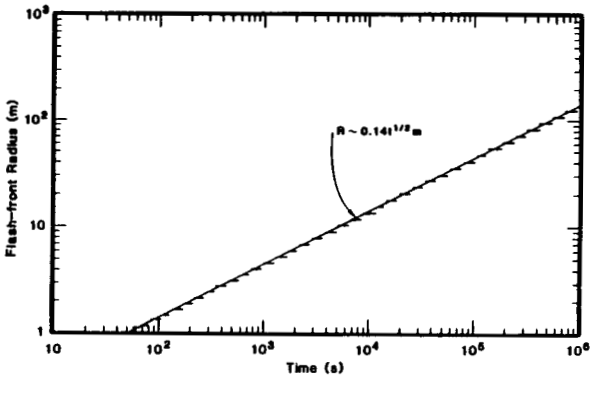


Figure 7. Flash-front radius versus drawdown time for Case No. 1.

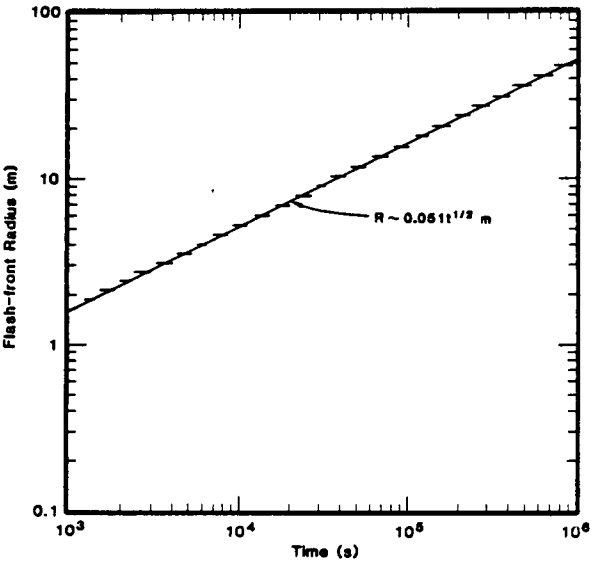


Figure 8. Flash-front radius versus drawdown time for Case No. 2.

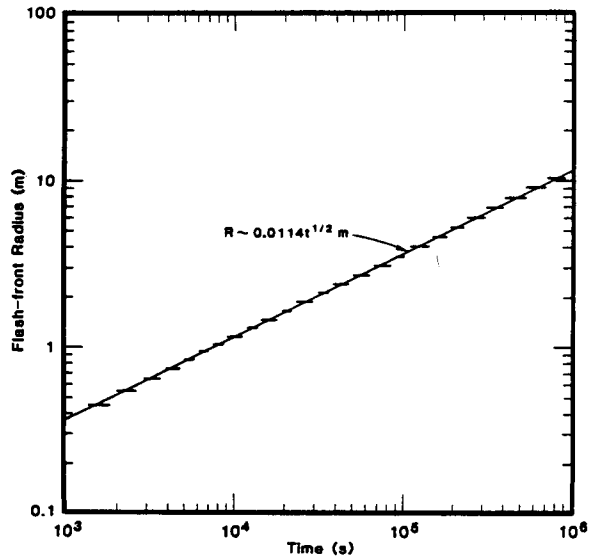


Figure 9. Flash-front radius versus drawdown time for Case No. 3.

small error in A (10 • 4 percent), one may be tempted to conclude that the linear solution should be sufficient for analyzing pressure interference data. This is, however, not always true. In that the nondimensional parameter λ occurs in the exponential term in Equation (15), a small error in A (and hence λ) can lead to a relatively large error in the calculated reservoir transmissivity.

Finally, the kinematic transmissivities kh/ν_ℓ (Equation 15) and the ratio of apparent flow rate M_{app} to the actual flow rate (Equation 12) are also given in Table 3. A comparison of the calculated transmissivities (Table 3) with the input value of $4.02\ 10^{-5}$ m-s shows that the agreement between the computed and the input values gets progressively worse as the two-phase effects become more pervasive. In Case 1, the computed value is only two-thirds of the actual transmissivity; note that in this case the apparent mass flow rate M_{app} is only ~ 5 percent of the input mass rate M. The latter results are to be contrasted with those for Case 3 wherein $M_{app}/M \sim 0.97$, and the computed value of kh/ν_ℓ is in close agreement with the input value. These numerical results suggest that the theoretical method of Section II can always be used (even in the presence of a large two-phase zone) to provide a first estimate for reservoir transmissivity. In cases wherein an extensive two-phase zone develops as a result of fluid production, it would seem prudent to check the computed value of kh/ν_ℓ by a forward simulation using a numerical reservoir simulator.

For a single-phase reservoir, superposition can be utilized to construct solutions for pressure buildup response. Thus, for a constant rate of mass production, the shutin pressure Δp_s at a time Δt after the cessation of production operations is given by:

$$\Delta p_s = \Delta p\ (t + \Delta t) - \Delta p\ (\Delta t), \qquad (17)$$

where $\Delta p\ (t + \Delta t)$ and $\Delta p(\Delta t)$ are the pressure drawdowns at times $(t + \Delta t)$ and Δt, respectively, computed from the line-source solution. Assuming that a match of the drawdown data to the line source solution is available, Equation (17) implies that

$$\Delta p\ (\Delta t) = \Delta p\ (t + \Delta t) - \Delta p_s\ . \qquad (18)$$

should also lie on the line source curve. Because of nonlinear effects in two-phase flow, superposition does not, strictly speaking, apply. Nevertheless, we decided to compute $\Delta p\ (\Delta t)$ (Equation 18) and to test the applicability (or lack thereof) of superposition empirically. Figures 5 and 6 (Cases 2 and 3) show that about one-half log cycle after the return of reservoir to single-phase conditions, the buildup data are closely approximated by the line-source solution. (In Case 1, the reservoir did not return to single-phase conditions during the time scale of interest. As a matter of fact, the two-phase zone advanced farther into the reservoir and engulfed the observation well. The buildup pressures in this case are quite different from those implied by Equation (18).) These results suggest that superposition may be used to model the pressure response of the observation well after the return of reservoir to single-phase conditions.

CONCLUDING REMARKS

The principal purpose of this paper is to develop a practical procedure for analyzing pressure interference data from a two-phase (water/steam) geothermal reservoir. It is assumed that the geothermal reservoir is initially all liquid and that the two-phase zone is created on initiation of production operations. The observation well is, however, assumed to always remain in the single-phase region of the reservoir. Garg (1980) derived an approximate solution for the pressure (drawdown) response of hot water reservoirs which undergo flashing on production. A numerical reservoir simulator was employed to test the applicability of the latter solution for analyzing pressure interference data. Application of the analysis procedure discussed in this paper requires pressure data from both the production and the observation wells in addition to information regarding the thermomechanical properties (i.e. specific heat, temperature, porosity, density, etc.) of the reservoir rocks. As far as the pressure drawdown response of the observation well is concerned, the effect of the two-phase zone can be represented by a reduced (or apparent) mass flow rate. The calculation of this apparent mass flow rate can, however, only be made after solving for reservoir transmissivity and diffusivity. If the two-phase zone created during drawdown is very large, then the apparent mass flow rate will be a small fraction of the actual production rate. In the latter case, the analytical method will yield only a first rough estimate of reservoir transmissivity; a more accurate estimate may then be obtained by forward modeling (history-matching) using a numerical reservoir simulator.

Because of nonlinear effects in two-phase flow, the superposition principle does not usually apply in two-phase problems. More specifically, Garg and Pritchett (1984) showed that the buildup response of the production well cannot be constructed from the drawdown solution. The numerical results in this paper, however, suggest that the buildup response of the observation well, subsequent to the return of the reservoir to single-phase conditions, does obey the superposition principle. The buildup data can, therefore, be used to check the consistency of formation properties derived from an analysis of drawdown pressures.

REFERENCES

ASME (1967), ASME Steam Tables, *The American Society of Mechanical Engineers*, New York.

Earlougher, R. C. (1977), Advances in Well Test Analysis, *Monograph Series, Vol. 5, Society of Petroleum Engineers*, Dallas.

Garg, S. K. (1980), "Pressure Transient Analysis for Two-Phase (Water/Steam) Geothermal Reservoirs," *Society of Petroleum Engineers Journal, Vol. 20*, pp. 206-214.

Garg, S. K. and J. W. Pritchett (1984), "Pressure Transient Analysis for Two-Phase Geothermal Wells: Some Numerical Results," *Water Resources Research, Vol. 20*. pp. 963-970.

Grant, M. A. (1978), "Two-Phase Linear Geothermal Pressure Transients: A Comparison With Single-Phase Transients," *New Zealand Journal of Science, Vol. 21*, pp. 355-364.

Grant, M. A. and M. L. Sorey (1979), "The Compressibility and Hydraulic Diffusivity of a Water-Steam Flow," *Water Resources Research, Vol. 15*, pp. 684-686.

Moench, A. F. and P. G. Atkinson (1978), "Transient Pressure Analysis in Geothermal Steam Reservoirs With an Immobile Vaporizing Liquid Phase," *Geothermics, Vol. 7*, pp. 253-264.

Pritchett, J. W. (1982), "User's Guide to the THOR Thermal Reservoir Simulator," S-CUBED Report No. SSS-R-83-5795.

Riney, T. D. and S. K. Garg (1985), "Pressure Buildup Analysis for Two-Phase Geothermal Wells: Application to the Baca Geothermal Field," *Water Resources Research, Vol. 21*, pp. 372-382.

Sorey, M. L., M. A. Grant and E. Bradford (1980), "Nonlinear Effects in Two-Phase Flow to Wells in Geothermal Reservoirs," *Water Resources Research, Vol. 16*, pp. 767-777.

PROCEEDINGS, Thirteenth Workshop on Geothermal Reservoir Engineering
Stanford University, Stanford, California, January 19-21, 1988
SGP-TR-113

A Convolution Boundary Element Method for Unsteady State Groundwater Flow in Homogeneous Aquifers

Jitendra Kikani and Roland N. Horne

Stanford Geothermal Program

Abstract

In this paper, Boundary Element (BEM) solutions were obtained for the transient flow of fluids through homogeneous, anisotropic porous media. The Green's function method with Euler method of forward time differencing and Laplace transform method have been used by previous authors. Unlike these methods, this paper uses the fundamental solution to the differential equation and the convolution behavior of the resulting integrals to obtain an implicit and stable solution. This allows large time steps to be taken without significant loss in accuracy. Comparison with the Laplace transform method and Green's function method with discrete time stepping, for two test cases, show that the method is very accurate. The computations however, become quite storage intensive owing to the dynamic increase in the number of stored matrices. It has been shown elsewhere that for certain problems with both Dirichlet and Neumann boundary conditions, asymptotic expression generated from exact solution is needed for starting the computational procedure. The present formulation alleviates this requirement.

These solutions are developed for use in the analysis of pressure transients in complex reservoir problems.

INTRODUCTION

Solution of reservoir engineering problems associated with fluid injection and fluid movement in reservoirs and its related pressure response at the well is of major importance in the exploitation of geothermal reservoirs. Usually these reservoirs are of complex geometries (shapes) and are produced by means of numerous wells. These problems are difficult to treat accurately and efficiently by numerical methods which suffer from dispersion and grid orientation effects. Analytical techniques are not available except for a very few regular geometries. In this paper we explore the use of the boundary element method to solve such problems.

The Boundary Integral Equation Method (BIEM), or Boundary Element Method (BEM) as it is often called, is gaining popularity in solving problems encountered in solid mechanics, heat transfer, groundwater hydrology and various other fields. The methodology of solving partial differential equations follows closely that of finite element method where the governing differential equation is cast in an integral form. Instead of choosing basis functions which approximate the differential equations in the domain as in the finite element method, fundamental solutions to the differential operator are used to reduce the problem to quadratures. The solution becomes a pure boundary procedure if inhomogeneities in the differential operators are removed.

The primary advantage which has encouraged people to explore and use this technique is that the dimensionality of the problem is reduced by one. A 3-D problem is reduced to a 2-D problem and so forth. Since it is a boundary procedure, it conforms well to boundaries. The results obtained with this method are usually more accurate than finite difference or finite element methods, as it is an analytic technique requiring only numerical evaluation of integrals. Integration is a smoothing procedure and for well behaved functions can be performed quite accurately. In BEM the governing differential equation is exactly satisfied in the domain of the problem, it is only on the boundaries that the approximations are made. The only bottleneck in this procedure is finding the fundamental solutions to the differential operators.

The efficiency and accuracy of the method has been proved for elliptic operators. *Numbere et al.*(1986), and *Masukawa et al.*(1986) have used BEM as a useful streamline generating method for Laplace's equations with odd shaped boundaries and with moving interfaces. A variety of problems arising in groundwater hydrology have been solved by *Liggett* and coworkers [*Liggett and Liu* (1983), *Lafe and Liggett* (1981), *Taigbenu and Liggett* (1985)] using Boundary Element Methods.

The present work involves solution of unsteady state (transient) problems with BEM. A slightly different formulation than the one presented by *Liggett et al.*(1979) has been used. Another similar problem, the solution of the diffusivity equation by integral equations, which govern the transient heat conduction in materials, was looked at by *Rizzo and Shippy* (1970). They removed the time derivative by converting the problem into Laplace space.

Taigbenu and Liggett (1985), use the fundamental solution to the diffusion equation and cast it in terms of an integral equation. Depending on the interpolating functions used between nodes, some of the integrals, in the discretized equations, can be performed analytically. They performed the analytic integrations in space first and then used Euler's method of time stepping to evaluate the solution at each time step. Use of this method in a mixed type problem [with both Neumann (flux) and Dirichlet (potential) boundary conditions] requires that the initial normal derivatives of the velocity potential be known. They derived an asymptotic expression from the exact solution and used it to start the computational procedure at early time.

We use the convolution character of the integral equation as observed by *Wrobel and Brebbia* (1981) and *Pina* (1984) to develop a boundary element code. The formulation is implicit in nature and thus very stable with respect to time

step sizes. Performing the time integrations analytically removes the singularity of the fundamental solution in the time dimension. The space integrals are then evaluated analytically or by the use of accurate Gaussian quadrature techniques. This formulation does not require knowledge of the analytic solutions beforehand in order to develop asymptotic expressions at early times to start the computational procedure. *Wrobel and Brebbia* (1984) suggested a term by term integration of the series to find values of singular integrals obtained when the collocation point is on the same boundary element as the field point. The series converges very slowly for large arguments which are frequent due to the small time step sizes used. We provide here an analytic integration technique in terms of smoothly behaved functions which are easier to evaluate.

In the solution process with constant time step size, the left hand side coefficient matrix is generated once, inverted and stored. At every step, one additional matrix needs to be generated. However, all the previous coefficient matrices and solution vectors need to be stored because of the convolution character of the problem. But with high speed auxiliary memory access and large swap spaces in modern computers this extra storage requirement is not much of a problem.

Some simple test problems which have exact solutions were used to check the efficacy of the technique.

FORMULATION

The continuity equation for two-dimensional flow of a slightly compressible, single phase fluid in a homogeneous, anisotropic and confined reservoir is (*Aziz and Settari* (1979))

$$\nabla\bullet(\frac{K\rho}{\mu}\nabla P) = \frac{\partial(\phi\rho)}{\partial t} + Q^* \tag{1}$$

where Darcy's law has been used. Q^* is the strength of a sink in mass per unit volume per unit time. Using the equation of state for small and constant compressibility fluid and assuming that the permeability tensor can be diagonalized and also that the viscosity of the fluid and the porosity of the medium are constant, we obtain in a cartesian coordinate system, with the coordinate axes aligned with the principal permeability directions, the following equation

$$\frac{\partial}{\partial x'}\left[\frac{k_{xx}}{\mu}\frac{\partial P}{\partial x'}\right] + \frac{\partial}{\partial y'}\left[\frac{k_{yy}}{\mu}\frac{\partial P}{\partial y'}\right] = \phi c\frac{\partial P}{\partial t} + \frac{Q^*}{\rho} \tag{2}$$

Assuming k_{xx} and k_{yy} to be constants and performing a coordinate transformation given by

$$x = x' ; \qquad y = y'\left[\frac{k_{xx}}{k_{yy}}\right]^{1/2} \tag{3}$$

we obtain

$$\frac{\partial^2 P}{\partial x^2} + \frac{\partial^2 P}{\partial y^2} = \frac{1}{\eta}\frac{\partial P}{\partial t} + \frac{Q^*\mu}{\rho k_{xx}} \tag{4}$$

where, $\eta = \dfrac{k_{xx}}{\phi\mu c}$

Since the system geometry can be odd, the above system can be normalized with respect to the area (A) of the system. A description of a typical system geometry is shown in Fig. 1. Thus, defining

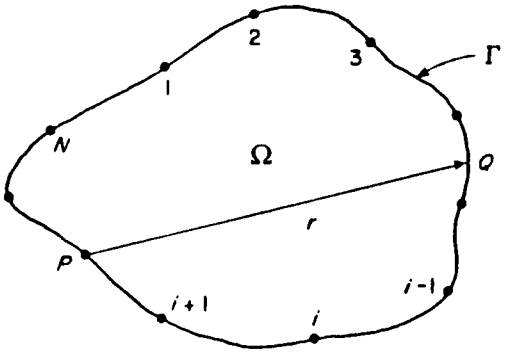


Figure 1. Typical computational domain

$$t_{DA} = \frac{k_{xx}\,t}{\phi\mu cA} = \frac{\eta t}{A} ; \qquad P_D = \frac{P_i - P}{P_i}$$

$$x_D = \frac{x}{\sqrt{A}} ; \qquad y_D = \frac{y}{\sqrt{A}} \tag{5}$$

gives

$$\frac{\partial^2 P_D}{\partial x_D{}^2} + \frac{\partial^2 P_D}{\partial y_D{}^2} = \frac{\partial P_D}{\partial t_{DA}} + Q_D \tag{6}$$

where,

$$Q_D = \frac{Q^*\mu A}{\rho k_{xx}}$$

and Q_D is non-dimensionalized with respect to a flow rate of unity.

We drop the subscripts hereafter for convenience. Now, three types of boundary conditions can be applied to Eqn. (6)

$$P = P_1 \qquad on\ \Gamma_1 \in \Gamma \quad (Dirichlet)$$

$$\frac{\partial P}{\partial n} = q \qquad on\ \Gamma_2 \in \Gamma \quad (Neumann) \tag{7}$$

$$\alpha P + \beta\frac{\partial P}{\partial n} = \gamma \qquad on\ \Gamma_3 \in \Gamma\ (Robin,\ Radiation\ or\ Mixed)$$

The free space Green's function for the above equation has been derived by *Greenberg* (1971), *Zauderer* (1983), *Morse and Feshbach* (1953). A two dimensional free space Green's function is defined [*Carslaw and Jaegar* (1959)] as the pressure at (x,y) at a time t due to an instantaneous line source of strength unity generated at the line $P(\xi,\eta)$ at the time τ. The medium is initially at zero pressure and infinite in extent. The integral equation formulation of equation(6) using the divergence theorem of Gauss has been given by *Liggett and Liu* (1983). The integral equation is

$$2\alpha P(x,y,t) = \int_t d\tau \int_\Gamma (G\frac{\partial P}{\partial n} - P\frac{\partial G}{\partial n})ds + \int_\Omega G_0 P_0\, dA$$

$$+ \int_t d\tau \int_\Omega GQ\, dA \tag{8}$$

where,

$$G = \frac{1}{(t-\tau)} H(t-\tau) \exp\left[-\frac{r^2}{4(t-\tau)}\right] \quad (9)$$

is the free space Green's function for the diffusion equation. and

H(t - τ) is the Heaviside step function.

also

$$r^2 = (x-\xi)^2 + (y-\eta)^2$$

where, ξ and η are the coordinates of a fictitious source point, and

$$\alpha = 2\pi \qquad \text{if } (x,y) \in \Omega \quad (10a)$$

$$\alpha = \theta \qquad \text{if } (x,y) \in \Gamma \quad (10b)$$

SOLUTION OF THE INTEGRAL EQUATION

If there is no inhomogeneity in the governing equation i.e.; Q_D is zero and also the equation is non-dimensionalized such that the initial condition is homogeneous, then the solution becomes strictly a boundary procedure. This is not a limitation because the forcing function on the right hand side of the differential equation is usually a source or a sink term. Since the differential operator is linear, we can use the concept of singularity programming to superpose the contribution due to sources and sinks separately onto the solutions free of sources and/or sinks.

Equation(8) can then be solved by choosing a finite number of elements on the boundary. An interpolating function for pressure and flux on a boundary element both in space and time dimensions is assumed. The integral equation could be solved by a collocation type technique by moving a fictitious source point to all the nodes and generating enough equations so that they match the number of unknowns. The problem then reduces to one of solving a matrix equation.

For simplicity we choose interpolating functions between boundary elements that are linear in space and constant in time. Higher dimensional elements could be chosen. *Wrobel and Brebbia* (1981) show some of the integrals arising from choosing higher dimensional interpolating functions in time. Pressure or the normal derivative of pressure at any point on the element is expressed in terms of the nodal values as follows :

$$P = [(P_{j+1} - P_j)\,\xi + (\xi_{j+1}P_j - \xi_j P_{j+1})]/(\xi_{j+1} - \xi_j) \qquad \xi_j < \xi < \xi_{j+1} \quad (11)$$

$$\left(\frac{\partial P}{\partial n}\right) = \left\{\left[\left(\frac{\partial P}{\partial n}\right)_{j+1} - \left(\frac{\partial P}{\partial n}\right)_j\right]\xi + \left[\xi_{j+1}\left(\frac{\partial P}{\partial n}\right)_j - \xi_j\left(\frac{\partial P}{\partial n}\right)_{j+1}\right]\right\} / (\xi_{j+1} - \xi_j) \qquad \xi_j < \xi < \xi_{j+1} \quad (12)$$

where, ξ is the local coordinate varying along the element. Integrations are performed after transferring every element in a moving local coordinate system. An illustration of a local coordinate system is given in Fig. 2. After performing all the

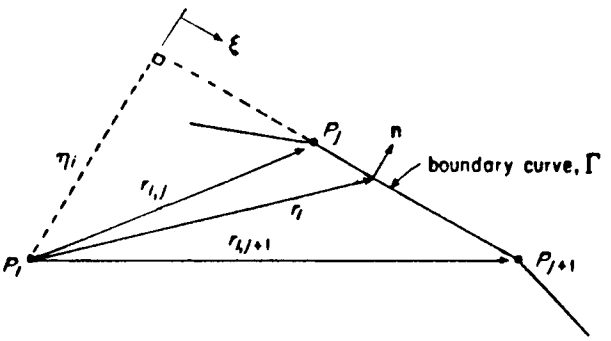


Figure 2. Local co-ordinate system

integrations which can be done analytically we obtain,

$$\sum_{j=1}^{N} 2\alpha_i\,\delta_{ij}\,P_j = A_i + B_i + \sum_{j=1}^{N}\left[(AA)_{I_{ij}} + (AA)_{II_{ij}}\right]; \quad i = 1,N \quad (13)$$

where

$$A_i = \int_{\Omega} \exp\left[\frac{-\frac{r^2}{4(t-\tau)}}{(t-\tau)}\right] P_0\, dA \quad (14)$$

$$B_i = \int_{t} d\tau \int_{\Omega} \exp\left[\frac{-\frac{r^2}{4(t-\tau)}}{(t-\tau)}\right] Q\, dA \quad (15)$$

$$(AA)_{I_{ij}} = \frac{\eta_i}{(\xi_{j+1} - \xi_j)}(P_{j+1} - P_j)\left[E_1\left[\frac{\xi_j^2 + \eta_i^2}{4(t-\tau)}\right] - E_1\left[\frac{\xi_{j+1}^2 + \eta_i^2}{4(t-\tau)}\right]\right]$$

$$+ \frac{2\eta_i}{(\xi_{j+1} - \xi_j)} \exp\left[-\frac{\eta_i^2}{4(t-\tau)}\right](\xi_{j+1}P_j - \xi_j P_{j+1})$$

$$\left[\int_{\xi_j}^{\xi_{j+1}} \frac{d\xi}{(\xi^2 + \eta_i^2)} \exp\left[-\frac{\xi^2}{4(t-\tau)}\right]\right] \quad (16)$$

and

$$(AA)_{II_{ij}} = \frac{(P_{n_{j+1}} - P_{n_j})}{(\xi_{j+1} - \xi_j)}\left[\frac{1}{2}\left\{(\xi_{j+1}^2 + \eta_i^2)\,E_1\left[\frac{\xi_{j+1}^2 + \eta_i^2}{4(t-\tau)}\right]\right.\right.$$

$$\left.\left. - (\xi_j^2 + \eta_i^2)\,E_1\left[\frac{\xi_j^2 + \eta_i^2}{4(t-\tau)}\right]\right\} + 2(t-\tau)\exp\left[-\frac{\eta_i^2}{4(t-\tau)}\right]$$

$$\left\{\exp\left[-\frac{\xi_j^2}{4(t-\tau)}\right] - \exp\left[-\frac{\xi_{j+1}^2}{4(t-\tau)}\right]\right\}\Bigg] + \frac{(\xi_{j+1}P_{n_j} - \xi_j P_{n_{j+1}})}{(\xi_{j+1} - \xi_j)}$$

$$\left[\int_{\xi_j}^{\xi_{j+1}} E_1\left[\frac{\xi^2 + \eta_i^2}{4(t-\tau)}\right] d\xi\right] \quad (17)$$

where,

$$E_1(x) = \int_x^\infty \frac{e^{-u}}{u}\, du \qquad (18)$$

Singular Integral Evaluation

When the collocation point is on the same boundary element as the field point we obtain integrals which are singular at one of the limits. This can be seen easily from Fig. 2. This happens when η is zero and ξ_j or ξ_{j+1} is zero. The usual techniques for numerical integration are unsuitable and special care needs to be taken. Such a functions is $E_1(z)$, which is singular at $z = 0$. *Pina(1984)* used series expansion of $E_1(z)$ which is uniformly and absolutely convergent [*Abramowitz and Stegun* (1964) page 229] and integrated it term by term. For arguments greater than 1.0 the series converges very slowly. Since the time step sizes used are usually very small thus the argument of the function tends to be large. We present here a simple closed form integration in terms of very smoothly behaved functions.

The singular integrals that are encountered are of the form :

$$\int_0^c E_1(\frac{x^2}{4t})\, dx$$

We obtain the following result;

$$\int_0^c E_1(x^2/4t)\, dx = cE_1(\frac{c^2}{4t}) + \sqrt{\frac{\pi}{\alpha}}\, erf\,(\sqrt{\alpha}c) \qquad (19)$$

The details of the derivation are given in Appendix-A.

Solution of Matrix Equations

At every node, one piece of information is prescribed by the boundary condition, and the other is unknown. Thus, one could move the fictitious source point to all the boundary nodes. This will generate N equations for N boundary nodes. The system of N equations in N unknowns can then be solved, in principle. The matrix equation generated is

$$\sum_{\alpha=1}^{t} H^{n\alpha} u^\alpha = b^\alpha \qquad (20)$$

Note that the integrals that are obtained have time both in the limit and in the integrand and thus are of the form,

$$\int_0^t f(\tau)\, G(t-\tau)\, d\tau \qquad (21)$$

The convolution character of the above equation is evident. If we assume a constant time step size then, $t = t_0 + n\Delta t$, where Δt is the step size. If the solution up to $(n-1)^{th}$ time step is known then the solution at the n^{th} time level could be found from the above equations as

$$H^{n1}u^1 + H^{n2}u^2 + ... + H^{nn}u^n = b^n \qquad (22a)$$

which on transposing becomes

$$H^{nn}u^n = b^n - \sum_{\alpha=1}^{n-1} H^{n\alpha}u^\alpha \qquad (22b)$$

The matrix $H^{n\alpha}$ depends entirely on the geometry of the system and the step size. At the n^{th} time level for example, Equation(22b) suggests that the unknown vector u^n at time step n is multiplied by a coefficient matrix H^{nn}. Because of the convolution character of the matrices $H^{nn} = H^{11}$, if the time step size is constant. Similarly $H^{(n)(n-1)} = H^{21}$. Similar relations could be derived between various matrices. What this provides is the need to create only one extra matrix at every time step. Another way to solve the same problem would be to start the time integrations from zero at every time step. This becomes quite time consuming, whereas the above method needs extra storage space. *Taigbenu and Liggett* (1985) have used the solution obtained after the first time step as the initial condition to advance in time. This too reduces the storage requirement but introduces a domain integral in the integral equation. To evaluate such an integral the entire domain has to be discretized once every time step in a finite element type subdivision. This reduces the charm of the method as being a boundary procedure, though it may improve the efficiency of calculations.

VERIFICATION

A computer code has been developed on the foregoing lines. The program has been tested on four simple problems until now. These problems have closed form analytical solutions to compare with.

A Neumann Problem

The first example is a solution to the diffusivity equation in a porous medium with a step change in the flux at the inlet end. All the boundary conditions are of Neumann type and the initial condition is homogeneous. Figure 3 shows the problem domain. The governing equation and the boundary conditions are as follows :

$$\nabla^2 P = \frac{\partial P}{\partial t}$$

$$P(x,y,0) = 0$$

$$\frac{\partial}{\partial n}P(0,y,t) = 1 \qquad \frac{\partial}{\partial n}P(1,y,t) = -1$$

$$\frac{\partial}{\partial n}P(x,0,t) = \frac{\partial}{\partial n}P(x,1,t) = 0$$

The results are shown in Figs. 4 and 5. Pressure at the inlet end is plotted as a function of time. Smaller step sizes give more accurate results but the implicit nature of the solution procedure allows us to take large step sizes.

A Mixed Problem

The problem domain is the same as the previous one. The governing equation and the initial condition is also the

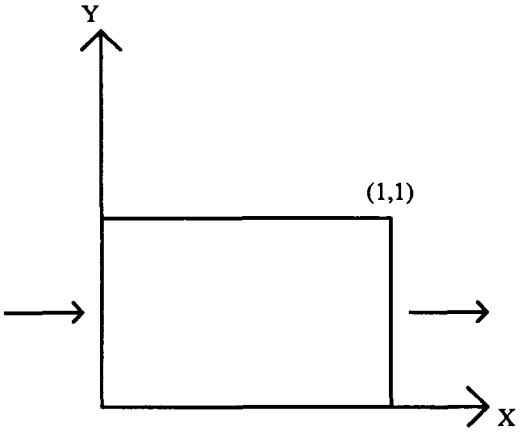


Figure 3. Domain used for example calculations

same. The boundary conditions are

$$P(0,y,t) = 1 \qquad P(1,y,t) = 0$$

$$\frac{\partial}{\partial n}P(x,0,t) = \frac{\partial}{\partial n}P(x,1,t) = 0$$

In this problem the inner and the outer boundaries are held at constant pressures and the other two boundaries at a no flux condition. Figures 6 through 9 show the comparisons with the analytical solution. Pressure solutions match very well even for large time steps. But flux is infinite at early times and thus poses a problem for large time steps. On taking sufficiently small time steps the fluxes match well. The effect of time step size on the solutions for pressures are shown in Figs. 6 and 7 whereas Figs. 8 and 9 show the effect of time step size on the calculation of fluxes at the inner boundary.

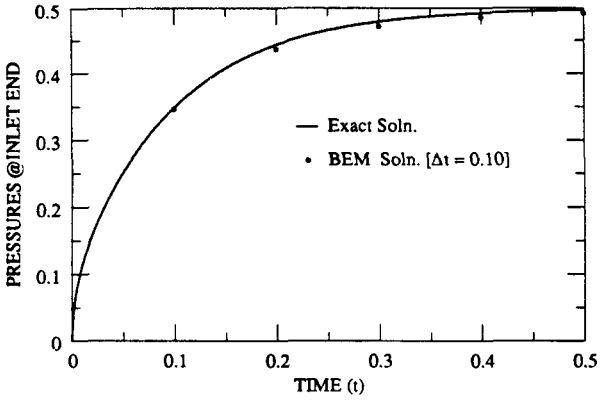


Figure 4. Neumann problem

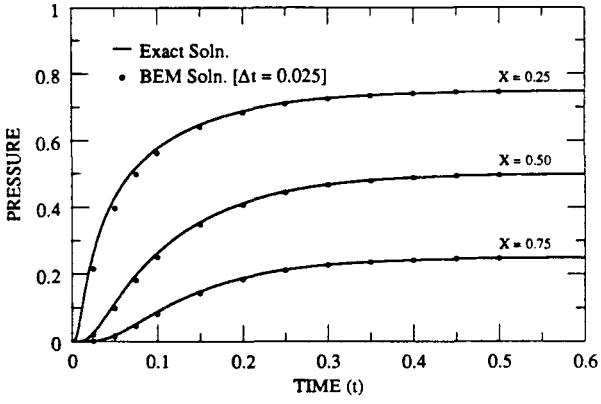


Figure 6. Mixed problem

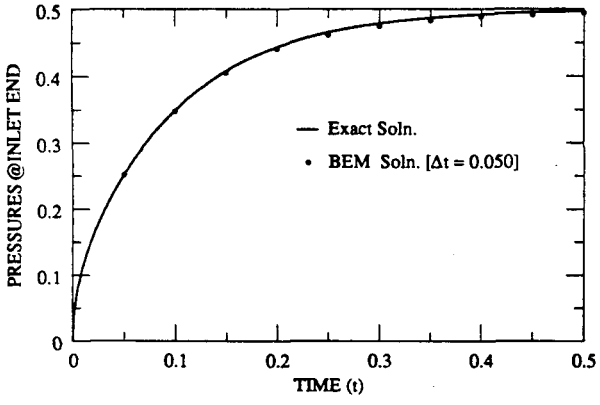


Figure 5. Effect of step size on the solution for Neumann problem

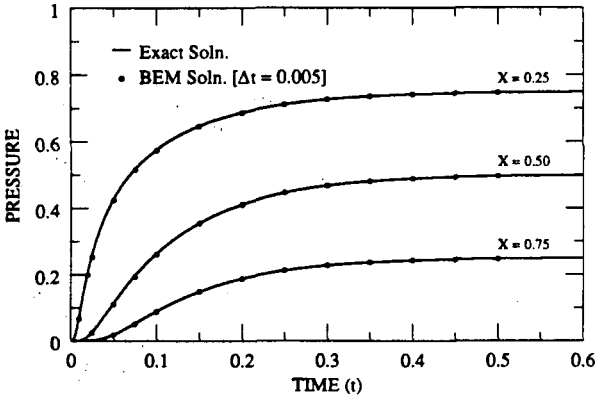


Figure 7. Effect of step size on the solution for mixed problem

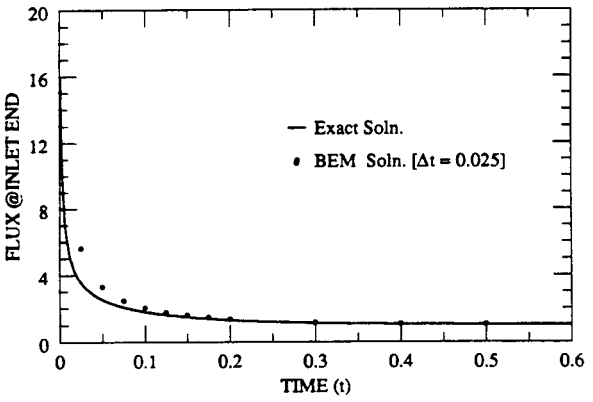


Figure 8. Mixed problem: Matching of flux singularity at the inlet

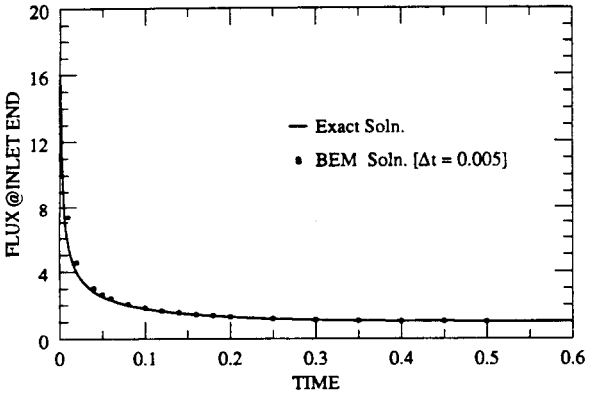


Figure 9. Effect of step size on flux for mixed problem

Problems with Radiation Boundary Conditions

The problem domain remains the same as the previous problems. Two different inner boundary conditions were used. The outer boundary conditions are the same in both the examples considered below. The outer boundary conditions for the two problems are

$$P + \frac{\partial}{\partial n}P(1,y,t) = 0$$

Figure 10 shows the pressure response at the outer boundary with time for the case of a constant pressure inner boundary condition. It is the flux at the inner boundary which has a singular behavior and is difficult to match. With refinement of step sizes we could match the fluxes well at early times. Figure 11 shows the flux at the inner boundary as a function of time, for a step size of 0.005.

Figure 12 shows the pressure response at inner and outer boundaries with time. This is for the case of a prescribed flux inner boundary condition and radiation outer boundary condition. The BEM solution matches the analytical solution very closely.

These problems are very simple but they do show the efficacy of the method which can now be used on complicated and odd shaped domains with accuracy.

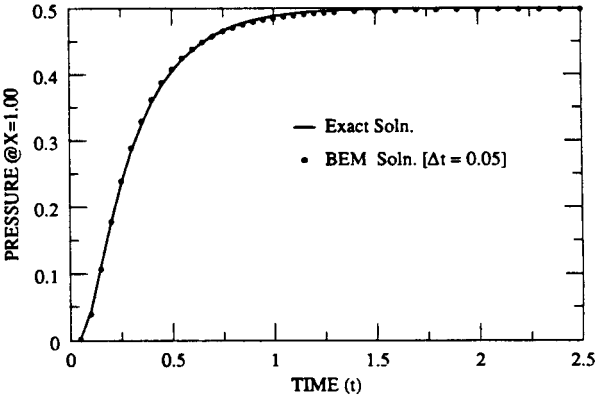


Figure 10. Constant pressure inner boundary and radiation outer boundary

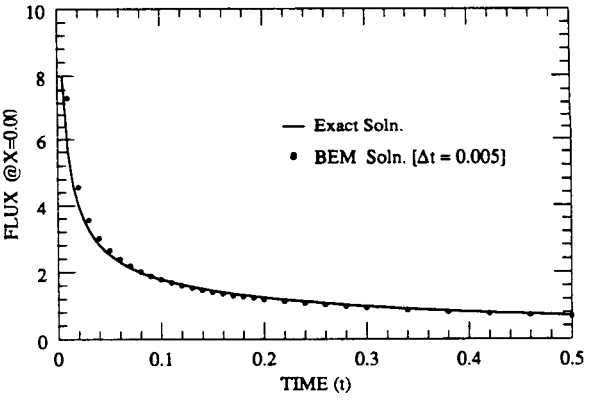


Figure 11. Matching fluxes for constant pressure IBC and radiation OBC

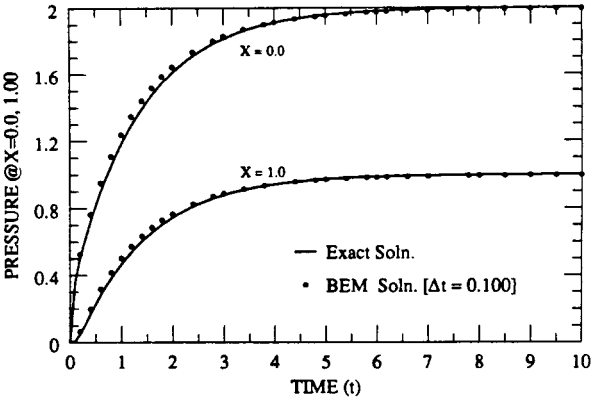


Figure 12. Constant flux inner boundary and radiation outer boundary

CONCLUSIONS

Problems governed by diffusivity equation in odd shaped boundaries can be solved efficiently and accurately by the Boundary Element Method. A slightly different formulation compared to other authors has been discussed and implemented. Simple problems with analytical solutions have been tested to check the validity of the method. All combinations of the three boundary conditions *viz;* Dirichlet, Neumann and Radiation (mixed) have been used. The solution methodology holds promise for solution of problems leading to pressure transient testing for single phase flow.

ACKNOWLEDGMENTS

Financial support was provided by the Stanford Geothermal Program, DOE Contract No. DE-AS07-84ID12529 and by Stanford University.

REFERENCES

Abramowitz, M., and Stegun, I. A., *Handbook of Mathematical Functions*, 1964.

Aziz, K., and Settari, A., *Petroleum Reservoir Simulation*, Pub. Elsevier, 1979.

Brebbia, C. A., "Weighted Residual Formulation of Approximate Methods", *Boundary Element Methods in Computer Aided Engineering*, Ed. Brebbia, C. A., 1984.

Carslaw, H. S., and Jaegar, J. C., *Conduction of Heat in Solids*, 1959.

Connor, J. J., and Brebbia, C. A., "Boundary Element Methods", *Boundary Element Methods in Computer Aided Engineering*, Ed. Brebbia C. A., 1984.

Greenberg, M. D., *Application of Green's Functions in Science and Engineering*, Pub. Prentice Hall, Inc., 1971.

Lafe, O. E., Liggett, J. A., and Liu, P. L-F, " BIEM Solutions to Combinations of Leaky, Layered, Confined, Unconfined, Nonisotropic Aquifers, *WRR*, 1970.

Ligget, J. A., and Liu, Phillip L-F, *The Boundary Integral Equation Method for Porous Media Flow*, Pub. George Allen & Unwin, 1983.

Liggett, J. A., and Liu, Phillip L-F, "Unsteady Flow in Confined Aquifers : A Comparison of Two Boundary Integral Methods", *WRR*, Aug. 1984.

Masukawa, J, and Horne, R.N., "The Application of the Boundary Intetgral Method to Immiscible Displacement Problems", *SPE Paper #15136*, April, 1986.

Morse, P. M., and Feshbach, H., *Methods of Theoretical Physics*, Pub. McGraw Hill, 1953.

Numbere, D.T., and Tiab, D., "An Improved Streamline Generating Technique Using Boundary (Integral) Element Method", *SPE Paper #15135*, April, 1986.

Pina, H. L. G., "Time Dependent Potential Problems", *Boundary Element Methods in Computer Aided Engineering*, Ed. Brebbia, C. A., 1984.

Rizzo, F. J., and Shippy, D. J., "A Method of Solution for Certain Problems in Transient Heat Conduction", *AIAA J*, 1970.

Taigbenu, A. E., and Liggett, J. A., "Boundary Element Calculations of Diffusion Equation", *J. of Eng. Mech, Division* of ASCE, April, 1985.

Wrobel, L. C., and Brebbia, C., "Time Dependent Potential Problems", *Progress in Boundary Element Methods, vol.* 1, Ed. Brebbia, C.A., 1981.

Zauderer, E., *Partial Differential Equations in Applied Mathematics*, Pub. Wiley-Interscience, 1983.

APPENDIX-A

We evaluate here the singular integral obtained when the collocation point is on the same boundary element as the field point.

$$I = \int_0^c E_1(\alpha x^2)\, dx \tag{A1}$$

where,

$$\alpha = \frac{1}{4t} \tag{A2}$$

Integrating once by parts, we obtain

$$I = x\, E_1(\alpha x^2)\Big|_0^c - \int_0^c \frac{d}{dx}\left[E_1(\alpha x^2)\right] dx \tag{A3}$$

$$= cE_1(\alpha c^2) - xE_1(\alpha x^2)\Big|_0 + 2\int_0^c \exp(-\alpha x^2)\, dx \tag{A4}$$

Since $E_1(\alpha x^2)$ as $x \to 0$ grows logarithmically and hence grows slower than any polynomial, thus $x \to 0$ faster than E_1 grows.

$$\Rightarrow \qquad x\, E_1(\alpha x^2)\Big|_0 \to 0 \ \ as \ \ x \to 0 \tag{A5}$$

thus,

$$\int_0^c E_1(\alpha x^2)\, dx = cE_1(\alpha c^2) + \sqrt{\frac{\pi}{\alpha}}\, erf(\sqrt{\alpha} c) \tag{A6}$$

where

$$erf(z) = \frac{2}{\sqrt{\pi}} \int_0^z \exp(-x^2)\, dx \tag{A7}$$

For large arguments $E_1(\alpha c^2)$ goes to zero asymptotically and $erf(\sqrt{\alpha} c)$ goes to 1 asymptotically. Thus a very stable and easy to evaluate form is obtained.

PROCEEDINGS, Thirteenth Workshop on Geothermal Reservoir Engineering
Stanford University, Stanford, California, January 19-21, 1988
SGP-TR-113

ANALYSIS OF INTERNAL WELLBORE FLOW

M. Ripperda and G.S. Bodvarsson

Earth Sciences Division, Lawrence Berkeley Laboratory
University of California, Berkeley, California 94720

ABSTRACT

Most two-phase geothermal wells are located in fractured rocks and intersect a few major feedzones. It is well known that internal wellbore flow between feedzones often occurs during warmup or pressure recovery periods. The internal flow can occur even when the reservoir is initially in pressure equilibrium, because of the different phase composition that develops within the wellbore. Internal flow can cause large apparent pressure drawdowns and significantly affect pressure and temperature surveys as well as pressure buildup tests. This paper presents an analytic method for using static pressure surveys to calculate internal flowrates between two zones when the reservoir characteristics are known. Conversely, the transmissivity of the feedzone with the lowest transmissivity can be calculated from measurements of internal flowrates and wellbore pressures.

INTRODUCTION

Internal wellbore flow occurs in many systems with multiple feedzones. In geothermal wells, relatively small pressure differences may cause substantial flows within a wellbore. Measurements of internal flowrates for wells in the Ngawha and Wairakei fields in New Zealand have ranged from several kg/s to 80 kg/s (Grant et al., 1983). This has significant effects on the interpretation of pressure transient tests and wellbore pressure and temperature profiles. The characteristics of internal flow on static pressure and temperature surveys have been well documented by several authors, including Grant et al. (1983) and Haukwa and O'Sullivan (1982). Bixley and Grant (1980) discussed a method for calculating internal flowrates during injection tests and using the results to estimate pressures and productivities of the individual feedzones.

This paper discusses an alternative method to calculate internal flow rates between the feedzones, using shut in pressure profiles. Under certain conditions, this method may also be used to calculate transmissivities.

CAUSES OF INTERNAL FLOW

A shut-in wellbore will obviously transmit fluids between feedzones that have different pressure potentials. However, internal wellbore flow often occurs even when the reservoir is initially in vertical pressure equilibrium. This happens after either drilling or production, when the density of the fluid in the wellbore does not match the reservoir fluid density at both feedzones. After drilling, the wellbore is filled with cold fluid, which has a much higher pressure gradient than the reservoir fluid. When circulation is stopped, the fluid level will fall so that pressures are in equilibrium at the pivot point (Fig. 1). If the pivot point is located somewhere between the two feedzones, then the reservoir pressure is higher than the wellbore pressure at the top feedzone and lower at the bottom feedzone. This causes the downflow as shown in Figure 1. If the fluids in the top feedzone are cooler and denser than the fluids in the bottom feedzone, then these flow conditions may last for a long period of time.

Upflow will occur when the conditions are similar to those shown in Figure 2. During production, the pressure in the wellbore is lower than the reservoir pressure at both feedzones. After the well is shut in, the pressure gradient in the wellbore will be smaller than the reservoir pressure gradient if the fluids in the bottom layer are hotter and less dense than the fluids in the top layer. A continued influx of hotter fluids from the bottom feedzone causes large apparent pressure drawdowns. Thus, the measured pressure conditions within the wellbore provide little or no information about in-situ pressures when crossflow occurs. However, the rate of crossflow and the relative strengths of the two aquifers can be estimated from the wellbore pressure measurements.

CALCULATION OF INTERNAL FLOWRATES

Figure 4 shows an idealized system with internal upflow. Because there is generally very little heat loss within the wellbore, the fluid entering the top feedzone has a temperature T_2. The rock and fluid properties are as shown. The radial, transient pressure equations can be written for each layer as

$$\frac{\delta^2 P_1}{\delta r^2} + \frac{1}{r}\frac{\delta P_1}{\delta r} = \left[\frac{\phi_1 \mu_1 c_1}{k_1}\right]\frac{\delta P_1}{\delta t} \qquad (1)$$

$$\frac{\delta^2 P_2}{\delta r^2} + \frac{1}{r}\frac{\delta P_1}{\delta r} = \left[\frac{\phi_2 \mu_2 c_1}{k_1}\right]\frac{\delta P_2}{\delta t} \qquad (2)$$

The initial conditions and outer boundary conditions for both layers are

$$P_1(r,0) = P_{1_i} \tag{3a}$$

$$P_1(\infty,t) = P_{1_i} \tag{3b}$$

$$P_2(r,0) = P_{2_i} \tag{3c}$$

$$P_2(\infty,t) = P_{2_i} \tag{3d}$$

The inner boundary conditions are slightly more complicated because the pressures will be changing with time. But we do know that flow out of one layer must equal flow into the second layer if wellbore storage is negligible. Thus,

$$\frac{k_1 h_1}{\mu_1} \frac{\delta P_1(r_w,t)}{\delta r} = -\frac{k_2 h_2}{\mu_2} \frac{\delta P_2(r_w,t)}{\delta r} \tag{4}$$

Also, the relationship between wellbore pressures for layers one and two, $P_1(r_w)$ and $P_2(r_w)$, can be written as

$$P_2(r_w,t) - P_1(r_w,t) = P^* \tag{5}$$

where $P_2(r_w,t)$ and $P_1(r_w,t)$ are taken directly from the wellbore pressure surveys. Although the wellbore pressures change with time, P^* is usually fairly constant.

The problem may be put in dimensionless form by introducing the following parameters:

$$\zeta = \left[\frac{k_1 \phi_2 \mu_2 c_2}{k_2 \phi_1 \mu_1 c_1}\right]^{1/2} \tag{6a}$$

$$\eta = \frac{k_2 h_2 \mu_1}{k_1 h_1 \mu_2} \tag{6b}$$

$$r_D = \frac{r}{r_w} \tag{6c}$$

$$t_D = \frac{k_1 t}{\phi_1 \mu_1 c_1 r_w^2} \tag{6d}$$

$$P_{D_1} = \frac{P_{1_i} - P_1}{P_{2_i} - P_{1_i}} \tag{6e}$$

$$P_{D_2} = \frac{P_{2_i} - P_2}{P_{2_i} - P_{1_i}} \tag{6f}$$

$$P_D^* = \frac{(P_{2_i} - P_{1_i}) - P^*}{P_{2_i} - P_{1_i}} \tag{6g}$$

Solutions to the above equations in the Laplace domain are

$$\bar{P}_{D_1} = -\frac{(\frac{1}{s})P_D^* K_0(r_D\sqrt{s})}{\left[\frac{K_1(\sqrt{s})K_0(\zeta\sqrt{s})}{\zeta\eta K_1(\zeta\sqrt{s})} + K_0(\sqrt{s})\right]} \tag{7}$$

$$\bar{P}_{D_2} = \frac{(\frac{1}{s})P_D^* \frac{1}{\zeta\eta} \frac{K_1(\sqrt{s})}{K_1(\zeta\sqrt{s})} K_0(r_D\sqrt{s})}{\left[\frac{K_1(\sqrt{s})K_0(\zeta\sqrt{s})}{\zeta\eta K_1(\zeta\sqrt{s})} + K_0(\sqrt{s})\right]} \tag{8}$$

The flowrate is then

$$\bar{q}_D = \frac{\delta \bar{P}_{D_1}}{\delta r_D} = \eta \frac{\delta \bar{P}_{D_2}}{\delta r_D} \tag{9}$$

The above expressions may easily be inverted using numerical techniques such as the Stehfast algorithm. The actual flowrate is then

$$q = 2\pi\rho \frac{k_1 h_1}{\mu_1} (P_{1_i} - P_1(r_w))\, q_D \tag{10}$$

where q_D represents the numerical Laplace inversion of equation (9).

RESULTS

The factors that strongly affect the internal well flowrate are the transmissivities and storage properties of the two zones. Increasing the transmissivity of both layers has a direct effect on the flowrate, as expected. When both layers have single-phase liquid, the initial flowrate ranges from approximately 10 to 200 kg/s for transmissivities ranging from 1 to 30 Dm (Fig. 4). After 3 years, the flowrates are still significant and vary between about 2 and 50 kg/s, respectively. The effects of changing the compressibility (phase composition) and transmissivity ratio of the two aquifers are shown in Figures 5 and 6. For the results shown in these figures, the transmissivity of layer 1 was held constant at 1 Dm, while the transmissivity of layer 2 was varied. Both figures show that the internal flowrate is strongly controlled by the feedzone with the lowest transmissivity. In Figure 5, for example, increasing the transmissivity of layer 2 by an order of magnitude (from $(kh)_1/(kh)_2$ = 0.1 to $(kh)_1/(kh)_2$ = 0.01) has almost no effect. However, when the transmissivity of layer 2 is less than layer 1, increasing its value from $(kh)_1/(kh)_2$ = 100 to $(kh)_1/(kh)_2$ = 10 increases the flowrate by a factor of 3. When both layers have high compressibility, two-phase fluids (Fig. 6), the initial flowrate is increased by a factor of 3 compared to single-phase conditions (Fig. 5). But the decline is much steeper for the case with high compressibilities, and after 3 years the flowrates are almost equal.

CONCLUSIONS

An analytical model of internal flow between two feedzones has been developed. The equations can be used to calculate the pressure distributions in the two aquifers and the internal flowrates. The flowrates will be higher if the reservoir fluids have a high compressibility (two-phase conditions). The properties of the aquifer with the lowest transmissivity controls the internal flowrate. The predicted flowrates range from about 1 to over 100 kg/s for reasonable reservoir characteristics. This range is similar to flowrates measured in several geothermal fields in New Zealand. The flowrates are predicted to decline by a factor of between 2 and 10 after 3 years, depending primarily on the phase compositions.

REFERENCES

Bixley, P.F. and Grant, M.A., 1981, Evaluation of Pressure-Temperature Profiles in WElls with Multiple Feed Points, *Proceedings, The New Zealand Geothermal Workshop,* Auckland, pp. 121-124.

Grant, M.A., Bixley, P.F., Donaldson, I.G., 1983, Internal Flows in Geothermal Wells: Their Identification and Effect on the Wellbore Temperature and Pressure Profiles, *Society of Petroleum Engineers Journal.*

Haukwa, C.B. and O'Sullivan, M.J., 1982, A Study of Cycling in Geothermal Wells, *Proceedings, The New Zealand Geothermal Workshop,* Auckland, pp. 425-431.

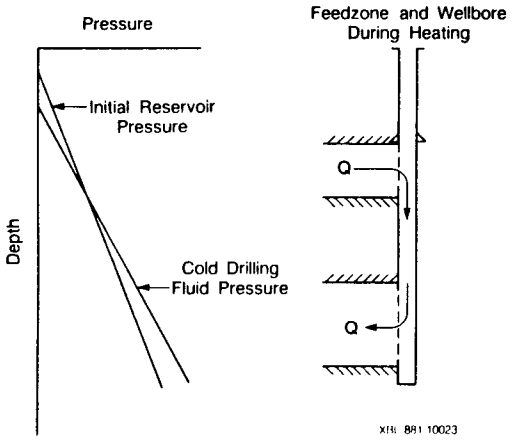


Figure 1. Wellbore pressure and flow conditions during the warmup period after drilling.

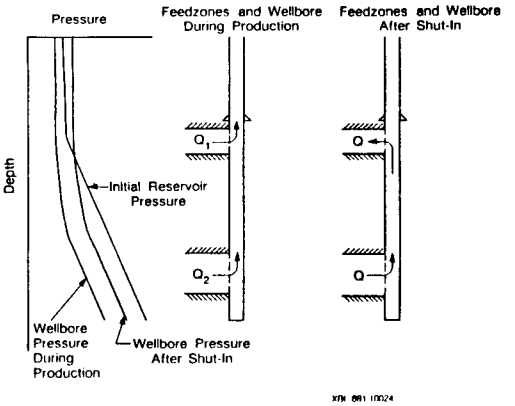


Figure 2. Wellbore pressure and flow conditions during and after production.

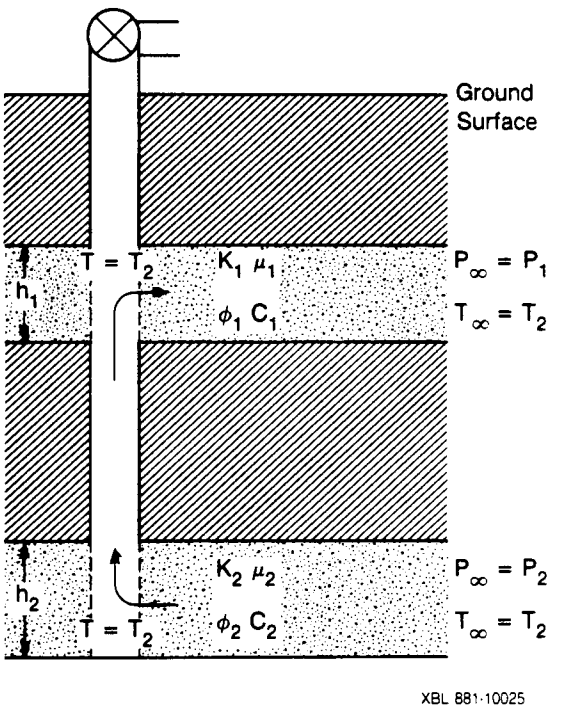


Figure 3. Idealized reservoir with two feedzones used in analytic model.

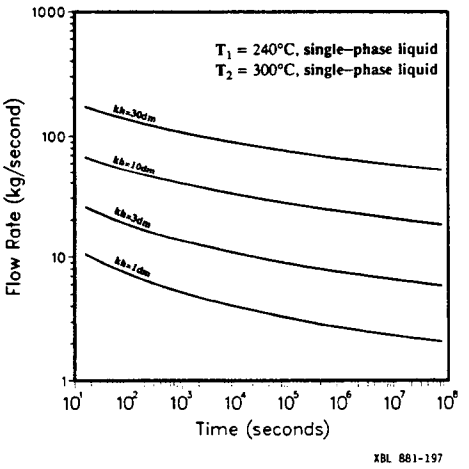
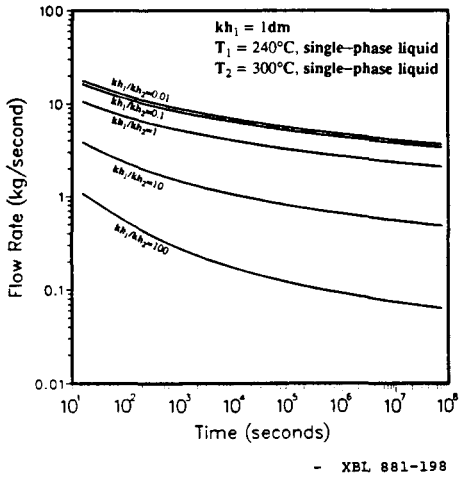
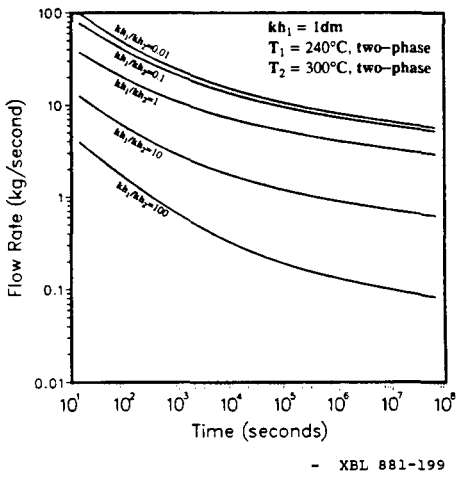


Figure 4. Flowrate versus time for various reservoir transmissivities. The transmissivity of the two feedzones are equal.



- XBL 881-198 -

Figure 5. Flowrates versus time for various ratios of the transmissities between the two feedzones. The reservoir fluid is single phase liquid in both layers.



- XBL 881-199 -

Figure 6. Flowrates versus time for various ratios of the transmissities between the two feedzones. The reservoir fluid is two-phase in both layers.

PROCEEDINGS, Thirteenth Workshop on Geothermal Reservoir Engineering
Stanford University, Stanford, California, January 19-21, 1988

DUAL PERMEABILITY MODELING OF SOLUTE TRANSPORT IN DISCRETE FRACTURE SYSTEMS

John D. Miller and Tom M. Clemo

Idaho National Engineering Laboratory
P.O. Box 1625
Idaho Falls, ID 83415

ABSTRACT

The flow and transport properties of a dual permeability model have been evaluated in a form which allows discrete simulation of the complete range of fracture size in a series of successively larger models up to reservoir scale.

In matrix dual permeability modeling, the flow and transport processes occur in both matrix cells and the superimposed discrete fractures. The matrix cell models use Darcian flow and Fickian transport relationships to represent processes occurring in the numerous small channels which make up the micro-structure of the rock. The macro-fractures are modeled discretely up to the size of the multi-cell model. If the overall properties of the multi-cell model can be determined they can be used to represent this model as a single cell in a larger model along with the next larger set of fractures. Since its cells represent the rock matrix and the distributed effect of small fractures, the larger model is termed a distributed or representative element dual permeability model. Successively larger models then allow simulation up to the scale of the reservoir.

An initial step in this development has been achieved by numerically determining the non-Darcian, non-Fickian properties of a two-dimensional model composed of Darcian and Fickian matrix cells and a discrete fracture system. The porous matrix properties were assumed to be those measured in a visibly unfractured core. The discrete fracture system was a realization of the smaller fractures in a stochastic system. The FRACSL code was used to determine flow coefficients and residence time distributions for the porous matrix combined with each of five different realizations of the stochastic fracture system. Reservoir scale simulation could be achieved with reasonable computer resources and with fidelity to the fractured media by incorporating this type of results in successively larger models.

INTRODUCTION

The modeling of transport in fractured porous media has been the subject of considerable recent research in the areas of petroleum recovery, geothermal energy and waste management. These studies have recognized the limitations of porous media approaches in representing the physical nature of the media and, consequently, in modeling observed flow and transport characteristics. Recent development has been enhanced by advances in computer size and speed and in improved borehole techniques for fracture characterization.

Models developed for this application may be categorized as porous equivalent, dual porosity, discrete fracture-without-rock matrix and dual permeability. In the porous media equivalent, zones of high permeability are described by changing conductivity in selected grid cells.

In the dual porosity approach the rock matrix and the fracture system are each represented as a distinct continuum with a distinct head distribution. An intercontinua flow is calculated from the differences in head between the two continua. The fractures are, of necessity, treated as a repeated geometric pattern, such as parallel planes with fixed spacing.

The discrete-fracture-without-rock-matrix models are much closer to the actual fractured-matrix structure. They represent fractures in an impermeable matrix and are valid to the extent that the finer structure which provides the intimate communication with the rock mass is represented.

Dual permeability modeling is the most physically realistic of any of the approaches since the actual continuous distributions of head and concentration are used to relate the flow and transport processes in the fractures and in the rock mass. This void space in the fractured rock mass is divided into three components. A single set of probability

density functions is used to represent the complete range of macro fracture sizes. Faults and fracture zones are of different structural origins and are assumed to be specifically mapped by borehole geophysical techniques. At the other end of the size regime, the microstructure of the rock has a distinct physical origin. Microstructure flow and transport properties are found by direct measurements from cores, bypassing the need for geometric description.

Another advantage of dual permeability modeling is the computational relief provided by the separation of void space into discrete and distributed components. At any model size there are many distinct voids or passages. The smallest of these can be considered uniformly distributed over the model and can therefore be represented in a distributed manner. The properties of these distributed features are found by the numerical techniques given in this paper. Analytic studies of these properties have been given by Clemo (1986, 1987).

FLOW AND TRANSPORT MODELS

Under saturated conditions, each of the dual permeability codes calculates laminar flow in uniform parallel sided fractures from the cubic law (Lamb, 1945):

$$Q = \frac{\rho g}{12\mu} b^3 W \frac{\Delta H}{\Delta L} \qquad (1)$$

where

Q	=	volumetric flow	(L^3/T)
μ	=	viscosity	(M/LT)
ρ	=	density	(M/L^3)
g	=	acceleration of gravity	(L/T^2)
b	=	fracture aperture	(L)
W	=	fracture width	(L)
ΔH	=	head differential	(L)
ΔL	=	fracture length	(L)

In the matrix dual permeability model, matrix flow is calculated from Darcy's Law:

$$Q = kA \frac{\Delta H}{\Delta L} \qquad (2)$$

where

k	=	conductivity	(L/T)
A	=	flow area	(L^2)

This equation is strictly valid only for porous media, i.e., one in which a very large number of small passages of random orientation result in a flow which varies linearly with the head gradient and is the same direction. Transport is calculated by a numerical implementation of the advection-dispersion equation which is based on Fick's Laws. The one-dimensional form of this equation is given by Prickett et al., (1981) as:

$$\frac{\partial C}{\partial t} = \frac{\partial}{\partial x}\left(\frac{D}{R_d}\frac{\partial C}{\partial x}\right) - \frac{v \partial C}{R_d \partial x} \qquad (3)$$

$$D = d_L v + D_m$$

where

C	=	concentration	$(-)$
t	=	time	(T)
D	=	hydrodynamic dispersion coefficient	(L^2/T)
d_L	=	longitudinal dispersivity	(L)
D_m	=	molecular diffusion coefficient	(L^2/T)
v	=	interstitial velocity	(L/T)
R_d	=	retardation factor	$(-)$

and the terms in the concentration equation, from left to right, are accumulation, dispersion and convection.

FRACSL TRANSPORT MODEL

In the FRACSL matrix dual permeability code (Miller et.al., 1987) the advection-dispersion equation is implemented by tracing the movement of imaginary marker particles, each tagged with a specified amount of solute, through the fractures and the "matrix". The advective motion of particles in the matrix follows a second order head distribution. Within a fracture, the particle moves in a direction parallel to the fracture axis with a longitudinal velocity which varies with its distance from the wall according to the Poiseuille velocity profile. The transverse velocity is computed from the fracture-to-matrix flux dictated by the local mass balance.

A diffusive motion, in either host, is computed by a random walk process in which the direction is random and the magnitude is normally distributed with standard deviation equal to the diffusion coefficient.

The hydrodynamic dispersion in the fractures is explicitly defined by the advective motion. Hydrodynamic dispersion in the "matrix" is computed by another random walk process, this time using the dispersion coefficient. Execution times are reduced by the use of higher-order stoichastic models of the transfer between fractures and matrix.

It should again be noted that the random or Fickian diffusion and dispersion in the "matrix" are only appropriate for a porous media or the microstructure of a fractured media, i.e., a multitude of short interconnected passages.

MEDIA TRANSPORT CHARACTERISTICS

The differences in transport characteristics between a fracture, a porous matrix and a fractured-porous matrix were shown by Hull and Clemo (1987) in a study using the FRACSL Code. A two dimensional fractured-porous aquifer (Figure 1) was established in a vertical plane bounded by an injection well and a production well. Two other models provided the same conductivity between the wells but were composed of a single fracture and a porous matrix, respectively. The transport characteristics of the these models were determined by establishing a steady state flow between the two wells, sending a tracer front through the model and measuring the concentration-time (break through) curves at the production well as shown in Figure 2. The single fracture shows the earliest arrival. Diffusion has homogenized concentration gradients across the Poiseuille velocity profile resulting in a near step-like response. The porous matrix response is the slowest, and has the classic sigmoidal porous media characteristic. The fractured-porous matrix response is intermediate in arrival and approximates the rapid early rise and the long tail observed in this media.

Clearly the transport characteristics of the fractured-porous system cannot be represented in a larger scale model by merely increasing the conductivity of a porous media Also, the conductivity in the orthogonal direction would not be found by the same transformation used in the horizontal direction. This departure from Darcian and Fickian behavior is consistent with the physical structure of the fractured-porous matrix since there are straight line paths at all scales.

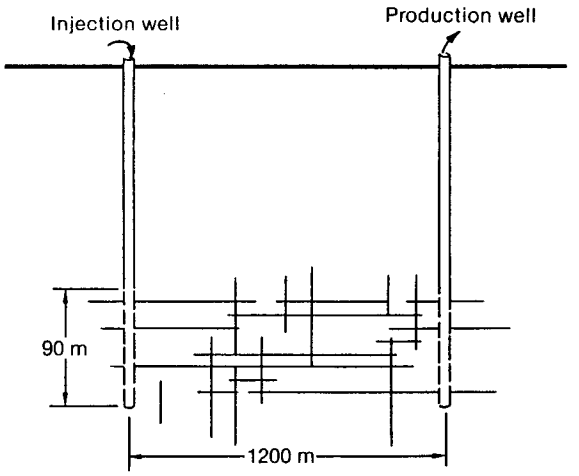
The implication for dual permeability modeling is that the Darcian flow - Fickian transport model is only valid for a cell as long as it only includes the microstructure of the rock, i.e., that approximating a porous media. The remainder of this paper presents the results of a FRACSL study to define the flow and transport characteristics of a cell or representative element which incorporates both porous matrix and discrete fractures. These elements could then be used in a larger scale model with large discrete fractures.

MODEL DESCRIPTION

A fractured porous matrix aquifer has been described in terms of those properties which can be found by coring and borehole characterization. A porous matrix has been combined with five different realizations of a stoichastic fracture system. These five models have been analyzed using the 2-dimensional FRACSL Code. Each model was tested to determine its conductivity and transport characteristics. The form of these characteristics permits a non-Darcian, non-Fickian distributed representation in a larger scale dual permeability model along with large discrete fractures. The distribution of these characteristics is described and interpreted.

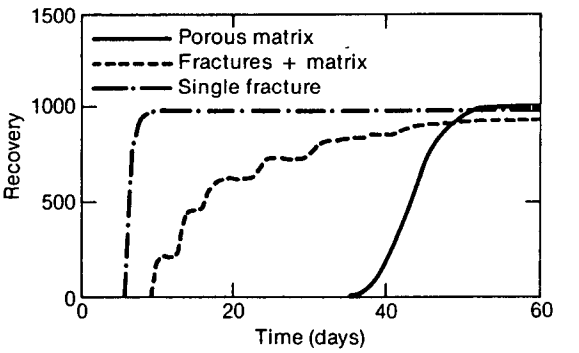
The model is 10 m square by 0.305 m thick and is divided into 100 1 m square blocks. The "matrix" properties given in Table 1 are characteristic of granites and are assumed to be defined by measurements of cores which are visually unfractured.

The fracture system consists of three independent fracture sets which are generally consistent with a geothermal test site in schist and other crystalline rocks from the literature. The fractures in the three sets are vertical, horizontal or 45° diagonally



From Hull and Clemo, 1987 7-1619

Figure 1. Reference Fracture System.



From Hull and Clemo, 1987 7-1611

Figure 2. Breakthrough Curves for Hydraulically Equivalent Reservoirs

upwards to the right, respectively. Their lengths are assumed to be exponentially distributed. Fracture centers are distributed throughout the model region following the procedure given by Andersson et al. (1984) and summarized in Figure 3 and the following discussion.

The center position in the direction normal to the fracture orientation is selected randomly over the length of a scanline. The fracture length is then chosen from an exponential distribution. The other coordinate of the fracture center is then chosen as equally likely over the range which will result in the fracture at least touching the model. This treats the subset of interest, i.e., that which lies at least partially within the model. This random process corresponds (Priest and Hudson, 1979) to an exponential distribution of spacing.

Fracture lengths are limited to the maximum values given in the table since longer fractures are to be implemented discretely in the next larger dual permeability model. Fractures shorter than the minimums given in this table cannot be implemented in the subject model and are excluded by modifying the exponential distribution. Fractures are synthesized until the number which intercepts the scanline provide the mean separation appropriate for the set. The mean separation used is not that given in Table 1 for the entire population but is the larger separation for the distribution above the minimum. Fractures larger than the maximum are rejected after selection from the bottom truncated distribution. Apertures are selected from identical exponential distributions for the three sets. While a larger aperture may be postulated for the longer fractures when fresh, it is not clear that the same trend exists after in-filling.

After synthesis each fracture is displaced laterally to the nearest grid node. Each of the ends is then moved to the nearest node. The apertures of multiple synthesized fractures in a particular location are combined under the cube root since they essentially act independently in carrying flow. This process has the effect of eliminating small fractures.

Figure 4 shows one of the five synthesized models. The dominance of the vertical fracture set is clearly evident -- almost every

TABLE 1. MODEL PROPERTIES

Matrix			
Conductivity (x and y)	8.69 E-4 m/day		
Longitudinal dispersivity	.914 m		
Transverse dispersivity	.305 m		
Porosity	1. E-4		
Water, Solute			
Water temperature	121.1°C		
Diffusion coefficient	4.50E-4 m^2/day		
Fractures			
Mean[a] aperture	100 micron		
	Set 1	Set 2	Set 3
Orientation	Vertical	Horizontal	Diagonal
Mean Spacing	.621 m	3.05 m	4.33 m
Mean[a] Length	2.67 m	13.1 m	18.6 m
Maximum Length	10 m	10 m	14.1 m
Minimum Length	.5 m	.5 m	.707 m
Boundary Conditions			
Head differential	3.05 E-4 m		

a. Uncorrelated exponential distributions.

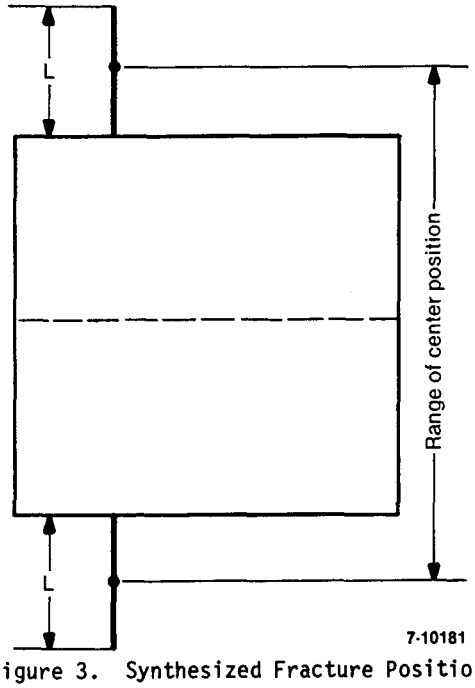
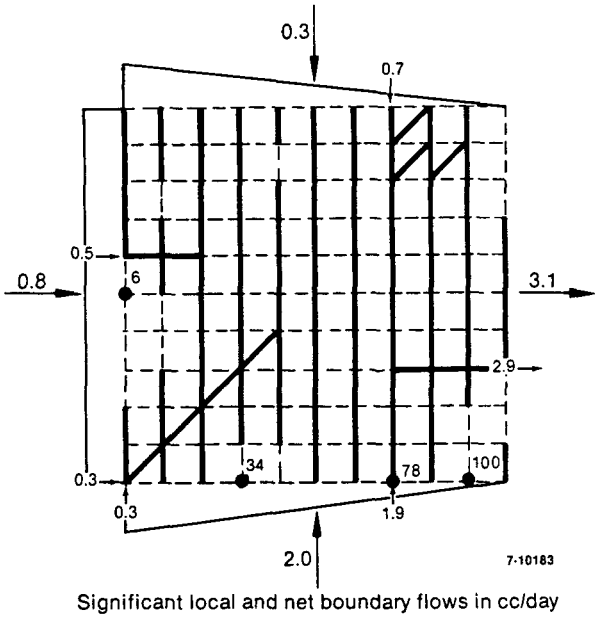


Figure 3. Synthesized Fracture Position



Significant local and net boundary flows in cc/day

Figure 4. Model 5 horizontal gradient flows

possible vertical model fracture location is occupied. Lateral connection, via horizontal or diagonal fractures, is relatively limited. The boundary condition is that presented by Endo (1984). A steady-state linear head gradient is imposed across the entire model, first in the x direction, as shown in Figure 4 and then in the y direction, as shown in Figure 5. Matrix and fracture flow through the model boundary is permitted.

After the flows have been established, a pulse of marker particles is introduced at each boundary node with substantial inflow. Particle exit at the various boundary nodes is monitored and the residence times are recorded.

RESULTS

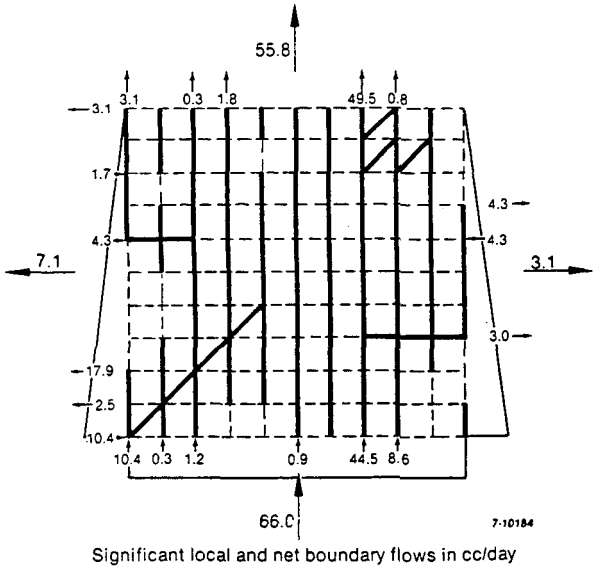
Figures 4 and 5 show the significant flow rates (small figures close to the sketch) at the boundary nodes and the net flow rate through the four edges for the two head gradients in the system previously discussed.

The data again demonstrates the dominance of the vertical fractures. The net flows through the four edges are described by a non-Darcian flow model given as follows and illustrated in Figure 6.

$$Q_i = \sum_{j=1}^{2} g_{ij} \Delta H_j \qquad (4)$$

where

Q_i	=	flow through ith boundary	(L^3/T)
g_{ij}	=	flow coefficient	(L^2/T)
ΔH_j	=	jth head differential	(L)



Significant local and net boundary flows in cc/day

Figure 5. Vertical gradient flows.

and flows at a model corner are split equally between the two faces. It should be noted that a flow coefficient is given rather than a conductivity since the value is only valid for the specific model size and is not a material property.

The individual flow coefficients are given in Table 2 along with the population mean and standard deviation. The data shows the dominance of vertical flow under most conditions, the greater flow coefficients for a vertical head differential and standard deviations on the order of the means. The mean values of the eight flow coefficients would be used in a large scale dual permeability model along with the appropriate head differentials.

The non-Fickian transport model is given as follows and illustrated in Figure 7.

$$t_x = \frac{z\ DY\ x}{Q_x} \qquad (5)$$

$$t_y = \frac{z\ DX\ y}{Q_y}$$

where

$t_{x,y}$	=	time to reach the x,y boundary	(T)
z	=	model thickness	(L)
DX,DY	=	length of boundary	(L)
x,y	=	distance to boundary	(L)
$Q_{x,y}$	=	boundary flow	(L^3/T)

An iterative process is used to find the distance x,y to the first boundary impacted and the mean boundary flow in the appropriate direction, based on linear interpolation between values on opposite boundaries. The

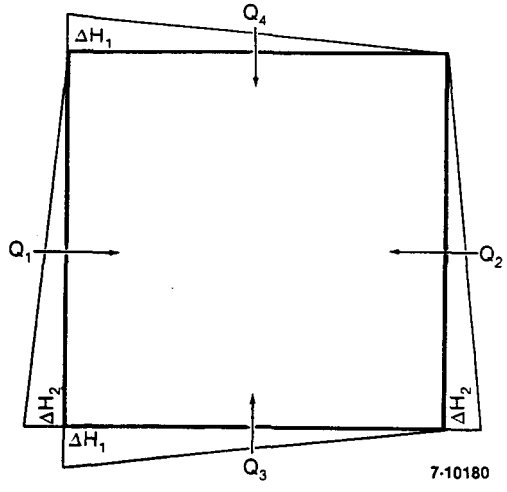


Figure 6. Non-Darcian flow model.

particle trajectories would therefore be consistent with the mass flow calculations and individual impact points would reflect the average flow pattern rather than specific fracture locations which are only valid for a particular realization. This process provides the mean residence time for particular entrance location and head distribution.

The final element of the transport model is the variation of residence time from the mean.

Figure 8 shows the distribution of residence times for five different combinations of model, head differential and injection node.

In each case, 1000 particles were injected at time zero and the exit locations and times recorded. An average exit or residence time was computed at each exit node as the mean of those values without substantial holdup in the matrix. The figure gives histograms of the ratio of residence time to mean residence time for that particular exit node. Since frequency values at ratios beyond the mean are two orders of magnitude smaller than at the mean, the natural logarithm of the frequency has been shown in order to make the small values visible. In each case the majority of residence times occur in a narrow band characteristic of plug flow. A small number are increased by as much as a factor of 55, due to holdup in the matrix.

In usage in a large scale dual permeability model the mean arrival time, for a particular particle entry position, would be calculated from the mean flow coefficients and the appropriate pressure gradients using equations 4 and 5. A weighted mean residence time factor would then be chosen from the residence time factor distribution and multiplied by the mean arrival time.

Additional residence time variation would be introduced in the discrete fracture marker transport algorithm to account for the path variability due to fracture roughness. The extension of the FRACSL marker particle capability to heat transport was initiated during 1987 and is nearly complete. Initial development of 3D version of the dual permeability FRACSL code was reported by Miller and Allman (1986). Development has been limited to the flow portion of the code.

TABLE 2. FLOW COEFFICIENTS - cm^2/day

	HORIZONTAL GRADIENT			
MODEL	BNDRY 1(W)	BNDRY 2(E)	BNDRY 3(S)	BNDRY 4(N)
1	.006E+3	-.012E+3	.090E+3	-.084E+3
2	.005E+3	-.008E+3	0.0	.004E+3
3	1.69E+3	-.006E+3	-1.14E+3	-.543E+3
4	.605E+3	-.370E+3	-.503E+3	.268E+3
5	.026E+3	-.100E+3	.064E+3	.010E+3
MEAN	.466E+3	-.099E+3	-.298E+3	-.069E+3
STD DEV	.731E+3	.158E+3	0.53E+3	.30E+3
STD DEV / MEAN	1.57	1.60	1.78	4.30

	VERTICAL GRADIENT			
MODEL	BNDRY 1(W)	BNDRY 2(E)	BNDRY 3(S)	BNDRY 4(N)
1	-.004E+6	.271E+6	.748E+6	-1.02E+6
2	.001E+6	.026E+6	.124E+6	-.151E+6
3	-.731E+6	.036E+6	2.98E+6	-2.29E+6
4	-1.61E+6	.063E+6	2.63E+6	-1.09E+6
5	-.232E+6	-.102E+6	2.16E+6	-1.83E+6
MEAN	-.515E+6	.059E+6	1.73E+6	-1.28E+6
STD DEV	.680E+6	.134E+6	1.24E+6	0.82E+6
STD DEV / MEAN	1.32	2.27	0.71	0.64

Positive values indicate flows into the model.

CONCLUSIONS

An initial investigation has been made of the non-Darcian flow and non-Fickian transport characteristics of a representative element suitable for use in large scale dual permeability model. The representative element properties were determined for a subscale dual permeability model composed of a porous matrix and a synthesized discrete fracture system. The integration of the resulting simplified representative element model with large scale discrete fractures would permit the application of dual permeability simulation economy through several staged model scales to the ultimate modeling of a complete reservoir.

ACKNOWLEDGMENTS

Funding for this study was provided by the U.S. Department of Energy, Geothermal Injection Technology Program, under contract DE-AC07-76ID01570.

REFERENCES

Andersson, J., A. M. Shapiro, and J. Bear, "A Stochastic Model of a Fractured Rock Conditioned by Measured Information," Water Resources Research, 20, 1, January 1984, pp. 79-88.

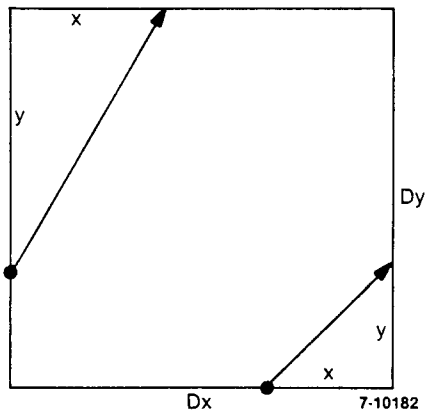


Figure 7. Non-Fickian transport model.

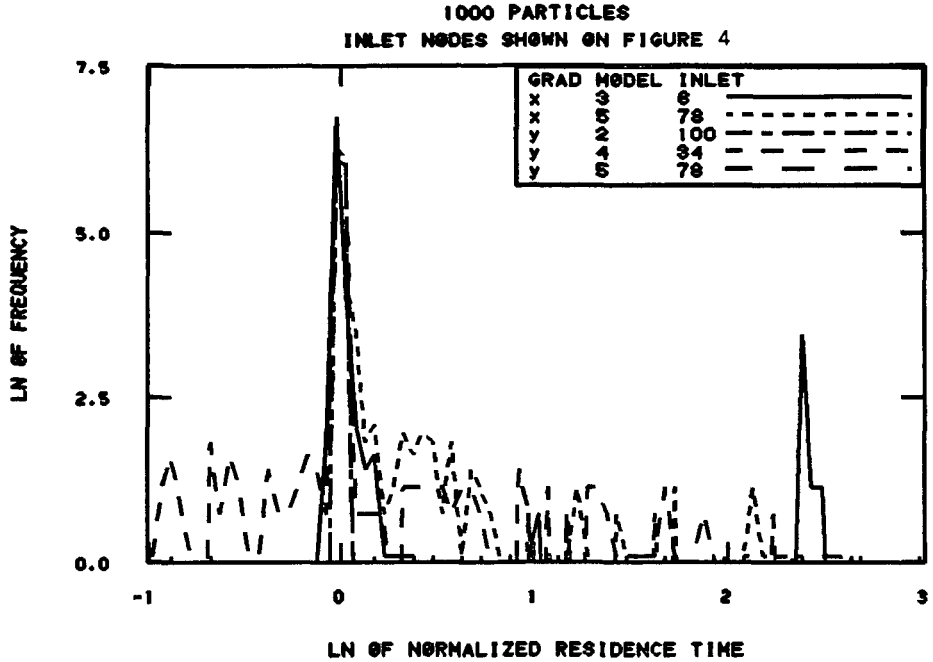


Figure 8. Residence Time Distributions.

Clemo, T. M., Representative Element Modeling of Fracture Systems Based on Stochastic Analysis, Proceedings: Eleventh Workshop on Geothermal Reservoir Engineering, Stanford University, SGP-TR-93, Stanford, CA, pp. 71-76, 1986.

Clemo, T. M., Representative Elements: A Step to Large-Scale Fracture System Simulation, Proceedings: DOE/AECL '87 Conference on Geostatistical, Sensitivity and Uncertainty Methods for Ground Water Flow and Radionuclide Transport Modeling, San Francisco, September, 1987.

Endo, H. K., Mechanical Transport in Two-Dimensional Networks of Fractures, Lawrence Berkeley Laboratory LBL-17491, 1984.

Hudson, J. A. and S. D. Priest, Discontinuities and Rock Mass Geometry, Int. J. Rock Mech. Min. Sci. and Geomech. Abstr. V.16, pp. 339-362, 1979.

Hull, L. C. and T. M. Clemo, Sensitivity Analysis of Dual-Permeability Systems, Proceedings: Twelfth Workshop on Geothermal Reservoir Engineering, Stanford University, 1987.

Lamb, H., Hydrodynamics, Dover Publications, New York, 1945.

Miller, J. D., and D. W. Allman, Dual-Permeability Modeling of Flow in a Fractured Geothermal Reservoir, Proceedings: Eleventh Workshop on Geothermal Reservoir Engineering, Stanford University, SGP-TR-93, Stanford University, CA, pp. 77-84, 1986.

Miller, J. D., T. M. Clemo, and L. C. Hull, FRACSL User's Manual, EG&G Idaho ST-ES-06-87, 1987.

Prickett, T. A., T. G. Naymik, and C. G. Lonnquist, A "Random-Walk" Solute Transport Model for Selected Groundwater Quality Evaluations. Illinois Department of Energy and Natural Resources, 1981.

PROCEEDINGS, Thirteenth Workshop on Geothermal Reservoir Engineering
Stanford University, Stanford, California, January 19-21, 1988
SGP-TR-113

TRACER FLOW MODEL FOR NATURALLY FRACTURED GEOTHERMAL RESERVOIRS

Jetzabeth Ramírez
Jesús Rivera and
Fernando Rodríguez
Universidad Nacional Autónoma de México

ABSTRACT

The model proposed has been developed to study the flow of tracers through naturally fractured geothermal reservoirs. The reservoir is treated as being composed of two regions: a mobil region where diffusion and convection take place and a stagnant or immobile region where only diffusion and adsorption are allowed.

Solutions to the basic equations in the Laplace space were derived for tracer injection and were numerically inverted using the Stehfest algorithm. Eventhough numerical dispersion is present in these solutions, starting at moderate dimensionless time values, a definite trend was found as to infer the behavior of the system under different flow conditions. For practical purpouses, it was found that the size of the matrix blocks does not seem to affect the tracer concentration response and the solution became equivalent to that previously presented by Tang et al. Under these conditions, the behavior of the system can be described by two dimensionless parameters: the Peclet number for the fractures, P_{e1}, and a parameter α ($\alpha = \xi \sqrt{P_{e2}}$), where ξ is $\xi = \phi_e D_e/v(w-\delta)$ and P_{e2} is the Peclet number for the matrix. Tracer response for spike injection was also derived in this work. A limiting analytical solution was found for the case of α approaching zero and a given P_{e1}, which corresponds to the case of a homogeneous system. It is shown that this limiting solution is valid for $\alpha < 10^{-2}$. For the case of continuous injection this solution reduces to that previously presented by Coats and Smith. For the spike solution it was found that the breakthrough time for maximum tracer concentration is directly related to the dimensionless group $\frac{\sqrt{9+X_D^2 P_{e1}^2}-3}{P_{e1}}$. Therefore it is possible to obtain the value of P_{e1} or X_D. A set of graphs of dimensionless concentration in the fracture vs. dimensionless time for tracer response were developed. It was found that if P_{e1} is held constant while α is changing, the limiting solution becomes a limiting curve for a family of curves in a plot of C_D vs t_D. In this graph P_{e1} fixes the range in which the family of curves evolves. It was also found that the breakthrough time for a given concentration is a strong function of α.

INTRODUCTION

Reinjection of separated hot brine back into the geothermal reservoir can be considered as a promising reservoir pressure maintenance technique. In addition to this, secondary heat mining from the reservoir seems to be desirable. However, several field experiences in the past years indicate that unless careful and detailled studies on the selection of the reinjection-production pattern are made, adverse effects such as early thermal breakthrough can result (Horne, 1982). Therefore, before a reinjection project could be implemented, a proper reservoir characterization should be given a major role in designing the project.

Geothermal reservoirs are highly-fractured, complex systems, which require the use of sophisticated techniques in order to be properly characterized. In addition to well testing, tracer flow interpretation techniques provide the means to obtain basic reservoir parameters, as well as the connectivity between several regions of the reservoir and a good estimation of transit times of injected fluids. Most interpretation models published to describe tracer flow through both aquifers and oil reservoirs cannot be directly applied to geothermal reservoirs, because they treat the flow system as

a homogeneous porous medium, which does not correspond to the case of most geothermal fields. Most of the models for geothermal reservoirs published to date provide only qualitative estimation of reservoir parameters (Fossum, 1983, Tester et al, 1982, Jensen, 1983) and only a few of them allow quantitative determination of these parameters (Walkup and Horne, 1985, Tang et al., 1981).

In this study a fractured, two flow region model was developed to quantitatively determine basic geothermal reservoir parameters from tracer return curves. This model takes into account the main mass transport mechanisms that take place in the reservoir when a tracer is flowing under actual reservoir conditions. In spite of this, the model can still be considered as simpler than other published models (Walkup and Horne, 1985), since it requires only one numerical inversion in order to bring to real space the analytical solution for the concentration profile, which was written in Laplace's Space. It is also shown that under certain conditions, the fractured system can be properly characterized by a minimum of two fitting parameters, which compare favorable with four or five fitting parameters required by other published models.

MODEL DESCRIPTION

The model proposed in this work is actually an extension of that previously presented (Rivera et al., 1987) at the Eleventh Workshop on Geothermal Reservoir Engineering. Dimensionless parameters were redefined in order to simplify the solution to the model and also to eliminate some numerical dispersion that was present in the solution to the former model. In this work the characteristc length was taken as the distance from the injection point to that in which the concentration profile has to be calculated.

The proposed model is shown in Fig. 1. The fractured heterogeneous medium is represented by means of a system of equally spaced parallel fractures alternated with porous blocks. As shown in Fig. 1, this system is made of two connected regions; a mobile region constituted by the fracture itself, where diffusion and convection processes are taking place and an immobile region where only diffusion and adsorption are allowed. Connecting both regions there is a very thin, stagnant fluid layer of thickness δ, which acts as a resistance to mass transfer from the mobile region to the immobile one. For a more detailed description of the model the reader should refer elsewhere (Ramírez, 1987, Rivera et al., 1987). The idea of representing the flow system by means of two interconnected regions has been used in the past by several anthors (Deans, 1963, Walkup and Horne, 1985, Maloszewski and Zuber, 1985, among others).

The governing equations of the model are as follows:

a) For the mobile region:

$$D_m \frac{\partial^2 C_m}{\partial x^2} - V_m \frac{\partial C_m}{\partial x} - \lambda C_m - \frac{\phi_e}{w-\delta} D \frac{\partial C_e}{\partial y}\bigg|_{(w-\delta)} - \frac{\partial C_m}{\partial t} = 0 \qquad ...(1)$$

b) For the immobile region:

$$\frac{D_e}{1 + \frac{\rho k (1-\phi_e)}{\phi_e}} \frac{\partial^2 C_e}{\partial y^2} - \lambda C_e - \frac{\partial C_e}{\partial t} = 0 \qquad ...(2)$$

The main assumptions for development of the model are the following: a) no production by reaction of the chemical species within the control volume; b) continuous injection of tracer into the fracture system; c) tracer transport in the fractures is due to diffusion and convection; d) tracer distribution across the fracture width can be assumed constant due to efficient transverse diffusion and dispersion; e) constant density; f) in the immobile region only diffusion in the y-direction is important; g) reversible adsorption with a linear adsorption isotherm is taking place.

In dimensionless form, eqs. (1) and (2) can be expressed as follows:

$$\frac{1}{P_{e1}} \frac{\partial^2 C_{D1}}{\partial x_D^2} - \frac{\partial C_{D1}}{\partial x_D} - \gamma C_{D1} + \xi \frac{\partial C_{D2}}{\partial y_D}\bigg|_{\frac{w-\delta}{L}} - \frac{\partial C_{D1}}{\partial t_D} = 0 \qquad ...(3)$$

$$\frac{R}{P_{e2}} \frac{\partial^2 C_{D2}}{\partial y_D^2} - \gamma C_{D2} - \frac{\partial C_{D2}}{\partial t_D} = 0 \qquad ...(4)$$

where:

$$P_{e1} = \frac{V_m L}{D_m} \qquad \ldots(5)$$

$$P_{e2} = \frac{V_m L}{D_e} \qquad \ldots(6)$$

$$\xi = \frac{\phi_e D_e}{V_m (w-\delta)} \qquad \ldots(7)$$

$$\gamma = \frac{L\lambda}{V_m} \qquad \ldots(8)$$

$$R = \frac{\phi_e}{\phi_e + \rho k (1-\phi_e)} \qquad \ldots(9)$$

The initial and boundary conditions are as follows:

$$C_{D1}(x_D, 0) = 0 \qquad \ldots(10)$$

$$C_{D2}(x_D, y_D, 0) = 0 \qquad \ldots(11)$$

$$C_{D1}(0, t_D) = 1 \qquad \ldots(12)$$

$$C_{D1}(\infty, t_D) = 0 \qquad \ldots(13)$$

$$C_{D2}\left(x_D, \frac{w-\delta}{L}, t_D\right) = C_{D1}(x_D, t_D) \qquad \ldots(14)$$

$$\left.\frac{\partial C_{D2}}{\partial y_D}\right|_{\left(x_D, \frac{E}{2L}, t_D\right)} = 0 \qquad \ldots(15)$$

where:

$$C_{D1} = \frac{C_m - C_i}{C_o - C_i} \qquad \ldots(16)$$

$$C_{D2} = \frac{C_e - C_i}{C_o - C_i} \qquad \ldots(17)$$

$$x_D = \frac{x}{L} \qquad \ldots(18)$$

$$y_D = \frac{y}{L} \qquad \ldots(19)$$

$$t_D = \frac{V_m t}{L} \qquad \ldots(20)$$

Equations (3) and (4) can be solved by means of the Laplace's transform. Solution for concentration distribution in the mobile and immobile regions in Laplace's space are as follows:

$$\bar{C}_{D1} = \frac{C_o}{s} \exp\left\{\frac{P_{e1} x_D}{2}\left[1 - \sqrt{1 + \frac{4}{P_{e1}}(s + \gamma + \alpha\sqrt{\frac{s+\gamma}{R}}\tanh(a_1)}\right]\right\} \qquad \ldots(21)$$

$$\bar{C}_{D2} = \left\{\frac{\exp[-m_1(\frac{E}{L} - y_D)] + \exp(-m_1 y_D)}{\exp[-m_1(\frac{E-w+\delta}{L})] + \exp[-m_1(\frac{w-\delta}{L})]}\right\} \bar{C}_{D1} \qquad \ldots(22)$$

where:

$$m_1 = \sqrt{\frac{P_{e2}}{R}(s+\gamma)} \qquad \ldots(23)$$

$$a_1 = \frac{m_1(E - 2w + 2\delta)}{2L} \qquad \ldots(24)$$

$$\alpha = \xi\sqrt{P_{e2}} \qquad \ldots(25)$$

A particular case of eq.(21) results when α as defined by eq.(25) above becomes very small. In a given situation, this can be produced by either one of the following factors or any combination of them: the porosity or the diffusion coefficient for the immobile region are very small, or the velocity in the mobile region is very large. In this case, the immobile region will behave as if it were impermeable, so that only one flow region will contribute to any change in the tracer concentration. Under these conditions, eq.(21) becomes:

$$\bar{C}_{D1} = \frac{1}{s}\exp\left[\frac{x_D P_{e1}}{2}\right]\exp\left[-x_D\sqrt{\frac{P_{e1}^2}{4} + P_{e1}(s+\gamma)}\right] \qquad \ldots(26)$$

In real space, the inverse transform of eq. (26) can be written as follows:

$$C_{D1}(x_D, t_D) = \frac{1}{2}\exp\left[-x_D(\sqrt{a_2} - \frac{P_{e1}}{2})\right]\operatorname{erfc}\left(\frac{x_D}{2}\sqrt{\frac{P_{e1}}{t_D}} - \sqrt{\frac{a_2 t_D}{P_{e1}}}\right) + \frac{1}{2}\exp\left[x_D(\sqrt{a_2} + \frac{P_{e1}}{2})\right]\operatorname{erfc}\left(\frac{x_D}{2}\sqrt{\frac{P_{e1}}{t_D}} + \sqrt{\frac{a_2 t_D}{P_{e1}}}\right) \qquad \ldots(27)$$

where:

$$a_2 = \frac{P_{e1}^2}{4} + \gamma P_{e1} \qquad ...(28)$$

Eq.(27) corresponds to that case in which the influence of the immobile region is negligible. This equation will reduce to that previously presented by Coats and Smith (1963) for an infinite homogeneous system when $\gamma=0$.

On the other hand, if for practical purpouses the size of the immobile region in the vertical direction, E, does not show any influence on the behavior of the system, eqs. (21) and (22) can be expressed as follows:

$$\bar{C}_{D1} = \frac{C_o}{s} \exp\left\{\frac{P_{e1} x_D}{2}\left[1 - \sqrt{1+\frac{4}{P_{e1}}(s+\gamma+\alpha\sqrt{s})}\right]\right\} \qquad ...(29)$$

$$\bar{C}_{D2} = \exp\left[-m_1(y_D - \frac{w}{L})\right] \qquad ...(30)$$

The system described by eqs. (29) and (30) was previously studied by Tang et al. (1981) and their solutions in Laplace's space agree very well with the solution presented here. Numerical inversion was used for the evaluation of eqs. (29) and (30) in real space. The algorithm presented by Stehfest (1970) was used for this purpouse. Data reported by Tang et al were used in the evaluation of eqs. (29) and (30) and then compared with those obtained from the integral solution previously presented by Tang et al. Results obtained from both evaluations agreed very well with each other.

To determine the influence that the size of the repetitive element, E, could have under several combinations of practical values for the parameters involved in the solution to the model, extensive evaluations of the general solution, eq. (21), and the particular solution when the effect of E is negligible, eq. (29), were carried out. It was observed that for all conditions considered, the results obtained that can be expected in practical applications, the size of the repetitive element, E, does not have influence in the magnitude of the tracer concentration obtained at the producing end, or at any other location within the flow path. Under these conditions the system can be properly described by just two dimensionless parameters: the Peclet number for the mobile region, P_{e1}, and α. If the tortuosity of the fractured medium is considered, then x_D should be added to these parameters.

Thus far, all discussion has been centered in the continuous injection case. However, in field applications tracers are injected as finite slugs in a short period of time , which has been called the "spike injection case" in the literature. As it was pointed out by Walkup and Horne, the solution for an spike-input is the time derivative of a step input, that is:

$$(C_{D1})_{spike} = \frac{\partial C_{D1}}{\partial t_D} = L^{-1}\left\{s\bar{C}_{D1}\right\} \qquad ...(31)$$

Therefore to obtain the solution for a spike-input all that is needed is to multiply the expression for the step input in the (x,y,s) space by s and then invert the resulting equation to the (x,y,t) space. Two cases can be considered; the first one results by considering the solution when the effect of E is negligible. From eq. (29):

$$(\bar{C}_{D1})_{spike} = s\,\bar{C}_{D1} = C_o \exp\left\{\frac{P_{e1} x_D}{2}\left[1-\sqrt{1+\frac{4}{P_{e1}}(s+\gamma+\alpha\sqrt{s})}\right]\right\} \qquad ...(32)$$

By analyzing eq. (32) it can be seen that a maximum (or limiting) solution can be obtained when $\alpha=0$. Applying the inverse transformation to eq. (32) when $\alpha=0$ the following expression is obtained:

$$(C_{D1})_{\substack{spike\\limit}} = \frac{x_D}{2t_D}\sqrt{\frac{P_{e1}}{\pi t_D}} \exp\left\{\frac{P_{e1}}{4}\left[x_D(2-\frac{x_D}{t_D}) - t_D(1+\frac{4\gamma}{P_{e1}})\right]\right\} \qquad ...(33)$$

An estimation of the time of arrival of the maximum tracer concentration can be obtained by equating to zero the time derivative of eq. (33). Thus, the following expression is obtained:

$$t_{D_{cmax}} = \frac{\sqrt{9 + x_D^2 P_{e1}^2} - 3}{P_{e1}} \qquad ...(34)$$

This corresponds to that dimensionless time when the maximum dimensionless tracer concentration breaks through at the producing point location. Since it has been calculated from eq. (33), it will hold for $\alpha=0$. However, from the cases studied, it has been determined that although the maximum tracer concentration at a given location will change with α departing from zero, the time of arrival of the maximum concentration will have a small variation compared with that value predicted by eq. (34). Therefore, this expression should be considered as a good estimation for the time of arrival of the maximum tracer concentration.

DISCUSSION OF RESULTS

Analysis of results generated from Eqns. (21) and (26) show that for practical purposes, $w/L \geq 0.005$, $1 \leq P_{e1} \leq 10^2$ and $10^7 \leq P_{e_2} \leq 10^{12}$, tracer response seems not to be affected by the size of the matrix blocks, this is, diffusion into the matrix blocks does not reach far enough as for matrix boundary effects to be felt in the solution. Under these conditions the system can be described by two dimensionless parameters, α and P_{e1}, as seen from equation (29)

Diffusion of tracer into the matrix is governed by α. When $\alpha \leq 0.01$, tracer response is the same as would be for $\alpha=0$, which corresponds to the zero diffusion into the matrix case.

An analytical solution, equation (26), was found for this limiting case; this is shown in Fig.2 for $P_{e1}=2$ and $x_D=1$ along with solutions for $\alpha \neq 0$, generated from the numerical inversion of Eq. (26). As α becomes larger, for a given t_D, concentration becomes smaller, thus indicating that more tracer has been transferred into the matrix along the injection path. Also, notice in Fig.2 that instabilities on the solutions, due to the numerical Laplace space invertor used, become worst as $\alpha \longrightarrow 0$ and t_D becomes larger.

The effect of P_{e_1} on the tracer response at $X_D=1$, for $\alpha=0.01$, is presented in Fig. 3. These results were obtained from the numerical inversion of Eq. (29). It can be seen that as P_{e_1} becomes larger, the time for tracer breaktrough become also larger. This seems to be contradictory, note however that both α and P_{e_1} depend on velocity and system length and that setting α to a constant implies that changes in P_{e_1} migth only be produced by changing the diffusivity of the tracer on the fractures, Dm. Then, as Dm becomes smaller, P_{e_1} becomes larger and so will the breakthrough time. Fig. 4 shows the same results as Fig. 3 but obtained analytically from Eq. (27).

Figure 5 shows tracer concentration responses at $X_D = 1$ for the case of a spike injection, $P_{e_1} = 2$ and several values of α. These results were obtained by numerical inversion of Eq.(29) and as it can be seen, instabilities due to the inversion algorithm become worse as time increases and for samll values of α. Dimensionless concentration values greater than unity were obtanied for relatively small and large values of P_{e_1}, ≤ 2 and ≥ 20, when $\alpha \leq 0.01$. This indicates that the mathematical treatment of the spike injection, $C_{D_1}(0, t_D) = \delta(t_D)$, must only be valid under certain conditions. These conditions are currently being investigated.

NOMENCLATURE

a_1= Dimensionless constant defined by eq.(24)

a_2= Dimensionless constant defined by eq.(28)

C= Concentration, (M/L^3)

D= Diffusion coefficient, (L^2/t)

E= Fracture spacing, (L)

k= Adsorption constant, (L^3/M)

L^{-1}= Inverse Laplace's operator

m_1 = Dimensionless group defined by eq. (23)

P_e = Peclet number, (dimensionless)

R= Dimensionless group defined by eq. (9)

s= Laplace parameter

t= Time, (t)

V= Velocity, (L/t)

w= Fracture half-width, (L)

x= Distance in x-direction, (L)

y= Distance in y-direction, (L)

Greek Symbols

α = Dimensionless group defined by eq. (25)

γ = Dimensionless group defined by eq. (8)

δ = Stangnant fluid film thickness, (L)

ξ = Dimensionless group defined by eq. (7)

ϕ = Porosity, referred to total-bulk volume, (dimensionless)

λ = Radioactive decay constant, (t^{-1})

ρ = Density, (M/L^3)

Subscripts

D = Dimensionless variable (distance, time or concentration)

e = Refers to the immobile (stagnant) region

i = Refers to initial conditions

m = Refers to the mobile (fractured) region

0 = Refers to inlet conditions

1 = Refers to mobile region

2 = Refers to immobile region

REFERENCES

1. Deans, H.A.: "A Mathematical Model for Dispersion in the Direction of Flow in Porous Media", Soc.Pet. Eng. Jour. (March, 1963) 49-52.

2. Fossum, M.P.: Tracer Analysis in a Fractured Geothermal Reservoir: Field Results from Wairakei, New Zealand, Stanford Geothermal Program, SGP-TR-56, (June, 1982), Stanford, CA.

3. Horne, R.N.: "Geothermal Reinjection Experience in Japan", Jour. Pet. Tech., (March, 1982) 495-503.

4. Hugakorn, P.S., Lester, B.H., and Mercer, J.W.: "An Efficient Finite Element Technique for Modeling Transport in Fractured Porous Media -1. Single Species Transport", Water Resources Research, Vol.19, No. 3 (June, 1983) 841-854.

5. Jensen, C.L.: Matrix Diffusion and Its Effect on the Modeling of Tracer Returns from the Fractured Geothermal Reservoir at Wairakei, New Zealand, SGP-TR-71 (Dec. 19830, Stanford, CA.)

6. Maloszewski, P. and Zuber, A.: "On the Theory of Tracer Experiments in Fissured Rocks with a Porous Matrix", Journal of Hydrology, 79 (1985) 333-358.

7. Ramirez, J.S.: Modelo de Fracturas Paralelas Para el Estudio del Flujo de Trazadores en Yacimientos Geotermicos, MSc. Report, Division de Estudios de Posgrado, Facultad de Ingeniería, Universidad Nacional Autonoma de Mexico, (1987).

8. Rivera, J.R., Vides, A.R., Cuellar, G., Samaniego, F.V., and Neri, G.I.: "A Status Report on the exploitation Conditions of the Ahuachapan Geothermal Field", Proceedings, Ninth Workshop on Geothermal Reservoir Engineering, Stanford, CA (Dec. 1983).

9. Rivera, J.R., Ramirez, J.S. and Rodriguez, F.G.: "Parallel Fractures Model for Tracer Flow Through Geothermal Reservoirs- Preliminary Results", proceedings, Eleventh Workshop on Geothermal Reservoir Engineering, Stanford University, Stanford, CA. (January, 1987).

10. Stehfest, H.: "Algorithm 368 Numerical Inversion of Laplace Transforms", Communications of the ACM, January (1970)

11. Tester, J.N., Bivens, R.L., and Potter, R.M.: "Interwell Tracer Analysis of Hydraulically Fractured Granitic Geothermal Reservoirs", Soc. Pet. Eng. Jour., (1982), Vol. 22,537-545

12. Walkup, G.W., Jr., and Horne, R.N.: "Characterization of Tracer Retention Processes and Their Effect on Tracer Transport in Fractured Geothermal Reservoirs", paper SPE 13610 presented at the 1985 SPE California Regional Meeting, Bakersfield, CA (March, 1985) 229-240.

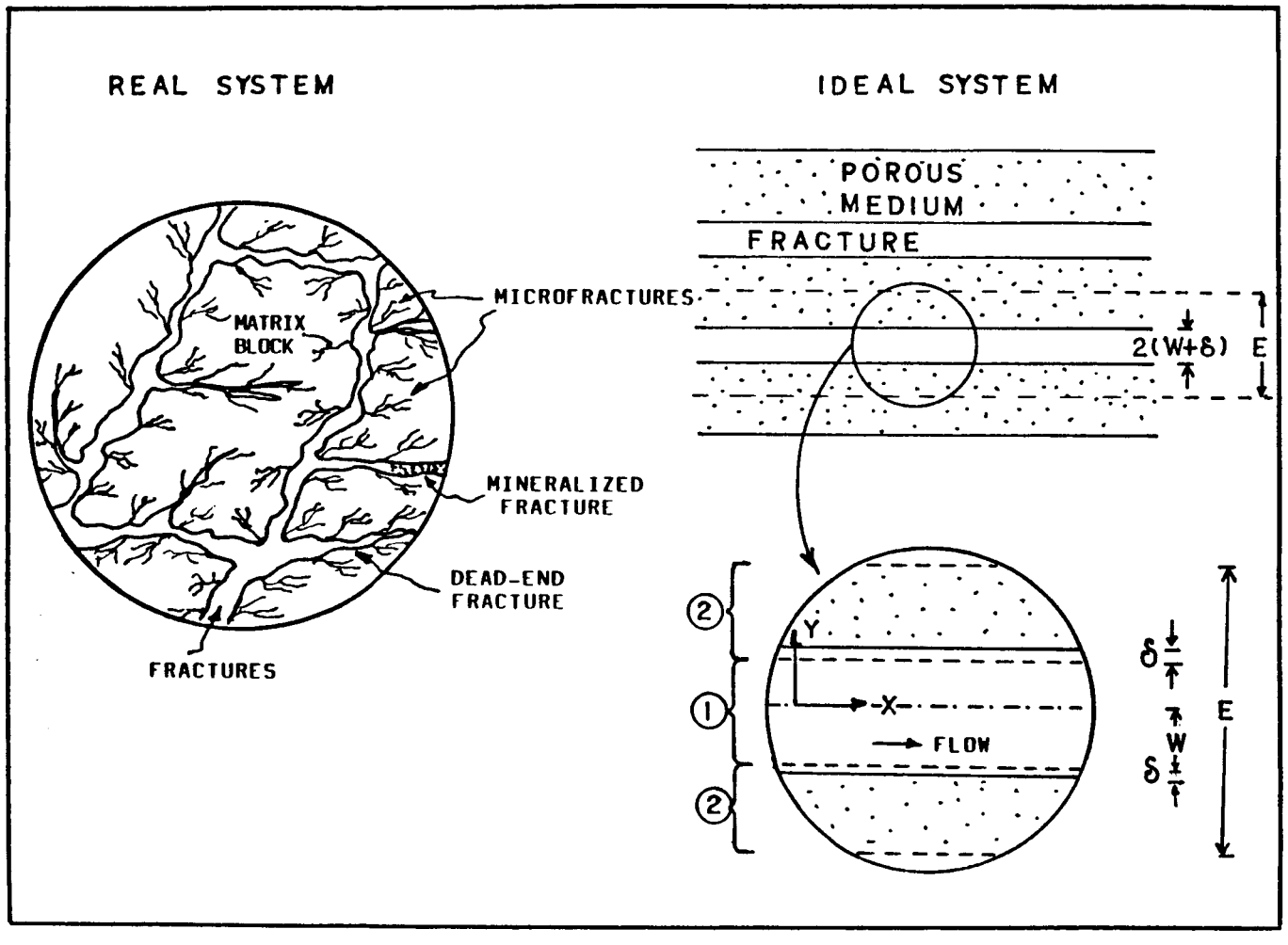


Fig. 1. Idealized proposed model for representation of the naturally fractured medium.

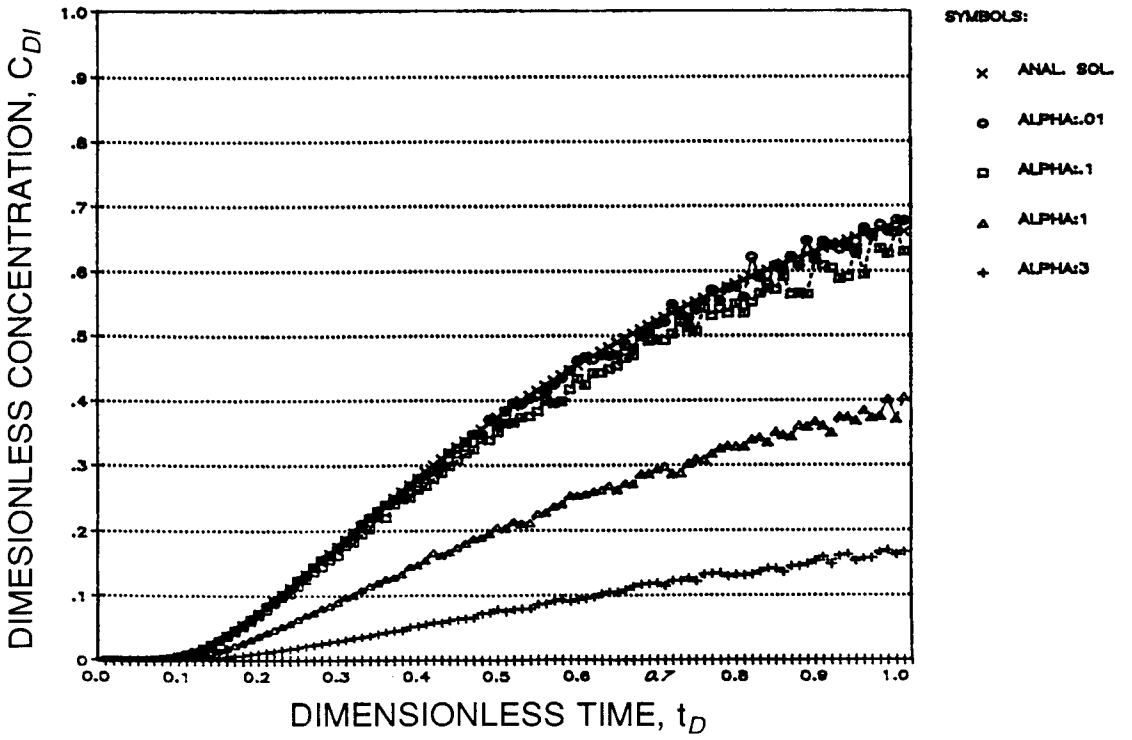


Fig. 2. Effect of α on the concentration profile at X_D=1.0. Step up injection case.

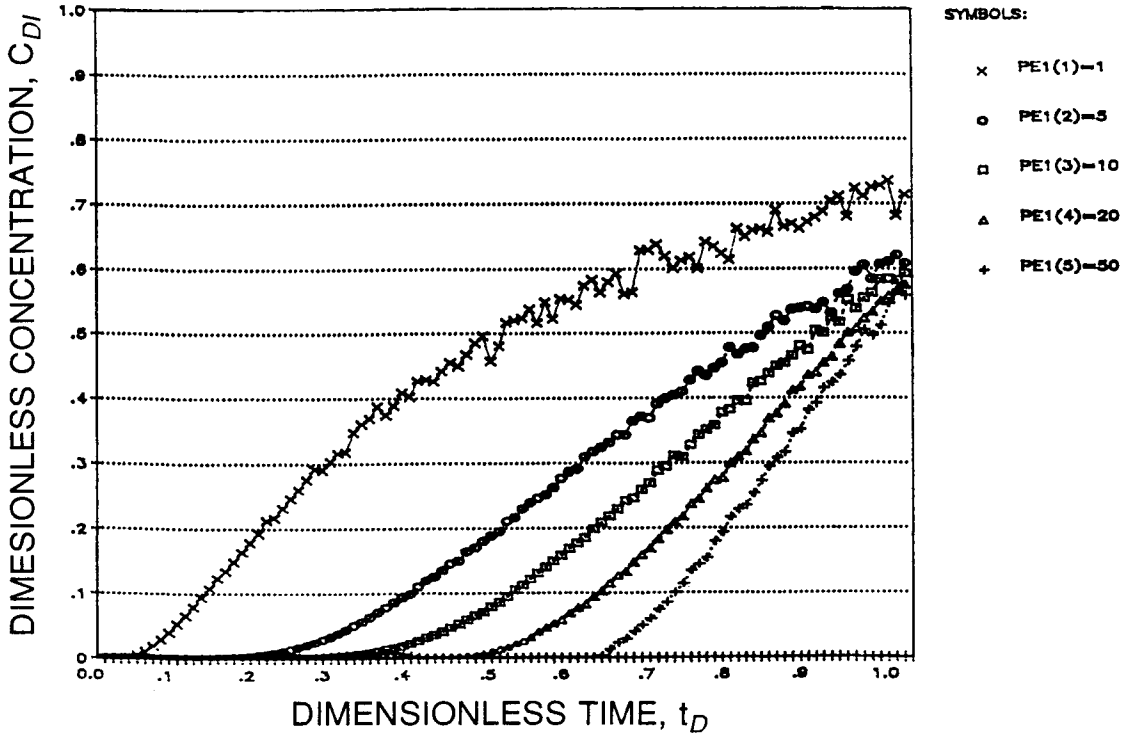


Fig. 3. Effect of the Peclet number in the mobile region, P_{e1}, on the concentration profile X_D=1.0. Step injection, α=0.01

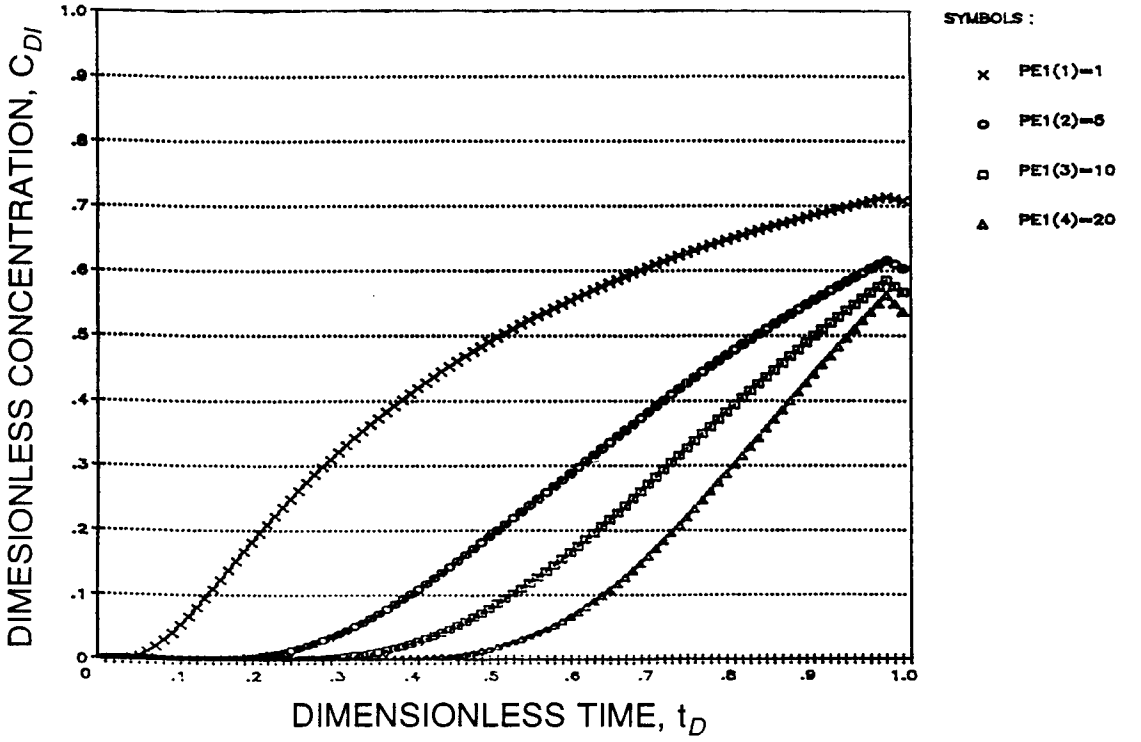


Fig. 4. Limiting analitical solution given by Eq. (27), as a function of P_{e1}. Step injection case.

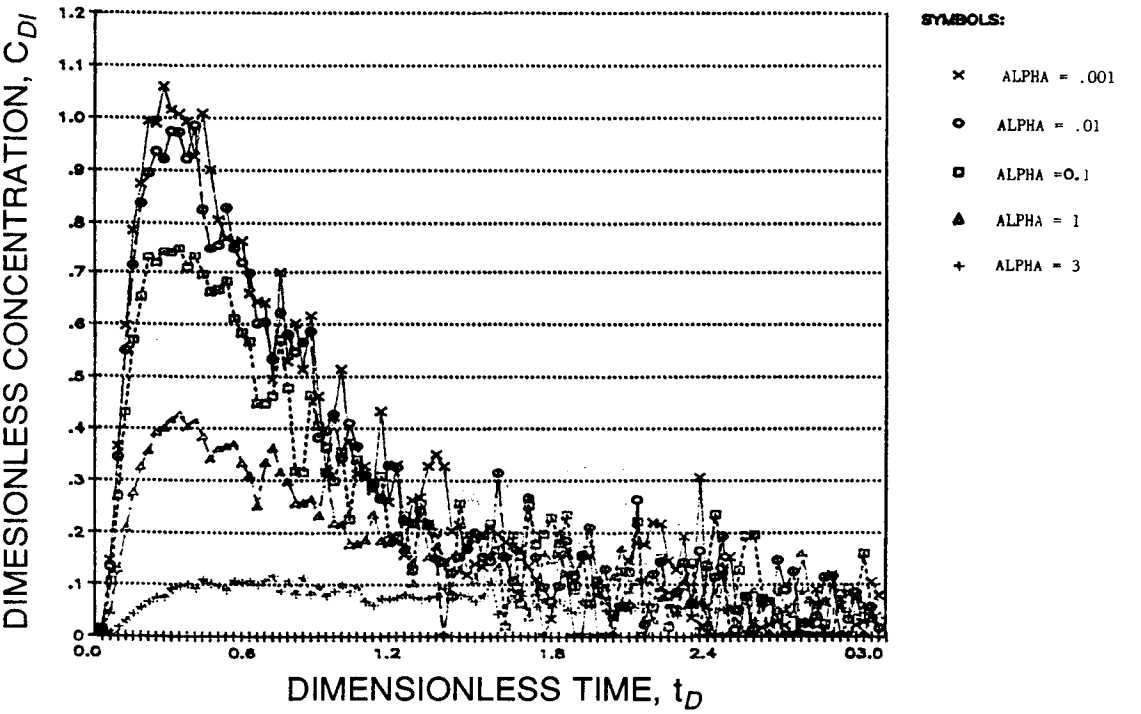


Fig. 5. Tracer concentration responses at X_D=1, P_{e1}=2 and several values of α. Spike injection case.

ANAPPRES: AN EXPERT SYSTEM FOR INTERFERENCE WELL-TEST ANALYSIS

V.M. Arellano, E.R. Iglesias, J. Arellano and M. Schwarzblat

Instituto de Investigaciones Eléctricas
Cuernavaca, Mor., México, Apdo. Postal 475.

ABSTRACT

We present ANAPPRES V1.0, the first version of a computerized expert system capable of analyzing constant- and variable-flowrate interference tests, in which there is one active well and an arbitrary number of observation wells, in liquid-saturated homogeneous reservoirs. ANAPPRES succesfully couples mathematical models, optimization techniques, heuristic knowledge and computerized graphics, a combination not often found in published expert systems. Its main advantages are that it is user friendly, requires essentially no experience on the part of the analist, eliminates subjectivity associated with earlier techniques of analysis, can handle complex cases and large data sets, completes the analysis of even the most complex cases (including plotting the results) in one run, and is significantly faster than a human expert.

INTRODUCTION

Interference tests, in which one or more active wells, and one or more observation wells participate, have distinct advantages over conventional well test in which only one well is involved. They ussually produce transmissivity and storativity values averaged over greater areas, can detect anisotropies in those properties, and can provide information about the existence and type (e.g., no-flow, constant-pressure) of hidrologic boundaries, and on their location.

For interference test analysis, a type-curve graphical technique (e.g., Earlougher, 1977) has been the standard of the trade for many years. In practice, this technique has the disadvantages of being restricted to relatively simple cases and of requiring subjective judgement for curve fitting. The popularization of digital computers brought about computerized analysis techniques (e.g., Earlougher and Kersch, 1972; Mc Edwards and Benson, 1981). These techniques, by use of regression and least-squares linear programming, eliminated the subjectivity previously associated with fitting a model to the observations, and provided the possibilities to study complicated systems and handle large quantities of data. However, the application of these techniques still requieres extensive experience on the part of the analyst, and, except in the simpler cases, is laborious. The laboriosity is associated with the necessity of running many times the same program, in cleverly selected sequences, with different subsets of data. The experience is required mainly for provinding initial guesses of the parameter solutions to start the programs, for applying adequate quantitative criteria for accepting a computed fit to the data (i.e., a solution), and for selecting the proper sequence to run the program and the corresponding data subsets.

This work describes ANAPPRES V1.0 (ANAlizador de Pruebas de PRESion, Spanish for "Well Test Analist") a computerized expert system developed to analyze interference tests in homogeneous reservoirs. ANAPPRES is user friendly, requires essentially no experience on the part of the analist, eliminates subjectivity, can handle complex cases and large data sets, and completes the analysis of even the most complex cases, including plotting the results, in one run. In the current version ANAPPRES can analyze interference tests including 1 active well and an arbitrary number (as currently implemented, up to 20) observation wells. The user can be a beginner: the only requirement is that he (she) can create computerized files with the test data, for input. If prompted by the user, ANAPPRES explains how and why it arrived at the current conclusion(s). This feature

has obvious didactic advantages for non-expert users and provides verification capabilities for expert analists. These characteristics of ANAPPRES were obtained applying artificial inteligence techniques, mathematical models, optimization techniques, heuristic knowledge and graphics software.

HARDWARE AND SOFTWARE

ANAPPRES was developed and is currently used in a VAX-11/780, a computer system widely used in universities and R&D institutions. For input-output it uses the graphics terminal Digital VT241, and for hardcopy output the Digital LA210 Letterprinter and the Hewlett Packard HP-7585B pen plotter.

For intercomputer portability the software is written in Fortran 77.

ARCHITECTURE OF ANAPPRESS

The architecture of ANAPPRES is represented in Fig. 1. There are 5 main modules, with 4 of them (the User Interface, the Computational Module, the Knowledge Base and the Explanatory Module) linked to the central Inference Engine which drives the analysis. The functions of the different modules are described below.

The user must provide 2 types of data files, corresponding respectively to the active well, and the observation wells. These files are created with a word processing (editor) program and must conform to specified formats. The data files are read directly from the Computational Module.

Having created the data files, the user can run ANAPPRES. This is an interactive process in which the program prompts the user for information and instructions. The interaction is driven by the User Interface module.

User Interface. Its main goal is to provide a friendly environment for communication with the user. Communication proceeds via questions and answers. The main functions of this module (Fig. 1) are to generate menus, to display diagnostics and numerical results, to generate graphics, and to display explanations. Figs. 2-5 illustrate the presentation of menus, results, graphics and explanations, respectively (Note: the single-well test option depicted in Fig. 2 is not implemented in ANAPPRES's current version). A general

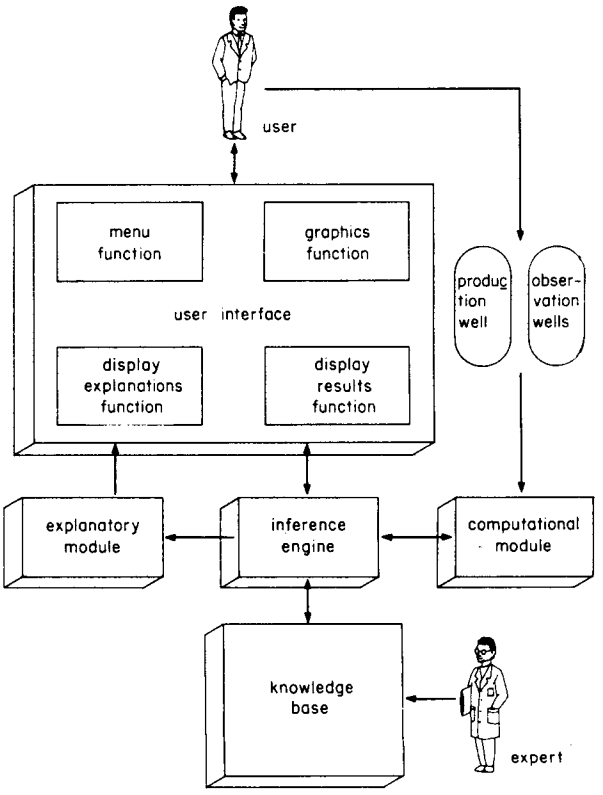


Fig. 1. Architecture of ANAPPRES.

graphics package, developed in-house (Rodriguez et al., 1987), is used by the Graphics function.

Computational module. This is a modified version of the program ANALYZE (Mc Edwards and Benson, 1981), developed for analysis of interference tests in single (liquid) phase, homogeneous, isotropic reservoirs. ANALYZE assumes a constant-thickness, infinite, radial reservoir, and models the active well as a totally penetrating line source. This module determines reservoir parameters by minimizing the differences between observed and model pressure histories. Pressure histories are modeled with the Theis (1935) solution. The minimization is achieved by means of a non-linear least-squares routine (Beals, 1966), which requires initial guesses of reservoir parameters for its use. A Chi-square statistic, normalized to the observed pressures, provides a quantitative measure of the goodness of the fit.

The modifications to the original code were designed to obtain a good coupling with the architecture of ANAPPRES. They include refreshing the memory in succesive calls to this

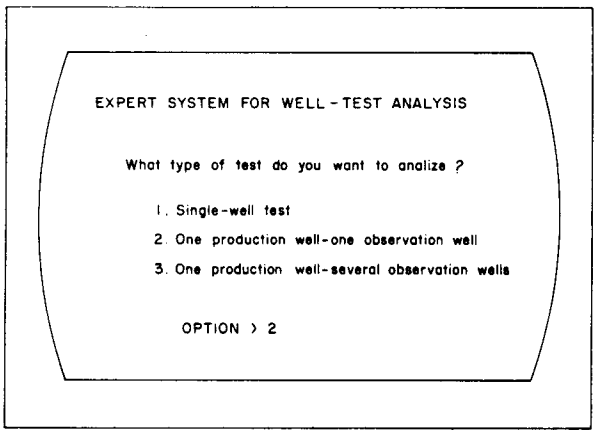


Fig. 2. Example of a display generated by the Menu Function.

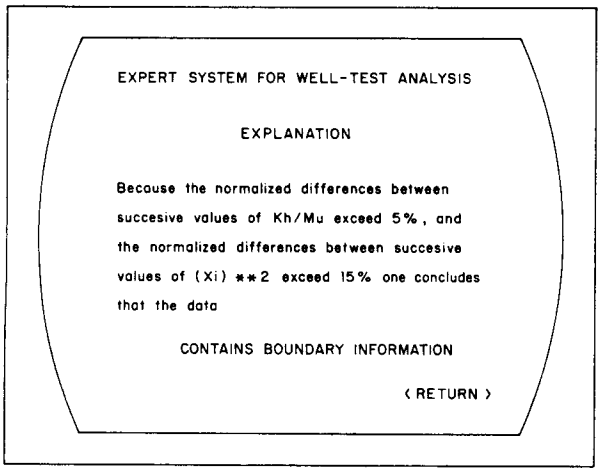


Fig. 3. Example of a screen generatred by the Display Explanations function.

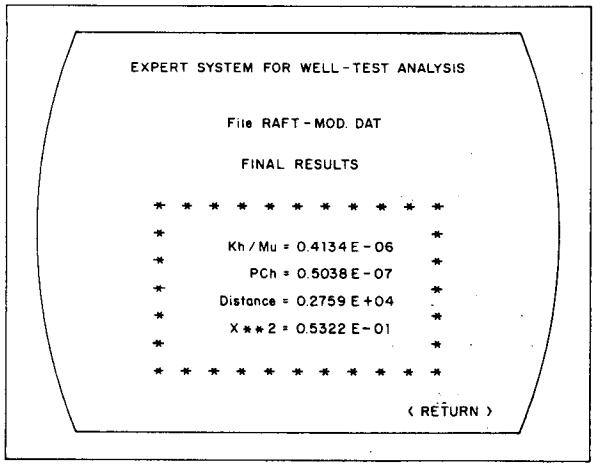


Fig. 4. Example of a screen generated by the Display Results function.

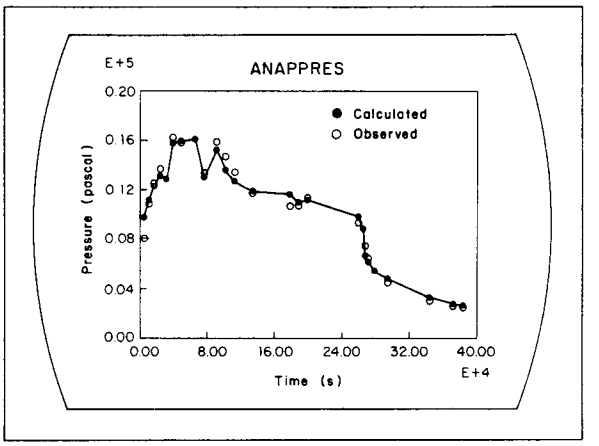


Fig. 5. Example of a screen generated by the Graphics function.

module, automatic handling of error conditions, and the inclusion of criteria to decide whether a run with given reservoir parameter initial guesses will converge (a time-saving feature).

Knowledge Base. It contains the knowledge necessary to perform the analysis of interference tests. This knowledge includes quantitative criteria to decide whether a particular fit is acceptable, how to diagnostic whether there is a hidrologic boundary and its type, what initial guesses to use in order to start the Computational Module, etc. For example, Fig. 6 is a map in the transmissivity-storativity plane, illustrating 16 trigger points, and the corresponding areas of convergence, that ANAPPRES will use as initial guesses to start the Computational Module, if the user chooses not to provide an initial guess, or if the initial guess provided by the user failed to promote convergence. The Knowledge Base is organized in production rules, with the well-known IF-THEN format (Arellano, 1987).

Inference Engine. This module drives the analysis of the test, on the basis of its built-in information, the options selected and the input data given by the user, the partial results provided by the Computational Module, and the information provided by the Knowledge Base. The Inference Engine controls the operation of the Computational Module, and gets results, such as Chi-square and reservoir parameter values, from it. With this information, the Inference Engine interacts with the Knowledge

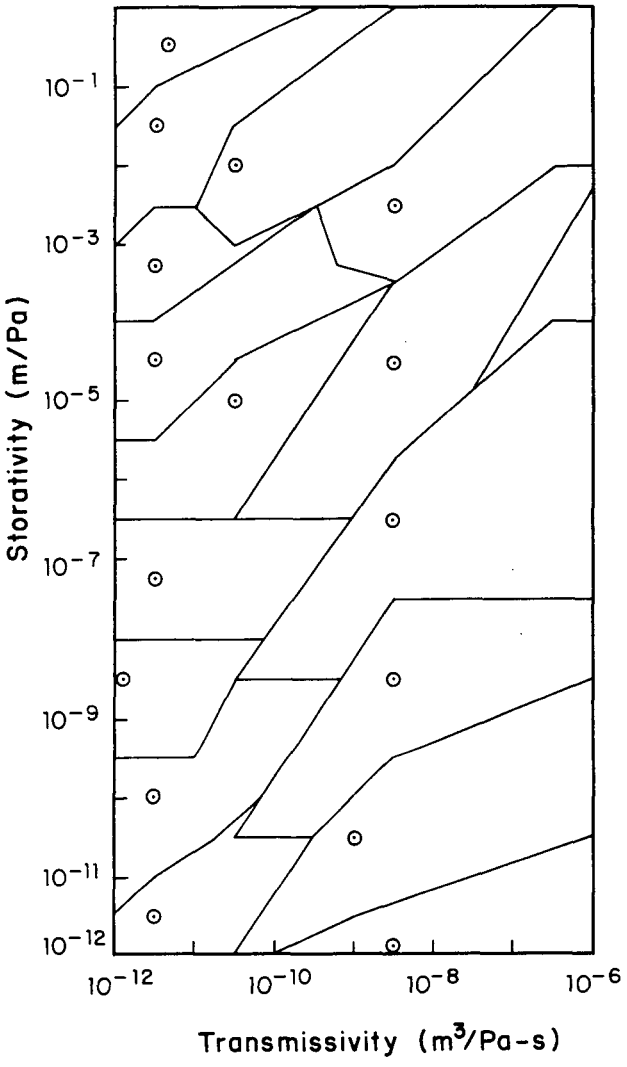


Fig. 6. Trigger points, and the corresponding convergence regions, used by ANAPPRES as initial guesses to start the Computational Module if the user chooses not to provide initial guesses, or if the initial guesses provided by the user failed to promote convergence.

Base in order to reach conclusions. Every time the Inference Engine reaches a conclusion, it commands the User Interface to display it in the screen of the VT241 terminal and ask the user if an explanation is requested, sets flags that enable the Explanatory Module to support the conclusion(s), and commands the User Interface to ask whether a graphic display of the resulting fit is requested. These interactions are repeated as necessary (several to many times, depending on the complexity of the case under analysis) in each run of ANAPPRES.

Explanatory Module. It contains preformatted explanations for all the diagnostics and conclusions ANAPPRES can reach. These explanations are supplemented with information provided by the Inference Engine each time it reaches a conclusion or diagnostic. If the user chooses to request an explanation, the Explanatory Module passes on the corresponding explanation to the User Interface, which displays it through its Display Explanation function (Fig. 1).

METHOD OF ANALYSIS

Unlike previous computerized analysis techniques, ANAPPRES performs a totally automatic interference tests analysis in a single run. That is, it finds out whether there is evidence of a hydrologic boundary in the test data and determines its type, computes storativity and transmissivity values for each observation well, and, if possible, computes storativity and transmissivity values averaged over the participating wells, and distance and angle from an arbitrary origin to the hydrologic boundary. Furthermore, it can provide, on request, screen or hardcopy plots of the model fits obtained in the process.

Fig. 7 briefly illustrates the method of analysis. For ech observation well ANAPPRES determines whether the corresponding data indicate the existence of a boundary, and if there is one, its type (either no-flow or constant-pressure). At this stage, estimates of the storativity and transmissivity associated with the well are obtained; these are taken as final results for the well if no boundary is detected. If a boundary is detected, the values of the transmissivity, storativity and distance of the boundary to the origin are simultaneously determined, using the estimates of transmissivity and storativity as initial guesses. This is sequentially done for each and all the observation wells participating in the test.

If 2 wells detected a boundary, a final analysis simultaneously including both wells is performed to obtain the average values of storativity and transmissivity, the distance of the boundary to the origin and β, the angular location of the boundary. However, in this case β is not uniquelly determined and the true angular location could be $2\pi-\beta$. If

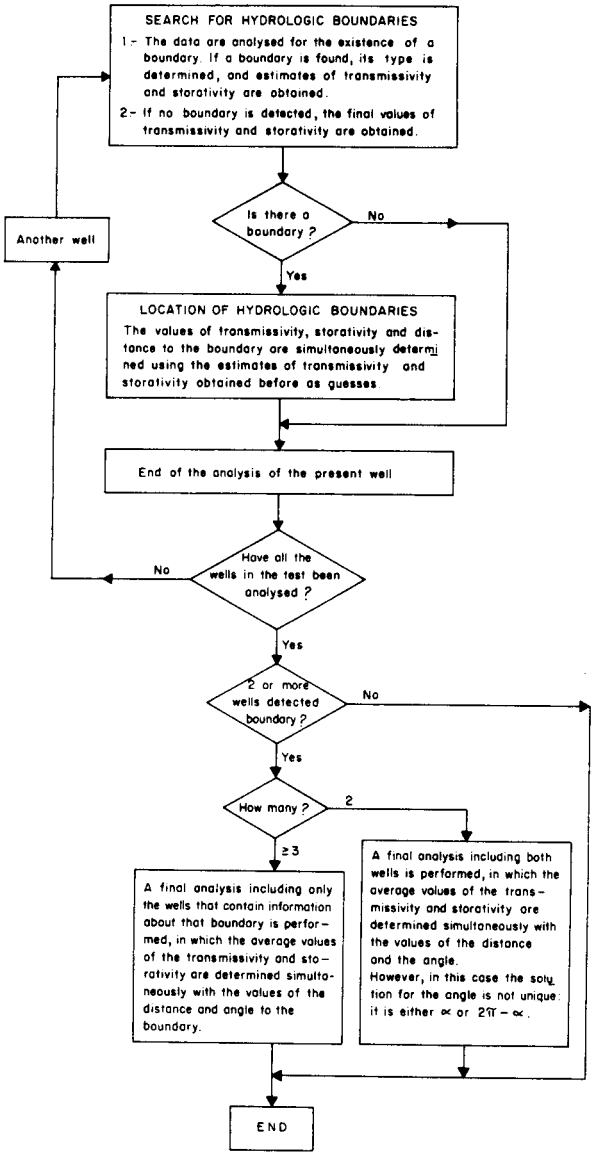


Fig. 7. Method of analysis used by ANAPPRES.

more than 2 wells detected a boundary, a final analysis simultaneously including all these wells is performed to obtain storativity, transmissivity, distance and angle; in this case the angle is uniquely determined.

VALIDATION

At the time of this writting ANAPPRES V1.0 had been validated against 3 problems with known solutions. They include: (a) a constant-flowrate match of the Theis curve, modeling the simplest interference case in an infinite reservoir (Mc Edwards and Benson, 1981); (b) a two-well (active and observation), constant-flowrate production interference test in the Raft River, Idaho, geothermal project that detected a no-flow boundary (Narasimhan and Witherspoon, 1977); and (c) a multiwell, highly-variable flowrate, injection interference test in a shallow groundwter aquifer under consideration for an aquifer thermal energy storage project (Mc Edwards and Benson, 1981). In all three cases ANAPPRES obtained the correct diagnostics and quantitative results, whether or not initial guesses were provided by the user. In case (a), where the synthetic "data" are noiseless and no deviations from the idealized reservoir model exist, the results were exactly coincident with those of the original source. In case (b), in which the original analysis was done using the type-curve graphical technique, with its unavoidable subjectivity, the differences were about 7%. In case (c), in which the original analysis was performed with ANALYZE in a vastly different computer system, the numerical results differed by about 4%. These differences are totally negligible for all practical purpouses.

For brevity, only the analysis of case (c), the most difficult by far, is illustrated here. Fig. 8 presents the relative locations of the 5 wells. Fig. 9 displays the highly variable injection flowrate. Figs. 10-13 illustrate the well by well search for hidrologic boundaries. Figs. 14-17 show the results of the simultaneous determinaton of transmissivity, storativity and distance of the boundary, well by well. And Fig. 18 presents the results of the final analysis, that includes all the wells simultaneously.

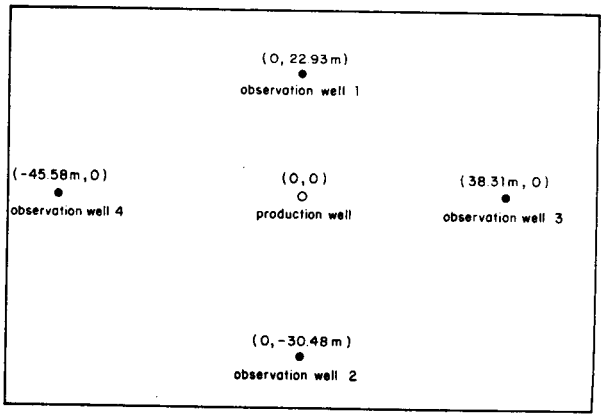


Fig. 8. Relative locations of the wells in case (c) (after Mc Edwards and Benson, 1981).

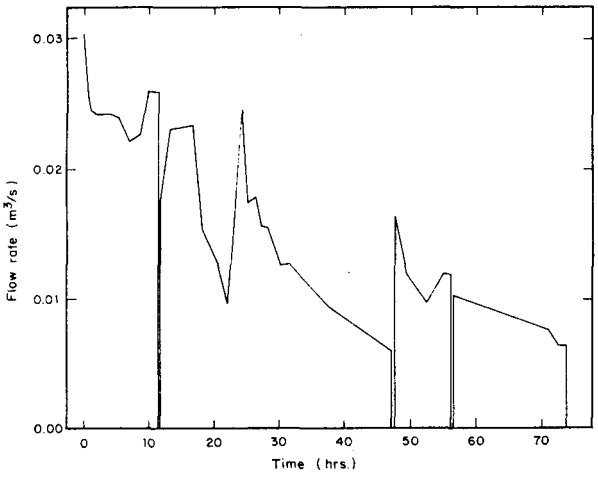


Fig. 9. Highly variable injection flowrate for case (c) (after Mc Edwards and Benson, 1981).

OPTION 1 PRODUCTION WELL - SEVERAL OBSERVATION WELLS

Time considered	(K*h)/Mu	Fl*C*h	X**2
0.1137 E+06	0.5382 E-06	0.4475 E-06	0.4460 E-02
0.2274 E+06	0.5079 E-06	0.5451 E-06	0.4772 E-02
0.4547 E+06	0.4656 E-06	0.7678 E-06	0.6053 E-02

Well 1 File CONVER21.DAT

THE DATA CONTAIN BOUNDARY INFORMATION

EXPLANATION ? [Y/N] › Y

Fig. 10. Results of the search for hydrologic boundary for well #1 in case (c).

OPTION 1 PRODUCTION WELL - SEVERAL OBSERVATION WELLS

Time considered	(K*h)/Mu	Fl*C*h	X**2
0.9613 E+05	0.5406 E-06	0.6327 E-06	0.2765 E-02
0.1923 E+06	0.4957 E-06	0.7789 E-06	0.3704 E-02
0.3845 E+06	0.4509 E-06	0.1022 E-05	0.4789 E-02

Well 2 File CONVER22.DAT

THE DATA CONTAIN BOUNDARY INFORMATION

EXPLANATION ? [Y/N] › Y

Fig. 11. Results of the search for hydrologic boundary for well #2 in case (c).

OPTION 1 PRODUCTION WELL - SEVERAL OBSERVATION WELLS

Time considered	(K*h)/Mu	Fl*C*h	X**2
0.9613 E+05	0.5679 E-06	0.4468 E-06	0.2713 E-02
0.1923 E+06	0.5140 E-06	0.5628 E-06	0.3787 E-02
0.3845 E+06	0.4546 E-06	0.7810 E-06	0.5199 E-02

Well 3 File CONVER23.DAT

THE DATA CONTAIN BOUNDARY INFORMATION

EXPLANATION ? [Y/N] › Y

Fig. 12. Results of the search for hydrologic boundary for well #3 in case (c).

OPTION 1 PRODUCTION WELL - SEVERAL OBSERVATION WELLS

Time considered	(K*h)/Mu	Fl*C*h	X**2
0.9613 E+05	0.5631 E-06	0.3297 E-06	0.2597 E-02
0.1923 E+06	0.5132 E-06	0.4080 E-06	0.3618 E-02
0.3845 E+06	0.4597 E-06	0.6220 E-06	0.9578 E-02

Well 4 File CONVER24.DAT

THE DATA CONTAIN BOUNDARY INFORMATION

EXPLANATION ? [Y/N] › Y

Fig. 13. Results of the search for hydrologic boundary for well #4 in case (c).

EXPERT SYSTEM FOR WELL-TEST ANALYSIS

Well 1 File CONVER21.DAT

FINAL RESULTS

Kh/Mu = 0.5188 E-06
PCh = 0.6836 E-06
Distance = 0.4442 E+03
X**2 = 0.2770 E-02

‹ RETURN ›

Fig. 14. Final results for well #1, case (c).

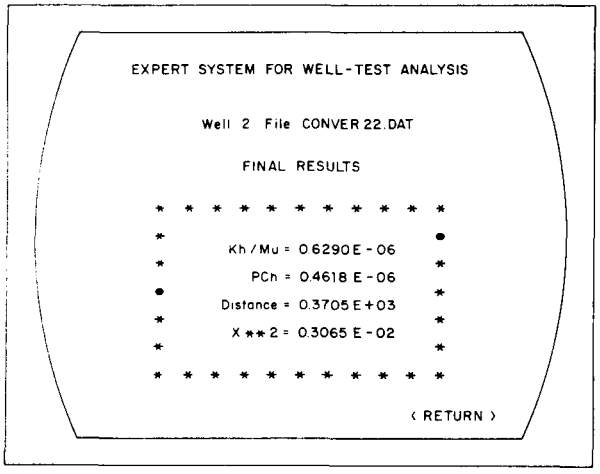


Fig. 15. Final results for well #2, case (c).

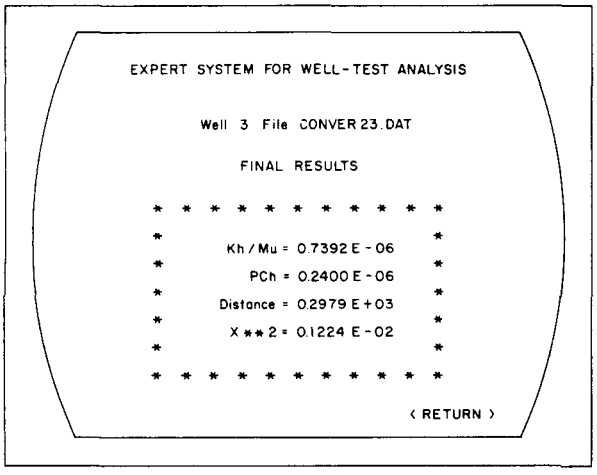


Fig. 16. Final results for well #3, case (c).

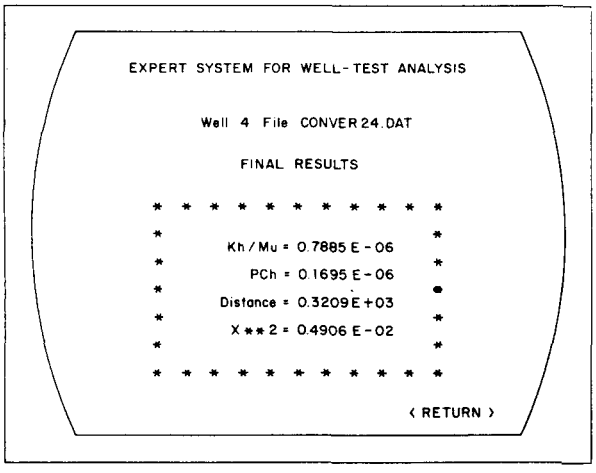


Fig. 17. Final results for well #4, case (c).

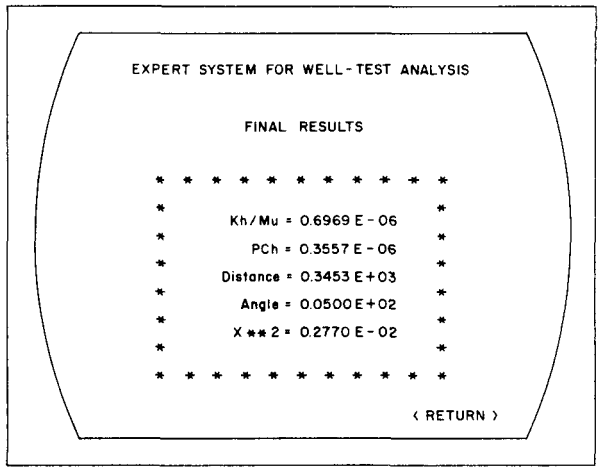


Fig. 18. Final results, averaged over the observation wells, for case (c).

CONCLUSIONS AND FUTURE WORK

We have developed and validated the first version of a computerized expert system capable of analyzing constant- and variable-flowrate interference tests, in which there is one active well and an arbitrary number of observation wells, in liquid-saturated homogeneous reservoirs. The main advantages of this system are that it is user friendly, requires essentially no experience on the part of the analist, eliminates subjectivity associated with earlier techniques of analysis, can handle complex cases and large data sets, completes the analysis of even the most complex cases (including plotting the results) in one run, and is significantly faster than a human expert.

The next version of ANAPPRES, which is already in an advanced stage of development, will include, in addition to the current capabilities, the possibility of analyzing interference tests including an arbitrary number of active wells, and several lesser upgrades. We are also working on the capability to analyze single-well pressure tests.

ACKNOWLEDGEMENTS

The authors are indebted to the Earth Sciences Division of the Lawrence Berkeley Laboratory for providing a copy of ANALYZE, and to Carlos Juarez Badillo for its adaptation to the VAX-11/780 computer system.

REFERENCES

Arellano, V.M., (1987), Desarrollo de un Sistema Experto para el Análisis de Pruebas de Presión. Tesis para obtener el grado de Maestro en Ingeniería Industrial, Universidad Autónoma del Estado de Morelos. Cuernavaca, Mor.

Beals, E., (1966), A computer Program for Nonlinear Least Squares Procedure, No. E2, BKY-LSQVMT, Lawrence Berkeley Laboratory (Computer Center Library), Univ. of Calif. Berkeley.

Earlougher, R.C., and K.M. Kersch , (1972), Field Examples of Automatic Transient Test Analysis, Paper SPE-3363, presented at SPE 46th Annual Fall Meeting, held in New Orleans, Oct. 4-7.

Earlougher, R.C., (1977), Advances in Well Test Analysis, SPE Monograph No. 5, Dallas, Texas.

McEdwards, D.G. and S.M. Benson, (1981), User's Manual for Analyze Multiple-well, Least Squares Matching Routine for Well-test Analysis, LBL-10907, Lawrence Berkeley Laboratory, Univ. of Calif. Berkeley.

Narasimhan, T.N. and P.A. Witherspoon, (1977), Reservoir Evaluation Tests on RRGE 1 and RRGE 2, Raft River Geothermal Proyect, Idaho, LBL-5958, Report Prepared for the U.S. Energy Research and Development Administration, contract No. W-7405-ENG-48. Univ. of Calif. Berkeley.

Rodriguez, A., M. Angeles, L.A. Pineda y J.S. Santana, (1987), DIGRAF Diseño de Graficas, DECUS México, Conferencia Nacional.

Theis, C.V., (1935), The Relation between the Lowering of the Piezometric Surface and the Rate and Duration of Discharge of a Well Using Groundwater Storage, Trans. AGU, 519-524.

PROCEEDINGS, Thirteenth Workshop on Geothermal Reservoir Engineering
Stanford University, Stanford, California, January 19-21, 1988
SGP-TR-113

Application of the Spread–Spectrum Technique in Well Logging

Constantinos V. Chrysikopoulos † and Simos D. Dadakarides ‡

†Environmental Engineering and Science, Department of Civil Engineering
‡Department of Electrical Engineering
Stanford University, Stanford, CA 94305

Abstract—This paper presents the novel concept of employing the noise insensitive spread–spectrum technique in well logging. The proposed design of a spread–spectrum device improves the performance of well logging tools, particularly within highly noisy environments. The heart of the device is a shift register which generates a pseudorandom binary code sequence. A coder is connected to the transmitter and codes the probing signal by utilizing the pseudorandom sequence. A decoder is connected to the receiver and correlates the return signal to the same sequence, which is used as a sliding reference. Shifts as small as a fraction of a bit are unambiguously resolvable, and distance resolution of the order of micrometers is achievable. Spread–spectrum well logging tools can operate even with coded signal–to–noise ratio below zero–dB. The spread–spectrum device can be interfaced with any available wave transmitting logging tool. However, tools employing acoustic waves are favorable because the acoustic wave propagation velocity is low and allows the use of inexpensive electronics. The problems associated with high temperatures which are commonly encountered in geothermal reservoirs are bypassed, since the spread–spectrum device can be located either inside the well logging tool or together with the supporting electronics on the surface.

Introduction

Many well logging techniques utilize electromagnetic, acoustic or optical waves. Acoustic waves are advantageous because their propagation velocity is five to six orders of magnitude lower than that of electromagnetic or optical waves. The time intervals involved in acoustic waves require slow or moderately fast processing electronics. Therefore, the cost is lower, the reliability is higher, and complicated real–time data processing is possible. The methods described in this treatment apply to all wave techniques, but the examples as well as the references are drawn from the acoustic well logging field.

Acoustic logging is a continuous record of the amplitude and time required for an elastic wave to travel a given distance of subsurface formation immediately adjacent to the borehole versus depth. Since rock formation is not ideally elastic, part of the energy of an elastic wave is absorbed and dispersed in the rocks. Absorption occurs due to the mutual friction of rock particles and dispersion due to the heterogeneity of the rock.

Waves are characterized by two basic parameters, amplitude and frequency. The first parameter is related to attenuation and wave shape, while the second is related to phase and timing. Since the velocity and attenuation of sound waves in a reservoir depend on the formation properties, acoustic data may be used to calculate, detect or estimate among others the porosity, lithology, synthetic seismograms, fractures, borehole ellipticity, as well as casing defects and perforations.

Acoustic logging is usually carried out with the transmission and reflection procedures. In the transmission method, a transmitter emits acoustic energy, and part of this energy is guided by the formation or casing and is sensed by one or several receivers. In the reflection method a transducer emits acoustic energy that is beamed horizontally toward the borehole wall. Part of this energy is reflected back and sensed by the same transducer.

This paper introduces the conceptual design of a well logging devise utilizing the noise insensitive spread spectrum technique, and summarizes some acoustic well logging tools which can utilize such technique. The theoretical background of spread spectrum systems is presented in a non–mathematical fashion, so that complex and sophisticated derivations can be avoided. The advantages of the spread–spectrum technique and expected performance of the improved well logging tools are also discussed.

Common Acoustic Logging Tools

Tools available for acoustic logging include among others the single–transmitter sonde, the borehole compen-

sated system, the long–spacing sonic, the circumferential sonde, and the borehole televiewer. The continuous velocity sonde contains one large transmitter and one or two receivers (Summers and Broding, 1952). Consequently, these tools are known as single or dual receiver systems. The transmitter generates an acoustic wave which travels through the borehole fluid to the formation. At the borehole wall the transmitted wave gives rise to compressional, shear and fluid waves which return to the receiver following different pathways. A *single receiver system* measures the time required for the wave to travel from the transmitter to the receiver. Obviously, the total time measured by the system exceeds the desired value by the amount equal to the travel time in the borehole fluid. The *dual receiver system* measures the time required for the wave to travel the distance between receivers. This method eliminates the effect of the travel time in the borehole fluid, provided that the time intervals from the two receivers to the formation are equal. The technique can give incorrect results if the tool is tilted in the hole, or if the receivers are staggered across a cave boundary.

To overcome the problems of the single transmitter sondes, the *borehole compensated acoustic tool* was developed (Kokesh et al., 1965). This tool consists of two transmitter–receiver arrays, one inverted relative to the other. Two values of acoustic wave travel time are measured and averaged. The result of this averaging technique is the elimination of incorrect measurements. Typically, a compensated acoustic tool has a transmitter–receiver spacing of 3–ft and receiver–receiver spacing of 2–ft.

The *long–spacing sonic tool* consists of two transmitters spaced 2–ft apart at the bottom of the tool, and two receivers spaced 2–ft apart at the top with 8–ft separation between the nearest transmitter and receiver. The long transmitter–receiver spacing is required in order to obtain wave travel time measurements from the formation further from the borehole, to allow for adequate time separation between the various arrivals, as well as to achieve a good signal–to–noise ratio and minimum signal distortion. This tool records the entire received wave–form, not only the first arrival, from which compressional, shear and fluid arrivals can be distinguished and separated. To assure correct well logging the tool's internal bias level must be set such as to detect the difference between noise and first wave arrival time. The ability to separate compressional and shear wave velocities is very useful in lithological formation investigations (Pickett, 1963).

The *Circumferential sonde* designed by Vogel and Worrell (1977) is a device employing ultrasonic transmitters and receivers mounted on four wall–contacting arms placed 90° apart along the circumference of the borehole wall. The tool is approximately 8.5–ft long and 4–in in diameter when the arms are closed. The transmitters and receivers are cylindrical in shape, perpendicularly fixed to the tool axis. It is reported that the tool can be used for vertical fracture detection because the transmitted shear and guided fluid waves are impaired by open fracture of sufficient width (Vogel and Herolz, 1981).

The *Borehole Televiewer* is a logging tool that records acoustic waves reflected from the borehole wall (Zemanek et al., 1969). The tool contains a piezoelectric transducer that acts as both the transmitter and receiver. The transducer is rotated at 3 revolutions per second by a motor, and it probes the borewall with pulses 500 times each revolution. A magnetic compass is used to generate a trigger pulse that sets the direction reference. The amplitude of the reflected acoustic signal is displayed as a gray–scale image of the borehole wall. A smooth surface reflects better than a rough one, and a hard surface produces larger reflections than a soft. Therefore, fractures and other rough parts of the wall are displayed as dark lines. If the televiewer is off center or tilted in a circular borehole, a low amplitude is recorded and images exhibit two vertical stripes. If the borehole is elliptical, acoustic waves are reflected away from the tool and only reflections from the major and minor axes are recorded. These stripes may be interpreted as a fractured zone, or can make the precise fracture identification difficult (Georgi, 1985).

Recent advances have increased the interest of the borehole televiewer utilization in well logging applications. An acoustic borehole televiewer for operation in geothermal environments with temperatures up to 280°C has also been developed (Heard and Bauman, 1983). Pasternack and Goodwill (1983) have shown that digital borehole televiewer data provide more informative images than analog televiewer images. Tay-

lor (1983) has developed a method for recording not only a picture of amplitude versus azimuth and depth, but also a picture showing the arrival time of the reflected wave. Rambow (1984) reports that combining amplitude and travel time improves the data interpretation. Although the borehole televiewer has been used extensively in several investigations of hydraulic fracturing stress and other applications (Zoback et al., 1985; Stock at al., 1985), not all of the information provided by the tool is utilized to full advantage (Paillet et al., 1985).

Instrumentation capable of operating sufficiently in the hostile geothermal environments had not been available until quite recently. Some of the advances in geothermal instrumentation are presented by Adorni et al. (1985). The existing acoustic well logging tools emit proper signals, record the associated distorted reflections and apply a series of processing techniques to clean the received signals and extract the desired information. The complexity of the return signal and the low signal–to–noise ratio make the processing difficult and the final results partially reliable. Recently, digital techniques improved the signal processing but there are still inaccuracies inherent to the process of signal sensing.

Spread Spectrum Signal Coding

A fundamentally different approach of well logging tool operation is to transmit a series of pulses instead of one pulse at a time. A set of such pulses forms a digital codeword with internal structure. Consequently, a coded signal is transmitted and the received word–echoes are compared to the transmitted word. The observed differences between the sent and received signals are indicative of the properties of the medium in which the signal propagates. The codeword structure makes it possible for the tool to operate at low signal–to–noise ratio, and still have good performance. Therefore, for a given signal–to–noise ratio the tool response is by far superior when coded signals are used.

There are many digital coding techniques (Blahut, 1983; Wozenkraft and Jacobs, 1965), but the most appropriate for well logging applications is the *spread–spectrum*. This coding technique maps a single binary pulse onto a long string of pulses which constitute the code sequence. The two basic properties of code sequences are the syntax of ones and zeroes and the shape of their correlation (auto–correlation and cross–correlation) functions (Dixon, 1984). A shift register with ℓ–stages generates sequences of variable length depending on the feedback connections. In sequences with maximum length, $(2^\ell - 1)$ bits, the amounts of ones and zeroes differ only by one. The positions where these two values appear in the sequences are described by a pseudorandom probability density function, and their correlation has a unique shape. The decoding process in the receiver is based on the correlation between the reference (transmitted) signal and the received signal. The output of the correlator is a signal relatively free of noise, even if the environment of the propagated coded word is very noisy. In fact, spread spectrum techniques can give valuable information even at coded signal–to–noise ratios far below zero–dB. When the code sequence and its identical image are perfectly synchronized, their correlation reaches an absolute maximum. In maximum length sequences a shift more than one bit from the complete overlap reduces the correlation function by a factor $G_p = 2^\ell$, where G_p is the processing gain. Figure 1, shows such a correlation function.

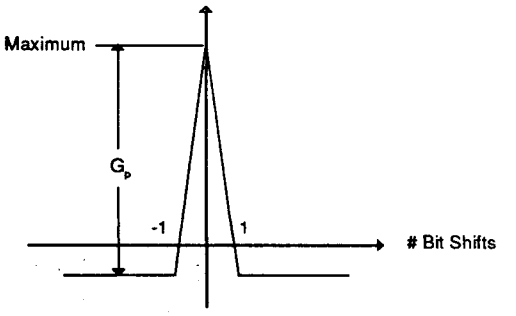


Figure 1. Correlation function of a maximum length code sequence generated by an ℓ-stage shift register.

(a) Noise Insensitivity

The disturbance, $d(t)$, that actually reaches the receiver consists of two parts, namely the signal, $s(t)$, and the random noise, $n(t)$:

$$d(t) = s(t) + n(t). \tag{1}$$

The receiver performs the detection by correlating the incoming disturbance to the transmitted signal reference. When the relative shift of the signals is k bits,

then the correlation R_k in terms of discrete representation is:

$$R_k = \sum_{j=1}^{M} s_j(s_{j-k} + n_{j-k})$$

$$= \sum_{j=1}^{M} s_j s_{j-k} \qquad (2)$$

where M is the number of bits in the sequence. The signal and the random noise are uncorrelated and the $(s_j n_{j-k})$ products are zero. When perfect alignment is achieved the correlation reaches its maximum value of $\sum_{j=1}^{M} s_j^2 = M$. In any detection system a vital parameter is the signal–to–noise ratio. At the receiver input the signal–to–noise power ratio is

$$\left(\frac{S}{N}\right)_{input} = \alpha \quad [dB] \qquad (3)$$

while the signal–to–noise ratio at the correlator output, in terms of the processing gain, is G_p times higher than that of the received coded signal

$$\left(\frac{S}{N}\right)_{output} = \alpha + 10\ell og_{10}G_p \quad [dB]. \qquad (4)$$

The basic trade off is between processing gain and required bandwidth. A processing gain of G_p implies a bandwidth increase of G_p.

Accurate time measurements are accomplished by sliding slowly the reference code sequence until its correlation with the received coded signal is maximum. From the amount of sliding the round trip delay is calculated. The temporal information is combined with the known propagation velocity to calculate the travel distance. Accuracy as high as a small fraction (1/8 to 1/10) of a bit length is easily accomplished (Dixon, 1984). Figure 2, describes the measuring process and shows the shift register. This particular sift register generates a sequence of $2^5 - 1 = 31$ maximum length, and yields a processing gain of 32 or approximately 15dB.

The length of the code sequence used for distance measurements must be such that when the receiver starts to receive back the codeword's leading bits, the transmitter still emits the same sequence. This is accomplished

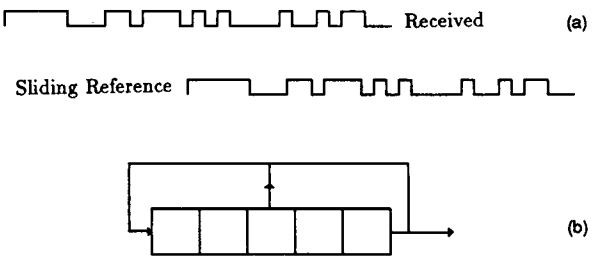


Figure 2. (a) Schematic representation of the time measuring process, (b) Five stage shift register and feedback connections.

whenever round–trip delay is shorter than the sequence duration. In this way the time reference for the round trip delay is precisely known.

The distance resolution measurement is given by the following equation:

$$\Delta s = up\frac{T_b}{2} \qquad (5)$$

where Δs is the distance resolution, u is the wave propagation velocity, p ($p \leq 1$) is the resolvable fraction of a bit length, and T_b is the duration of a single pulse.

It has been shown that systems using spread spectrum techniques achieve high spatial resolution, and can operate with very poor signal–to–noise ratio. This noise immunity results from the decision making process of the electronic detector which is quite independent of the received noise power. In other words, factors such as reflectivity amplitude variation do not degrade the accuracy of the measurement. Spread spectrum decouples amplitude degradations from temporal data, which is very advantageous for spatial measurements.

(b) Multiple Signal Interference Suppression

In typical well logging applications, the transmitted signal gives rise to a multiplicity of returned signals. Compressional, shear, and delayed echoes are mixed with reflections at different interfaces and the compound signal that reaches the receiver becomes highly distorted and degraded by noise. Furthermore, the different amplitudes associated with each one of these signals make their identification difficult. In contrast, the digital spread–spectrum coded signals are insensitive to signal–to–noise ratio fluctuations, and multiple coded signals are easily separable as long as the spacing between consecutive interfaces is longer than the distance resolution limit, Δs.

Signal identification can be achieved either in real time by using more than one time shifted correlators, or by postprocessing of the recorded data. Discrimination of signals can also be obtained by compound sequences, such as the Jet Propulsion Laboratory (JPL)–sequences. These sequences are long, and consist of shorter ones. They have multiple correlation peaks, one for every component–sequence, which are advantageous in signal discrimination and synchronization.

The Conceptual Design

The proposed spread spectrum device consists of two units, the coder and the decoder. The coder is placed before the transmitter and the decoder after the receiver. The coder consists of a local oscillator that provides the carrier, a shift register that generates the code sequence and a modulator that imposes the code on the carrier wave. The output of the coder drives the transmitter that emits the signal wave–form. The decoder consists of a mixer that multiplies the locally generated coded carrier with the incoming signal, a correlator and a bandpass filter that rejects the out of band unwanted signals. The equipment required to build the device are commercially available (Rappaport and Grieco, 1984; Shreve, 1985). The device can be interfaced to the present well logging tools without any major modifications. It is light–weight with characteristic dimensions of a few inches, and possibly can be located either inside the tool or together with the supporting electronics on the surface. Figure 3, shows a block diagram of the spread spectrum device.

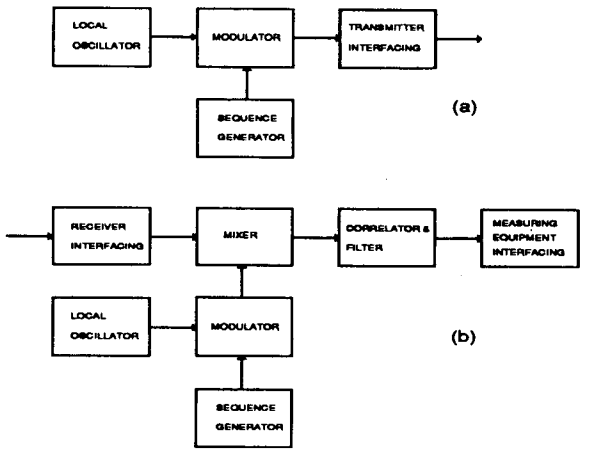


Figure 3. The spread–spectrum device, (a) Transmitter and (b) Receiver.

Discussion

One distinct advantage of well logging tools employing the spread–spectrum device is the ability to operate in noisy environments with excellent performance. Because of this noise immunity, signals can propagate longer distances, experience high attenuations, and still the weak return signal can reveal the carried information. Amplitude and timing information are virtually decoupled and variations of the amplitude do not degrade the tool performance.

Parameters such as formation porosity, fracture locations, and borehole geometry are commonly obtained by the present well logging tools through wave travel distance measurements. The dramatic increase of the distance or time measurement resolution achieved by well logging tools combined with the spread spectrum device leads to much more accurate determination of formation characteristics. A wide variety of devices can be built depending on the requirements. However, for high operating speeds fast electronics and transducers are required, but formation microdetails can be observed.

The ability of the spread spectrum device to discriminate closely spaced or overlapping signals, independently of relative amplitudes, indicates that signals propagated with different velocities or reflected from different surfaces can be resolved with minimum ambiguity. Standard well logging tools may yield inaccurate data measurements when more than one signals are received simultaneously.

Besides accurate temporal information, penatration increase is another advantage of the spread spectrum coding. Since the technique offers a gain of G_p, for a given level of transmitted power, the acoustic wave can travel further and experience higher round-trip attenuation compared to uncoded waves. Figure 4 shows the penetration advantage when the 5–stage shift register coder discussed previously is used for several typical rocks. Attenuation and velocity data for the calculations of Figure 4 were obtained from Knopoff [1965], and Tittman [1986]. The wave penetration depth increases as the carrier frequency decreases or as the number of shift register stages increases.

If more information is desired from well logging, the device can transmit several code sequences concur-

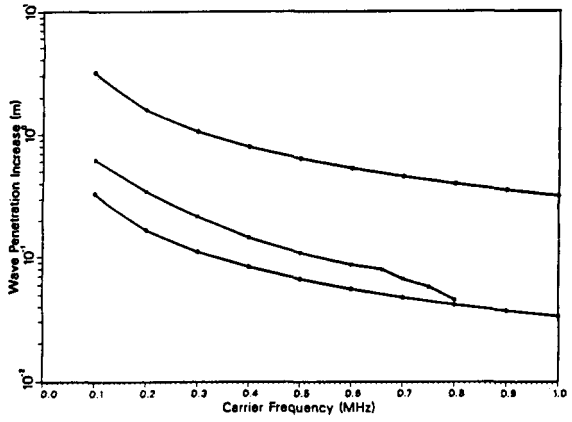


Figure 4. Wave penetration increase versus carrier frequency for (a) Limestone, (b) Westerly Granite, and (c) Sandstone.

rently using only one transmitter–receiver pair and process all of them simultaneously. The cross–correlation function shape of different, suitably selected sequences guarantees the unambiguous recovery of the information carried by each one of them.

Since the information is retrieved from the correlation function of the digital signal any amplitude variation is masked. If amplitude information is necessary, the received signal can be monitored before it enters the correlator by using analog processing techniques. Therefore, amplitude information can be gained from each and every one of the returned pulses.

Conclusions

Well logging can be improved tremendously with the new device utilizing spread spectrum techniques. Overlapping signals are discriminated and signals propagated with different velocities or reflected from different surfaces are resolved accurately. Distance resolution of the order of micrometers is achievable. Parameters related to the device such as shift register length, code sequence length, resolution, dynamic range, and noise immunity can be tailored according to the specific requirements. Constrains imposed by the existing transducers can also be met by proper selection of these parameters. The device can be interfaced with any presently available well logging tool or can be incorporated into any newly designed tool. Operational problems due to high temperatures and pressures can be avoided by locating the spread–spectrum device at the surface together with the other electronics. The cost of the device is only a small fraction of the total cost of a well logging tool, because the necessary components are commercially available and relatively inexpensive. Some of the fields where upgraded well logging tool performance is applicable are: geothermal, oil and gas, lithology, and seismology.

Acknowledgement—The authors appreciate the assistance provided by Mary Kenney in the preparation of the illustrations.

References

Adorni, N., L. Ceppatelli, R. Papale, and A. Parmeggiani, Instrumentation for geothermal wells: Present status and future prospects, *Geothermics*, **14(2/3)**, 287–307, 1985.

Blahut, R. E., *Theory and Practice of Error Control Codes*, Addison Wesley, New York, NY, 1983.

Dixon, R. C., *Spread Spectrum Systems*, Wiley Interscience, New York, NY, 1984.

Georgi, D. T., Geometrical Aspects of Borehole Televiewer Images, *SPWLA Twenty–Sixth Annual Logging Symposium, Transactions*, paper O, 20pp., 1985.

Heard, F. E., and T. J. Bauman, Development of a geothermal acoustic borehole televiewer, *Tech. Rep. SAND83–0881*, 85pp., 1983.

Knopoff, L., Attenuation of elastic waves in the earth, in *Physical Acoustics, Volume III–Part B*, ed. W. P. Mason, Academic Press, New York, NY, 1965.

Kokesh, F. P., R. J. Schwartz, W. B. Wall, and R. L. Morris, A new approach to sonic logging and other acoustic measurements, *J. Petr. Tech.*, **17**, 282–286, 1965.

Paillet, F. L., W. S. Keys, and A. E. Hess, Effects of lithology on televiewer–log quality and fracture interpretation, *SPWLA Twenty–Sixth Annual Logging Symposium, Transactions*, paper JJJ, 31pp., 1985.

Pasternack, E. S., and W. P. Goodwill, Applications of digital borehole televiewer logging, *SPWLA Twenty–Fourth Annual Logging Symposium, Transactions*, paper X, 12pp., 1983.

Pickett, G. R., Acoustic character logs and their applications in formation evaluation, *J. Petr. Tech.*, **15**, 659–667, 1963.

Rambow, F. H. K., The borehole televiewer: Some field examples, *SPWLA Twenty–Fifth Annual Logging Symposium, Transactions*, paper C, 21pp., 1984.

Rappaport, S. S., and D. M. Grieco, Spread spectrum signal acquisition: Methods and technology, *IEEE Commun. Magaz.*, **22(6)**, 6–21, 1984.

Shreve, W. R., Signal processing using surface acoustic waves, *IEEE Commun. Magaz.*, **23(4)**, 6–11, 1985

Stock, J. M., J. H. Healy, S. H. Hickman, and M. D. Zoback, Hydraulic fracturing stress measurements at Yucca Mountain, Nevada, and relationship to the regional stress field, *J. Geoph. Reser.*, **90(B10)**, 8691–8706, 1985.

Summers, G. C., and R. A. Broding, Continuous velocity logging, *Geophysics*, **17**, 598–614, 1952.

Tittman, J., *Geophysical Well Logging*, Academic Press, London, UK, 1986.

Taylor, T. J., Interpretation and application of borehole televiewer surveys, *SPWLA Twenty–Fourth Annual Logging Symposium, Transactions*, paper QQ, 1983.

Vogel, C. B., and R. A. Herolz, The CAD - a circumferential acoustical device for well logging, *J. Petr. Tech.*, **33**, 1985–1987, 1981.

Vogel, C. B., and G. T. Worrell, Circumferential acoustical detector, *U. S. Patent 4,130,816*, 1977.

Wozencraft, J. M., and I. M. Jacobs, Principles of Communication Engineering, Wiley Interscience, New York, NY, 1965.

Zemanek, J., R. L. Caldwell, E. E. Glenn Jr., S. V. Holcomb, L. J. Norton, and A. J. D. Straus, The borehole televiewer: A new logging concept for fracture location and other types of borehole inspection, *J. Petr. Tech.*, **25**, 762–774, 1969.

Zoback, M. D., D. Moos, and L. Mastin, Well bore breakouts and in situ stress, *J. Geoph. Reser.*, **90(B7)**, 5523–5530, 1985.

PROCEEDINGS, Thirteenth Workshop on Geothermal Reservoir Engineering
Stanford University, Stanford, California, January 19-21, 1988
SGP-TR-113

USE OF DERIVATE FOR DETECTING LINEAR IMPERMEABLE BARRIERS BY TRANSIENT PRESSURE TEST

F. Ascencio and R. Molinar

Comisión Federal de Electricidad
Gerencia de Proyectos Geotermoeléctricos
Morelia, Michoacán, México

ABSTRACT

The goal of this paper is to show a numerical method for evaluate distance at an impermeable barrier, using buildup and drawdown pressure test analysis.

This technical needs of derivates evaluation in transition zone defined between two classics semilog straight lines with slopes "m" and "2m" that are present in these systems.

Complementary to shis study the authors propose type curves for application in alternatives analysis.

An illustrative example is showed using the proposed method.

INTRODUCTION

The identification of heterogeneities in geothermal reservoir takes an important place in evaluation of these. Accurate predictions from simulation works require of true conceptual models and propper caracterizations.

The transient well testing are very useful tools to evaluate the hydraulic parameters of reservoir and identify of heterogeneities of this, for example the impermeable barriers that are the main objective of this paper.

Horner (1951) was the first which pointed out that from buildup well testing is possible to detect impermeable boundaries, he reported that the graphic of Pws vs. log ($t/(t_p+ t)$) shows two straight lines with slopes "m" and "2m".

Davis and Hawkins (1963), Witherspoon et. al. (1976) and Erlougher (1977) gave methods to evaluate the distance to impermeable barriers using the profile of the straight lines. Nevertheless these methods are restricted if the lines are not developed completely.

Gray (1965) established that the difference between the extrapolated pressure data of the first semilog straight line gives a useful method to obtain the distance to barrier and Martinez and Cinco (1983) extended further this method.

The objective of this study to carry out an interpretation algorithm, oriented in the transition zone between one and other semilog straight using the numerical derivates of pressure. The method proposed does not require definition of the second straight line.

BASIC EQUATIONS

The dimensionless pressure drop caused by one well at constant rate producing in an infinite medium, homogeneous and isotropic, can be given by the line source solution of the diffusivity equation and is expressed in terms of exponential integral as:

$$P_D = -0.5Ei(-r_D^2 / (4t_D)) \quad \text{.....(1)}$$

Where the dimensionless variables are defined with conventional form by:

$$P_D = (\rho\, kh\, \Delta p)/(\beta W \mu)$$

$$t_D = (\alpha\, kt)/(\emptyset\, \mu c_t r_w^2)$$

$$r_D = r/r_w \quad \text{.....(2)}$$

The effect of one impermeable barrier can be simulated from the images theory, locating one production well at the other side of the barrier and simetric to the real well, this is showed in figure 1. The solution for this system is given by:

$$P_D = -0.5(Ei(-r_{D1}^2/(4t_D)) + Ei(-r_{D2}^2/(4t_D))) \quad \text{...(3)}$$

The r_{D1} and r_{D2} are dimensionless distance between the observation point (x,y) and the real well and image well respectively, and are defined as:

$$r_{D1} = r_1/r_W$$

$$r_{D2} = r_2/r_W \quad \text{.....(4)}$$

For the system of figure 1, the following relations are valid:

$$r_{D1}^2 = x_D^2 + y_D^2$$

$$r_{D2}^2 = (2d_D - x_D)^2 + y_D^2 \quad \text{.....(5)}$$

Where dD is dimensionless distance between real well and impermeable barrier and is expressed in the form of:

$$d_D = d/r_w \qquad \text{.....(6)}$$

The right hand term on equation (3) is related to the drop pressure in the acting well, also the second one, describes the drop pressure due to the barrier (Image Well).

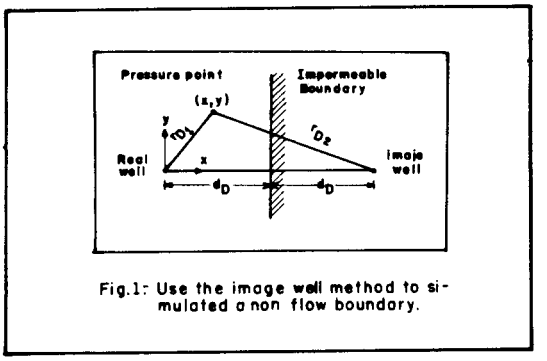


Fig.1: Use the image well method to simulated a non flow boundary.

DRAWDOWN TEST

On the drawdown test, the equation (3) is evaluated at $r_{D1}=1$ and $r_{D2}=2d_D$ for larger value times, so the dimensionless drop pressure in the wellbore could be written as:

$$P_D=0.5(\ln(t_D)-Ei(-d_D^2/t_D)+0.8097)\text{.....(7)}$$

Getting the derivate of equation (7) with time and rearranging:

$$t_D P_D' = 0.5(1+EXP(-d_D^2/t_D))\text{.....(8)}$$

Figure (2) shows the type curve for equation (8). Two straight lines are defined here: in the first one, the behavior of the pressure in the wellbore is according to one well producing into an infinite medium; in the second one, the behavior of the pressure is affected by the impermeable boundary effects.

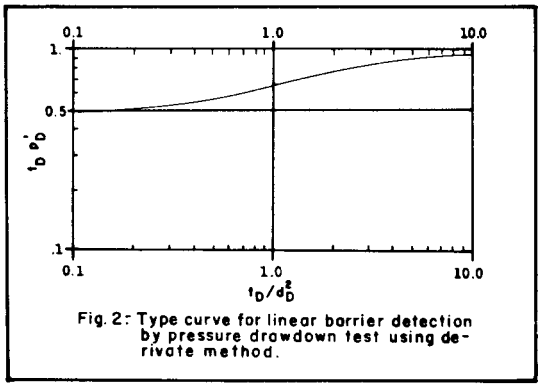


Fig. 2: Type curve for linear barrier detection by pressure drawdown test using derivate method.

Type curve showed at figure 2, has no problem of unicity, making easy the analysis since it can be moved just horizontally.

As a matter of fact, we need just a correct definition of the first horizontal line a short part of the transition zone to make the match.

Analysis Technique. Equation (8) can be written as:

$$2t_D P_D - 1 = EXP(-d_D^2/t_D) \qquad \text{.....(9)}$$

so, taking natural logarithm and writing it in real variables we get:

$$\ln(t(dP_w/dt)/m_1' - 1) = -d^2/(\eta t)\text{.....(10)}$$

where:

η = hydraulic diffusivity coefficient.

$m_1' = m_1/\ln(10)$.

m_1 = slope of the first straight line in a P_w vs. log(t) plot.

Equation (10) suggests that an $\ln(t(dP_w/dt)/m_1'-1)$ vs. $1/t$ plot could be a straight line with a slope proportional to the square distance to the fault.

Another analysis technique can be proposed, if we get the product of equation (11) by $-\eta t$, this is;

$$d^2 = -\eta t \ln(t(dP/dt)/m_1'-1) \text{ .....(11)}$$

the above equation says that in the transition zone the right hand term is a constant equal to the square distance to the barrier.

BUILDUP TEST

In a buildup test, formaly trated by Horner (1951), Mathews (1967) and Earlougher (1977), the behavior of the dimensionless pressure in the wellbore is given by:

$$P_D=0.5(\ln((t_{pD}+\Delta t_D)/\Delta t_D)-Ei(-d_D^2/(t_{pD}+\Delta t_D))+Ei(-d_D^2/\Delta t_D)) \text{ .....(12)}$$

Derivating by time in both sides of the equation and rearranging:

$$((t_{pD}+\Delta t_D)/t_{pD})\,\Delta t_D P_D' = 0.5(1+EXP(-d_D^2/\Delta t_D)-(\Delta t_D/t_{pD})(EXP(-d_D^2/t_{pD}+\Delta t_D)-EXP(-d_D^2/\Delta t_D)) \qquad \text{.....(13)}$$

The type curve showed in figure (3) is obtained of equation (13), for different relation values of dimensionless variables t_{pD}/d_D^2.

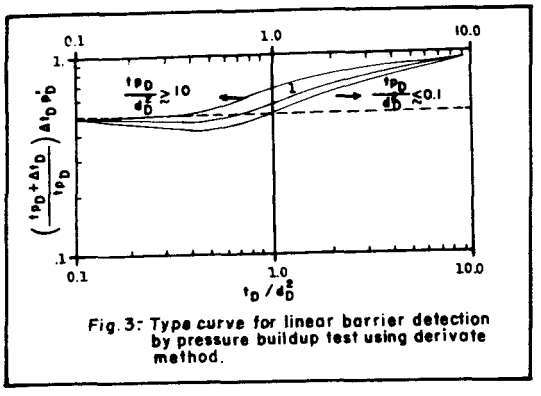


Fig.3: Type curve for linear barrier detection by pressure buildup test using derivate method.

This type curves shows that the shape of transition zone defined between the two horizontal lines is determinated by t_{pD}/t_D^2, and for values of $0.1 > t_{pD}/d_D^2 > 10$ all curves trend to form a group of one curve only.

Also, values of $t_{pD}/d_D^2 > 10$ are required to avoid desviations from the pressure data below of the first semilog straight line.

More over, as in the case of drawdown test, this type curve does not present any unicity problems.

Analysis Technique: Rearranging equation (13), we get:

$$2((t_{pD}+\Delta t)/ t_{pD})\Delta t_D P_D' - 1 + f) = EXP(-d_D^2/\Delta t) \quad \ldots\ldots\ldots\ldots\ldots (14)$$

Where:

$$f = (\Delta t_D / t_{pD})(EXP(-d_D^2/(t_{pD}+\Delta t_D) - EXP(-d_D^2/\Delta t_D))$$

and taking the logarithms in both sides of equation (14) and multiplying by $-\eta t_D$ the equation stablished is:

$$-\eta t_D \ln(2((t_{pD}+\Delta t_D)/t_{pD})\Delta t_D P_D' - 1 + f) = d_D^2 \quad \ldots\ldots\ldots\ldots\ldots (15)$$

in terms of real variables:

$$d^2 = -\eta t \ln(2(t_p+\Delta t)/t_p \Delta t(dp_{ws}/d\Delta t)/m_1' - 1 + f) \quad \ldots\ldots\ldots\ldots\ldots (16)$$

An iterative procces of solution for equation (16) can be writing assuming an initial valve of $d(d^k)$ in equation "f" and solving for a new valve of d (d^{k+1}), and so on, until we reach the convergence criterian as:

$$\left| \frac{d^{k+1} - d^k}{d^k} \right| < Tol.$$

APPLICATION EXAMPLE

To show proposed technique in present paper a theoretical example for a buildup pressure test is generated, locating an impermeable barrier at 20 m. of distance, and considering a production time of 100,000 seconds, the remaining information for this example is the next:

N = 60 Kg/q

P_i = 8.0E6Pa

kh = 5.0E-13 m^3

$\phi C_t h$=3.0E-7m/Pa

ρ = 722.Kg/m^3

Figure (4) shows the Horner plot of this example, in this it can be seen that second straight line does not appear. Figure (5) presents log-log plot of $(t_p+\Delta t)/t_p)\ \Delta t\ dp/dt$ versus Δt. The value of $m_1 = m_1'/\ln(10) = 610{,}000$ can be obtained from both graphics.

From graphics were selected three points in transition zone, as follows the test data are presented:

	Δt	p_{ws}	$(t_p+\Delta t)/t_p)\Delta t(dp_w/dt)$
1	0.63E4	6.7E6	0.38E6
2	0.10E5	6.8E6	0.42E6
3	0.20E5	7.1E7	0.46E6

The initial value of "d" was 10 m. and taking a tolerance of 0.001 the calculated values of "d" were; 20.04, 20.02 and 19.89, which are very similar to value used for generating this theoretical test.

Complementary it is mentioned that the convergency of this method is to speedy.

As an alternative, these data were matched with type curve of figure (3), obtaining a value of distance to a barrier of 19.5 m.

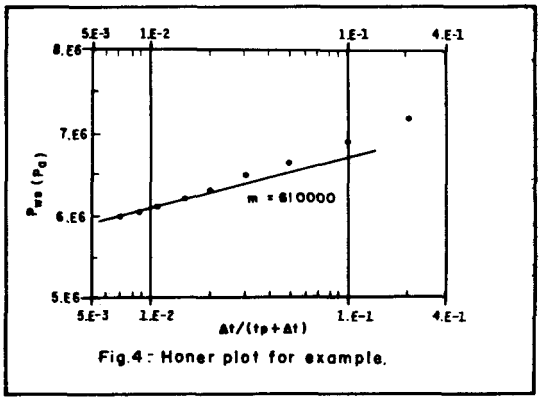


Fig.4: Horner plot for example.

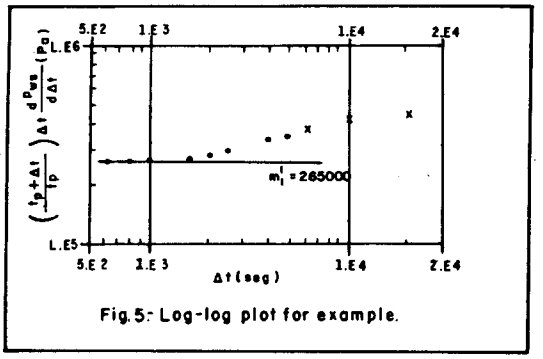


Fig.5: Log-log plot for example.

CONCLUSIONS

Analysis techniques were presented in this paper for evaluating distance from one well to an impermeable barrier, as well as in drawdown buildup tests. These do not need development of second straight line, because they are focussed in a transition zone that is defined between two classic straight lines.

At least, one point is needed in order to use this method, to verify distances, a good collection pressure data is suggested. Only, for buildup tests the technique is iterative and its convergency is to speedy. As an alternative type curves are proposed, mentioning that total development of transition zones are not needed. It was also founded that for values of t_{pD}/δ 10 there are no irregular behaviors of graphics for buildup tests.

ACKNOWLEDGEMENTS

The authors wish to give acknowledgement to CFE for the time given to make this study, and to Alfonso Aragón, Oscar Campos and Héctor Gutiérrez for their constructive discusions.

NOMENCLATURE

c_t : Total compressibility (Pa^{-1}).

d : Distance between source well and impermeable barrier (m).

d_D : Dimensionless distance between source well and impermeable barrier.

h : Formation thickness (m).

k : Permeability (m^2).

m_1 : Slope of the first straight line.

m_1': m_1 ln(10).

P_D : Dimensionless pressure.

P_i : Initial reservoir pressure (Pa).

p_w : Wellbore pressure (Pa).

p_{ws}: Shut-in wellbore pressure (Pa).

r_D : Dimensionless radial distance, r/rw.

r_1 : Distance between source well and observation well (m).

r_2 : Distance between image well and observation well (m).

r_w : Radius of well (m).

t_D : Dimensionless time.

t : Time (s).

t_{pD}: Dimensionless production time.

t_p : Production time (s).

t : Shut-in time during buildup (s).

W : Mass flow rate (Kg/s).

α : Constant convertion (=1).

β : Constant convertion ($=1/2\pi$).

ρ : Density (kg/m^3).

η : Hydraulic diffusivity.

$\emptyset$: Porosity (fraction).

μ : Viscosity (Pa-s).

SPECIAL FUNCTION

$E_i(-x)$ = Exponential integral, $-\int_x^\infty (EXP(-u)/u)du$.

EXP(x) = Exponential of x.

REFERENCES

1. Davis, G.E.; Hawkins, M.F. (1963): "Linear Fluid-Barrier Detection by Well Pressure Measurements". J. Pet. Technol., Oct., pp. 1077.

2. Earlougher, R.C. (1977): "Advances in Well Test Analysis". Monograph Series, Society of Petroleum Engineers of AIME, Texas, Jan. Vol. 5.

3. Gray, K.E. (1965): "Approximating Well-to-Fault Distance from Pressure Measurements Discussion". J. Pet. Techno., Jul. pp 761-767.

4. Horner, D.R. (1951): "Pressure Build-up in Wells". Proc. Third World Petroleum Congress, Section II, The Haque, pp 503-523.

5. Martinez, R.N.: Cinco H. (1983): "Detection of Linear Impermeable Barriers by Transient Pressure Analysis". Paper SPE 11833, May, pp. 237-245.

6. Matthews, C.S.; Russell, D.G. (1967): "Pressure Buildup and Flow Test in Wells". Monograph Series, Society of Petroleum Engineers of AIME, Dallas, Vol. 1.

7. Witherspoon, P.A.; Javandel, I; Newman, S. P.; Freeze, R.A. (1967): "Interpretation of Aquifer Gas Storage Conditions from Water Pumping Tests". Monograph on Project NS-38, American Gas Association, New York, pp. 93-128.

PROCEEDINGS, Thirteenth Workshop on Geothermal Reservoir Engineering
Stanford University, Stanford, California, January 19-21, 1988
SGP-TR-113

CHEMISTRY OF A LOW TEMPERATURE GEOTHERMAL RESERVOIR : THE TRIASSIC SANDSTONE AQUIFER AT MELLERAY, FRANCE.

François-David Vuataz, Christian Fouillac, Sylvie Detoc and Michel Brach

Institut Mixte de Recherches Géothermiques
BRGM - BP 6009, 45060 ORLEANS CEDEX 2 - FRANCE

ABSTRACT

The Triassic sandstone aquifer offers on a regional scale, a large potential for low-temperature geothermal exploitation in the Paris Basin. The Na-Cl water in the aquifer has highly variable mineralization (TDS = 4 to 110 g/l) and a wide range of temperature (50° to >100°C). Chemical studies have been carried out on the Melleray site near Orléans, where a single well was producing a Na-Cl geothermal water (TDS = 35 g/l) at a wellhead temperature of 72°C to provide heat for greenhouses.

The purpose of these studies is to understand the chemical phenomena occurring in the geothermal loop and to determine the treatment of the fluid and the exploitation procedures necessary for proper reinjection conditions to be achieved. During the tests performed after the drilling operations, chemical variations in the fluid were noticed between several producing zones in the aquifer. Daily geochemical monitoring of the fluid was carried out during two periods of differing exploitation conditions, respectively pumping at 148 m^3/h and artesian flow at 36 m^3/h. Vertical heterogeneities of the aquifer can explain the variations observed for the high flowrate.

Filtration experiments revealed that the particle load varies with the discharge rate and that over 95 weight % of the particles are smaller than 1 μm. The chemistry of the particles varies greatly, according to their origin as corrosion products from the well casing, particles drawn out of the rock or minerals newly formed through water-rock reactions.

Finally, small-scale oxidation experiments were carried out on the geothermal fluid to observe the behaviour of Fe and SiO_2 and to favour particle aggregates for easier filtration or decantation processes.

INTRODUCTION

During the late 1970s, the sandstone aquifer in the Triassic of the Paris Basin was drilled for geothermal purposes. The first drillhole, at Cergy, west of Paris, gave insufficient yield. The two following operations at Melleray (near Orléans) and Achères (west of Paris), despite showing good reservoir productivity, gave poor performance on reinjection (Fig. 1). Solving these reinjection problems was the main task of a research program supported by the Commission of the European Communities (Fouillac et al., 1986).

The present paper summarizes a detailed study of the chemical aspects of the fluid and solid particles at the Melleray geothermal site carried out to acquire a comprehensive knowledge of the chemical interactions occurring between the fluid, the reservoir rock and the casing and tubing materials. The understanding of these phenomena is necessary for the future design of water treatment and reinjection procedures.

The chemical and hydrogeological information obtained from the wells penetrating the Triassic aquifer is much less than that available for the Dogger aquifer in the overlying Jurassic rocks (Rojas et al., 1987). Figure 1 shows the location of the wells on which fluid chemical data were obtained and shows the extension of the Triassic geothermal aquifer (> 10000 km^2). Three types of well have been considered :

- geothermal wells (Cergy, Melleray 1 and 2, Achères 1 and 2);
- wells drilled for potential gas storage (Romorantin, Chemery);
- oil exploration wells (Marchenoir, Pasnes, Blancafort, Etampes, Mantes, Chaunoy).

The fluids from the Triassic aquifer are characterized by a wide range of temperature (45° to 155°C) related to aquifer depths between 950 and 2440 m. The geothermal waters are of Na-Cl type with important amounts of Ca and SO_4. Their mineralization is also strongly variable with Total Dissolved Solids from 4 to 110 g/l, according to their location within the aquifer. As a general rule, the mineralization of the fluids increases with depth but the linear correlation between these two parameters is only fair. The amount of dissolved chemical species is of course related to the distance that the water circulates between the recharge zone and the

wells, and also to the occurrence of soluble minerals such as evaporites leached by the groundwater.

Na exhibits a very good linear trend against Cl (Fig. 2) which could mean that neither element is controlled by secondary minerals. The slope of the linear curve is not compatible with halite being the source of both Na and Cl and therefore another mineral source for sodium (plagioclase ?) is needed (Fouillac et al., 1986).

At Melleray, near Orléans (120 km south of Paris) one production well (GMY1) and one injection well (GMY2) were drilled in 1980 to depths of respectively 1669 and 1661 m. The producing zones of the Triassic aquifer are equipped with slotted liners from about 1400 to 1600 m. Both wells are artesian and at the level of the reservoir are separated horizontally by 1000 m.

Saline water (TDS = 35 g/l) pumped from the production well GMY1 at 150 m^3/h with a wellhead temperature of 73°C, has been used intermittenly for several years to heat a complex of greenhouses. Due to great difficulties of reinjection, the geothermal water was discharged after cooling in the nearby Loire River.

VARIATIONS IN FLUID CHEMISTRY

During the first sampling carried out at Melleray at the end of drilling, variations of chemical composition were established related to the different producing layers of the Triassic reservoir. Physical and chemical monitoring of the fluid was therefore carried out to improve the knowledge of the geothermal fluid and its variations with time and space, and to draw up a program of treatment of the fluid with a view to reinjection.

Daily monitoring of the production well

Measurements and sampling were carried out at the GMY1 wellhead on a daily basis for two periods of about one month, corresponding to periods of differing production rates. Five days a week, water samples were collected and measurements of pressure, discharge rate, temperature and pH were made at the wellhead. The total alkalinity (HCO_3) was analyzed within the next few hours. To obtain maximum analytical precision and to avoid problems of drift, Fe, SiO_2 and Cl were analyzed only at the end of each survey on filtered (0.45 μm) and acidified water samples.

Table 1 shows that at the different discharge rates and pressures corresponding to the two survey periods, four of the six parameters compared display absolute variations. The temperature decreased by 3°C between the first and second surveys owing to decreasing fluid velocity in the well. The pH decreased by 0.23 units while HCO_3 increased by 13 mg/l. Fe increased by 13 mg/l. Fe increased notably, by 2.2 mg/l. Note that as the bubble-point pressure is very high (17-20 bars), the geothermal fluid was more degassed at 1.8 bars (2^{nd} survey) than at 5 bars (1^{st} survey).

Table 1 - Mean and standard deviation of parameters measured during the two daily survey periods of production well GMY1.

Parameters	1^{st} survey mean ± stand. dev.	2^{nd} survey mean ± stand. dev.
Flowrate (m^3/h)	148 (pumped)	36 (artes.)
Pressure (bars)[a]	5	1.8
Temperature (°C)[a]	72.4 ± 0.1	69.4 ± 0.3
pH[a]	6.30 ± 0.02	6.07 ± 0.01
HCO_3 (mg/l)	295 ± 5	308 ± 2
Fe "	7.9 ± 0.5	10.1 ± 0.1
SiO_2 "	37.4 ± 0.3	36.8 ± 0.3
Cl "	19520 ± 800	19870 ± 40
nb of measurements	30	25

[a] Wellhead measurements

In terms of time-variations, important differences have also been noted between the first and the second surveys. During the first (under pumping), the five chemical parameters, respectively pH, HCO_3, SiO_2, Fe and Cl show relatively large variations, cleary greater than the precision of the measurements (Fig. 3A). The variations of the different parameters are not always in phase and no repetitive events have been detected. On the 25^{th} day, major variations were simultaneous for four parameters. During the second survey (artesian flowrate), the pH and the dissolved species vary only slightly with time but the variations remain very close to the limit of reproducibility of the measurements (Fig. 3B).

Several phenomena can tentatively be invoked to explain these variations :

1) Unstable pumping rate, contrary to the flowmeter indication (148 ± 2 m^3/h) ; electromagnetic flowmeters are often unprecise in two-phase flow.
2) Increase of fluid/casing interaction due to slower ascent during the second survey. For a total fluid volume of 84 m^3 and for discharge rates of 140 and 36 m^3/h, 36 min. and respectively 140 min. are needed for the fluid to reach the wellhead.
3) Further degassing for the second survey due to reduced pressure, with the result that the large amount of gas can create around each gas bubble an acidic water-gas emulsion, which intensely corrodes the casing.

4) Chemical variations as a function of discharge rates may be linked to production of different layers of the Triassic aquifer. Indeed, the lower pH of the second survey is in contrast to the more pronounced degassing when the loss of CO_2 should have increased the pH of the water at the wellhead. Variations in Cl also relatively important at 148 m^3/h, suggest heterogeneity of the fluids contained in the sandstone reservoir.

Variations of the fluid with depth and production rates

At the end of drilling in well GMY1 in 1980, two downhole samples (GMY1 80.1 and 80.2) were collected between packers at different depths. The concentration of major ions show important differences (Table 2) with TDS values of 32.4 g/l for the shallow sample (1441-1471 m) and 37.0 g/l for the deep one (1561-1593 m). Spinner surveys indicated that these two zones provide respectively 20 and 25 % of the total production in well GMY1. Such low and high TDS values have not been found for any subsequent samples collected at the wellhead and thus representing the average of all the producing layers of the Triassic aquifer (TDS = 35.0 to 35.8 g/l).

Finally, the vertical and possibly horizontal heterogeneity in fluid composition between the different producing layers seems to be confirmed by the sample collected at the wellhead of GMY2. For a similar discharge rate (85 m^3/h), the total mineralization of the fluid (34.7 g/l) is lower than that for GMY1 (35.3 g/l) (Table 2).

Table 2 - Chemical composition of selected samples of the geothermal fluid from wells GMY1 and GMY2, Melleray.

Samples	GMY2 1	(1) GMY1 1	(1) GMY1 2	GMY1 3	GMY1 4	GMY1 5	GMY1 30	GMY1 70
Month/Year	12/80	1/80	1/80	2/80	12/83	11/85	3/86	12/86
Flowrate m^3/h (2)	85	-	-	138	170	85	146	36
Temperature °C (3)	69	-	-	69.5	67	71	72.4	69.5
pH (3)	6.28	-	-	6.75	6.17	6.34	6.33	6.07
Na mg/l	10900	10760	11960	11680	11000	10880	11860	11700
K "	309	295	340	319	320	316	249	310
Ca "	1166	1132	1344	1236	1236	1210	1174	1200
Mg "	374	331	417	390	409	358	366	363
Cl "	19738	17572	20963	19312	20000	20280	19009	19808
SO_4 "	1800	1900	1550	1840	1760	1820	1890	1950
HCO_3 "	305	442	397	360	319	292	293	308
SiO_2 "	37	-	-	38	37	31	37.3	36.6
Fe "	-	-	-	36	6.1	9.7	7.2	10.2
Sr "	41.2	-	-	44.1	45.0	35.8	38.8	37.7
Li "	13.1	-	-	14.6	10.6	-	11.2	11.3
Ba "	$\leqslant 1$	-	-	-	0.26	0.165	0.176	0.154
B "	-	-	-	13	16.1	-	16.5	16.4
F "	-	-	-	1.4	1.3	4.3	3.5	2.8
Al "	-	-	-	-	0.030	0.332	0.638	0.451
TDS g/l	34.7	32.4	37.0	35.3	35.2	35.2	35.0	35.8
Sum cations meq/l	574	559	630	614	585	572	614	609
Sum anions meq/l	599	542	630	589	606	615	581	605

(1) Samples GMY1 1 and 2 were collected between packers between the depths of 1441-1471 m and 1561-1593 m respectively. All the other samples are from wellheads.
(2) Flowrates are pumping rates, with the exception of 36 m^3/h in 1986, which represents artesian discharge.
(3) Temperature and pH were measured at the wellheads.

Because the pH and HCO_3 measurements were not standardized, not all the parameters of fluid samples collected from the wellhead of GMY1 for various production rates over six years, can be readily compared. Fe content however increases as discharge falls, which confirms the evolution observed during the two daily surveys (Fig. 4). As mentioned before, both the time of contact between fluid and casing during ascent in the well and the degassing rate, parameters which are essential for corrosion phenomena, are highly variable.

PARTICLE DISTRIBUTION

Numerous filtration experiments have been carried out at Melleray, mainly on the wellhead of GMY1, using a small stainless steel filtration unit (filter area 1.73 x 10^{-3} m^2), which limited the volume of fluid filtered (1 to 40 x 10^{-3} m^3). The method was checked using a large filtration unit (filter area 0.36 m^2) and volumes of fluid (27 to 113 m^3). The particle load is very variable according to the production rate. Under pumping at 148 m^3/h, the total load of particles $\geqslant$0.01 μm equals 4.8 mg/l, whereas for the artesian discharge ($\sim$ 36 m^3/h), the total amount of particles reaches 7.5 mg/l (Table 3). These values should be considered carefully because the particle load will be reinjected into the aquifer unless the fluid is treated by physical and/or chemical processes to remove the particles.

Table 3 - Particle load and weight, geothermal fluid at the GMY1 wellhead.

Flowrate (m^3/h)	Particle load $\geqslant$0.01 μm (mg/l)	Total weight (kg/day)	Total weight ton/7 months[a]
148 (pumping)	4.8	17	3.6
~36 (artesian)	7.5	6.5	1.4

[a]Seven months is the length of a normal heating season.

Particle distribution as a function of size has been evaluated using values of the solid load obtained in filtration experiments during artesian discharge (36 m^3/h). It appears that more than 94 weight % of the particles are less than one micron in size and more than half is $\leqslant$0.1 μm (Fig. 5). With the exception of the interval 0.2-0.45 μm, the particle distribution decreases logarithmically from small to large particles.

SCALING AND CORROSION PRODUCTS

In 1984, a mineralogical study of the particles contained in the geothermal fluid at the GMY1 wellhead showed the lack of amorphous phases (Boulmier, 1984). All the particles retained on the filter, even the finest, were more or less crystalline. Fe, a major element, occurred essentially as magnetite but also as sulphide, associated with Cu, and in phyllosilicates. Cu was relatively abundant but poorly crystallized (Cu + S, Cu + Fe + S). Zn and Pb were also detected. Free SiO_2 was seldom seen, but Si and Al were associated in kaolinite and illite. In some filter residues, the presence of gypsum, dolomite, quartz, marcasite and pirsonnite ($Na_2Ca(CO_3)_2 \cdot 2H_2O$) was detected by X-ray diffraction.

Two series of filter residues analyzed in 1986 for different production rates (150 and 36 m^3/h), differ considerably from each other as well as from the 1984 residue. The particle-size distribution is similar but an important amorphous phase of complex composition was found in the later filtration residues. The chemical nature of the particles is extremely varied (quartz, Fe sulphide, phyllosilicates, Fe oxides and hydroxides, complex carbonates, etc.), as is their size ($<$ 0.1 μm to $>$5 μm). On the other hand the amorphous phase is relatively homogeneous in composition, consisting essentially of Fe, with which is associated, in order of decreasing importance, Al, Si, S, P, Cl, Ca and Pb. For particles collected in the heating plant after cooling of the geothermal fluid, several elements were found in greater proportions in the amorphous phase, such as Cr, Pb, V, Ti and Zn. These are indicators of corrosion of the pipes and the heat exchanger in the heating plant.

Scaling products have been collected in the 200 μm protection filter of the plant. Their large particle size (0.1 to 1 cm), their platy shape and their composition (75-82 % Fe_2O_3) indicate their origin in the well casing and the pump suspension tubing. Magnetite, goethite and traces of siderite were the principal minerals found by X-ray diffraction.

Finally a series of filters of various sizes and qualities (Millipore, Sartorius, Nuclepore) and of different porosities (3, 1.2, 0.4 μm) was analyzed after deposition of particles from the artesian discharge of 36 m^3/h. Most particles are amorphous and remain undetected by X-ray diffraction. With the electron microscope an amorphous coating of S + Fe + Zn was found. In contrast of the previous residues, ZnS was a major phase, determined by microscopy as well as by chemical analysis with a Zn/Fe ratio ranging from 1 to 5. Cu and clay were also more abundant than in the earlier filtration residues.

The major variations observed with time consist in a progressive increase of the amorphous phase and the disappearance of Cu sulphide, replaced by Zn sulphide as the main particulate mineral phase in the geothermal fluid. Although no proof has yet been found, the abundant Zn could originate from either corrosion of the sampling port couplings or from the aquifer rock. As for sulphur, though it may exist in infra-trace quantities, it has not been detected in the fluid. Temporary occurrence of ZnS as a major amorphous phase could also be explained by "puffs" of fluid enriched in Zn, which mix with fluids from another productive zone containing S. In support of this suggestion, seven analyses of the geothermal fluid carried out between 1983 and 1986 for various producing conditions

revealed high variations of Zn ($\leqslant$ 50 to 500 ppb), which shows the considerable changes in certain dissolved chemical species.

FLUID/MINERAL EQUILIBRIUM

Water/rock interactions have been approached using a computer code to determine which minerals exert a control on fluid chemistry under downhole conditions. The code WATRA2 (Sevèque et al., 1984) is a modified version of WATEQ F (Plummer et al., 1976). Prior to computing the degrees of saturation of the fluid in selected minerals, it was necessary to calculate independently the redox potential (Eh) and the pH value in the reservoir, as these two parameters are modified during the ascent of the fluid in the well due to slight conductive cooling and partial degassing.

The results of these computations show that the deep fluid is very close to equilibrium with carbonates, particularly with calcite, magnesite and siderite. Equilibrium is also attained to varying degrees for several SO_4-minerals, fluorite and chalcedony, whereas quartz was identified as the newly formed silica phase in the reservoir rock (Cautru and Robelin, 1984). The difficulty in computing equilibrium with H_4SiO_4 is due to the estimation of activity coefficients for this species, which could explain the discrepancies between calculations and observations.

With two input values for aluminum, the program indicates oversaturation of the solution with respect to kaolinite and illite, which have been positively identified (Cautru and Robelin, 1984). This places some doubt on either the accuracy of aluminum determinations or the reliability of the thermodynamic data set for aluminous species. The solution is also oversaturated with respect to K-feldspar, although secondary orthoclase was described in the Triassic sandstone. This suggests that the same comment is valid as for aluminum.

PRELIMINARY WORK ON FLUID TREATMENT

In order to establish a fluid treatment with a view to reinjection into the Triassic sandstone, several oxidation experiments have been carried out. Three oxidizers were tested: air, water saturated with dissolved O_2 and NaOCl. Only the last enables quantitative control of the oxidation of Fe^{2+} to Fe^{3+}. This can be induced very quickly and appears to involve about 5 % of SiO_2 during the precipitation of Fe^{3+}. The procedure allowed injection of a precise amount of NaOCl during the fluid treatment for an adjusted oxidation of 95 to 98 % of Fe^{2+} and thus avoided an excess of oxidizer, which would be corrosive toward the pipes of the geothermal loop. Other oxidizers will be tested to determine which will induce the coarsest aggregates, likely to be easily decanted and/or filtered.

If, during the treatment used for the reduction of Fe content, the geothermal fluid becomes slightly undersaturated toward minerals such as calcite, siderite and chalcedony, the reinjected fluid would tend of dissolve these minerals in the aquifer and increase or at least maintain the porosity around the reinjection well. Finally, complete degassing of the fluid would avoid the clogging of the pores by micro-bubbles of gas.

CONCLUSIONS

Comprehensive study of the geothermal fluids of the Triassic sandstone aquifer established that the producing zones are very heterogeneous at the scale of the Paris Basin, as well as at kilometer scale, between two boreholes or even between two producing layers in the same borehole. Consequently, the distribution of the slotted liners and the modification of the exploitation conditions for a given well (flowrate, pressure) can significantly change the fluid chemistry.

It is clear that the chemical variations of the fluid observed at Melleray during the two one-month survey periods are more important for the high than for the low flowrate. This is true even for non-reactive dissolved species such as Cl and supports the hypothesis of local vertical heterogeneity of fluid composition in different layers of the Triassic, as established from previous downhole sampling and differences between production and reinjection wells.

Filtration experiments showed that particles between 0.1 and 0.01 μm constitute more than 50 % of the total solid load and about 90 % of this is composed of particles $\leqslant$ 0.45 μm. The amount of particles is inversely proportional to the discharge rate of the well. At a flowrate of 150 m^3/h, 17 kg of residues enter the heating plant daily.

The chemical composition of these particles indicate different origins : Fe-oxides and hydroxides and traces of Cr and Ti represent mainly products of corrosion of the well casing. On the other hand elements such as Al, Si, S, Ca and Mg originate in the geological environment. The existence of a significant amorphous phase has been established but its composition varied with time. At first Fe was the major component (associated with S, Al, Si and Pb) but then ZnS became the most abundant phase.

The Melleray geothermal fluid is in chemical equilibrium with respect to calcite, siderite, magnesite fluorite and chalcedony,

whereas the nature of the Al-limiting phase is still debatable. Problems of reinjection of the fluid into the Triassic sandstone have shown the necessity for treatment of the fluid. The study of the parameters which induce clogging of the rock matrix is underway, but possible steps in the fluid treatment can already be suggested, namely degassing, oxidation, decantation, filtration and injection of corrosion inhibitors.

ACKNOWLEDGEMENTS

This work was carried out under contract n° EN 3G-0006-F (CD) of the Commission of the European Communities and received financial support from the Bureau de Recherches Géologiques et Minières and the Agence Française pour la Maîtrise de l'Energie. The authors wish to thank all those in the BRGM who contributed to this phase of the project. Special thanks are due to Annie Criaud, IMRG, for her critical comments on the draft and to J. Kemp, BRGM, for improving the English of the final version. B. Gayet and J. Rabian, IMRG, are respectively thanked for drafting and typing.

REFERENCES

Boulmier J.L., 1984 - Exploitation des formations gréso-argileuses du Trias. Etude des particules en suspension dans l'eau du forage de Melleray (Loiret). BRGM report, 84 SGN 279 MGA, 16 p. (unpubl.).

Cautru J.P. and Robelin C., 1984 - Etude d'un réservoir argilo-gréseux. Cas du Trias du doublet géothermique de Melleray, Loiret. BRGM report 84 SGN 124 IRG-GEO, 34 p. (unpubl.).

Fouillac C., Vuataz F.D., Brach M. and Criaud A., 1988 - Water-rock reactions in a Triassic sandstone aquifer. Detailed study of a low temperature geothermal system, Melleray, France. European Community Contractors Meeting, Geochemistry, Antwerp, Nov. 1986, 12 p. (in press).

Institut Mixte de Recherches Géothermiques, 1987 - Exploitation géothermique des formations argilo-gréseuses : Trias. Rapport annuel d'activités 1986 (unpubl.).

Plummer L.N., Truesdell A.H. and Jones B.F., 1976 - WATEQ F. A Fortran IV version of WATEQ, a computer program for calculating chemical equilibrium of natural waters. U.S.G.S. WRI, 76-13, 61 p.

Rojas J., Menjoz A., Martin J.C., Criaud A. and Fouillac C., 1987 - Development and exploitation of low enthalpy geothermal systems : example of the Dogger in the Paris basin, France. 12th Workshop on Geothermal Reservoir Engineering, Stanford, 6 p.

Sevèque J.L., Oustrière P. and Criaud A., 1985 - WATRA 2, programme de calcul d'équilibre dans les eaux. Une version de WATRA étendue aux espèces métastables du soufre : polysulfures, thiosulfates et sulfites, données thermodynamiques révisées et complétées. BRGM report 85 SGN 061 GMX, 123 p. (unpubl.).

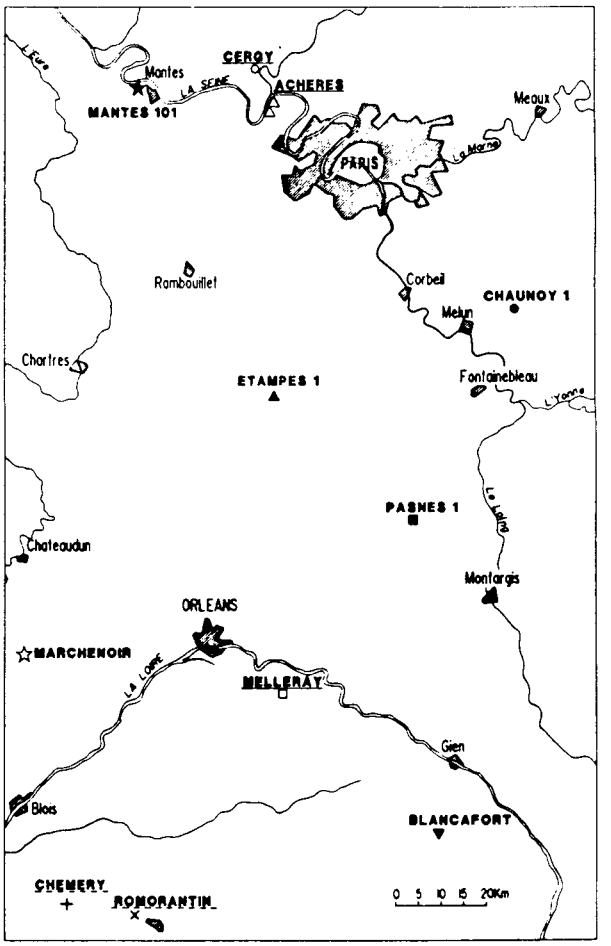


Fig. 1 - Location map of the wells on the Triassic sandstone aquifer.

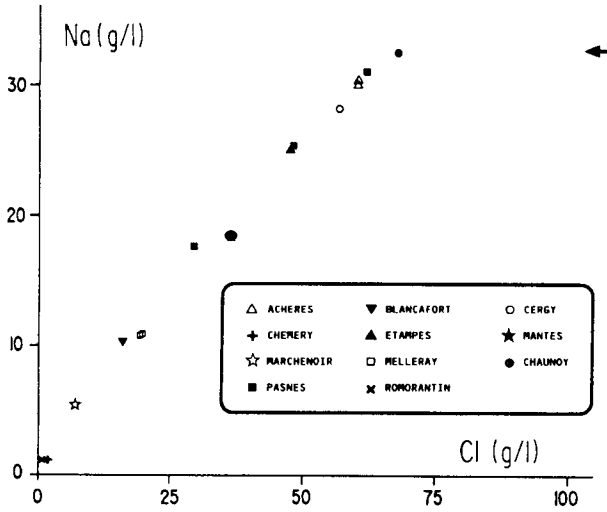


Fig. 2 - Plot of sodium versus chloride contents for the Triassic fluids.

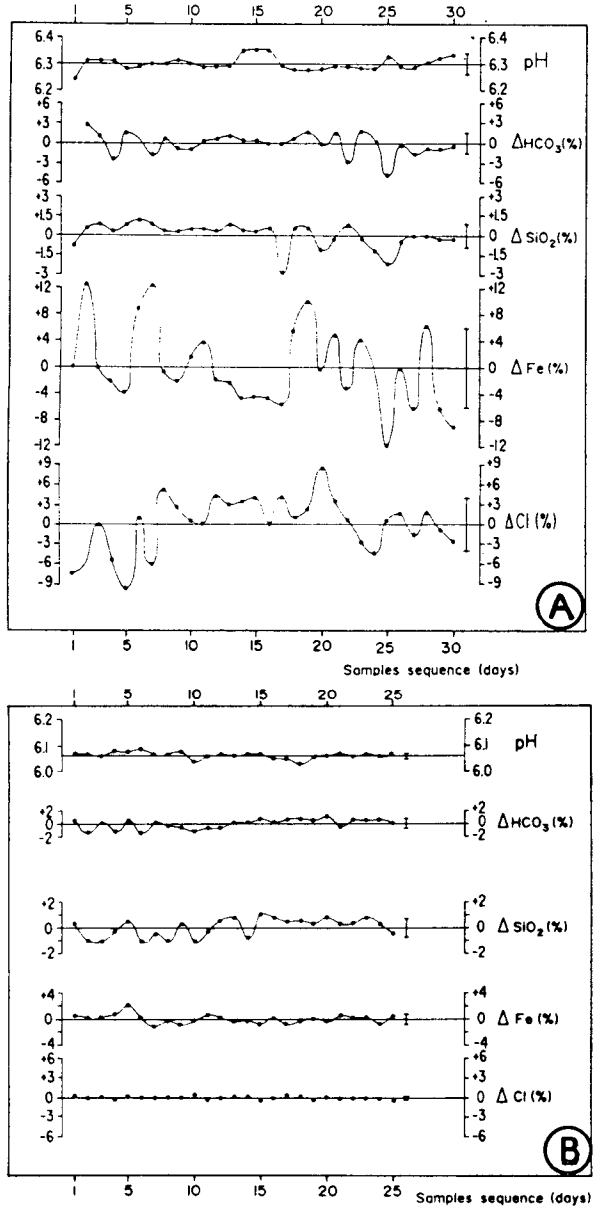


Fig. 3 - Time variations of pH and selected chemical species, expressed in % around the mean. Errors-bars correspond to 1 standard deviation.
A : 1st survey under pumping (148 m^3/h)
B : 2nd survey under artesian flow (~ 36 m^3/h)

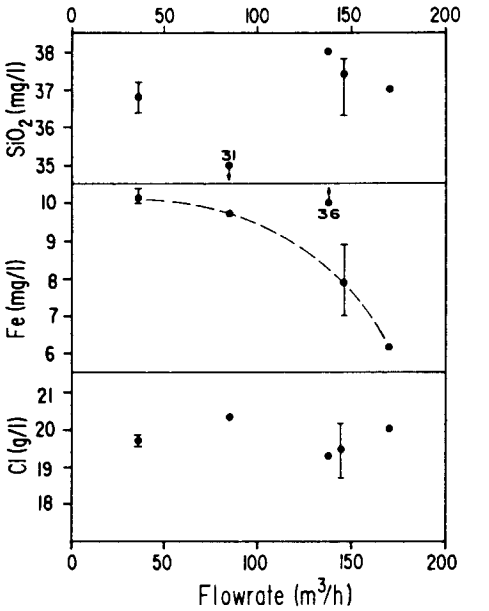


Fig. 4 - Variation of selected dissolved species in the geothermal fluid for various production rates of well GMY 1.

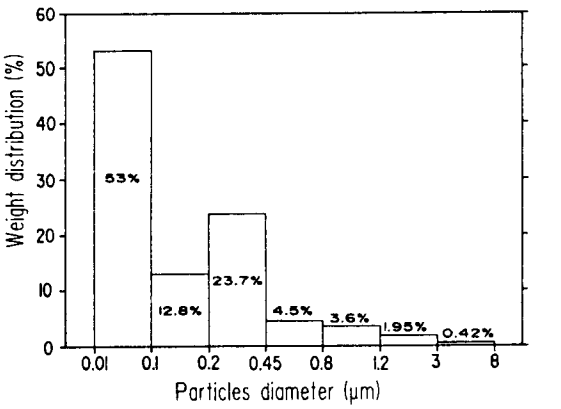


Fig. 5 - Distribution of particle sizes in the geothermal fluid at 36 m^3/h. Percentages are calculated from the particle load weighed on 8 filters.

PROCEEDINGS, Thirteenth Workshop on Geothermal Reservoir Engineering
Stanford University, Stanford, California, January 19-21, 1988
SGP-TR-113

PREDICTION OF KIZILDERE RESERVOIR BEHAVIOR UNDER EXPLOITATION

Ender Okandan

Petroleum Engineering Dept., METU
Ankara-TURKEY

ABSTRACT

Kızıldere geothermal reservoir is under exploitation since 1984. During the four years of operation, electricity production showed a decline from the initially designed power output of 20.4 MW_e. The scaling in wells necessitates periodic mechanical cleaning. However decline in well flow rates even after cleaning, indicate either decrease in productivity index due to scaling in fractures or due to rapid decline in reservoir pressure due to insufficient recharge and strong interference between wells.

In this paper the results of a lumped parameter model prepared for Kızıldere will be presented with the analysis of natural state of the field.

KIZILDERE FIELD

The geologic and geochemical models of Kızıldere were presented elsewhere (1,2). The present well field is located in one of the fault blocks generated on the northern flanks of Büyük Menderes Graben (Fig.1). There are 9 wells that are producing, three of which KD-20, 21 and 22 were drilled in 1986 to supplement the declining power output (Fig.2).

The field is believed to have cool water recharge from Büyük Menderes river (1,2). The drilled holes had encountered two formations that contained hot fluid. The shallow formation, Sazak, at 180 C, is not planned for production, however the deeper formation Igdecik at 200 C is used to supply fluid to the power plant.

Energy potential of Kızıldere field was calculated using reported areal extent of the field as 2 km^2 and thickness of 1000 meters. When optimistic values for porosity as 10% and recovery factor of 15% were assumed, it was calculated that the present area can support only 10 MW power plant for 25 years (3) (Table 1.).

Table 1. Available Work at Well Head and Electricity Producing capacity of Kızıldere
ϕ=10% Res.vol.=2 km^3

R_g, %	10	15	20	25
$W_A x10^{-5}$ Joule	21.8	32.7	43.5	54.4
$Ex10^{-15}$ Joule N_u = 25%	5.5	8.2	10.9	13.7
MW_e (25 years)	7.0	10.4	13.8	17.4

The initial pressure measurements in production zones, indicate a single aquifer feeding the wells (Fig.3.). Temperatures measured in drilled wells indicate a temperature inversion at about -700 m BSL. The pressures in feed zones indicate a possibly high potential area in the north-east direction of the presently producing field.

The CO_2 content of the geothermal fluid had the major effect on the flashing pressure of the reservoir fluid. Bubble point pressure of water with 1.5% (by weight) CO_2 was calculated using Sutton's correlation (4). When this data is carried to the vertical pressure distribution in the field an approximate location of two phase zone is constructed (Fig. 4). So wells producing shallower than this depth should experience $CaCO_3$ deposition in the reservoir which will cause decline in productivities and hence in production rates.

PRODUCTION FROM KIZILDERE AND THE LUMPED PARAMETER MODEL

There is continuous data on power output of the power plant. The flow rate measurements in each well were taken after each cleaning operation. The decline curve analysis of each

well indicate KD-15 and KD-16 show a rapid decline in their flow rates. On the average wells show 50% yearly decline.

The lumped parameter model of the field was prepared assuming there is negligible amount of vapor and original state of the field is compressed liquid. Using the material balance approach, the cumulative mass of water produced is

$$M_{pt} = V.C_w.\rho_w (P_i - P_f) + \rho_w \; B \; \Sigma Q_D \; \Delta P$$

where V = the storage volume of reservoir
C_w = isothermal coefficient of compcompressibility of reservoir fluid
ρ_w = density of reservoir fluid
P_i = initial reservoir pressure
P_f = current reservoir pressure
B = aquifer influx constant
Q_D = dimensionlees influx function
ΔP = drop in reservoir pressure

The recharged mass was calculated using Van Everdingen and Hurst method. The unknown parameters necessary for determining B, influx constant, was estimated using a history match procedure using fluid production data from the wells (5). During history match the pressures were estimated using productivity index data presented in initial reports. Aquifer, feeding the reservoir is taken to be infinite in extent and only supplies fluid around half of the periphery of the reservoir. This was chosen due to geologic setting of the field.

Production from wells were interrupted during cleaning operations (Fig.5.). For influx calculations the pressure drop estimated during a production period was assumed to buildup by 50% during shut in periods. The data used for this purpose are given on Table 2.

The model results are plotted on figure 6, which can be used for future prediction and decline in reservoir pressure can be estimated. The data show an appreciable drop in pressure with small amount of mass produced.

By the time this paper was written only one set of well pressure data was available (5). The pressures measured in wells during Dec. 1986, after the cleaning operation are given on Table 3.

CONCLUSION

The analysis of available data show that the presently producing area in Kızıldere field is located in an overflow zone. The main hot upflow zone should be located by an extended exploration program.

The interference between 9 wells that are drilled so close is unavoidable. It is recommended that wells that showed the highest decline rates be closed and deeper wells to be produced at high well head pressures that will cause scaling to occur in well bores and not in the reservoir.

Table 2. Production from Kızıldere wells during Feb.1984 to Dec.1986

Periods	Cum. time (days)	Production x 10^{-9}kg	Cumulative Prod. x10^{-9} kg
1	75	2.581	2.581
2	167	wells closed	
3	289	2.724	5.305
4	410	wells closed	
5	471	1.275	6.580
6	654	wells closed	
7	1050	13.221	19.800

Table 3. Pressure in Wells after the Cleaning Operation in December 1986 (5)

Well no.	KD-6	KD-7	KD-13	KD-14	KD-15	KD-16
Pressure, bar at production depth	74.8	49.2	54.6	34.5	39.8	39.5
Initial pressure, bar at-production depth	81.24	54.9	61.2	48.2	44.9	44.6

REFERENCES

1. Geothermal Energy Survey of Western Anatolia, Turkey, Project Findings and Recommendations : United Nations Project DP/UN/TUR-66-517/1 final report, 1974.

2. First Turkish-Italian Seminar on Geothermal Energy : Proceedings Vol.II, Ankara, 1982.

3. Okandan E. : Assessment of Denizli-Sarayköy and Aydın-Germencik geothermal Fields: Proceedings IV.Turkish Energy Conference, Izmir, Nov. 1986 (In Turkish)

4. Sutton E.M. : Pressure-Temperature Curves for a Two-phase Mixture of Water and Carbon-dioxide. New Zealand Journal of Science, Vol.19, 291-301, 1976.

5. Data provided by Turkish Electricity Authority.

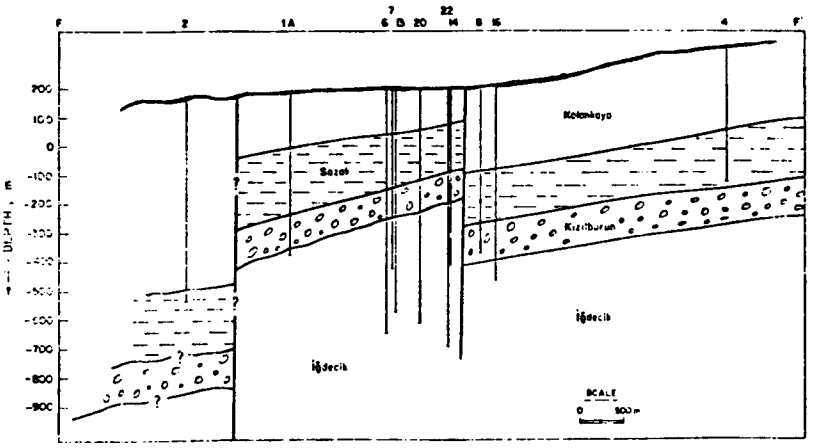


Figure 1. Well Locations and Cross-section along SW-NE Direction in Kızıldere Field

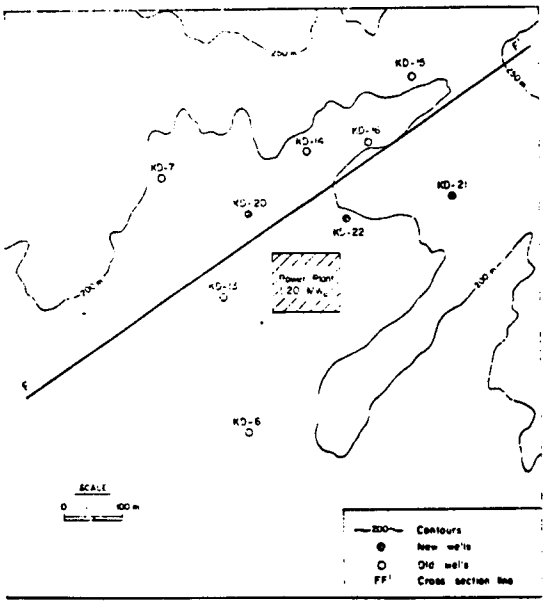


Figure 2. Location of Producing Wells in the Present Well-Field

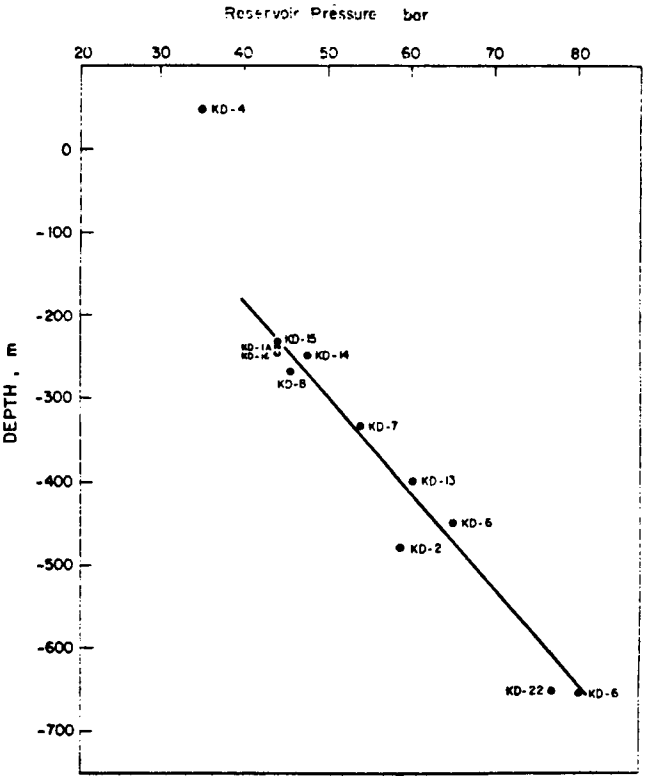


Figure 3. Producing Pressures in Wells of Kızıldere

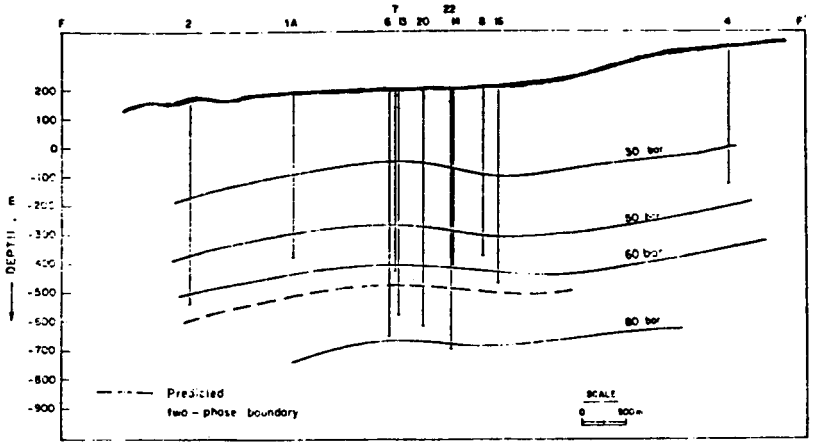


Figure 4. Predicted Two-Phase Boundary and Pressure Distribution along SW-NE Section in the Field

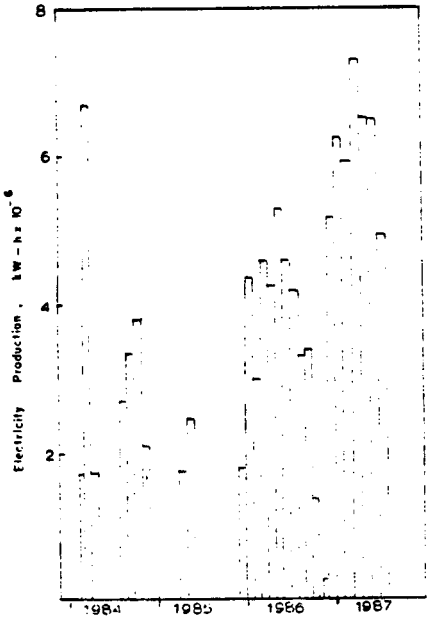


Figure 5. Electricity Production from Kızıldere Power Plant Since its Establishment

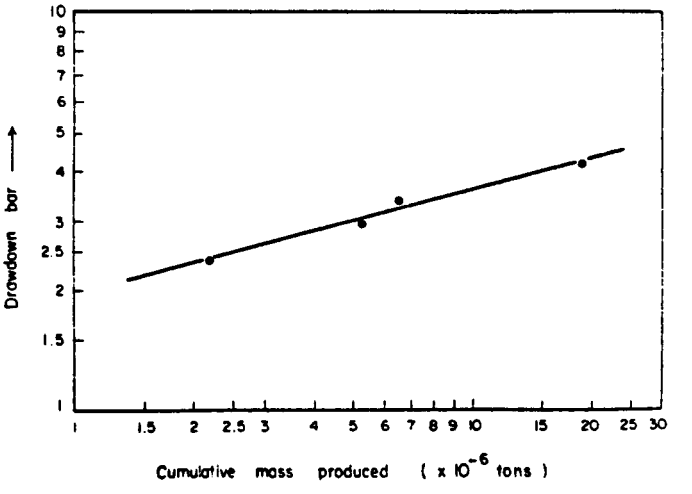


Figure 6. Model Results for Pressure Drawdown due to Mass Production from the Reservoir

PREDICTING THERMAL CONDUCTIVITY OF ROCKS FROM THE LOS AZUFRES GEOTHERMAL FIELD, MEXICO, FROM EASILY MEASURABLE PROPERTIES

Alfonso García, Enrique Contreras,
Departamento de Geotermia, División Fuentes de Energía
Instituto de Investigaciones Eléctricas
Apartado Postal 475, Cuernavaca, Mor., 62000-México

and

Bernardo Domínguez A.
Comisión Federal de Electricidad
Av. Las Camelinas 3527, 10^0 Piso
Morelia, Michoacán, México

ABSTRACT

A correlation is developed to predict thermal conductivity of drill cores from the Los Azufres geothermal field. Only andesites are included as they are predominant. Thermal conductivity of geothermal rocks is in general scarce and its determination is not simple. Almost all published correlations were developed for sedimentary rocks. Typically, for igneous rocks, chemical or mineral analyses are used for estimating conductivity by using some type of additive rule. This requires specialized analytical techniques and the procedure may not be sufficiently accurate if, for instance, a chemical analysis is to be changed into a mineral analysis. Thus a simple and accurate estimation method would be useful for engineering purposes. The present correlation predicts thermal conductivity from a knowledge of bulk density and total porosity, properties which provide basic rock characterization and are easy to measure. They may be determined from drill cores or cuttings, and the procedures represent a real advantage given the cost and low availability of cores. The multivariate correlation proposed is a quadratic polynomial and represents a useful tool to estimate thermal conductivity of igneous rocks since data on this property is very limited. For porosities between 0% and 25%, thermal conductivity is estimated with a maximum deviation of 22% and a residual mean square deviation of 4.62E-3 in terms of the $\log_{10}(k\rho_b)$ variable. The data were determined as part of a project which includes physical, thermal and mechanical properties of drill cores from Los Azufres. For the correlation, sixteen determinations of thermal conductivity, bulk density and total porosity are included. The conductivity data represent the first determinations ever made on these rocks.

NOMENCLATURE

A_i	coefficients of proposed model
F	formation factor
k	thermal conductivity
s	standard deviation
y	$\log_{10}(k\rho_b)$
ρ_b	bulk density
ρ_s	solids density
ϕ_t	total porosity

INTRODUCTION

Maximum recovery of the energy content of a geothermal resource is a basic objective of geothermal energy development. The determination of the resource's size, heat and mass reserves and deliverability are tasks undertaken by geothermal reservoir engineering. These studies require data on the thermal and physical properties of the reservoir's fluids and rocks among which, thermal conductivity, density and porosity are very important. Reservoir rock properties are normally obtained through core analysis, but core extraction requires special sampling which makes cores expensive and not so readily available. Furthermore, determination of thermal conductivity is not straightforward but it may be indirectly estimated from other rock properties which are easier to measure or are more readily available. It thus becomes convenient to have correlations to predict rock properties such as thermal conductivity from a knowledge of other rock properties which may be measured both on cores and drill cuttings, the latter being much more abundant. Notwithstanding, published correlations to predict thermal conductivity include sedimentary rocks but not igneous rocks.

The objective of the present study is to present a correlation to predict thermal conductivity of igneous rocks

from density and porosity data measured on andesitic rocks from the Los Azufres geothermal field [1]. A more extensive treatment of this work will be published in the series Developments in Geothermal Energy in Mexico [2].

A summary of experimental methods used to determine thermal conductivity of rocks is presented in [3]. Correlations to predict thermal conductivity variation with temperature were developed in [4] while pressure effects were considered in [5]. Estimation of conductivity from the rock mineral composition and the conductivity of the rock-forming minerals has been the subject of a number of studies [6-10]. Birch and Clark [6] found that a series combination of the rock-forming minerals is appropriate for this purpose. Woodside and Messmer [8] claimed that the geometric mean arrangement was more satisfactory while Beck [9] proposed a Maxwell-type model which accounts for thermal contact resistance effects. Horai and Baldridge [10] proposed three methods for estimating the conductivity of non-porous, macroscopically isotropic and homogeneous rocks. To obtain the conductivity of the rock as a consolidated medium, a correction for porosity is needed. On the other hand, a common disadvantage of all these methods is the need for specialized equipment to perform the chemical or mineral analysis. Even if the analysis is available, the procedure might not be sufficiently accurate if, for instance, a chemical analysis is to be converted into a mineral analysis or if the thermal conductivity of a rock-forming mineral is not available Although these methods are typically used for igneous rocks, some are also applicable to other rocks.

Other published correlations include Krupiczka's theoretical models [11] for granular material arranged in cylindrical and spherical packings for which the porosity was 21.5 % and 47.6 % respectively. Martinez [7] extended this model to account for intergranular effects through the use of grain size. Anand et al [12] developed multivariate correlations for dry and saturated rocks. Zierfuss and Van der Vliet [13] developed a correlation which included the formation factor F. This factor must be determined from electrical resistivity measurements. Reddy [14] modified the model of [13] and proposed a simple correlation of conductivity with density and porosity as independent variables, properties which are easy to measure. These correlations were developed for sedimentary rocks, except for Krupiczka's model [11], but none for igneous rocks. This fact lends further support to the correlation presented here and in [2] for igneous rocks.

THE EXPERIMENTS

Thermal conductivity, porosity and density were determined. Conductivity was measured using oven-dried cylindrical specimens, 2" diameter by 4" lentgh employing the thermal needle transient method which simulates a line source in an infinite homogeneous medium [15]. Fig. 1 shows the experimental set-up: an electric heater and its attached type-K thermocouple are introduced along a longitudinal borehole in the sample, with the thermocouple tip sensing temperature at mid-length in the cylindrical sample. Any gaps left in the hole are stuffed with copper powder to minimize contact resistance.

Controlled power is then applied which results in a constant heat generation per unit length. The temperature history is then recorded using an automatic data logger along with the heat input and finally, conductivity is computed from the slope of a best-fit straight line of the curve of temperature versus the logarithm of time. Test runs on a standard sample of fused quartz showed an error of ± 0.03W/(m-K) for the present determinations. Density was measured employing standard techniques [16]. Mass was measured using an electronic balance and bulk volume was measured in a Ruska Universal porometer by mercury injection, and from these, bulk density was computed. Solids (grain) volume was determined by the pulverization method whereby grain volume was measured by displacing an equivalent volume of liquid in a volumetric flask. Total porosity was then computed from its definition:

$$\phi_t = 1 - (\rho_b/\rho_s) \qquad (1)$$

RESULTS AND CORRELATION ANALYSIS

The experiments were performed on fifteen cores from eleven wells from Los Azufres. Fig. 2 shows the location of the wells under study. Samples tested include basaltic andesites and andesites of igneous origin which are the predominant type of rock in the field. The results of the present study include sixteen determinations of thermal conductivity,

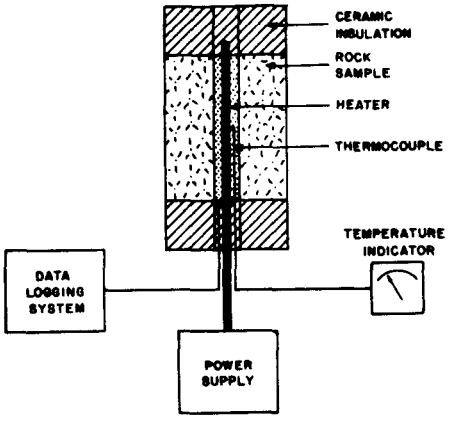


FIG. 1 SCHEMATICS OF EXPERIMENTAL SET-UP FOR THERMAL CONDUCTIVITY MEASUREMENT.

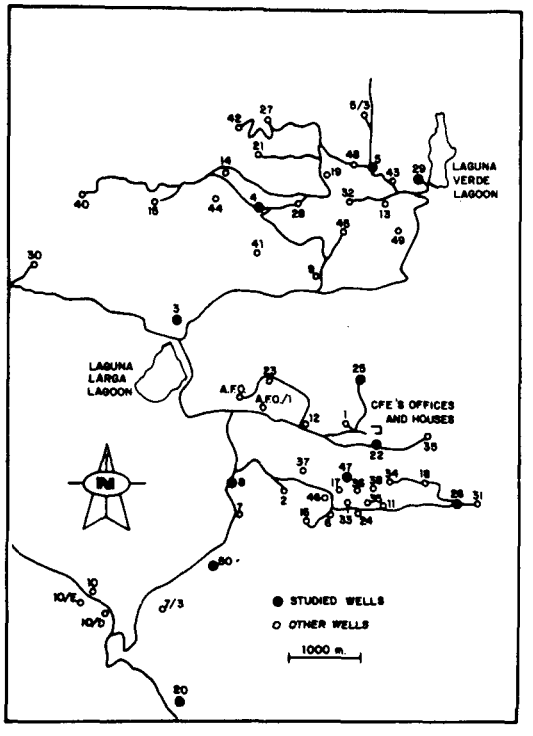


FIG. 2 MAP OF LOS AZUFRES GEOTHERMAL FIELD SHOWING THE LOCATION OF THE WELLS STUDIED.

bulk and solids density and total porosity and are shown in Table 1. It may be noted that thermal conductivity varied between 1.05W/(m-K) and 2.34W/(m-K) with a mean conductivity value of 1.72W/(m-K) and a standard deviation of 0.34W/(m-K) for the 16 determinations. Similarly, the range of variation of solids density is from 2610 to 2940kg/m^3 whereas that for bulk density is from 2050 to 2740kg/m^3 The corresponding mean density values are 2760kg/m^3 and 2450kg/m^3, respectively. Total porosity varied from 1.9 to 24.7 %, with an average value of 11.2 %.

Table 1 Measured thermophysical properties of cores from The Los Azufres geothermal field

Well, core and sample	Density (kg/m^3) bulk	solids	Total porosity (%)	Thermal conductivity [W/(m-K)]
AZ3-N1-1	2340	2760	15.5	1.68
AZ3-N4.1-1	2560	2940	13.2	1.84
AZ3-N5-1	2740	2800	2.2	1.99
AZ4-N3-1	2440	2790	12.7	1.58
AZ4-N3-2	2430	2790	12.9	1.53
AZ5-N1-1	2050	2730	24.7	1.17
AZ8-N2-1	2600	2790	6.9	2.34
AZ20-N1-1	2270	2610	13.0	1.58
AZ20-N3-1	2690	2810	4.2	1.71
AZ22-N2-1	2450	2800	12.6	2.17
AZ25-N1-1	2320	2730	14.8	1.75
AZ26-N2-1	2610	2740	4.9	2.20
AZ26-N3-1	2430	2700	10.1	1.55
AZ29-N1-1	2050	2660	23.1	1.05
AZ47-N4-1	2740	2790	1.9	1.89
AZ50-N3-1	2490	2680	7.2	1.52

With the data just described, a correlation to predict thermal conductivity from density and porosity was developed. In developing the correlation, bulk density and total porosity were selected as independent variables since they are easy-to-measure or may be readily available. Also, they have a direct effect on heat flow path through a rock and affect the thermal conductivity of the rock. This contrasts with correlations which have been developed for sedimentary rocks and include variables such as formation factors which might be widely available for sedimentary rocks but not for igneous rocks. Furthermore, formation factors may be as difficult to measure as the thermal conductivity itself.

For the correlation, a new variable $y = \log_{10}(k\rho_b)$ is defined and a polynomial regression of y as function of total porosity was performed. Polynomials tested include first and second degree models. Figures 3 and 4 show plots of experimental values of the $y-\phi_t$

pairs as well as the corresponding fitted curves. It is seen from Fig. 3 that the linear model follows reasonably well the central points but fails to follow the points at both left and right ends while Fig. 4 shows that the quadratic model follows such points better and its behavior in the central part of the figure is quite similar to that of the linear case. Statistical computations revealed a correlation coefficient of 0.83 and a r.m.s. deviation of 5.23E-3 for the linear fit. Correspondig values for the quadratic model are a correlation coefficient of 0.87 with a r.m.s. deviation of 4.62E-3. These observations show that the quadratic model is the best of the two. The resulting equation is

$$\log_{10}(k\rho_b) = A_0 + A_1\phi_{tot} + A_2\phi_{tot}^2 \quad (2)$$

where:

A_0=3.7228809, A_1=-0.94476092E-3

and A_2=-0.581068E-3

Comparison between predicted and measured conductivity values showed a maximum difference of ±22% for fifteen of the sixteen points. The discrepancy for the other point was 28% and may be due to a possible error in the determination of the total porosity which resulted to be less than its corresponding effective porosity value, a fact that is physically incongruent. The density and porosity values for this case are being reviewed. However, the point is included to show the complete set of data. This correlation will be updated as more data are gathered.

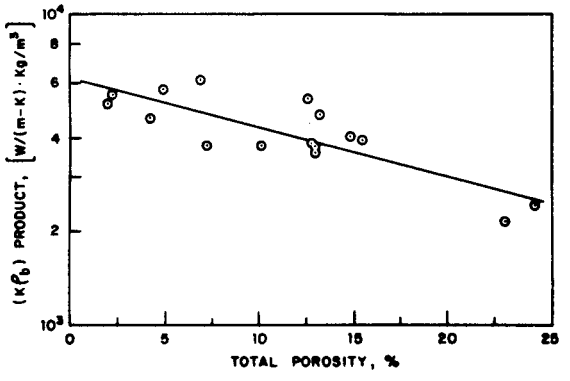


FIG. 3 EXPERIMENTAL POINTS AND LINEAR MODEL FITTED

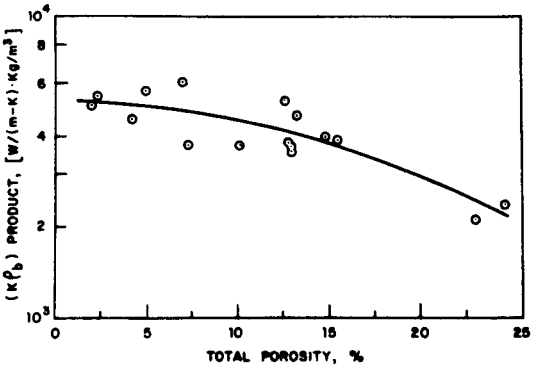


FIG. 4 EXPERIMENTAL POINTS AND QUADRATIC MODEL FITTED

CONCLUSIONS

Sixteen determinations of thermal conductivity, density and porosity were performed on drill cores from Los Azufres. The mean conductivity value was found to be 1.72W/(m-K) while mean values of bulk density and total porosity were 2451kg/m^3 and 11.2% respectively. A regression analysis was made using two models which included thermal conductivity, density and porosity. A quadratic polynomial correlation in the form of the log of the product between thermal conductivity and bulk density as function of total porosity proved to be better on the basis of statistical and error analysis. For such model, the correlation coefficient was 0.87 and the r.m.s. deviation was 4.62E-3 with a maximum error of ±22% for 94% of the cases. This correlation should have a significant practical value since it predicts thermal conductivity from a knowledge of density and porosity, properties which are simple to determine and may be measured not only on drill cores but also on drill cuttings which are more abundant and less expensive than cores. The model could be used to perform numerical studies of the Los Azufres field.

Acknowledgements-Thanks are due to Dr. David Nieva, for his encouragement to publish this work. Thanks are also due to the staff of Gerencia de Proyectos Geotermoeléctricos of C.F.E. for their valuable collaboration.

REFERENCES

1. Apoyo para diagnósticos de perforación de pozos mediante la determinación de propiedades

físicas de rocas en medios geotérmicos-Fase I: Correlaciones entre Petrología y Petrofísica en campos del eje neovolcánico, Informe IIE/11/2014/I 03/F, Instituto de Investigaciones Eléctricas, Cuernavaca, Mor., México, in preparation, (1987).

2. A. García, E. Contreras, E. Iglesias and B. Domínguez, Developments in geothermal energy in Mexico--Part seventeen: Thermal conductivity of drill cores from the Los Azufres geothermal field: experimental results and accurate prediction method, J. Heat Recovery Systems, in press, (1988).

3. A. García, and E. Contreras, Métodos para la determinación de la conductividad y la difusividad térmica de rocas: estudio bibliográfico, Informe IIE/10/11/1663/FE-G29/I 07/P, Instituto de Investigaciones Eléctricas, Cuernavaca, Mor., México, (1985).

4. W. H. Somerton and G. D. Boozer, Thermal characteristics of porous rocks at elevated temperatures, Petroleum Trans. of AIME, Vol. 219, pp. 418-422, (1960).

5. G. Backstrom, Measurement of thermophysical properties of solids under high pressure, Invited paper, Proc. Seventh Symposium on Thermophysical Properties, Standing Committee on Thermophysical Properties, Heat Transfer Division of ASME, Gaithersburg, Md., pp. 169-180, 10-12 May, (1977).

6. F. Birch and H. Clark, The thermal conductivity of rocks and its dependence upon temperature and composition, Am. Jour. Sci., **238**, 527-558, 613-635, (1940).

7. L. F. Martínez, Thermal conductivity of core samples from the Cerro Prieto geothermal field: experimental results and an improved prediction method, Proc. First Symp. on the Cerro Prieto Geothermal Field, Baja California, México, Lawrence Berkeley Laboratory, Report LBL-7098, pp. 342-351, (1978).

8. W. Woodside and J. H. Messmer, Thermal conductivity of porous media: I-unconsolidated sands; II-consolidated rocks, J. Appl. Phys., **32**, 1688-1699, 1699-1706, (1961).

9. A. E. Beck, An improved method of computing the thermal conductivity of fluid-filled sedimentary rocks, The Log Analyst, p. 30, (1976).

10. K. Horai and S. Baldridge, Thermal conductivity of nineteen igneous rocks, II: Estimation of the thermal conductivity of rock from the mineral and chemical compositions, Phys. Earth Planet Interiors, **5**, 157-166, (1972).

11. R. Krupiczka, Analysis of thermal conductivity in granular materials, Intl. Chem. Engng. **7**, 122-144, (1967).

12. J. Anand, W. H. Somerton and E. Gomaa, Predicting thermal conductivities of formations from other known properties, J. Soc. Pet. Engrs., **13**, 267-273, (1973).

13. H. Zierfuss and G. van der Vliet, Laboratory measurements of heat conductivity of sedimentary rocks, Bull. Amer. Assoc. of Pet. Geol., **40**, 2475-2488, (1956).

14. M. S. Reddy, Estimating the thermal conductivity of rocks-an analytical approach, Proc. Seventh Symposium on Thermophysical Properties, Standing Committee on Thermophysical Properties, Heat Transfer Division of ASME, Gaithersburg, Md., pp. 404-411, 10-12 May, (1977).

15. H. S. Carslaw and J. C. Jaeger, Conduction of heat in solids, 2nd. ed., Oxford, Oxford University Press, (1959).

16. ISRM, Suggested methods for determining water content, porosity, density, absorption and related properties, Society for Rock Mechanics, Commission on Standarization of Laboratory and Field Tests, Document No. 2, Lisbon, Portugal, (1972).

THIRTEENTH ANNUAL WORKSHOP ON
GEOTHERMAL RESERVOIR ENGINEERING
STANFORD UNIVERSITY
JANUARY 19-21, 1988

PARTICIPANTS LIST

R. H. Adams
Consultant
20 Point Loma Drive
Corona Del Mar, CA
(714) 759-0684

Percival F. delas Alas
Philippine Geothermal Inc.
P.O. Box 7336 Airport
Metro Manila, Philippines
63-2-8178876

Anil K. Ambastha
Petroleum Engineering Dept.
Stanford University
Stanford, CA 94305
(415) 723-4744

Emilio Antunez
GeothermEx, Inc.
5221 Central Avenue, Suite 201
Richmond, CA 94804
(415) 527-9876

Benjamin G. Aquino
PNOC - EDC
Ft. Bonifacio
Manila, Philippines
8158961

Paul Atkinson
UNOCAL - Geothermal Division
3576 UNOCAL Place
Santa Rosa, CA 95401
(707) 545-7600

Zosimo P. Aunzo
PNOC - Energy Development Corp.
Ft. Bonifacio, Makati
Metro Manila, Philippines

Elwood L. Baldwin
Baldwin Engineering, Inc.
13612 Midway Road, #490
Dallas, TX 75244
(214) 980-0784

Judith M. Ballantyne
University of Utah Research Institute
391 Chipeta Way, Suite C
Salt Lake City, UT 84108
(801) 524-3422

Benjamine J. Barker
Philippine Geothermal Inc.
P.O. Box 7336 Airport
Metro Manila, Philippines
63-2-8178876

A. S. Batchelor
Geoscience Limited
Falmouth Business Park,
Bickland Water Rd.,
Falmouth, Cornwall, England, TR11 4SZ
01-144-326-211070

Dick Benoit
Oxbow Geothermal Corp.
200 S. Virginia St., Suite 450
Reno, Nevada 89501
(702) 322-1300

Sally Benson
Lawrence Berkeley Laboratory
Earth Sciences Division
One Cyclotron Road, Bldg. 50E
Berkeley, CA 94720
(415) 486-6766

Domingo B. Beraquit
Philippine Geothermal Inc.
P.O. Box 7336 Airport
Metro Manila, Philippines
63-2-8178876

Gudmundur Bodvarsson
Lawrence Berkeley Laboratory
Earth Sciences Division
One Cyclotron Road, Bldg. 50E
Berkeley, CA 94720
(415) 486-4789

William Brigham
Petroleum Engineering Dept.
Stanford University
Stanford, CA 94305
(415) 723-0611

Paul Brophy
California Energy Co., Inc.
3333 Mendocino Ave., Suite 100
Santa Rosa, CA 95403
(707) 526-1000

Gustavo Calderon
Inter-American Development Bank
1300 New York Ave. NW
Washington, DC 20577
(202) 623-1978

Chieh Chu
Texaco Inc.
P.O. Box 770070
Houston, TX 77215-0070
(713) 954-6000

Gene T. Cole
Chevron Resources Co. - Geothermal
P.O. Box 5049
San Ramon, CA 94583-0949
(415) 842-5303

Jim Combs
Geothermal Resources Int'l., Inc.
1825 S. Grant St., Suite 900
San Mateo, CA 94402
(415) 349-3232

Richard Corbaley
Calif. Division of Oil and Gas
485 Broadway, Suite B
El Centro, CA 92243
(619) 353-9900

Derek Corlett
Camborne School of Mines
Geothermal Energy Project
Rosemanowes Quarry, Herniss, Penryn,
Cornwall, TR10 9DU, England
(0209) 860141

John Counsil
Consultant
1148 Shadyoak Place
Santa Rosa, Ca 95404
(707) 538-2288

B. Lea Cox
Lawrence Berkeley Laboratory
Earth Sciences Division
One Cyclotron Road, Bldg. 50E
Berkeley, CA 94720
(415) 486-4717

Annie Criaud
Bureau de Recherches Geologiques
et Minieres (BRGM)
BP 6009 - Avenue de Concy
45060 Orleans Cedex - France
33-38-64-34-34 or 33-38-64-31-72

R. Curtis
Geoscience Limited
Falmouth Business Park,
Bickland Water Rd.,
Falmouth, Cornwall, England, TR11 4SZ
01-144-326-211070

William D'Olier
Thermal Power Company
601 California St.
San Francisco, CA 95401
(415) 765-0306

Jeff Davarzani
Atlas Wireline Services
P.O. Box 1407, DC-15
Houston, TX 77251
(713) 972-4866

Richard F. Dondanville
UNOCAL - Geothermal Division
3576 UNOCAL Place
Santa Rosa, CA 95401
(707) 545-7600

Andy Drenick
GEO Operator Corp.
1330 N. Dutton
Santa Rosa, CA 95401
(707) 523-4272

Herman Dykstra
Petroleum Engineering Consultant
4180 Treat Blvd., Suite I
Concord, CA 94518
(415) 676-7464

Carlos Echeverria
State Dept. of Water Resources
1416 9th Street
Sacramento, CA 95814
(916) 322-0445

Michael J. Economides
Dowell Schlumberger
2346 Underwood
Houston, TX 77030
(713) 556-7726

Kathleen L. Enedy
Geysers Geothermal Company
1160 N. Dutton, Suite 200
Santa Rosa, 95401
(707) 578-2710

Steven Enedy
Northern California Power Agency
P.O. Box 425
Healdsburg, CA 95448
(707) 987-3101

Richard M. Estabrook
Bureau of Land Management
555 Leslie St.
Ukiah, CA 95482
(707) 462-3873

Don J. Everitts
Calif. State Lands Commission
245 W. Broadway, Suite 425
Long Beach, CA 90802
(213) 590-5204

David D. Faulder
Chevron Resources
6001 Bollinger Canyon
San Ramon, CA 94583
(415) 842-5319

David H. Fleisig
Pacific Gas and Electric Co.
Law Dept., Room 2749
P.O. Box 7442
San Francisco, CA 94120
(415) 972-6649

Robert O. Fournier
U.S. Geological Survey
345 Middlefield Rd., MS 910
Menlo Park, CA 94025
(415) 329-5205

Pat Gallagher
Bureau of Land Management
800 Truxtun
Bakersfield, CA 93301
(805) 861-4356

Sabodh K. Garg
S-Cubed
3398 Carmel Mountain Road
San Diego, CA 92121
(619) 453-0060

Scott Gaulke
Lawrence Berkeley Laboratory
Earth Sciences Division
One Cyclotron Road, Bldg. 50E
Berkeley, CA 94720
(415) 486-6760

Malcolm A. Grant
DSIR
Box 1578
Wellington, New Zealand

L. Eric Greenwade
Idaho National Eng. Lab.
P.O. Box 1625, Mail Stop 2212
Idaho Falls, ID 83415
(208) 526-1276

J. S. Gudmundsson
Geothermal Division
National Energy Authority
Grensasvegur 9, Reykjavik, Iceland
354-1-83600

Marianne Guffanti
U.S. Geological Survey
922 National Center
Reston, VA 22203
(703) 648-6725

Jill Robinson Haizlip
GEO Operator Corp.
1330 N. Dutton
Santa Rosa, CA 95401
(707) 523-4272

Ronald Hedges
UNOCAL - Geothermal Division
3576 UNOCAL Place
Santa Rosa, CA 95401
(707) 545-7600

James Hoagland
UNOCAL - Geothermal Division
3576 UNOCAL Place
Santa Rosa, CA 95401
(707) 545-7600

Manifred Hochstein
Geothermal Institute
University of Auckland
Private Bag, Auckland, New Zealand
737999 x8403

John Holtzapple
Pacific Gas and Electric Company
77 Beale Street
San Francisco, CA 94120
(415) 972-4115

Roland N. Horne
Petroleum Engineering Dept.
Stanford University
Stanford, CA 94305
(415) 723-9595

Glenn D. Horton
Pacific Gas and Electric Company
111 Stony Circle
Santa Rosa, CA 95401
(707) 577-7062

Eduardo Iglesias
IIE
Apdo. Postal 475, Cuernavaca
Mor., Mexico
(73) 14-3811 x3210

Joe Iovenitti
2337 Panoramic Drive
Concord, CA 94520
(415) 798-8449

Younes Jalali
Petroleum Engineering Dept.
Stanford University
Stanford, CA 94305
(415) 723-9476

Cathy Janik
U.S. Geological Survey
345 Middlefield Rd., MS 910
Menlo Park, CA 94025
(415) 329-5213

Dawn Janney
Naval Weapons Center
Code 2606, NWC
China Lake, CA 93555-6001
(619) 939-3411 x234

Jitendra Kikani
Petroleum Engineering Dept.
Stanford University
Stanford, CA 94305
(415) 723-4744

Hideaki Kitamura
New Energy Development Organization
Sunshine 60, 29F
1-1, 3-Chome, Higashi-Ikebukuro
Toshimu-ku, Tokyo, 170 Japan

Paul Kruger
Civil Engineering Dept.
Stanford, CA 94305
(415) 725-2382 or 723-4123

Kwabena Kwakwa
Camborne School of Mines
Geothermal Energy Project
Rosemanowes Quarry, Herniss, Penryn,
Cornwall, TR10 9DU, England
(0209) 860141

Catherine Laky
Lawrence Berkeley Lab.
Berkeley, CA 94720
(415) 486-4160

P. Ledingham
Geoscience Limited
Falmouth Business Park,
Bickland Water Rd.,
Falmouth, Cornwall, England, TR11 4SZ
01-144-326-211070

John K. Leong
Philippine Geothermal Inc.
P.O. Box 7336 Airport
Metro Manila, Philippines
63-2-8178876

Wilhelmino Q. Lim
Philippine Geothermal Inc.
P.O. Box 7336 Airport
Metro Manila, Philippines
63-2-8178876

Grant S. Lyddon
947 Berkeley St.
Santa Monica, CA 90403-2307
(213) 829-0049

Mark Malzahn
Los Alamos National Lab.
3789 Gold St., #2
Los Alamos, NM 87541
(505) 667-4318

R. A. McCartney
Geoscience Limited
Falmouth Business Park,
Bickland Water Rd.,
Falmouth, Cornwall, England, TR11 4SZ
01-144-326-211070

Gregory M. McFadden
UNOCAL- Geothermal Division
Box 1805
Indio, CA 92202
(619) 342-4723

Robert McKibbin
Geothermal Institute, Univ. of Auckland
Private Bag, Auckland, New Zealand

M. G. Mefferd
Calif. Div. of Oil and Gas
1416 9th St., Rm. 1310
Sacramento, CA 95814
(916) 445-9686

Anthony J. Menzies
GeothermEx, Inc.
5221 Central Avenue, Suite 201
Richmond, CA 94804
(415) 527-9876

Frank G. Miller
Petroleum Engineering Dept.
Stanford University
Stanford, CA 94305
(415) 723-2938

John D. Miller
Idaho National Eng. Lab.
P.O. Box 1625
Idaho Falls, ID 83415
(208) 526-0881

Richard J. Miller
Cascadia Pacific Corp.
1000 E. Walnut Ave., #237
Pasadena, CA 91106
(818) 795-3214

Phil Mogen
UNOCAL - Geothermal Division
3576 UNOCAL Place
Santa Rosa, CA 95401
(707) 545-7600

George M. Moore
Pacific Gas and Electric Co.
Law Dept., Room 2733
P.O. Box 7442
San Francisco, CA 94120
(415) 972-6642

Joe Moore
University of Utah Research Institute
391 Chipeta Way
Salt Lake City, UT 84108
(801) 524-3428

Paul B. Mount
Calif. State Lands Commission
245 W. Broadway, Suite 425
Long Beach, CA 90802
(213) 590-5995

Patrick Muffler
U.S. Geological Survey
345 Middlefield Rd., MS 910
Menlo Park, CA 94025
(415) 329-5239

Hugh Murdifi
Los Alamos National Lab.
Mail Stop J979
Los Alamos, NM 87545
(505) 667-3185

Larry Murray
UNOCAL-Science and Technology Div.
376 S. Valencia Ave.
Brea, CA 92621
(714) 528-7201 x1593

K. Ben Naceur
Dowell Schlumberger
P.O. Box 2710
Tulsa, OK 74101
(918) 250-4426

Giuseppe Neri
ENEL - UNG
Via A. Pisano
Pisa, Italy
(50) 535111 or (50) 535815

David Nieva
I. I. E.
Apdo. Postal 475
Cuernavaca, Monelos, Mexico
(73) 14-14-33

Kosuke Nishi
Univ. of Tokyo
Dept. of Mineral Dev. Eng., Faculty of Eng
Hongou, Bunkyou-ku, Tokyo 113
Japan

Al Pingol
UNOCAL - Geothermal Division
3576 UNOCAL Place
Santa Rosa, CA 95401
(707) 545-7600

Lyndon F. Pittinger
Philippine Geothermal Inc.
P.O. Box 7336 Airport
Metro Manila, Philippines
63-2-8178876

Susan M. Prestwich
U. S. Dept. of Energy
785 D.O.E. Place
Idaho Falls, ID 83402
(208) 526-1147

John W. Pritchett
S-Cubed
3398 Carmel Mountain Road
San Diego, CA 92121
(619) 453-0060

Karsten Pruess
Lawrence Berkeley Laboratory
Earth Sciences Division
One Cyclotron Road, Bldg. 50E
Berkeley, CA 94720
(415) 486-6732

Greg Raasch
UNOCAL - Geothermal Division
3576 UNOCAL Place
Santa Rosa, CA 95401
(707) 545-7600

Henry J. Ramey, Jr.
Petroleum Engineering Dept.
Stanford University
Stanford, CA 94305
(415) 723-1774

Jetzabeth Ramirez
Universidad Nacional Autonoma De Mexico
Division De Estudios De Posgrado,
Facultad De Ingeneria
04510 Mexico, D.F.
(525) 286-3181

Marshall Reed
U.S. Dept. of Energy
Washington, D.C 20585
(202) 586-8076

Joel Renner
Idaho National Eng. Lab.
P.O. Box 1625
Idaho Falls, ID 83415
(208) 526-9824

Kenneth Riedel
UNOCAL - Geothermal Division
3576 UNOCAL Place
Santa Rosa, CA 95401
(707) 545-7600

Mark Ripperda
Lawrence Berkeley Laboratory
Earth Sciences Division
One Cyclotron Road, Bldg. 50E
Berkeley, CA 94720
(415) 486-7107

Jesus Rivera
Univ. Nacional Autonoma De Mexico
Division De Estudios De Posgrado,
Facultad De Ingeneria
04510 Mexico, D.F.
(525) 550-8712

Bruce Robinson
Los Alamos National Lab.
Mail Stop J981
Los Alamos, NM 87545
(505) 667-4318

Joel Robinson
UNOCAL - Geothermal Division
3576 UNOCAL Place
Santa Rosa, CA 95401
(707) 545-7600

Don Ross
Bureau of Land Management
7109 Wilford Ct.
Bakersfield, CA 93309
(805) 861-4129

Tim Rossknecht
UNOCAL - Geothermal Division
3576 UNOCAL Place
Santa Rosa, CA 95401
(707) 545-7600

Subir K. Sanyal
GeothermEx, Inc.
5221 Central Avenue, Suite 201
Richmond, CA 94804
(415) 527-9876

Zosimo F. Sarmiento
PNOC - Energy Development Corp.
Merritt Rd., Ft. Bonifacio,
Metro Manila, Philippines
815-89-61

Gerald K. Smith
Chevron Resources
6001 Bollinger Canyon
San Ramon, CA 94583
(415) 842-5311

Mike Sorey
U.S. Geological Survey
345 Middlefield Rd., MS 439
Menlo Park, CA 94025
(415) 329-4420

Mary Stallard
U.S. Geological Survey
345 Middlefield Rd., MS 910
Menlo Park, CA 94025
(415) 329-5214

Neil Stefanides
Union Oil - Geothermal Div.
Box 7600
Los Angeles, CA 90051
(213) 977-7740

Valgardur Stefansson
United Nations - DTCD
One United Nations Plaza
Room DCI - 784
New York, NY 10017

Benedik Steinigrumsson
Lawrence Berkeley Laboratory
Earth Sciences Division
One Cyclotron Road, Bldg. 50E
Berkeley, CA 94720
(415) 486-6760

Kenneth Stelling
State of California
50 "D" Street, Rm. 300
Santa Rosa, CA 95405
(707) 576-2385

Jeffrey Sternfeld
GEO Operator Corp.
1330 N. Dutton
Santa Rosa, CA 95401
(707) 523-4272

Chandler A. Swanberg
Geothermal Resources Int'l., Inc.
1825 South Grant St., Suite 900
San Mateo, CA 94402
(415) 349-3232

Masahiro Takahashi
Japan Metals and Chemicals Co., Ltd.
24-Ukai, Takizawa-mura, Iwate
020 -01 Japan
0196-84-4112

Larry Taylor
Pro-Technics International, Inc.
14760 Memorial Drive., Suite 206
Houston, TX 77079
(713) 496-3734

Wilbur M. Thompson
Calif. State Lands Commission
245 W. Broadway, Suite 425
Long Beach, CA 90802
(213) 590-5243

Franco B. Tonani
University of Palermo
Instituto Di Mineralogia
Via Archirafi 36 - Palermo Italy
(3991) 6161516

Alfred Truesdell
U.S. Geological Survey
345 Middlefield Rd., MS 910
Menlo Park, CA 94025
(415) 329-5212

William C. Walkey
GEO
61419 S. Hwy. 97, Suite A
Bend, OR 97701
(503) 389-6681

Mark Walters
GEO Operator Corp.
1330 N. Dutton
Santa Rosa, CA 95401
(707) 523-4272

Charles W. Whitcomb
Bureau of Land Management
555 Leslie St.
Ukiah, CA 95482
(707) 462-3873

Ken Williamson
UNOCAL - Geothermal Division
P.O. Box 0854
Santa Rosa, CA 95406
(707) 545-7600

Mike Woodruff
GEO Operator Corp.
P.O. Box 748
Holtville, CA 92250
(619) 356-4613

Phillip M. Wright
University of Utah Research Institute
391 Chipeta Way, Suite C
Salt Lake City, UT 84108
(801) 524-3422

John Ziagos
Geothermal Resources Int'l., Inc.
1825 S. Grant St., Suite 900
San Mateo, CA 94402
(415) 349-3232

SUBJECT INDEX VOLUME 14

Acoustic logging: 299
Adsorption: 281
Agarwal slope: 56
Anhydrite deposition: 69
Artificial intelligence: 292
Asymptotic expression: 261
Basement aquifer system: 25
Beijing Geothermal System: 25
Binary code sequence: 299
Biot number: 114
Borehole:
  stability: 2
  televiewer: 2, 300
Boundary layer: 174
Budiansky's formula: 256
Bulalo field, Philippines: 35
Casa Diablo Geothermal Project:
  geology and hydrology of: 5
  well test program: 7
Cascades range: 2
Chi-square statistic: 292
Chloride concentration: 93
Circumferential sonde: 300
Clapeyron equation: 166
Collocation: 263
Composition:
  mobile phase: 143
Compressibility:
  isentropic: 20
  steam/water mixtures: 19
Computer codes:
  FEHM: 225,
  FRACSL: 273,
  MULKOM: 86, 165, 173, 220
  THOR: 256
  WATRAZ: 313
  WBGHT: 226
Convection: 77, 102
  double-diffusive: 101
  natural: 32, 47
  near-critical: 173
  secular: 25
Convective-dispersion equation:
  114, 211, 274
Convolution:
  Boundary Element Method: 261
  integral: 246
Cooldown curve: 117
Corey curves: 129, 167
Correlation coefficient : 326
Corrosion: 94
Crank-Nicholson scheme: 115
Crater Lake, Oregon: 2
Crossflow: 269
Cullender-Smith method: 45
Debye-Huckel equation: 95
Deconvolution: 113
Department of Energy: 1
Detoxifying sludges: 3
Diffusion:
  binary: 165
  matrix: 211, 215
  molecular: 165
Dipole tests: 249
Discrete sampling: 142
Dissociation reaction: 95
Divergence theorem of Gauss: 262
Doublet: 27
Dual permeability: 273
Dual porosity systems: 205
East Mesa, California:
  heat cycle research facility: 2
Energy:
  extraction, Magma: 4
Enthalpy: 43, 85, 193, 254
  reservoir water, of: 59
Equation of state: 164
  Haar: 173
Exponential decline: 182
Fenton Hill, NM: 113, 225
Fickian transport: 273
Finite element: 115, 225
Five-spot pattern: 222
Flash front: 254
Flash point: 151
Flow impedance: 227
Flow probable planes: 231
Fourier Series: 221
Fracture: 84, 103, 205, 226
  275, 282, 303
  aperture: 211
  mapping tool, radar: 2
  network modeling: 211
  plugging mechanics: 2
  orientation: 211, 276
  spacing: 205, 211
Fumeroles: 6

Gas Wedge: 168
Gaussian distribution: 211
Geochemical mud logging (GML): 141
Geochemistry: 78
Geophysical:
  measurements: 2
  tools, surface and borehole: 2
Geothermal:
  Energy Systems: 1
  reservoir, vapor-dominated: 73
  93, 125
  reservoirs, assessment of: 1,
  reservoir, liquid dominated: 80,
  125, 191,
Geysers, Sonoma County, CA: 73,
  93,
  geologic setting: 74
Graben: 25
Gravity:
  fields, surface: 35
  measurement, precision: 35
Green's function: 261
Heat:
  exchangers: 2
  extraction: 114
  sweep: 219
  transport, convective: 105, 173
Heat Capacity: 20
Heat-pipe mechanism: 93, 125, 165
Henry's Law: 152, 166
Heterogeneities: 133
Heuristic knowledge: 291
Horner slope: 56
Illite Geothermometer: 145
Impermeable barrier: 305
Infinite-acting radial flow: 53
Influence function: 183
Integral equation: 261
Interference testing: 49
Internal flow: 64
Interwell crossflow/interference: 41
Isosalinity curves: 134
Isotopes: 73, 85
Jemez Mountains, New Mexico: 3
Kirishima field, Japan: 47
Kizildere geothermal reservoir: 317
Lacustrine: 109
Laminar flow: 212
Laplace Transform: 114, 261
Larderello Geothermal field: 181
Line Source: 12
Linear model: 326
Logs:
  lithology: 11
  mud: 8
  neutron density: 8
Long Valley Caldera, California: 121
Los Azufres Geothermal field: 125, 323
Mass flow potential: 31
Mass spectrometry: 108
Matrix equation: 264
Mean square deviation: 323
Metamorphic processes: 107
Meteoric water: 65
Microseismic events: 228, 249
Modal volume: 247
Model:
  conceptual: 85, 251
  heat sweep: 113
  lumped parameter: 317
  natural state: 47, 86
  wellbore: 151
Monte Carlo technique: 211
Multiple interacting continua
  (MINC): 220
Multivariate correlation: 323
Natural-state model: 47, 86
Nesjavellir geothermal field
  Iceland: 83
Neumann Problem: 264
Newberry Crater: 2
Nicklin correlation: 160
Nigorikawa field, Japan: 151
Non-condensible gas: 59, 78, 165
Numerical:
  modeling: 36, 86
  simulation: 47, 87, 221
Nusselt number: 173
Orkiszewski correlation: 160
Palinpinon reservoir, Philippines: 63
Parallel plate law: 227
Particle tracking: 211
Peclet numbers: 249, 281
Petrogeothermal system: 114
Phase:
  behavior: 159
  composition: 269
  composition, mobile: 143

diagram: 160
Pipeline scaling: 69
Polynomial regression: 325
Potentiometric titration: 134
Pressure:
bubble point: 160
buildup analysis: 5, 53, 253
derivative type-curves: 53
drawdown: 5, 65
partial: 153
transient tests: 50
Pressure Temperature Spinner
tool (PTS): 41
(TPS): 76
Probability density function:
273, 301
Producing time effects: 57
Proximity function: 220
Pseudo steady state: 206
Quadratic model: 326
Radiation boundary condition: 266
Random walk model: 274
Rayleigh number: 103, 174
Recharge: 182
Redox-potential (Eh): 313
Reinjection: 63, 194
Reservoir:
connectivity: 253
fractured: 219
geopressure: 3
high temperature, (HTR): 73
hot dry rock: 113, 211, 231
impedance, intrinsic: 239
monitoring techniques: 1
Residence time: 114
distribution (RTD): 115
213, 245, 273
Retention-release: 248
Runge-Kutta method: 166
Salton Sea Geothermal System: 101, 107
Saturation pressure: 167
Scale:
deposition: 151
inhibiting chemical: 151
Seismic clouds: 231
Sericite: 145
Singularity: 262
Solute retardation: 211
Sonic velocity: 19
Sorption: 211
Spectrophotometry: 134
Standard deviation: 277
Steady state: 239
Steam soak: 219
Stochastic: 220
Superposition principle: 253,
Test: 68, 193, 245
backpressure: 241
buildup: 5, 53, 306
drawdown: 206, 306
interference: 206, 253
oscillation: 250
pressure transient: 50
tracer: 68, 193, 245
Thermal: 102
anomalies: 32, 232
boundary layer: 102
conductivity: 323
drawdown: 66, 113, 227
equilibrium: 166
fronts: 2
gradients: 2, 110
Thermal conductivity igneous
rocks, of: 323
Thermal needle transient
method: 324
Thermodynamic properties: 159
Three point method: 231
Time constant: 113
Tortuosity: 284
Tracer:
anomolous spikes: 142
flow model: 281
flow through fractures: 2
gas phase, research: 2
response: 113
return profiles: 2
tests, reactive: 249
tests, inert: 247
Two-phase flow: 2, 153, 159
VAPLIQ Hydrothermal Systems: 125
Vapor:
expansions, supersaturated: 2
pressure: 153, 194
Vaporization:
supercritical: 2
superheated steam: 93
Vaporstatic: 126

Vertical permeability: 125
Viscous fracturing operation: 246
Wairakei Geothermal field: 191
Water influx: 39
Wellbore:
  flow, adiabatic: 19
  flow, internal: 269
  interference: 239
  saturated steam: 41
Well-closure tests: 181
X-ray diffraction (XRD): 145

AUTHOR INDEX VOLUME 14

Abe, I. : 47
Adams, M.C. : 107
Ambastha, A.K. : 53
Amistoso, A.E. : 63
Arellano, J. : 291
Arellano, V.M. : 125, 291
Arpaci, M. : 205
Ascencio, F. : 305
Atkinson, P.G. : 35
Ballantyne, J.M. : 145
Birdsell, S.A. : 225
Bjornsson, S. : 83
Bodvarsson, G.S. : 83, 269
Brach, M. : 133, 309
Chrysikopoulos, C.V. : 299
Clemo, T.M. : 273
Combs, Jim : 73
Contreras, E. : 323
Cox, B.L. : 173
Criaud, A. : 133
Dadakarides, S.D. : 299
Detoc, S. : 309
Dominguez, A.B. : 323
Dreesen, D. : 231
Drenick, A.F. : 73
Enedy, K.L. : 41
Fehler, M. : 231
Fouassier, P. : 133
Fouillac, C. : 133, 309
Fournier, R.O. : 101
Garcia, A. : 323
Garg, S.K. : 253
Grant, M.A. : 191
Gudmundsson, J.S. : 19
Guidi, M. : 141
Gunnarsson, A. : 83
Gunnlaugsson, E. : 83
Haizlip, J.R. : 73, 93
Hochstein, M.P. : 25
Horne, R.N. : 261
Iglesias, E.R. : 125, 291
Ishido, T. : 47
James, R. : 59
Johnson, S.D. : 141
Jónsson, V.K. : 19
Kikani, J. : 261
Kitamura, H. : 47
Kruger, P. : 113
Kwakwa, K.A. : 245
Malzahn, M.V. : 231, 239
McKibbin, R. : 165, 173
Miller, J.D. : 273
Miller, R.J. : 5
Miyazaki, S. : 47
Mock, J.E. : 1
Molinar, R. : 305
Moore, J.N. : 107, 145
Murphy, H.D. : 239
Neri, G. : 181
Nishi, K. : 159
Nobumoto, R. : 47
Okandan, E. : 205, 317
Öngen, J. : 205
Pedersen, J.R. : 35
Pritchett, J.W. : 253
Pruess, K. : 165, 173, 219
Ramey, H.J.,Jnr. : 53
Ramirez, J. : 281
Ripperda, M. : 269
Rivera, J. : 281
Robinson, B.A. : 113, 211, 225
Rodriguez, F. : 281
Sarmiento, Z.F. : 63
Schwarzblat, M. : 291
Sigurdsson, O. : 83
Sorey, M.L. : 121
Stefansson, V. : 83
Steingrimsson, B. : 83
Sternfield, J.N. : 73
Sveinsson, S. : 19
Takahashi, M. : 151
Tanaka, S. : 159
Tonani, F.B. : 141
Truesdell, A.H. : 93
Vasquez, R. : 5
Vuataz, F.D. : 309
Walters, M.A. : 73
Wu, Y.S. : 219
Zhongke, Y. : 25